



PHYSICAL CHEMISTRY 2021

15th International Conference
on Fundamental and Applied Aspects of
Physical Chemistry

Proceedings
Volume I

The Conference is dedicated to the

*30th Anniversary of the founding of the Society of Physical
Chemists of Serbia*

and

100th Anniversary of Bray-Liebhafsky reaction

**September 20-24, 2021
Belgrade, Serbia**

Title: Physical Chemistry 2021 (Proceedings) **ISBN** 978-86-82475-40-8

Volume I: ISBN 978-86-82475-38-5

Editors: Željko Čupić and Slobodan Anić

Published by: Society of Physical Chemists of Serbia, Studentski Trg 12-16, 11158, Belgrade, Serbia

Publisher: Society of Physical Chemists of Serbia

For Publisher: S. Anić, President of Society of Physical Chemists of Serbia

Printed by: "Jovan", <Printing and Publishing Company, 200 Copies

Number of pages: 6+344, Format A4, printing finished in December 2021

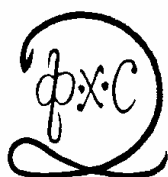
Text and Layout: "Jovan"

Neither this book nor any part may be reproduced or transmitted in any form or by any means, including photocopying, or by any information storage and retrieval system, without permission in writing from the publisher.

200 - *Copy printing*

CONTENT

<i>Volume I</i>	
<i>Organizer</i>	IV
<i>Comittes</i>	V
<i>Plenary Lecture</i>	1
<i>Chemical Thermodynamics</i>	41
<i>Spectroscopy, Molecular Structure, Physical Chemistry of Plasma</i>	55
<i>Kinetics, Catalysis</i>	107
<i>Nonlinear Dynamics, Oscillatory Reactions, Chaos</i>	197
<i>Electrochemistry</i>	273
<i>Biophysical Chemistry, EPR investigations of Bio-systems</i>	305



PHYSICAL CHEMISTRY 2021

*15th International Conference on
Fundamental and Applied Aspects of
Physical Chemistry*

Organized by

*The Society of Physical Chemists of
Serbia*

in co-operation with

Institute of Catalysis Bulgarian Academy of Sciences

and

*Borekov Institute of Catalysis Siberian Branch of
Russian Academy of Sciences*

and

University of Belgrade, Serbia:

*Faculty of Physical Chemistry
Institute of Chemistry, Technology and Metallurgy
Vinča Institute of Nuclear Sciences
Faculty of Pharmacy*

and

Institute of General and Physical Chemistry, Belgrade, Serbia

International Organizing Committee

Chairman: S. Anić (Serbia)
Vice-chairman: M. Gabrovska (Bulgaria)
A. A. Vedyagin (Russia)
S. N. Blagojević (Serbia)

Members: N. Cvjetičanin (Serbia), S. M. Blagojević (Serbia), M. Daković (Serbia), J. Dimitrić Marković (Serbia), T. Grozdić (Serbia), Lj. Ignjatović (Serbia), D. Jovanović (Serbia), M. Kuzmanović (Serbia), D. Marković (Serbia), B. Milosavljević (USA), M. Mojović (Serbia), N. Pejić (Serbia), M. Petković (Serbia), A. Popović-Bjelić (Serbia), B. Simonović (Serbia), M. Stanković (Serbia), B. Šljukić (Serbia), G. Tasić (Serbia), S. Veličković (Serbia), N. Vukelić (Serbia)

International Scientific Committee

Chairman: Ž. Čupić (Serbia)
Vice-chairman: V. Bukhtiyarov (Russia)
S. Todorova (Bulgaria)
B. Adnađević (Serbia)

Members: S. Anić (Serbia), A. Antić-Jovanović (Serbia), A. Azizoglu (Turkey), R. Cervellati (Italy), G. Ćirić-Marjanović (Serbia), V. Dondur (Serbia), I. I. Grinvald (Russia), R. Jerala (Slovenia), M. Jeremić (Serbia), G. N. Kaluderović (Germany), E. Kiš (Serbia), A. V. Knyazev (Russia), Lj. Kolar-Anić (Serbia), U. Kortz (Germany), T. Kowalska (Poljska), A. Lemarchand (France), G. Lente (Hungary), Z. Marković (Serbia), S. Mentus (Serbia), K. Novaković (UK), N. Ostrovski (Serbia), V. Parmon (Russia), Z. Petkova Cherkezova-Zheleva (Bulgaria), M. Plavšić (Serbia), J. Savović (Serbia), G. Schmitz (Belgium), I. Schreiber (Czech), L. Schreiberova (Czech), D. Stanisavljev (Serbia), N. Stepanov (Russia), M. Stojanović (USA), E. Szabó (Slovakia), Zs. Szakacs (Romania), Z. Šaponjić (Serbia), Á. Tóth (Hungary), M. Trtica (Serbia), V. Vasić (Serbia), D. Veselinović (Serbia), V. Vukojević (Sweden)

Local Executive Committee

Chairman: S. N. Blagojević
Vice-chairman: A. Ivanović-Šašić
N. Jović-Jovičić
A. Stanojević

Members: M. Ajduković, I. N. Bubanja, A. Dobrota, J. Dostanić, D. Dimić, S. Jovanović, Z. Jovanović, D. Lončarević, M. Kragović, J. Krstić, B. Marković, S. Maćešić, J. Maksimović, S. Marinović, D. Milenković, T. Mudrinić, M. Pagnacco, N. Potkonjak, B. Stanković, I. Stefanović, G. Stevanović, A. Stoilković, M. Vasić

SPONSORS

Ministry of Education, Science and Technological Development of the
Republic Serbia

Institute of General and Physical Chemistry, Belgrade
Belgrade Analysis d.o.o.

PL- Plenary lecture

DISSIPATIVE STRUCTURES AND BIOLOGICAL RHYTHMS

A. Goldbeter

Unité de Chronobiologie théorique, Service de Chimie physique et Biologie théorique,
Faculté des Sciences, Université Libre de Bruxelles (ULB), Brussels, Belgium

ABSTRACT

Sustained oscillations abound in biological systems. They occur at all levels of biological organization over a wide range of periods, from a fraction of a second to years, and with a variety of underlying mechanisms. They control major physiological functions, and their dysfunction is associated with a variety of physiological disorders. The goal of this presentation is (i) to give an overview of the main rhythms observed at the cellular and supracellular levels, (ii) to briefly describe how the study of biological rhythms unfolded in the course of time, in parallel with studies on chemical oscillations, (iii) to present the major roles of biological rhythms in the control of physiological functions, and (iv) the pathologies associated with the alteration, disappearance, or spurious occurrence of biological rhythms. Among the rhythms discussed are neural and cardiac rhythms, metabolic oscillations such as those occurring in glycolysis in yeast, intracellular Ca^{++} oscillations, cyclic AMP oscillations in *Dictyostelium* amoebae, the segmentation clock that controls somitogenesis, pulsatile hormone secretion, circadian rhythms which occur in all eukaryotes and some bacteria with a period close to 24h, the oscillatory dynamics of the enzymatic network driving the cell cycle, and oscillations in transcription factors such as NF-KB and tumor suppressors such as p53. The concept of dissipative structures applies to temporal oscillations and allows us to unify within a common framework the various rhythms observed at different levels of biological organization, regardless of their period and underlying mechanism.

REFERENCES

- [1] Goldbeter, A. (2017) Dissipative structures and biological rhythms. *Chaos* **27**, 104612. doi: 10.1063/1.4990783
- [2] Goldbeter, A. (2018) Dissipative structures in biological systems: bistability, oscillations, spatial patterns and waves. *Phil. Trans. R. Soc. A* **376**:20170376. (<http://dx.doi.org/10.1098/rsta.2017.0376>).

SYNCHRONISATION OF GLYCOLYTIC ACTIVITY IN YEAST CELL POPULATIONS

M.J. B. Hauser

*Otto-von-Guericke-Universität Magdeburg,
Institute of Biology, Department of Regulation Biology,
Pfälzer Straße 5, 39106 Magdeburg, Germany.
marcus.hauser@ovgu.de*

ABSTRACT

Glycolysis is the central metabolic pathway of almost every cell and organism. We report on glycolytic oscillations of intact yeast cells at the level of the cell population as well as at the level of individual cells. Synchronisation depends on the cell density of a population, because the collective oscillatory behaviour of a yeast cell population ceases when the cell density of the population falls below a threshold. At high cell densities, the dynamics is oscillatory, but below a critical density the collective dynamics becomes quiescent. Whereas cells in stirred cell suspension ceased to oscillate, immobilized cells were found to show glycolytic oscillations, even at very low cell densities. This means, the transition between oscillatory and stationary dynamics in immobilized or suspended cells follows different phase types of transitions.

The pathway to synchrony of originally quiescent, immobilized cells was achieved by a the synchronisation of the frequencies of the cellular oscillations, which was followed by a synchronisation of their phases. The pathway leading to synchronisation involved a narrowing of the frequency distribution in conjunction with a shift in the mean frequency of the glycolytic oscillations to larger values. The population was entrained by those cells that oscillated at higher frequencies; this is typical for synchronisation due to phase advancement.

Two spatial aspects of self-organization observed in extended populations of immobilized yeast cells were addressed: (1) the emergence of regional clusters and (2) the emergence of travelling waves of glycolytic activity. Although the cells were either completely or partially synchronised, travelling glycolytic waves arise due to a phase difference in space. These waves propagated though the field of view; however, the intracellular dynamics of each cell is homogeneous in space, due to the small diameter of the cell.

INTRODUCTION

Glycolysis, i.e., the enzymatic conversion of glucose to pyruvate and ATP, is the central metabolic pathway of almost every cell and organism. Under suitable conditions, glycolytic oscillations may occur in cells as well as in entire cell populations. Oscillations at the population level require the cells to synchronize their metabolism. In fact, yeast cells may achieve complete synchronisation, where the metabolism of all cells join a common rhythm.

We have studied glycolytic oscillations of intact yeast cells at the level of the cell population as well as at the level of individual cells. Synchronisation is a quorum-sensing phenomenon because the collective oscillatory behaviour of a yeast cell population ceases when the cell density of the population falls below a threshold. At high cell densities, the dynamics is oscillatory, but below a critical density the collective dynamics becomes quiescent. We address the question, under which conditions individual cells in such sparse populations continue or cease to oscillate. Whereas cells in stirred cell suspension ceased to oscillate [1], immobilized cells were found to show glycolytic oscillations, even at very low cell densities [2,3]. This means, the transition between oscillatory and stationary dynamics in immobilized or suspended cells follows different pathways, namely an

amplitude death phenomenon in stirred cell suspensions [1] and a so-called Kuramoto transition [2,3,4], respectively. In sparse populations of immobilized cells, the transition in the collective dynamics is caused by the loss of coherence (or desynchronisation) of the oscillations of individual cells.

RESULTS AND DISCUSSION

To identify the pathway how the transition between synchronous and asynchronous behaviour of intact, immobilized yeast cells occurs, we have studied populations of intermediate cell densities [3]. Here, a partially synchronized as well as an asynchronous state were accessible for experimental studies. In the partially synchronized state (Fig. 1), the degree of synchronisation increased substantially, whereas the distributions of the frequencies and phases of the oscillations in the cells narrowed. In fact, the synchronisation of the frequency of the glycolytic oscillations preceded the synchronisation of their phases. The pathway leading to synchronisation involved a shift in the mean frequency of the glycolytic oscillations in the cells: the mean oscillatory frequency was larger than that of the cells in the asynchronous state, suggesting that the cells were entrained by those cells that oscillated more rapidly (at a higher frequency). This is typical for synchronisation due to phase advancement (Fig. 2). However, the cells did not synchronize completely, as the distribution of the oscillatory frequencies only narrowed but failed to collapse on a unique frequency.

When investigating immobilized cell populations of intermediate cell densities, the spatial organization of the dynamics within the population must also be considered. Cells may form regional clusters where they are more densely packed than on average. These clusters may affect the dynamics at the population level because, here, cells may be better synchronized. During partial synchronisation, spatial domains of slightly higher cell density were indeed observed, however, in such clusters a number of cells oscillating at substantially different phases than the bulk of the population were found to be dispersed within the cluster [3,5,6]. Thus, at low and intermediate cell densities, clustering may slightly enhance the degree of synchronisation, but it did not lead to the formation of domains where the cells oscillate homogeneously at distinctively different phases than in other sites of the population.

Another aspect of spatial self-organization observed in populations of immobilized yeast cells is the emergence of travelling waves of glycolytic activity [3,5,6,7] in populations of high and intermediate cell densities. Although the cells were either completely or partially synchronised, travelling glycolytic waves arise due to a phase difference in space (i.e., in the cell population). The waves propagated through the field of view; however, the intracellular dynamics of each cell is homogeneous in space, due to the small diameter of the cell (of 8 – 10 μ m).

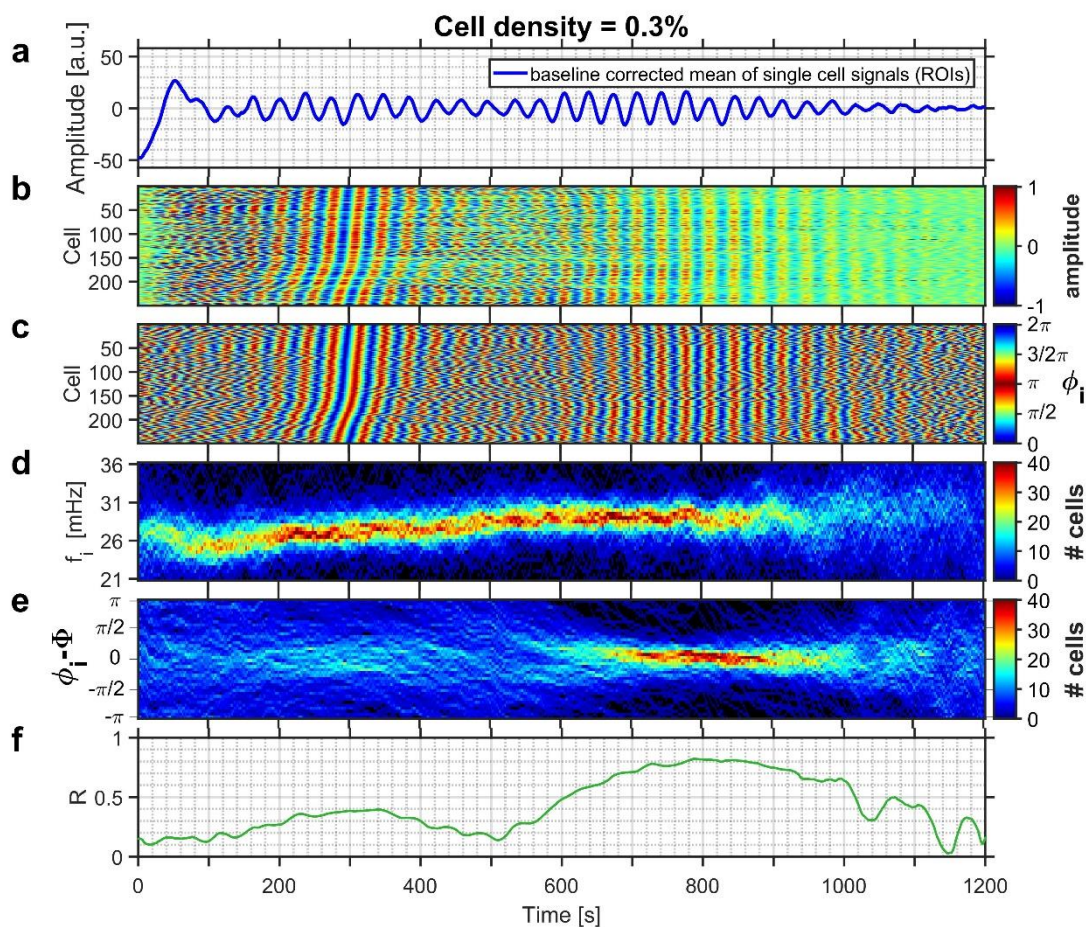


Figure 1. Partial synchronisation in a yeast cell population of intermediate cell density. (a) Time-series of the collective NADH fluorescence signal of immobilized yeast. Partial synchronisation was achieved from 580 s to 1080 s. (b) Relative amplitudes of oscillations and (c) phases of each cell. Time-dependent distributions of (d) the instantaneous frequencies f_i of the cells and (e) of the distribution of the phase difference between the phase ϕ_i of each cell and the average phase Φ of all cells of the population. (f) Time dependence of the order parameter R , i.e., the degree of synchronisation. Figure taken from ref. [3].

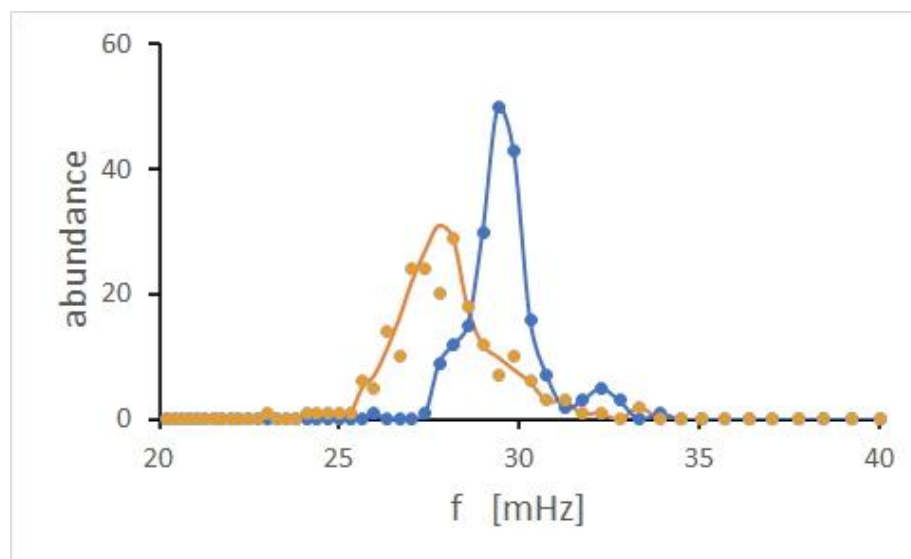


Figure 2. Distribution of oscillation frequencies of individual cells in a population of intermediate cell density. During asynchronous collective behaviour, the cells showed a fairly broad frequency distribution (in orange), whereas during partial synchronisation, the frequency distribution of periods narrowed and was shifted to higher frequencies (in blue). Figure taken from [5].

REFERENCES

- [1] S. De Monte, F. d'Ovidio, S. Danø, P. G. Sørensen: Dynamical quorum sensing: Population density encoded in cellular dynamics. *Proc. Natl. Acad. Sci. USA* **104**, 18377-18381 (2007). <https://doi.org/10.1073/pnas.0706089104>
- [2] A. Weber, W. Zuschratter, M. J. B. Hauser: Desynchronisation of glycolytic oscillations in yeast cell populations. *PLoS One* **7**, e43276 (2012). <https://doi.org/10.1371/journal.pone.0043276>
- [3] A. Weber, W. Zuschratter, M. J. B. Hauser: Partial synchronisation of glycolytic oscillations in yeast cell populations. *Sci. Rep.* **10** 19714 (2020). <https://doi.org/10.1038/s41598-020-76242-8>
- [4] A.-K. Gustavsson, D. D. van Niekerk, C. B. Adiels, F. B. du Preez, M. Goksör, J. L. Snoep: Sustained glycolytic oscillations in individual isolated yeast cells. *FEBS J.* **279**, 2837-2847 (2012). <https://doi.org/10.1111/j.1752-4658.2012.08639.x>
- [5] M. J. B. Hauser: Synchronisation of glycolytic activity in yeast cells. A min-review. *Curr. Genetics*, under consideration.
- [6] M. Mojica-Benavides, D. D. van Niekerk, M. Mialkov, J. L. Snoep, B. Mehlig, G. Volpe, M. Goksör, C. B. Adiels: Intracellular communication introduces glycolytic synchronization waves between individually oscillating cells. *Proc. Natl. Acad. Sci.* **118**, e2010075118 (2021). <https://doi.org/10.1073/pnas.2010075118>
- [7] J. Schütze, T. Mair, M. J. B. Hauser, M. Falcke, J. Wolf: Metabolic synchronization by travelling waves in yeast cell layers. *Biophys. J.* **100**, 809-813 (2012). <https://doi.org/10.1016/j.bpj.2010.12.3704>

MAKING NON-BIOCHEMICAL ARTIFICIAL LIFE IN A TEST TUBE

J.Perez-Mercader^{1,2}

¹ *Department of Earth and Planetary Sciences and Origins of Life Initiative
Harvard University, Cambridge, MA 02138, United States (jperezmercader@fas.harvard.edu)*

² *Santa Fe Institute, 1399 Hyde Park Rd., Santa Fe, NM 87501, United States*

ABSTRACT

Living systems on Earth are broadly characterized as complex chemical systems capable of concomitantly (i) process information, (ii) metabolize (including making their own parts from simpler components), (iii) self-reproduce and (iv) evolve. These properties are traditionally associated with the presence in extant living systems of three common universal and interdependent features: the existence of a membrane boundary, metabolism and information-carrying molecules. For each of these there exists an origins-of-life school of thought positing that one of them preceded the others in the path from non-life to proto-life to life. However, their interconnectedness makes exploring any of the three in the absence of the rest extremely difficult.

Notwithstanding the above, we show that properties (i) through (iv) can be described by a small set of unifying equations whose solutions, remarkably, display the above properties. Inspired and guided by these solutions, we present progress in the area of life's origins and its chemical synthesis resulting from experiments on autonomous system boot-up during the chemically controlled non-equilibrium self-assembly of functional, non-biochemical and small molecule-based polymeric vesicles. We follow their dynamical evolution with membrane growth and metabolism working in concert under autonomous chemical control. All this is achieved by implementing a PISA (Polymerization Induced Self-Assembly) polymerization/encapsulation scenario in an aqueous medium, which solves the concentration problem and generates an all-important free-energy gradient which provides the necessary boot-up conditions for these fully artificial systems. By design, our 1-pot chemical system ("test tube") uses reversible addition-fragmentation-chain transfer (RAFT) polymerization and completely avoids bio-chemistry. We monitor the consequences of the on-going active amphiphilic block copolymer synthesis with their resulting molecular self-assembly and evolution using electron and optical microscopy. (We will present actual microscope movies of the resulting active vesicles and their population.) We find that this dissipative self-assembly process leads to vesicles with diameters between 0.5 and 10's of microns which exhibit several emergent, life-like, properties. These include periodic growth and partial collapse, system self-reproduction, together with homeostasis, competition and phototaxis at the population level. We will briefly discuss the extension of the above by executing the PISA process with oscillatory chemical reactions which are actually able to compute as chemical Turing machines and control the assembly sequence and time evolution of their self-generating, entrapping and self-replicating vesicles. Taken together these results offer insights into artificial life, as well as into the formation of small-molecule protocells as a route to the earliest living systems on the Earth as precursors to extant life and biochemistry.

REFERENCES

- [1] Anders N. Albertsen, Jan K. Szymański, and Juan Pérez-Mercader (2017). “Emergent Properties of Giant Vesicles Formed by a Polymerization-Induced Self-Assembly (PISA) Reaction”. *Scientific Reports* 7, 41534. doi:10.1038/srep41534
- [2] Bishnu Prasad Bastakoti and Juan Pérez-Mercader (2017). “Autonomous Ex Novo Chemical Assembly with Blebbing and Division of Functional Polymer Vesicles from a "Homogeneous Mixture"”. *Advanced Materials*. doi:10.1002/adma.201704368
- [3] Kaixuan Ren and Juan Pérez-Mercader (2018). “Light-induced Evolution of Microaggregates: Transformation to Vesicles, Cyclic Growth and Collapse and Vesicle Fusion”. *Polymer Chemistry*. doi:10.1039/C8PY00546J (cover of issue)
- [4] Gong Chen and Juan Pérez-Mercader (2018). “Polymerization-induced self-assembly for artificial biology: opportunities and challenges”. *Macromolecular Rapid Communications*. 40(2). doi:10.1002/marc/201800513. (backcover of issue)
- [5] Juan Pérez-Mercader (2020), De novo laboratory synthesis of life mimics without biochemistry, *ALIFE 2020: The 2020 Conference on Artificial Life*. 483-490. doi:10.1162/isal_a_00282
- [6] Chenyu Lin, Sai Katla. and J. Perez-Mercader (2021), “Photochemically induced cyclic morphological dynamics via degradation of autonomously produced, self-assembled polymer vesicles”, *Nature’s Communications Chemistry*. 4, 25. doi:10.1038/s42004-021-00464-8
- [7] Marta Dueñas-Diez and Juan Pérez-Mercader (2019). “How Chemistry Computes: Language Recognition by Non-Biochemical Chemical Automata. From Finite Automata to Turing Machines”. *iScience*, 19, 514-526. doi:10.1016/j.isci.2019.08.007.
- [8] Marta Dueñas-Diez and Juan Pérez-Mercader (2021), “Native Chemical Computation. A Generic Application of Oscillating Chemistry Illustrated with the Belousov-Zhabotinsky Reaction. A Review”, *Frontiers in Chemistry*. 9:611120. doi:10.3389/fchem.2021.611120
- [9] Besides visiting www.fas.harvard.edu/~topdownsynthbio for more information you can also look at *Advanced Science* October 2018, <https://www.advancedsciencenews.com/mimicking-living-systems-using-polymer-chemistry>.
- [10] Harvard Gazette, March 2017, “Mimicking life in a chemical soup”, <https://news.harvard.edu/gazette/story/2017/03/harvard-researcher-creates-chemical-system-that-mimics-early-cell-behavior/>
- [11] “Scientists Create Self-Replicating Chemicals [Chemical Systems] to Help Explain the Origins of Life” by M. Rorvig in VICE, March 2021 ,<https://www.vice.com/en/article/y3g7ev/scientists-create-self-replicating-chemicals-to-explain-the-origins-of-life>

DESIGN OF A PHOTOCROMIC OSCILLATOR TO BE USED AS DYNAMICAL MODEL OF PACEMAKER NEURONS

P. L. Gentili, L. Baldinelli, B. Bartolomei

Department of Chemistry, Biology, and Biotechnology of the Università degli Studi di Perugia (Italy). E-mail: pierluigi.gentili@unipg.it

ABSTRACT

Neuromorphic engineering implements surrogates of neurons to develop Artificial Intelligence. A strategy to devise artificial neuron models is to use non-linear chemical systems that can mimic neural dynamics. This work presents the design of a new photochemical oscillator to be used as a dynamical model of pacemaker neurons. Such photochemical oscillator is based on two photochromic compounds. The spectral and kinetic features required to have oscillations are presented rigorously using numerical integration of non-linear differential equations. The designed artificial pacemaker neuron can communicate with other chemical neuron models through the transmitted and/or emitted light.

INTRODUCTION

A strategy to develop Artificial Intelligence is neuromorphic engineering [1, 2]. Neuromorphic engineering implements surrogates of neurons through non-biological systems either for neuro-prosthesis [3] or to devise brain-like computing machines. Brain-like computing machines are designed to mimic some performances of human intelligence, such as learning, recognizing variable patterns, and computing with words. Brain-like computing machines will have an architecture different from that of our electronic computers, devised by Von Neumann, and having memory physically separated from the processor. It is expected that brain-like computers will have the advantage of requiring much less power and occupying much less space than our best electronic supercomputers. The elementary unit of any brain-like computing machine is the surrogate of the neuron or some of its constitutive parts, such as the synapses. In our brain, neurons are cells specialized in encoding, collecting, processing, and storing information. The synapses constitute the terminal part of a neuron, and they send signals to other neurons or cells. At the cellular level, information is encoded in the values of neurons' transmembrane potentials. Every neuron receiving signals responds by changing its transmembrane potential value. The kind of response depends on the dynamical feature of the neuron. Neurons are non-linear dynamic systems [4, 5] that can work in either oscillatory or chaotic or excitable regimes.

Different methods for engineering surrogates of neurons have been proposed so far. Most of these methods are based on the hardware implementation of neurons and their constitutive element. Such hardware is rigid if it is made of the conventional passive and active circuit elements, either analog [1, 6] or digital [7]. It is also rigid when it consists of two-terminal devices with multiple-valued internal states that can be tuned in either a non-volatile or quasi-stable manner, mimicking synaptic interconnections [8–10]. There is also the possibility of using phase-change devices wherein the actual membrane potential of the artificial neuron is stored in the form of the phase configuration of a chalcogenide-based material, which can undergo phase transition on a nanosecond timescale and at the nanometric level [11]. The hardware might be flexible if it is based on organic film working as artificial synapses [12]. An alternative approach implements neural models in wetware by using liquid solutions of specific non-linear chemical systems [13–17]. Finally, there is the possibility of using hybrid electrochemical systems as surrogates of neurons [18, 19].

In wetware, dynamical models of pacemaker neurons are often implemented by using well-known oscillatory chemical systems, such as the Belousov-Zhabotinsky, Orbán, and Briggs-Rauscher reactions [20]. These reactions can work indefinitely in time, just in open reactors if fresh reagents are constantly introduced, and the products are sucked out. One of our goals is to design photochemical oscillators based on photochromic compounds [21]. Photochromic compounds change structure and colour when they are upon irradiation (see Figure 1). The structural modification is reversible.

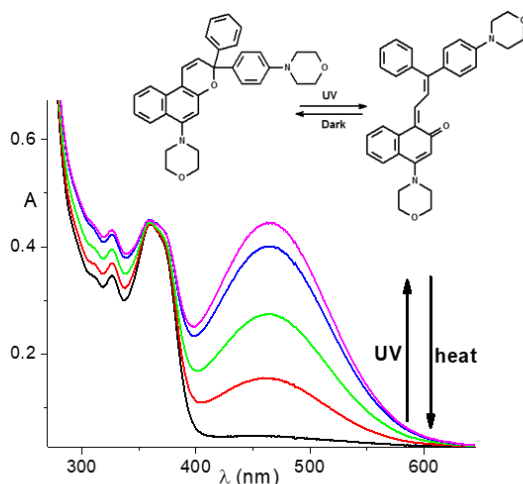


Figure 1. Spectral modification generated by UV irradiation of 6-morpholino-3-(4-morpholinophenyl)-3-phenyl-3H-naphtho[2,1-b]pyran.

Photochromic oscillators give rise to oscillations upon irradiations. When the light is off, the chemical system returns to the original equilibrium state, and it is not a surrogate of a neuron. It is ready to become the dynamical surrogate of a pacemaker neuron as soon as the light is turned on again. If this system is implemented, it will be a breakthrough with respect to the other models of pacemaker neurons in wetware [22].

In this work, we present the design and computational analysis of a new artificial neuron model based on a system of two thermally reversible photochromic compounds. One of them is peculiar because it shows an autocatalytic photo-activation through its intrinsic fluorescence. Together, they give rise to photochemical oscillations when they have specific spectral and kinetic properties.

METHODS

The systems of non-linear differential equations have been solved numerically by using the solver ode15s implemented in MatLab. The linear stability analyses of the steady-state solutions have been performed by MatLab.

RESULTS AND DISCUSSIONS

There is just one theoretical example of photochemical oscillations promoted by light in a batch reactor and isothermal conditions in the scientific literature. This case is based on two direct thermally reversible photochromic compounds presented in reference [21]. This work proposes another brand-new case, which involves two direct thermally reversible photochromic compounds, A and S, as shown in Figure 2a.

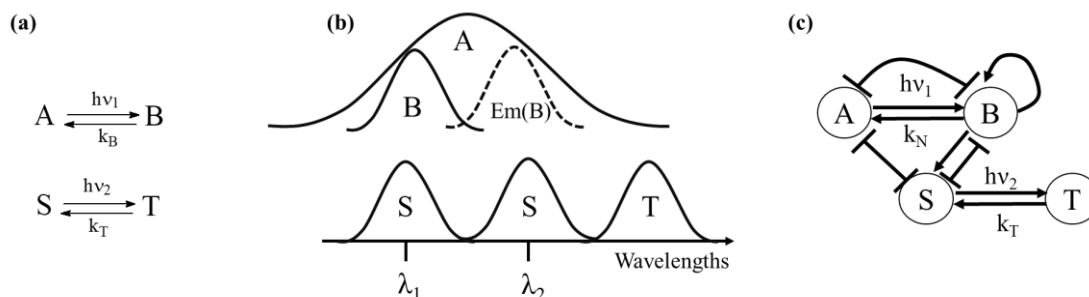


Figure 2. Principal reactions (a), spectral features (b), and reciprocal optical relationships (c) for the chemical system constituted by two thermally reversible photochromic compounds: A and S, which reversibly transform into B and T, respectively. In (c), the flattened arrowheads mean inhibitory actions whereas the traditional arrows represent activating actions.

The species A absorbs at both λ_1 and λ_2 , and it jumps to its excited state A^* (see steps 1 and 2 of Table 1). A^* can transform to B (step 3) that does not absorb appreciably at λ_2 . A^* can also relax spontaneously to A by internal conversion or other plausible processes, such as fluorescence (step 4). B absorbs at λ_1 and jumps to its excited state B^* (step 5). B^* relaxes to its ground state B by emitting light with λ_2 as wavelength (step 6) or through internal conversion (step 7). B self-activate its own production, because its emission at λ_2 is re-absorbed by A. B^* can also be quenched by A (step 8). Finally, B transforms back to A, thermally (step 9).

Table 1. Elementary steps relative to the direct thermally reversible photochromism of A producing B^* when irradiated at ν_1 . B^* emits at ν_2 that is re-absorbed by A.

Elementary steps	Molecular event	Description	Rate
1	$A + hv_1 \rightarrow A^*$	Absorption of hv_1 by A	$I_1(A)$
2	$A + hv_2 \rightarrow A^*$	Absorption of hv_2 by A	$I_2(A)$
3	$A^* \xrightarrow{k_{RA}} B$	Photo-reaction	$k_{RA}[A^*]$
4	$A^* \xrightarrow{k_{CI(A)}} A + \text{heat (+light)}$	Deactivation processes	$k_{CI(A)}[A^*]$
5	$B + hv_1 \rightarrow B^*$	Absorption of hv_1 by B	$I_1(B)$
6	$B^* \xrightarrow{k_F} B + hv_2$	Emission of hv_2 by B^*	$k_F[B^*]$
7	$B^* \xrightarrow{k_{CI(B)}} B + \text{heat}$	Internal Conversion for B^*	$k_{CI(B)}[B^*]$
8	$B^* + A \xrightarrow{k_{EX}} B + A$	Quenching of B^* by A	$k_{EX}[B^*][A]$
9	$B \xrightarrow{k_B} A$	Thermal bleaching	$k_T[B]$

The differential equation describing how the concentration of A changes over time, when it is irradiated at λ_1 is:

$$\frac{d[A]}{dt} = -I_1(A) - I_2(A) + k_{CI(A)}[A^*] + k_T[B] \quad (1)$$

In nondimensionalized form, equation (1) becomes:

$$\begin{aligned} \frac{dA}{d\tau} = & -\frac{i_1 A}{(A + EBA(1 - A))} (1 - e^{-E_1(A + EBA(1 - A))}) \\ & - \frac{\phi_F i_1 EBA(1 - A)}{(1 + \beta' A)(A + EBA(1 - A))} (1 - e^{-E_1(A + EBA(1 - A))}) (1 - e^{-E_1 EAA \times A}) \\ & + (1 - A) \end{aligned} \quad (2)$$

In (2), $i_1 = \frac{\phi_{RA} I_{0,1}}{k_T [A]_0}$, $\phi_F = \frac{k_F}{k_F + k_{CI(B)}}$, $\beta' = \frac{k_{EX}}{k_F + k_{CI(B)}} [A]_0$, $EAA = \frac{\epsilon''_A}{\epsilon'_A}$, $EBA = \frac{\epsilon'_B}{\epsilon'_A}$, $E_1 = \epsilon'_A d [A]_0$,

wherein ϕ_{RA} is the photochemical quantum yield of A, $I_{0,1}$ is the intensity at λ_1 , ϵ'_A and ϵ'_B are the absorption coefficients of A and B at λ_1 , ϵ''_A is that of A at λ_2 . $[A]_0$ is the analytical concentration of A, and d is the optical path length. Usually, photochromic compounds exhibit just one stable photo-stationary state. On the other hand, such a system can give rise to bi-stability. When the self-quenching process is faster than the sum of the emissive and internal conversion processes, i.e., when $k_{EX} > (k_F + k_{CI(B)})$, and $\beta > 1$, the rate of A's consumption has a maximum as shown by the black curve in Figure 3. For a proper value of i_1 , the thermal rate of A's production (see the red straight line of Figure 3) intersects the black curve in three points. The stabilities of the intersection points that appear in Figure 3 can be easily inferred by looking at the relative positions of the two pairs of curves. Among the three intersection points, the intermediate one represents an unstable solution, whereas the other two represent stable states. Therefore, A exhibits bi-stability.

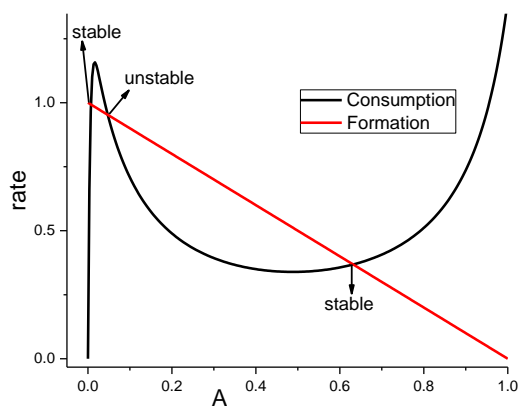


Figure 3. Rates of A's consumption (in black) and A's production (in red) obtained after fixing $i_1 = 1.4$, $EBA = 10$, $E_1 = 20$, $EAA = 10$, $\phi_F = 1$, $\beta' = 10$. There are three intersection points highlighted by the three arrows: the intermediate one represents an unstable photo-stationary state.

An empirical rule for devising oscillatory chemical reactions in open reactors affirms that any bistable system can be transformed in an oscillating one by adding a suitable inhibitory reaction [23]. In this case, the introduction of a second thermally reversible photochromic compound, $S=T$, which optically interferes with $A=B$, can originate an oscillatory system. The spectral properties of the photochrome $S=T$ are depicted in Figure 2b. The species S absorbs in the same regions of A and B.

Species T absorbs at longer wavelengths. If the chemical system, constituted by a mixture of A and S, is irradiated at both λ_1 and λ_2 , the elementary steps that can occur are not only those reported in Table 1, but also those listed in Table 2. When S absorbs one photon with λ_1 as wavelength is excited to the S^{**} state (step 10), whereas when it absorbs a photon with λ_2 as wavelength is excited to the S^* state (step 11). S^{**} relaxes directly to the ground state S by dissipating the absorbed energy (step 12). It also relaxes to S^* (step 13). On the other hand, S^* can either transform to T (step 14) or relaxes to the ground state S (step 15). The species T can transform back to S, thermally (step 16).

Table 2. Supplementary elementary steps for the chemical system constituted by A=B and S=T irradiated at both λ_1 and λ_2 (see Figure 1).

Elementary steps	Molecular event	Description	Rate
10	$S + hv_1 \rightarrow S^{**}$	Absorption of hv_1 by S	$I_1(S)$
11	$S + hv_2 \rightarrow S^*$	Absorption of hv_2 by S	$I_2(S)$
12	$S^{**} \xrightarrow{k_{CI2}} S + heat$	Deactivation processes	$k_{CI2}[S^{**}]$
13	$S^{**} \xrightarrow{k_{CI3}} S^* + heat$	Deactivation processes	$k_{CI3}[S^{**}]$
14	$S^* \xrightarrow{k_{RS}} T$	Coloration reaction	$k_{RS}[S^*]$
15	$S^* \xrightarrow{k_{CI1}} S + heat(+light)$	Deactivation processes	$k_{CI1}[S^*]$
16	$T \xrightarrow{k_T} S$	Thermal bleaching	$k_T[T]$

The ordinary differential equation describing how [S] changes over time is:

$$\frac{d[S]}{dt} = -I_2(S) - I_1(S) + k_T[T] + k_{CI2}[S^{**}] + k_{CI1}[S^*] \quad (3)$$

The introduction of the photochromic S=T does not affect the chemical behavior of A=B. The only form of interaction between the two photochromes is through mutual inner filter effect (see Figure 2c). In nondimensionalized form, the differential equations describing how [A] and [S] change over time are:

$$\begin{aligned} \frac{dA}{d\tau} = & -\frac{\Phi_{RA}A}{(A + EBA(1-A) + ESA_1S)} (1 - e^{-E_1(A+EBA(1-A)+ESA_1S)}) \\ & - \frac{\Phi_{RA}i_1EAA_2A}{(EAA_2A + ESA_2S)} (1 \\ & - e^{-E_1(EAA_2A+ESA_2S)}) \left(\left(\frac{\Phi_F}{1 + \beta'A} \right) \frac{EBA(1-A)}{(A + EBA(1-A) + ESA_1S)} i_1 (1 \right. \\ & \left. - e^{-E_1(A+EBA(1-A)+ESA_1S)}) + i_2 \right) + (1 - A) \end{aligned} \quad (4)$$

$$\begin{aligned} \frac{dS}{d\tau} = & -\frac{\phi_{RS}ESA_2S}{(EAA_2A + ESA_2S)} \left(1 \right. \\ & - e^{-E_1(EAA_2A + ESA_2S)} \left(\left(\frac{\phi_F}{1 + \beta'A} \right) \frac{EBA(1-A)}{(A + EBA(1-A) + ESA_1S)} i_1 \left(1 \right. \right. \\ & \left. \left. - e^{-E_1(A + EBA(1-A) + ESA_1S)} \right) + i_2 \right) \\ & - \frac{ki_1ESA_1S}{(A + EBA(1-A) + ESA_1S)} \left(1 - e^{-E_1(A + EBA(1-A) + ESA_1S)} \right) \\ & \left. + \rho(SA - S) \right) \end{aligned} \quad (5)$$

In equations (4) and (5), $i_1 = \frac{I_{0,1}}{k_B[A]_0}$, $i_2 = \frac{I_{0,2}}{k_B[A]_0}$, $\beta' = \left(\frac{k_{EX}}{k_F + k_{CI(B)}} \right) [A]_0$, $k = \frac{k_{CI3}k_{RS}}{(k_{CI2} + k_{CI3})(k_{RS} + k_{CI1})}$, $SA = \frac{[S]_0}{[A]_0}$, $\rho = \frac{k_T}{k_B}$, $E_1 = \epsilon'_{A1}d[A]_0$, $EBA = \frac{\epsilon'_B}{\epsilon'_{A1}}$, $ESA_1 = \frac{\epsilon'_{S1}}{\epsilon'_{A1}}$, $ESA_2 = \frac{\epsilon'_{S2}}{\epsilon'_{A1}}$, $EAA_2 = \frac{\epsilon'_{A2}}{\epsilon'_{A1}}$, ϕ_{RA} and ϕ_{RS} are the photochemical quantum yields. Such system can give rise to photochemical oscillations. Figure 4 reports two cases.

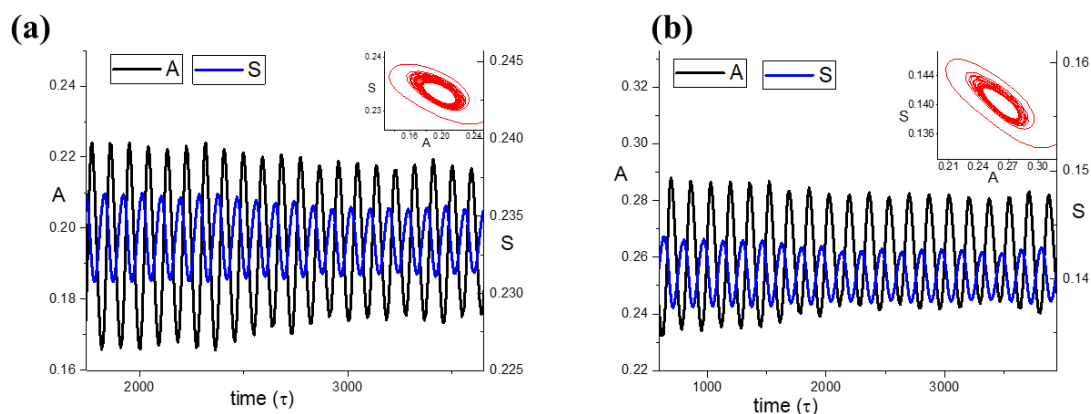


Figure 4. Trends of the relative concentrations A (black traces) and S (blue traces) vs. the relative time τ when $i_1 = 1.755$, $i_2 = 0.1$, $\phi_{RA} = 0.9$, $\phi_{RS} = 0.05$, $\phi_F = 0.9$, $E_1 = 10$, $\beta' = 2.3$, $k = 0.025$, $\rho = 0.02$, $SA = 1$, $EBA = 8$, $ESA_1 = 15$, $ESA_2 = 0.01$, $EAA_2 = 3$ in (a), and $i_1 = 2.75$, $i_2 = 0$, $\phi_{RA} = 0.9$, $\phi_{RS} = 0.05$, $\phi_F = 0.9$, $E_1 = 10$, $\beta' = 6.25$, $k = 0.025$, $\rho = 0.0088$, $SA = 1$, $EBA = 15$, $ESA_1 = 10$, $ESA_2 = 0.001$, $EAA_2 = 1.05$ in (b). The initial conditions in both simulations are $[A; S] = [1; 1]$. The insets report the phase space of the photochemical oscillator.

When ϕ_{RA} is larger than ϕ_{RS} and the thermal recovery of A from B is much faster than that of S from T (i.e., $\rho \ll 1$), then A and S oscillate. Their oscillations are always out-of-phase. The periods are $\approx 100\tau$ in (a) and $\approx 170\tau$ in (b). In a nutshell, it is the mutual optical feedback action between two photochromes, one autocatalytic (i.e., $A=B$) and the other rather slow in both photochemical and thermal reactions (i.e., $S=T$), that originates another photochemical oscillator.

CONCLUSIONS

This work shows that photochromic compounds can be used to mimic dynamics of not only phasic [15, 24, 25], and chaotic neurons [26], but also pacemaker neurons. The photochemical oscillator described in this work is based on two photochromic compounds having specific spectral and kinetic

properties. Such photochemical oscillator is an alternative to the traditional pacemaker neuron models, which are oscillatory reactions, such as the Belousov-Zhabotinsky (BZ) one [27, 28]. The BZ reaction is powered by chemical affinity, whereas the photochemical oscillator proposed herein is powered by light. Since it is based on two thermally reversible photochromic compounds, it can oscillate indefinitely in time and in a closed reactor as long as the irradiation source is on. On the other hand, the BZ reaction can oscillate indefinitely in time only if it is carried out in an open reactor by constantly feeding reagents. The next challenge is the implementation of photochemical oscillators such as those described in this contribution and a previous paper [21].

REFERENCES

- [1] C. Mead; "Neuromorphic Electronic Systems." Proc. IEEE 1990, 78, 1629-1636.
- [2] I. K. Schuller, R. Stevens; "Neuromorphic Computing: From Materials to Systems Architecture – Report of a Roundtable Convened to Consider Neuromorphic Computing Basic Research Needs." 2015, US Department of Energy.
- [3] J. P. Donoghue; "Bridging the brain to the world: a perspective on neural interface systems neuron." vol. 60. 2008. p. 511–521.
- [4] M. Izhikevich; "Dynamical systems in neuroscience." 2007, MIT Press, Cambridge, MA.
- [5] M. I. Rabinovich, P. Varona, A. I. Selverston; "Dynamical principles in neuroscience." Rev. Mod. Phys. 2006, 78, 1213-1265.
- [6] R. F. Service; "The brain chip." Science 2014; 345: 614–616.
- [7] P. A. Merolla, J. V. Arthur, R. Alvarez-Icaza, A. S. Cassidy, J. Sawada, F. Akopyan, B. L. Jackson, N. Imam, C. Guo, Y. Nakamura, B. Brezzo, I. Vo, S. K. Esser, R. Appuswamy, B. Taba, A. Amir, M. D. Flickner, W. P. Risk, R. Manohar, D. S. Modha. "A million spiking-neuron integrated circuit with a scalable communication network and interface." Science 2014; 345: 668–673.
- [8] S. D. Ha, S. Ramanathan; "Adaptive oxide electronics: a review." J Appl Phys. 2011; 110: 071101.
- [9] M. Di Ventra, Y. V. Pershin; "The parallel approach." Nat Phys 2013; 9: 200–202.
- [10] K. Pilarczyk, A. Podborska, M. Lis, M. Kawa, D. Migdal, K. Szacilowski; "Synaptic behavior in an optoelectronic device based on semiconductor-nanotube hybrid." Adv. Electron. Mater. 2016: 1500471.
- [11] T. Tuma, A. Pantazi, M. Le Gallo, A. Sebastian, E. Eleftheriou; "Stochastic phase-change neurons." Nat Nanotechnol 2016; 11: 693–699.
- [12] Y. Lee, T.-W. Lee; "Organic Synapses for Neuromorphic Electronics: From Brain-Inspired Computing to Sensorimotor Nervetronics." Acc. Chem. Res. 2019, 52, 964-974.
- [13] A. Adamatzky, B. De Lacy Costello, T. Asai; "Reaction–diffusion computers." Elsevier, 2005, New York (NY, USA).
- [14] P. L. Gentili; "Small steps towards the development of chemical artificial intelligent systems." RSC Adv. 2013, 3, 25523-25549.
- [15] P. L. Gentili, M. S. Giubila, R. Germani, A. Romani, A. Nicoziani, A. Spalletti, B. M. Heron; "Optical Communication among Oscillatory Reactions and Photo-Excitable Systems: UV and Visible Radiation Can Synchronize Artificial Neuron Models." Angew. Chem. Int. Ed. 2017, 56, 7535-7540.
- [16] V. Vanag; "Hierarchical network of pulse coupled chemical oscillators with adaptive behavior: Chemical neurocomputer." Chaos 2019, 29, 083104.
- [17] T. Litschel, M. M. Norton, V. Tserunyan, S. Fraden; "Engineering reaction–diffusion networks with properties of neural tissue." Lab on a Chip 2018, 18, 714-722.
- [18] H. Okamoto, N. Tanaka, M. Naito; "Analogy between the stimulus-response characteristics of neuronal and electrochemical cells." Chem. Phys. Lett. 1995, 237, 432-436.

- [19] Y. Liu, M. Sebek, F. Mori, I. Z. Kiss, "Synchronization of three electrochemical oscillators: From local to global coupling." *Chaos*, 2018, 28, 045104.
- [20] P. L. Gentili; "Untangling Complex Systems: A Grand Challenge for Science." CRC Press, Taylor & Francis Group, 2008, Boca Raton (FL, USA).
- [21] P. L. Gentili, B. Bartolomei, J.-C. Micheau; "Light-driven artificial neuron models based on photoswitchable systems." *Dyes and Pigments*, 2021; 187: 109086.
- [22] P. L. Gentili, J. C. Micheau; "Light and Chemical Oscillations: review and perspectives" *J. Photochem. Photobiol. C* 2020, 43, 100321.
- [23] J. Biossonade, P. De Kepper; "Transitions from bistability to limit cycle oscillations. Theoretical analysis and experimental evidence in an open chemical system" *J. Phys. Chem. A* 1980, 84, 501-506.
- [24] Pier Luigi Gentili, Amanda L. Rightler, B. Mark Heron, Christopher D. Gabbutt; "Extending human perception of electromagnetic radiation to the UV region through biologically inspired photochromic fuzzy logic (BIPFUL) systems." *Chem. Commun.* 2016, 52, 1474-1477.
- [25] Pier Luigi Gentili, Maria Sole Giubila, Raimondo Germani, B. Mark Heron; "Photochromic and luminescent compounds as artificial neuron models." *Dyes and Pigments* 2018, 156, 149-159.
- [26] Pier Luigi Gentili, Milos Dolnik, Irving R. Epstein; "Photochemical Oscillator": Colored Hydrodynamic Oscillations and Waves in a Photochromic System." *J. Phys. Chem. C*, 2014, 118, 598-608.
- [27] P. L. Gentili, V. Horvath, V. K. Vanag, I. R. Epstein; "Belousov-Zhabotinsky "chemical neuron" as a binary and fuzzy logic processor." *Int. Journ. of Unconventional Computing* 2012, 8, 177-192.
- [28] V. Horvath, P. L. Gentili, V. K. Vanag, I. R. Epstein; "Pulse-Coupled Chemical Oscillators with Time Delay." *Angew. Chem. Int. Ed.* 2012, 51, 6878-6881.

NUCLEOPEPTIDE NETWORKS OUT-OF-EQUILIBRIUM

G. Ashkenasy¹, A.K. Bandela¹, H. Sadihov¹, N. Wagner¹ and A. de la Escosura²

¹*Department of Chemistry, Ben-Gurion University of the Negev, 84105 Beer-Sheva, Israel*

²*Department of Organic Chemistry, Universidad Autónoma de Madrid, Campus de Cantoblanco, 28049 Madrid, Spain.*

ABSTRACT

Many fundamental cellular functions, including replication and translation, involve synergistic activity between nucleic acids and proteins/peptides. Yet, studies with synthetic replicators have focused largely on the activity of each class of these molecules separately. We show here that short nucleopeptide chimeras can replicate through autocatalytic and cross-catalytic processes, governed synergistically by nucleobase hybridization and the assembly of peptide segments. Remarkably, within small networks of complementary nucleopeptides, unequal replication kinetics induces clear selectivity toward the formation of a certain species. The selectivity may be maximized to almost extinction of the weakest replicator when the system operates far from equilibrium and manipulated through changes in the physical and chemical conditions.[1] We will discuss how similar processes may have led to the emergence of the first functional nucleic-acid-peptide assemblies prior to the origin of life.

REFERENCES

- [1] A.K. Bandela, N. Wagner, H. Sadihov, S. Morales-Reina, A. Chotera-Ouda, K. Basu, R. Cohen-Luria, A. de la Escosura, G. Ashkenasy. "Primitive selection of the fittest emerging through functional synergy in nucleopeptide networks" *Proceeding of the National Academy of Sciences USA*, **2021**, 118, 9 e2015285118.

COMPETITIVE ADSORPTION AND SELECTIVITY ASPECTS OF CARBON DIOXIDE, WATER VAPOUR, NITROGEN, AND SULFUR DIOXIDE ON ACTIVATED CARBON FOR CAPTURE FROM FLUE GASES

M. Thomas

Wolfson Northern Carbon Reduction Laboratories, School of Engineering, Newcastle University, Newcastle upon Tyne, United Kingdom, mark.thomas@newcastle.ac.uk

ABSTRACT

There is extensive interest in post combustion flue gas treatment for mitigating CO₂ emissions and removal of acid gases. Adsorption on porous materials is a potential low energy method for capturing CO₂. In recent years, many novel porous materials have been synthesized. However, the knowledge of selectivity and competitive adsorption of complex mixtures on porous materials remains superficial. In this study we investigate the adsorption of the main flue gas components (CO₂, N₂, SO₂, and water vapour) on Filtrasorb 400 activated carbon in order to understand adsorption characteristics of the main flue gas components and competitive adsorption effects. The adsorption isotherms of the pure components of flue gas CO₂, N₂, SO₂ and H₂O vapour were investigated. The isosteric enthalpies of adsorption were determined as a function of surface excess. The enthalpies at zero surface coverage have the order: SO₂ > H₂O > CO₂ > N₂. However, the SO₂ isosteric enthalpy decreases with increasing surface excess and is lower than that of water vapour at high surface excess uptake values. The temperature range for CO₂ adsorption covers the subcritical to supercritical gas transition. There was no evidence for isosteric enthalpy differences over this temperature range. The adsorption kinetics for SO₂ and H₂O adsorption were measured for each isotherm pressure increment. In both cases the adsorption kinetics followed the linear driving force model. The adsorption mechanisms for both SO₂ and H₂O kinetic trends are discussed in terms of the adsorption mechanisms. The water vapour adsorption kinetics showed a minimum in the region where water molecules form clusters around functional groups, which merge in the pores. The SO₂ adsorption kinetics also show a minimum with increasing surface coverage and this is attributed to dipole-dipole interactions. The activation energies for diffusion of both SO₂ and H₂O into F400 were very low. The adsorption kinetics of both pure N₂ and CO₂ were too fast to be measured accurately by the gravimetric method used in this study. Ideal Adsorbed Solution Theory (IAST) was used to calculate competitive adsorption of SO₂/CO₂ and CO₂/N₂ from the isotherms of the pure components. In the case of CO₂/H₂O adsorption, the adsorption mechanisms of H₂O and CO₂ are different and therefore, IAST was not applicable. The competitive adsorption of CO₂/N₂ was investigated using the Integral Mass Balance (IMB) experimental method and this was used for validation of the IAST. The competitive adsorption of CO₂/H₂O is the most important for CO₂ capture and this was also investigated using the IMB method. The results show that both thermodynamic and kinetic effects are important. The results provide an insight into the role of competitive adsorption in the capture of CO₂ and SO₂ from flue gases by adsorption on porous materials from both thermodynamic and kinetic perspectives.

FUNCTIONAL BIODYNAMICS: THE YIN COMPLEMENT

J. Mau

*Chair of Medical Kybernetika, Bashkir State Medical University, Ufa, Russia;
Professor (em) School of Medicine, Heinrich Heine University Duesseldorf, Germany*

ABSTRACT

Background

A previous paper elaborated on holistic functional dynamics of human-body system with assumptions about “driving forces” of physiological processes from a phenomenological viewpoint. At the behavioral level of person’s operations in body’s outside world, in particular in interaction with other persons in society, motivations had been considered in more detail though still without attempts to expand the mathematical model accordingly.

AIMS

For an integrative model perspective, in-body resonance of operational decision-making will be incorporated into the holistic modeling of physiological dynamics.

METHODS

From a philosophical viewpoint, one may invoke the Taoist Principle of Shadow-Light (Yin-Yang 阴 阳) to complement previous axiomatics of Yang. The Yin then appears as a person’s ambitions in pursuit of operational goals within the prevalent life-sphere setting. The holistic approach of a hierarchical drill-down in System Functional Architecture (SFA) is adopted. A generic daily wake-sleep dynamics for a single functional unit is considered first, next extended to a multiplet of functional units, and finally translated one scale upwards to functional aggregate level. Technically, a three-compartment model with charge-transfer intensities is used with any single functional unit.

RESULTS

The Yang dynamics of consumable-charge transfers from ubiquitous ‘source’ to supply-part capacitor and from its content-mirrored demand-part capacitor to the consumer are complemented with an equally ubiquitous ‘drain’ that reflects general desire to consume, the driving force, in order to maintain physiological functions and to pursue operational goals in body’s outside world, the Yin dynamics. By parallel connection of Yin complements of functional units that compose a functional aggregate, the structure can be carried forward consistently to next upper functional level.

CONCLUSION

This extension of axiomatic functional biodynamics within SFA reflects “desire to consume” irrespective of whether generated inside or outside of human body; it then lends itself to investigations in a spectrum of behavioral attitudes and internal disorders, in neuroeconomics, addiction, and metabolism. As mere axiomatics, it provides the feed from person’s surroundings into internal dynamics which was not addressed previously.

COILED-COILS FOR THE DESIGN OF CELLULAR LOGIC CIRCUITS AND NEW PROTEIN FOLDS

R. Jerala

Department of synthetic biology and immunology,
National institute of chemistry, Hajdrihova 19, SI-1000 Ljubljana, Slovenia
roman.jerala@KI.si

ABSTRACT

Coiled-coil (CC) dimers are ubiquitous building modules in natural proteins. Rules that defined interactions in CC dimers are relatively well known which allows us to design new CC dimers with selected stability and selectivity. Although CC dimers have been known since Francis Crick, recently their application in cell regulation and construction of new building modules are experiencing an explosive growth. We have designed new CC pairs that can be fused to and incorporated into other proteins, that enables new type of regulation of biological processes with increased response and fast kinetics (1,2).

CC dimers can be concatenated into longer chains which enables construction of new modular protein folds based on topological principles distinct from natural proteins. Coiled-coil protein origami (CCPO) have interesting properties and we are designing new modalities of their construction that enable multiple use of the same building modules and design of the folding pathways and other properties (3-6).

REFERENCES

- [1] Fink T., Lonžarić J... Jerala R. *Nat Chem Biol.* (2018) 15 (2), 115-122.
- [2] Lebar T.. Jerala R. *Nat. Chem.Biol.* (2020) 16 (5), 513-519.
- [3] Gradišar H, ... Jerala R. *Nat Chem Biol.* (2013) 9:362-6.
- [4] Ljubetič A, Lapenta F, .. Jerala R. *Nat Biotechnol.*(2017) 35:1094-1101.
- [5] Lapenta F.... Jerala R. *Nat Commun.* (2021) 29:939.
- [6] Aupič J.... Jerala R. *Nat Commun.* (2021) 12:940.

HYBRID ORGANIC-INORGANIC PEROVSKITES

A. Stroppa

National Research Council, Italy

ABSTRACT

Hybrid Organic-Inorganic Perovskites (HOIPs) are introducing new directions in the materials science landscape. In this talk, we will discuss the intriguing origin of ferroelectricity in HOIPs. In particular, we highlight the hybrid improper mechanism where Jahn-Teller cooperative distortions are subtly coupled to inversion symmetry breaking giving rise to a switchable electric polarization. Symmetry invariants theory permits to predict a magneto-electric coupling which has been recently confirmed by experiments. We propose further examples of the complex multifunctional behaviour arising from the organic and inorganic dual nature as well as from the interplay between ferroelectricity and spin-related properties in hybrid perovskites. In particular we discuss a recently synthesized ferroelectric layered two-dimensional HOIP, *i.e.* (AMP)PbI₄ (AMP=4-aminomethyl-piperidinium). We report a new effect, *i.e.*, an extraordinarily large Rashba anisotropy that is tunable by ferroelectric polarization: as polarization is reversed, not only the spin texture is inverted, but also the major and minor axes of the Rashba anisotropy ellipse in \mathbf{k} -space are interchanged, *i.e.* a pseudo-rotation. A $\mathbf{k}\cdot\mathbf{p}$ model Hamiltonian and symmetry-mode analysis reveal a quadrilinear coupling between the cation-rotation modes responsible for the Rashba ellipse pseudo-rotations, the framework rotation, and the polarization.

ANTITUMOR DRUGS IMMOBILIZED INTO MESOPOROUS SILICA SBA-15

G. N. Kaluđerović

*Department of Engineering and Natural Sciences, University of Applied Sciences Merseburg, Eberhard-Leibnitz-Strasse 2, DE-06217 Merseburg, Germany.
(goran.kaluderovic@hs-merseburg.de)*

ABSTRACT

Conventional therapeutics, such as cisplatin, beside their benefit effects in fight against cancers confronts quite a few challenges [1]. The main goals of chemotherapeutics are to hinder the tumor expansion, reduce growth of tumor cells and increase the patient's survival period. Cisplatin alone or in combined therapy is a first-line agent for several cancers (e.g. testicular, ovarian, lung, head and neck tumors). However, its antitumor efficiency is limited due to dose-dependent toxicities (e.g. nephro- and neurotoxicities) and intrinsic or acquired cellular resistance [2].

Silica-based materials are already highly promising candidates in several fields of medicine including cancer therapy [3,4]. The rationale of loading of highly active anticancer compounds into particles lie in the following: prevention of hydrolysis and accumulation in the healthy tissues/organs, tailorable drug release, as well as local application in tumor tissues in high doses.

SBA-15 or its functionalized forms potentiate and modify mechanism of action of metal-based (e.g. cisplatin, ruthenium(II), organotin(IV) compounds) or natural occurring compounds (e.g. emodin) [3-9]. For instance, SBA-15 loaded with cisplatin induced senescence in survived clones of B16F10 mouse melanoma cells [3]. SBA-15 grafted with $\text{Ph}_3\text{Sn}(\text{CH}_2)_6\text{OH}$ triggers apoptosis in B16 cells followed by the development of a nonproliferative melanocyte-like phenotype of surviving cells [5]. Moreover, same nanomaterial almost completely abolished tumor progression *in vivo* in melanoma syngeneic C57BL/6 mouse model without visible side effects. $\text{Ph}_3\text{Sn}(\text{CH}_2)_3\text{OH}$ loaded into SBA-15 reduces metastatic potential of highly invasive serous ovarian carcinoma A2780 cells [6]. Importantly, functionalization of SBA-15 has an influence on the mode of action and differentiation inducing properties [7]. SBA-15 potentiates action of $[\text{Ru}(\eta^6\text{-}p\text{-cymene})\text{Cl}_2\{\text{Ph}_2\text{P}(\text{CH}_2)_3\text{SPh-}\kappa\text{P}\}]$ and emodin against B16 cells [8,9]. These approaches present a safer mode in tumor treatment compared to induced apoptosis alone.

REFERENCES

- [1] S. Ghosh, *Bioorg. Chem.* 2019, 88, 102925.
- [2] S. Sears, L. Siskind, *J. Am. Soc. Nephrol.* 2021, ASN.2020101455
- [3] D. Edeler, M. R. Kaluđerović, B. Dojčinović, H. Schmidt, G. N. Kaluđerović, *RSC Advances* 2016, 6, 111031.
- [4] D. Drača, D. Edeler, M. Saoud, B. Dojčinović, D. Dunđerović, G. Đmura, D. Maksimović-Ivanić, S. Mijatović, G. N. Kaluđerović, *J. Inorg. Biochem.* 2021, 217, 111383;
- [5] M. Z. Bulatović, D. Maksimović-Ivanić, C. Bensing, S. Gómez-Ruiz, D. Steinborn, H. Schmidt, M. Mojić, A. Korać, I. Golić, D. Pérez-Quintanilla, M. Momčilović, S. Mijatović, G. N. Kaluđerović, *Angew. Chem. Int. Ed.* 2014, 53, 5982.
- [6] C. Bensing, M. Mojić, S. Gómez-Ruiz, S. Carralero, D. Maksimović-Ivanić, S. Mijatović, G. N. Kaluđerović, *Dalton Trans.* 2016, 45, 18984.
- [7] D. Edeler, D. Drača, V. Petković, F. Natalio, D. Maksimović-Ivanić, S. Mijatović, H. Schmidt, G. N. Kaluđerović, *Mat. Sci. Eng. C* 2019, 100, 315-322.

- [8] D. Edeler, S. Arlt, V. Petković, G. Ludwig, D. Drača, D. Maksimović-Ivanić, S. Mijatović, G. N. Kaluđerović, J. Inorg. Biochem. 2018, 180, 155-162.
- [9] T. Krajnović, D. Maksimović-Ivanić, S. Mijatović, D. Drača, K. Wolf, D. Edeler, L. A. Wessjohann, G. N. Kaluđerović, Nanomaterials 2018, 8, 322.

CEREBRAL HYPOPERFUSION AND PROGESTERONE TREATMENT ALTER PARAMETERS OF OXIDATIVE STRESS AND ANTIOXIDANT DEFENCE IN MALE RATS

I. Guševac Stojanović¹, A. Todorović¹, S. Pejić¹, N. Tatalović², D. Blagojević², J. Martinović¹, I. Grković¹, N. Mitrović¹, M. Zarić¹, and D. Drakulić¹

¹ *University of Belgrade, VINČA Institute of Nuclear Sciences – National institute of the Republic of Serbia, P.O.Box 522, 11001 Belgrade, Republic of Serbia. (drakulic@vin.bg.ac.rs)*

² *University of Belgrade, Institute for Biological Research “Siniša Stanković”, National Institute of Republic of Serbia, Bulevar despota Stefana 142, 11060 Belgrade, Republic of Serbia.*

ABSTRACT

Numerous natural compounds, like progesterone (P4), a sex steroid hormone, are highlighted as promising agents for treatment of different disorders including prolonged disturbance of blood flow. However, its action on several oxidative stress markers (pro/antioxidant balance, products of lipid peroxidation and phosphatidylcholine to lysophosphatidylcholine intensity ratio) and one of the major components of antioxidant system, superoxide dismutase in rat prefrontal cortex (PFC) following permanent bilateral occlusion of common carotid arteries (2VO) is not completely investigated. According to the obtained results, levels of investigated oxidative stress markers and SOD activity were altered in 2VO animals treated with vehicle, while P4 treatment returned them to control values. Overall, presented data indicate that P4 might manifest antioxidative features in PFC of 2VO rats.

INTRODUCTION

In pathophysiological conditions, including cerebrovascular insufficiency, the imbalance might be created between the generation of reactive species and their abolition by the components of antioxidant system, mostly by superoxide dismutase (SOD), catalase and glutathione peroxidase. Due to their inadequate removal, these over-synthesized highly toxic intermediates are capable of causing structural and functional cellular changes by oxidation of biomolecules, such as lipids, proteins and DNA that may initiate oxidative injury and even cell death in neurons. In the rat two vessel occlusion (2VO), model when both common carotid arteries are permanently ligated, the most prominent neuronal damage is detected in cortical pyramidal neurons in layer III and hippocampal CA1 neurons, as well as in the other vulnerable brain regions and cell types [1].

Different therapeutic strategies are proposed for protecting brain from the deleterious effects of restricted cerebral blood flow that causes limitation of tissue oxygen and nutrients supply. Their aim is to decrease the activation of toxic pathways and increase the activity of endogenous protective mechanisms. Recently, a few neuroprotectants are suggested, including sex steroid hormones, such as progesterone (P4) and its metabolites. Previous reports indicate that P4 treatment in various models of neuronal injury exhibits multiple neuroprotective outcomes by reducing blood-brain barrier leakage, cerebral edema, lesions' volume, thus promoting functional recovery, etc. This pleiotropic hormone might achieve its genomic and non-genomic actions via binding to the appropriate hormone receptors, controlling signalling cascades in neurons, astrocytes and microglia, modulating the inflammatory response, and regulating glutamate excitotoxicity [1, 2]. P4-mediated protection might be also related to membrane stabilization and reactive species scavenging, either of which might attenuate the damage provoked by oxidative stress [3]. However, the additional research is necessary to better analyse the antioxidant mechanisms underlying this hormone's neuroprotective effects in the state of cerebral hypoperfusion and allow its use in preclinical and clinical studies.

To address these disputable issues, in the present study, the rat 2VO model and P4 treatment were used to investigate the potential alterations of several parameters of oxidative stress (pro/antioxidative balance (PAB), products of lipid peroxidation (LPO products) and phosphatidylcholine (PC) to lysophosphatidylcholine (LPC) intensity ratio) and one of the major components of antioxidant system, superoxide dismutase (SOD). These changes were evaluated in prefrontal cortex (PFC), a brain region that might be directly affected by mild and prolonged disturbance of blood flow as well as hormone therapy.

METHODS

All research procedures were conducted on adult male Wistar rats (350 – 400 g) and approved by the Ethical Committee for the Use of Laboratory Animals of VINČA Institute of Nuclear Sciences – National institute of the Republic of Serbia, Belgrade (authorization numbers 02/11 and 323-07-04253/2016-05). The animals were randomly divided into three groups: controls subjected to sham operation and treated with vehicle (commercial flaxseed oil, dose 1 mg/kg/day, Sham + V) (n = 5); rats subjected to permanent common carotid artery ligation and vehicle treatment (commercial flaxseed oil, dose 1 ml/kg/day, 2VO + V) (n = 5); and animals with permanently occluded common carotid arteries treated with P4 dissolved in commercial flaxseed oil in dose 1.7 mg/kg/day (2VO + P4) (n = 5). The surgical procedures were conducted by neck ventral midline incision and exposition of both common carotid arteries, followed by their careful separation from carotid sheaths, cervical sympathetic and vagus nerves. In 2VO groups, both common carotid arteries were permanently double-ligated with 5-0 silk suture, while controls underwent the same surgical intervention but without actual occlusion of carotid arteries. The treatments in all experimental groups were administrated in the form of subcutaneous injections for seven consecutive days [2]. On the last day of the experiment, 4 h following the last injection, rats were decapitated with guillotine (Harvard Apparatus, Holliston, USA). PFCs were isolated on the ice, frozen in liquid nitrogen and stored at -70°C until processing.

All analyses were performed on samples homogenized in iced-cold medium (0.25 M sucrose, 1 mM Tris-HCl EDTA buffer pH 7.4) that were then centrifuged two times per 10 min, at 3000 rpm, 4°C (Beckman, Germany). The obtained supernatants were pooled, additionally centrifuged per 20 min, at 10000 rpm, 4°C (Beckman, Germany) and obtained pellets were resuspended in ice-cold 5 mM TRIS HCl pH 7.4 [4].

For PAB assay, as previously reported [5], 10 µl of sample/standard (dilution series of hydrogen peroxide)/blank (dH₂O) were incubated with 200 µl of working solution (1 ml TMB (3,3',5,5'-tetramethylbenzidine) cation solution with 10 ml TMB solution) in a dark place for 12 min, at 37°C. Then, the reaction was stopped by adding 100 µl of 2 N HCl. The absorbencies were read on microplate reader (WALLAC 1420-Victor2 Multilabel Counter, PerkinElmer, USA) at 450 nm.

To estimate the LPO levels, the methane sulfonic acid was added to the reaction mixtures containing samples/standards (dilution series of 10 mM TMOP (1,1,3,3,-tetramethoxypropane))/blank (acetonitrile:methanol in the ratio 3:1) and working solution. Then the mixtures were heated at 45°C/60 min, centrifuged (15 min, 13000 rpm, 4°C) (Eppendorf 5417, Germany) and the absorbencies were measured at 580 nm in a microplate reader (WALLAC 1420-Victor2 Multilabel Counter, PerkinElmer, USA). The LPO levels were determined using the corresponding standard curve, as described earlier [5].

The activity of total SOD was evaluated by the adrenaline method of Misra and Fridovich, where one SOD unit (U) is defined as the amount of enzyme needed to exhibit 50 % dismutation of the superoxide radical at pH 10.2 [6].

The modified Folch procedure using a chloroform/methanol/water solvent system was used for total lipid extracts preparation. Obtained pallets were subsequently redissolved in matrix solution

(0.5 M DHB (2,5-dihydroxybenzoic acid, Merck Millipore, Germany) in methanol (Merck Millipore, Germany)), applied onto the stainless steel target plate and dried under warm steam of air [7]. All mass spectra were obtained in the reflector mode and “delayed extraction” conditions (delay time was approximately 130 ns) on a commercial matrix assisted laser desorption/ionization time of flight (MALDI-TOF) Voyager-DE PRO mass spectrometer (Sciex, USA). The raw data were processed with the “Data Explorer Software” version 4.9 (Applied Biosystems, USA).

Statistical analysis was performed by one-way analysis of variance (one-way ANOVA) followed by Tukey’s *posthoc* test using GraphPad Prism 5 Software (USA). The significance level was $p < 0.05$, with values expressed as a percentage of the mean of the values in Sham + V group \pm SEM (standard error of the mean).

RESULTS AND DISCUSSION

The brain tissue with its elevated metabolic activity, high oxygen consumption, lipid-rich content and low antioxidant capacity is highly prone to oxidative stress. A critically low oxygen supply to the brain in pathophysiological conditions is capable to modulate oxidative phosphorylation by mitochondria and considerably decrease cellular ATP production. As a result of rapid decline in cellular ATP to a level insufficient to sustain the activity of ion pumps, a prompt and widespread membrane depolarization of neurons and astrocytes arise. In parallel, mitochondria increase the production of highly reactive species that enhance lipid peroxidation and protein oxidation and induce the alteration of prooxidant/antioxidant balance in the cerebral tissues and lead to cell death. Although it is reported that reperfusion injury initiates intensive oxidative damage, there are also indications that enduring ischemic/oligemic condition provoked by 2VO creates mild, but permanent oxidative stress, which might be the cause of persistent and progressive neuronal damage [1]. These pathological processes might be prevented or even attenuated by different agents that are shown to exert protective effects in several experimental models, like those that mimic certain pathogenic features of brain dysfunction observed in advanced age- or age-related neurodegenerative diseases. Although P4 is reported to be protective against oxidative insults induced by glutamate, glucose deprivation, and FeSO₄/ amyloid β -peptide-provoked toxicity in primary hippocampal cultures [8], its effect in PFC in the state of cerebral hypoperfusion are still unclear. In current experimental setup, a relatively new but well defined assay for estimating the levels of PAB was used. As presented in **Figure 1.**, in 2VO group that received vehicle treatment, PAB level was augmented compared to the controls for 38 % ($p < 0.05$) and it was also increased ($p < 0.05$) regarding to P4 treatment. Previous study has shown a significant elevation of PAB level in acute cerebral ischemia and proposed that it could be used as a predictive marker of disease outcome [9]. To our knowledge, there are no available data about the effect of P4 on PAB levels in 2VO rat model, which makes them unique in the scientific literature.

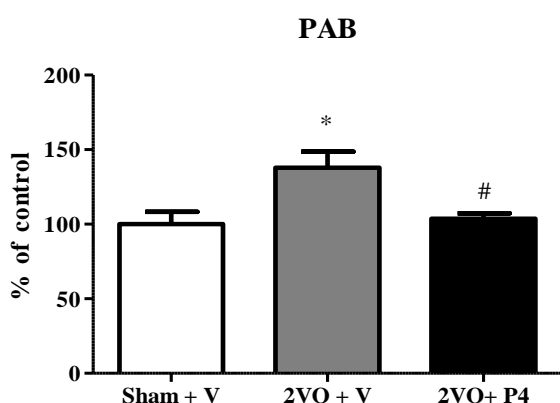


Figure 1. Levels of oxidative stress marker (pro/antioxidative balance (PAB) in prefrontal cortex of sham operated rats treated with vehicle, Sham + V, rats subjected to permanent ligation of common carotid arteries and either vehicle treatment, 2VO + V or P4 treatment, 2VO + P4. Data are presented as the mean \pm SEM, whereas the values Sham + V are set as 100%. * $p < 0.05$, vs. control group; # $p < 0.05$ between 2VO groups.

Moreover, it was found that PAB status was positively correlated with other parameters of oxidative stress, such as LPO products [9]. Thus, in parallel with PAB levels, we estimated the level of LPO products. In comparison to Sham + V, in 2VO + V group the formation of LPO products was increased by 64 % ($p < 0.001$) (**Figure 2.**). Previous reports indicate that elevated levels of prooxidants lead to lipid peroxidation and formation of lipid radicals, like the aldehydes. These most abundant LPO products inactivate many cellular proteins and cause a rapid decrease and inhibition of the enzymatic and nonenzymic components of the antioxidative defense system. This provokes the overproduction of other reactive species and plays an important role in ischemic cell death, which might be associated with our previous findings [2]. Namely, previously we reported that prolonged reduction of cerebral blood flow alters the neuronal morphology, the amount of DNA fragmentation, along with the expression of progesterone receptors and the expression of the key elements of Akt/Erk/eNOS signal pathway. These modifications were attenuated by P4 treatment [2]. Although P4 does not have the characteristic chemical structure of an antioxidant, in the present study, it progressively modulated the levels of LPO products compared to vehicle treatment ($p < 0.01$) and returned them to values observed in controls (**Figure 2.**). This is consistent with literature data on P4 neuroprotective properties that are accomplished via its capacity to mitigate the lipid peroxidation by blocking the formation of free radicals and increasing the efficiency of their elimination by regulating antioxidant defense components [10]. These effects might be also achieved by controlling the isoprostanes production and pro-inflammatory genes activation [3] as detected in models of global cerebral ischemia, traumatic brain injury and subarachnoid hemorrhage [11]. Thus, the observed modulation of investigated parameters promoted by cerebral hypoperfusion might be indicative of a P4-induced reduction of oxidative stress and downregulation of proapoptotic signalling studied earlier [2].

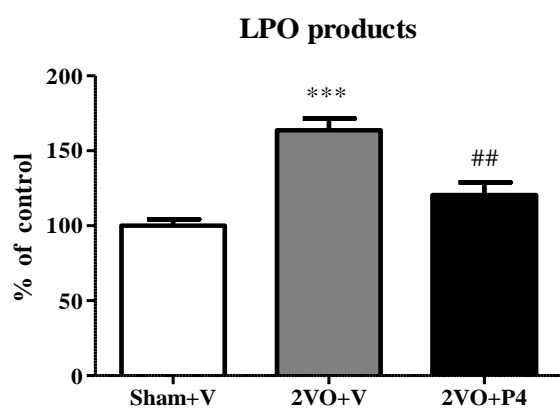


Figure 2. Levels of oxidative stress marker (products of lipid peroxidation (LPO products)) in prefrontal cortex of sham operated rats treated with vehicle, Sham + V, rats subjected to permanent ligation of common carotid arteries and either vehicle treatment, 2VO + V or P4 treatment, 2VO + P4. Data are presented as the mean \pm SEM, whereas the values Sham + V are set as 100%. *** $p < 0.001$ vs. control group; ## $p < 0.01$ between 2VO groups.

PCs, the most abundant phospholipids, and PC-derived products, including LPCs (lipid species produced by spontaneous hydrolysis or enzymatic degradation of PCs) beside their structural functions and regulation of the physical properties of membranes, act as precursors of various lipid secondary messengers in diverse signalling cascades. The literature indicates that total concentrations of PCs and LPCs, as well as their intensity ratio, might be used as markers positively associated not only with normal aging but also with the onset and progression of different pathological conditions, including cerebrovascular and neurodegenerative diseases [7]. Since there are no available data about the lipid metabolism in PFCs' of 2VO rats treated either with vehicle or P4, this study attempted to add new knowledge about PC/LPC intensity ratio in both groups of hypoperfused animals in comparison to controls by employing MALDI TOF method followed by appropriate statistical analysis.

The observed PCs and LPCs peaks are listed in **Table 1**.

Table 1. List of phosphatidylcholine (PC) and lysophosphatidylcholine (LPC) species identified by MALDI TOF MS detected in positive ion mode.

Phospholipid Class	Adduct	m/z
LPC (16:0)	H	496.5
LPC (16:0)	Na	518.5
LPC (18:1)	H	522.5
LPC (18:0)	H	524.5
LPC (16:0)	K	534.5
LPC (18:1)	Na	544.3
LPC (18:0)	Na	546.4
LPC (22:6)	K	568.5
PC (32:0)	H	734.6
PC (32:0)	Na	756.6
PC (34:2)	H	758.6
PC (34:1)	H	760.6
PC (32:0)	K	772.6
PC (34:1)	Na	782.6
PC (36:4)	H	782.7
PC (36:3)	H	784.6
PC (36:2)	H	786.6
PC (36:1)	H	788.6
PC (34:1)	K	798.6
PC (36:4)	Na	804.6
PC (36:3)	Na	806.6
PC (36:2)	Na	808.6
PC (38:4)	H	810.6
PC (36:1)	Na	810.6
PC (36:4)	K	820.5
PC (36:1)	K	826.7
PC (38:4)	K	848.6

Figure 3. illustrates characteristic PC and LPC peaks observed in all three experimental groups, detected in positive ion MALDI spectra in the presence of DHB.

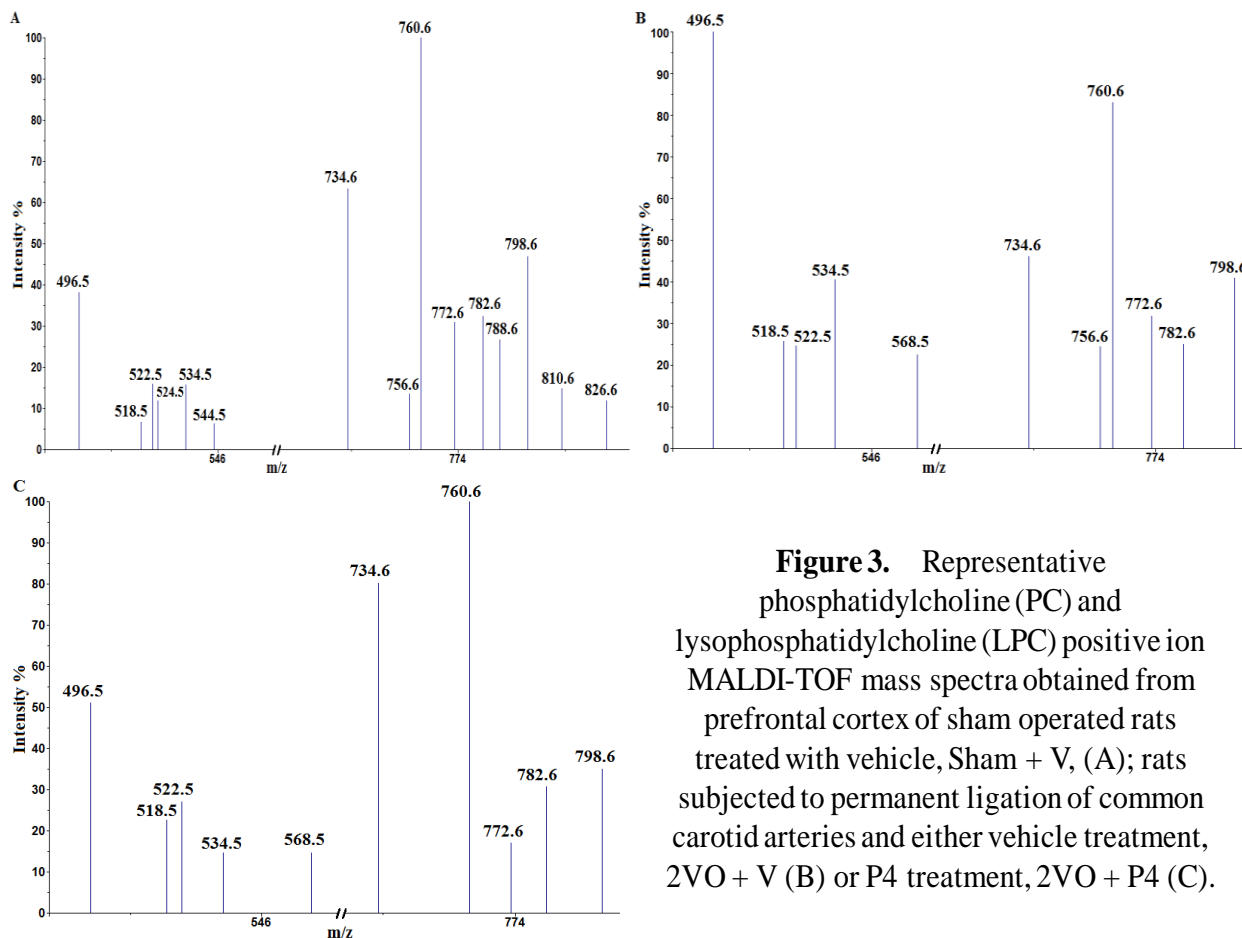


Figure 3. Representative phosphatidylcholine (PC) and lysophosphatidylcholine (LPC) positive ion MALDI-TOF mass spectra obtained from prefrontal cortex of sham operated rats treated with vehicle, Sham + V, (A); rats subjected to permanent ligation of common carotid arteries and either vehicle treatment, 2VO + V (B) or P4 treatment, 2VO + P4 (C).

The most intense peaks that correspond to PC 34:1 [M+H]⁺ (m/z 760.6), PC 34:1 [M+Na]⁺ (m/z 782.6) and PC 34:1 [M+K]⁺ (m/z 798.6); and LPC 16:0 [M+H]⁺ (m/z 496.5), [M+Na]⁺ (m/z 518.5) and LPC 16:0 [M+K]⁺ (m/z 534.5) were used to calculate the PC/LPC intensity ratio (**Figure 4**). The other detected PC and LPC peaks detected in samples had much lower intensities and they were not used for further analyses.

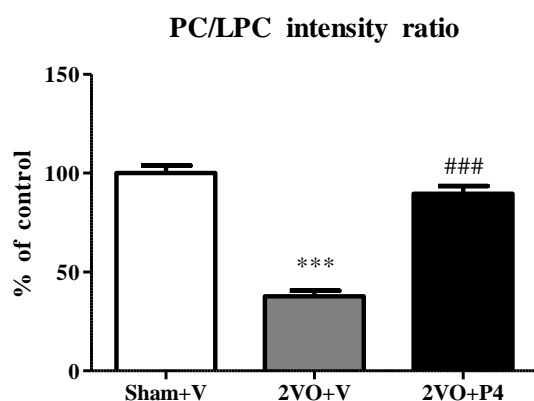


Figure 4. Phosphatidylcholine (PC) to lysophosphatidylcholine (LPC) (PC/LPC) intensity ratio calculated using most intense PC and LPC peaks (D). Intensities obtained from prefrontal cortex of sham operated rats treated with vehicle, Sham + V, rats subjected to permanent ligation of common carotid arteries and either vehicle treatment, 2VO + V or P4 treatment, 2VO + P4. Data are presented as the mean ± SEM, whereas values in Sham + V are set as 100%. ***p < 0.001 vs. control group; ###p < 0.001 between 2VO groups.

The observed decrease of PC/LPC ratio implies the abnormal phospholipid metabolism in 2VO + V group comparing to Sham + V (p < 0.001) which is most likely the result of increased activity of phospholipase A2 (PLA2). PLA2 is a lipolytic enzyme responsible for removal of the acyl group from the sn-2 position of PCs initiating the loss of vital membrane phospholipids and

generation of free fatty acids and LPCs. These species and products of their metabolism further react with other biomolecules and increase accumulation of lipid peroxides, alter membrane permeability, and ion homeostasis. Aforementioned processes, along with the loss of ATP and massive cellular calcium influx and calcium overload, may provoke the impairment of cellular components, trigger proapoptotic signalling and subsequent changes in neuronal morphology and even cell death [7] that were confirmed in our prior study [2]. Furthermore, in 2VO rats treated with P4, the PC/LPC ratio was increased in comparison to 2VO + V ($p < 0.001$) and returned to the values detected in controls (**Figure 4.**), indicating decline of the intensity of oxidative stress presented herein and amelioration of its downstream prosurvival signalling pathways revealed in our previous report [2].

A detoxification enzyme, SOD, catalyzes dismutation of the superoxide anion radical into less harmful oxygen and hydrogen peroxide. Thus, it contributes to the protection of the cells from detrimental agents that promote cell death [12]. In 2VO + V group the SOD activity was enhanced in comparison to controls ($p < 0.01$) (**Figure 5.**). The observed increased levels of prooxidants (**Figure 1., Figure 2., Figure 3., and Figure 4.**) along with previously reported apoptotic events [2], in current experimental setup however, indicate that investigated component of antioxidant system is not capable to completely compensate the overproduction of reactive species. These compounds further oxidize biomolecules, potentiate the accumulation of oxidative cell damage and finally, most likely provoke, at least partially, previously investigated cell death signalling pathway [2]. In contrast, as presented in **Figure 5.**, P4 decreased SOD activity in PFC regarding to vehicle treatment ($p < 0.05$) and returned it to basal values. The unchanged SOD activity along with no alteration of the other tested parameters when compared to controls, indicate that applied hormone might exert neuroprotective effect by attenuating 2VO-induced oxidative stress. The protective outcome in neuronal cells might also arise due to P4-binding to specific receptors in the nucleus and activation of gene transcription. In particular, SOD is one of the P4 target genes implicated in oxidative stress tolerance [11].

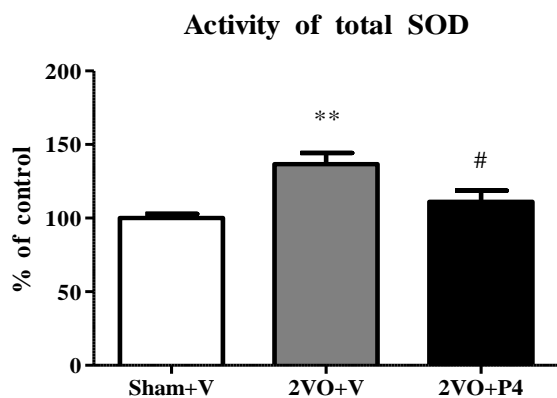


Figure 5. Activity of principal antioxidant marker (total superoxide dismutase (SOD) in prefrontal cortex of sham operated rats treated with vehicle, Sham + V; rats subjected to permanent ligation of common carotid arteries and either vehicle treatment, 2VO + V or progesterone (P4) treatment, 2VO + P4. Data are presented as the mean \pm SEM, whereas the values of Sham + V are set as 100%. ** $p < 0.01$ vs. control group; # $p < 0.05$ between 2VO groups.

CONCLUSION

Disturbed cognitive and behavioural functions observed in aging, senescence and/or patients with cerebrovascular diseases or cardiovascular pathologies are associated with cerebrovascular insufficiency/hypoperfusion. Even the pathophysiology of this type of brain injury is still ambiguous, the literature highlights that various pathways might be implicated, including the generation of reactive species, inflammation, cell death, and signaling pathway disturbance. Since there is a lack of efficient pharmacotherapy, cerebral hypoperfusion is still a challenging condition in clinical medicine. Among many proposed agents, those preventing the initiation of oxidative stress and targeting the components of antioxidant system might be the promising neurotherapeutic tools. According to the presented results, hormone treatment modified 2VO-induced increase of investigated prooxidant markers, activity of main component of antioxidant defence system and

PC/LPC intensity ratio that were all restored to control values. Overall, repeated low-dose P4 treatment in PFC of animals subjected to permanent cerebral hypoperfusion, characteristic for elders and patients with cerebrovascular disorders, might exhibit neuroprotective outcome by stimulating its antioxidative capacity.

Acknowledgement

This work is supported by Ministry of Education, Science and Technological Development, Republic of Serbia (grants no. 451-03-9/2021-14/200017-0902102, 451-03-9/2021-14/200017-0902107 and 451-03-9/2021-14/200017-0502110).

REFERENCES

- [1] E. Farkas, P.G.M. Luiten, F. Bari, *Brain Res Rev.*, 2007, **54**, 162-180.
- [2] M. Stanojlović, I. Guševac Stojanović, M. Zarić, J. Martinović, N. Mitrović, I. Grković, D. Drakulić, *Cell Mol Neurobiol.*, 2019, doi: 10.1007/s10571-019-00777-2.
- [3] M. Singh, C. Su, *Horm Behav.*, 2013, **63**, 284-290.
- [4] M. Stanojlović, A. Horvat, I. Guševac, I. Grković, N. Mitrović, I. Buzadžić, D. Drakulić, *Folia biol (Praha)*, 2014, **60**, 123-132.
- [5] S. Đurašević, G. Nikolić, A. Todorović, D. Drakulić, S. Pejić, V. Martinović, D. Mitić-Ćulafić, D. Milić, T.J. Kop, N. Jasnić, J. Đorđević, Z. Todorović, *Food Chem Toxicol.*, 2020, **140**, 111302-2020.
- [6] H.P. Misra, I. Fridovich, *J Biol Chem.*, 1972, **247**, 3170-3175.
- [7] J. Miletić Vukajlović, D. Drakulić, S. Pejić, T.V. Ilić, A. Stefanović, M. Petković, J. Schiller, *Rapid Commun Mass Spectrom.*, 2020, **28**, e8595.
- [8] A.N. Siddiqui, N. Siddiqui, R.A. Khan, A. Kalam, N.R. Jabir, M.A. Kamal, C.K. Firoz, S. Tabrez, *CNS Neurosci Ther.*, 2016, **22**, 342-350.
- [9] J. Kotur-Stevuljevic, N. Bogavac-Stanojevic, Z. Jelic-Ivanovic, A. Stefanovic, T. Gojkovic, J. Joksic, M. Sopic, B. Gulan, J. Janac, S. Milosevic, *Atherosclerosis*, 2015, **241**, 192-198.
- [10] J. Wei, G. Xiao, *Acta Pharmacol. Sin.*, 2013, **34**, 1485-1490.
- [11] Ishihara, Y., Takemoto, T., Ishida, A., Yamazaki, T. *Oxid. Med. Cell. Longev.*, 2015, 1-16.
- [12] O.M. Ighodar, O.A. Akinloye, *Alexandria Med J.*, 2018, **54**, 287-293.

SELF-CREATION OF COMPLEX CHEMICAL ENTITIES THAT CREATE COMPLEX CELLS, GROWING AND FORMING UNUSUAL STRUCTURES, MOVEMENTS AND MACHINES THAT CAN SWITCH ITSELF TO ANOTHER

J. Maselko

Technical University, Chemical Department, Wroclaw, Poland, jmaselko2@alaska.edu
University of Alaska, Anchorage, Chemistry Department, USA,

First Law of Thermodynamic describe that everything cannot be -self creator or destroyed in an isolator system. In open systems far from thermodynamic equilibrium. However, they exist systems that exist far from Thermodynamic Equilibriums that are supplied by chemical systems and continuously moving fater from equilibrium. They are building chemical cells that can take compounds from outside, react and one compound will stay inside and next move outside. May create very complex towers. Machines cand move in different ways and may produce different complex structures. It is the basic Law of Chemical Self-creation.

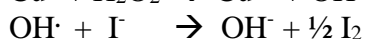
Self-Creation chemical cells and theirs functions. $\text{CaCl}_2 - \text{Na}_2\text{CO}_3$.

Here few inorganic compounds will create spontaneously chemical cell. Inorganic chemicals move to cell, produce another chemical that will diffuse outside.

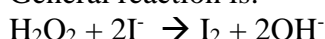
CaCl_2 was inversed to solution of Na_2CO_3 producing formation of a cell surrounded by a semi permeable membrane. The water and small molecules diffuse through the membrane. If the CaCl_2 is doped with CuCl_2 and solution contain $\text{NaI} + \text{H}_2\text{O}_2$ the membrane is larger and has violet color from iodine. Iodide and hydrogen H_2O_2 diffuse into a cell, react inside and producing iodine and hydroxy ions. The process is catalyzed by Cu (II) ions

The process is catalyzed by Cu (II) ions inside the cell. The products diffuse out of the cell. Chemical reaction occurs only inside the cell.

The mechanism of iodine formation appears to follow:



General reaction is:

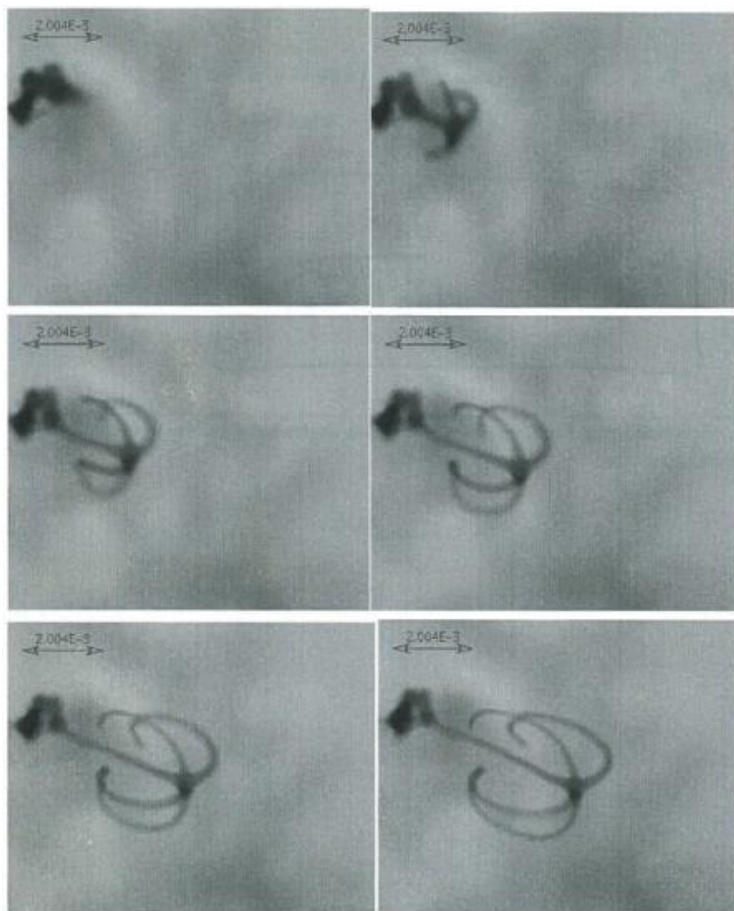


Finally, iodine diffuses out of the cell.

Chemical cell is a chemical machine. This sound like an incredible accident but it is the rule in Creation Chemistry. Iodine is essential element of life.

Self-controlling unusually complex tube networks. $\text{AlCl}_3 + \text{NaOH}$ system.

The injection has about 0,01s with 2.5 ml/min, concentration 2-4 M. AlCl_3 was saturated.



Growing tuba network.

AlCl_3 was injected into solution through a needle. The stem is a single tuber from balloon to branchers. Four branches grow at the same time. They distribute symmetrically around the stems at common junction. The number of branches can be from 2 to 5. The single brunch was never observed. Branches and stem grow together. The circle is constant all the time. Usually from one fluid into another do not move far. The H_2O is controlling chemical compound and chemical compound is controlling H_2O . It may be used in nanotechnology.

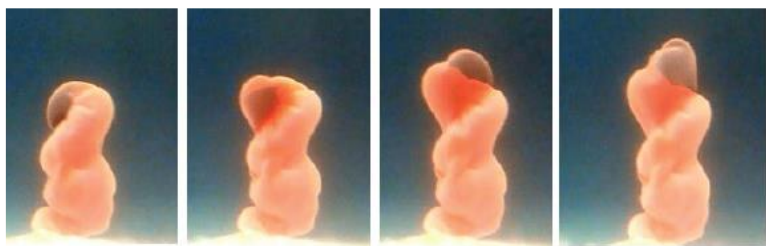
Chemical Machines. Self-building complex towers. $\text{Al}^{3+} - \text{OH} - \text{CO}_3^{2-}$

This system has presented many different structures in time. First is self-formation of Solomonic Columns that climb itself forming spiral. Next step where solution reaches the surface, the different structures are formed. They are channels A and B. Next steps is formation of fingers C and D. The D fingers growth from tip to crescent and from crescent to tip. This process is creating many times. The final structures are streams E with 0.1 mm long and length about few cm.

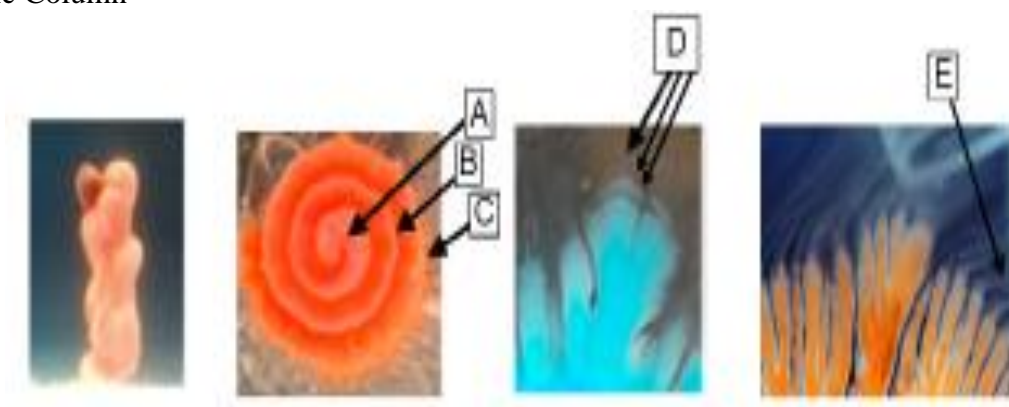
The next system is a cell that is growth by itself and forming legs that are moving the cell. On the top is jumping. On the bottom is a cell that is creating another attached cell that is moving and become bigger when mother cell is disappearing.

The last cell has membrane with CO_2 bubbles inside. The cells are moving up and down and shrinking in this process. If bubble is released is the cell is moving down and is cell is shrinking is moving up. It is great example of a Chemical Machine. (It is reproduced from Langmuir, 2014, 30, 5727-5731 with permission of American Chemical Society)

In this system we observed self-creations where simple chemical systems may produce many different Chemical Machines. Many Machines can switch many different Machines.



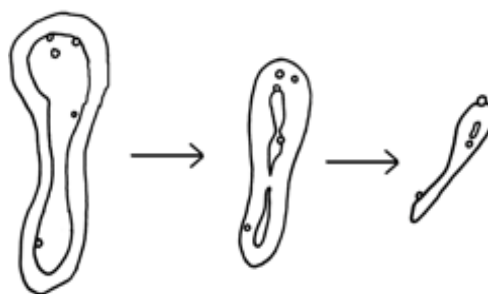
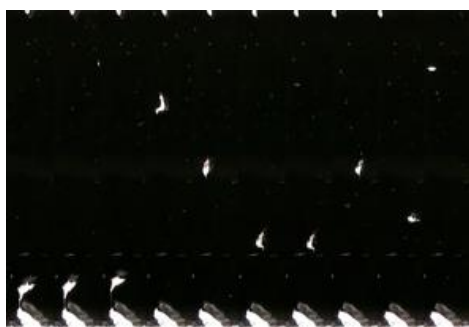
Solomonic Column



Spirals and Flowers



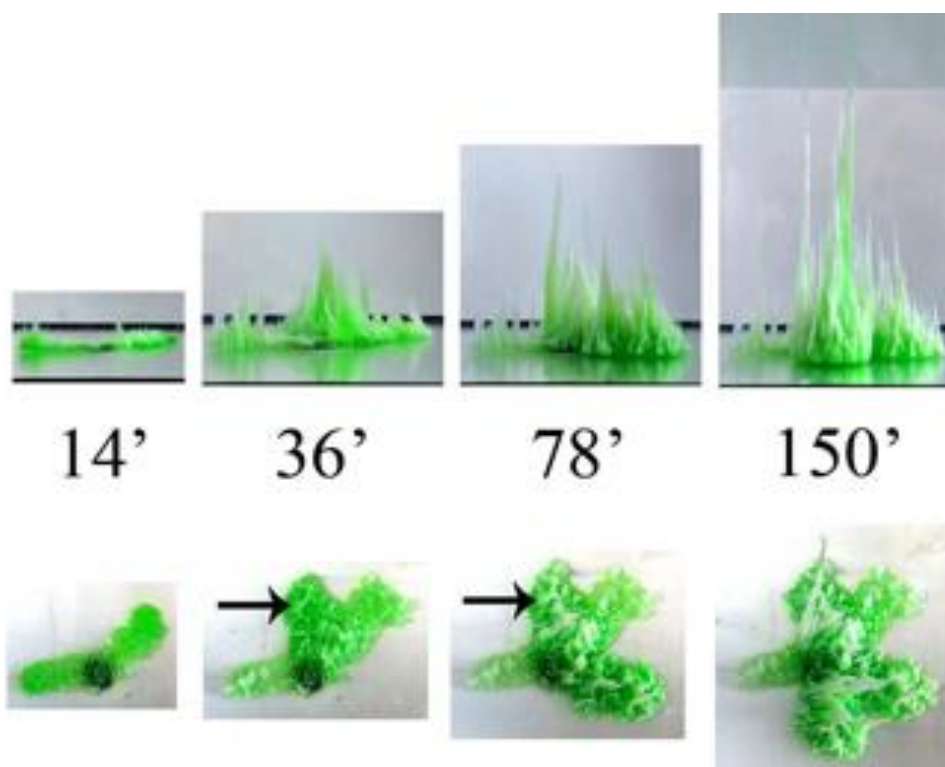
Chemical Machines



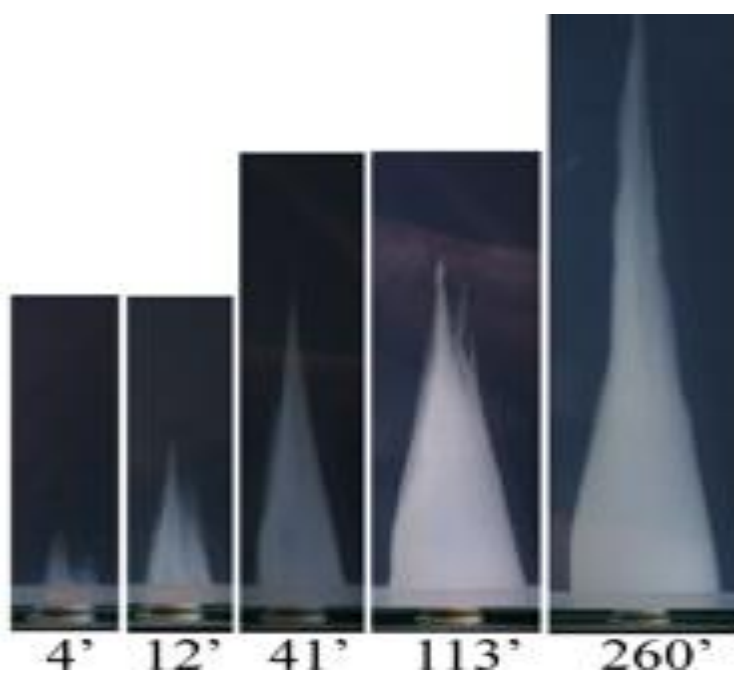
Cell membrane with CO₂ inside

Self-creation of multicellular chemical organism. Behaviors as a whole. AlCl₃ - SiO₄

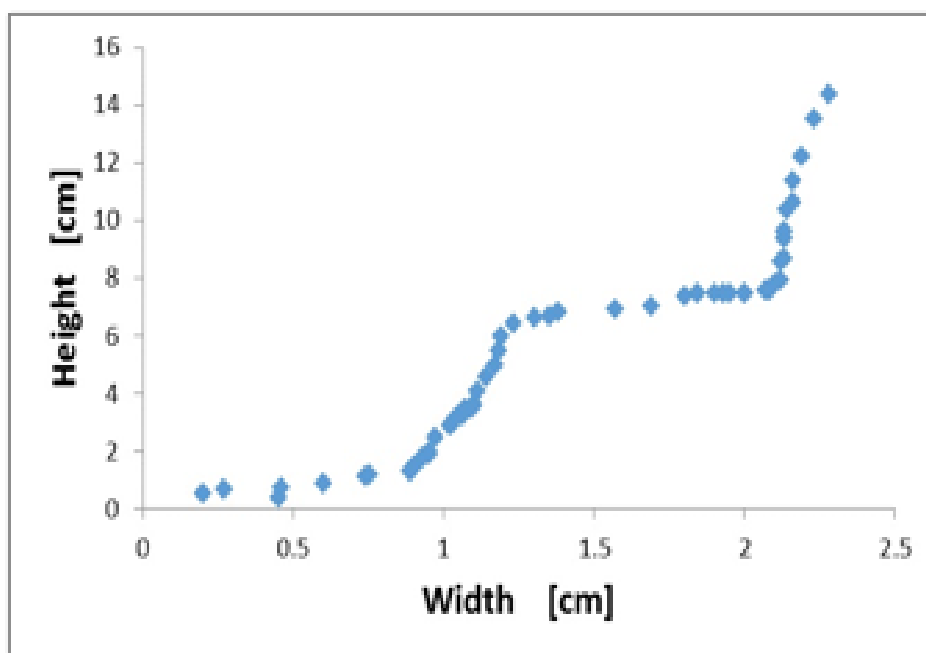
Many towers are building city and metropolis. One tower stop building and new is building itself. At the beginning the new structure growing horizontally, next is growing vertically and it is repeating. When growth is critical then new cell will growth. In the systems always tree cells growth at the same time. The cells communicate between itself. When one is dying then next is growing. It is property of chemical systems.



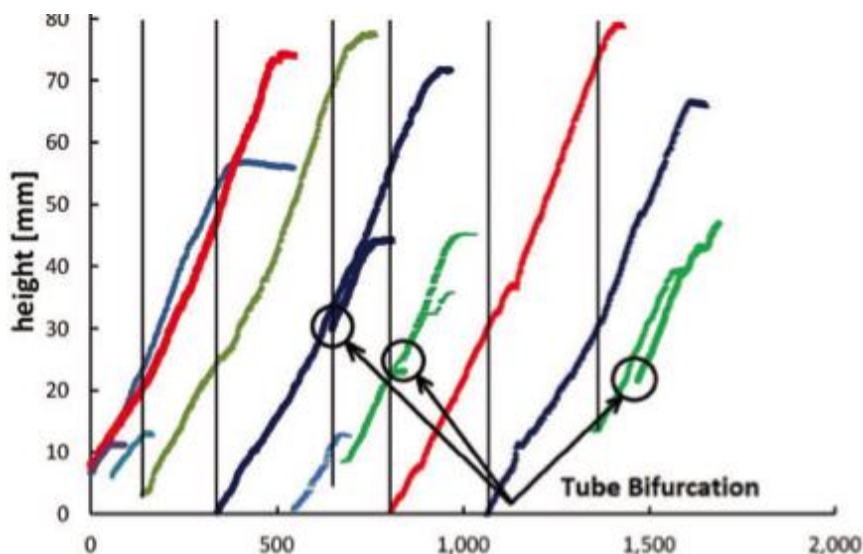
Growth of chemical metropolis from side and top



Growth of pyramid



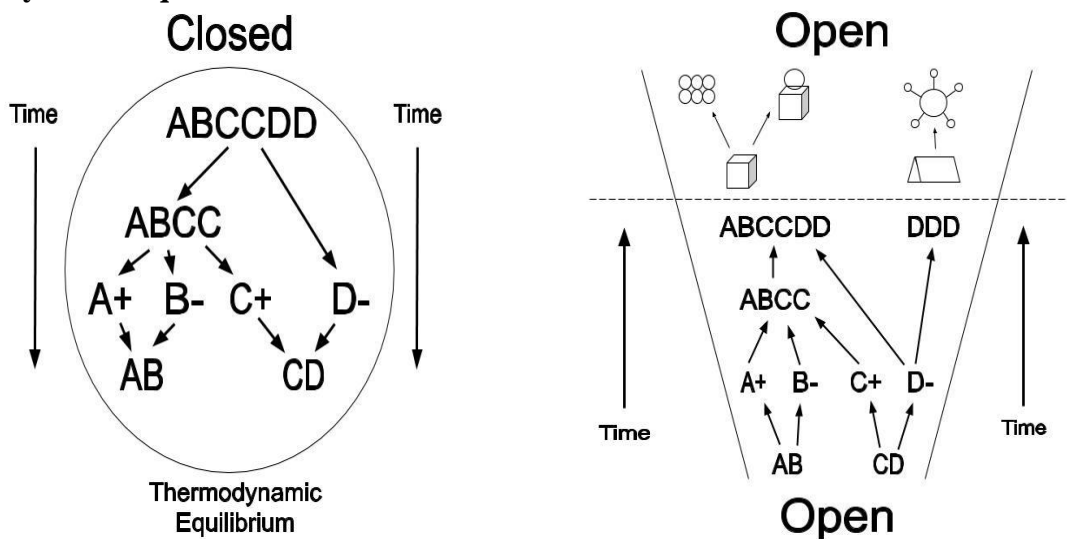
Growth of pyramid



Vertical growth of cells.

The first Law of thermodynamic states: everything cannot be self-creating or destroyed in isolated system. On left are closed systems that are moving to Thermodynamic Equilibrium. On the right, with open systems and with energy and mass, complex structures continuously create itself.

Thermodynamic Equilibrium and Law of Creation.



On the left Th. Eq. on write Law of Creation

On the right-chemical reactions were formed. They can form chemical cells, multicellular structures, chemical Machines, self-growing cities These new chemical complex processes created itself very fast and in simple temperatures.

DISCUSSION

1. Using two simple compounds the self-create will grow to infinity.
2. If there will be no Law of chemistry, there will be no biology.
3. Biology is relatively known. Self-create is known very little.
4. The Law of Self-creation is controlling development of the Universe.

REFERENCES

- [1] J. Maselko, J. Pantaleone. Universal Chemical Machine: Continuous Increase of Complexity and Chemical Evolution. *Journal of Systems Chemistry*. 2019/vol7/ 1-52, 38-51
- [2] J. Maselko, Self-creation of chemical structures. Experimental study. *Nature Journal*, Accepted. May 2021

A - Chemical Thermodynamics

THERMODYNAMIC PROPERTIES OF PURINE

A.V. Knyazev, A.S. Shipilova, S.S. Knyazeva, A.M. Kusutkina,
A.A. Panova, A.S. Logacheva, E.V. Gusarova

*Chemistry Department, Lobachevsky State University of Nizhni Novgorod Gagarin Av.
23/2,603950, Nizhni Novgorod, Russia (knyazevav@gmail.com)*

ABSTRACT

In the present work the temperature dependence of the molar heat capacity for purine CAS 120-73-0 has been measured for the first time over the temperature range from 5 K to 350 K and $p = 0.1$ MPa by the precision adiabatic vacuum calorimeter. Based on the experimental data, the thermodynamic functions of the sample have been determined for the range $T = (0 - 350)$ K. Using combination of the adiabatic and combustion calorimetry results the thermodynamic functions of formation of purine at $T = 298.15$ K and $p = 0.1$ MPa have been calculated. The low-temperature X-ray diffraction was used for the determination of sample thermal expansion coefficients.

INTRODUCTION

A purine is an aromatic heterocyclic compound composed of carbon and nitrogen. Purines include adenine and guanine, which participate in DNA and RNA formation. Purines are also constituents of other important biomolecules, such as ATP, GTP, and can serve as cofactors, such as NADH (reduced form nicotinamide adenine dinucleotide) and coenzyme A. [1]. A limited amount of thermodynamic information is available on the fundamental properties of the purine bases. The goals of this work include calorimetric determination of the standard thermodynamic functions of purine with the purpose of improved description of biochemical and industrial processes with its participation.

EXPERIMENTAL

The studied sample of purine (CAS: 120-73-0) was purchased from Sigma-Aldrich. An x-ray diffraction pattern of purine was obtained in the 2θ range from 5° to 60° on a XRD-6000 X-ray diffractometer from Shimadzu (CuK α radiation, scanning step 0.02°) to identify the phase. X-ray data and estimation of the impurity content in the studied substance allowed us to conclude that the investigated sample is an individual crystal compound (Pna21, $a = 1.555$ nm, $b = 0.937$ nm, $c = 0.366$ nm) [2].

To measure the molar heat capacity of the studied substances at $p = 0.1$ MPa in the temperature range from 5 K to 350 K a BKT-3.0 automatic precision adiabatic vacuum calorimeter with discrete heating, was used. The calorimeter design and the operation procedure are described earlier [3].

To study the thermal expansion of studied sample in the temperature range from 150 K to 450 K, a powder diffractometer XRD-6000 Shimadzu described earlier and the low temperature attachment TTK- 450 Anton Paar were used. X-ray diffraction analysis was performed using the XRAY software [4].

RESULTS AND DISCUSSION

Molar heat capacity

The measurements were carried out in temperature range between 5 K and 350 K. The molar heat capacity of the sample varied from 20% to 50% of the total heat capacity of calorimetric ampoule + substance over the investigated temperature range.

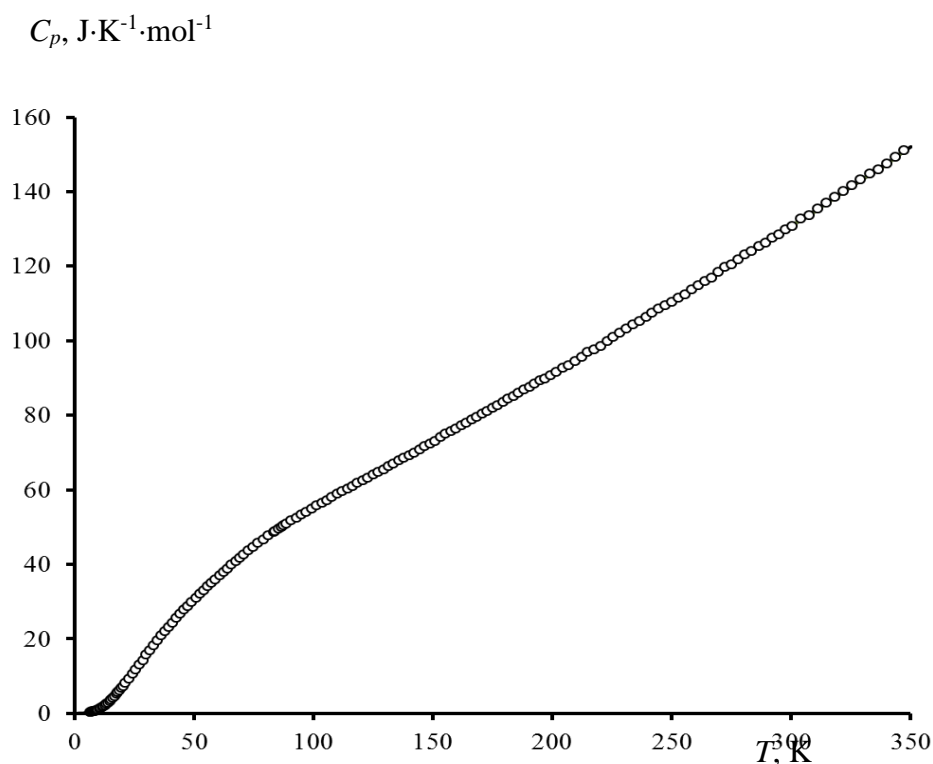


Figure 1. Temperature dependence of molar heat capacity of purine.

The experimental points in the investigated temperature range were fitted by means of the least-squares method and polynomial equations of the molar heat capacity versus temperature.

The experimental values of the molar heat capacity of purine over the range from 5 to 350 K and the averaging $C_p^\circ = f(T)$ plot are presented in Figure 1. The molar heat capacity C_p° of this substance gradually increases with rising temperature and does not show any peculiarities.

The experimental data were used to calculate standard thermodynamic functions, namely the heat capacity, enthalpy $H^\circ(T) - H^\circ(0)$, entropy $S^\circ(T) - S^\circ(0)$ and Gibbs energy $G^\circ(T) - H^\circ(0)$, in the temperature range from 0 K to 350 K. The standard entropy of formation $\Delta_f S^\circ$ of the compounds under study at 298.15 K were calculated from the absolute entropy of the compound and the corresponding simple substances.

Table 1. Thermodynamic properties of formation and absolute entropy of purine ($T = 298.15$ K, $p = 0.1$ MPa)

$\Delta_f H^\circ(298)$ (kJ/mol)	S° (J·K ⁻¹ ·mol ⁻¹)	$\Delta_f S^\circ(298)$ (J/(mol·K))	$-\Delta_f G^\circ(298)$ (kJ/mol)
169.41 ± 2.65 [5]	140.9 ± 0.5	-532 ± 7	328 ± 3

Low-temperature X-ray diffraction

Calculation of the thermal expansion coefficients was performed in the DTC (Deformation Tensor Computing) software package developed in the St. Petersburg State University [6]. To construct 2D figures of thermal expansion, the software complex KTR-B2 was used.

Table 2. Unit cell parameters and coefficients of thermal expansion of purine.

T (K)	a (nm)	b (nm)	c (nm)	V (nm ³)
150	1.5591 (19)	0.9418 (13)	0.3648 (5)	0.5356 (12)
300	1.5598 (16)	0.9408 (12)	0.3655 (5)	0.5363 (10)
450	1.5585 (14)	0.9395 (10)	0.3659 (4)	0.5357 (9)
$\alpha \cdot 10^5$ (K ⁻¹)	0.06	-0.63	1.01	0.43

The unit cell parameters and the coefficients of thermal expansion of the investigated sample are presented in the Table 2. Thermal expansion of purine is anisotropic, and its coefficient of thermal expansion depends on temperature. The greatest thermal deformations are observed along the crystallographic axis c , due to the weakest hydrogen bonds along this direction. The anisotropy of thermal expansion is demonstrated most clearly by the 2D figures of thermal expansion values shown in Fig. 2.

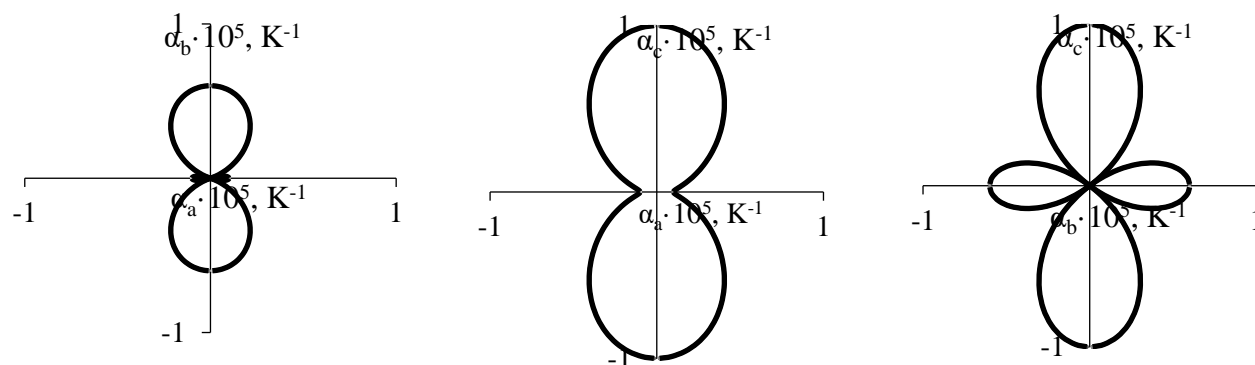


Figure 2. 2D figures of thermal expansion values of purine.

CONCLUSION

The general aim of these investigations was to report the results of the thermodynamic study of purine and to study the thermal expansion of this compound along with calculation of its coefficients. The molar heat capacity of this sample is measured in the temperature range from 5 K to 350 K and the appropriate thermodynamic functions, calculated.

Acknowledgement

The work was supported by the Ministry of Science and Higher Education of the Russian Federation (Project Part of the State Assignment No 0729-2020-0039).

REFERENCES

- [1] A. M. Pedley, S. J. Benkovic, Trends in Biochemical Sciences, 2017, 42 (2), 141-154.
- [2] D. G. Watson, The crystal and molecular structure of purine, Acta Crystallographica, 1965, 19, 573-580.
- [3] R. H. Stern, Journal of Clinical Lipidology, 2007, 1, 191–193.
- [4] L. M Kovba, V.K. Trunov, X-ray analysis. Moscow: Moscow State University (1976).
- [5] D. R. Kirklin, E.S. Domalski, J. Chem. Thermodyn., 1984, 16, 633-641.
- [6] R. I. Belousov, S.K. Filatov, Glass Physics and Chemistry, 2007, 33(3), 271-275.

LOW-TEMPERATURE STUDIES OF AURIVILLIUS PHASE $\text{Bi}_5\text{Ti}_3\text{MnO}_{15}$

O.V. Krashennikova, A.V. Knyazev, E.V. Syrov and A.V. Barykin

Lobachevsky State University of Nizhni Novgorod, Gagarin Prospekt 23/2, 603950 Nizhni Novgorod, Russia (okkraska@gmail.com)

ABSTRACT

Manganese-containing multiferroic Aurivillius layered perovskite was synthesized and characterized by XRD and XRF. The obtained compound is isostructural to its ferrous analog. Second order insulator-metal phase transition was detected at 126 K using low-temperature XRD and DSC. Heat expansion of the material was studied in the temperature range of 80-400 K.

INTRODUCTION

Multiferroics have attracted much attention recently, mostly because of their potential application as detectors, power converters, and memory devices due to their ferroelectric and magnetic properties. Ecological reasons push the development of lead-free ceramic multi-component solid solutions based on relaxor ferroelectrics with special ferroelectric and magnetic properties.

Aurivillius phases are one of the families of layered perovskite structure type, and they have been known for their multiferroic properties [1]. They can be described with general chemical formula $\text{A}_{n-1}\text{Bi}_2\text{B}_n\text{O}_{3n+3}$, where $\text{A} = \text{Na}^+, \text{K}^+, \text{Ca}^{2+}, \text{Sr}^{2+}, \text{Ba}^{2+}, \text{Pb}^{2+}, \text{Bi}^{3+}$ and Ln^{3+} ; $\text{B} = \text{Ti}^{4+}, \text{Cr}^{3+}, \text{Ga}^{3+}, \text{Mn}^{4+}, \text{Fe}^{3+}, \text{Nb}^{5+}, \text{Ta}^{5+}$ and W^{6+} . The crystal structure of Aurivillius phases consists of n perovskite-like layers $[\text{A}_{n-1}\text{B}_n\text{O}_{3n+1}]^{2-}$ stacking between rock-salt-like layers $[\text{Bi}_2\text{O}_2]^{2+}$. The number of layers n ranges from 1 to 9. The first Aurivillius phase discovered to be ferroelectric was $\text{PbBi}_2\text{Nb}_2\text{O}_9$ in 1962 [2]. Many phases of this family with various electromagnetic properties were discovered since, including multiferroic system $\text{Bi}_4\text{Ti}_3\text{O}_{12} - \text{BiFeO}_3$ [3].

In this system, physical properties and stability are varying with the increasing number of layers n . It was established that thermal stability decreases with n increasing [3]. Moreover, orthorhombic – tetragonal phase transitions occur upon heating in the same temperature range as usual perovskites ferroelectric – paraelectric transition (Curie temperature). Curie temperatures in this system increasing for $1 \leq n \leq 3$, decreasing for $4 \leq n \leq 6$ and plateauing for $n > 6$ [3]. Compound $\text{Bi}_5\text{Ti}_3\text{FeO}_{15}$ with $n = 4$ demonstrates quite strong magnetoelectric behavior despite the fact that it is paramagnetic at room temperature. The nature of such electromagnetic properties is yet to be determined. Doping or changing d-elements in various atomic positions can dramatically change the crystal structure and electromagnetic properties of the materials. Even though the structure and properties of Fe-compound are studied, almost no data are available in the literature for the Mn-containing phase, which can be promising multiferroic material. To fill this gap, $\text{Bi}_5\text{Ti}_3\text{MnO}_{15}$ was synthesized and its low-temperature properties were studied.

METHODS

For the synthesis, stoichiometric quantities of Bi_2O_3 , TiO_2 , and Mn_2O_3 (Sigma-Aldrich) were grounded, pressed into pellets, and annealed at 1173 K for 12 h to perform the following reaction:



The phase purity of the obtained sample was studied using powder XRD on Shimadzu XRD-6000, Cu $\text{K}\alpha_{1,2}$ irradiation, 30 kV, 30 mA on the tube; $10-60^\circ 2\theta$ range; 0.02° step; $2^\circ/\text{min}$ scan speed.

The chemical composition and purity of the obtained sample were studied using wavelength dispersive X-ray spectroscopy on Shimadzu XRF-1800. Bi $L\alpha$, Ti $K\alpha$, Mn $K\alpha$ lines were measured 3 times from sample pellet in a vacuum with 40 kV, 50 mA on Rh-anode tube using SC detector. Fundamental parameters with a single standard calibration method was used for the oxide matrix corrections [4].

Low-temperature XRD studies were carried out using Anton Paar HTK-450 chamber on Shimadzu XRD-6000 diffractometer in the temperature range 80-400 K at 1 °/min scan speed. Cell parameters for every temperature were refined using UnitCell software. Thermal expansion coefficients were calculated using DTC software.

Differential scanning calorimetry measurements were carried out using Netzsch DSC 204 F1 Phoenix in the temperature range 100-400 K in the Ar atmosphere at 10 °/min speed with liquid nitrogen as a cooling agent.

RESULTS AND DISCUSSION

XRD phase analysis proved that the obtained sample is monophasic Aurivillius phase with an orthorhombic $Fmm2$ space group with unit cell parameters $a = 0.5397(2)$ nm, $b = 0.5425(2)$ nm, $c = 4.213(1)$ nm. The crystal structure of $\text{Bi}_5\text{Ti}_3\text{MnO}_{15}$ consists of stacking layers of $[\text{Bi}_3\text{Ti}_3\text{MnO}_{13}]^{2-}$ interchanging with $[\text{Bi}_2\text{O}_2]^{2+}$ slabs (Figure 1). Therefore, the synthesized compound is isostructural to $\text{Bi}_5\text{Ti}_3\text{FeO}_{15}$.

XRF analysis showed that the sample has 99.7 % purity (metal trace basis). The chemical composition of the obtained compound is close to theoretical: 78.1 mass. % Bi_2O_3 (theoretical 78.5); 16.4 mass. % TiO_2 (theoretical 16.2); 5.5 mass. % Mn_2O_3 (theoretical 5.3). Therefore, the measured chemical formula for the obtained compound can be written as $\text{Bi}_{4.9\pm 0.2}\text{Ti}_{3\pm 0.2}\text{Mn}_{1\pm 0.2}\text{O}_{14.9\pm 0.6}$. A slight lack of bismuth oxide is probably caused by its volatility at a high temperature of synthesis.

Low-temperature XRD studies show a leap of unit cell parameters in the temperature range of 125 – 150 K (Figure 2). Parameters before and after phase transition are fitting well with linear functions. No abrupt changes in the XRD pattern led us to conclude that this transition is happening within orthorhombic symmetry. According to literature data on resistivity measurements, the observed effect can be explained as an insulator-metal phase transition [5]. $\text{Bi}_5\text{Ti}_3\text{MnO}_{15}$ resistivity drops significantly below 126 K, right after the detected phase transition. Heat expansion coefficients were calculated for all measured temperatures. Heat expansion along the c axis is greater than along a or b axes in the temperature range of 80-150 K; anisotropy of heat expansion weakening after the phase transition.

The measured DSC curve corresponds well with XRD and literature data (Figure 3). A slight exo-effect on the curve peaking at 126 K demonstrates the presence of a phase transition. All observations mentioned above led us to conclude that the observed phenomenon is the second-order phase transition.

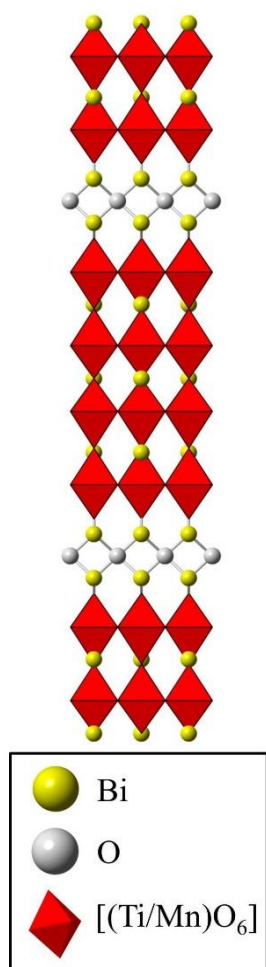


Figure 1. Crystal structure of Bi₅Ti₃MnO₁₅

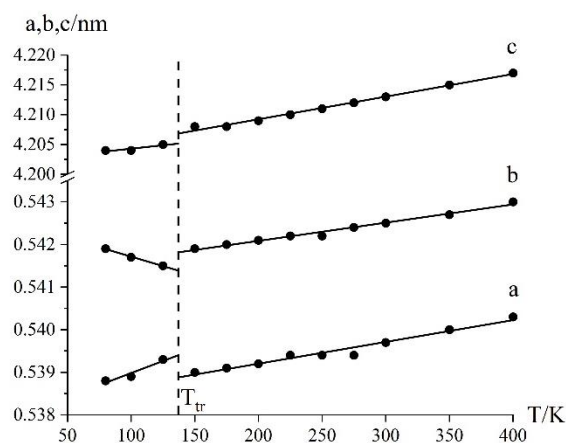


Figure 2. Unit cell parameters vs. temperature of Bi₅Ti₃MnO₁₅

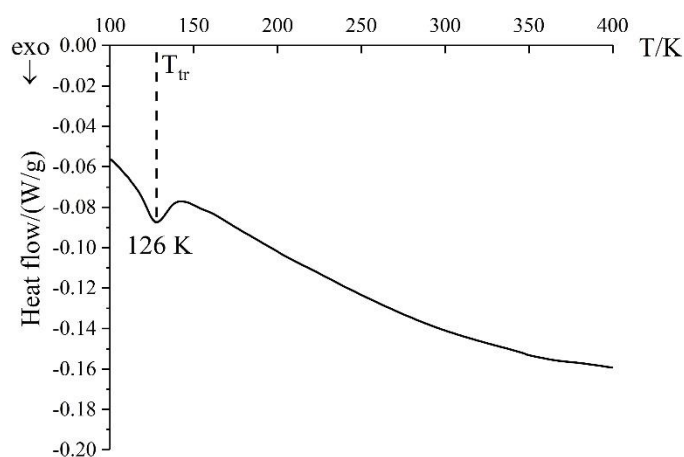


Figure 3. DSC curve of Bi₅Ti₃MnO₁₅

CONCLUSION

Therefore, synthesis, characterizing, and low-temperature measurements of Aurivillius phase Bi₅Ti₃MnO₁₅ were conducted. Conventional solid state reaction between respective oxides yields monophasic and chemically pure compound, isostructural to Bi₅Ti₃FeO₁₅ phase. Low-temperature heat expansion behavior was studied. Low-temperature insulator-metal phase transition within the same symmetry was detected by XRD and DSC measurements at 126 K, corresponding well with literature data on compound resistivity.

Acknowledgement

The work was supported by the Ministry of Science and Higher Education of the Russian Federation (Project Part of the State Assignment No 0729-2020-0039).

REFERENCES

- [1] B. Aurivillius, Mixed bismuth oxides with layer lattices. I. The structure type of CaNb₂Bi₂O₉, Arkiv för Kemi, V. 1 (1949) 463-480
- [2] E.C. Subbarao, A family of ferroelectric bismuth compounds, J. Phys. Chem. Solids, V.23 (1962) 665-676.

-
- [3] M. Krzhizhanovskaya, S. Filatov, V. Gusarov, P. Paufler, Aurivillius phases in the $\text{Bi}_4\text{Ti}_3\text{O}_{12}/\text{BiFeO}_3$ system: Thermal behaviour and crystal structure, *Z. Anorg. Allg. Chem.*, V.631 (2005) 1603-1608.
- [4] R. Sitko, B. Zawisza, Quantification in X-Ray Fluorescence Spectrometry, Chapter In book: *X-Ray Spectroscopy*, (2012) 137-162
- [5] M. Mahesh Kumar, A. Srinivas, G.S. Kumar, S.V. Suryanarayana, Synthesis and physical properties of $\text{Bi}_5\text{Ti}_3\text{MnO}_{15}$, *Solid State Comm.*, V. 104 No.12 (1997) 741-746

CONTRIBUTION OF DIFFERENT INTERACTIONS TO THE EXCESS GIBBS ENERGY OF MIXING IN AQUEOUS ELECTROLYTE SOLUTIONS

D. Ž. Popović¹, T. Ivanović², J. M. Miladinović³, Z. P. Miladinović⁴

¹ *Innovation Centre Faculty of Technology and Metallurgy, University of Belgrade, Karnegijeva 4, 11 001 Belgrade, Serbia (dpopovic@tmf.bg.ac.rs)*

² *Institute for Multidisciplinary Research, University of Belgrade, Kneza Višeslava 1, 11 030 Belgrade, Serbia*

³ *Faculty of Technology and Metallurgy, University of Belgrade, Karnegijeva 4, 11 001 Belgrade, Serbia*

⁴ *Institute of General and Physical Chemistry, Studentski trg 12-16, 11 000 Belgrade, Serbia*

ABSTRACT

The thermodynamic properties of the mixed electrolyte solutions are conveniently described in terms of excess quantities. The excess Gibbs energy of mixing, presents the difference between the excess free energy of a mixed electrolyte solution and free energies of the individual binary electrolyte solutions at the same temperature, pressure and total ionic strength. In this paper the excess Gibbs energy of mixing is calculated for series of mixed electrolyte solutions and possible pairs, triplets, quads or even higher order multiplets were discussed in respect to Scatchard's mixing parameter values.

INTRODUCTION

In thermodynamics of electrolyte solutions, for aqueous mixture of two electrolytes the excess free energy can be expressed as the sum of the contributions of single electrolyte solutions at the same ionic strength as the mixed one, plus excess free energy of mixing given as an expansion in the ionic strength fractions of electrolyte. The main contribution to the excess free energy of mixing appears due to interactions of pairs and triplets of ions. The contribution of triplet interactions are often considered negligible compared to binary ones. If a solution contains an electrolyte which tends to form complexes or has strong hydrophobic character, the contribution of higher-order multiplets to the excess free energy of mixing must be taken into account, in addition to the contributions due to pairs or pairs and triplets.

THEORY AND MODEL

The model used in calculations is Scatchard's neutral-electrolyte model [1], generally capable of representing osmotic coefficients of mixed electrolyte solutions accurately, given enough mixing parameters. This approach treats all electrolytes present formally as if they were completely dissociated. In the case of mixtures of strong electrolytes, the binary-solution mixing approximation can sometimes provide a fairly reliable estimate of the osmotic coefficients of the ternary solutions. The excess free energy of mixing for the mixed solution of A and B electrolytes, in terms of the Scatchard parameters is given by:

$$\frac{\Delta G_m^{\text{ex}}}{RT} = I y_A y_B \left[B_{AB}^{(0)} + (y_A - y_B) B_{AB}^{(1)} + (y_A - y_B)^2 B_{AB}^{(2)} + \dots + (y_A - y_B)^n B_{AB}^{(n)} \right] \quad (1)$$

where terms B_{AB} represent:

$$B_{AB}^{(n)} = \sum_{k=n+1}^{k'} \frac{I^k}{k} b_{AB}^{(n,k)} \quad \text{for } n \geq 0 \quad (2)$$

In previous relations, y is the ionic strength fraction of electrolyte A or B, I is the ionic strength of the mixed solution and b_{AB} are Scatchard's mixing parameters. The b_{AB} parameters are found by least squares method applied to either the osmotic coefficients or the activity coefficient data for the mixed systems containing A and B electrolytes. If we rearrange the terms in excess free energy of mixing through possible pairs, triplets, quads or even higher order multiplets (HOM), we obtain:

$$\frac{\Delta G_m^{\text{ex}}}{RT} = \left(\frac{\Delta G_m^{\text{ex}}}{RT}\right)_{\text{pairs}} + \left(\frac{\Delta G_m^{\text{ex}}}{RT}\right)_{\text{triplets}} + \left(\frac{\Delta G_m^{\text{ex}}}{RT}\right)_{\text{quads}} + \dots + \left(\frac{\Delta G_m^{\text{ex}}}{RT}\right)_{\text{HOM}} \quad (3)$$

where:

$$\left(\frac{\Delta G_m^{\text{ex}}}{RT}\right)_{\text{pairs}} = I^2 y_A y_B b_{AB}^{(0,1)} \quad (4a)$$

$$\left(\frac{\Delta G_m^{\text{ex}}}{RT}\right)_{\text{triplets}} = \left(I^3/2\right) y_A y_B \left[b_{AB}^{(0,2)} + (y_A - y_B) b_{AB}^{(1,2)} \right] \quad (4b)$$

$$\left(\frac{\Delta G_m^{\text{ex}}}{RT}\right)_{\text{quads}} = \left(I^4/3\right) y_A y_B \left[b_{AB}^{(0,3)} + (y_A - y_B) b_{AB}^{(1,3)} + (y_A - y_B)^2 b_{AB}^{(2,3)} \right] \quad (4c)$$

$$\left(\frac{\Delta G_m^{\text{ex}}}{RT}\right)_{\text{HOM}} = \left(I^{n+2}/n+1\right) y_A y_B \left[b_{AB}^{(0,n+1)} + (y_A - y_B) b_{AB}^{(1,n+1)} + \dots + (y_A - y_B)^n b_{AB}^{(n,n+1)} \right] \quad (4d)$$

RESULTS AND DISCUSSION

Excess Gibbs energy of mixing (Figure 1) was calculated by relation (1), for series of mixed electrolyte solutions at temperature 298.15 K. Scatchard's parameters (Table 1.) for each mixed solution were taken from our previous work on osmotic coefficients treatment[2-7].

Table 1. Scatchard's mixing parameters for different electrolyte systems, standard deviation of fitting the osmotic coefficient data for the system, s.d. (ϕ), the solution ionic strength interval, for which the parameters are valid (m^0 stands for standard molality, $1 \text{ mol}\cdot\text{kg}^{-1}$).

System	$b_{AB}^{(0,1)} (m^0)$	$b_{AB}^{(0,2)} (m^0)^2$	s.d. (ϕ) 10^3	Ionic strength interval ($\text{mol}\cdot\text{kg}^{-1}$)
{yKCl+(1-y)K ₂ HPO ₄ }(aq)[2]	-0.03724	0.047634	7.8	2-12
{yKNO ₃ +(1-y)K ₂ HPO ₄ }(aq)[3]	-0.028196	0.081518	4.2	2.5-6.5
{yKBr+(1-y)K ₂ HPO ₄ }(aq)[4]	-0.020035	0.020422	8.0	3-10
{yK ₂ SO ₄ +(1-y)K ₂ HPO ₄ }(aq)[5]	-0.010654	0.0062619	8.0	1.2-2
{yKH ₂ PO ₄ +(1-y)K ₂ HPO ₄ }(aq)[6]	-0.0025	0.0122	1.6	0.4-3.4
{yNa ₂ HPO ₄ +(1-y)K ₂ HPO ₄ }(aq)[7]	0.0084145	0.0	0.9	0.9-1.06

If pairwise interactions are truly the only interactions occurring in a mixed solution, then $b_{AB}^{(0,1)}$ parameter will be the only one required to fit the data, and the total excess free energy of mixing will be equal to $(\Delta G_m^{ex} / RT)_{pairs}$. This is the case with the system $\{y\text{Na}_2\text{HPO}_4 + (1-y)\text{K}_2\text{HPO}_4\}(\text{aq})$ where standard deviation of the fit is of 10^{-4} order even with only one mixing parameter.

If the sole use of $b_{AB}^{(0,1)}$ is found to be inadequate in fitting the data, then there must also be triplet interactions in the solution. Therefore, both $b_{AB}^{(0,2)}$ and $b_{AB}^{(1,2)}$ as well as $b_{AB}^{(0,1)}$ must be used in fitting the data, as it is the case for the systems $\{y\text{KCl} + (1-y)\text{K}_2\text{HPO}_4\}(\text{aq})$, $\{y\text{KBr} + (1-y)\text{K}_2\text{HPO}_4\}(\text{aq})$ and $\{y\text{K}_2\text{SO}_4 + (1-y)\text{K}_2\text{HPO}_4\}(\text{aq})$ where the standard deviation of the fit by using just two mixing parameters $b_{AB}^{(0,1)}$ and $b_{AB}^{(0,2)}$ is still relatively, high. Gibbs energy of mixing for these systems, specially with $\{y\text{KCl} + (1-y)\text{K}_2\text{HPO}_4\}(\text{aq})$, changes evidently with the increase of solution ionic strength reflecting possible triplet interactions.

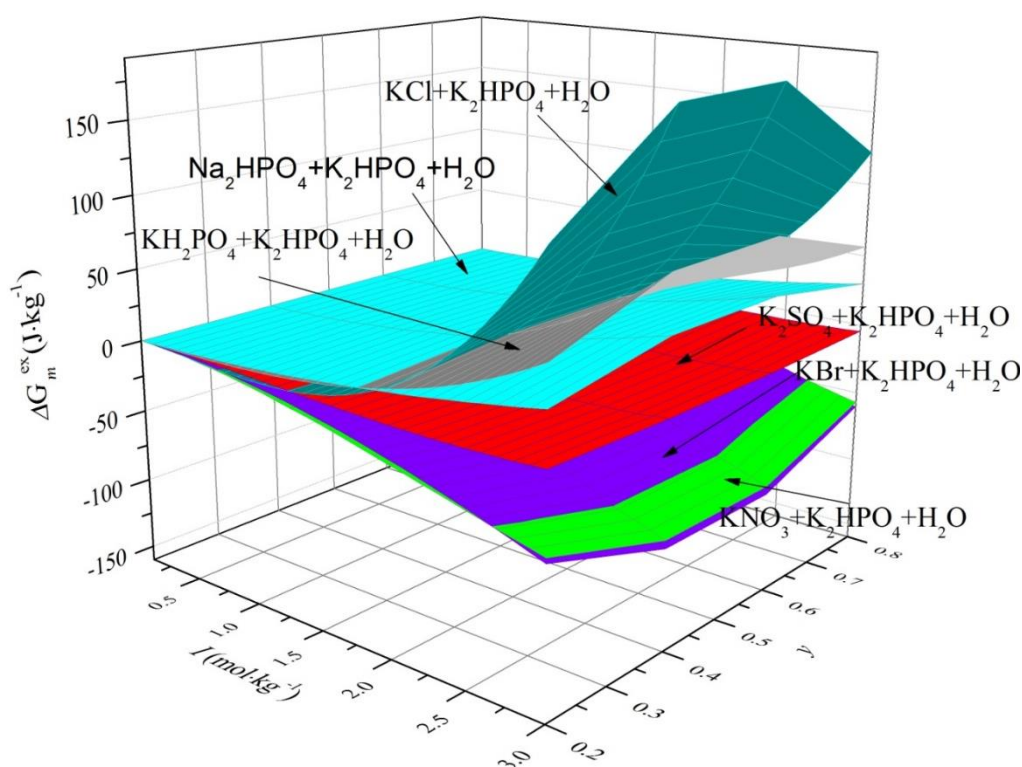


Figure 1.: Excess Gibbs energy of mixing per kilogram of solvent (water) for different mixed electrolyte solutions at $T = 298.15$ K in respect to solution ionic strength, I , and ionic strength fraction, y .

CONCLUSION

By obtaining detailed thermodynamic data on excess Gibbs energy of mixing for the aqueous electrolyte systems, using Scatchard's parameters, significant information regarding specific ion interactions can be obtained.

Acknowledgement

This work was supported by the Ministry of Education, Science and Technical Development of the Republic of Serbia (Contract No. 451-03-9/2021-14/200287).

REFERENCES

- [1] G. Scatchard, *J. Phys. Chem.*, 1961, 83, 2636-2642.
- [2] Daniela Z. Popović, Jelena Miladinović, Milica D. Todorović, Milorad M. Zrilić, Joseph A. Rard, *J. Chem. Thermodyn.*, 2011, 43, 1877-1885.
- [3] Daniela Z. Popović, Jelena Miladinović, Zoran P. Miladinović, Branislav B. Ivošević, Milica D. Todorović, Joseph A. Rard, *J. Chem. Thermodyn.*, 2012, 55, 172-183.
- [4] Daniela Z. Popović, Jelena Miladinović, Zoran P. Miladinović, Snežana R. Grujić, Milica D. Todorović, Joseph A., *J. Chem. Thermodyn.*, 2013, 62, 151-161.
- [5] Daniela Ž. Popović, Jelena Miladinović, Joseph A. Rard, Zoran P. Miladinović, Snežana R. Grujić, *J. Chem. Thermodyn.*, 2014, 79, 84-93.
- [6] T. Ivanović, Daniela Ž. Popović, Jelena Miladinović, Joseph A. Rard, Zoran P. Miladinović, Ferenc T. Pastor, *J. Chem. Thermodyn.*, 2020, 142, 105945.
- [7] Daniela Ž. Popović, Jelena Miladinović, Joseph A. Rard, Zoran P. Miladinović, Snežana R. Grujić, *J. Solution Chemistry*, 2016, 45, 1261-1287.

*B - Spectroscopy,
Molecular Structure,
Physical Chemistry of Plasma*

INSIGHTS FROM NUMERICALLY EXACT APPROACHES FOR THE CALCULATION OF THE ROVIBRATIONAL ENERGY STRUCTURE OF TRI- AND TETRATOMIC MOLECULES

M. Mladenović

*MSME, Univ Gustave Eiffel, CNRS UMR 8208, Univ Paris Est Créteil,
F-77454 Marne-la-Vallée, France (mirjana.mladenovic@univ-eiffel.fr)*

ABSTRACT

Numerically exact rotation-vibration solutions to the molecular Schrödinger equation for tri- and tetratomic molecules are applied. As a first example, the torsional structure of HOCO is analyzed using several adiabatic projection techniques. The torsional structure is found to exhibit two limiting cases associated with oscillator and rotor spectral patterns. Combining full-dimensional rovibrational calculations for N_2H^+ with the available experimental values for B_0 , the r_α and r_c structures of the ion are additionally determined and analyzed.

INTRODUCTION

Numerical approaches for full-dimensional rovibrational calculations are valuable tools for achieving a complete full-dimensional physical description of molecular behavior for a given potential energy surface (PES) constructed within the Born-Oppenheimer approximation. To obtain the maximum information possible in such a calculation, a good functional representation for the potential is desirable, satisfying at least the fundamental symmetries [1]. This request is not fulfilled by commonly used quartic force fields, based on near-equilibrium arrangements. With the help of full-dimensional rovibrational calculations, we may not only assess the validity of traditional methods, but also provide a hint at possible causes for their limitations.

METHODS

Methods for full-dimensional rovibrational calculations, which I have been developing for general tri- and tetratomic molecules, use the exact body-fixed kinetic energy operator in combination with flexible basis sets and efficient computational strategies [2,3]. The computation makes no approximation beyond the concept of the potential energy surface, involving no dynamical approximations and no re-expansion of the potential energy function. The computed rovibrational energy levels are quantitatively analyzed by several adiabatic projection techniques, which provide detailed information on anharmonic and coupling/mixing effects, allowing also for automatic quantum number assignments. The quantum state character correlation scheme is employed to monitor the evolution of the adiabatic representation [3].

RESULTS AND DISCUSSION

The hydrocarboxyl radical, HOCO, is an intermediate in the reaction between hydroxyl radical, HO, and carbon monoxide, CO, known to exhibit a significant nonstatistical (non-Arrhenius) behavior. The internal dynamics of HOCO is dominated by the torsional (out-of-plane) motion.

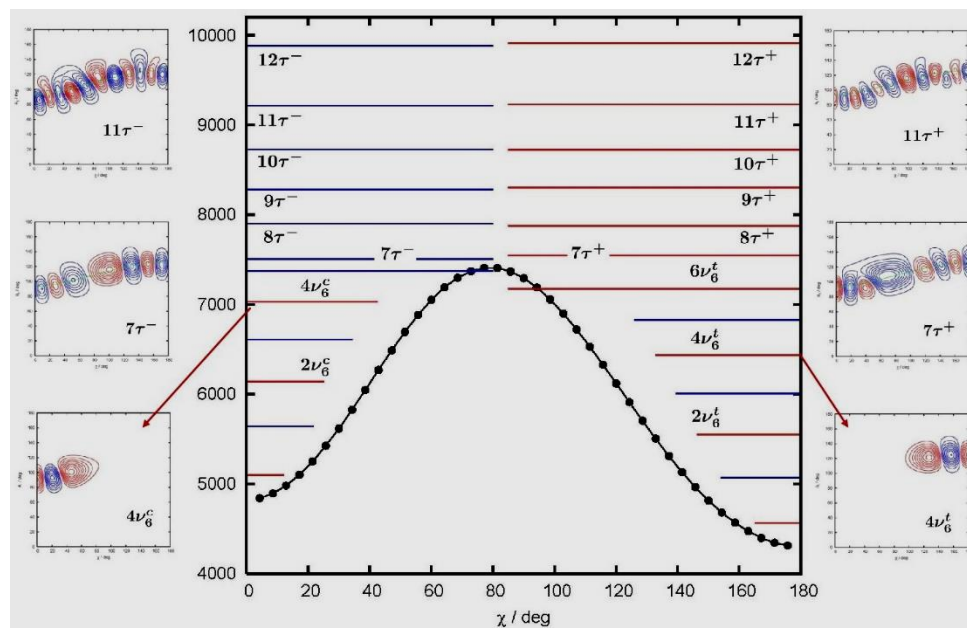


Figure 1. Two limiting cases associated with oscillator and rotor spectral patterns identified for the torsion in HOCO.

The torsional structure of HOCO is studied in great detail using the RCCSD(T)/cc-pVQZ PES developed earlier [4]. The torsion is described by a double-minimum anharmonic potential with a nonplanar barrier between the *trans* and *cis* arrangements. The electronic torsional saddle point is 3270 cm^{-1} above the *trans* form. The torsional saddle point $^{\text{adi}}V^0$ on the effective ground-state profile is at 7410 cm^{-1} , as seen in Figure 1. The pure torsional states below $^{\text{adi}}V^0$ follow the oscillator pattern associated either with the *trans* or *cis* form and described by the quantum number ν_6 . The first states having a nonzero wave function probability amplitude in both well regions occur in the vicinity of $^{\text{adi}}V^0$. The states above $^{\text{adi}}V^0$ exhibit the free-rotor behavior, with the even-parity and odd-parity levels of similar energies. The rotor states are described by the quantum number τ^p , where the parity label p is + or – for even or odd parity. The expectation value of the torsional angle in the first excited torsional state is about 25° for *trans*-HOCO and 20° for *cis*-HOCO. Due to this, alternative approaches to vibrational calculations based on the normal mode description (such as the vibrational configuration interaction approach) encounter difficulties in treating even the fundamental torsional transition of *trans*-HOCO and *cis*-HOCO [5].

Vibrational second-order perturbation theory is commonly used to derive effective spectroscopic constants from *ab initio* energy points, which typically cover only a narrow portion of the potential energy surface around the minimum. This traditional approach has been integrated into several popular quantum chemistry program packages with the motivation to routinely provide reference data for experimental measurements. However, the standard perturbational approach is not always sufficient to reliably predict all experimentally required spectroscopic properties. Huang *et al.* [6] strongly questioned the attribution of the transition at 11244 MHz to C_3H^+ on the basis of large discrepancies between the calculated equilibrium centrifugal distortion constants D_e and the experimentally derived D_0 value. Using their quartic force field in combination with our numerically exact rovibrational treatment, we found that the PES from Ref. [6] in fact supports the experimental identification of C_3H^+ [1]. Another example is provided by the protonated nitrogen molecule, N_2H^+ . The experimentally derived sextic centrifugal distortion constant is reported to be $H_0=73.5\text{ mHz}$ for N_2H^+ and $H_0=71.6\text{ mHz}$ for N_2D^+ [7]. The vibrational second-order perturbational results are much smaller, given by $H_e=48.8\text{ mHz}$ for N_2H^+ and $H_e=34.2\text{ mHz}$ for N_2D^+ [7]. Our rovibrational

calculations using a CCSD(T) PES of Ref. [8] provide $H_0=73.3$ MHz N_2H^+ and $H_0=65.8$ MHz N_2D^+ , in good agreement with the experimental findings.

Microwave rotational spectroscopy measures the energies of rotational transitions, frequently with stunning precision. The experimental observations are usually fitted to effective spectroscopic Hamiltonians and applied to find the molecular structure at equilibrium. In real vibrating-rotating molecules, corresponding to actual experimental situation, the ground vibrational state is described by a wave function, extended over other-than-equilibrium arrangements. The effects of zero-point vibrational motion produce an effective rotational constant B_0 , which is different from the equilibrium B_e value. Based on numerically exact rovibrational energy levels, we have designed a new two-step experimental/theoretical procedure for the derivation of molecular equilibrium structures [9,10]. This method has been applied on the formyl cation, HCO^+ , a key species in ion-molecule chemistry with a central role in astrochemical models [11].

Information about the correction $\Delta B_0=B_e-B_0$ is not easily accessible experimentally. The zero-point B_0 constant is usually corrected by the vibration-rotation α constants. The estimates for B_e obtained in this fashion produce the so-called r_α structure. On the other hand, the concepts of B_0 and B_e are both well founded in theoretical approaches based on numerically exact full-dimensional rovibrational calculations. The full correction $\Delta B_0=B_e-B_0$ only allows to derive the equilibrium r_e structure.

In Figure 2, we see the pairs of the bond distances $r(NH)$ and $r(NN)$ reproducing the estimates B^{est} modeled as B_0+S_0 and $B_0+\Delta B_0$ for eight isotopologues of N_2H^+ , involving H, D, ^{14}N , and ^{15}N . The intersection of the horizontal and vertical dashed lines shows the r_e and r_α parameters, computed by nonlinear least-squares methods. Two bond distances, describing a linear triatomic molecule such as N_2H^+ , are anti correlated.

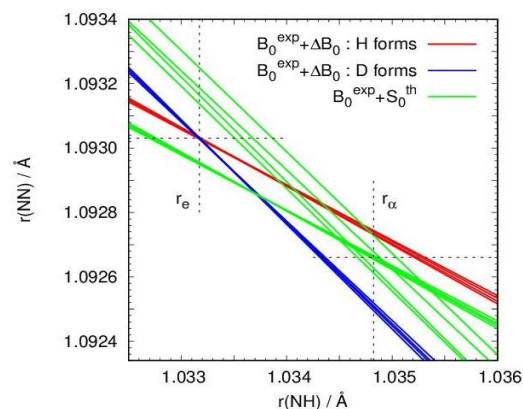


Figure 2. Parameters of N_2H^+ .

The spectroscopic α corrections S_0 for eight isotopic variants of N_2H^+ are approximately 200 MHz. They provide the dominant contribution to the full corrections ΔB_0 . The higher-order corrections ΔB_0-S_0 are in order of several MHz and much smaller than S_0 . In spite of that, the higher-order contributions are found to be essential for the determination of the molecular structure. To access the higher-order contributions experimentally, measurements on vibrational overtones and combination bands are required. But, this is not an easy task. In electronic-structure program packages, the spectroscopic correction S_0 from second-order vibrational perturbation theory is routinely used to obtain the zero-point rotational constant B_0 from the calculated equilibrium rotational constant B_e . However, the correction S_0 has its own fundamental deficiency due to neglecting higher-order effects.

In theoretical spectroscopy, quartic internal coordinate force fields are sometimes employed for the determination of spectroscopic parameters by perturbation methods. In rovibrational calculations beyond the perturbation treatment, they are commonly subjected to a Morse transformation. The quartic force fields are, however, often found to be insufficient to properly capture the angular behavior, important for describing the underlying physics of the system. In our study on N_2H^+ , we use the global three-dimensional PES of Schmatz [8] and the quartic force field of Huang *et al.* [12], both designed for this ion in its ground electronic state. The minimum energy paths V_{MEP} and the ground state adiabatic profile $^{(0,0)}V_{opt}$ along the bending angle θ computed for the two PESs are

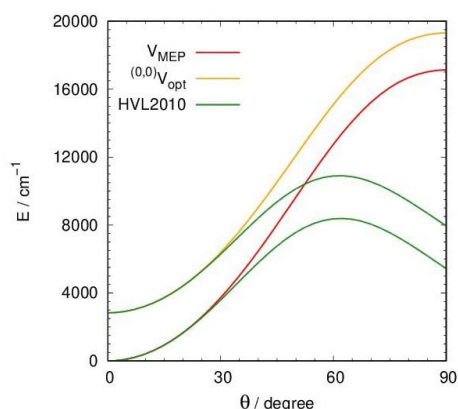


Figure 3. Minimum energy path V_{MEP} and effective bending potential ${}^{(0,0)}V_{\text{opt}}$ along the Jacobi angle θ computed for N_2H^+ using the PES of Ref. [8] (red and yellow) and the PES of Ref. [12] (green).

compared in Figure 3. The minimum energy paths are constructed by minimization of the potential energy with respect to the radial coordinates. The adiabatic (effective) bending profile is obtained by adding the zero-point energy of the stretching vibrations to the minimum energy path. Figure 3 clearly shows that the quartic force field of Ref. [12] provides a good description of the bending motion only for angles θ smaller than 30° .

CONCLUSION

The issues concerning the potential energy representations and numerically exact full-dimensional rovibrational calculations in combination with exact kinetic energy operators are not simply a technical matter: they are essential ingredients for achieving good, reliable results from high-level/high-accuracy *ab initio* points and for generating data to support/assist detailed spectroscopic studies. In connection with this, triatomic molecules are still important for examining the effect of the orientation of the axis system on the kinetic energy operator and tetratomic molecules for examining the effect of the out-of-plane motion in the internal molecular dynamics. Only full-dimensional rovibrational calculations are capable of providing the full correction ΔB_0 to the rotation constant B_0 in the ground vibrational state for the effects of zero-point motion in the molecule.

REFERENCES

- [1] M. Mladenović, J. Chem. Phys., 2014, 141, 224304.
- [2] M. Mladenović, J. Chem. Phys., 2000, 112, 1070-1081.
- [3] M. Mladenović, Spectrochim. Acta, Part A, 2002, 58, 795–807.
- [4] M. Mladenović, J. Phys. Chem. A, 2013, 117, 7224–7235.
- [5] M. Mladenović, J. Chem. Phys., 2012, 137, 014306.
- [6] X. Huang, R. C. Fortenberry, T. J. Lee, Astrophys. J. Lett. 2013, 768, L25.
- [7] L. Dore, L. Bizzocchi, E. S. Wirström, C. Degli Esposti, F. Tamassia, S. B. Charnley, Astron. Astrophys., 2017, 604, A26.
- [8] S. Schmatz, M. Mladenović, Ber. Bunsenges. Phys. Chemie 1997, 101, 372-386.
- [9] M. Mladenović, J. Chem. Phys., 2017, 147, 114111.
- [10] M. Mladenović, M. Lewerenz, Mol. Phys., 2018, 116, 3607-3620.
- [11] M. Mladenović, E. Roueff, Astron. Astrophys. 2014, 566, A144.
- [12] X. Huang, E. F. Valeev, T. J. Lee, J. Chem. Phys., 2010, 133, 244108.

STUDY OF NONCOVALENT INTERACTIONS USING CRYSTAL STRUCTURE DATA AND QUANTUM CHEMICAL CALCULATIONS

M. R. Milovanović¹, J. M. Živković¹, D. B. Ninković¹, J. P. Blagojević Filipović¹, D. Z. Vojislavljević–Vasilev¹, I. S. Veljković², I. M. Stanković², D. P. Malenov³, V. B. Medaković³, D. Ž. Veljković³, S. D. Zarić³

¹*Innovation center of the Faculty of Chemistry, Studentski trg 12-16, Belgrade, 11000, Serbia,*

²*Institute of Chemistry, Technology and Metallurgy, University of Belgrade, Njegoševa 12, 11000 Belgrade, Serbia,*

³*Faculty of Chemistry, University of Belgrade, Studentski trg 12-16, Belgrade, 11000, Serbia (szaric@chem.bg.ac.rs)*

ABSTRACT

The analysis of the crystal structures in the CSD was used to recognize and characterize new types of noncovalent interactions. It was also used to study already known noncovalent interactions. Based on the data from the CSD we can determine existence of the interactions, frequency of the interactions, and preferred geometries of the interactions in the crystal structures [1,2].

The quantum chemical calculations were performed to evaluate the energies of the interactions. For the preferred geometries in the crystal structures we can calculate the interaction energies. By calculating potential energy surfaces for the interactions, we can determine the most stable geometries, as well as stability of various geometries [1,2].

Using this methodology our group recognized stacking interactions of planar metal-chelate rings; stacking interactions with organic aromatic rings, and stacking interactions between two chelate rings. The calculated energies showed that the stacking of metal-chelate rings is stronger than stacking between two benzene molecules. Studies of interactions of coordinated ligands indicate stronger noncovalent interactions than interactions of noncoordinated molecules [2].

REFERENCES

- [1] Ninković, D. B., Blagojević Filipović, J. P., Hall, M. B., Brothers, E. N., Zarić, S. D. (2020) *ACS Central Science*, **6**, 420
- [2] Malenov, D. P., Zarić, S. D. (2020) *Cood. Chem. Rev.* **419**, 213338

FORMATION OF THE METHANE HALIDES FLUID-LIKE LAYERS AT AMBIENT CONDITIONS

I.I. Grinvald, R.V. Kapustin

*Nizhny Novgorod State Technical University n.a. R.E. Alekseev
Minin str. 24, 603950 Nizhniy Novgorod, Russia
(grinwald@mts-nn.ru)*

ABSTRACT

The work presents the IR-study of fluid-like methane halides (methyl iodide, carbon tetrachloride, chloroform, and methane dichloride) layers formation in the near-surface area at ambient conditions. It was shown that at vapors compression-expansion procedure in variable-thickness spectral cell, the phase state of matter, exhibiting both gas and liquid spectral properties appears. The reversible and continuous transition of gas-like and liquid-like shapes, not depending on thermodynamic characteristics of studied substances, was revealed.

INTRODUCTION

Fluids represent a unique phase state of matter generating under supercritical conditions and combining the properties of gas and liquid. It is conventional to divide fluids into gas-like and liquid-like states depending on which properties prevail in them, however, this definition is ambiguous due to the continuous nature of the transition between these two states.

Supercritical fluids have many applications as industrial solvents, largely due to their tunable density, and can be used as an environmentally friendly solvent for hazardous waste cleanup. However, the same properties that make fluids useful also make their generation quite difficult. Aside from the high pressures and temperatures required, fluids can be chemically active and corrode many components of experimental apparatus. Therefore, the formation of supercritical fluids is generally limited to the simplest compounds – water and carbon dioxide. FTIR studies of their behavior and the liquid-like to gas-like fluid transition are presented in a few of works to date. The spectral manifestations shown there are similar to FTIR observations of some organic liquids at ambient conditions. [1; 2]

In the present work, we set the aim to generate a fluid-like state of matter at ambient conditions and reveal it with FTIR methods by fixing a combination of gaseous and liquid properties and their transitions for methyl iodide, carbon tetrachloride, chloroform, and methane dichloride.

EXPERIMENTAL

To generate fluid-like layers, a variable thickness optical cell (VTC), shown in Figure 1, was used. At the first step, organic components were evaporated into the cell at atmospheric pressure and 295K during 20 – 70 hours. At the second step, the fluid-like state was formed by compressing of interwindow space in vapor-filled VTC. For the estimating of fluid-like layers, their IR bands were compared with the ones recorded in a 100-mm gas cell at 295K for gases and between optical windows for liquid state.



Figure 1. Spectral cell (VTC) used for generating the fluid-like layers.

IR-spectra were recorded by IR-Fourier spectrometer FSM 1202 (InfraSpec Co.) in $500\text{-}4000\text{ cm}^{-1}$ range with resolution 2 cm^{-1} and 60 scans. The VTC was manufactured by Perkin-Elmer Co. The purity of halides was not less than 99 perc as it was confirmed by chromato-mass spectrometry data obtained by GCMS - QP2010 Plus spectrometer (Shimadzu Co. Inc.).

RESULTS AND DISCUSSION

In the IR spectra of methyl iodide in the region of bending (H-C-H) vibrations, recorded at 6 mm thickness of VTC, the gas phase band at 1263 cm^{-1} (**B**, in the Fig. 2) and the liquid phase band at 1240 cm^{-1} (**C**, in the Fig. 2) were observed. Besides, a broad band with a rotational structure at 1426 cm^{-1} , assigning to gas phase, is revealed.

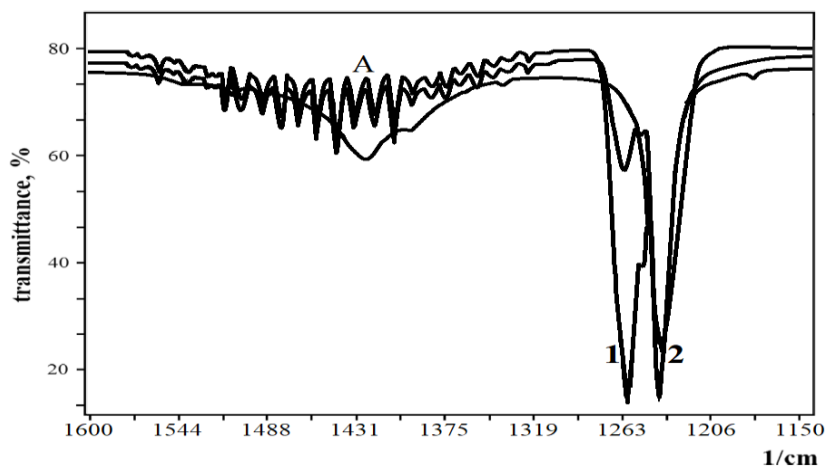


Figure 2. Fragment of methyl iodide spectra in H-C-H bending region.

The spectrum 2, recorded at 1 mm distance between the optical windows, demonstrates the presence of both gaseous and liquid phase components. At the distance 0.5 mm, the relative intensity of the gas state band decreases, and the intensity of the liquid state band grows (spectrum 3, Fig. 2). Since the IR spectra of gases cannot be observed at such distances, the mentioned bands can be assigned to the generated fluid-like layer.

The spectra of carbon tetrachloride (Fig. 3) show similar changes under the vapor compression procedure. The gas phase bands (**A**, **B**) at 795 and 779 cm^{-1} in spectrum 1 (at the 6 mm optical distance) are observed. In spectrum 2 the gas band **A** and liquid bands **C**, **D** at 784 and 761 cm^{-1} are observed. These data indicate that the formed “gas-liquid” state of carbon tetrachloride can also be determined as a fluid-like layer.

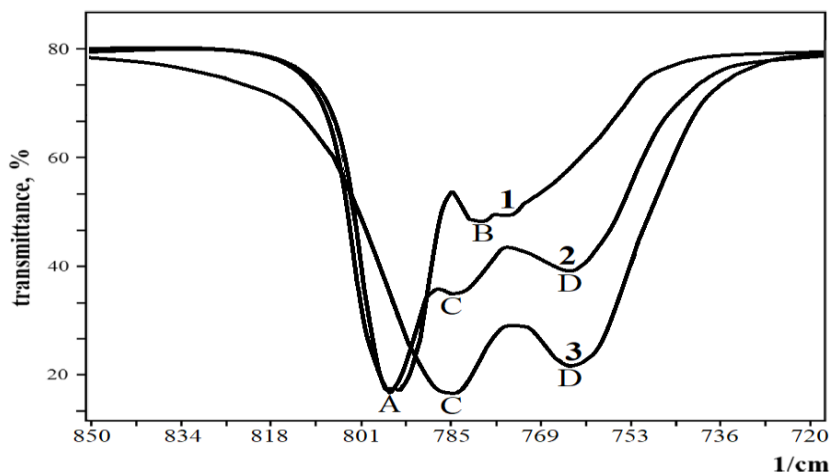


Figure 3. Fragment of carbon tetrachloride spectra in C-Cl stretching region.

In the spectra of methane dichloride (Fig. 4) the gas phase bands (bands **A**, **B**, spectrum 1) at 764 and 750 cm^{-1} at the optical distance 6 mm are revealed. At 1 mm thickness of VTC in the spectrum (Fig. 2, spectrum 2) both gas bands (**A**, **B**) and liquid band **C** at 738 cm^{-1} were observed. Under reduction of interwindow distance to 0.5 mm, the gas phase bands disappear, and only the liquid phase band remains. This transition is reversible: at the optical distance expansion to 6 mm, the gas phase bands appear again while liquid phase bands are absent. Since similar changes cannot be caused at these conditions by condensation or evaporation of the substance only, the presented data reasonably justify the formation of a layer with fluid-like properties.

The spectra of chloroform and chloroform-d (Fig. 5), manifesting similar behavior under the vapor compression procedure, at the same time have some differences.

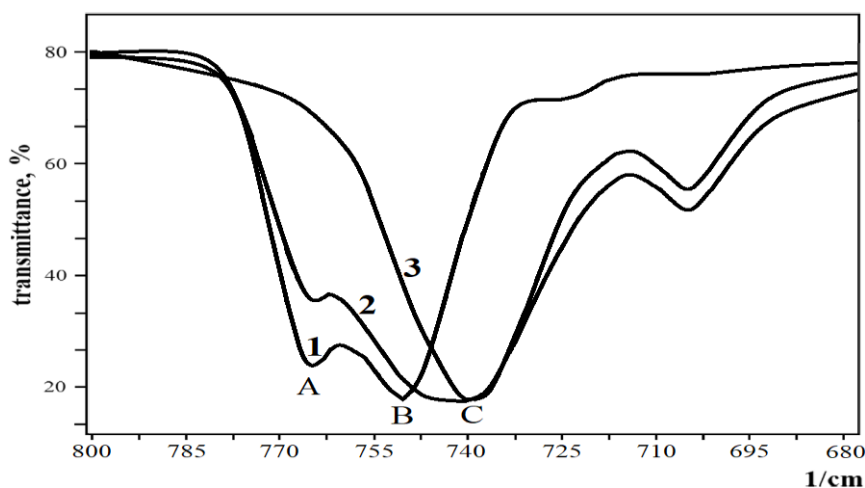


Figure 4. Fragment of methane dichloride spectra in C-Cl stretching region.

The gas and liquid bands of fluid-like layer locate much closer to each other than in spectra of other halides. Two overlapped components of liquid band, which are well-visible in chloroform-d spectrum, indicate on the symmetry breaking of (CCl_3) -group. This can be explained by the formation of intermolecular hydrogen bond in the fluid-like system.

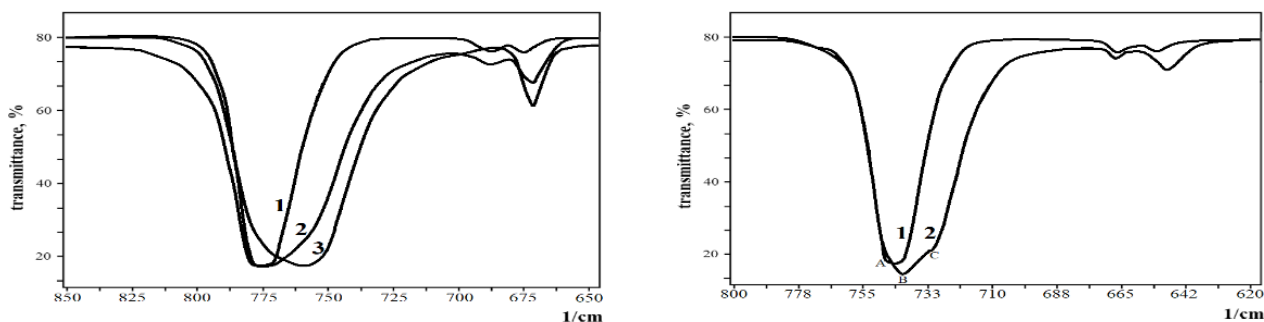


Figure 5. The fragment of chloroform and chloroform-d spectra in C-Cl stretching region.

CONCLUSION

As the reversible transition from gaseous to liquid properties occurs very quickly and does not depend on the thermodynamic characteristics of the substance, this phenomenon cannot be assigned to the process of evaporation-condensation only. Therefore, these systems, having the duality of phase state properties, were defined as fluid-like state. Since in the space of VTC ambient conditions remain, the solid surface should play a crucial role in fluid-like state arising mechanism.

REFERENCES

- [1] E.S. Alekseev, A.Yu. Alentiev et al., Russ. Chem. Rev. 89 (2020) 1337
- [2] N. J. Hestand, S.E.Strong et al., J. Chem. Phys. 150 (2019) 054505

STRUCTURAL TRANSFORMATIONS OF DICHLORO-ALKANES AT THE LIQUID-TO-GAS TRANSITION

I.I. Grinvald, R.V. Kapustin

*Nizhny Novgorod State Technical University n.a. R.E. Alekseev
Minin str. 24, 603950 Nizhniy Novgorod, Russia
(grinwald@mts-nn.ru)*

ABSTRACT

The work discusses the data obtained by IR study referring to the dual gas-liquid properties of thin layers forming in the cell near-surface (optical windows) area for dichloromethane, 1,2-dichloroethane and 1,2-dichloropropane. These layers represent the combination of gas-like and liquid-like states, which can be considered as the intermediate stage of the phase transition from gas to liquid. It was shown that the molecular interactions in dual gas-liquid systems of chloroalkanes are changing due to the restructuring of Cl...H hydrogen bonding.

INTRODUCTION

The problem of gas-liquid systems formation, considering different properties of substances, was studied by several methods from thermodynamic and molecular light scattering to quantum-chemical and dynamic simulation. The IR spectroscopy was used for these investigations as well. Some recent works devoted to the interactions in gas and liquid phases of organic species can be quoted [1].

It was revealed that at the formation of liquid phase a non-valence intermolecular bonding appears, which leads to supramolecular systems with shifted hydrogen or halogen atoms. However, the role of this transformations in the mechanism of phase-to-phase transitions at ambient conditions was not considered.

An attempt to use this phenomenon to interpret the processes occurring in the interfacial space during evaporation and condensation led to the idea of generating thin molecular layers in an optical cell and detecting their features by IR spectroscopy methods. As part of this study, results for dichloromethane, 1,2-dichloroethane and 1,2-dichloropropane are discussed here. The main reason for this choice is the assumption that the stretching vibrations of C-Cl in these systems can clearly demonstrate the existence of intermolecular bonds and its changing in the gas and liquid phases [2].

EXPERIMENTAL

The following procedure was used to create a thin layer in the spectral cell during the evaporation of organic liquids. The sample was placed under a Teflon gasket (1 mm thick) on a KBr optical window so that it did not fall into the optical beam. Then the gasket is closed with another window, and both windows are placed in the holder for spectra recording. Before spectral measurement, the sample was left between the windows at ambient conditions for 5-30 minutes, depending on the type of chloroalkanes.

IR-spectra were recorded for liquid sample between KBr windows, and for gas phase – in 100 mm gas cell, by IR-Fourier spectrometer FSM 1202 (InfraSpec Co.) in 500-4000 cm^{-1} range with 2 cm^{-1} resolution and 60 scans. The purity of dichloroalkanes was not less than 99 perc as it was confirmed by chromato-mass spectrometry data obtained by GCMS - QP2010 Plus spectrometer (Shimadzu Co. Inc.).

RESULTS AND DISCUSSION

Dichloromethane. In the IR spectra of liquid dichloromethane in the region of C-Cl stretching vibrations the bands at 740 and 706 cm^{-1} (labeled as **A**, **B** in the spectrum 1, Fig. 1) were observed. These bands can be assigned, taking the conception that they assign to two types of intermolecular binding. The first of them is attributed to $(\text{Cl}\cdots\text{H})$ hydrogen bonds in chains having (H-C-Cl) fragments and another one to $(\text{Cl}\cdots\text{H})$ bonds in chain with (Cl-C-Cl) fragments. The second binding option should be stronger, but less likely to form. Consequently, the intensity of band **B** is considerably lower.

In gas phase spectrum instead of bands **A**, **B** the two-components band (components at 763 and 750 cm^{-1}) is revealed (spectrum 2, Fig.1). Therefore, it can be assumed that the bands of C-Cl bond stretching in molecules bound in the chain, transform into a pair of isomers C-Cl bond stretching, the first with (Cl-C-Cl) fragment and the second with two (H-C-Cl) structural elements attributed to unbound shape of dichloromethane in the gas phase (Fig 1, bands **C**, **D**).

When a liquid sample was evaporated into the space between the optical windows at ambient conditions, complex bands containing both gas non-resolved (**C**, **D**) and liquid (**A**) bands were observed, while the band **B** was absent (spectrum 3, Fig. 1). Since a real gas spectrum cannot be obtained in such a thin cell, it can be assumed that the spectrum of the thin layer demonstrates the appearance of intermediate molecular shape arising at the liquid-to-gas phase transition.

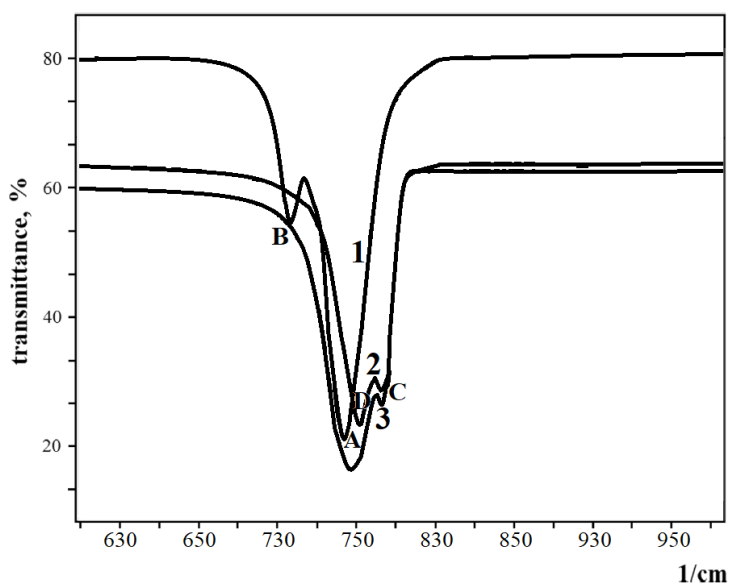


Figure 1. Fragment of dichloromethane IR spectra in C-Cl stretching region.

1,2-dichloroethane. The spectra of 1,2-dichloroethane in C-Cl stretching region (Fig. 2) exhibit two kinds of intermolecular binding as well: the shape with intermolecular $(\text{Cl}\cdots\text{H})$ bonds of *sin*-isomer (bands **A**, **B** at 766 and 655 cm^{-1} in spectrum 1, Fig.2) and the shape with $(\text{Cl}\cdots\text{H})$ bond of *anti*-isomer (band **C** at 711 cm^{-1} , spectrum 1, Fig.2)

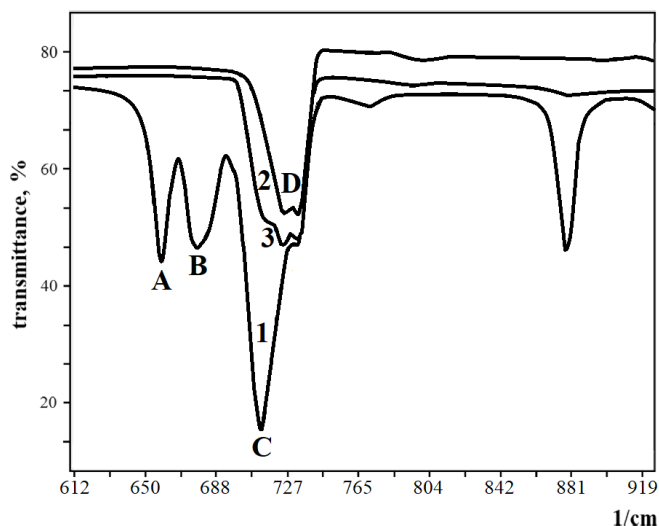


Figure 2. Fragment of dichloroethane spectra in C-Cl stretching region.

In the gas phase spectrum, band **D** has two components, at 731 and 724 cm^{-1} (spectrum 2, Fig. 2). These components can be assigned to the staggered and eclipsed conformers, which have a low barrier of transformation in the gas phase. The spectrum of the thin layer (spectrum 3, Fig. 2) has the combination of gas and liquid phase bands. However, band **C** here is assigned to *anti*-isomer only, and bands **A**, **B** are absent at all. It can be assumed that such a molecular form is a transitional one at the transformation of a liquid into a gas within the system.

1,2-dichloropropane. In the spectra of liquid 1,2-dichloropropane (spectrum 1, Fig. 3) two pair of bands are shown – one at 742 , 745 cm^{-1} (spectrum 1, pair **A**) and another one – at 670 , 620 cm^{-1} (spectrum 1, pair **B**). Such a complication of the spectrum for the considered dichloroalkane can be caused by the appearance of two structures with different spatial arrangement of CH_3 -group in each chlorine conformer. In the thin layer spectrum recorded after 15 minutes of evaporation procedure, two types of bands were observed – one with liquid components at 685 cm^{-1} (Fig. 3, spectrum 2, band **C**) and another one with two gas components – at 744 , 757 cm^{-1} (Fig. 3, spectrum 2, components **D**). After the 30-minutes of evaporation procedure instead of double-component gas band **D** the single band at 747 cm^{-1} remains.

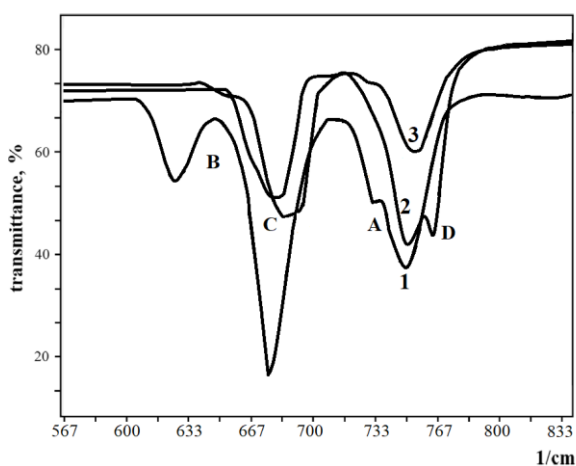


Figure 3. Fragment of 1,2-dichloropropane spectra in C-Cl stretching region.

CONCLUSION

The presented data show that during the phase liquid-to-gas transition the thin layer having combination of both gas and liquid phase properties, unambiguously manifesting in their IR spectra,

arises. Therefore, it can be assumed that the detected dual-phase state is a transitional substance shape formed when a liquid is converted into a gas at ambient conditions. In this state molecular binding is weaker than in the initial liquid bulk, and gas is also present inside it.

REFERENCES

- [1] I. I. Grinvald, I. Yu. Kalagaev, et al, *Rus. J. Phys. Chem. A* 93 (2019) 69
- [2] I. Grinvald, I. Kalagaev, et al, *Struct. Chem.* 30 (2019) 1659

A THEORETICAL CALCULATION OF THE RAMAN SPECTRUM OF INDIGO CARMINE

J. Senćanski¹, J. Maksimović² and M. Pagnacco³

¹University of Belgrade, Institute of General and Physical Chemistry,
Studentski trg 12-15, 11000 Belgrade, Serbia.(sencanskijelena@yahoo.com)

²University of Belgrade, Faculty of Physical Chemistry, Studentski trg 12-15, 11000 Belgrade,
Serbia.

³University of Belgrade, Institute of Chemistry, Technology and Metallurgy, Njegoševa 12, 11000
Belgrade, Serbia.

ABSTRACT

This paper presents the B97D functional added to the Hamiltonian in order to calculate Raman spectrum of indigo carmine. The experimental spectrum of the compound was recorded from indigo carmine, a commercial dye sold for use in food processing when used in a mixture with D-glucose. The Raman spectrum was calculated using the B97D/cc-pVTZ level of theory. The results obtained show lower deviation from 1000 cm⁻¹ to 2000 cm⁻¹ for the main bands compared with the data found in the literature.

INTRODUCTION

Synthetic dyes are commonly used across consumable goods. Indigo carmine (indigotine, E132) is a blue dye that is used in the food, pharmaceutical, medical and cosmetic industries [1]. Indigo carmine is an organic compound that has the chemical formula C₁₆H₈N₂Na₂O₈S₂[2].

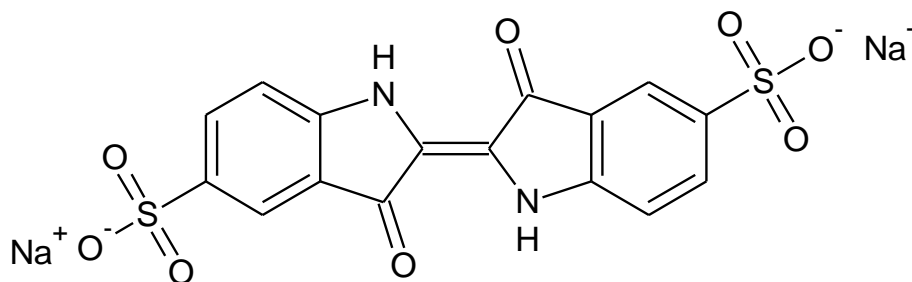


Figure 1. The structural formula of indigo carmine[2]

To calculate the Raman spectrum, Volkov et al [3] performed their calculation using a 6-31++g(d,p) basis set and the restricted B3LYP functional. Peica et al [2] optimized indigo carmine by BPW91/6311++G^{**}, B3PW91/LANL2DZ, B3LYP/6311++G^{**} and B3LYP/LANL2DZ.

The aim of the results presented here was to examine a method of calculation that had not already been used in the literature and to compare the results obtained by a theoretical calculation with an experimental one.

METHODS

An experimental spectrum of the compound was recorded for indigo carmine (E132), a commercial dye sold for use in food production as a dye in a mixture with D-glucose. The spectrum was recorded by a Thermo Scientific DXR Raman Microscope. The recording of the spectrum is done at $\lambda=532$ nm, laser strength 8mW, magnification 10x, and 2.1 μm laser spot size.

The geometry of the indigo carmine was optimized using the B97D/cc-pVTZ level of theory. After optimizing the geometry, the Raman spectrum was calculated to be the same level of theory. The calculations were carried out in *Gaussian 09*, Revision D.01[4].

RESULTS AND DISCUSSION

In order to simulate the Raman spectrum, firstly, geometrical optimization of the molecule was carried out. The optimized structure of the indigo carmine molecule is presented in **Fig. 2**.

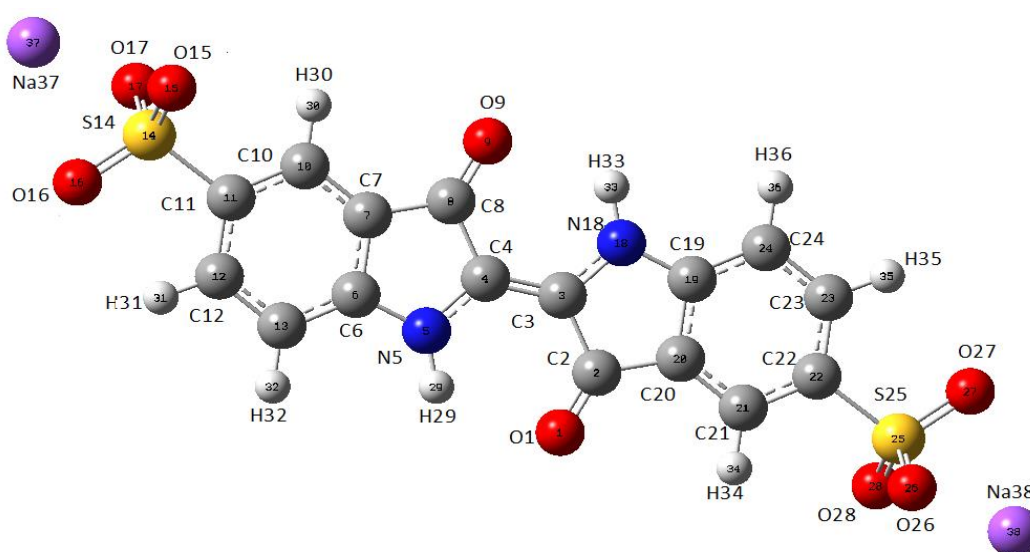


Figure 2. The optimized geometry of Indigo carmine

Table 1. The theoretical and experimental values of the vibration bands [2]

This study		Literature [2]				
	B97D		B3PW91		B3LYP	
experi- mental	cc- pVTZ	experi- mental	LANL2 DZ	6- 311G++ G**	LAN L2DZ	6- 311++G **
1039	1051	1036	1022	1074	1023	1068
1136	1155	1130	1164	1152	1157	1139
1248	1234	1240	1239	1243	1265	1244
1293	1291	1290	1288	1280	1288	1296
1347	1347	1344	1357	1345	1343	1352
1473	1457	1472	1472	1486	1482	1482
1577	1586	1576	1511	1509	1621	1616
1625	1623	1623	1640	1632	1635	1634
1698	1702	1698	1687	1701	1669	1681

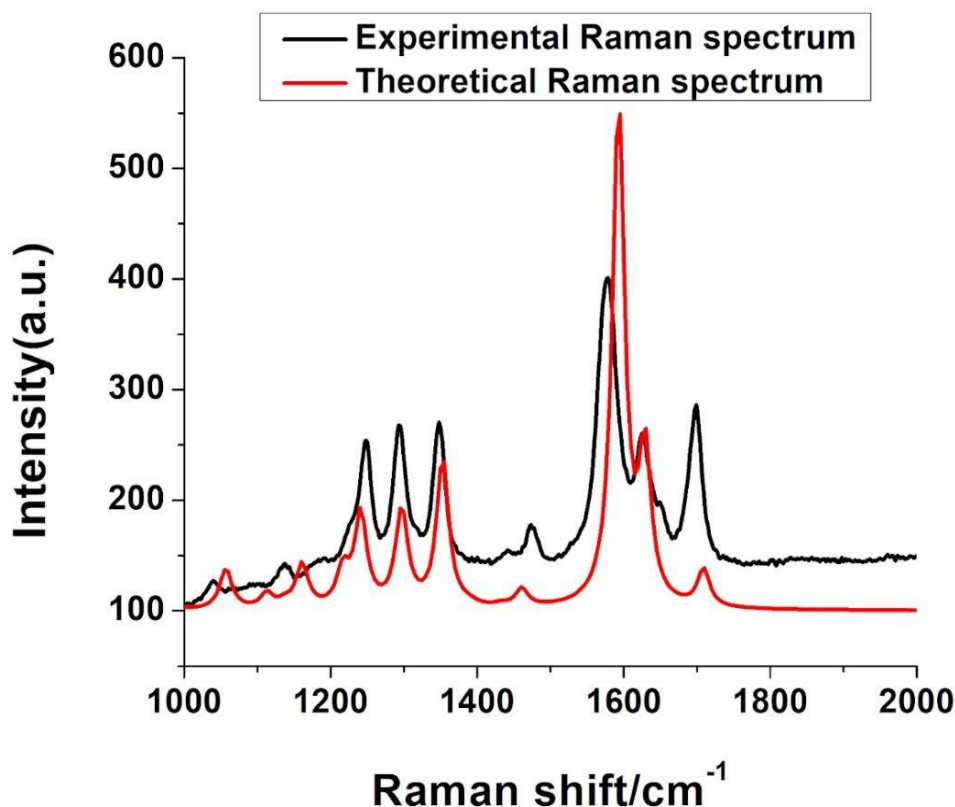


Figure 3. The experimental and calculated spectra

Fig. 3. lists the calculated and experimental spectra, whose good agreement is evident. The bands that have a lower or the same deviation compared to the data found in literature are marked in bold. The results obtained in terms of a lower deviation compared to the data in the literature were anticipated due to the fact that a higher basis set is taken to calculate the spectrum compared to the reference [2].

CONCLUSION

The data obtained for the simulated Raman spectrum of the indigo carmine indicates good agreement with the experimental spectrum as well as better agreement compared to the data found in literature. Therefore, the use of the B97D functional and the correlation consistent basis set may be applied to achieve a satisfactorily precise calculation of the vibrational spectra of indigo carmine.

Acknowledgement

This work was partially supported by the Ministry of Education, Science and Technological Development of the Republic of Serbia, no: 451-03-9/2021-14/200026, 451-03-9/2021-14/200051, 451-03-9/2021-14/200146.

REFERENCES

- [1] EFSA Panel on Food additives and Nutrient Sources added to Food (ANS), Scientific Opinion on the re-evaluation of Indigo Carmine (E 132) as a food additive, EFSA Journal 12, 2014, 12(7), 3768.

- [2] N. Peica, W. Kiefer, *Journal of Raman Spectroscopy: An International Journal for Original Work in all Aspects of Raman Spectroscopy, Including Higher Order Processes, and also Brillouin and Rayleigh Scattering*, 2008, 39, 47-60.
- [3] V. V. Volkov, R. Chelli, R. Righini, C. C. Perry, *Dyes and Pigments* 2020, 172, 107761.
- [4] M. J. Frisch, et al, *Gaussian 09*, Revision D.01, Gaussian Inc., Wallingford CT, 2009.

LIBS HYDROGEN DETECTION: TEA CO₂ LASER - POLYMETHYL METHACRYLATE INTERACTION

M. Trtica¹, M. Kuzmanovic², J. Savovic¹ and D. Rankovic²

¹ *University of Belgrade, VINCA Institute of Nuclear Sciences - National Institute of the Republic of Serbia, Mike Petrovica Alasa 12-14, 11001 Belgrade, Serbia. (etrtica@vin.bg.ac.rs)*

² *Faculty of Physical Chemistry, University of Belgrade, Studentski trg 12-16, 11158 Belgrade, 118, PAC 105305, Serbia*

ABSTRACT

Laser-Induced Breakdown Spectroscopy (LIBS) was applied to detect hydrogen in solid polymer - polymethyl methacrylate (PMMA). A pulsed Transversely Atmospheric Excited (TEA) CO₂ laser was used as the excitation source. Using a low laser intensity of ~ 58 MW/cm² and fluence of ~ 16.5 J/cm², the plasma above the PMMA was studied in a vacuum ambience (0.01 mbar). Under the applied experimental conditions, the plasma could be induced only in the presence of a metal sub-target, after a cavity in a PMMA was created by multipulse laser ablation. The spectrum of the plasma generated on a PMMA-metal sub-target system was dominated by the emission of intensive hydrogen, carbon, and oxygen atomic lines and molecular bands of C₂ and CN. The characteristics of laser-induced plasma were analyzed by evaluating the plasma parameters, such as the electron number density and temperature.

INTRODUCTION

Hydrogen detection and quantification in solids are of great importance in contemporary science and technology applications. Of particular importance is the detection of hydrogen in nuclear fission and fusion technology. Focusing only on the fusion area the significance can be twofold: (i) Consideration of the laser-polymer interaction is essential from the aspect of the fuel capsule design [1]. Namely, in laser-based direct-drive inertial confinement fusion, the D-T fuel is placed inside a capsule where the outer layer is typically the plastic forming the ablator and, (ii) the PMMA as a hydrogen-bearing material can be used to test and optimize the LIBS apparatus for hydrogen detection before analyzing an authentic reactor plasma facing material that has been exposed to H-isotope atoms fluxes, e.g., tungsten with incorporated hydrogen [2].

This paper describes the interaction of a pulsed IR laser with a polymethyl methacrylate (PMMA - (C₅O₂H₈)_n) target, focused on the detection of hydrogen by the TEA CO₂ laser-based Laser-Induced Breakdown Spectroscopy. The PMMA is a promising polymer for use in various fields such as electronics and biomedicine, and also in nuclear technology [3].

EXPERIMENTAL

The LIBS set-up used in this study is described in detail in Ref. [4,5]. The experimental apparatus, Figure 1, includes a pulsed laser, focusing and collecting optics, and a spectrometer coupled with a CCD detector. In order to provide conditions for the generation of plasma, a PMMA sample was placed on a steel sub-target.

A pulsed TEA CO₂ laser is a commercial version of a laser constructed at the VINCA Institute of Nuclear Sciences, having a pulse energy of up to 170 mJ at a wavelength of 10.6 μ m. The typical laser/optical pulse form is shown in Fig. 1(a). A sample, PMMA-steel sub-target system, was placed in a chamber evacuated to 0.01 mbar. The laser beam was transmitted through a NaCl window of the chamber and focused on the PMMA surface with a ZnSe lens ($f=13.0$ cm). Optical emission from the plasma was viewed in a direction parallel to the sample surface. The image of a plasma plume was

projected along a horizontal axis on the entrance slit of a spectrograph using a lens ($f=9.5$ cm). The spectrograph was coupled with a CCD detection system (Apogee Alta F1007 camera), and spectra were recorded using a time-integrated space-resolved method [4,5]. The typical integration time was 60 seconds.

RESULTS AND DISCUSSION

Initially, CO₂ laser-PMMA-steel sub-target interaction was accompanied by absorption of laser radiation by PMMA, resulting in its melting and vaporization without inducing the plasma.

Repeated laser shots hitting the same spot on the PMMA surface created a channel/cavity through PMMA. For PMMA thickness of 5 mm and applied laser energy of 160 mJ, the laser radiation reached the steel sub-target surface after accumulation of 150 laser pulses. At that point, plasma was induced on the steel sub-target, and a plasma plume appeared over the PMMA surface. A series of complex phenomena were involved in plasma creation and propagation. A simplified description includes two main processes: (i) absorption of laser radiation by steel, causing its ablation, vaporization, and plasma generation; (ii) propagation of the plasma through previously created PMMA channel causing PMMA heating, vaporization, and decomposition.

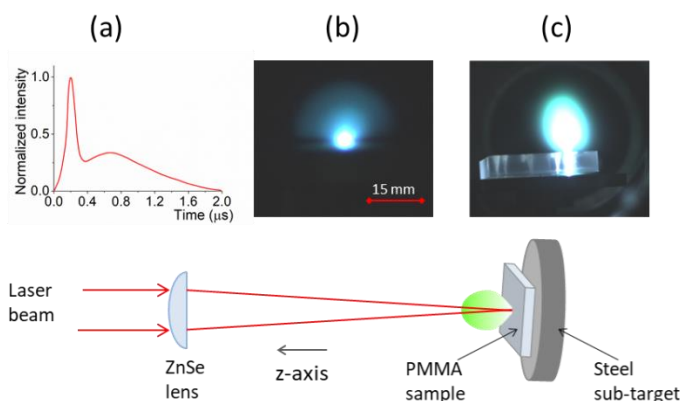
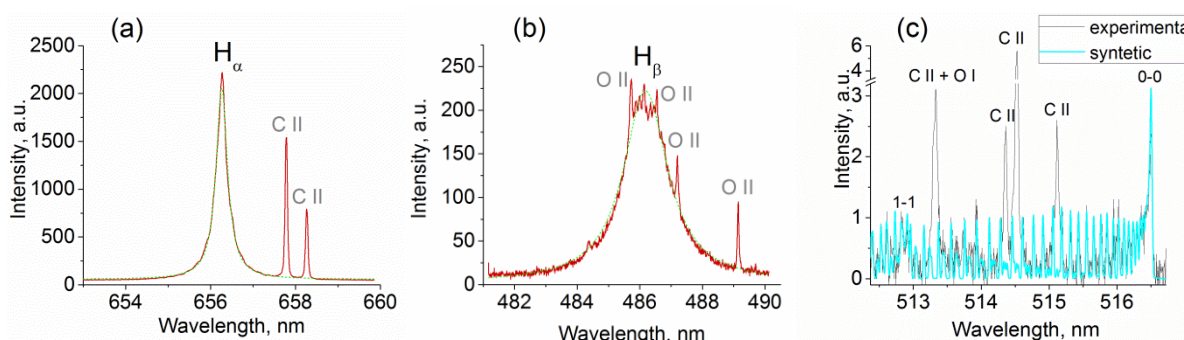


Figure 1. Schematic illustration of PMMA irradiation by CO₂ laser. (a) CO₂ laser pulse shape; (b) and (c) View of plasma created over the steel sub-target and PMMA-steel sub-target system, respectively.

Experimental conditions: vacuum ambience, 0.01 mbar; laser output pulse energy 165 mJ (intensity ~ 58 MW/cm², fluence ~ 16.5 J/cm²).



The plasma emission consisted of the spectral lines of the PMMA constitutive elements

Figure 2. LIBS spectra recorded 2 mm above the PMMA-steel sub-target system: (a) H_α 656.27 nm line; (b) H_β 486.13 nm line, and (c) C₂ Swan-band emission. Experimental conditions: vacuum ambience, 0.01 mbar; laser output pulse energy 165 mJ.

(hydrogen, carbon, and oxygen), Fig. 2 (a,b), and a band spectra of small molecular species created in the plasma, such as C₂ (Fig. 2(c)), and CN. For all atomic species, the highest emission intensity was recorded in the vicinity of the PMMA surface, at a distance 2 mm above the sample surface.

Estimation of the plasma parameters, electron number density (N_e), and ionization temperature (T) was done to characterize the excitation conditions in the laser-induced plasma. The electron density was inferred from the Stark broadened H α (656.27 nm) and H β (486.13 nm) linewidths [6]. Estimated from the spectra recorded from a plasma slice 2 mm above the PMMA surface, N_e was $1.6 \times 10^{16} \text{ cm}^{-3}$. The FWHM of both hydrogen lines decreased with increasing distance from the PMMA surface. For example, at a distance of 7 mm, the estimated N_e was $4.9 \times 10^{15} \text{ cm}^{-3}$.

The ionization temperature was determined from the measured intensity ratio of carbon ionic and atomic line pair (C II 250.9 nm/C I 247.9 nm) and previously obtained N_e . Depending on the distance from the PMMA surface, the temperature varied from 16500 K (at 2 mm) to 13600 K (at 7 mm).

Apart from atomic lines of H, C, and O, intensive molecular emission could be observed in the plasma. Figure 2 (c) shows LIBS spectra of the C₂ Swan band, recorded 0.5 mm above the PMMA surface. By increasing the air pressure to 0.1 mbar, a CN violet system could also be registered. The maximum CN emission intensity was located 2 mm above the PMMA surface. Formation of the CN molecules required recombination of atomic carbon or the C₂ molecules from the plasma with the atmospheric nitrogen. The rotational temperature of 4500 K was estimated by comparison of the experimental and simulated C₂ emission spectra.

CONCLUSION

In this work, TEA CO₂ laser-based LIBS was successfully applied to detect hydrogen from a solid polymer – PMMA. The low laser intensity of $\sim 58 \text{ MW/cm}^2$ and fluence of $\sim 16.5 \text{ J/cm}^2$ could not induce plasma on the PMMA under vacuum conditions. The plasma above the sample was created only when a sub-target made of steel was employed. The possible mechanism of plasma creation in a PMMA-steel sub-target system was proposed. Apart from hydrogen, the species like C, O, C₂ and CN were registered in the emission spectra.

Furthermore, the electron number density and the ionic, vibrational, and rotational temperatures were evaluated to characterize the laser-induced plasma. Depending on the observation distance, estimated N_e was in the range $1.6 \times 10^{16} \text{ cm}^{-3}$ to $4.9 \times 10^{15} \text{ cm}^{-3}$, at a distance of 2 mm, and 7 mm above the sample surface, respectively. The corresponding ionization temperature was 16500 K (2 mm) and 13600 K (7 mm). The rotational temperature of 4500 K was estimated by comparing the experimental and synthetic C₂ Swan bands.

Acknowledgment

This work was partially supported by: (i) International Atomic Energy Agency (IAEA), through contract, “Contemporary and New IF Structural-First Wall Materials: Conditions of High Thermal and Electromagnetic Fluxes“, Contract no. 24076, and (ii) The Ministry of Education, Science and Technological Development of the Republic of Serbia through Contract No. 451-03-9/2021-14/200017.

REFERENCES

- [1] G. McCracken, P. Stott, Inertial-Confinement Fusion, in: Fusion, Elsevier, 2013: pp. 82–83.
- [2] N. Moral, R.S. Hontoria, J. Alvarez, D. Garoz, M. Perlado, HiPER Fellows Meeting, Bordeaux, 3rd Feb. 2012. Book of abstracts, p. 10/37.
- [3] International Atomic Energy Agency - Contract 24076, “Contemporary and New IF Structural-First Wall Materials: Conditions of High Thermal and Electromagnetic Fluxes“, 2020-2024.

-
- [4] M. Momcilovic, M. Kuzmanovic, D. Rankovic, J. Ciganovic, M. Stoiljkovic, J. Savovic, M. Trtica, *Applied Spectroscopy*, 2015, **69**, 419-429.
- [5] M. Kuzmanovic, D. Rankovic, M. Trtica, J. Ciganovic, J. Petrovic, J. Savovic, *Spectrochimica Acta Part B*, 2019, **157**, 37-46.
- [6] N. Konjević, M. Ivković, N. Sakan, *Spectrochimica Acta Part B*, 2012, **176**, 16-26.

LASER-INDUCED BREAKDOWN SPECTROSCOPY STUDY OF ARCHEOLOGICAL GLASS SAMPLES

A. Šajić¹, M. Kuzmanović¹, D. Ranković¹, I. Stojić³, M. Stoiljković² and J. Savović²

¹ *University of Belgrade, Faculty of Physical Chemistry, Studentski Trg 12-16, 11000 Belgrade, Serbia.*

² *University of Belgrade, INN Vinca, Mike Petrovića Alasa 12-14, 11001 Belgrade, Serbia. (lelas@vinca.rs)*

³ *University of Belgrade, Institute of History, Knez Mihailova 36/II, 11000 Belgrade, Serbia.*

ABSTRACT

Two unclassified glass samples of medieval origin found in Belgrade were examined by the laser-induced plasma spectroscopy (LIBS) technique. Measurements were performed with a LIBS system based on a compact TEA CO₂ laser with low pulse energy ($E < 170$ mJ). The threshold energy required to induce plasma on a glass sample was 80 mJ per pulse. Depending on the sample, spectral lines of Si, Al, Ca, Fe, Ti, Mg, Mn, Sr, Cu, K, Ba, Na, and Ni were detected. Detection limits (LODs) were also estimated for several elements: Ni (18 ppm), Cu (2.5 ppm), Ti (25 ppm), Mn (32 ppm), and K (205 ppm). The plasma diagnostics was performed to determine plasma temperature and electron concentration. The excitation temperature of 8700 K was evaluated using a Boltzmann plot, constructed from the measured relative integral intensities of iron spectral lines. The electron number density, determined using the intensity ratio of Ti ionic and atomic lines, was $2 \cdot 10^{17}$ cm⁻³.

INTRODUCTION

Glass is a material that is unsuitable for the analysis by standard analytical techniques because the sample preparation of aluminosilicate glass matrix is complex. Moreover, glass as a sample is not convenient for X-ray fluorescence spectrometry (XRF) either, because essential elements that make up the glass are light elements that cannot be accurately determined using this method. On the other hand, Laser-Induced Breakdown Spectroscopy (LIBS) has characteristics that make it a suitable technique for the elemental analysis of glass [1]. Most elements of the periodic table, usually without the need for sample preparation, could be analyzed by LIBS.

The commonly used laser as a radiation source in LIBS is Nd:YAG laser. However, due to the high transparency of Nd:YAG laser radiation in the visible spectral region, it is hard to induce plasma on a glass sample. In addition, irradiation by high-energy laser pulses very often produces cracks in the sample. The mid-infrared lasers are more convenient for glass analysis because laser radiation is well absorbed, and LIBS plasma is easily created. This paper aims to demonstrate the analytical potential of LIBS for the chemical analysis of glass. For that purpose, two fragments of archaeological glass were used as samples. The first was a fragment of a bottom of a vessel made of dark green glass (Figure 1. a), the other was a fragment of a more delicate vessel in the shape of a vase made of opaque, pearly glass (Figure 1. b).

EXPERIMENTAL

Experiments were conducted using a setup based on the Transversely Excited Atmospheric pressure (TEA) CO₂ laser. It is a small, compact, laboratory-made laser. A working gas mixture in the laser chamber was CO₂/N₂/He in the volume ratio of 2:2:9. The energy of the laser pulse is up to 160 mJ. The laser emits radiation of 10.6 μm in the form of short pulses. The pulse repetition frequency is usually 1-2 Hz. The laser pulse of a TEA CO₂ laser consists of two parts, the initial peak and the tail. The initial peak has a full width at half maximum (FWHM) of 100 ns and contains about 35% of the

total radiated laser energy. The rest of about 65% is contained in the pulse tail, whose duration is over 2 μ s. The initial peak causes ablation of the target and initiation of plasma, while the pulse tail additionally and prolonged heats the plasma. These facts are responsible for the favorable properties of TEA CO₂ laser-induced plasma excitation conditions [2,3].

The laser beam was focused by a ZnSe lens of 125 mm focal length, while achromatic lenses were used to projected plasma optical emission on the entrance slit of a Carl Zeiss PGS-2 spectrometer. The spectrometer was equipped with a diffraction grating with 631 lines/mm, blazed at 290 nm. The U2C-16H11850 CCD camera (SOL Instruments.) with 2048 \times 64 chip (pixel size 14 \times 14 μ m) was used as a detection system. The spectral range of the camera is 200–1100 nm, with maximum spectral sensitivity at 600 nm. The target was set on the X-Y-Z translation stage and moved between two laser pulses to ensure that each laser pulse interacts with a new surface area. In this way, a stable plasma was produced. The camera was synchronized with the laser pulse, and the signal detection time was 10 ms.

Measurements were performed mainly using a laser pulse energy of 140 mJ, with the laser beam focused on the target. The radiation was detected from a plasma slice 1 mm above the target surface. Each measurement represents the mean value of at least ten consecutive individual spectra, whereby the spectra that deviated significantly in intensity from the mean value were discarded, after which the spectra were averaged again.

RESULTS AND DISCUSSION

Figure 1. c shows a part of the spectrum rich in narrow spectral lines of single-charged titanium ions. The lines of Mn, Cu, and Ni are also seen in the spectrum, together with spectral lines of the atmospheric air constituents (nitrogen and oxygen). The N II and O II lines emission originates from the early phases of plasma evolution, characterized by high temperature and electron number density. Because of that, these lines are very intense and broad. By carefully optimizing the laser focus, the observed plasma area, and delaying emission signal detection relative to the plasma generation, the emission of N and O lines can be eliminated. In this way, spectral lines of sample elements could be obtained with an even better signal-to-noise ratio.

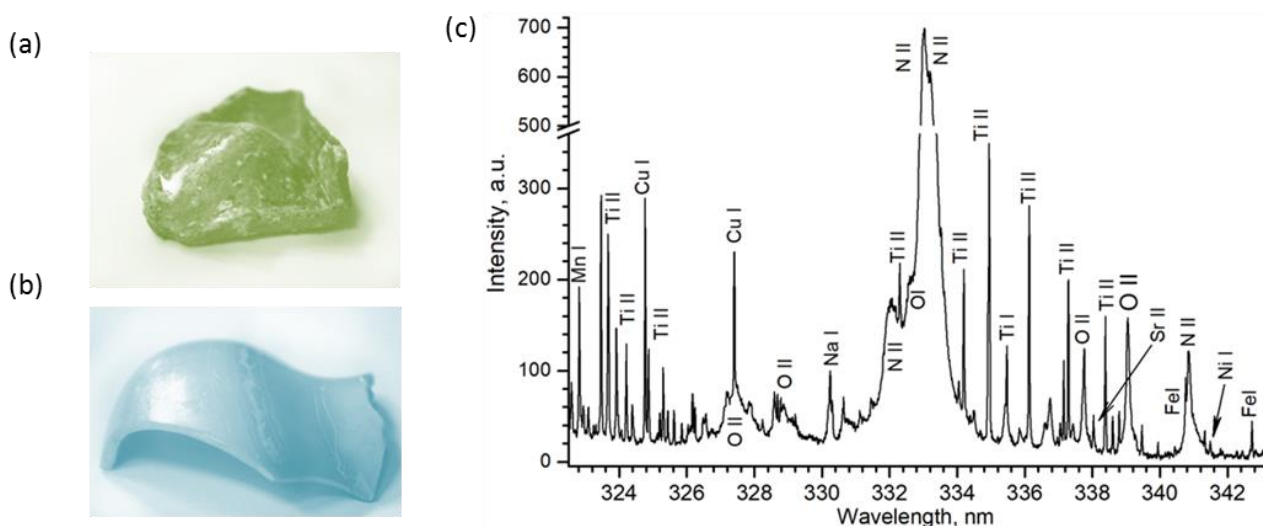


Figure 1. a) A green glass sample (flask bottom fragment); (b) Pearlescent glass sample (fragment of a vase); (c) Part of the UV spectra of the green glass sample.

In addition to the lines of elements that most often characterize ordinary (soda-lime-silica) glass (Si, Na, K, Ca, Al and Mg), high contents of Mn and Fe were registered in both samples, which were probably added in order to color the glass. Typically for non-modern glass samples, both samples have high concentrations of potassium, which was previously used instead of sodium for lowering the temperature necessary to produce glass. As known, the ordinary soda-lime glass appears colorless. Pigments (usually in a form of powdered metal oxides) are added in the manufacturing process to change the glass color. Although the elements identified in both samples were almost the same, the line intensities of characteristic elements were quite different. For instance, LIBS spectra of pearlescent glass were characterized by higher intensities of Ca and K and lower intensities of Fe and Mn lines compared to a green glass sample. In addition to the mentioned elements, Ti, Ba, Sr, and Cu were also detected.

In order to determine the limits of detection of the LIBS technique for glass analysis, elemental analysis of samples by X-ray fluorescence (XRF) was performed. The sensitivity of the LIBS technique was demonstrated for several elements, Ni, Cu, Ti, Mn, and K. The obtained LODs were 18, 2.5, 25, 32, and 205 ppm, respectively. LODs were determined as the concentration of an element whose spectral line intensity is equal to three times the standard deviation of the nearby background signal. The high LOD for K is a consequence of its low ionization energy and the fact that the most sensitive potassium lines were not used for the analysis as they are prone to self-absorption.

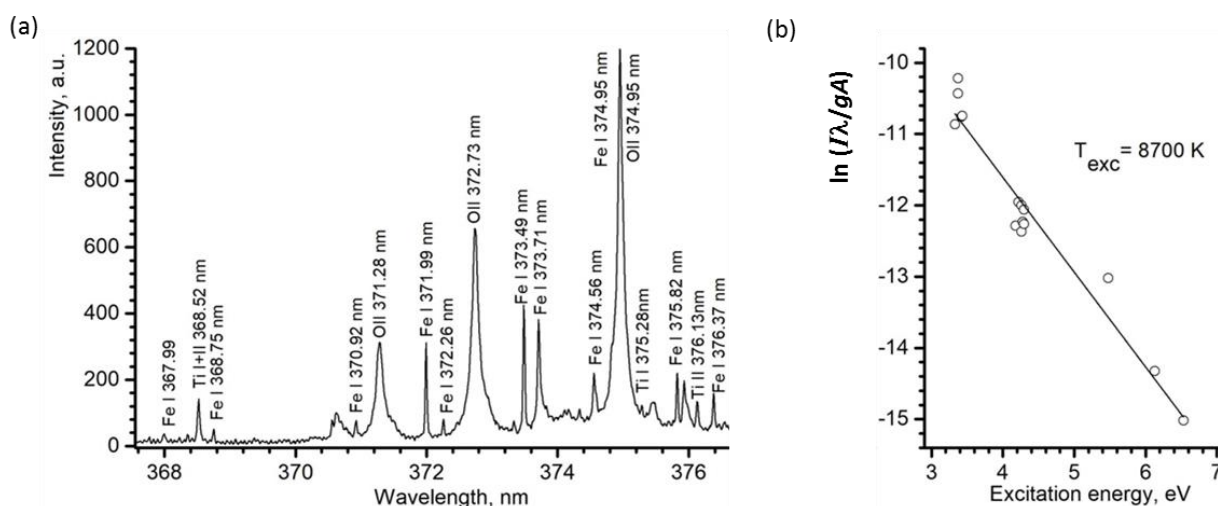


Figure 2. (a) Part of LIBS spectra of green glass sample; (b) The Boltzmann plot for the iron atomic spectral lines. The evaluated excitation temperature was 8700 ± 900 K.

Plasma diagnostics was performed using the spectral lines shown in Figure 2. a. Boltzmann plot method was used to evaluate the excitation temperature (Figure 2. b). The plot was constructed using suitable iron atomic lines, which in this spectral region have many spectral lines with a favorable distribution of excitation energies, and transition probabilities determined with high accuracy. A satisfactory linear fit was obtained from which the excitation temperature of 8700 K was determined, with a roughly estimated error of 900 K. The excitation temperature determined in this way was used to estimate the electron concentration using the intensity ratio of two spectral lines (ionic and atomic) of the same element [4]. For this purpose, the ratio of Ti II 376.13 nm and Ti I 375.28 nm lines were used. An electron concentration of $2 \cdot 10^{17} \text{ cm}^{-3}$ was obtained, with a relative error of about 30%. It should be underlined that the plasma parameters obtained in this way refer to the time interval and the volume of plasma from which the spectral lines of metal elements are predominantly emitted.

CONCLUSION

In this work, a potential of LIBS based on a TEA CO₂ laser for the spectrochemical analysis of glass has been demonstrated. The LIBS spectra consisted of sharp emission lines of main and minor glass constituents were obtained with a good signal-to-noise ratio. Limits of detection for Ni, Cu, and Ti were in the range of 2.5 to 32 ppm. The main parameters, temperature, and electron number density were determined to characterize excitation conditions in the plasma. The values of the excitation temperature and the electron number density were 8700 K and $2 \cdot 10^{17} \text{ cm}^{-3}$, respectively.

Acknowledgement

This work was partially supported by the Ministry of Education, Science and Technological Development of the Republic of Serbia through Contract No. 451-03-68/2020-14/200146, 451-03-9/2021-14/200017 and ИИИ 47025.

REFERENCES

- [1] M. Oujja, M. Sanz, F. Agua, J. Conde, M. García-Heras, A. Dávila, Pilar Oñate, J. Sanguino, J. R. V. D. Aldana, P. Moreno, M. Villegas, M. Castillejo, *J. Anal. At. Spectrom.* 2015, **30**, 1590-1599.
- [2] M. Momcilovic, M. Kuzmanovic, D. Rankovic, J. Ciganovic, M. Stoiljkovic, J. Savovic, M. Trtica, *Appl. Spectrosc.* 2015, **69**, 419-429.
- [3] J. Savovic, M. Stoiljkovic, M. Kuzmanovic, M. Momcilovic, J. Ciganovic, D. Rankovic, S. Zivkovic, M. Trtica, *Spectrochim. Acta Part B* 2016, **118**, 127-136.
- [4] E. Tognoni, M. Hidalgo, A. Canals, G. Cristoforetti, S. Legnaioli, A. Salvetti, V. Palleschi, *Spectrochim. Acta Part B* 2007, **62**, 435-443.

OPTICAL SPECTROSCOPY OF PLASMA INDUCED BY IRRADIATION OF ANIMAL BONE WITH TEA CO₂ LASER

M. Marković¹, D. Ranković¹, M. Savić Biserčić², M. Trtica², J. Savović² and M. Kuzmanović¹

¹ *University of Belgrade, Faculty of Physical Chemistry, Studentski Trg 12-16, 11000 Belgrade, Serbia. (miroslav@ffh.bg.ac.rs)*

² *University of Belgrade, INN Vinca, Mike Petrovića Alasa 12-14, 11001 Belgrade, Serbia.*

ABSTRACT

The application of laser-induced breakdown spectroscopy (LIBS) for the elemental analysis of pig shoulder bone samples is reported. Measurements were performed using a compact laboratory-made TEA CO₂ laser with low pulse energy. The recorded spectra consisted of well-defined lines of atoms and single charged ions of Ca, Mg, P, and other constituent elements, with a good signal-to-noise ratio suitable for spectrochemical analysis. Based on the ICP quantitative analysis of the bone sample, the limits of detection of LIBS analysis were estimated for Mg (16 ppm) and Na (940 ppm). Plasma parameters, temperature, and electron number density were determined by measuring Stark widths and relative intensities of the C and Mg ionic and atomic spectral lines.

INTRODUCTION

In forensic and archeological contexts, identifying isolated or fragmentary bones is essential since many non-osseous materials, like plastic, wood, or stones, can be mistaken for human/animal bone. Bones can be generally identified on three levels: gross skeletal anatomy, bone macrostructure, and bone histology (microstructure).

As a versatile, non-contact, multi-elemental, non-destructive sampling, powerful atomic spectrometry method LIBS provides elemental composition data of practically any forensic sample. LIBS utilizes a high power density laser pulse to ablate a sample and create a localized plasma plume. Plasma plume emits wavelengths characteristic of the elemental composition of the investigated sample.

TEA CO₂ laser has several advantages over the most common commercially used laser in LIBS, Nd:YAG laser. Unlike Nd:YAG laser, TEA CO₂ laser does much less damage to samples which is a benefit in applications such as forensics, archeology, or art where tolerance to damage and sample consumption is minimal. Its temporal pulse profile of the order of hundred nanoseconds, followed by a few μ s tail, produces a plasma plume with good analytical characteristics.

In this work, the applicability of a TEA CO₂ laser-based LIBS for qualitative analysis of the elemental composition of a pig shoulder bone was tested. The paper aims to demonstrate LIBS potential for relatively simple, fast, and sensitive analysis of complex organic matrices such as bones. The selection of a pig bone was based on its likeness with the human bones, i.e., only minor bone composition differences [1]. In addition, to characterize the excitation conditions in the laser-induced plasma, two main plasma parameters, electron number density and temperature were determined using standard spectroscopic methods. The calculated plasma parameters may be used to normalize the line intensities by intrinsically correcting for shot-to-shot fluctuations and are essential for quantitative LIBS analysis using a calibration-free approach.

EXPERIMENTAL

The Transversely Excited Atmospheric pressure carbon dioxide (TEA CO₂) laser, developed at the VINCA Institute of Nuclear Sciences, was used as the radiation source in the applied LIBS setup [2]. The operating laser wavelengths were 10.5709 and 10.5909 μ m, and the pulse repetition rate up to 2

Hz when in a multimode regime. The initial laser peak, which lasted around ~ 100 ns, carried approximately 35% of the total pulse energy. The initial peak was followed by a decaying tail which lasted around ~ 2 μ s.

The optimized measurement parameters were: laser pulse energy of 155 mJ, laser beam focused at the sample surface, acquisition of plasma emission from a plasma slice 1 mm above the sample surface. ZnSe lens was used for laser beam focusing. A plasma image was projected on the entrance slit of a Carl Zeiss PGS2 spectrograph by an achromatic quartz lens. U2C-16H11850 CCD camera with enhanced sensitivity in UV range was used to capture plasma emission spectra. The CCD camera was triggered at a minimal exposure time of 10 ms to reduce dark current and noise.

A preliminary quantitative analysis of samples was performed using the ICP OES technique (iCAP 6000, Thermo Scientific). Digestion procedure using mineral acids was performed to prepare bone samples for ICP analysis. Multi-element standard solutions were prepared from 1000 ppm ICP standard stock solution (Merck) and used for calibration. Concentrations of the phosphorus determined in the bone sample was 12.8 %. Other elements detected in ppm concentrations were Mg (3440 ppm), Na (4330 ppm) and Al (214 ppm).

RESULTS AND DISCUSSION

Part of the spectrum obtained by irradiating the bone sample with TEA CO₂ laser pulses is shown in Fig. 1. In the spectral region around 250 nm, atomic and ionic carbon lines and strong atomic phosphorus lines dominate the spectrum. In addition, oxygen and nitrogen ion lines from the atmosphere were observed in the spectrum.

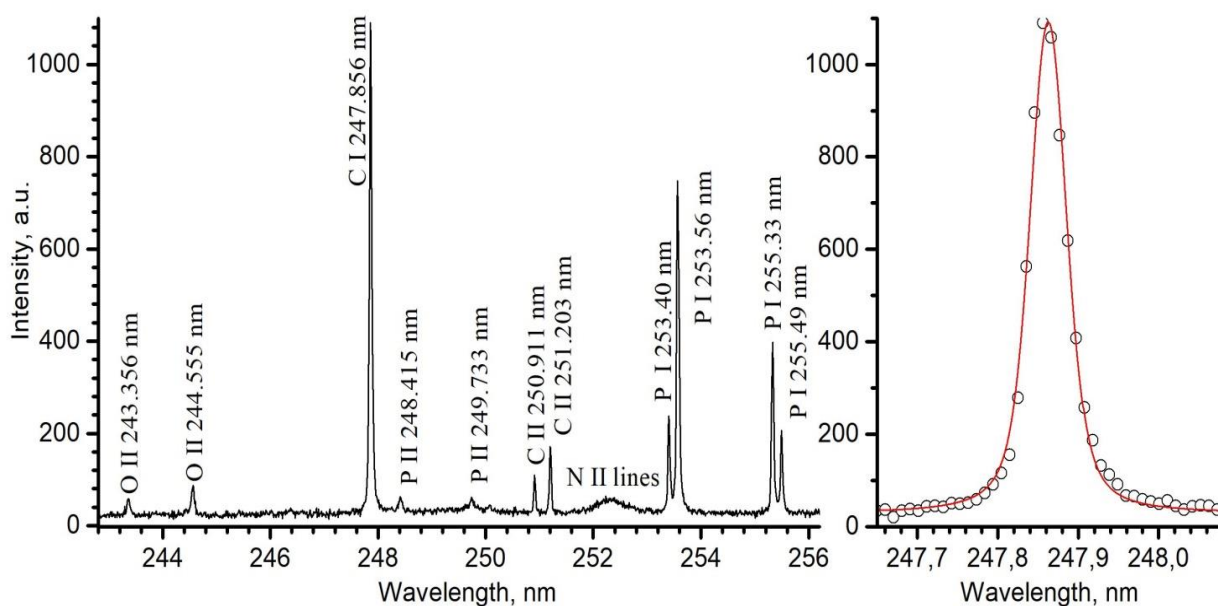


Figure 1. a) Part of UV spectra of the pig shoulder bone sample, b) Profile of C I 247.856 nm line fitted with Voigt profile (fixed Gaussian width of 0.040 nm)

The measurement of the ionic to atomic carbon line intensity ratio is a very suitable method for determining the ionic temperature (T_{ion}) in plasma [3]. Determination of temperature using the C II/C I intensity ratio required knowledge of the electron concentration, N_e . The electron number density was determined from the Stark-broadened profile of the C I 247.86 nm line. The experimental line profile was deconvolved to extract Lorentz width, assuming that the Stark broadening dominates the Lorentz profile. The ion broadening coefficient for the C I 247.86 nm line is very small (0.033 at 10^{16}

cm^{-3}) and due to considerable Gaussian width the Stark width was determined by deconvolution using Voigt fitting. The Gaussian component of the profile was fixed to the predetermined instrumental width (0.040 nm). The Stark width of carbon 247.86 nm line was 0.024 nm which corresponds to the electron number density of $2.9 \times 10^{17} \text{ cm}^{-3}$ [4]. The ionic temperature of $T_{ion} = 18100 \text{ K}$ was calculated from the measured intensity ratio of C II 250.91 nm and C I 247.86 nm lines (0.077) and the predetermined value of N_e .

An intense C I line at 247.86 nm is suitable for the determination of the carbon concentration. Using the measured intensity to background noise ratio of the carbon line and assuming the typical carbon concentration in bones (mainly in the form of CaCO_3) is about 5%, the detection limit (LOD) for carbon was estimated at 0.07%. Similarly, using the Na I line 330.23 nm line, LOD for sodium was estimated at 940 ppm. Despite a low sensitivity, this line is still usable for detecting Na in samples with larger quantities of this element, as our bone sample (4330 ppm). The Na I line at 588.00 nm is suitable to determine Na with higher sensitivity, but only in samples with low Na concentrations since this line is highly prone to self-absorption.

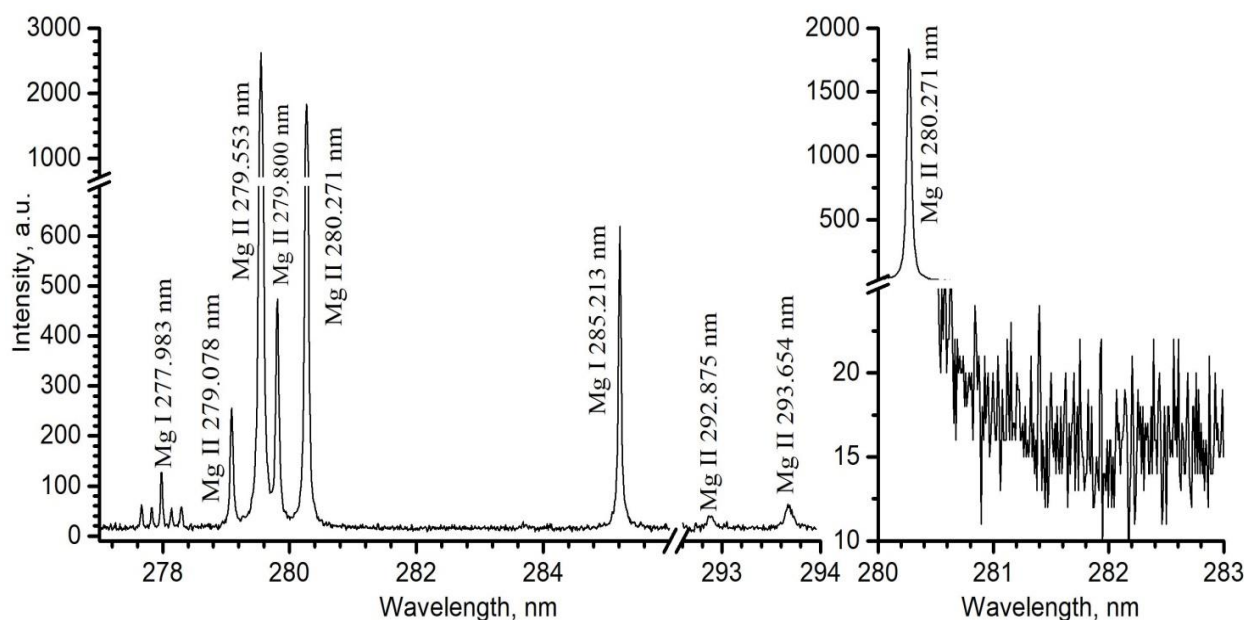


Figure 2. a) Part of LIBS spectra of the pig shoulder bone sample: Mg I and Mg II lines, b) Illustration of the determination of LOD for magnesium.

In Fig. 2a, a group of magnesium ionic and atomic lines suitable for plasma diagnostics is shown. Using the predetermined electron concentration, from the ratio of Mg II 280.27 nm and Mg I 285.21 nm line integral intensities [5], the ionization temperature of 10500 K was calculated. The difference in temperatures determined from carbon and magnesium lines is caused by the fact that the predominant emission of these lines comes from different plasma regions. Due to the significantly higher ionization and excitation energy of carbon regarding magnesium, the maximum carbon emission is located in the hotter plasma zones. The lines shown in Fig. 2 are also suitable for determining the magnesium content. Magnesium is present in the bones in a significant concentration, e.g., the Mg concentration in our sample was 0.344%. Figure 2b illustrates the determination of LOD using the Mg II ionic line at 280.27 nm. The obtained LOD for Mg was 16 ppm.

CONCLUSION

The applicability of the LIBS technique based on low pulse energy TEA CO₂ laser for the elemental analysis of bone samples was demonstrated. LIBS can be used to detect most metals in bones with detection limits between 10-100 ppm, as illustrated by the Mg example. The possibility of using Mg and C lines for plasma diagnostics was also demonstrated. Apparent values for electron concentration of $2.9 \times 10^{17} \text{ cm}^{-3}$ and ionization temperature in the range from 10500 to 18100 K were determined, depending on the properties of the element whose lines were used for diagnostics.

Acknowledgement

This work was partially supported by the Ministry of Education, Science and Technological Development of the Republic of Serbia through Contract No. 451-03-68/2020-14/200146 and 451-03-9/2021-14/200017.

REFERENCES

- [1] K. Franke, F. Schöne, A. Berk, M. Leiterer, G. Flachowsky, *Eur. J. Nutr.* 2008, **47**, 40–46.
- [2] M. Momcilovic, M. Kuzmanovic, D. Rankovic, J. Ciganovic, M. Stoiljkovic, J. Savovic, M. Trtica, *Appl. Spectrosc.* 2015, **69**, 419-429.
- [3] M. Kuzmanovic, D. Rankovic, M. Trtica, J. Ciganovic, J. Petrovic, J. Savovic, *Spectrochim. Acta* 2019, **157**, 37-46.
- [4] H. Griem, *Spectral Line Broadening by Plasmas*, Academic Press, New York, 1974.
- [5] E. Tognoni, M. Hidalgo, A. Canals, G. Cristoforetti, S. Legnaioli, A. Salvetti, V. Palleschi, *Spectrochim. Acta Part B* 2007, **62**, 435-443.

CONFORMATIONAL AND SPECTROSCOPIC ANALYSES OF 2-(4-FLUOROPHENYL)-2-HYDROXYPROPANOIC ACID

V. Vitnik and Ž. Vitnik

Department of Chemistry, Institute of Chemistry, Technology and Metallurgy, University of Belgrade, Njegoševa 12, 11000 Belgrade, Serbia. (vesnak@chem.bg.ac.rs)

ABSTRACT

The conformational and vibrational spectroscopic analyses of 2-(4-fluorophenyl)-2-hydroxypropanoic acid (FHPA) are represented in this research. Theoretical calculations were performed by density functional theory (DFT) with B3LYP method using 6-311++G(d,p) basis set. The FT-IR and Raman spectra of FHPA were recorded and analyzed. The comparison between the experimental and calculated spectra showed good agreement. Molecular electrostatic potential map (MEP) of the compound was calculated to predict chemical reactivity of the title molecule.

INTRODUCTION

Fluoro compounds are widely used in medicinal chemistry. Compounds with a C-F bond are well known drugs such as: cholesterol-absorption inhibitor Ezetimibe [1], Celecoxib [2] inhibitor of the cyclo-oxygenase 2, antimalarial drug Mefloquine and anticancer drug 5-fluorouracil. Fluoxetine [3] is approved as the drug for use in the treatment of both obsessive-compulsive disorder and bulimia. Many fluoroquinolones are highly active antibacterial agents that are widely used [4]. Fluoro compounds have broad spectrum of industrial applications like refrigerants fluoropolymers and fire extinguishants. Some fluoro compounds containing OCF₃-group have application in electro-optical materials and are used for the development of liquid crystal displays.

In an attempt to give our contribution to the structural analysis of fluoro compounds, in the present study, the stability of different possible conformers of monomer and dimer of FHPA are determined. The vibrational spectra of FHPA are analyzed to confirm the molecular structure. MEP surface is plotted over the optimized geometry to find out the reactivity of FHPA molecule.

EXPERIMENTAL DETAILS

The chemical structure and purity of the synthesized compound was confirmed by its melting point, ¹H and ¹³C NMR, FT-IR and UV spectra. FT-IR spectrum was recorded on a Bomem MB 100 spectrophotometer. The Raman spectrum of FHPA was recorded in the region of 50–3500 cm⁻¹ using Thermo DXR Raman microscope with the 532 nm laser excitation line, with a constant power of 10 mW and exposure time of 10.00 s.

COMPUTATIONAL DETAILS

All the calculations were performed using Gaussian 09 Revision D.01 program package. Geometry of FHPA was fully optimized at DFT/B3LYP/6-311++G(d,p) level of theory. The harmonic frequencies were calculated with the same method and scaled by 0.967. The assignments of the calculated wavenumbers were aided by the animation option of Gauss View 3.0 graphical interface from Gaussian programs. To investigate the reactive sites of FHPA, MEP for the 0.002 a.u. isosurfaces of electron density was evaluated using the B3LYP/6-311++G(d,p) level of theory.

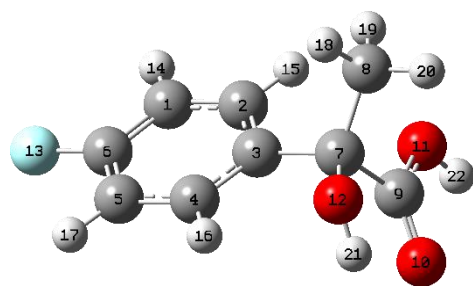


Figure 1. Optimized geometry of FHPA

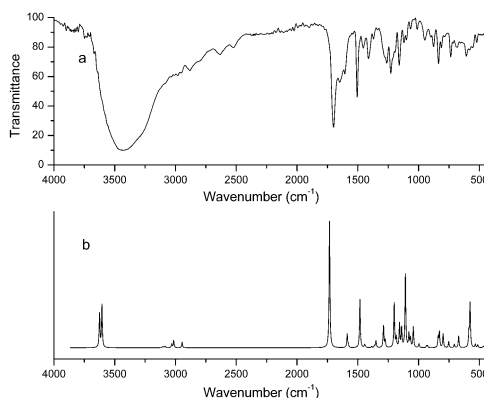


Figure 2. Experimental and predicted IR spectra of FHPA

RESULTS AND DISCUSSIONS

Detailed conformational analysis was evaluated to find all stable conformers of FHPA. Analysis shows that orientation of phenyl, OH and COOH groups attached in position C7 defines conformational characteristics of molecule. The position and different orientations of these groups give rise to eleven stable conformers. The DFT energy and the statistical Boltzmann distribution reveal that the two isomers acquire dominant stability among other isomers with 84.35 and 12.97 of percentage contribution. The stability of conformers highly depends on the orientation of phenyl ring and possibility to form intramolecular hydrogen bond. The phenyl ring in most stable conformers is in the same plane with α -OH group while in the least stable one is in the plane of COOH group. The optimized molecular structure of the most stable conformer with the atom numbering scheme of the title molecule is shown in Fig. 1.

In order to estimate the barrier height and confirm the transitions between conformers for the rotation around single bonds potential energy scan (PES) is done. The energy for rotation of phenyl ring when passing through a plane of C1-COOH bond is 2.5 kcal/mol while the rotation of COOH group requires 5.5 and 7.0 kcal/mol of energy when the group is in the plane of C7-C(Ph) bond.

Since FHPA possesses three groups that can form an intermolecular hydrogen bonds, in an additional part of the conformational analysis, the stability of potential dimers is investigated. Also the atom C7 represents stereocenter and two types of dimers can be formed: centrosymmetric (*R/S* or *S/R*) and with C_2 symmetry (*R/R* or *S/S*). From the DFT calculations it is evident that the most stable dimer is centrosymmetric dimer with intermolecular hydrogen bond between carboxyl groups of two molecules with different configuration of stereocenters (*R/S* or *S/R*).

As the exact geometrical parameters of the investigated molecule are not available, the literature data on crystal of the similar compound, 2-(4-fluorophenyl)-2-hydroxyacetic acid, are used for comparison. In the crystal structure of racemic form of this molecule the centrosymmetric dimer formed with intermolecular hydrogen bond between carboxyl group of one molecule and α -OH group of the other molecule is found (CCDC 1292366). Also, the dimer formed via intermolecular hydrogen bonds between carboxyl groups of two molecules is not found in the literature. Instead of that combined hydrogen bonding is found in crystal of optically active molecule a.i. pure enantiomer form (CCDC 131621) in a form of asymmetric trimer with α -OH \cdots O=C, OH \cdots O=C and α -OH \cdots α -OH hydrogen bonds.

In FT-IR spectrum of FHPA the broad absorption bands at 3425 and 3295 cm^{-1} are assigned to O11-H22 and O12-H21 stretching vibrations, respectively. In FT-Raman spectrum these vibrations are appeared as sharp peaks at 3230 and 3200 cm^{-1} . The bands at 3010/3010 cm^{-1} and 2984/3092 cm^{-1} (FT-IR/FT-Raman) are assigned to asymmetric and symmetric stretching vibrations of aromatic C-H groups, respectively. The bands observed at 2952/2989 and 2882/2944 cm^{-1} (FT-IR/FT-Raman)

are assigned to asymmetric and symmetric C-H stretching vibrations of C₈H₃ group, respectively. The C=O stretching vibrations appeared as very sharp and intense band at 1735 cm⁻¹ in FT-IR and weak band at 1696 cm⁻¹ in FT-Raman spectrum. The strong bands observed at 1649 and 1608 cm⁻¹ in FT-IR spectrum are assigned as C-C stretching vibrations of the phenyl ring. In FT-Raman spectrum the band corresponding to the same vibrations appears as a weak band at 1606 cm⁻¹. The bands at 813, 1229/773, 1195 cm⁻¹ (FT-IR/FT-Raman) are assigned to C-F stretching vibrations.

The medium to strong bands observed in the FT-IR/FT-Raman spectra at 1229/1165 and 1262/1220 cm⁻¹ are assigned to aromatic C-H in-plane bending vibrations, and weak and medium bands at 836, 900, 949 cm⁻¹, and strong band at 815 cm⁻¹ (FT-IR/FT-Raman) are assigned to C-H out-of-plane deformation modes. In-plane bending vibrations of O11-H22 group lead to two bands at 1121 and 1160 cm⁻¹ in FT-IR (1100 and 1128 cm⁻¹ in Raman) and bands centered at 461 and 785 cm⁻¹ in FT-IR (728 cm⁻¹ in Raman) are assigned to out-of-plane bending vibrations. The O12-H21 in- and out-of-plane bending vibrations appear as weak bands at 1338/1294 cm⁻¹ and 415, 420, 468/420 cm⁻¹ (FT-IR/FT-Raman), respectively. Bands of the in- and out-of-plane bending vibrations of C9=O10 bond appear at 1160/1128, 1121/1100 cm⁻¹ and at 461/ 785 cm⁻¹ (FT-IR/FT-Raman), respectively. The weak bands at 522/612 and 411, 480/500 cm⁻¹ (FT-IR/FT-Raman) are assigned to in- and out-of-plane bending vibrations of C-F bond, respectively. All the calculated wavenumbers show excellent agreement with the experimental data.

The maximum negative region of MEP (possible site for electrophilic attack) is spread over oxygen atoms O10, O11 and O12 of carboxyl and α-hydroxyl group, respectively. The maximum positive region (possible site for nucleophilic attack) is mainly localized on the hydrogen atom H22.

CONCLUSION

The structural, vibrational properties and chemical reactivity of FHPA were studied with DFT/B3LYP/6-311++G(d,p) method. The calculated results correlate well with the experimental values.

Acknowledgement

This work was financially supported by Ministry of Education, Science and Technological Development of the Republic of Serbia (Grant No. 451-03-68/2020-14/200026).

REFERENCES

- [1] J. W. Clader, *J. Med. Chem.* 2004, 47, 1-9.
- [2] D. Clemett, K. L. Goa, *Drugs*, 2000, 59, 957-980.
- [3] D. L. Roman, C. C. Walline, G. J. Rodriguez, E. L. Barker, *Eur. J. Pharmacol.*, 2003, 479 (1-3), 53-63.
- [4] P. Ball, *J. Antimicrob. Chemother.*, 2000, 46, 17-24

SPECTROSCOPIC AND COMPUTATIONAL STUDY OF NOVEL DIHYDROPYRIMIDINE AZO PYRIDONE DYE

Ž. Vitnik¹, J. Tadić², D. Mijin³ and V. Vitnik¹

¹ Department of Chemistry, ICTM, University of Belgrade, Belgrade, Serbia,
(vesnak@chem.bg.ac.rs)

² Innovation Center, Faculty of Technology and Metallurgy, University of Belgrade, Belgrade, Serbia

³ Department of Organic Chemistry, Faculty of Technology and Metallurgy, University of Belgrade, Belgrade, Serbia

ABSTRACT

Structural, vibrational, electronic, NMR and reactivity properties of ethyl 4-(4-((5-cyano-2-hydroxy-4-methyl-6-oxo-1-propyl-1,6-dihydropyridine-3-yl)diazenyl)phenyl)-6-methyl-2-oxo-1,2,3,4-tetrahydropyrimidine-5-carboxylate (PPD) were investigated by using density functional theory (DFT). Theoretical calculations were performed with B3LYP/6-311++G(d,p) method. The calculated data correlated well with the experimental ones. HOMO-LUMO energy gap for the title molecule confirmed the high reactivity of dye. The obtained results verified the hydrazone form as *more stable one*. In addition, molecular electrostatic potential (MEP) map of the dye was used to test its activity.

INTRODUCTION

The heterocyclic azo dyes have been *extensively* studied because of their significant coloration properties [1]. Also, some of arylazo pyridone dyes possess antibacterial [2] and anticancer [3] activity. It is well known that compounds based on the 3,4-dihydropyrimidine-2(1*H*)-one (DHPM) core have broad spectrum of activities like antibacterial, antiviral, antioxidant, anti-inflammatory and antitumor [4].

In this paper the structural and spectroscopic properties of newly synthesized DHPM azo pyridone dye were calculated. Also, azo-hydrazone tautomerism of dye PPD was analyzed.

EXPERIMENTAL DETAILS

The structure of the newly synthesized compound was elucidated by melting point and FT-IR, UV-Vis, MS, ¹H and ¹³C NMR spectral data. FT-IR spectrum was recorded on the Nicolet™ iS™ 10 FT-IR spectrometer in the region 500–4000 cm⁻¹ using ATR technique. The ultraviolet absorption spectrum of PPD was examined in the range of 200-600 nm using Shimadzu 1700 spectrophotometer. The UV pattern was taken from a 10⁻⁵ molar solution of ethanol. ¹H and ¹³C NMR spectra were recorded on a Bruker Ascend 400 instrument at 400 Hz and 100 MHz, respectively, in DMSO-*d*₆. Quadrupole ion trap mass spectrometer LCQ Advantage (Thermo Fisher Scientific, USA) was used for the compounds detection.

COMPUTATIONAL DETAILS

All the calculations were performed using Gaussian 09 program package. Geometry of PPD was fully optimized with DFT/B3LYP/6-311++G(d,p) method. The calculated harmonic frequencies are scaled by 0.968. ¹H and ¹³C NMR chemical shifts are calculated with GIAO approach. UV absorption energies of this compound in ethanol were calculated by TD-DFT method. The frontier molecular orbital energies and HOMO-LUMO energy gap are calculated with B3LYP/6-311++G(d,p) method.

The molecular electrostatic potentials for the 0.002 a.u. isosurfaces of electron density was evaluated using the same method.

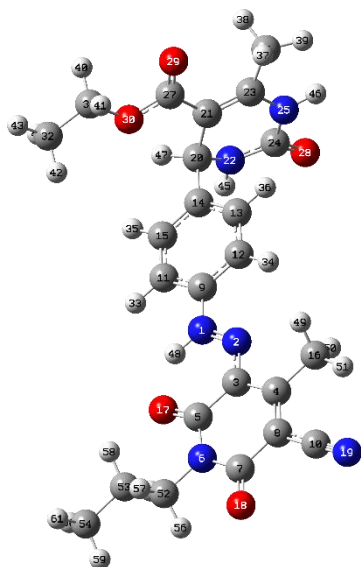


Figure 1. Optimized geometry of PPD

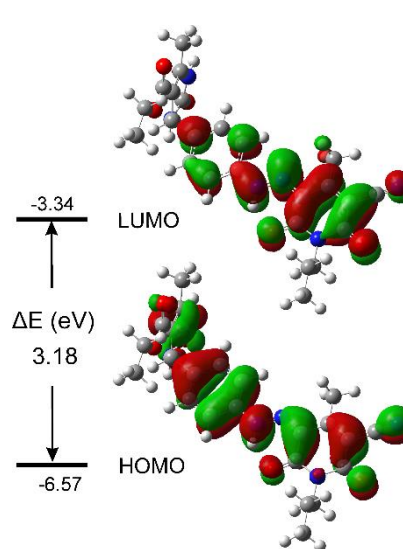


Figure 2. HOMO-LUMO plot of PPD

RESULTS AND DISCUSSIONS

The calculated energy data of possible tautomeric forms confirm that the most stable form of the dye is hydrazone one. The phenylazo pyridone part of PPD molecule is planar while the DHPM group is normal to that plane which prevents electron delocalization between these two parts of the molecule. The largest conformational difference in the molecule results from the rotation of the DHPM group around the C14-C21 bond. The calculation showed that the energy barrier for this rotation is just 2.0 kcal/mol and that the rotation produces two conformers with almost identical energies. The optimized geometry of the most stable conformer obtained with B3LYP method is presented in Fig. 1 with numbering of atoms. To the best of our knowledge, exact experimental structure data of PPD are not yet known in the literature.

In calculated IR spectrum of PPD, weak and broad absorption bands at 3513 and 3499 cm^{-1} are assigned to N25-H46 and N22-H45 stretching modes of the dihydropyrimidinone ring, respectively. These bands appear at 3593 and 3507 cm^{-1} in experimental FT-IR spectrum, respectively. The band at 3181 cm^{-1} is assigned to N1-H48 stretching mode of hydrazone group. The bands of symmetric and asymmetric C-H stretching modes of the phenyl group are at 3076 and 3061 cm^{-1} , respectively. The band calculated at 2255 cm^{-1} belongs to stretching vibration of nitrile group. The sharp and intensive bands observed at 1728 and 1687 cm^{-1} in calculated IR spectrum are assigned to C24=O28 and C27=O29 stretching vibrations of dihydropyrimidinone ring and ethoxycarbonyl group, respectively. For two polar carbonyl groups, C7=O18 and C5=O17, of pyridone ring the calculated energy values of stretching vibrations are 1682 and 1617 cm^{-1} , respectively. The band of the combined mode of C3=N2 stretching vibration and in-plane bending N1-H18 vibration appears at 1519 cm^{-1} in calculated spectrum and correlate well with experimental value of 1514 cm^{-1} . The shapes of the calculated and experimental infrared spectra reveal that hydrazone tautomer is predominant form of the dye in the solid state.

Additional evidence of hydrazone tautomeric form of PPD are characteristic signals of hydrogen of N-H groups in ^1H NMR spectrum as well as ^{13}C NMR signals of carbon atoms of carbonyl groups.

In ^1H NMR spectrum signal at 14.62 ppm marks hydrogen H48 which belongs to hydrazone group. The predicted value is 14.68 ppm. Two signals that appear at 9.23 and 7.77 ppm, assigned to H46 and H45, respectively, indicate the presence of two N-H groups as part of dihydropyrimidinone ring. In predicted ^{13}C NMR spectrum of the investigated dye, resonance maximum at 174.67 ppm, assigned to ethoxycarbonyl group, correlates with the experimental value of 165.72 ppm. Resonance maxima of C7 and C5 of carbonyl groups of pyridone ring are at 169.67 and 168.71 ppm while the experimental values are 161.18 and 160.66 ppm, respectively. The chemical shift value of C24 atom of carbonyl group in dihydropyrimidinone ring is observed at 152.46 ppm while the corresponding computed value is 158.1 ppm. The carbon atom C3 resonates at 123.48 ppm in the ^{13}C NMR spectrum and the computed value is 130.58 ppm. The chemical shift values predicted by TD-DFT are in close agreement with the experimental ones.

Density plots over the highest occupied molecular orbital (HOMO) and lowest unoccupied molecular orbital (LUMO) energy surface identifies the donor and acceptor groups in the molecule. However, it provides information about the intramolecular charge transfer (ICT) through the molecule. As can be seen from the Fig. 2, HOMO is spread over dihydropyrimidinone and phenyl rings. LUMO is mainly located over pyridone ring and support ICT through investigated molecule. The frontier orbital energy gap for PPD is 3.18 eV and reveals the high reactivity of molecule.

In attempt to predict reactive sites of electrophilic or nucleophilic attack for molecule PPD, the MEP at the B3LYP/6-311++G(d,p) optimized geometry is calculated. PPD molecule has three possible sites for electrophilic attack because negative regions in the studied molecule are found around the O28 and O18 atoms of carbonyl groups as well as nitrile group. The maximum positive region is localized on the H45 and H46 atoms of two N-H groups of dihydropyrimidinone ring indicating the possible sites for nucleophilic attack.

CONCLUSION

Detailed DFT and experimental analyzes of structural and spectroscopic properties of PPD have shed light on the existence of its hydrazone tautomeric form as the most stable form of the molecule.

Acknowledgement

This work was financially supported by Ministry of Education, Science and Technological Development of the Republic of Serbia (Grant No. 451-03-68/2020-14/200026, 451-03-68/2020-14/200135 and 451-03-68/2020-14/ 200287).

REFERENCES

- [1] M. A. Metwally, E. Abdel-Galil, A. Metwally, F. A. Amer, *Dyes Pigm.* 2012, 92(3), 902-908
- [2] S. M. Ashkar, M. A. El-Asasery, M. M. Touma, M. H. Elnagdi, *Molecules* 2012, 17, 8822-8831.
- [3] D. Mijin, B. Božić Nedeljković, B. Božić, I. Kovrlija, J. Lađarević, G. Ušćumlić, *Turk. J. Chem.* 2018, 42, 896-907.
- [4] Â. de Fátima, T. C. Braga, L. da S. Neto, B. S. Terra, B. G. F. Oliveira, D. L.da Silva, L. V. Modolo, *J. Adv. Res.* 2015, 6, 363-373.

EXPERIMENTAL AND THEORETICAL UV-VIS SPECTRAL STUDY OF SOME ARYLAZO PYRIDONE DYES IN AMIDE SOLVENTS

J. Lađarević ¹, Ž. Vitnik ², V. Vitnik ², B. Božić ³ and D. Mijin ¹

¹ Faculty of Technology and Metallurgy, University of Belgrade, Karnegijeva 4, Belgrade, Serbia

² Institute of Chemistry, Technology and Metallurgy, University of Belgrade, Njegoševa 12, 11000 Belgrade, Serbia. (vesnak@chem.bg.ac.rs)

³ Institute of Physiology and Biochemistry "Ivan Đaja", Faculty of Biology, University of Belgrade, Studentski trg 16, Belgrade, Serbia

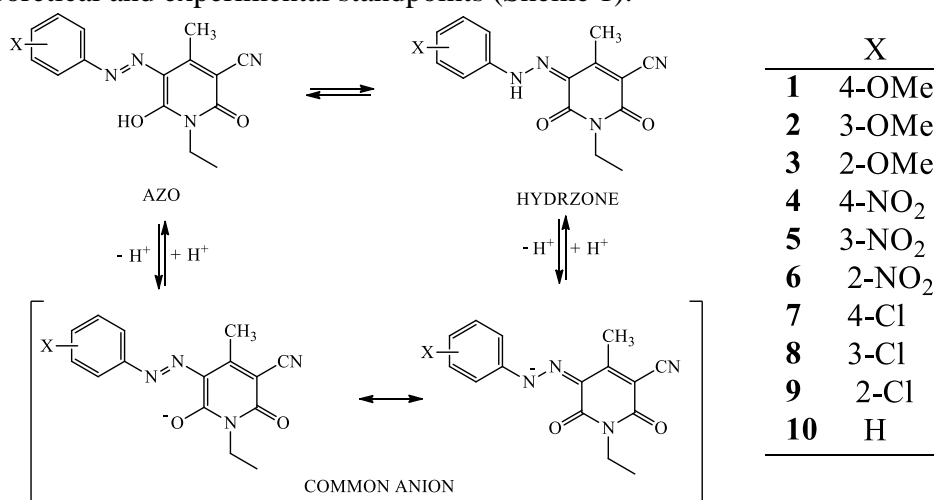
ABSTRACT

Spectral properties of ten 5-(substituted phenylazo)-3-cyano-1-ethyl-6-hydroxy-4-methyl-2-pyridones were investigated in formamide and *N,N*-dimethylformamide (DMF) by combining experimental study and density functional theory (DFT). In these two solvents, equilibrium between hydrazone and anionic forms is confirmed both experimentally and theoretically. Relative position of the absorption maxima of hydrazone and anion forms is highly affected by the substitution pattern in the phenyl ring. Theoretical absorption energies showed good agreement with experimental data.

INTRODUCTION

Arylazo pyridone dyes comprise a significant class of disperse dyes composed of pyridone ring, as coupling component, and carbocyclic and heterocyclic ring as diazo component. Their use in the textile industry have been known for a long time and is highly affected by their good wash and light fastness properties, vigorous colors and molar extinction coefficients [1,2]. In recent years, they are also utilized as suitable compounds for liquid crystal displays (LCD), ink-jet printing, hot melt or phase change inks [3]. One of the most interesting features of these dyes is the possibility of the azo-hydrazone tautomerism for the dyes bearing –OH group in *ortho*- and *para*-position to the azo bridge. This phenomenon has attracted a considerable attention since tautomers possess different physical, optical and toxicological properties, and most important different tinctorial strengths [4].

In this work, UV-Vis spectral properties of ten 5-(substituted phenylazo)-3-cyano-1-ethyl-6-hydroxy-4-methyl-2-pyridones of diverse substituents (R = –OMe, –NO₂, –Cl, H) in different positions of the phenyl moiety (*ortho*-, *meta*- and *para*-) have been analyzed in formamide and DMF both from theoretical and experimental standpoints (Scheme 1).



Scheme 1. Possible forms of the investigated dyes in solutions.

METHODS

UV-Vis spectra were collected on a Shimadzu 1700 spectrophotometer at a concentration of 5×10^{-5} mol dm⁻³. All spectra are recorded at room temperature.

Geometries of all investigated dyes have been calculated using the Gaussian 09 program package on M06-2X/6-311++G(d,p) method using a conductor-like polarisable continuum model (CPCM) for inclusion of solvent effects. UV absorption energies in formamide and DMF were calculated by TD-DFT approach on the same level of theory.

RESULTS AND DISCUSSION

DFT study show that investigated dyes adopt hydrazone form in the solid state and most of the solvents [5]. Intramolecular hydrogen bond between carbonyl group of pyridone ring and hydrogen of N–H hydrazone bond is considered to be the main reason for high stability of this form. In proton-accepting solvents, deprotonation takes place and equilibrium between hydrazone and common anion has been established (Scheme 1).

UV-Vis spectra of the dyes 1-10 in formamide and DMF clearly show the existence of two forms in the solution. Furthermore, all spectra exhibit bands in the region between 300–340 nm which have been proven to be an indicator of the anionic form in DMF [5]. In order to determine the position of the hydrazone form, acetic acid is added to the solution to eliminate the present anionic form, while the position of anionic form is confirmed upon addition of the solid NaOH (Table 1). It can be observed that the relative positions of the hydrazone and anionic form are dependent on the substitution pattern. Anion form appears at lower wavelength with respect to hydrazone form, except in the case of 4 whose anion form show bathochromic shift.

Table 1. Experimental and theoretical UV-Vis maxima of hydrazone and anionic forms and their differences ($\Delta\lambda = \lambda_{\text{anion}} - \lambda_{\text{hydrazone}}$) in formamide.

	Experimental			theoretical (scaled) ^a M06-2X		
	$\lambda_{\text{hydra.}}$, nm	λ_{anion} , nm	$\Delta\lambda$, nm	$\lambda_{\text{hydra.}}$, nm	λ_{anion} , nm	$\Delta\lambda$, nm
1	465.5	404.0	-61.5	463.83	432.87	-30.96
2	441.0	400.0	-41.0	443.79	433.75	-10.05
3	463.0	405.0	-58.0	461.69	429.49	-32.20
4	443.0	508.0	65.0	441.58	491.48	49.90
5	426.5	406.0	-20.5	426.38	439.80	13.42
6	450.0	410.0	-40.0	448.39	442.66	-5.73
7	440.5	405.0	-35.5	442.20	437.52	-4.69
8	433.5	403.0	-30.5	433.54	437.25	3.71
9	438.5	413.0	-25.5	438.67	438.27	-0.39
10	438.0	396.5	-41.5	438.28	430.78	-7.51

^a scaled by 1.16

Table 2. Experimental and theoretical UV-Vis maxima of hydrazone and anionic forms and their differences ($\Delta\lambda = \lambda_{\text{anion}} - \lambda_{\text{hydrazone}}$) in DMF.

	Experimental			theoretical (scaled) M06-2X [5]		
	$\lambda_{\text{hydra.}}$, nm	λ_{anion} , nm	$\Delta\lambda$, nm	$\lambda_{\text{hydra.}}$, nm	λ_{anion} , nm	$\Delta\lambda$, nm
1	458.0	420.5	-37.5	457.08	427.21	-32.87
2	437.0	408.0	-29.0	437.59	428.26	-9.33
3	454.5	408.5	-46.0	454.96	423.97	-30.99
4	438.0	483.0	45.0	435.26	485.55	50.29
5	421.5	414.0	-7.5	420.44	434.42	13.98
6	442.0	426.5	-15.5	441.88	437.31	-4.57
7	433.5	415.0	-18.5	436.03	432.00	-4.03
8	426.5	416.0	-10.5	427.48	431.81	4.33
9	431.5	418.0	-13.5	432.52	432.73	0.21
10	433.0	406.0	-27.0	432.11	425.37	-6.74

^a scaled by 1.1456

It is known that the TD-DFT M06-2X method gives underestimated wavelengths of absorption maxima so it is necessary to scale the calculated values. The best scaling factors for formamide and DMF of 1.16 and 1.1456 were determined by fitting. The scaled values show excellent agreement with the experimentally determined values for the hydrazone form. However, the calculated values for the anionic form show a significant overestimation of the maxima as well as a significant underestimation of the difference between maxima of anion and hydrazone forms.

CONCLUSION

In proton-accepting solvents, equilibrium between hydrazone and common anion has been established. The position of absorption maxima of the hydrazone and anionic forms are determined. The calculated values for the anionic form show significant overestimation of the maxima and underestimation of the difference between maxima of anion and hydrazone forms.

Acknowledgement

This work was financially supported by Ministry of Education, Science and Technological Development of the Republic of Serbia (Grant No. 451-03-68/2020-14/200026, 451-03-68/2020-14/200135 and 451-03-68/2020-14/200178)

REFERENCES

- [1] K. Hunger, *Industrial Dyes Chemistry, Properties, Applications*, Wiley-VCH, Weinheim, Germany, 2003.
- [2] H. Qian, X. Zhao, Y. Dai, W. Huang, *Dyes Pigm.* 2017, 143, 223-231.
- [3] J. M. Park, C. Y. Jung, W. Yao, C. J. Song, J. Y. Jaung, *Col. Tech.* 2017, 133, 158-164.
- [4] X. Zhao, F. Chang, Y. Feng, H. Qian, W. Huang, *Dyes Pigm.* 2017, 140, 286-296.
- [5] J. Mirković, B. Božić, V. Vitnik, Ž. Vitnik, J. Rogan, D. Poleti, G. Ušćumlić, D. Mijin, *Color. Technol.*, 2018, 134, 33-43.

CRYSTALLOGRAPHIC AND DFT STRUCTURAL ANALYSIS OF OCTOPAMINE-COUMARIN DERIVATIVE

D. Dimić¹, E. Avdović², D. Sretenović³, Ž. Milanović², G. Kaluđerović⁴ and J. Dimitrić-Marković¹

¹ *University of Belgrade, Faculty of Physical Chemistry, Studentski trg 12-16, 11000 Belgrade, Republic of Serbia. (ddimic@ffh.bg.ac.rs)*

² *Institute of Information Technologies, Department of Science, University of Kragujevac, Jovana Cvijića bb, 3400 Kragujevac, Serbia.*

³ *Lehrstuhl für Molekulare Physikalische Chemie, Heinrich-Heine-Universität Düsseldorf, Universitätsstraße 1, D 40225 Düsseldorf, Germany.*

⁴ *Department of Engineering and Natural Sciences, University of Applied Sciences Merseburg, Eberhard-Leibnitz-Straße 2, DE-06217 Merseburg, Germany*

ABSTRACT

Octopamine is a norepinephrine analog in invertebrates and acts as a neurotransmitter. The crystal structure of a novel octopamine-coumarin derivative is described in this contribution. The density functional theory optimization of a structure by several common functionals (APFD, B3LYP-D3BJ, M05-2X, and M06-2X) was performed. Based on the bond lengths and angles, B3LYP-D3BJ proved to be the most reliable functional with the lowest values of mean absolute error. The experimental and theoretical UV-Vis transition wavelengths are also discussed.

INTRODUCTION

Coumarin and its derivatives have gained much attention due to their significant antibacterial, antifungal, anticoagulant, anti-HIV, antioxidant and cytotoxic activities. These compounds consist of fused benzene and pyrone rings with a variety of active positions which are important for their biological functions, such as signaling and hormonal role, as well as defense functions. Octopamine is a phenol analog of norepinephrine. It is included in the signal transduction, neurotransmission, neuromodulation, recovery after high energy demand, and modulation of cellular immune responses [1].

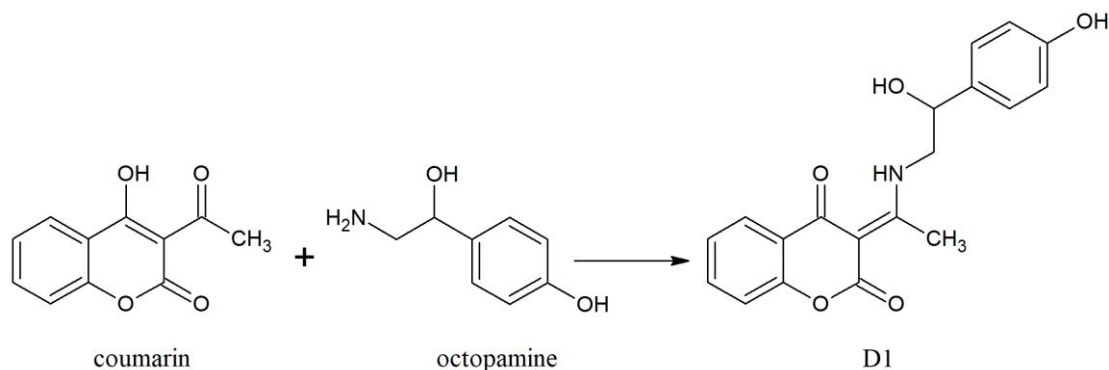
In this contribution, the synthesis under mild conditions of an octopamine-coumarin derivative is described. The experiments were performed because similar derivatives between coumarin and dopamine showed promising anti-tumor activity. The crystallographic structure was solved and presented. This structure was later used as a starting structure for geometry optimization by employing common functionals (APFD, B3LYP-D3BJ, M05-2X, and M06-2X). Based on the difference in experimental and theoretical bond lengths and angles, the suitable method for structure description was determined.

EXPERIMENTAL/THEORETICAL METHODS

Octopamine hydrochloride, methanol, toluene, acetone, and 96% ethanol were purchased from Sigma Aldrich (Munich, Germany). The synthesis of 3-(1-((2-hydroxy-2-(4-hydroxyphenethyl)amino)ethylidene)-chroman-2,4-dione (D1) followed the Scheme 1. The experimental UV-Vis spectrum was recorded on the Evolution 220 Thermo Scientific spectrophotometer in the region between 200 and 400 nm for the 6.25×10^{-5} M solution in methanol. The NMR spectra were obtained on the Varian Gemini Spectrometer with CHCl_3 as solvent and TMS as internal standard.

The data collection for the crystallographic structure was performed on the Oxford Diffraction Xcalibur2 diffractometer equipped with a Sapphire2 CCD detector with graphite-monochromatized

MoK α radiation (wavelength 0.71073 Å). CrysAlis CCD was used for data collection while CrysAlis RED was used for cell refinement, data reduction, and absorption correction. The structure was solved by SHELXT and subsequent Fourier series using SHELXL, implemented in the WinGX program suit. The anisotropic displacement parameters were refined for all non-hydrogen atoms. The analysis of bond distances, angles, and non-bonding interactions was performed in programs SHELX, PLATON, and DIAMOND.



Scheme 1. The synthesis route of the octopamine-coumarin derivative.

The optimization of the structure was done based on the crystallographic data in the Gaussian program package [2]. Several common functionals were used for the optimization, namely APFD, B3LYP-D3BJ, M05-2X, and M06-2X, in conjunction with the 6-311++G(d,p) basis set. These functionals are recommended for the calculation of the thermodynamic parameters and structural features (bond lengths and angles) of organic compounds. The absence of imaginary frequencies showed that the local minimum was found. The optimization was performed without any geometrical constraints. The parameter used for the comparison of the experimental and calculated bond lengths and angles was the mean absolute error (MAE). The Time-Dependent Density Functional Theory (TD-DFT) was applied for the theoretical analysis of possible electronic transitions for structure optimized at B3LYP-D3BJ level of theory. The ^1H and ^{13}C NMR chemical shifts were calculated within the Gauge Independent Atomic Orbital (GIAO) approach for previously mentioned optimized structure.

RESULTS AND DISCUSSION

The crystallographic structure of **D1** is presented in Figure 1.

The obtained substance consists of two rings of the coumarin core, aliphatic chain, hydroxyl group attached to the aliphatic chain, aromatic ring, and a phenolic hydroxyl group. The structure is additionally stabilized by the presence of an intramolecular hydrogen bond that encloses six-membered ring O–C–C–C–N–H. This ring determines the keto-amine tautomeric form of the molecule. This hydrogen bond leads to the equalization of two carbon-carbon bonds due to the delocalization of the π -electron system.

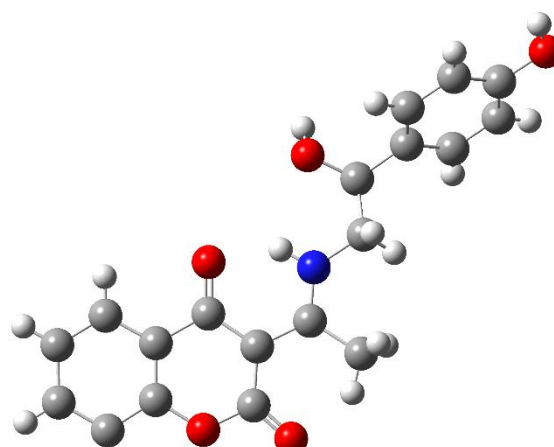


Figure 1. The crystallographic structure of **D1**.

The overall crystal structure also contains hydrogen bonds formed by the hydroxyl groups in the structure.

Table 1. Parameters R and MAE for the comparison of the experimental and theoretical bond lengths and angles.

	Funct.	APFD	B3LYP-D3BJ	M06-2X	M05-2X
Bond length [Å]	MAE	0.014	0.015	0.013	0.014
Bond angles [°]	MAE	0.819	0.779	0.882	0.868

The parameter MAE for the investigated functionals, given in Table 1, shows that all of the functionals describe well the experimental structure. The values for bond lengths were reproduced better in comparison to the values for bond angles. Therefore, parameters for bond angles can be used for the precise comparison of functionals. The values of MAE for bond lengths were between 0.013 and 0.015 Å, while for bond angles these values were in a range from 0.779 to 0.882°. Based on these two values, it can be concluded that the structure optimized at B3LYP-D3BJ/6-311++G(d,p) resembles the most experimental one.

Additionally, UV-Vis spectra were used to verify the applicability of the chosen level of theory. The experimental spectrum consists of three closely positioned peaks between 280 and 320 nm and one at 240 nm. The calculated values, at B3LYP-D3BJ level of theory, are 315 nm (HOMO→LUMO), 308 nm (HOMO-1→LUMO), 292 nm (HOMO-2→LUMO), and 245 nm (HOMO-1→LUMO+1). These results prove that the experimental wavelengths are well reproduced. The differences can be attributed to the specific interactions with the solvent as they change the energy of electronic levels.

The experimental NMR spectra were also well-reproduced with parameters R and MAE being 0.994 and 0.15 ppm for ¹H NMR and 0.999 and 7.37 ppm for ¹³C NMR. The lowest differences in values were obtained for aromatic and coumarin hydrogen and carbon atoms due to the rigidity of these moieties. The noticeable differences are observed for the methyl group and aliphatic chain because atoms in these parts are more flexible and there is a possibility of free rotation.

CONCLUSION

In this contribution, the synthesis under mild conditions of the octopamine-coumarin derivative is presented, together with the crystallographic structure. The bond lengths and angles were well-reproduced by the optimization employing common functionals, although, the lowest mean average errors were obtained for the structure optimized at the B3LYP-D3BJ/6-311++G(d,p) level of theory. The theoretical wavelengths of electronic transitions are very close to the experimental ones. High values of R (0.994 and 0.999) and low values of MAE (0.15 and 7.37 ppm) were obtained when theoretical and experimental ¹H and ¹³C NMR spectra were compared.

Acknowledgement

The authors acknowledge the Ministry of Education, Science and Technological Development of the Republic of Serbia for the financial support (Agreement No. 451-03-9/2021-14/200146 and 451-03-9/2021-14/200378) and the Science Fund of the Republic of Serbia (Serbian Science and Diaspora Collaboration Program: Knowledge Exchange Vouchers, No. 6388843, Project Acronym: TumorSelCoup)

REFERENCES

- [1] D. Dimić, Ž. Milanović, G. Jovanović, D. Sretenović, D. Milenković, Z. Marković, J. Dimitrić Marković, *Comput. Biol. Chem.*, 2019, 84, 107170
- [2] M.J. Frisch, G. W. Trucks, H. B. Schlegel, et al. *Gaussian 09, Revision C. 01*, Gaussian Inc. Wallingford, CT. USA, 2010.

DFT OPTIMIZATION AND FUKUI ANALYSIS OF SELECTED 1,4-BENZODIAZEPIN-2-ONE DRUGS

D. Dimić¹, N. Ristivojević¹, J. Đorović-Jovanović² and A. A. Rakić¹

¹University of Belgrade, Faculty of Physical Chemistry, Studentski trg 12-16, 11000 Belgrade, Republic of Serbia. (ddimic@ffh.bg.ac.rs)

²Department of Science, Institute of Information Technologies, University of Kragujevac, Jovana Cvijića bb, 34000 Kragujevac, Republic of Serbia

ABSTRACT

1,4-Benzodiazepin-2-ones are an important class of drugs with a variety of structural modifications. Five of them (nordiazepam, diazepam, oxazepam, temazepam, and nitrazepam) were optimized at the M06-2X/6-311++(d,p) level of theory based on the crystallographic structure. After the comparison, quantified by the correlation coefficient and mean average error, these structures underwent the Natural Bond Orbital (NBO) analysis and the Condensed Fukui functions (CFFs) were calculated. The most reactive positions for electrophilic, nucleophilic, and radical attack were determined.

INTRODUCTION

Benzodiazepin-2-ones are a class of drugs that are in use for over 50 years for various conditions, such as epilepsy, alcohol withdrawal, depression, and insomnia [1,2]. Various other beneficial physiological effects are also known. The plethora of structural modifications led to the refinement of their physicochemical properties, stabilities, and activities. Besides extensive experimental investigations, quantum-chemical methods have proven to be important for the analysis, reactivity, and prediction of drug behavior [1].

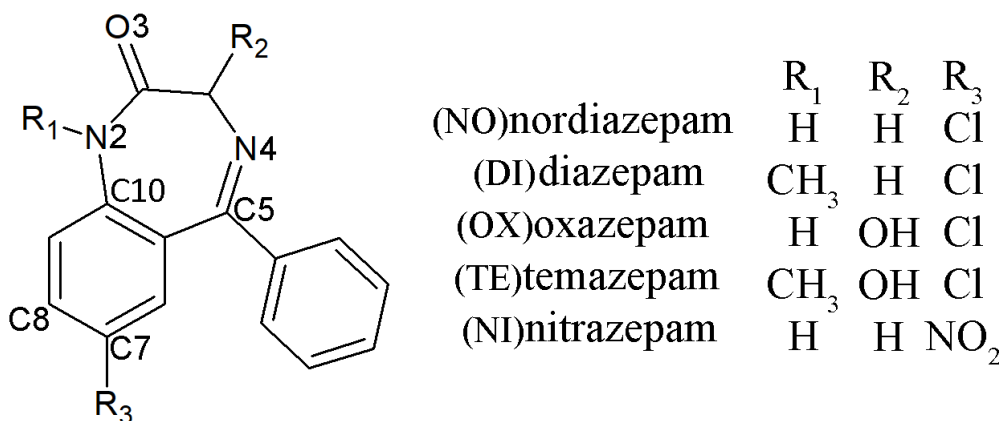


Figure 1. Structures of investigated 1,4-benzodiazepin-2-one drugs

In this contribution five of the 1,4-benzodiazepin-2-one drugs, namely nordiazepam (NO), diazepam (DI), oxazepam (OX), temazepam (TE), and nitrazepam (NI) (Figure 1) are optimized by DFT methods based on the crystallographic structures. After the comparison of bond lengths and angles of experimental and theoretical structures, the NBO analysis is performed to calculate the Fukui functions. These molecules were selected so that the influence of the specific substituents could be examined.

THEORETICAL METHODS

The crystallographic structures were obtained from the Cambridge Crystallographic Data Centre (CCDC) (CCDC: 149151 (NO), 1142317 (DI), 1226369 (OX), 1317863 (TE), and 1219355 (NI)) and later reoptimized at the M06-2X/6-311++G(d,p) level of theory as implemented in the Gaussian program package [3]. This functional was suggested by the authors since it adequately described the thermodynamic parameters and structure of various molecules. The Natural Bond Orbital (NBO) analysis, implemented in the Gaussian program package, was performed to obtain the natural charges so that Condensed Fukui functions (CFFs) can be calculated as follows:

$$f_A^+ = q_N^A - q_{N+1}^A \quad (1)$$

$$f_A^- = q_{N-1}^A - q_N^A \quad (2)$$

$$f_A^0 = [q_{N-1}^A - q_{N+1}^A]/2 \quad (3)$$

The given equations can be used for the determination of the affinity of atom A towards nucleophilic, electrophilic, and radical attack. The values of q_N^A , q_{N-1}^A , and q_{N+1}^A represent the NBO charges for the neutral, anionic, and cationic species, respectively.

RESULTS AND DISCUSSION

The experimental and theoretical bond lengths and angles were compared based on two parameters, namely the correlation coefficient (R) and mean average error (MAE). These values for each of the analyzed drugs are given in Table 1.

Based on the results presented in Table 1, it can be concluded that the chosen level of theory, M06-2X/6-311++G(d,p) describes well the experimental structures. The values of R are above 0.99 for bond lengths and above 0.93 for bond angles. On the other hand, MAE values for bond lengths and angles are below 0.01 Å and 0.06° for all of the investigated structures. It should be kept in mind that the optimization of the structure was performed for an isolated molecule in a vacuum and some discrepancy is expected. Nevertheless, this result proved that these structures could be used for further analysis. From the structural point of view, these molecules represent rigid structures with extended delocalization between aromatic ring and heterocycle. The only rotatable part is the aromatic ring without substituents.

Table 1. The correlation coefficient and mean average error for investigated structures.

Molecule		NO	DI	OX	TE	NI
Bond lengths (Å)	R	0.99	0.99	0.99	0.99	0.99
	MAE	0.01	0.01	0.01	0.01	0.01
Bond angles (°)	R	0.98	0.93	0.99	0.98	0.96
	MAE	0.58	0.65	0.51	0.55	0.68

The reactivity of molecules is investigated by calculating the CFFs. The structural differences between these molecules are substituents on the aromatic ring (Cl, NO₂, and Br), presence of methyl group on N1 (DI, and TE), and presence of OH group in structures of OX and TE. It is not expected that the values of CFFs of atoms in the rotatable aromatic ring will be influenced by the substituents, therefore only atoms with the three highest values of CFFs are discussed in the proceeding paragraphs.

The most reactive position for the electrophile attack is the nitrogen atom in position 2, with the following values ND (0.160 *e*), DI (0.193 *e*), OX (0.136 *e*), TE (0.171 *e*), and NI (0.183 *e*). This position is not influenced by the presence of various substituents. The O3 atom is another active position in ND, DI, OX, and TE. The electronegative atom Cl is very reactive towards electrophile attack. The f_A^- values are between 0.128 and 0.145 *e*. In NI third most reactive position is C7 (0.138 *e*) due to the presence of the electron-withdrawing NO₂ group.

The reactive positions for nucleophile attack include N4, C5, and C8 of NO, DI, OX, and TE. This result shows that the interactions with amino acids in proteins can occur both with the aromatic ring and heterocycle. In mentioned molecules, these values are around 0.160 *e* for N4, 0.130 *e* for C5, and 0.120 *e* for C8. The carbon atoms of the aromatic ring are slightly negatively charged (-0.2 *e*) except for C10 which is a neighboring atom of N2. The atoms of the nitro group in the structure of NI have negative charges as well, with values -0.494, 0.390, and -0.390 *e* for nitrogen and two oxygen atoms, respectively. These atoms are a very potent position for nucleophilic attack, with f_A^+ being 0.121 *e* (N), 0.198 *e* (O), and 0.198 *e* (O).

The attack of radical species can be expected for the atoms in positions O2, N4, and Cl of NO, DI, OX, and TE. It is important to mention that the electron delocalization in investigated species includes all of these atoms except for Cl. The values for f_A^0 are around 0.1 *e* for all mentioned atoms, which shows no difference in their reactivity. On the other hand, the NI molecule differs since N4 and oxygen atoms of the NO₂ group are the most reactive sites, with oxygen atoms being more probable with f_A^0 of around 0.13 *e*.

Based on the presented values, the most reactive positions in investigated structures are the electronegative atoms (N2, N4, O3, and Cl), electronegative group (NO₂), the carbon atom in position 8 of the aromatic ring, and the carbon atom of heterocycle in position 5. This analysis leads to the conclusion that these atoms and groups are most likely to form the interactions in the active positions of proteins. The choice of substituents allows the introduction of new active positions, therefore careful selection is needed for the desired pharmacological effects and further experimental and theoretical analyses are needed.

CONCLUSION

The theoretical analysis of 1,4-benzodiazepin-2-one molecules is an effective way for the prediction of their reactivity and interactions with proteins. Structures of nordiazepam, diazepam, oxazepam, temazepam, and nitrazepam were optimized at the M06-2x/6-311++G(d,p) level of theory and compared with crystallographic data. The correlation coefficients between experimental and theoretical bond lengths and angles are higher than 0.99 and 0.93. The mean average error is below 0.01 Å and 0.6°. The values of Condensed Fukui Functions (CFFs) showed various active positions including hetero- and carbon atoms of heterocycle, carbon atoms of the aromatic ring, and substituents (Cl and NO₂).

Acknowledgement

The authors acknowledge the financial support by the Ministry of Education, Science and Technological Development of the Republic of Serbia (Agreement No. 451-03-9/2021-14/200146 and 451-03-9/2021-14/200378)

REFERENCES

- [1] B. Pem, V. Vrček, *Int. J. Qunatum. Chem.*, 2018, 118, e25523.
- [2] J. Spencer, R.P. Rathnam, B.Z. Chowdhry, *Future Med. Chem.*, 2010, 2, 1441.
- [3] M.J. Frisch, G. W. Trucks, H. B. Schlegel, et al. *Gaussian 09*, Revision C. 01, Gaussian Inc. Wallingford, CT. USA, 2010.

THE NATURE OF STACKING INTERACTIONS OF THE RESONANCE-ASSISTED HYDROGEN-BRIDGED RINGS

J. P. Blagojević Filipović¹, S. D. Zarić²

¹ Innovation Centre of the Faculty of Chemistry,
Studentski trg 12-16, 11000 Belgrade, Serbia, (jbfilipovic@chem.bg.ac.rs)

² University of Belgrade, Faculty of Chemistry, Studentski trg 12-16, 11000 Belgrade, Serbia

ABSTRACT

The Symmetry Adapted Perturbation Theory (SAPT) energy decomposition analysis is applied for studying the nature of stacking interaction occurring in homodimers of resonance-assisted hydrogen-bridged (RAHB) rings and heterodimers of RAHB and benzene rings. The contribution of various energy terms is dependent on the composition of a RAHB ring and can be rationalized based on electrostatic potential maps.

INTRODUCTION

The existence of mutual stacking interaction between Resonance-Assisted Hydrogen-Bridged (RAHB) rings (Figure 1a), as well as stacking interactions between RAHB and C₆-aromatic rings is confirmed by analysing the crystal structures from the Cambridge Structural Database (CSD) and by quantum-chemical calculations in the gas phase [1,2]. It is observed that both RAHB/RAHB and RAHB/C₆-aromatic rings form parallel layers in the crystal structures and that these layers are in both cases separated by 3.0-4.0 Å in the majority of the structures. Thus, contacts between the layers can be assigned to stacking interactions. Namely, we used malonaldehyde molecule (Figure 1b), its mononitrogen (Figure 1c) and dinitrogen analogue (Figure 1d) as prototypes for the RAHB rings, since these rings are the most frequently present in both sets of structures in the CSD (RAHB/RAHB rings and RAHB/C₆-aromatic rings) [1,2]. We used benzene molecule as a prototype for a C₆-aromatic molecule. In this work, we present a Symmetry Adapted Perturbation Theory (SAPT2+3, [3]) energy decomposition, calculated for RAHB/RAHB and RAHB/benzene stacking interactions and discuss the nature of these interactions.

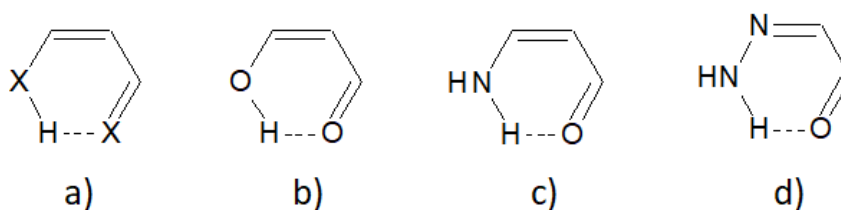


Figure 1. Examples of the RAHB rings; a) general formula, electronegative atoms, usually N, O and S forming intramolecular hydrogen bond are connected by a π -system; b) malonaldehyde; c) the mononitrogen analogue of malonaldehyde; d) the dinitrogen analogue of malonaldehyde

METHODS

On the basis of the SAPT energy decomposition scheme the interaction energy is consisted of the electrostatic, induction, dispersion and exchange-repulsion terms. Dispersion and exchange-repulsion terms are sometimes combined into a net dispersion term [4]. A SAPT2+3 energy decomposition analysis was performed in this work on structures corresponding to the lowest minima on the RAHB/RAHB and the RAHB/benzene potential energy curves [1,2]. The SAPT2+3 calculations were performed at cc-pVQZ level, since it was shown to be in good agreement with CCSD(T) method at the Complete Basis Set limit (CCSD(T)/CBS) [1,2]. To perform SAPT2+3 calculations we used PSI4 program package [5]. The electrostatic potential maps were calculated at the outer contour of electron density of 0.001 a. u. using Wavefunction Analysis Surface Analysis Suite (WFA-SAS) program [6] by the wavefunctions calculated in Gaussian09 [7] at MP2/cc-pVTZ level.

RESULTS AND DISCUSSION

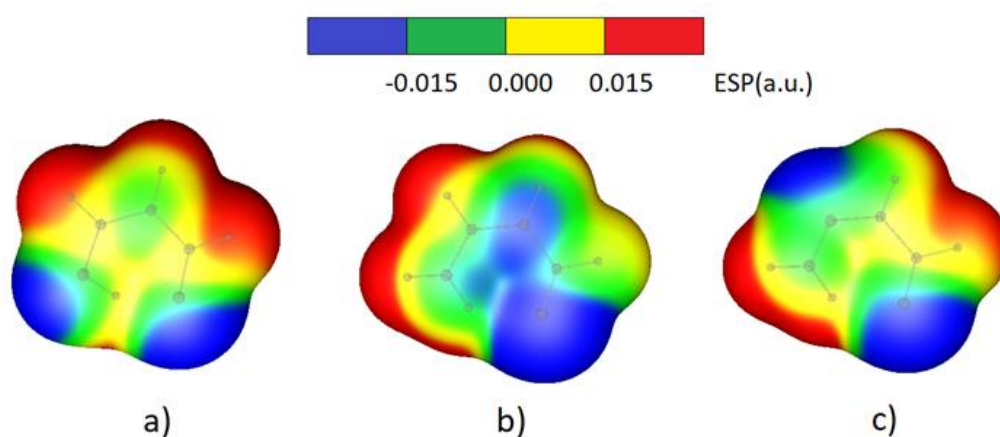
The dispersion term is dominant in all studied systems (Table 1), but it is significantly cancelled or even surpassed by the exchange-repulsion term. Thus, when we compare RAHB/RAHB stacked systems [1] we can see that the electrostatic term is dominant in $\text{H}_4\text{C}_3\text{O}_2/\text{H}_4\text{C}_3\text{O}_2$ and $\text{H}_5\text{C}_3\text{NO}/\text{H}_5\text{C}_3\text{NO}$ systems, since net dispersion is quite small (in $\text{H}_4\text{C}_3\text{O}_2/\text{H}_4\text{C}_3\text{O}_2$ system) or even repulsive (in $\text{H}_5\text{C}_3\text{NO}/\text{H}_5\text{C}_3\text{NO}$ system). The main reason for significantly smaller total interaction energy in $\text{H}_4\text{C}_2\text{N}_2\text{O}/\text{H}_4\text{C}_2\text{N}_2\text{O}$ system, compared to the other two RAHB /RAHB stacking interactions is a smaller electrostatic contribution. On the other hand, in this system, net dispersion contribution is almost equal to the electrostatic contribution (Table 1).

Similar observations apply to RAHB/benzene stacked dimers [2]. Dispersion terms are almost cancelled in $\text{H}_4\text{C}_3\text{O}_2/\text{benzene}$ and $\text{H}_5\text{C}_3\text{NO}/\text{benzene}$ systems, while net dispersion significantly contributes to the interaction in $\text{H}_4\text{C}_2\text{N}_2\text{O}/\text{benzene}$ system. However, even in this system the electrostatic contribution is more pronounced than net dispersion (Table 1). Electrostatic contribution is dominant in $\text{H}_4\text{C}_3\text{O}_2/\text{benzene}$ and $\text{H}_5\text{C}_3\text{NO}/\text{benzene}$. Induction energy term contributes to the interaction energy in all studied RAHB/RAHB and RAHB/benzene systems, but to a smaller extent (Table 1).

We can observe that differences occur in the nature of RAHB stacking interactions for the three rings. These differences can be explained by electrostatic potential maps (Figure 2). It can be seen that $\text{H}_4\text{C}_3\text{O}_2$ and $\text{H}_5\text{C}_3\text{NO}$ molecules both have a dipole moment. At the other hand, a clearly pronounced dipole moment can not be observed in case of $\text{H}_4\text{C}_2\text{N}_2\text{O}$ molecule. Thus, significant contribution of electrostatic interaction in antiparallel $\text{H}_4\text{C}_3\text{O}_2/\text{H}_4\text{C}_3\text{O}_2$ and $\text{H}_5\text{C}_3\text{NO}/\text{H}_5\text{C}_3\text{NO}$ can be attributed to antiparallel dipole-dipole interactions. Benzene molecule does not possess a dipole moment, but it possesses a quadrupole moment, thus a smaller electrostatic term in $\text{H}_4\text{C}_3\text{O}_2/\text{benzene}$ and $\text{H}_5\text{C}_3\text{NO}/\text{benzene}$ systems than in the corresponding RAHB/RAHB systems is a consequence of a dipole-quadrupole interaction. For that reason, the overall interaction is stronger in $\text{H}_4\text{C}_3\text{O}_2/\text{H}_4\text{C}_3\text{O}_2$ and $\text{H}_5\text{C}_3\text{NO}/\text{H}_5\text{C}_3\text{NO}$ systems than in $\text{H}_4\text{C}_3\text{O}_2/\text{benzene}$ and $\text{H}_5\text{C}_3\text{NO}/\text{benzene}$ systems. Since $\text{H}_4\text{C}_2\text{N}_2\text{O}$ molecule does not possess a clearly pronounced dipole moment, the electrostatic terms are less dominant than in systems involving $\text{H}_4\text{C}_3\text{O}_2$ and $\text{H}_5\text{C}_3\text{NO}$ molecules. Also, net dispersion is significant, which can be attributed to the smaller exchange-repulsion term (Table 1).

Table 1. SAPT2+3 energy decomposition analysis; all energy values are in kcal/mol. Net dispersion is a sum of exchange-repulsion and dispersion terms.

Model system	ELST	EXCH	IND	DISP	NET DISP	SAPT 2+3
H ₄ C ₃ O ₂ /H ₄ C ₃ O ₂	-3.55	5.92	-0.60	-6.10	-0.18	-4.32
H ₅ C ₃ NO/H ₅ C ₃ NO	-4.81	7.86	-1.12	-6.74	1.12	-4.81
H ₄ C ₂ N ₂ O/H ₄ C ₂ N ₂ O	-0.89	3.76	-0.33	-4.64	-0.88	-2.09
H ₄ C ₃ O ₂ /benzene	-2.68	6.51	-0.80	-6.63	-0.12	-3.60
H ₅ C ₃ NO/benzene	-2.60	6.51	-0.92	-6.52	-0.01	-3.53
H ₄ C ₂ N ₂ O/benzene	-1.61	4.70	-0.51	-5.69	-0.99	-3.11

**Figure 2.** The electrostatic potential maps of a) malonaldehyde; b) the mononitrogen analogue of malonaldehyde; c) the dinitrogen analogue of malonaldehyde (Figure 1)

CONCLUSION

The SAPT2+3 energy decomposition analysis is performed on RAHB/RAHB and RAHB/benzene model systems. The dispersion contribution is dominant in all studied systems. Depending on the dipole moment intensity, the electrostatic term is dominant or comparable with a net dispersion term, which is often presented as a sum of dispersion and exchange-repulsion terms. In a system that does not possess a pronounced dipole moment, the electrostatic contribution is smaller than in systems with a pronounced dipole moment. Also, exchange-repulsion term is smaller, which leads to a more significant net dispersion term. The induction energy term contributes to the stacking interaction energy in all systems, but not to a large extent.

Acknowledgement

This work was supported by the Serbian Ministry of Education, Science and Technological Development (Contract numbers: 451-03-9/2021-14/200168 and 451-03-9/2021-14/200288).

REFERENCES

- [1] J. P. Blagojević Filipović, M. B. Hall, S. D. Zarić, *Cryst. Growth Des.* 2019, 19, 5619-5628.
- [2] J. P. Blagojević Filipović, M. B. Hall, S. D. Zarić, *Phys. Chem. Chem. Phys.* 2020, **22**, 13721-13728.
- [3] T. M. Parker, L. A. Burns, R. M. Parrish, A. G. Ryno, C. D. Sherrill, *J. Chem. Phys.* 2014, 140, 094106.
- [4] E. G. Hohenstein, C. D. Sherrill, *J. Phys. Chem. A*, 2009, 113, 878-886.
- [5] R. M. Parrish, L. A. Burns, D. G. A. Smith, A. C. Simmonett, A. E. DePrince, E. G. Hohenstein, U. Bozkaya, A. Y. Sokolov, R. Di Remigio, R. M. Richard, et al. *J. Chem. Theory Comput.*, 2017, 13, 3185-3197.
- [6] F. A. Bulat, A. Toro-Labbé, T. Brinck, J. S. Murray, P. J. Politzer, *Mol. Model.* 2010, 16, 1679–1691.
- [7] M. J. Frisch, G. W. Trucks, H. B. Schlegel, G. E. Scuseria, M. A. Robb, J. R. Cheeseman, G. Scalmani, V. Barone, G. A. Petersson, H. Nakatsuji, et al. *Gaussian 09*, Revision D.01; Gaussian, Inc., 2016.

C - Kinetics, Catalysis

ROLE OF MECHANOCHEMISTRY IN ECO-FRIENDLY AND SUSTAINABLE PREPARATION AND RECYCLING OF CATALYSTS

Z. Cherkezova-Zheleva

*Institute of Catalysis, Bulgarian Academy of Sciences,
Acad. G. Bonchev St., Bldg. 11, 1113 Sofia, Bulgaria*

*E-mail: zzhel@ic.bas.bg, fax: +359 2 971-29-69

ABSTRACT

Ensuring a secure, reliable and unhindered supply of raw materials is crucial for the competitiveness and growth of the European Union (EU) economy. The EU is taking actions to secure the access of all raw materials, but some of them are defined as ‘critical’. Difficulties in the access to critical raw materials (CRMs) are expected to depress industrial sectors vital to European Union. The current conditions of material supply and their evolution in EU and international markets strongly affect the present-day list of CRMs. The current Fourth list of CRMs was published in 2020 and covers a larger number of materials. The sustainable solution of the CRM problem is design of advanced CRM-free or low content materials, but also the optimal use, enhanced recycling and sustainable mining. In this context, the European Commission set up a number of initiatives to promote innovative solutions and accelerate the innovations in the field of raw materials. A lot of efforts are concentrated on the substitution of CRMs together with preservation and improvement of the advanced properties of the respective materials. However, the more realistic option relates to optimisation of CRM life cycle covering extraction and processing of the raw materials, manufacturing, distribution, use, recycling, and final disposal, as well as the environmental impact of a product through its life cycle.

Currently preparation of heterogeneous catalysts with advanced properties is strongly related to the use of one or more CRM such as Cr, rare earths, platinum group metals, etc. Criticality assessment of some raw materials in regard of catalysts preparation will be presented.

Mechanochemical treatment can be successfully used as a method for CRM recovery and recycling. On the other hand, the role of Mechanochemistry in synthesis and/or activation of CRM-free catalysts is a large and growing field of research and innovations. The research activities in this fast-moving area are focused on the development of new concepts for design and synthesis of non-CRM catalysts with the same or better activity and selectivity compared to the current ones. Improvement of full material life cycle of obtained non-CRM catalysts together with better recycling, reuse and repair of CRM-based catalysts are open areas for new ideas, scientific and innovative projects.

Acknowledgement

The authors gratefully acknowledge the financial support of the Bulgarian National Science Fund at the Ministry of Education and Science - Project № KII-06-KOCT/18/ 2019. This article is based on the project activities of COST Action CA 18112 “Mechanochemistry for Sustainable Industry” (Mech@SustInd), supported by COST (European Cooperation in Science and Technology).

Keywords: Mechanochemistry, Catalysis, Critical Raw Materials (CRM), CRM-free Catalysts, Material preparation and characterization.

ARTIFICIAL SECONDARY STRUCTURES IN THE DESIGN OF NEW CATALYSTS AND NEW MATERIALS

S. I. Kirin

*Ruđer Bošković Institute, Bijenička 54, HR-10000 Zagreb, Croatia
(Srecko.Kirin@irb.hr)*

ABSTRACT

In this conference paper, an author's review in the field of bioinorganic chemistry, stereochemistry, homogeneous catalysis and medicinal inorganic chemistry is presented, with particular emphasis on physical chemistry aspects. Within this work, bioconjugates of amino acid containing phosphine or nitrogen ligands were utilized for metal coordination. The metal complexes were extensively characterized by a number of instrumental spectroscopic or crystallographic techniques and by DFT calculations. The metal complexes were used as catalysts in the selective preparation of intermediates in the synthesis of active pharmaceutical ingredients. Special attention was paid to the formation of specific supramolecular artificial secondary structures formed by the amino acid moieties that control the stereochemical outcome of the catalytic reactions. In addition, the metal complexes served as building blocks for supramolecular architectures as well as potent anticancer agents.

INTRODUCTION

Proteins and nucleic acids are natural macromolecules that contain a large number of amino acid or nucleotide monomers, respectively. The secondary structures of these macromolecules are particularly important for their function in a biological environment. In nature, out of the wide variety of potentially possible secondary structures, proteins and nucleic acids are known to adopt only a very small number of secondary structures. Those privileged secondary structures are for example α -helix and β -sheet for proteins, or B-DNA for nucleic acids.

Ferrocenes 1,*n*'-disubstituted with amino acids are an interesting class of compounds that adopt only a limited number of secondary structures as well.[1] Most commonly, a *Herrick* conformation is found, with two inter-strand hydrogen bonds forming two formal 10-membered rings, Figure 1. Also known are the *van Staveren* conformation, with one inter-strand hydrogen bond forming a formal 7-membered ring and the *Xu* conformation (or open conformation) without any hydrogen bonds.[1] If the amino acids in these ferrocene bioconjugates are chiral, the inter-strand hydrogen bonding induces a new chiral element, namely helical chirality of the central ferrocene moiety. Most importantly, in both the *Herrick* and the *van Staveren* conformation, L-chirality of the pendant amino acids induced a *P*-helix at the ferrocene, Figure 1. The working hypothesis of our research is that this specific induction of chirality can find applications, for example in asymmetric catalysis.

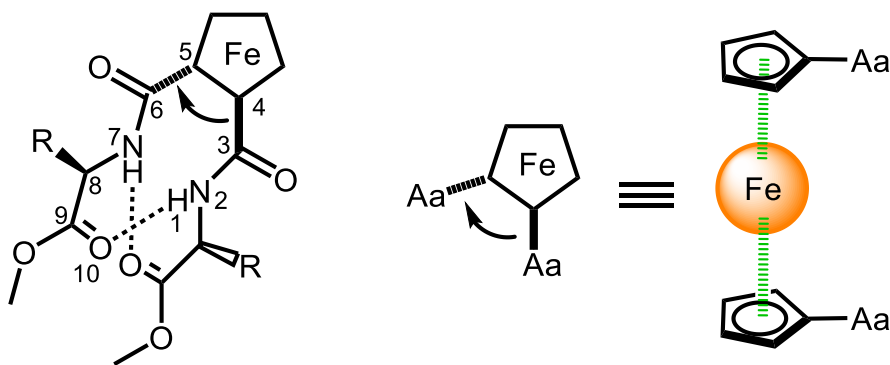


Figure 1. Herrick conformation (left), helical chirality of ferrocene (right). Aa = amino acid(s), curved arrows indicate sign of helical chirality.

RESULTS AND DISCUSSION

Metalloenzymes are in general very selective catalysts with high reaction rates, but work often only with a limited number of substrates and their application can be expensive. On the other hand, if a small metal complex is catalytically active, it can have a rather broad substrate scope and it can be much cheaper, but selectivity and reaction rates are far behind enzymes. The difference between metalloenzymes and small metal complexes is the outer-coordination sphere present in the metalloenzymes. Consequently, in order to model the catalytic function of an enzyme, it is not enough to consider only the active site, but at least some of the outer-coordination sphere should be included as well. However, this approach can only be efficient, if the outer-coordination sphere of the small metal complex is very well defined, for example as shown for ferrocene amino acids, Figure 1.

Prominent examples of small metal complexes with a well-defined outer-coordination sphere are rhodium triphenylphosphines substituted with chiral amino acids or chiral diamines, Figure 2.

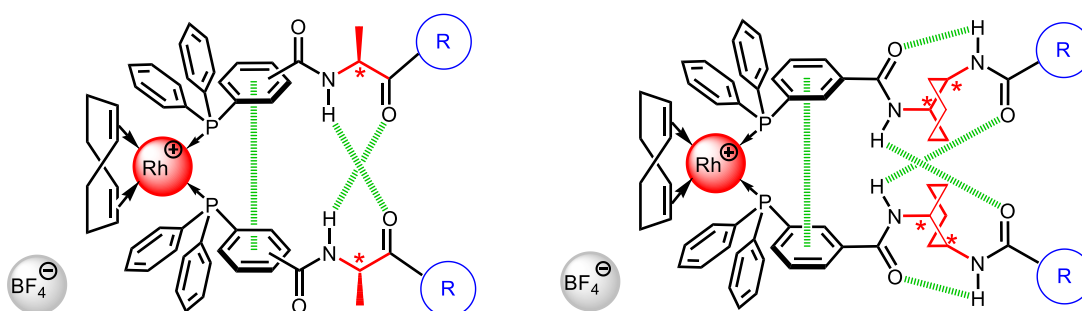


Figure 2. Schematic representation of rhodium catalysts, amino acid based (left) and diamine based (right).

These complexes can be used as catalysts in asymmetric hydrogenation reactions of α,β -unsaturated amino acids or as model compounds of intermediates in the synthesis of active pharmaceutical ingredients.[2,3] While optimized amino acid derivatives achieve up to 84% ee, the selectivity of diamine derivatives is up to 97% ee. Moreover, these catalytic systems are particularly interesting because they feature "backdoor induction" of chirality. The coordination sphere of the catalytic metal is only prochiral, while the chirality is transmitted from the distant chiral amino acids or diamines forming a *Herrick-like* conformation.

The higher selectivity of the diamine catalysts, if compared to the amino acid derivatives, prompted a study of 1, n' -disubstituted ferrocene diamines, Figure 3 (left), as opposed to their amino acid derivatives, Figure 3 (right).[4] Diamine ferrocenes expectedly showed a high stability of a *Herrick-like* conformation in DCM solution. In addition, it was surprisingly found that they could act as chiroptical switches between two stable states. The ferrocene absorption in the visible part of the CD spectrum can be inverted by solvent exchange or acid addition. The inversion is achieved through a change of the hydrogen-bonding pattern.

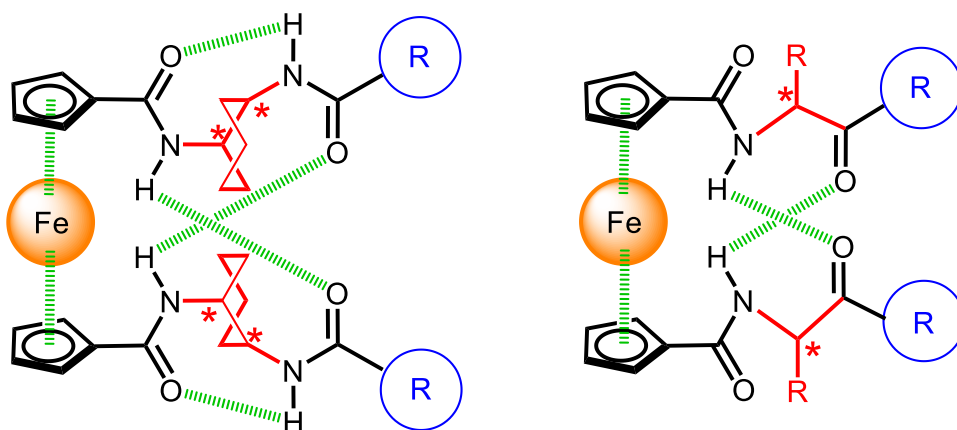


Figure 3. Schematic representations of ferrocene diamines (left) and ferrocene amino acids (right).

As shown in the previous paragraphs, in order to define the outer-coordination sphere of the metal complex by hydrogen bonding, spatial proximity of the two organic ligands in a *cis*-isomer is beneficial. An example where a *trans*-arrangement of the ligands results in a tightly bound dimer is provided by a palladium complex with amino acid substituted triphenylphosphines, Figure 4.[5] The self-assembly of the dimer is governed by the *cis-trans* isomerisation of the palladium metal centre. The dimer has a molecular mass of about 3000 g mol⁻¹ and is held together by 16 hydrogen bonds and aromatic stacking.

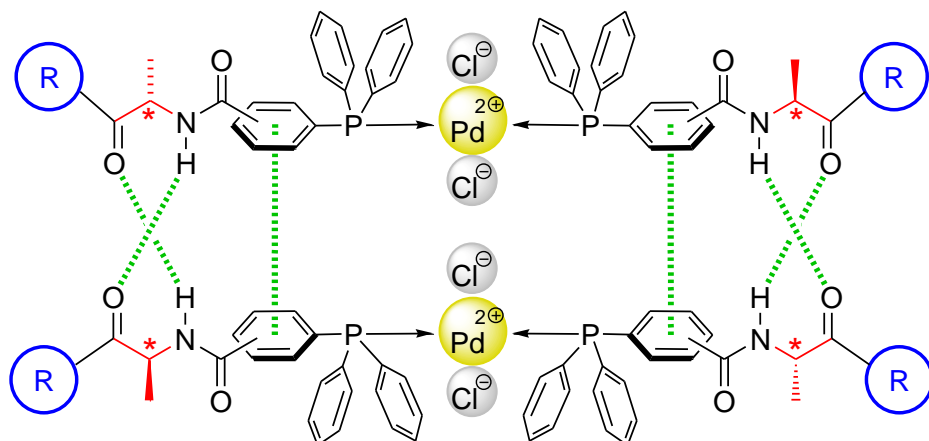


Figure 4. Schematic representation of a palladium complex dimer.

So far, organometallic and inorganic examples were discussed in this review. However, for the selective formation of a *Herrick-like* conformation, the presence of a metal cation is not required, Figure 5 (left).[6] An aminopyridine ligand exhibits supramolecular chirality in solution, based on self-assembly of the building blocks. Interestingly, this is the first reported system where the supramolecular chirality is completely inverted by addition of metal ions, e.g. zinc.

Finally, (*p*-cymene)-ruthenium bioconjugates with *Herrick-like* secondary structures have significant anticancer activity. An investigation using human cervical carcinoma cell lines revealed IC₅₀ values as low as 5 μM, Figure 5 (right).[7] These metal complexes have been shown to cause non-oxidative protein damage and induce autophagy.

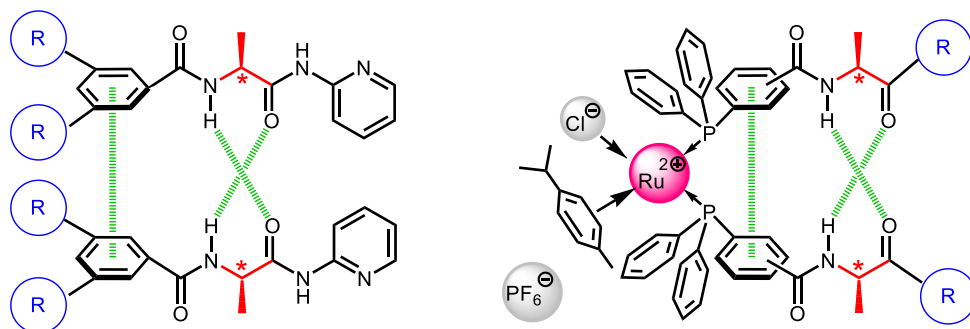


Figure 5. Schematic representations of an all-organic derivative (left) and a ruthenium complex (right).

CONCLUSION

Herein, a number of amino acid bioconjugates is discussed, including their metal complexes with rhodium(I), iron(II), palladium(II), zinc(II) and ruthenium(II). A common feature of these rather different compounds is the superior stability of a small number of secondary structures. Obviously, the concept of privileged secondary structures does apply not only to natural macromolecules like proteins and nucleic acids, but also to significantly smaller artificial systems forming *Herrick-like* conformations. The general goal of this research is to study these systems and to find appropriate applications in catalysis, activity in biological environment and beyond. Current efforts are directed towards the development of amino acid bioconjugates of tridentate nitrogen ligands, potentially capable of forming similar artificial secondary structures. [8,9]

Acknowledgement

This work was partially supported by CAT Pharma (KK.01.1.1.04.0013), a project co-financed by the Croatian Government and the European Union through the European Regional Development Fund – the Competitiveness and Cohesion Operational Programme.

REFERENCES

- [1] S. I. Kirin, H.-B. Kraatz, N. Metzler-Nolte, *Chem. Soc. Rev.*, 2006, 35, 348-354.
- [2] Z. Kokan, Z. Glasovac, M. Majerić Elenkov, M. Gredičak, I. Jerić, S. I. Kirin, *Organometallics*, 2014, 33, 4005-4015.
- [3] S. Opačak, Z. Kokan, Z. Glasovac, B. Perić, S. I. Kirin, *Eur. J. Org. Chem.* 2019, 2115-2128.
- [4] S. Opačak, B. Perić, D. Babić, Ž. Marinić, V. Smrečki, B. Pem, I. Vinković Vrček, S. I. Kirin, *Dalton Trans.*, 2021, 50, 4504-4511.
- [5] Z. Kokan, B. Kovačević, Z. Štefanić, P. Tzvetkova, S. I. Kirin, *Chem. Commun.*, 2018, 54, 2094-2097.
- [6] Z. Kokan, B. Perić, M. Vazdar, Ž. Marinić, D. Vikić-Topić, E. Meštrović, S. I. Kirin, *Chem. Commun.*, 2017, 53, 1945-1948.
- [7] M. Pernar, Z. Kokan, J. Kralj, Z. Glasovac, L.-M. Tumor, I. Piantanida, D. Eljuga, I. Turel, A. Brozovic, S. I. Kirin, *Bioorg. Chem.*, 2019, 87, 432-446.
- [8] N. Pantalon Juraj, G. I. Miletić, B. Perić, Z. Popović, N. Smrečki, R. Vianello, S. I. Kirin, *Inorg. Chem.*, 2019, 58, 16445-16457.
- [9] N. Pantalon Juraj, S. I. Kirin, *Coord. Chem. Rev.*, 2021, accepted.

VISIBLE LIGHT PROMOTED PHOTOREDOX CATALYSIS IN MICROFLOW SYSTEMS

B. P. Bondžić

*University of Belgrade, Institute of Chemistry, Technology and Metallurgy – National Institute of the Republic of Serbia, Njegoševa 12, 11000 Belgrade, Serbia.
(bbondzic@chem.bg.ac.rs)*

ABSTRACT

Lately, the application of microfluidic devices has been a very promising strategy in organic chemistry, and one of the research fields in which microfluidics have shown great potential is visible light photochemistry. There are several advantages when conducting transformations in flow compared to the batch reactions, in particular: a more predictable reaction scale-up, decreased safety hazards, improved reproducibility and yields, shorter residence time, higher reaction selectivity and product purity and lower catalyst loading. In addition, for photochemical transformations, the high surface-area-to-volume ratios typical of flow reactors allow for improved light efficiency. Light penetration in batch reactors is limited by decreasing light transmission over distance in a liquid medium.

Having all these advantages in mind, it comes as no surprise that visible light promoted photoredox chemistry in flow has been applied in functionalizations biologically active organic molecules.

A merger of organocatalysis and visible light photoredox catalysis performed in flow allowed access to a wide range of functionalized *N*-aryl-substituted tetrahydroisoquinolines (THIQs) in a formal C–H oxidation/Mannich reaction. Strecker type functionalization and copper-catalyzed alkynylation of several *N*-aryl-substituted THIQs were also successfully performed in flow, giving valuable products with high efficiencies. Three types of microreactors i.e., PFA microtube flow reactor, PDMS polymeric microreactor and glass/silicon reactor were designed and applied in these model reactions. The application of custom-made porous polymeric type microreactors proved to be crucial regarding the C–H oxidation step and overall reaction performance.

METAL DUSTING AS A KEY ROUTE TO PRODUCE FUNCTIONALIZED CARBON NANOFIBERS

A. Vedyagin , I. Mishakov and Yu. Bauman

*Department of Materials Science and Functional Materials,
Boreskov Institute of Catalysis SB RAS,
Pr. Lavrentieva 5, 630090 Novosibirsk, Russia. (vedyagin@catalysis.ru)*

ABSTRACT

The catalytic chemical vapor deposition (CCVD) method is frequently used to produce carbon nanomaterials, which are characterized by unique properties. Such materials are applied in various fields of science and technology, and their attractiveness grows year by year. Both the size and chemical, and phase composition of the catalysts are responsible for their activity and stability. In some cases, amorphous carbon being formed blocks the active sites and thus interrupts the CCVD process. On the other hand, the metal dusting process, known as a negative phenomenon causing the destruction of the industrial metal reactors, has started to be considered as a preparative route to obtain active and stable CCVD catalysts from bulk metal precursors. The present paper is aimed to demonstrate the current state of art in the claimed field of science.

INTRODUCTION

Carbon nanomaterials are a class of materials composed of carbon atoms. Due to their unique and easily tunable properties, they are widely used in numerous fields of application, including composite materials, lubricants, capacitors, adsorbents, catalysts, biomedical delivery systems, etc. Among them, carbon nanofibers (CNF) are of special interest due to the variety of their morphologic structure and relative cheapness. The exact area of application of CNF is also determined by the presence of functional groups on the fibers' surface. The introduction of heteroatoms into the structure of CNF, as usual, noticeably modifies their properties.

One of the most commonly used approaches to obtain CNF is the catalytic chemical vapor deposition (CCVD) method. The process undergoes in accordance with the so-called carbide cycle mechanism [1]. Initially, hydrocarbon molecules (methane, ethane, propane, etc.) serving as the carbon source are decomposed into carbon and hydrogen. During this stage, the formation along with the subsequent degradation of intermediate surface carbide-like compounds on the frontal facets of the dispersed particles of iron-subgroup metals (Fe, Co, and Ni) or their alloys takes place. The second physical stage is connected with the diffusion transfer of carbon atoms through the bulk of a metal particle from the frontal facet to the rear facet. Carbon atoms reach the rear facet and initiate the formation of a graphite phase nucleus followed by the growth of graphite-like fibers of different morphology and texture. Such a complex mechanism imposes special requirements on the composition and size of metal particles. Non-compliance with these requirements turns the CCVD process to the formation of amorphous carbon, blockage of the frontal facets, and deactivation of the catalyst. Therefore, the synthesis of the catalyst's particles with the required characteristics is an actual challenge.

On the other hand, one of the major problems of the modern chemical industry is the self-destruction of metal reactors working under the carburizing atmosphere. The phenomenon underlying this process is called metal dusting or carbon erosion. Quite recently, this generally negative process was considered as a possible route for the preparation of dispersed metal particles of uniform size and chemical composition [2-6]. As reported, in the case of Ni-based systems, the induction period of the metal dusting process can be effectively shortened by using halogenated hydrocarbons as a carbon

source. Moreover, the addition of alloying metals to nickel also affects the activity and efficiency of the catalyst [7-10].

The present paper summarizes all the experimental data accumulated during the last decade. The fundamental aspects of the metal dusting process were studied using the McBain balances, while the batch production of the CNF via the CCVD process was performed in a pilot-scale tubular reactor. 1,2-dichloroethane was used as the main carbon source. One-pot functionalization was provided by the addition of heteroatom-containing substances into the reaction mixture. The collected samples of CNF were characterized by a number of physicochemical techniques.

METHODS

Nickel-chrome alloy (80% Ni, 20% Cr, nichrome wire) was used as a bulk Ni-based precursor. Model Ni_{1-x}M_x (where M is Cr, Cu, Co, Fe, Pt, Mo, W, or Pd) bulk alloys were synthesized via the co-precipitation method. Thus, obtained sediments were filtered, dried, heated in hydrogen flow at a ramping rate of 20 °C/min up to 800 °C and calcined at this temperature for 30 min. The samples are labeled as Ni-M (*cp*). The formation of alloys was confirmed by the powder X-ray diffraction (XRD) analysis, which was performed at room temperature on a Shimadzu XRD-7000 diffractometer (CuK α radiation, Ni filter on the reflected beam).

The kinetics experiments on the metal dusting process were carried out at 600 °C in a quartz flow reactor equipped with McBain microbalance, which allowed measuring of the sample's weight during the process. The volume of the produced CNF was limited by the volume of the quartz basket that corresponds to the CNF weight of a few mg. The batch production of CNF samples (a few kg) for their detailed characterization was realized in a tubular quartz reactor placed inside a high-temperature furnace. Photos of both reactors as well as carbon products are shown in Figure 1.

The CCVD experiments were arranged as follows. The specimen of the alloy was loaded inside one of the reactors. The reactor was purged with argon and hydrogen and heated up to the reaction temperature. Then, the reaction gas feed containing argon and hydrogen was passed through the saturator filled with 1,2-dichloroethane (DCE). The excess of hydrogen (37.5 vol.%) in the reaction mixture was required to promote chemical corrosion of the metallic surface and prevent it from complete chlorination. In order to provide a one-pot synthesis of CNF and their functionalization with nitrogen-containing groups, acetonitrile (8 vol.%) was added to the reaction mixture.

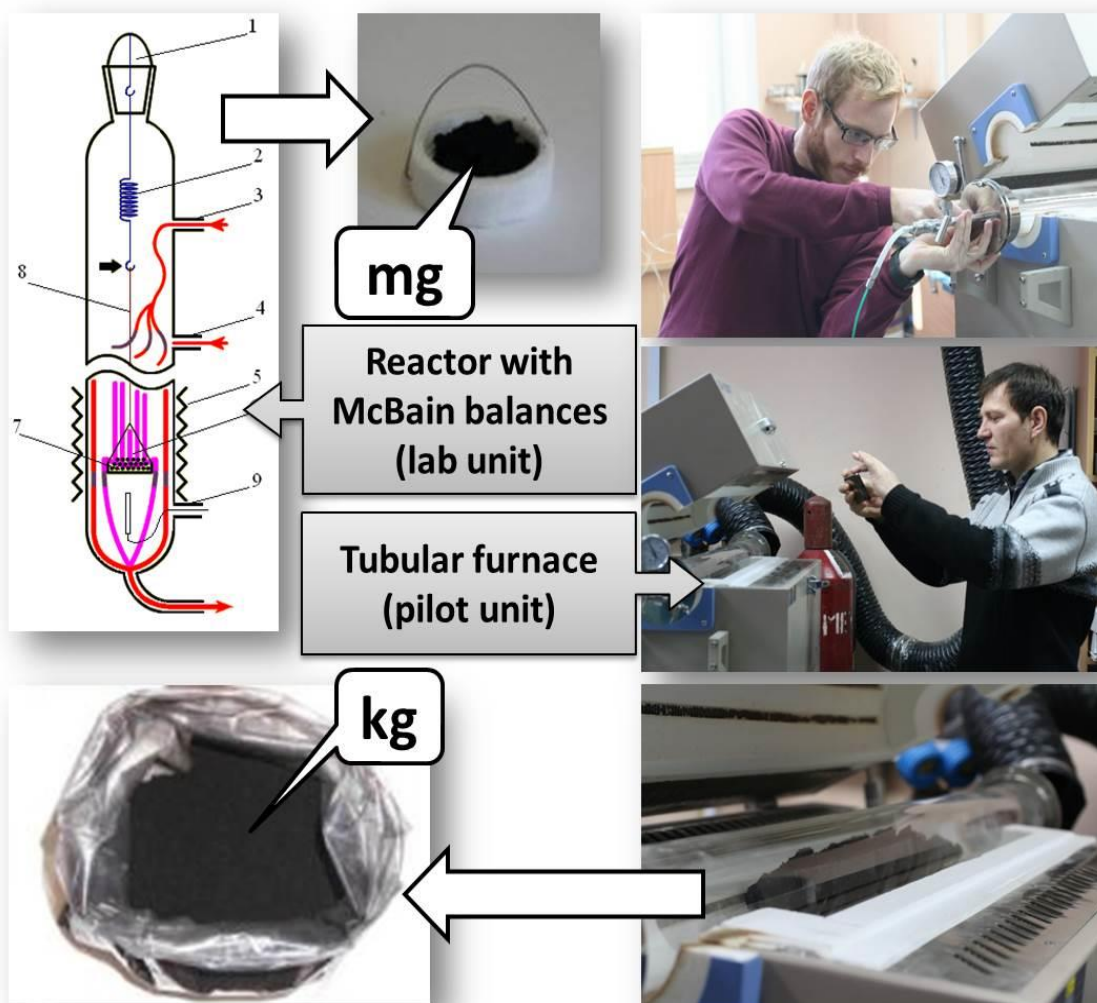


Figure 1. Experimental equipment used in the present research: McBain balances for the kinetics studies of the CCVD process (left); tubular furnace for batch production of CNF (right).

The structure and morphology of the CNF samples were studied by scanning electron microscopy (SEM) on a JSM-6460 scanning electron microscope (JEOL, Japan) at magnification factors from 8 to 300000. The transmission electron microscopy (TEM) studies were performed on a JEM-2010CX instrument (JEOL, Japan) with an accelerating voltage of 100 kV, an objective lens spherical aberration coefficient of 2.8 mm, and a line resolution of 1.4 Å. The instrument is equipped with XFlash (Bruker, Germany) X-ray energy dispersion spectrometer (EDX) having the Si-detector with an energy resolution of 130 eV. The test samples were applied as a suspension in ethanol to perforated carbon base layers fixed on a copper grid. The genesis of surface changes happening under the influence of the reaction medium at different times of exposure was also monitored by the TEM method. The measurements were carried out at 80 kV accelerating potential (JEM-1400, JEOL, Japan). The sample of NiCr wire was fixed in a standard grid holder. Then, a piece of wire was arc-curved in order to assure that the sample is fixed properly within the TEM holder. The beam was focused on the same edge of the wire.

The textural characteristics of the CNF samples were studied by a nitrogen adsorption method. The isotherms were obtained at 77.4 K on an Autosorb-iQ (Quantachrome Instruments, USA) instrument. The samples were degassed under an oil-free vacuum using a step-wise procedure, including treatment at 90 °C for 5 h and 300 °C for 10 h.

RESULTS AND DISCUSSION

Initially, the metal dusting process was studied for the bulk nichrome alloy subjected to the action of DCE vapors. For this purpose, the same piece of nichrome wire was treated under the reaction conditions for a varied period of time and then fixed in a standard grid holder of the microscope. It should be mentioned that the process starts with a prolonged induction period when no noticeable changes in the sample's weight can be registered. However, during the induction period, the surface of the nichrome wire undergoes significant alteration. As presented by a set of TEM images in Figure 2, the surface of the initial wire is relatively smooth. After just 1 minute of interaction with DCE vapor, it became evidently rough. Already after 10 minutes of the metal dusting process, the formation of dispersed metal particles accompanied by the growth of CNF takes place. 20 minutes of interaction is enough for the process to go deep inside the bulk of the wire. After 3 h of the experiment, as demonstrated by the SEM image in Figure 2, the initial wire does not exist anymore. The sample is represented by agglomerates composed of CNF with evenly distributed metal particles. Carbon yield achieves the value of 67.5 g/g_{cat}, while the specific surface area of CNF product exceeds 400 m²/g (see Table 1).

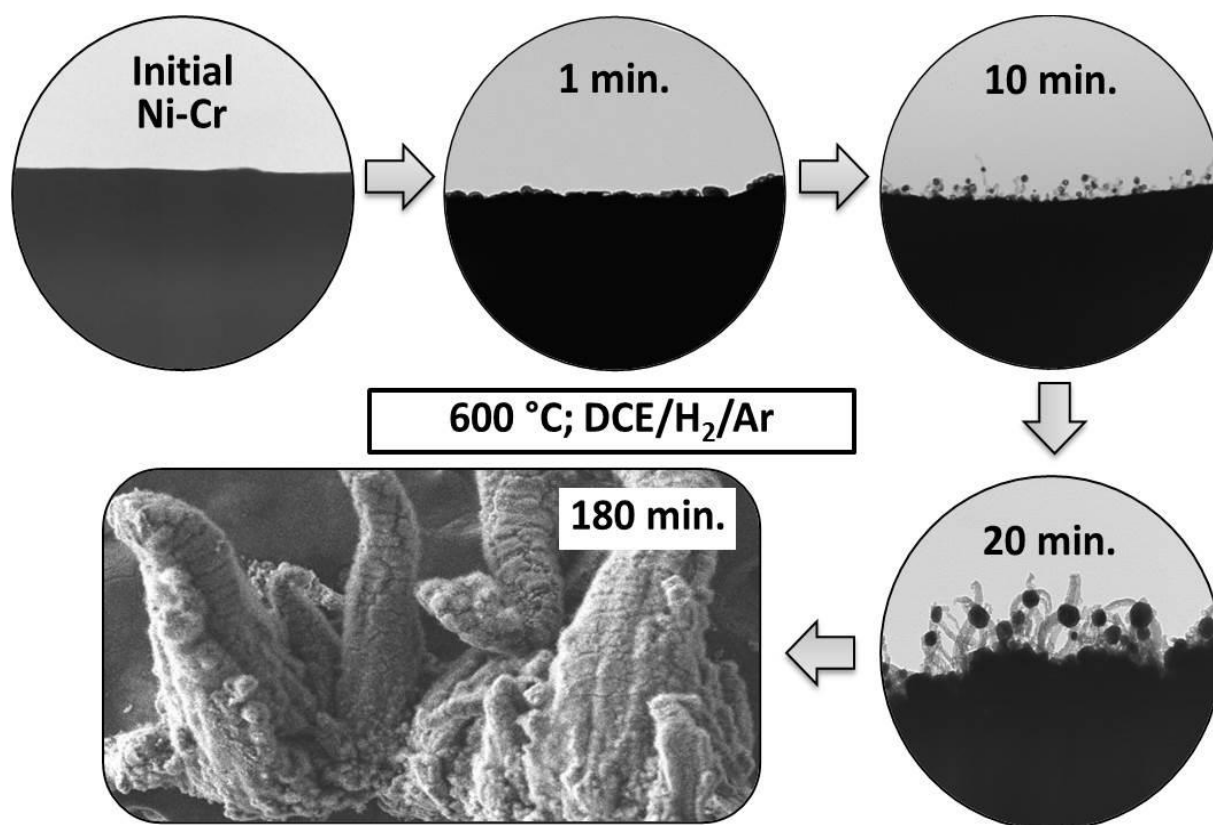


Figure 2. Scheme demonstrating the metal dusting process for the Ni-Cr wire exposed to the DCE/H₂/Ar reaction mixture at 550 °C.

Based on the detailed results of the TEM study, the general process scheme consisting of the following stages was proposed: i) adsorption and decomposition of DCE on the NiCr surface; ii) diffusion of carbon atoms to the bulk through the grain boundaries; iii) nucleation of the graphite phase; iv) disintegration of the alloy and appearance of the active nanoparticles catalyzing the CNF growth. It should be emphasized that the metal dusting process is significantly promoted by the use of chlorinated hydrocarbons in combination with H₂ excess that can be explained by the action of an aggressive corrosive medium generated by the decomposition of DCE. Therefore, the controllable metal dusting process of the bulk Ni-based alloys can be considered as a new platform for the synthesis of efficient catalysts for CNF production.

Table 1. Yield and specific surface area (SSA) of the obtained CNF over Ni-based catalysts of different compositions.
Reaction conditions: DCE/H₂/Ar; 600 °C; 2 h.

Catalyst	Carbon yield, g/g _{cat}	SSA, m ² /g
Ni-Cr (wire)	67.5*	401
Ni (cp)	22.6	325
Ni-Cr (1%, cp)	29.7	280
Ni-Cu (1%, cp)	23.6	320
Ni-Co (1%, cp)	24.8	330
Ni-Fe (1%, cp)	4.1	-
Ni-Pt (4%, cp)	27.0	380
Ni-Mo (4%, cp)	33.7	311
Ni-W (4%, cp)	26.1	307
Ni-Pd (5%, cp)	24.0	382
Ni-Pd (5%, cp)	50.9**	454

*Duration of the experiment was 3 h.

**Reaction mixture contained 8 vol.% acetonitrile.

The effect of the alloying metal on the efficiency of the overall CCVD process was investigated on a series of specially prepared Ni-M alloys. It should be noted here that the concentration of each

studied metal was varied in a wide range from 1 to 25 wt%, and only the samples with optimal concentration showing the best performance are compared below. The obtained data are summarized in Table 1. A monometallic Ni sample prepared via the same precipitation approach was used as a reference. As seen, the effect of the alloying metal can be positive or negative. For instance, the addition of iron (1 wt%) almost deactivates the catalyst. The corresponding carbon yield hardly reaches 4.1 g/g_{cat}. The addition of other metals improves the performance and significantly shortens the induction period of the metal dusting stage. The highest SSA values (380 m²/g and above) were obtained in the case of samples Ni-Pt (4%, cp) and Ni-Pd (5%, cp).

Finally, it was found that the addition of acetonitrile to the reaction mixture doubles the carbon yield value, increases the SSA value to 454 m²/g, and allows incorporation of almost 2 wt% of nitrogen atoms into the CNF structure.

CONCLUSION

It was established that the metal dusting process of bulk metal items could serve as an alternative method to prepare active and stable catalysts for the formation of carbon nanofibers via catalytic chemical vapor deposition. The metal dusting stage takes place during the induction period, when no noticeable weight changes can be seen. Under the action of aggressive medium containing hydrogen and chlorinated hydrocarbons, the metal surface undergoes restructuring and disintegration. The dispersed metal particles being formed catalyze the intensive growth of CNF. The catalytic performance of such systems depends on the alloying metal. Iron was found to worsen the activity of nickel. At the same time, its alloying with copper, chromium, cobalt, platinum, palladium, molybdenum, or tungsten shortens the induction period and increases the values of carbon yield and specific surface area of CNF. The addition of heteroatom-containing co-substrate to the reaction mixture, for an example of acetonitrile, allows producing of CNF functionalized with nitrogen-containing groups.

Acknowledgement

This work was by the Russian Foundation for Basic Research (project No. 18-29-19053_mk).

REFERENCES

- [1] I.V. Mishakov, R.A. Buyanov, V.I. Zaikovskii, I.A. Strel'tsov, A.A. Vedyagin, *Kinet. Catal.*, 2008, **49**, 868-872.
- [2] I.V. Mishakov, Y.I. Bauman, D.V. Korneev, A.A. Vedyagin, *Top. Catal.* 2013, **56**, 1026-1032.
- [3] Y.I. Bauman, A.S. Lysakova, A.V. Rudnev, I.V. Mishakov, Y.V. Shubin, A.A. Vedyagin, R.A. Buyanov, *Nanotechnol. Russia*, 2014, **9**, 380-385.
- [4] Y.I. Bauman, A.A. Vedyagin, I.V. Mishakov, *Protection of Metals and Physical Chemistry of Surfaces*, 2016, **52**, 309-315.
- [5] Y.I. Bauman, Y.V. Shorstkaya, I.V. Mishakov, P.E. Plyusnin, Y.V. Shubin, D.V. Korneev, V.O. Stoyanovskii, A.A. Vedyagin, *Catal. Today*, 2017, **293–294**, 23-32.
- [6] Y.I. Bauman, I.V. Mishakov, A.A. Vedyagin, S. Ramakrishna, *Mater. Lett.*, 2017, **201**, 70-73.
- [7] Y.I. Bauman, I.V. Mishakov, Y.V. Rudneva, P.E. Plyusnin, Y.V. Shubin, D.V. Korneev, A.A. Vedyagin, *Ind. Eng. Chem. Res.*, 2019, **58**, 685-694.
- [8] Y.I. Bauman, Y.V. Rudneva, I.V. Mishakov, P.E. Plyusnin, Y.V. Shubin, D.V. Korneev, V.O. Stoyanovskii, A.A. Vedyagin, R.A. Buyanov, *Heliyon*, 2019, **5**, e02428:1-10.
- [9] I.V. Mishakov, A.A. Vedyagin, Y.I. Bauman, A.R. Potylitsyna, A.S. Kadtsyna, V.V. Chesnokov, A.Y. Nalivaiko, A.A. Gromov, R.A. Buyanov, *Catalysts*, 2020, **10**, 1446:1-17.
- [10] Y.V. Shubin, Y.I. Bauman, P.E. Plyusnin, I.V. Mishakov, M.S. Tarasenko, M.S. Mel'gunov, V.O. Stoyanovskii, A.A. Vedyagin, *J. Alloys Compnd.*, 2021, **866**, 158778:1-12.

PEROXO-Zr/Hf CONTAINING POLYOXOMETALATES: SYNTHESIS, STRUCTURE AND DETAILED RAMAN SPECTROSCOPIC STUDIES

A. Sundar ¹, B. S. Bassil ^{1,2}, D. Bajuk-Bogdanović ³, G. Ćirić-Marjanović ³, O. V. Zalomaeva ⁴, N.V. Maksimchuk ⁴, O.A. Kholdeeva ⁴, and U. Kortz ¹

¹ *Department of Life Sciences and Chemistry, Jacobs University, Campus Ring 1, 28759 Bremen, Germany, Email u.kortz@jacobs-university.de*

² *Department of Chemistry, Faculty of Arts and Sciences, University of Balamand, P.O. Box 100, Tripoli, Lebanon*

³ *University of Belgrade-Faculty of Physical Chemistry, Studentski trg 12-16, 11158 Belgrade, Serbia*

⁴ *Boreskov Institute of Catalysis, Lavrentieva Ave. 5, Novosibirsk, 630090, Russia.*

ABSTRACT

Polyoxometalates (POM) are discrete anionic metal-oxo clusters of early *d*-block metal addenda ions in high oxidation states (e.g. W^{VI}, Mo^{VI}, V^V). POMs exhibit a large variety of shapes, sizes and compositions with multiple associated physicochemical properties and potential applications in catalysis, biomedicine and material science. The substitution of addenda atoms by other *d* or *f*-block metals such as Zr or Hf can lead to novel compounds with unprecedented properties, and some peroxo-derivatives are also known. Here we report on the synthesis and structural characterization of four novel peroxo-Zr and Hf-containing polyanions of the Wells-Dawson type. The solution stability was investigated by multinuclear NMR and detailed Raman and IR spectroscopic studies were performed in the solid state. The catalytic activity of the novel POMs in the H₂O₂-based oxidation of organic substrates was also investigated.

CATALYTIC PROPERTIES OF CARBON NANOTUBES AND REDUCED GRAPHENE OXIDE IN ETHYLENE HYDROGENATION BY MOLECULAR HYDROGEN

P.E. Strizhak, A.A. Abakumov, I.B. Bychko

L. V. Pisarzhevsky Institute of Physical Chemistry of the National Academy of Sciences of Ukraine, Prosp. Nauky, 31 Kyiv 03028, Ukraine. (pstrizhak@hotmail.com)

ABSTRACT

In the last years, several studies dedicated to the carbon nanomaterials such as multi-walled carbon nanotubes (CNT) and reduced graphene oxide (rGO) catalytic activity in the hydrogenation reactions have been reported. Particularly, for the first time, we showed that rGO and CNTs are active in the gas-phase hydrogenation reactions with molecular hydrogen.

The work is dedicated to the determination of the influence of the structure and functionality of CNT and rGO on the catalytic activity in the hydrogenation of ethylene by molecular hydrogen. The ethylene hydrogenation is a simple model gas-phase reaction that convenient to establish a dependence between the method of catalyst activation, the diameter of CNT, and the procedure of rGO preparation and their catalytic activity.

The catalytic activity of rGO strongly depends on its structural characteristics. An increase in the surface area and a decrease in the oxygen content enhance the catalytic activity of rGO. The defectiveness and oxygen content are crucial for the catalytic performance of rGO obtained either by thermal reduction of graphene oxide in hydrogen or by reduction of graphene oxide with hydrazine. This conclusion has significant implications for the potential applications of rGO as a hydrogenation catalyst.

Obtained results show that non-activated carbon nanomaterials do not exhibit catalytic activity. Increasing the temperature of activation from 100°C to 400°C increases the catalytic activity by three orders of magnitude. Further temperature increase leads to a decrease in catalytic activity. An increase in the CNT diameter significantly decreases the catalytic activity. The highest obtained activity for CNT is $6.2 \cdot 10^{-6} \text{ mol} \cdot \text{s}^{-1} \cdot \text{m}^{-2}$ which is higher compared to rGO.

Our results indicate the high stability of CNT and rGO compared to the typical hydrogenation catalysts in hydrogen-rich and ethylene-rich atmospheres. That offers new opportunities for the application of nanocarbon-based catalysts in the hydrogenation reaction at high temperatures. That is extremely important to replace catalysts operating under conditions where the metal-containing catalysts deactivate due to the formation of the carbonaceous deposits.

This research received funding from the National Research Foundation of Ukraine, grant number 2020.02/0050.

PREDICTING PARTICLE SIZE DISTRIBUTION IN NANOPARTICLE FORMATION BY STOCHASTIC AND DETERMINISTIC APPROACHES

R. Szabó and G. Lente

*University of Pécs, Institute of Chemistry, Department of Physical Chemistry and Materials Science,
Ijjúság útja 6, Pécs, 7624 Pécs, Hungary. (lente@gamma.ttk.pte.hu)*

ABSTRACT

A class of nucleation-growth type models for nanoparticle formation were investigated by deterministic and stochastic kinetic methods. Four different kernel functions were used for characterizing the dependence of the reactivity of a nanoparticle on its size in the growth reaction. The final distribution of nanoparticles formed were determined as a function of the ratio of the rate constants characterizing nucleation and particle growth. It was found that the final size distributions predicted by the stochastic and deterministic approaches for the same model agree very well. Furthermore, it was also shown that the average size of nanoparticles formed can be given as a function of the rate constant ratio with a simple power expression, where the value of the exponent depends on the identity of the kernel function used.

INTRODUCTION

Nanoparticles play an increasingly significant role in chemistry research mostly because of their excellent catalytic properties [1-3]. By now, it has become clear that their usefulness (and also toxicity) is primarily determined by the particle size [1-3]. Therefore, controlling the average size and the distribution of particle size is one of the most important aspects of nanoparticle synthesis. It is also clear that these properties are determined by kinetic factors rather than thermodynamics [4-6].

In this paper, we report mathematical kinetic investigations on a class of models used to interpret nanoparticle formation. Both the deterministic and stochastic approaches were used and their results are compared with special emphasis on the particle size distribution, which is the most common characteristic determined in experimental works.

METHODS

The model studied in this work consist of two different kinds of steps. The first type is nucleation, in which n monomeric units come together to form a nanoparticle seed that is capable of later growth (n is a parameter, its value is an integer). The second reaction step type is the growth of a nanoparticle. In this step, one monomeric unit is added to a seed or nanoparticle of larger size. It is noted that the reaction of two nanoparticles (usually termed aggregation) is not present in this model. Although its role is known in many nanoparticle formation systems [1-3], the usual strategy of mathematical modeling is to start from the simplest models and consider more complicated aspects when necessary [7-11].

The model studied here can be represented by the following two generic reactions, both of which show mass action type kinetics. In this following equation, M denotes the monomeric unit, whereas C_i is a nanoparticle containing i monomeric units:



This model gives rise to a set of simultaneous ordinary differential equations. Originally, the concentrations are the dependent variables in such equation and time is the independent variable, but it has been shown to be more advantageous to use dimensionless concentrations and dimensionless time instead [12-14]:

$$\begin{aligned}\frac{dm}{d\tau} &= -\alpha m^n - m \sum_{j=n}^{\infty} K(j) c_j \\ \frac{dc_n}{d\tau} &= \alpha m^n - K(n) m c_n \\ \frac{dc_i}{d\tau} &= K(i-1) m c_{i-1} - K(i) m c_i \quad i > n\end{aligned}\tag{2}$$

Here m denotes the dimensionless concentration of the monomeric unit M , c_i is the dimensionless concentration of the nanoparticle containing i monomeric units (C_i). The additional physical quantities are dimensionless time τ , and the ratio of the nucleation and particle growth rate constants, which is denoted α . In this ratio, the dependence of the growth rate constants of the particle size must also be considered. This is done through the $K(i)$ kernel function, for which four possibilities are given in Table 1.

Table 1. Typical kernel functions in the nucleation-growth type nanoparticle formation model

Name	Kernel function
mass kernel	$K(i) = i$
surface kernel	$K(i) = i^{2/3}$
Brownian kernel	$K(i) = i^{1/3}$
diffusion kernel	$K(i) = 1$

In Table 1, the mass kernel implies that the growth rate constant is directly proportional to the mass of the particle (so in effect, the number of monomeric units in it). The surface kernel takes the growth rate constant as directly proportional to the surface of the nanoparticle. Without having to specify further shape parameters, the nanoparticles are assumed to have roughly spherical shape, the surface of which is proportional to the 2/3th power of the volume (which is directly proportional to the mass). The Brownian kernel works in a similar way, but here the rate constant is proportional to the linear size of the nanoparticle. Finally, the diffusion kernel implies that the growth rate constant is independent of the size of the particle. This is commonly rationalized by the fact that the diffusion controlled rate constant is also independent of the size of a species: a larger particle moves slower but it is also a larger target, and the two opposing effects cancel each other [15].

In the deterministic approach, the symbolic solution of Eq. 2 was sought. It is to be noted that numerical solutions are not really viable in this case because the number of dependent variables is infinitely high.

Stochastic calculations were done using Monte Carlo simulations [16-20], which is commonly called the Gillespie algorithm. In this method, the dimensionless concentrations are measured in absolute molecule number rather than molarity based values (this is emphasized by introducing a bar over the concentration symbols m and c_i), and a time-dependent propensity p_i , analogous to deterministic reaction rates, is defined for each step:

$$p_1(t) = \binom{\bar{m}(t)}{n} \quad (3)$$

$$p_i(t) = \alpha K(i) \bar{m}(t) \bar{c}_i(t) \quad i \geq n$$

The essence of the simulation is that in each step, two independent, uniformly distributed random numbers are generated between 0 and 1, these are rnd_1 and rnd_2 . The first random number is used to increment the time according to the following equation [16-20]:

$$t^{\text{new}} = t^{\text{old}} - \frac{\ln rnd_1}{\sum_{j=1}^n p_j(t^{\text{old}})} \quad (4)$$

The second random number is used to decide which of the steps with non-zero propensity occurs. Step i occurs if and only if the following inequity is satisfied:

$$\frac{\sum_{j=1}^{i-1} p_j(t^{\text{old}})}{\sum_{j=1}^n p_j(t^{\text{old}})} \leq rnd_2 < \frac{\sum_{j=1}^i p_j(t^{\text{old}})}{\sum_{j=1}^n p_j(t^{\text{old}})} \quad (5)$$

The occurrence of step i causes the following changes in the molecule numbers:

$$\left. \begin{aligned} \bar{m}(t^{\text{new}}) &= \bar{m}(t^{\text{old}}) - n; \quad \bar{c}_n(t^{\text{new}}) = \bar{c}_n(t^{\text{old}}) + 1 \quad \text{if } i = 1 \\ \bar{m}(t^{\text{new}}) &= \bar{m}(t^{\text{old}}) - 1; \\ \bar{c}_i(t^{\text{new}}) &= \bar{c}_i(t^{\text{old}}) - 1; \quad \bar{c}_{i+1}(t^{\text{new}}) = \bar{c}_{i+1}(t^{\text{old}}) + 1 \end{aligned} \right\} \quad \text{if } i > n \quad (6)$$

These steps are repeated until $c_1 = 0$, which means that all the propensities are zero, i.e. an unchangeable final state is reached.

RESULTS AND DISCUSSION

Full symbolic solutions were obtained for three different models [12, 14], which means that a formula was found to give the dependence of all dimensionless concentrations on dimensionless time. For other cases, some partial results are also reported in our earlier works [12-14].

For the diffusion kernel and $n = 1$, the following general formula has been found to be valid [14]:

$$c_i = \alpha - \alpha e^{-\mu_0/\alpha} \sum_{j=0}^{i-1} \frac{1}{j!} \left(\frac{\mu_0}{\alpha} \right)^j \quad (7)$$

For the mass kernel and $n = 1$, the symbolic solution takes the following form [14]:

$$\begin{aligned} m &= \frac{\alpha + 1}{\alpha e^{(\alpha+1)\tau} + 1} \\ c_i &= \frac{\alpha}{i} \left(\frac{1-m}{\alpha+1-m} \right)^i \end{aligned} \quad (8)$$

The symbolic solution has also been found for the mass kernel and $n = 2$, although this is somewhat more complicated than the previous ones [12]:

$$\begin{aligned}
 m &= \frac{1}{1 - 2\alpha + 2\alpha e^\tau} \\
 c_i &= \frac{\alpha(i-1)!(-1)^{i-1}(m-1)}{\prod_{j=2}^i (2\alpha - j - 1)} + \\
 &\quad + \sum_{j=2}^i \frac{\alpha(j^2 - 1)}{j(2\alpha - j - 1)} \binom{i-1}{j-1} (-1)^j \left[\left(\frac{1-m}{2\alpha} + m \right)^{j/(2\alpha-1)} - 1 \right]
 \end{aligned} \tag{9}$$

In addition, a special numerical method was developed for the diffusion kernel and $n = 2$ [13], in which the individual c_i values could be calculated for $i = 2$ first and then for successively larger and larger i values.

Fortunately, programming the Gillespie algorithm in stochastic studies does not really depend on the complexity of the model, so these simulations could be carried out for every kernel and n value. We selected the range $n = 1-5$, so altogether did these calculations in 20 different models.

Since almost all earlier attempts on treating nanoparticle formation models involved the deterministic approach [1-3] only, it was important to compare the results from the two approaches. This is really essential because the typical particle numbers are very low in the system, which are the exact conditions where stochastic kinetics may describe behavior very different from the deterministic approximation.

Generally, it was found that the stochastic approach predicts substantial fluctuations in the time course of the reactions. However, when the final nanoparticle size distribution is concerned, the two approaches give essentially the same final results, which implies that even despite the anticipated problems, the deterministic approach is suitable for predicting size distributions. As an example, the two sets of data are compared for the diffusion kernel and $n = 2$ with $\alpha = 5 \times 10^{-7}$ in Figure 1. It is notable that in this graph, the x axis shows i values, which means that it is proportional to the mass of the nanoparticles rather than the linear size. The linear size would be obtained as the cube root of this axis. Also, the graph shows the cumulative distribution function (the probability that the size of the particle is smaller than i). From earlier examples, it is understood that this sort of representation is much better suited for comparison with experimental data than histograms, which tend to rely on the arbitrary categorization of data.

As already pointed out, the stochastic simulations could be done for every nucleation-growth type model. This means that the final distributions could be characterized for all these cases as a function of the rate constant ratio α . Such a dependence is shown for different values of n of the Brownian kernel in Figure 2.

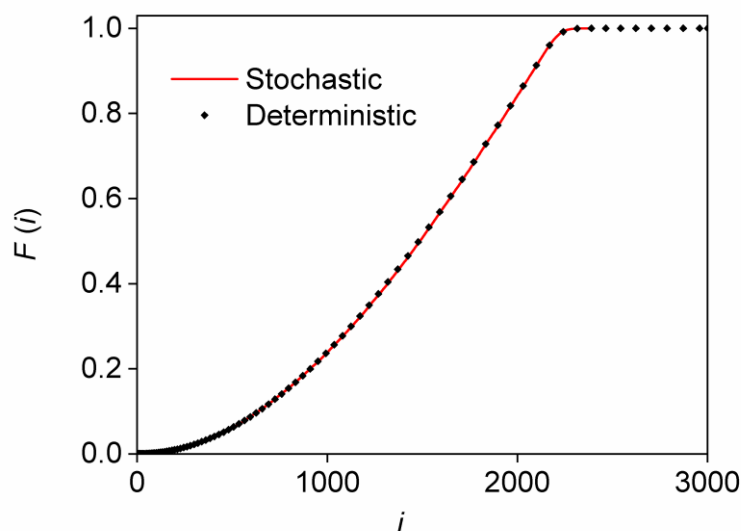


Figure 1. Final particle size distribution in stochastic simulations and the deterministic prediction for the diffusion kernel with $n = 2$ with $\alpha = 5 \times 10^{-7}$.

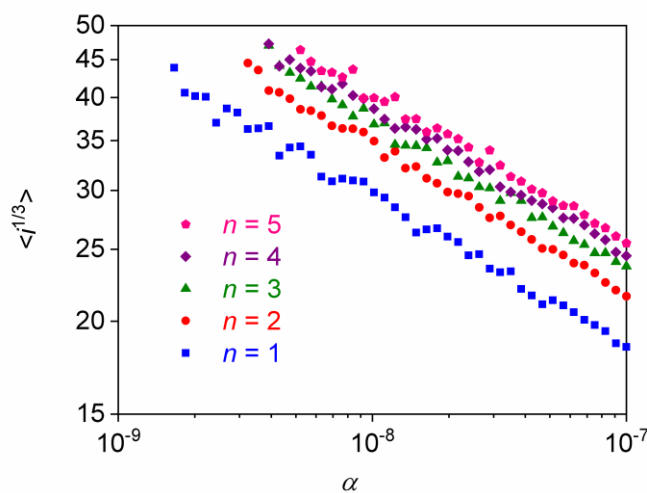


Figure 2. Dependence of average particle size on the value of α for different values of n with the Brownian kernel

A detailed analysis of the data showed that the average particle size (which is the average of the cube root of the monomeric units in the particles) can be given with a power function as follows:

$$\langle i^{1/3} \rangle = X \alpha^\rho \tag{10}$$

The values of the ρ exponents for the 20 different models studies in this work are given in Table 2.

Table 2. Power function exponents (ρ) for the dependence of average particle size on the value of α

Kernel	1	2	3	4	5
mass	0.258	0.249	0.241	0.235	0.230
surface	0.261	0.272	0.246	0.247	0.260
Brownian	0.200	0.201	0.200	0.194	0.197
diffusion	0.166	0.167	0.166	0.166	0.167

Table 2 shows that the exponent ρ only depends somewhat on the value of n for the mass kernel. This observation may be used to identify the suitable kernel functions for interpreting experimental data.

CONCLUSION

It is concluded that the mathematical methods developed in this work are capable of providing mechanism-based predictions for the size distributions of nanoparticles formed. The methods are readily extended to other models as well, so they will be directly suitable for comparing theoretical mechanistic considerations with experimental data.

Acknowledgement

This work was supported by the Higher Education Institutional Excellence Program of the Ministry of Human Capacities in Hungary, within the framework of the 1st thematic program of the University of Pécs. The National Research, Development, and Innovation Office of Hungary also supported this work under grant No. SNN 125739.

REFERENCES

- [1] S. T. Hunt, Y. Román-Leshkov, *Accounts of Chemical Research*, 2018, 51, 1054-1062.
- [2] I.V. Zibareva, L. Y. Ilina, A. A. Vedyagin, *Reaction Kinetics Mechanisms and Catalysis*. 2019, 127, 19-24.
- [3] Z. Li, S. Ji, Y. Liu, X. Cao, S. Tian, Y. Chen, Z. Niu, Y. Li, *Chemical Reviews*, 2020, 120, 623-682.
- [4] A. F: Lisovsky, *Science of Sintering*, 2010, 42, 15–24.
- [5] L. M. Wheeler, N. J. Kramer, U. R. Kortshagen, *Nano Letters*, 2018, 18, 1888–1895.
- [6] A. F: Lisovsky, *Journal of Superhard Materials*, 2020, 42, 9–17.
- [7] G. Lente, I. Fábián, *Inorganic Chemistry*, 1998, 37, 4204-4209.
- [8] G. Lente, I. Fábián, *Inorganic Chemistry*, 1999, 38, 603-605.
- [9] G. Lente, J. H. Espenson, *Inorganic Chemistry*, 2000, 39, 4809-4814.
- [10] G. Lente, *Journal of Physical Chemistry A*, 2006, 110, 12711-12713.
- [11] G. Lente, *Physical Chemistry Chemical Physics*, 2007, 9, 6134-6141.
- [12] R. Szabó, G. Lente, *Journal of Mathematical Chemistry*, 2019, 57, 616-631.
- [13] R. Szabó, G. Lente, *Chemistry of Materials*, 2021, DOI: 10.1021/acs.chemmater.0c04688.
- [14] R. Szabó, G. Lente, *Journal of Mathematical Chemistry*, 2021, 10.1007/s10910-021-01265-z.
- [15] G. Lente, *Current Opinion in Chemical Engineering*, 2018, 21, 76-83.
- [16] T. Sipos, J. Tóth, P. Érdi, *Reaction Kinetics and Catalysis Letters*, 1974, 1, 113-117.
- [17] T. Sipos, J. Tóth, P. Érdi, *Reaction Kinetics and Catalysis Letters*, 1974, 1, 209-213.
- [18] D. T. Gillespie, *Journal of Computational Physics*, 1976, 22, 403-434.
- [19] D. T. Gillespie, *Journal of Physical Chemistry*, 1977, 81, 2340-2361.
- [20] D. T. Gillespie, A. Hellander, L. R. Petzold, *Journal of Chemical Physics*, 2014, 138, 270901

FREE RADICAL SCAVENGING POTENCY OF EQUOL

A. Amić¹, D. Milenković², J. M. Dimitrić Marković³ and Z. Marković²

¹ Department of Chemistry, Josip Juraj Strossmayer University of Osijek, Ulica cara Hadrijana 8A, 31000 Osijek, Croatia (aamic@kemija.unios.hr).

² Institute of Information Technologies, Department of Science, University of Kragujevac, 34000 Kragujevac, Serbia.

³ The Faculty of Physical Chemistry, University of Belgrade, Studentski trg 12-16, 11000 Belgrade, Serbia.

ABSTRACT

Kinetic analysis performed by using Transitivity Code indicates that phenolic hydrogens of physiologically active equol molecule are much more abstractable than C-ring hydrogens. Obtained results are opposite to very recently published statements that aliphatic C–H bonds of natural compounds may play significant role in antioxidant action. Unequivocally, phenolic O–H bonds are responsible for antiradical activity of equol. The contribution of equol's C-ring hydrogens to free radical scavenging is negligible.

INTRODUCTION

It is well-known that oxyl radicals (peroxyl radicals ROO[•]) react $\sim 10^4$ faster with O–H bonds than with C–H bonds of comparable strength [1]. A few decades ago breaking of phenolic O–H bond was recognized as a cornerstone of antioxidant (free radical scavenging) activity of polyphenolic compounds [2]. Such breaking may be homolytic (e.g., *via* hydrogen atom transfer (HAT) mechanism) or heterolytic (e.g., *via* sequential proton loss electron transfer (SPLET) mechanism) [3]. Despite that, very recently in several reports it has been claimed that C–H bond hydrogen abstraction may play notable role in free radical scavenging by natural compounds, even more significant than phenolic O–H bond hydrogen abstraction [4]. Such statements are mainly based on using of inappropriate level(s) of theory: B3LYP functional which underestimates barrier heights [5] and/or such tunneling corrections that highly overestimate importance of tunneling for C–H bond abstraction [6].

Equol, a product of human intestinal bacterial metabolism of soy isoflavones [7], is particularly suitable molecule to reinvestigate the role of C–H hydrogens in antiradical activity. Equol possesses five C-ring hydrogens which may compete with two phenolic hydrogens in free radical quenching (Fig. 1).

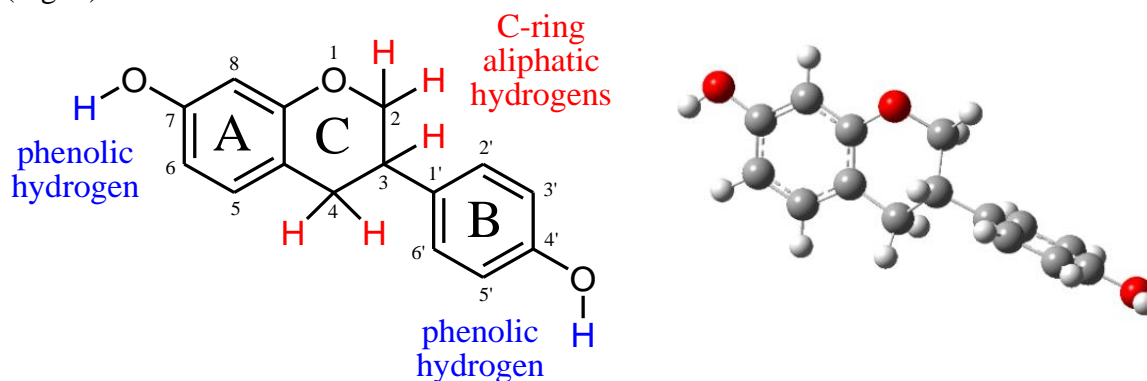


Figure 1. Structure of equol

METHODS

Geometry optimizations and frequency calculations for equol and all species involved in studied mechanism of hydroperoxyl (HOO^\bullet) scavenging were performed at M06-2X/6-311++G(d,p) level of theory in gas-phase at 298.15 K by using the Gaussian 09. Local minima and transition states (TS) were identified by the number of imaginary frequencies (0 and 1, respectively). IRC calculation was performed on both sides of the TS to confirm that it properly connects the corresponding reactants and products. The rate constants (k) were calculated by using transition state theory (TST) as implemented in the Transitivity Code [8]. For kinetic calculations, this code needs only the electronic structures of reactants, transition state and products.

For a general bimolecular reaction, the rate constant (k) is given by:

$$k = \kappa \frac{k_B T}{h} \frac{Q^\ddagger}{Q_1 Q_2} \exp\left(-\frac{\varepsilon^\ddagger}{k_B T}\right)$$

where, κ accounts for tunneling corrections, k_B is the Boltzmann constant, T is the temperature, h is the Planck constant, Q_1 , Q_2 and Q^\ddagger are partition functions of reactants and of the transition state, respectively, and ε^\ddagger is the barrier height. The one-dimensional tunneling corrections in the Transitivity Code include Skodje-Truhlar (ST), Bell's and the deformed (d -TST) tunneling corrections.

The branching ratios (Γ , in %) calculated from rate constants can be used to identify the reaction pathways contributing the most to the total reaction:

$$\Gamma = (k_i/k_{\text{overall}}) \times 100$$

where k_i represents the rate constant of independent path. The overall rate constant (k_{overall}) is calculated as the sum of rate constants of all reaction paths.

RESULTS AND DISCUSSION

The simplest approach to study the rate constants is TST with one-dimensional tunneling corrections. Tunneling in HAT reactions is significant and must be taken into account. Results of performed calculations at the M06-2X/6-311++G(d,p) level of theory and kinetic calculations using the Transitivity Code are summarized in Table 1.

Table 1. TS imaginary frequency ν (cm^{-1}), barrier height ε^\ddagger (kcal/mol) and rate constant k ($\text{M}^{-1} \text{s}^{-1}$) in HAT reaction of equol with HOO^\bullet radical

path	ν	ε^\ddagger	$k(\text{TST})$	$k(d\text{-TST})$	$k(\text{ST})$	$k(\text{Bell35})$
C2-H	-1819	10.39	1.7×10^0	2.3×10^1	8.6×10^2	8.8×10^2
C3-H	-1919	10.93	6.2×10^{-1}	1.1×10^1	7.2×10^2	7.3×10^2
C4-H	-1740	7.08	3.7×10^2	3.5×10^3	2.8×10^4	2.9×10^4
7-OH	-2110	6.72	1.9×10^3	3.6×10^4	3.9×10^5	3.9×10^5
4'-OH	-2201	7.18	1.1×10^3	2.7×10^4	3.9×10^5	3.9×10^5
k_{overall}			3.5×10^3	6.6×10^4	8.1×10^5	8.2×10^5

As can be seen from Table 1, phenolic OH groups of equol are preferred sites for H-atom abstraction. Branching ratios clearly indicate major role of equol's phenolic C7-OH and C4'-OH groups (>90%) in HOO^\bullet inactivation (Table 2). Amongst C-ring hydrogens, only those from C-4 site slightly contribute to the HOO^\bullet scavenging (<10%).

Table 2. Branching ratios Γ (%) at 295.15 K

path	Γ_{TST}	$\Gamma_{d\text{-TST}}$	Γ_{ST}	Γ_{Bell35}
C2-H	0.0	0.0	0.1	0.1
C3-H	0.0	0.0	0.1	0.1
C4-H	10.7	5.3	3.5	3.6
7-OH	56.4	54.3	47.9	47.9
4'-OH	32.9	40.4	48.4	48.3

Without tunneling corrections, the $k(\text{TST})$ values for O–H paths are by $\sim 10^3$ ($\sim 10^1$) higher than corresponding values for C2-H and C3-H (C4-H) paths, respectively. The same relationships remain by including tunneling corrections. Depending on applied tunneling corrections k_{overall} increase by $\sim 10^1$ (for $d\text{-TST}$) and by $\sim 10^2$ (for ST and Bell35). If we recall that phenolic O–H bonds are by a factor of $\sim 10^4$ more reactive than C–H bonds of similar strength [1], then it is obvious that used one-dimensional tunneling corrections are not fully appropriate. We suppose that more accurate results could be obtained by using canonical variational transition state theory (CVT) corrected by multidimensional small-curvature tunneling (SCT) [9]. The CVT/SCT method is successfully applied to the reactions of radical scavenging by natural antioxidants [10].

CONCLUSION

By using appropriate level of theory for electronic calculations and simple kinetic approach, we qualitatively found that phenolic hydrogens of equol are more abstractable than C-ring aliphatic hydrogens. To achieve reliable quantitative results more sophisticated kinetic approach (CVT/SCT) must be applied.

Acknowledgement

This work was partially supported by the Croatian Ministry of Science and Education, and the Ministry of Education, Science and Technological Development of Republic of Serbia (Contract number: 451-03-68/2020-14/200146).

REFERENCES

- [1] J. M. Mayer, *Acc. Chem. Res.*, 2011, **44**, 36-46.
- [2] W. Bors, W. Heller, C. Michel, M. Saran, *Method. Enzymol.*, 1990, **186**, 343-355.
- [3] A. Galano, G. Mazone, R. Alvarez-Diduk, T. Marino, J. R. Alvarez-Idaboy, N. Russo, *Annu. Rev. Food Sci. Technol.*, 2016, **7**, 335-352.
- [4] see, for example: a) Q. V. Vo, P. C. Nam, N. M. Thong, N. T. Trung, C-T. D. Phan, A. Mechler, *ACS Omega*, 2019, **4**, 8935-8942; b) T. C. Ngo, T. H. Nguyen, D. Q. Dao, *J. Chem. Inf. Model*, 2019, **59**, 766-776; c) H. Boulebd, *Free Radic. Res.*, 2020, **54**, in press.
- [5] Y. Zhao, N. Gonzalez-Garcia, D. G. Truhlar, *J. Phys. Chem. A*, 2005, **109**, 2012-2018.
- [6] E. Dzib, J. L. Cabellos, F. Ortiz-Chi, S. Pan, A. Galano, G. Merino, *Int. J. Quantum. Chem.*, 2018, **119**, e25686.
- [7] B.-J. Li, *J. Food Process. Preserv.*, 2019, **43**, e14205.
- [8] H. G. Machado, F. O. Sanches-Neto, N. D. Coutinho, K. C. Mundim, F. Palazzetti, V. H. Carvalho-Silva, *Molecules*, 2019, **24**, 3478.
- [9] J. L. Bao, D. G. Truhlar, *Chem. Soc. Rev.*, 2017, **46**, 7548-7596.
- [10] S. G. Chiodo, M. Leopoldini, N. Russo, M. Toscano, *Phys. Chem. Chem. Phys.*, 2010, **12**, 7662-7670.

APPLICATION OF QUANTUM CHEMICAL CALCULATION IN DEFINING PEAKS IN UV-VIS SPECTRA OF OXIDATIVE TARTRAZINE DEGRADATION

M. Popadić¹, S. Marinović², T. Mudrinić², A. Milutinović-Nikolić²,
P. Banković², I. Đorđević² and G. Janjić²

¹University of Belgrade–Faculty of Chemistry, Studentski trg 12-16, 11000 Belgrade, Republic of Serbia.

²University of Belgrade, Institute of Chemistry, Technology and Metallurgy, National Institute, Njegoševa 12, 11000 Belgrade, Republic of Serbia (goran.janjic@ihm.bg.ac.rs)

ABSTRACT

Degradation of tartrazine in presence of cobalt activated Oxone[®] (potassium peroxymonosulfate) was investigated. Aluminium pillared clay acted as a support for catalytically active Co²⁺. Oxone[®] was a precursor of SO₄^{•-} radical anions. Along with decolorization of tartrazine solution, the degradation of tartrazine and formation of oxidation products was monitored using UV-Vis spectroscopy. Quantum chemical calculations were performed in order to predict UV-Vis spectra. Different models were tested, and the results of calculation have shown that the combination of TPSS-D3 method and aug-cc-pVDZ basis set is quite satisfactory level of theory. The experimentally obtained peaks that arose during degradation were identified using this method.

INTRODUCTION

Catalytic oxidative degradation in the presence of sulfate radical anions (SO₄^{•-}), has received much attention recently [1]. Oxone[®] (KHSO₅·0.5·KHSO₄·0.5·K₂SO₄) has been widely utilized as a source of HSO₅⁻ ions that yield into SO₄^{•-} radical anions. In order to be efficient, the Oxone[®] should be activated. In our previous work, pillared montmorillonite impregnated with cobalt, was found to be efficient catalyst in catalytic oxidation of tartrazine in the presence of Oxone[®] [2]. The process was monitored using UV-Vis spectroscopy. It was found that changes in UV-Vis spectra were the result of tartrazine decolorization as well as formation of oxidative products. In this paper quantum chemical calculation were applied in order to assign newly formed peaks in UV-Vis spectra to defined products of tartrazine degradation.

EXPERIMENTAL

The 2 μm fraction of clay rich in montmorillonite was pillared with aluminium, impregnated with cobalt. The obtained catalyst was fully characterized [2]. The catalytic test was performed by stirring (300 rpm) tartrazine solution (C₀ = 50 mg dm⁻³) in the presence of 0.130 mmol Oxone[®] and 10 mg of catalyst [2]. The experiments were conducted at 50 °C at unadjusted pH (pH = 3.6). The sampling was performed at a predetermined periods of time (5, 10, 20, 30, 60, 120 and 240 min). The supernatant was separated from the catalyst by centrifugation and the obtained solution was monitored by using UV-Vis spectrophotometry (Thermo Scientific Evolution 220 UV-Vis Spectrophotometer).

All theoretical calculations were performed with the Gaussian 09 program package [3]. Structures of all investigated tartrazine forms were optimized with Density functional theory (DFT), by using the TPSS-D3 functional and 6-31g basis set. Time dependent density functional theory (TD-DFT) has been employed to compute the absorption spectra. To determine the level of theory which achieves the best agreement of experimental with calculated UV-Vis spectra, several functionals (cam-B3LYP, M06-2X, and TPSS-D3) and two basis sets (aug-cc-pVDZ and def2-TZVP) were used.

The calculations were performed using restricted formalism, the tight convergence criteria and without any symmetry constraints. The effect of water, as solvent, was simulated using the Solvation Model based on Density (SMD).

RESULTS AND DISCUSSION

Experimentally obtained UV-Vis spectra after selected reaction times are given in Figure 1a. The only change in spectra of starting solution (0 min) up to 60 min of reaction, was diminishing of the characteristic peaks at 257 nm and 426 nm. Besides these changes, a new peak at 231 nm appeared after 120 min of reaction, Later on, after 240 min of reaction the intensity of this peak decreased along with formation of another additional peak at 275 nm.

The possible reaction pathways were analyzed in order to estimate the origin of 231 nm and 275 nm peaks. Afterwards, for each potential product of the reaction, the theoretical UV-Vis spectra obtained by quantum chemical calculations were established (Figure 1b).

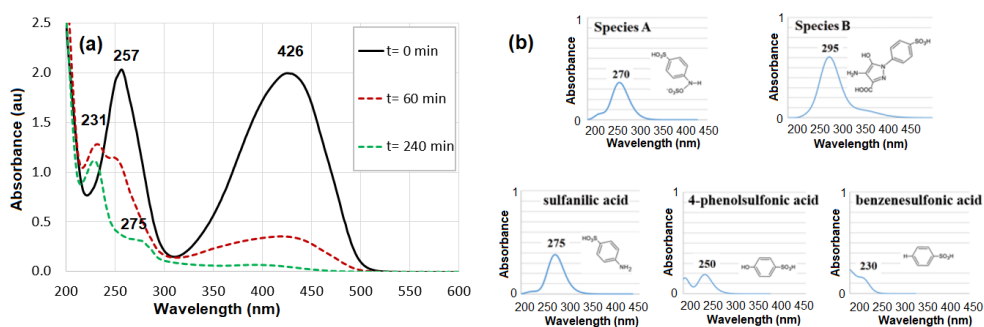


Figure 1. Experimental UV-Vis spectra for degradation of tartrazine (a) and calculated UV-Vis spectra of its oxidation products (b).

In the proposed mechanism $\text{SO}_4^{\cdot-}$ radical anion attacked the N atom of the azo group of tartrazine bonded to the benzene ring, producing a sulfate tartrazine derivative. Degradation started with the azo bond cleavage by $\text{SO}_4^{\cdot-}$ radical anion [4] (Figure 2). In this manner, two products were formed: sulfanilic acid derivative (species A) and the derivative of benzenesulfonic acid with pyrazole ring as substituent (species B).

After NH_3 and CO_2 release from species B and degradation of pyrazole ring, the sulfanilic acid might be formed. Further degradation sulfanilic acid can lead among other products into formation of 4-phenolsulfonic and benzenesulfonic acid. In calculated spectra of species B the peak was estimated at 300 nm. This peak was not pronounced in the experimental spectra, indicating the fast degradation of this product. The spectra of species A and sulfanilic acid have peaks at 270 nm and 275 nm, respectively. Therefore, the experimentally obtained peak at 275 nm can be assigned to these two species. The occurrence of the peak at 230 nm could be assigned to 4-phenolsulfonic and benzenesulfonic acid since they showed peak at around 230 nm in calculated spectra.

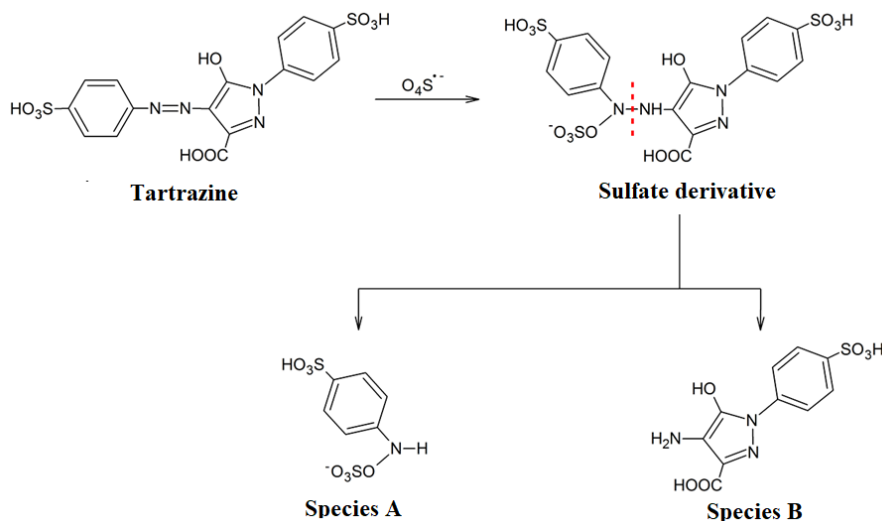


Figure 2. The first step of main reaction path of tartrazine degradation i.e. the azo bond cleavage.

CONCLUSION

Oxidative degradation of tartrazine by $\text{SO}_4^{\bullet-}$ radical anions was monitored by UV-Vis spectroscopy. In the first period of the reaction (up to 60 min) the only registered change in spectra was diminishing of the tartrazine originated characteristic peaks at 257 nm and 426 nm. After 120 min and 240 min of the catalytic reaction additional peaks at 231 nm and 275 nm, respectively, were monitored. The possible reaction pathways were analyzed in order to estimate the origin of 231 nm and 275 nm peaks. For each potential product of reaction quantum-chemical calculations were performed and theoretical UV-Vis spectra were calculated. The combination of TPSS-D3 method and aug-cc-pVDZ basis set was found to be the most appropriate. Based on calculated UV-Vis spectra peak at 275 nm can be assigned to sulfanilic acid derivatives. On the other hand, peak at 231 nm can be the result of further degradation of derivative of the benzenesulfonic acid with pyrazole ring as substituent. The products of degradation for which the calculated UV-Vis spectra had maxima in vicinity of 231 nm were 4-phenolsulfonic and benzenesulfonic acid. The quantum chemical calculations have proven beneficial for the identification of the products of tartrazine degradation.

Acknowledgement

This work was financially supported by the Ministry of Education, Science and Technological Development of the Republic of Serbia (Grant No: 451-03-9/2021-14/200026).

REFERENCES

- [1] Y. Yang, J. Jiang, X. Lu, J. Ma, Y. Liu, *Environ. Sci. Technol.* 2015; 49: 7330–7339. doi.org/10.1021/es506362e
- [2] M. Marković, S. Marinović, T. Mudrinić, M. Ajduković, N. Jović-Jovičić, Z. Mojović, J. Orlić, A. Milutinović-Nikolić, P. Banković, *Appl Clay Sci* 2019, **182**, 105276 (10 pages).
- [3] M. J. Frisch et al., *Gaussian 09* (Gaussian, Inc., Wallingford CT, 2009).
- [4] L. H. Mendoza-Huizar, *J Mex Chem Soc* 2014, **58**, 416–423.

KINETICS OF THE REDUCTION OF DICYANOBIS(2,2'-BIPYRIDYL)IRON(III) BY IODIDE IN AQUEOUS MEDIUM

R. Khattak¹ and M. S. Khan²

¹Department of Chemistry, Shaheed Benazir Bhutto Women University, Peshawar 25000, Pakistan.
(rznkhattak@yahoo.com; rznkhattak@sbbwu.edu.pk)

²Department of Chemistry, University of Malakand, Chakdara 18800, Pakistan.

ABSTRACT

The redox reaction between dicyanobis(2,2'-bipyridyl)iron(III) and iodide may have potential application in dye-sensitized solar cells. In this study, kinetics of the reduction of dicyanobis(2,2'-bipyridyl)iron(III) was studied in aqueous medium. Iodide was used as a reducing agent at 60 mM ionic strength and a temperature of 293 ± 0.5 K. The reaction was of zero and fractional (0.5) order in the oxidant and reductant, respectively. The reaction was in general fractional (0.5) order. With increasing acidity in the reaction mixture, the measured zero order rate constant decreased, but was unaffected by increasing ionic strength. The thermodynamic parameters of activation were also computed for the redox process.

INTRODUCTION

Dicyanobis(2,2'-bipyridyl)iron(III) has potential application in the dye-sensitized solar cells (DSSCs). Its photosensitive nature and high reduction potential (0.76 V) make it a good candidate for DSSC to be used as a sensitizer [1]. It has been used as an oxidizing agent for several reductants that include hexacyanoferrate(II), glutathione, L-cystein and iodide in different solvent media [2-5]. We used this complex to oxidize iodide in binary solvent media (aqueous-alcohol) and studied the effect of ionic strength on the redox reaction [6]. In this study, we have been interested in the reduction of dicyanobis(2,2'-bipyridyl)iron(III) by using potassium iodide in aqueous medium. Potassium iodide is easily oxidized by our selected mixed ligand complex without any application of an external triggering such as catalyst or external factors including ultra sensitive experimental conditions. The electrochemical series shows iodine's reduction potential as 0.54 V. Oxidation of iodide is an important facet of solar cells such as perovskite and dye-sensitized solar cells where it is oxidized in different ways [7-10]. In the dye-sensitized solar cells, different complexes have been used to oxidize the iodide ion in order to improve the efficiency of the DSSCs [11-12]. We studied the kinetics of our selected redox reaction and determined the effect of various parameters on the rate constant of the reaction and deduced the rate law.

METHODS

Analar grade (Sigma-Aldrich) materials (dicyanobis(2,2'-bipyridyl)iron(III) nitrate, potassium iodide, potassium nitrate and nitric acid) were used in this study. The aqueous solutions were prepared in deionized water. The spectra of reactants and products were recorded in aqueous medium (Figure 1). The time course graph was monitored upon formation of dicyanobis(2,2'-bipyridyl)iron(II) and the increase in absorbance was recorded. While determining the order of reaction with respect to the reactants, the pseudo-first order condition was maintained by keeping the oxidant at a low concentration (0.08 mM) and the reductant at a high concentration (80 – 2400 μ M). To evaluate the influence of H⁺ ions and ionic strength, this ratio was kept at 80 μ M : 800 μ M (oxidant : reductant). Each experiment was repeated thrice to acquire accuracy. The integration method was implemented to determine the order of reaction and the rate constant. The observed rate constant was the average of three readings.

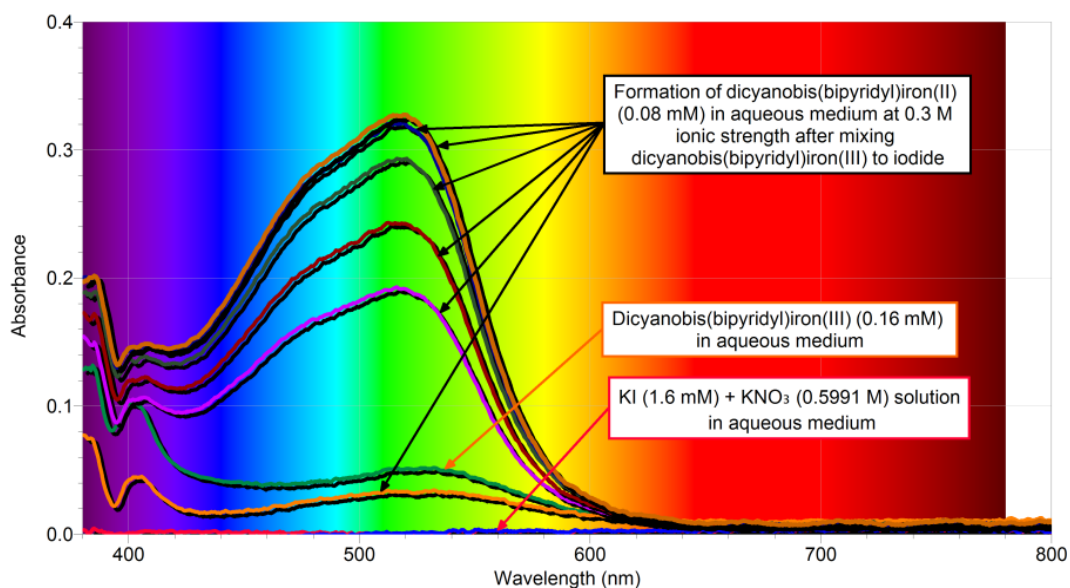


Figure 1. Spectral analysis (visible region) of reactants and product.

RESULTS AND DISCUSSION

The reaction was found to undergo the zero order kinetics in dicyanobis(2,2'-bipyridyl)iron(III) at 293 ± 0.5 K and 60 mM ionic strength (I) in aqueous medium. The observed zero order rate constant was determined at different concentration of iodide (0.08 – 2.4 mM) keeping all other parameters constant. The concentration of the oxidant was maintained at 80 μ M. The plot of the observed rate constant versus the fractional (0.5) power of the concentration of iodide yielded a straight line passing through the origin (Figure 2). The slope of the plot provided the fractional order rate constant as $5 \times 10^{-6} \text{ M}^{0.5} \text{ s}^{-1}$. The overall order of reaction was found fractional (0.5) consequently.

The effect of the increasing acidity was also studied on the observed rate constant by adding nitric acid to the reaction mixture. The value of the rate constant was decreased with increasing acidity that showed the rate resisting effect of the hydrogen ions on the rate constant (Figure 3). These results helped to conclude that the slow-step of the reaction involves the unprotonated iodide or triiodide ion. The results were refined by the neutral effect of the ionic strength on the observed zero order rate constant.

The effect of ionic strength was studied by increasing the concentration of potassium nitrate in the reaction mixture keeping all other parameters constant. The ionic strength was varied between 5 – 370 mM. The plot of log rate constant versus square root of ionic strength showed no effect according to the formulation of the primary salt effect (Figure 4). This confirms the formation of triiodide ion and its rate-leading effect in the reaction mechanism because the neutral iodine plays a vital role of limiting reactant in the formation of triiodide ion.

The activation parameters of the reaction were determined by varying the temperature between 10 – 40 $^{\circ}$ C. The Arrhenius and Eyring plots were drawn that yielded activation parameters such as activation energy; $E_a = 46.23 \text{ kJ mol}^{-1}$, pre-exponential factor; $A = 24.62 \text{ M s}^{-1}$, change in enthalpy of activation; $\Delta H^{\ddagger} = 43.76 \text{ kJ mol}^{-1}$, change in entropy of activation; $\Delta S^{\ddagger} = -226.5 \text{ J mol}^{-1} \text{ K}^{-1}$, and change in Gibbs free energy of activation; $\Delta G^{\ddagger} = 111.26 \text{ kJ mol}^{-1}$ (25 $^{\circ}$ C).

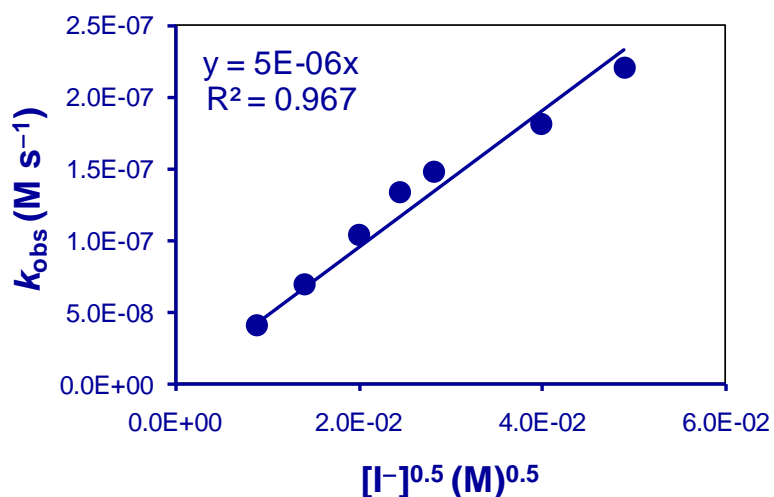


Figure 2. Fractional order with respect to reductant in aqueous medium.

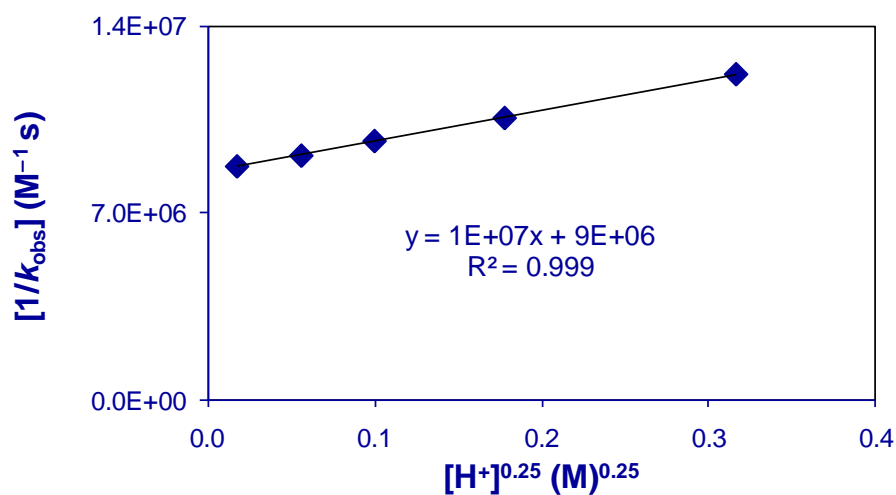


Figure 3. Rate resisting effect of H^+ ions on the rate constant in aqueous medium.

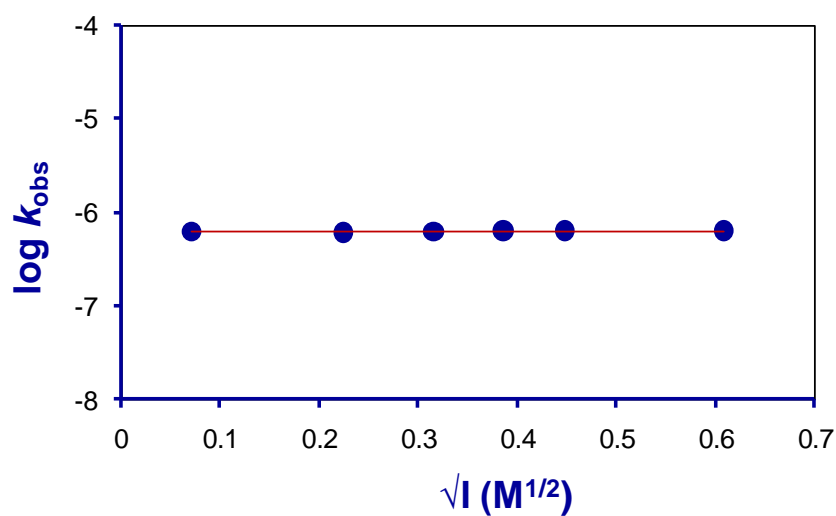


Figure 4. Primary salt effect in aqueous medium.

CONCLUSION

The reduction of dicyanobis(2,2'-bipyridyl)iron(III) by iodide conforms an overall fraction (0.5) order kinetics in aqueous medium. The reaction is zero order in oxidant and fractional order in reductant. The rate-determining step of the reaction is lead by the triiodide ion. The concentration of triiodide ion depends upon the concentration of the iodine in the reaction mixture. As a result, the concentration of iodine is limiting reactant for triiodide ion. The protonation of triiodide ion decelerates the reaction consequently as per our observations. The rate law of the reaction is proposed as follows.

$$\text{Rate} = [I^-]^{0.5} \left(k + \frac{k'}{[H^+]^{0.25}} \right)$$

REFERENCES

- [1] R. Khattak, PhD, University of Karachi, **2011**.
- [2] X. Wang, D. M. Stanbury *J. Phys. Chem. A*. **2004**, 108, 7637-7638.
- [3] X. Wang, D. M. Stanbury *Inorg. Chem.* **2008**, 47, 1224-1236.
- [4] X. Wang, D. M. Stanbury *Inorg. Chem.* **2006**, 45, 3415-3423.
- [5] N. Bhattarai, D. M. Stanbury *Inorganic Chemistry*. **2012**, 51, 13303-13311.
- [6] R. Khattak, M. S. Khan, R. Ullah, Zainab, Sony, M. Ali, W. Rahman, F. Hakeem, K. Ayaz, Z. Bibi *International Journal of Chemical Kinetics*. **2021**, 53, 16-26.
- [7] M. Kokkonen, P. Talebi, J. Zhou, S. Asgari, S. A. Soomro, F. Elsehrawy, J. Halme, S. Ahmad, A. Hagfeldt, S. G. Hashmi *Journal of Materials Chemistry A*. **2021**, 9, 10527-10545.
- [8] Y. Yang, L. Wu, X. Hao, Z. Tang, H. Lai, J. Zhang, W. Wang, L. Feng *RSC Advances*. **2019**, 9, 28561-28568.
- [9] G. Boschloo, A. Hagfeldt *Acc. Chem. Res.* **2009**, 42, 1819-1826.
- [10] M. Zhang, J. Bing, Y. Cho, Y. Li, J. Zheng, C. F. J. Lau, M. A. Green, S. Huang, A. W. Y. Ho-Baillie *Nano Energy*. **2019**, 63, 103853.
- [11] C. A. Bignozzi, R. Argazzi, R. Boaretto, E. Busatto, S. Carli, F. Ronconi, S. Caramori *Coord. Chem. Rev.* **2013**, 257, 1472-1492.
- [12] R. Khattak, M. S. Khan, S. Summer, R. Ullah, H. Afridi, Z. Rehman, S. Masood, H. Noreen, R. A. Qazi, B. Begum *International Journal of Chemical Kinetics*. **2021**, 53, 230-241.

MODELING OF THE LINSEED OIL EPOXIDATION: THE USE OF DIFFERENT EXPRESSIONS FOR THE REACTION RATE OF THE PERACETIC ACID FORMATION

O. Govedarica, M. Janković, S. Sinadinović-Fišer, J. Pavličević, V. Teofilović, N. Vukić, J. Blagojević

*University of Novi Sad, Faculty of Technology, Bul. cara Lazara 1, 21000 Novi Sad, Serbia.
(ogovedarica@uns.ac.rs)*

ABSTRACT

The published pseudohomogeneous model for the vegetable oil epoxidation with *in situ* formed peracetic acid in the presence of the ion exchange resin as a catalyst was modified considering, besides the heterogeneously catalyzed, previously neglected homogeneously catalyzed peracetic acid formation. Comparison of the original and two proposed models shows that introduced modification improves the modeling of the epoxidation process.

INTRODUCTION

In industry, vegetable oils are epoxidized with percarboxylic acid formed *in situ* from carboxylic acid and hydrogen peroxide [1]. The formation of commonly applied peracetic acid is carried out in the presence of an acidic catalyst. When ion exchange resin Amberlite IR120-H is the catalyst, the formation of peracid is catalyzed heterogeneously, by the active sites of the resin [1,2], as well as homogeneously, by hydronium ions originating from acetic acid dissociation [3]. The aim of the present work is to modify existing pseudohomogeneous model of the vegetable oil epoxidation with peracetic acid [2] as to better describe changes of epoxy group and residual vegetable oil's unsaturation amounts. The model was modified by taking into consideration also homogeneously catalyzed peracetic acid formation.

METHODS

The epoxidation of linseed oil with peracetic acid formed *in situ* from acetic acid and hydrogen peroxide in the presence of Amberlite IR120-H was carried out in a batch reactor as described in the literature [1]. The process was followed by determining the amount of residual unsaturation and the amount of epoxy group in the samples of epoxidized linseed oil. The experimental data of 96 epoxidation runs have been given previously [1].

RESULTS AND DISCUSSION

The epoxidation of vegetable oils involves peracetic acid (P) and water (W) formation from acetic acid (A) and hydrogen peroxide (H):



conversion of double bond in oil triglycerides (D) into epoxy group (E):



and several side reactions of epoxy group, among which is prominent the one with acetic acid yielding the hydroxy acetate (HA) [1,2]:



The reaction system of epoxidation process, conducted as the batch process, can be mathematically described with the pseudohomogenous model (Model 0) found in the literature [2]:

$$d[A]/dt = (d[H]/dt)_1 + k_2[P][D] - k_3[E][A]^n \quad (4)$$

$$d[P]/dt = -(d[H]/dt)_1 - k_2[P][D] \quad (5)$$

$$d[W]/dt = -(d[H]/dt)_1 \quad (6)$$

$$d[D]/dt = -k_2[P][D] \quad (7)$$

$$d[E]/dt = k_2[P][D] - k_3[E][A]^n \quad (8)$$

$$d[HA]/dt = k_3[E][A]^n \quad (9)$$

where square brackets denote amounts of compounds and functional groups as mole per 100 g oil. t (min) is the reaction time. k_2 (100 g oil/mol·min) and k_3 [(100 g oil) ^{n} /(mol ^{n} ·min)] are the rate coefficients for the reactions (2) and (3), respectively. n is the order of the reaction (3) with respect to acetic acid. Model 0 takes into consideration only the consumption of H by heterogeneously catalyzed reaction of P formation:

$$(d[H]/dt)_1 = (d[H]/dt)_{1,\text{het}} = -m \cdot C_s \cdot k_{1,\text{het}} ([A][H] - [P][W]/K_1) \quad (10)$$

where $k_{1,\text{het}}$ (100 g oil/mol²·min) is the rate coefficient for heterogeneously catalyzed reaction (1). m_c (g) and C_s (mol/g cat) are the mass of the catalyst and the amount of sulpho groups in the catalyst, respectively. K_1 is the chemical equilibrium constant for the reaction (1) [1].

In this study, Model 0 was modified by taking into consideration the change of H amount caused by homogeneously catalyzed P formation, $(d[H]/dt)_{1,\text{hom}}$. Therefore, the total consumption of H for P formation was considered as:

$$(d[H]/dt)_1 = (d[H]/dt)_{1,\text{het}} + (d[H]/dt)_{1,\text{hom}} \quad (11)$$

In Model 1, for the change of H amount caused by homogeneously catalyzed P formation, expression proposed by Zhao et al [3] was used:

$$\begin{aligned} (dC_H/dt)_{1,\text{hom}} = & -10^8 \sqrt{K_{D,A} C_A} \left[6.83 \cdot \exp(-57846.15/R \cdot T) C_A C_H \right. \\ & \left. - 6.73 \cdot \exp(-60407.78/R \cdot T) C_P C_W \right] \end{aligned} \quad (12)$$

where C_i (mol/L) is the concentration of component i in the aqueous phase. $K_{D,A}$ is the dissociation constant of acetic acid [4].

In Model 2, for $(dC_H/dt)_{1,\text{hom}}$ the modification of Eq. (12) was proposed:

$$(dC_H/dt)_{1,\text{hom}} = k_{1,\text{hom}} \sqrt{K_{D,A} C_A} [C_A C_H - (C_P C_W / K_1)] \quad (13)$$

where $k_{1,\text{hom}}$ ($\text{L}^{1.5}/\text{mol}^{1.5}\cdot\text{min}$) is the rate coefficient for homogeneously catalyzed reaction (1). Its temperature dependency was not taken from the expression (12); instead, it was determined by fitting the model to the experimental data.

In Eqs. (12) and (13) the concentrations of components in the aqueous phase were calculated as follows: $C_A = [A]/(K_A v^o + v^{\text{aq}})$, $C_H = [H]/v^{\text{aq}}$, $C_W = [W]/v^{\text{aq}}$ and $C_P = [P]/(K_P v^o + v^{\text{aq}})$. K_A and K_P are the partition coefficients for acetic acid and peracetic acid, respectively. v^o and v^{aq} ($\text{L}/100 \text{ g oil}$) are the volumes of the aqueous and oil phases, respectively. Since the change of molar volume of aqueous phase with time was neglected, the expression $(d[H]/dt)_{1,\text{hom}} = v^{\text{aq}}(dC_H/dt)_{1,\text{hom}}$ was used when fitting the proposed modified models to the experimental data. The expression for $k_{1,\text{hom}}$ in Eq. (13) was presented, like the other reaction rate coefficients in all studied models, with the modified form of Arrhenius equation:

$$k_i = \exp\left[k_{i,0} - k_{i,\text{Ea}}/R(1/T - 1/T_{\text{ref}})\right] \quad (14)$$

where $k_{i,0}$ and $k_{i,\text{Ea}}$ are the constants related to the frequency factor and the activation energy for reaction i , respectively. R [$8.3143 \text{ J}/(\text{mol}\cdot\text{K})$] is the universal gas constant. T (K) is the temperature of the epoxidation process, whereas T_{ref} is the reference temperature (accepted as 346 K). $k_{i,0}$ and $k_{i,\text{Ea}}$ for all reaction rate coefficients were obtained by fitting models to the experimental data obtained for the linseed oil epoxidation by applying the following objective function:

$$F = \sum_{i=1}^{\text{NE}} \left[\left([D]_i^{\text{calc}} - [D]_i^{\text{exp}} \right)^2 + \left([E]_i^{\text{calc}} - [E]_i^{\text{exp}} \right)^2 \right]$$

where NE is the number of the experimental points.

Parameter estimation results with related statistics for fitting the models with different expressions for the reaction rate of the P formation to the experimental data for the linseed oil epoxidation are given in Table 1. All reaction rate coefficients, calculated using values of $k_{i,0}$ and $k_{i,\text{Ea}}$ given in Table 1, have positive values and increase with rising in temperature. This confirms the validity of the proposed models as do the positive values of calculated amounts of all reactants and products.

Table 1. Comparison of the models with different P formation reaction rates

	Model 0		Model 1		Model 2	
	Ref. [2]					
	Order of the reaction (3) with respect to acetic acid, n					
	1	2	1	2	1	2
Error						
F	0.1492	0.1454	0.1436	0.1399	0.1173	0.1166
Constant of the reparameterized Arrhenius equation <i>i.e.</i> model parameter						
$(k_{1,\text{het}C_s})_0$	-11.26	-11.28	-11.44	-11.45	-12.43	-12.34
$(k_{1,\text{het}C_s})_{\text{Ea}}$	20364	20875	15851	16543	50631	52142
$k_{1,\text{hom},0}$	-	-	-	-	-2.292	-2.338
$k_{1,\text{hom},\text{Ea}}$	-	-	-	-	16389	13163
$k_{2,0}$	-2.348	-2.238	-2.122	-2.017	0.6635	0.6084
$k_{2,\text{Ea}}$	82546	88860	94291	100715	215070	219520
$k_{3,0}$	-6.608	-5.744	-6.603	-5.745	-6.599	-5.773

$k_{3,Ea}$	35397	40086	34993	40095	35966	42396
------------	-------	-------	-------	-------	-------	-------

According to the lower F , $n=2$ and both modified models better describe the epoxidation process than the published one, but in this work proposed Model 2 is better than Model 1.

CONCLUSION

Improving of the model for the vegetable oil epoxidation with *in situ* formed peracetic acid in the presence of the heterogeneous catalyst by adding the parameter for the homogeneously catalyzed reaction of the peracetic acid formation was the best when the reaction rate coefficient constants for the latter reaction were determined by fitting the model to the epoxidation data.

Acknowledgement

The Ministry of Education, Science and Technological Development of Serbia (Project #451-03-9/2021-14/200134).

REFERENCES

- [1] M. Janković, O. Govedarica, S. Sinadinović-Fišer, *Ind. Crop Prod.*, 2020, **143**, 111881
- [2] M. Janković, S. Sinadinović-Fišer, O. Govedarica, J. Pavličević, J. Budinski-Simendić, *Chem. Ind. Chem Eng. Q.*, 2017, **23**, 97-111.
- [3] X. Zhao, T. Zhang, Y. Zhou, D. Liu, *J. Mol. Catal. A Chem.*, 2007, **271**, 246–252.
- [4] K. Sue, F. Ouchi, K. Minami, K. Arai, *J. Chem. Eng. Data*, 2004, **49**, 1359–1363.

EFFICACY OF ZIRCONIA BASED NANOPOWDERS IN REMOVAL OF PHARMACEUTICALS USING SOLAR IRRADIATION

D. Šojić Merkulov¹, V. Despotović¹, S. Armaković¹, N. Finčur¹, M. Lazarević¹, M. Uzelac¹, N. D. Abazović², T. D. Savić², M. Čomor², and B. Abramović¹

¹University of Novi Sad Faculty of Sciences, Trg D. Obradovića 3, 21000 Novi Sad, Serbia
(biljana.abramovic@dh.uns.ac.rs).

²Vinča Institute of Nuclear Sciences, National Institute of RS, University of Belgrade, P. O. Box 522, 11001 Belgrade, Serbia.

ABSTRACT

Photocatalytic/adsorption efficacy of pure ZrO₂ and ZrO₂ powders with incorporated Si⁴⁺ ions was obtained following kinetics of degradation reaction and adsorption/desorption of some pharmaceuticals under solar irradiation. All selected pharmaceuticals have been found in surface waters in Serbia as organic micropollutants with ability to impact water quality, ecosystems and human health. Removal efficacy was followed using UFLC technique. All used zirconia based nanopowders can be used for removal of selected pharmaceutical.

INTRODUCTION

Photocatalytic processes based on the application of oxide semiconductors (such as TiO₂, ZnO, ZrO₂) are among the most popular methods for removing pollutants from the environment by overcoming the shortcomings of conventional technologies [1]. A great deal of efforts has been made to improve the photocatalytic efficiency of different nanopowders by modifying the surface of the photocatalyst or by doping with various dopants [2]. In recent years, pharmaceuticals have been discovered in the environment, especially in surface waters. Some drugs were detected in concentrations of the order of µg/L, which are concentrations that may have a physiological effect on aquatic organisms [3]. Their presence and persistence is a very current environmental problem.

Within this study, the photolytic/photocatalytic degradations of three model pharmaceuticals are presented: amitriptyline, tricyclic antidepressant used in the treatment of psychiatric disorders, 4-amino-6-chlorobenzene-1,3-disulfonamide, stable hydrolysis product of frequently used pharmaceutical hydrochlorothiazide, and ceftriaxone, hemi-synthetic broad-spectrum third generation cephalosporin antibiotic. ZrO₂ and ZrO₂ nanopowders doped with Si⁴⁺ ions were used as photocatalysts with solar irradiation.

METHODS

All chemicals used in the investigation were of reagent grade and were used without further purification. Amitriptyline hydrochloride (AMI, C₂₀H₂₃N x HCl, M_r=313.9, CAS No. 549-18-8, ≥ 98%), 4-amino-6-chlorobenzene-1,3-disulfonamide (ABSA, M_r=285.73, CAS No. 121-30-2, 98%), and ceftriaxone disodium salt hemi(heptahydrate) (CEF, C₁₈H₁₆N₈Na₂O₇S₃ x 3.5H₂O, M_r=661.6, CAS No 104376-79-6) were purchased from Sigma–Aldrich.

ZrO₂ and ZrO₂ nanopowders doped with Si⁴⁺ ions were used as photocatalysts with solar irradiation. Nanopowders were synthesized using hydrothermal method; precursors were zirconyl chloride (Sigma Aldrich, 98%) without/with tetraethoxysilane (TEOS, Alfa Aesar, 98%). Assignment referred to quantity of used Si⁴⁺ precursor: ZrO₂-1 obtained with 0.5 mL and ZrO₂-2 obtained with 5 mL TEOS, detailed characterization presented in [4]. Experiments were performed at natural pH of suspensions (for ZrO₂ it was 6-7, for doped samples 9-10) and pH of dissolved pharmaceuticals.

Removal experiments were performed as previously described [5]. Solar irradiation was carried out using a 50 W halogen lamp (Philips) with the intensity of 0.1 W/cm^2 in the visible region and $2.2 \times 10^{-4} \text{ W/cm}^2$ in the UV region. Experiments were performed using 20 mL of emerging pollutant aqueous solution, where their initial concentration in all experiments was 0.05 mM, while catalyst loading was 1.0 mg/mL.

To monitor the photodegradation of pharmaceuticals, high pressure liquid chromatography with a diode array detector (UFLC-DAD, Shimadzu Nexera, Tokyo, Japan) was used. Aliquots of the reaction mixture (0.5 mL) were taken before the start of irradiation and at specific time intervals during the irradiation (volume variation ca. 10%). All samples with photocatalyst were filtered through a Millipore (Millex-GV, MA, USA, $0.22 \mu\text{m}$) membrane filter in order to separate the catalyst particles. Prepared aliquots were analyzed on UFLC-DAD as described previously in ref. [6] for AMI, [7] for ABSA, and [8] for CEF.

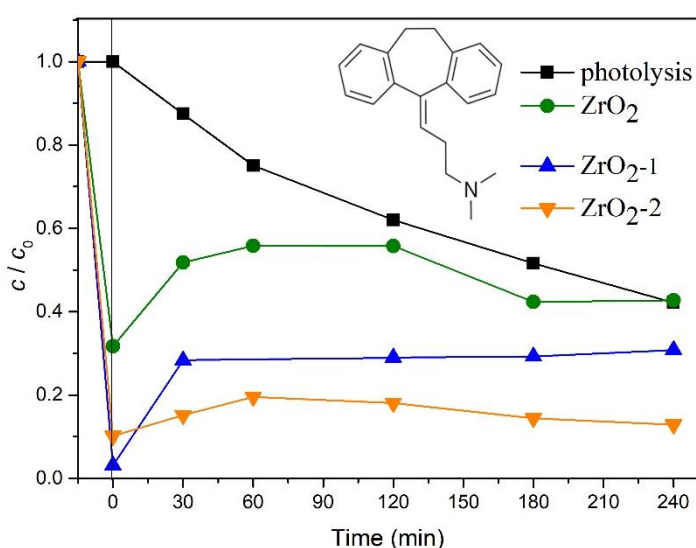


Figure 1. Kinetics of adsorption and photodegradation of AMI.

RESULTS AND DISCUSSION

Applied hydrothermal method for synthesis and Si^{4+} doping of zirconia powders produced crystalline powders: monoclinic in the case of pure ZrO_2 with particle diameter $\sim 25 \text{ nm}$ and doped samples with tetragonal crystalline phase and particles of 3-6 nm in diameter [4]. The presence of Si^{4+} ions in zirconia matrix induced decrease of effective band gap of doped samples: pure ZrO_2 had $E_g \sim 5 \text{ eV}$, $\text{ZrO}_2\text{-1}$ had $E_g \sim 4.7 \text{ eV}$ and $\text{ZrO}_2\text{-2}$ had $E_g \sim 3.8 \text{ eV}$. This method induced a great number of different intraband states in all nanopowders, defects like oxygen vacancies, resulting in the significant tailing of absorption in the visible part of the spectra. These findings were inspiration for to

photocatalytic experimental setup with simulated Solar light source.

Among chosen pharmaceuticals only amitriptyline (AMI) has significant photolysis, after 240 min 57.3% (the same as with ZrO_2 nanopowder) was degraded (Fig. 1). The photocatalytic removal efficiency of AMI (Fig. 1) increases with increasing content of incorporated Si^{4+} ions in zirconia based photocatalyst. After 240 min of irradiation in the systems with $\text{ZrO}_2\text{-2}$, ZrO_2 and $\text{ZrO}_2\text{-1}$, 87.1%, 57.3 and 69.2% of AMI was removed, respectively. In the presence of the catalyst, after sonication in the dark, significant adsorption of AMI occurs on the catalyst surface. During irradiation, desorption occurs [9,10], as well as degradation of AMI. The degree of adsorption/desorption of AMI depends on the type of the catalyst. Since a significant adsorption of AMI on the tested nanopowders was found (Fig. 1), the effect of pH on adsorption of AMI using $\text{ZrO}_2\text{-2}$ was investigated. The pH of AMI suspension using $\text{ZrO}_2\text{-2}$ without pH adjustment was 10, and in order to test the effect of pH, it was adjusted to 5. It was found that with decreasing pH, the adsorption of AMI is significantly lower (only 30.3%), which indicates the importance of pH value. This finding can be assigned to differences in surface charges of ZrO_2 , with IEP=6, negative at pH=10 and mainly positive at pH=5 and present forms of AMI in the solution, with $\text{p}K_a=9.4$ [11].

ZrO₂ and ZrO₂-2 nanopowders had slightly higher efficiency in the removal of ABSA, i.e. 9% of ABSA was removed after 120 min of irradiation, while only 5% when ZrO₂-1 was used (Fig. 2). When ABSA was removed in the presence of undoped ZrO₂, the initial pH was 7.7, but using ZrO₂-1 and ZrO₂-2 pH=9.8. Reduction of the initial pH to 7.4 upon removal of ABSA with ZrO₂-1 practically does not affect its efficacy, although the adsorption of ABSA on the nanopowder surface was slightly reduced. pK_a values for ABSA were estimated using DFT analysis, and were: 8.8, 10, 12.5 [12]. Bearing in mind that in all cases photocatalyst's surfaces were negatively charged obviously, adsorption was not crucial for photodegradation of ABSA.

In Fig. 3 results of adsorption, photolysis and photocatalysis of CEF are presented. Adsorption of CEF (pK₁=2.37, pK₂=3.03, pK₃=4.21 and pK₄=10.74 [13]; and natural pH of suspensions) is insignificant as in the case of ABSA. Namely, using ZrO₂, ZrO₂-1, and ZrO₂-2 percent of adsorption is only 7.2, 0.4, and 0.0, and the removal efficiency after 240 min of irradiation was 18.0%, 1.1%, and 7.9%, respectively. The most effective nanopowder was pure ZrO₂, either for adsorption and photodegradation.

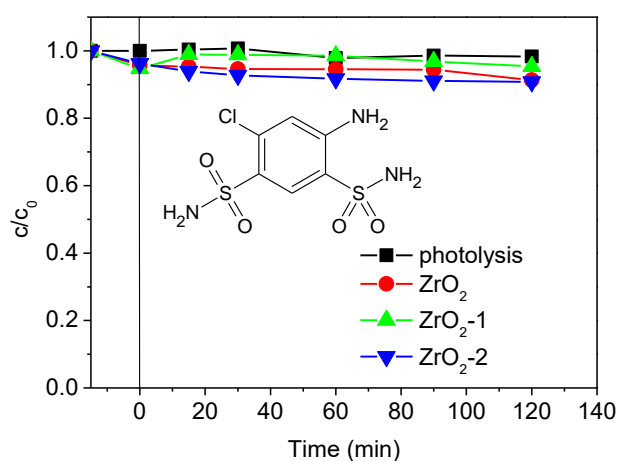


Figure 2. Kinetics of adsorption and photodegradation of ABSA.

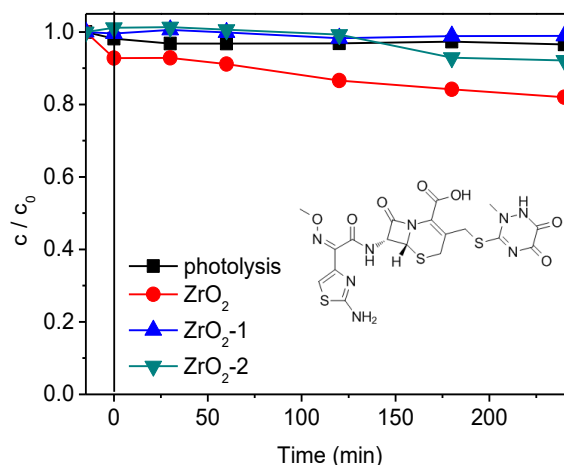


Figure 3. Kinetics of adsorption and photodegradation of CEF.

CONCLUSION

Presented results indicated that applied nanopowders are efficient adsorbents/photocatalysts for AMI, almost inactive for ABSA and slightly active for CEF. After 240 min of irradiation, 57.3% of AMI was removed by photolysis, while in the presence of ZrO₂-2 87.1% was removed. In the case of ABSA, the best photocatalysts were pure ZrO₂ and ZrO₂-2, although only 9% of starting concentration was removed. CEF was removed the most efficiently by pure ZrO₂, (7.2% after 240 min of process). pH of the suspensions was obviously important due to different ionic species present during irradiation and surface charges of the photocatalysts.

Acknowledgement

The authors acknowledge financial support of Ministry of Education, Science and Technological Development of the RS (Grant No. 451-03-9/2021-14/200125 and 451-03-9/2021-14/200017).

REFERENCES

- [1] H. Dong, G. Zeng, L. Tang, C. Fan, C. Zhang, X. He, Y. He, *Water Research*, 2015, 79, 128-146.
- [2] P. V. L. Reddy, K.-H. Kim, *Journal of Hazardous Materials*, 2015, 285, 325-335.
- [3] J. S. Murray, P. Politzer, *Wires Computational Molecular Science*, 2011, 1, 153-163.
- [4] M. V. Carević, N. D. Abazović, T. B. Novaković, V. B. Pavlović, M. I. Čomor, *Applied Catalysis B: Environmental*, 2016, 195, 112-120.
- [5] B. F. Abramović, V. N. Despotović, D. V. Šojić, D. Z. Orčić, J. J. Csanádi, D. D. Četojević-Simin, *Chemosphere*, 2013, 93, 166-171.
- [6] T. B. Ivetić, N. L. Finčur, B. F. Abramović, M. Dimitrievska, G. R. Štrbac, K. O. Čajko, B. B. Miljević, L. R. Đačanin, S. R. Lukić-Petrović, *Ceramics International*, 2016, 42, 3575-3583.
- [7] S. J. Armaković, S. Armaković, D. D. Četojević-Simin, F. Šibul, B. F. Abramović, *Environmental Pollution*, 2018, 233, 916-924.
- [8] B. F. Abramović, M. M. Uzelac, S. J. Armaković, U. Gašić, D. D. Četojević-Simin, S. Armaković, *Science of the Total Environment*, 2021, 768, No 144991.
- [9] J. Zhu, F. Chen, J. Zhang, H. Chen, M. Anpo, *Journal of Photochemistry and Photobiology A: Chemistry*, 2006, 180, 196-204.
- [10] D. V. Šojić, V. N. Despotović, N. D. Abazović, M. I. Čomor, B. F. Abramović, *Journal of Hazardous Materials*, 2010, 179, 49-56.
- [11] B. Kasprzyk-Hordern, R. M. Dinsdale, A. J. Guwy, *Analytical and Bioanalytical Chemistry*, 2008, 39, 1293-1308.
- [12] S. J. Armaković, Photocatalytic stability of selected active components of cardiovascular drugs: kinetics, mechanism and toxicity of the intermediates, PhD Thesis, Faculty of Sciences, Novi Sad, 2016.
- [13] S. Budavari, *The Merck Index*, 13th ed., Merck & Co. Inc., Rahway, NJ, USA, 2001, p. 335.

ZIRCONIA BASED PHOTOCATALYSTS IN DEGRADATION OF SELECTED HERBICIDES

M. Čomor¹, N. Abazović¹, T. Savić¹, D. Šojić Merkulov², V. Despotović², S. Armaković², N. Finčur², M. Lazarević², M. Uzelac², and B. Abramović²

¹*Vinča Institute of Nuclear Sciences, National Institute of RS, University of Belgrade, P.O. Box 522
11001 Belgrade, Serbia*

²*University of Novi Sad Faculty of Sciences, Trg D. Obradovića 3, 21000 Novi Sad, Serbia*

ABSTRACT

Hydrothermally synthesized zirconia nanopowders: pure and doped with Si⁴⁺ ions were spectroscopically characterized and used as photocatalysts for degradation of herbicides sulcotrione and fluroxypyr. Zirconia is wide band gap ceramic ($E_g \sim 5$ eV) however, synthesized nanopowders showed unexpected, modest absorbance in visible light range. That fact inspired photocatalytical degradation of herbicides with wide utilization, using solar irradiation (SI) in laboratory conditions. In the scope of this study, degradation of herbicides was only slightly achieved (irradiation time 2h).

INTRODUCTION

Zirconia (ZrO₂) is a member of transition metal oxides group of wide band gap materials. ZrO₂ is an important ceramic material widely used in variety of applications [1]. Due to its nature as n-type semiconductor, it has been considered as a photocatalyst in photocatalytical heterogeneous reactions. The values of the zirconia bandgap energy (E_g) is in the range between 3.25 and 5.1 eV, depending on the used preparation technique and the presence of dopants and defects, for the most usual value is $E_g = 5$ eV, conduction band potential would be -1.0 V and the valence band potential would be $+4.0$ V vs. NHE at pH 0, excellent values for variety of oxidation/reduction reactions in the solution. In the scope of this study, hydrothermal method for synthesis of zirconia nanopowders was chosen. In order to overcome necessity for UV irradiation, zirconia was doped with Si⁴⁺ ions. Literature already showed that Si⁴⁺ ions can introduce defects in zirconia matrix and change effective band gap. Simultaneously Si-doping process increase specific surface area of zirconia [2].

Both herbicides used as model molecules for photocatalytical degradation are widely used for control of grass and broad-leaf weeds in agriculture. Due to their solubility in water, they can be found in environment, especially in rivers and lakes. Sulcotrione belongs to class of triketone herbicides used for weed control in corn [3, 4]. Fluroxypyr is a selective post-emergent systemic herbicide widely used in agriculture. It was introduced in Europe for post-emergence control of annual and perennial broad-leaf weeds in small grains such as wheat, barley, oats and croplands [5].

METHODS

All chemicals were of reagent grade and used without further purification. Pesticides sulcotrione (CAS No. 99105-77-8, C₁₄H₁₃ClO₅S, $M_r = 328.8$, PESTANAL®, analytical standard, 99.9%) and fluroxypyr (CAS No. 99105-77-8, C₇H₅Cl₂FN₂O₃, $M_r = 255.03$, PESTANAL®, analytical standard, 99.9%) were purchased from Fluka.

Zirconia nanopowders were synthesized using hydrothermal method; precursors were zirconyl chloride (Sigma Aldrich, 98%) without/with tetraethoxysilane (TEOS Alfa Aesar, 98%). Assignment referred to quantity of used Si⁴⁺ precursor: ZrO₂-1 obtained with 0.5 mL and ZrO₂-2 obtained with 5 mL TEOS, detailed characterization presented in [1], as a part of this study, FTIR spectra (taken by using attenuated total reflection mode of a Nicolet 380 FTIR spectrometer) and UV/Vis absorption/reflectance spectra (obtained using an Evolution 600 spectrophotometer Thermo Scientific,

reflectance was converted to absorption using Kubelka-Munk method) are presented. Natural pH of suspensions was for ZrO₂ 6-7, for doped samples 9-10.

Removal experiments were performed as previously described [6]. Solar irradiation was carried out using a 50 W halogen lamp (Philips) with the intensity of 0.1 W/cm² in the visible region and 2.2×10^{-4} W/cm² in the UV region. Experiments were performed using 20 mL of emerging pollutant solution, where their initial concentration in all experiments was 0.05 mM, while catalyst loading was 1.0 mg/mL. Photodegradation was monitored at natural pH values of the suspensions without adjustment.

To monitor the photodegradation of pesticides, high pressure liquid chromatography with a diode array detector (UFLC-DAD, Shimadzu Nexera, Tokyo, Japan) was used. Aliquots of the reaction mixture (0.5 mL) were taken before the start of irradiation and at specific time intervals during the irradiation (volume variation ca. 10%). All samples with photocatalyst were filtered through a Millipore (Millex-GV, MA, USA, 0.22 μm) membrane filter in order to separate the catalyst particles. Prepared aliquots were analyzed on UFLC-DAD. For the sulcotrione and fluroxypyr UV/Vis DAD detector was set at 231 and 212 nm (wavelength of maximum absorption), respectively. The mobile phase with flow rate of 1.0 mL/min was a mixture of ACN and water in ratio 50:50 (v/v).

RESULTS AND DISCUSSION

Hydrothermally synthesized zirconia nanopowders: pure and doped with Si⁴⁺ ions [1], were successfully synthesized. One of the easiest ways to prove presence of Si⁴⁺ ions in zirconia matrix is FTIR spectroscopy. A characteristic band at 950 cm⁻¹ (Fig. 1a) can be seen; this band assigned to Zr-O-Si [2]. It is present only in doped samples with intensity that follows concentration of Si⁴⁺ ions in the samples. Also, UV/Vis spectra (Fig. 1b) show significant differences in reflection/absorption due to presence of dopant and, most probably, defects induced through synthesis. Even for pure ZrO₂ defect-related absorption can be seen at ~ 400 nm, in the visible light region. Doped samples showed higher absorption intensity at 400 nm and, especially ZrO₂-2, broad band from 400 nm to NIR region. This effect, absorption of visible light, by zirconia samples was inspiration for probing photocatalysis degradation reactions by solar irradiation in laboratory conditions.

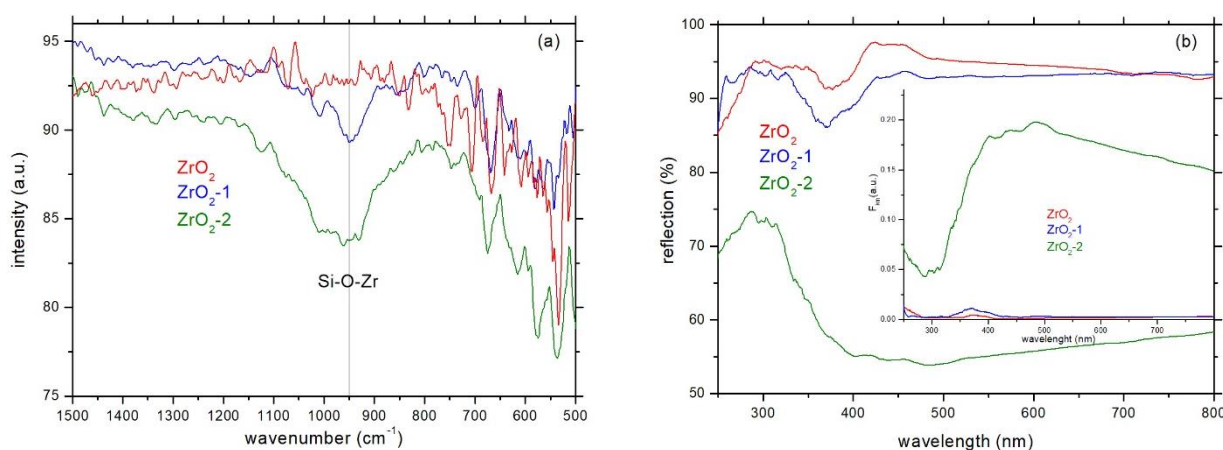


Figure 1. FTIR (a) and UV/Vis (b) reflection/absorption (inset) spectra of pure and Si⁴⁺ doped zirconia nanopowders.

In order to test the stability of sulcotrione, a direct photolysis experiment was performed (Fig. 2), where no degradation was observed after 120 min of irradiation, from which it can be concluded that the compound is stable. After that, the efficiency of photocatalytic degradation of sulcotrione using of ZrO₂, ZrO₂-1 and ZrO₂-2 nanopowders and solar irradiation was examined (Fig. 2a). As can be

seen in the presence of these nanopowders, almost no degradation of sulcotrione occurs during 120 min of irradiation. Only about 4% of sulcotrione was degraded by using doped zirconia samples, pure ZrO_2 showed no photocatalytic efficacy.

The photocatalytic activity of pure ZrO_2 , as well as ZrO_2 nanopowders doped with different content of Si^{4+} ions (ZrO_2 -1 and ZrO_2 -2) was investigated in the photodegradation of fluroxypyr using solar irradiation. The obtained results were compared with the results of direct photolysis (Fig. 2b). On the basis of the obtained results for the efficiency of photocatalytic degradation of fluroxypyr using solar irradiation, it can be concluded that the synthesized nanopowders slightly accelerate the degradation of fluroxypyr compared to the process of direct photolysis.

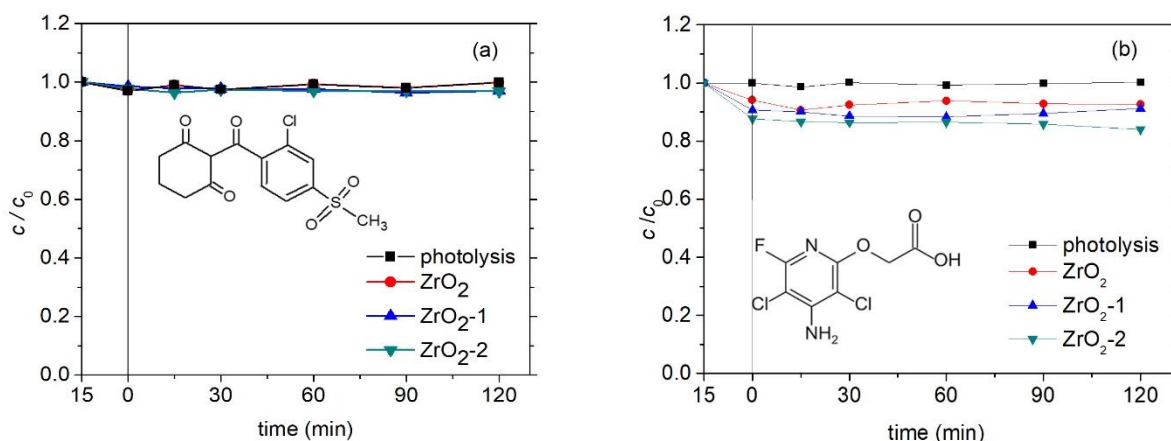


Figure 2. Adsorption and kinetics of photolysis and photocatalytical degradation of sulcotrione (a) and fluroxypyre (b).

Based on the obtained results, it was found that after 120 min irradiation in the presence of ZrO_2 and ZrO_2 -1, respectively about 91% of fluroxypyr is still present in solution. ZrO_2 -2 proved to be somewhat more efficient, with 17% of fluroxypyr being removed from solution after 120 min of irradiation. During equilibration of reaction dispersions, before irradiation, fluroxypyr was adsorbed at the surface of zirconia nanopowders; about 6% on ZrO_2 , 9% on ZrO_2 -1 and 12% on ZrO_2 -2. Obviously more experimental optimization is needed for better application of zirconia nanopowders for removal/photodegradation of fluroxypyr.

CONCLUSION

Hydrothermal method for synthesis of pure and Si^{4+} doped zirconia nanopowders proved to be efficient. FTIR spectroscopy reveals presence of Si-O-Zr bonds in the doped samples. Also, improvement of UV/Vis absorption in visible part of the spectra for all samples can be ascribed to formation of defects and/or presence of dopant ions in the samples. Usage of Solar light for irradiation in photodegradation reactions of sulcotrione and fluroxypyr showed modest results in the scope of presented reaction conditions. These are not ideal photocatalysts for degradation of sulcotrione. Adsorption and photodegradation of fluroxypyr was achieved, best photocatalyst was ZrO_2 -2 with 17% of degradation after 2 h of irradiation which was expected due to its UV/Vis absorption spectrum.

Acknowledgement

The authors acknowledge financial support of Ministry of Education, Science and Technological Development of the RS (Grant No. 451-03-9/2021-14/200125 and 451-03-9/2021-14/ 200017).

REFERENCES

- [1] M. V. Carević, N. D. Abazović, T. B. Novaković, V. B. Pavlović, M. I. Čomor, *Applied Catalysis B: Environmental*, 2016, 195, 112-120.
- [2] S. F. Yin, B. Q. Xu, *ChemPhysChem*, 2003, 277-281.
- [3] H. Chaabane, E. Vulliet, F. Joux, F. Lantoine, P. Conan, J.-F. Cooper, C.-M. Coste, *Water Research*, 2007, 41, 1781-1789.
- [4] <https://sitem.herts.ac.uk/aeru/ppdb/en/Reports/600.htm>
- [5] J. Hu, T. Wang, J. Long, Y. Chen, *International Journal Environmental Analytical Chemistry*, 2014, 94, 211-222.
- [6] B. F. Abramović; V. N. Despotović, D. V. Šojić, D. Z. Orčić, J. J. Csanádi, D. D. Četojević-Simin, *Chemosphere*, 2013, 93, 166-171.

COBALT SUPPORTED CHITOSAN-DERIVED CARBON-SMECTITE COMPOSITE FOR CATALYTIC ACTIVATION OF PEROXYMONOSULFATE IN WATER

G. Stevanović¹, N. Jović-Jovičić¹, J. Krstić¹, A. Milutinović-Nikolić¹, B. Milovanović¹, K. Radulović², M. Ajduković¹

¹*University of Belgrade, Institute of Chemistry, Technology and Metallurgy, National Institute, Center for Catalysis and Chemical Engineering, Njegoševa 12, 11000 Belgrade, Serbia. (gordana.stevanovic@ihtm.bg.ac.rs)*

²*University of Belgrade, Institute of Chemistry, Technology and Metallurgy, National Institute, Department of Microelectronic Technologies, Njegoševa 12, 11000 Belgrade, Serbia.*

ABSTRACT

In this work cobalt supported on chitosan-derived carbon-smectite composite catalyst was synthesized using impregnation-carbonization method (Co/cCh-S). The carbonization temperature was 400 °C. The obtained catalyst was tested as peroxymonosulfate (in form of Oxone[®]) activator for the food dye tartrazine degradation. The textural properties were obtained using low temperature N₂ physisorption. The calculated textural parameters of the Co/cCh-S catalyst were compared with properties of the carbonized chitosane-smectite composite (cCh-S). The catalytic tests confirmed that neither Oxone[®] without catalyst nor cCh-S were unable to activate Oxone[®]. The catalyst Co/cCh-S was found to be effective for tartrazine degradation in presence of Oxone[®].

INTRODUCTION

Recently, sulfate radical-based advanced oxidation processes with peroxymonosulfate (PMS) as the oxidant have attracted attention as solution for the removal of persistent organics in air, water, and soil [1]. Due to the chemical stability of PMS in mild conditions, various methods for its activation were employed: heat, UV irradiation, ultra-sound, chemicals, transition metal etc. [2] Among transition metals cobalt was found to be the most efficient [3]. Cobalt was applied supported on different materials such as the molecular sieve, metal oxides, and carbonaceous materials [4]. The two main roles of the support are to achieve the well-dispersed cobalt active sites and to suppress the leaching of cobalt ions via the metal-support interaction [5, 6]. The advantage of carbonaceous supports is related to variety of active sites, adsorptive properties toward organic contaminants and synergistic effect with cobalt. These properties facilitate the electron transfer and favorize their application as supports [5]. Smectite (S) that belongs to the layered silicate clay minerals, has been widely used in environmental remediation as adsorbent or supporting material in catalytic application [7, 8]. Various organic compounds can be adsorbed on S due to its layered structure, expandable interlayer, and chemically inert siloxane surface [9]. Hence, transition metal ion-organomodified S would be a suitable precursor to fabricate metal carbon-smectite composites via carbonization process.

In this work cobalt was supported on chitosan-derived carbon-smectite composite and used for activation of peroxymonosulfate. Activated PMS (commercially available as Oxone[®]) was applied in catalytic oxidation of tartrazine dye used as model of the water pollutant.

EXPERIMENTAL

The chitosan-derived carbon-smectite composite was obtained according to the previously described procedure [10]. Smectite rich bentonite clay from Bogovina, Serbia was used in this work. After milling, sieving and hydroseparation, the fractions containing particles up to 2 μm in diameter were separated and denoted as S. Thus, chitosan solution was prepared by the addition of 12.8 g of chitosan into 0.500 dm^3 of 1% (v/v) acetic acid and stirred until complete dissolution. After the pH was adjusted to 4.6–5, the chitosan solution was slowly dropped into a 2% clay dispersion (5.0 g clay in 0.250 dm^3 bidistilled water) and stirred at room temperature for 48 h. The obtained sample was centrifuged, air-dried at 50 $^\circ\text{C}$ and grounded to powder and denoted as Ch-S.

Incipient wetness impregnation method was used for Co^{2+} impregnation [11]. The impregnation was performed by slow addition of $\text{Co}(\text{NO}_3)_2$ solution to Ch-S powder resulting in 0.03 g Co^{2+} per 1 g of Ch-S. After drying at 85 $^\circ\text{C}$ for 2 h, sample was placed into tube furnace and heated at 400 $^\circ\text{C}$. The carbonization was performed in N_2 atmosphere with gas flow of 0.075 $\text{dm}^3 \text{min}^{-1}$ and heating rate of 5 $^\circ\text{C} \text{min}^{-1}$. After reaching the pre-set temperature of 400 $^\circ\text{C}$ the sample was kept for 1 h at this temperature and then rested to cool down to room temperature. The sample was denoted as Co/cCh-S. Sample without cobalt was treated under the same carbonization conditions and denoted as cCh-S.

Nitrogen adsorption–desorption isotherms of samples were determined using a Sorptomatic 1990 Thermo Finnigan at -196°C . The samples were outgassed at 80 $^\circ\text{C}$ for 2 h and 16 h at 200 $^\circ\text{C}$. Obtained isotherms were analyzed applying various models included in the ADP Ver. 5.1. software. Total pore volume, $V_{0.98}$, was calculated according to the Gurvitsch method. Specific surface area, S_{BET} , was calculated according to the Brunauer, Emmett and Teller method. Mesopore volume was calculated according to the Barrett, Joyner and Halenda method. Dubinin–Radushkevich method was used for the calculation of micropore volume, V_{mic} [12, 13].

Catalytic tests were performed by stirring 10 mg of catalyst (m_{kat} in aqueous tartrazine solution ($C_0=50.0 \text{ mg dm}^{-3}$, $V_0=0.200 \text{ dm}^3$) in the presence of 0.130 mmol Oxone[®]. The tests were conducted in a 0.500 dm^3 Pyrex reactor equipped with a mechanical stirrer and thermostatted using a Julabo[®] circulating bath at temperature of 30 $^\circ\text{C}$. The catalyst was added to the reaction mixture 5 min after the Oxone[®] was introduced into the tartrazine solution. This moment was taken as the initial (0 min) moment of the reaction. With the respect to this moment, aliquots were taken at predetermined periods of time. Supernatant solutions were separated from the solid phase by centrifugation at 17000 rpm for 3 min and analyzed using UV–Vis spectrophotometry (Thermo Scientific, Evolution 220 UV–Visible Spectrophotometer). The peak at 426 nm indicating decolorization of the reaction solution was monitored and analyzed.

RESULTS AND DISCUSSION

Nitrogen adsorption-desorption isotherms of the investigated samples are presented in Figure. 1, while textural properties calculated from these isotherms are presented in Table 1.

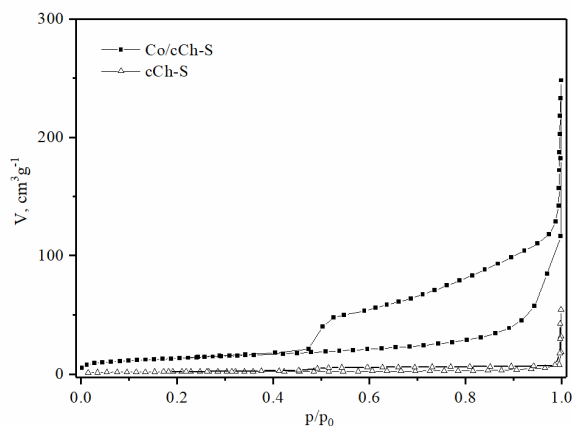


Figure 1. The N₂ low temperature adsorption-desorption isotherms of investigated samples.

appears. Such type of the adsorption-desorption isotherms indicates multilayer nitrogen adsorption and capillary condensation.

Table 1. Selected textural properties of investigated samples.

Sample	S_{BET} [m ² g ⁻¹]	$V_{0,98}$ [cm ³ g ⁻¹]	$V_{\text{mes}}^{\text{BJH}}$ [cm ³ g ⁻¹]	$V_{\text{mic}}^{\text{DR}}$ [cm ³ g ⁻¹]
cCh-S	7.4	0.010	0.012	0.003
Co/cCh-S	47.9	0.148	0.214	0.019

Where: S_{BET} – specific surface area; $V_{0,98}$ – total pore volume; V_{mes} -mesopore volume (Barrett, Joyner and Halenda) and V_{mic} - micropore volume (Dubinin-Radushkevich) and BJH

The obtained values of textural parameters for Co/cCh-S in comparison to cCh-S increased between 6 times (for micropore volume) and almost 15 times for total pore volume. It can be assumed that presence of cobalt nitrate during carbonization had significant impact on textural properties.

The comparison of the effect of pure Oxone®, and Oxone® activated with cCh-S and Co/cC-S on tartrazine decolorization versus time is presented in Figure 2.

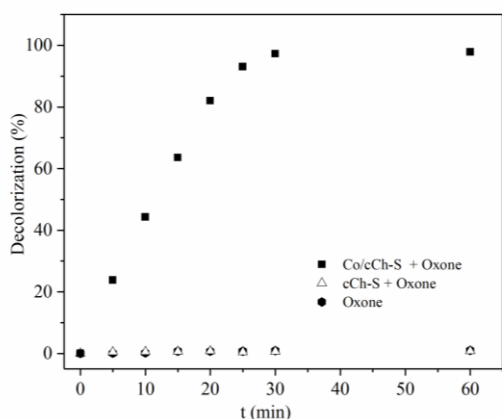


Figure 2. Decolorization of tartrazine solution monitored at 426 nm ($m_{\text{cat}}=10.0$ mg, $V_0=0.200$ dm³, $C_0=50.0$ mg dm⁻³; 40 mg of Oxone®; $T=30$ °C).

There is a significant difference in appearance of N₂ low temperature isotherms between carbonized material cCh-S and cobalt containing Co/cCh-S. The result obtained for cCh-S rivaled almost nonporous sample. On the other hand, the existence of cobalt species during the thermal carbonization process has obviously changed the texture of the Co/cCh-S. This sample has the Type II isotherm according to the IUPAC classification [14]. This type of isotherm is characteristic for materials that contain aggregated planar particles forming slit shape pores. At higher equilibrium pressures $p/p_0 < 0.4$ hysteresis loop of the H3 type

appears. Such type of the adsorption-desorption isotherms indicates multilayer nitrogen adsorption and capillary condensation. For cobalt containing catalyst, already after 30 min of the reaction, decolorization was almost complete. On the other hand, under the investigated conditions in referent Oxone®/tartrazine and cCh-S/Oxone®/tartrazine systems the decolorization of dye was less than 1 % even after 60 min of reaction. Unambiguously, the presence of cobalt as catalytically active species is necessary for catalytic activation of Oxone®, and consequently dye degradation. Also, it should be kept in mind that more developed surface of Co/cCh-S enhances catalytic activity.

CONCLUSION

In this work cobalt supported on chitosan-derived carbon-smectite composite catalyst (Co/cCh-S) was synthesized using impregnation-carbonization method. The carbonization temperature was 400 °C. The obtained catalyst was tested as peroxymonosulfate (in form of Oxone[®]) activator for the degradation of food dye tartrazine. The existence of cobalt species during the thermal carbonization process enhanced the textural properties for the Co/cCh-S in comparison to cCh-S. The catalytic tests confirmed that neither Oxone[®] without catalyst nor cCh-S were unable to activate Oxone[®]. The catalyst Co/cCh-S was found to be effective for tartrazine degradation in presence of Oxone[®].

Acknowledgement

This work was supported by the Ministry of Education, Science and Technological Development of the Republic of Serbia (Contract 451-03-9/2021-14/200026)

REFERENCES

- [1] W.-D. Oh, Z. Dong, T.-T. Lima, *Applied Catalysis B: Environmental*, 2016, 194, 169–201.
- [2] F. Ghanbari, M. Moradi, *Chemical Engineering Journal*, 2017, 310, 41–62.
- [3] G.P. Anipsitakis, D.D. Dionysiou, *Environmental Science & Technology*, 2003, 37, 4790-4797.
- [4] J. Hou, X. He, S. Zhang, J. Yu, M. Feng, X. Li, *Science of The Total Environment*, 2021, 770, 145311.
- [5] Y. Wang, Z. Ao, H. Sun, X. Duan, S. Wang. *Applied Catalysis. B Environmental*, 2016, 198, 295-302.
- [6] P.-f. Xiao, L. An, D-d. Wu, *New Carbon Materials*, 2020, 35 (6), 667-683.
- [7] S. Marinović, T. Mudrinić, N. Jović-Jovičić, M. Ajduković, Al. Milutinović–Nikolić, P. Banković, Z. Mojović, *Journal of Electroanalytical Chemistry*, 2019, 848 113280.
- [8] N. Jović-Jovičić, Z. Mojović, M. Mojović, P. Banković, M. Ajduković, A. Milutinović-Nikolić, D. Jovanović, *Applied Surface Science*, 2017, 400, 347-354.
- [9]. Q. Chen, R. Zhu, W. Deng, Y. Xu, J. Zhu, Q. Tao, H. He, *Applied Clay Science*, 2014, 100, 112-117.
- [10] N. Jović-Jovičić, Z. Mojović, M. Darder, P. Aranda, E. Ruiz-Hitzky, P. Banković, D. Jovanović, A. Milutinović-Nikolić, *Applied Clay Science*, 2016, 124-125, 62-68.
- [11] M. Marković, S. Marinović, T. Mudrinić, M. Ajduković, N. Jović-Jovičić, Z. Mojović, J. Orlić, A. Milutinović-Nikolić, P. Banković, *Applied clay science* 2019, 182, 105276.
- [12] S.H. Gregg, K.S. Sing, *Adsorption, Surface Area and Porosity*, Academic Press, New York (1967)
- [13] F. Rouquerol, J. Rouquerol, K. Sing, *Adsorption by Powders and Porous Slides*, Academic Press, London (1999)
- [14] P. Cañizares, J.L. Valverde, M.R. Sun Kou, C.B. Molina, *Microporous and Mesoporous Materials*, 1999, 29, 267-281.

HYDROGEN PRODUCTION FROM GLYCEROL PHOTO-REFORMING OVER Pt/N-DOPED TITANATE PHOTOCATALYSTS

H. Šalipur, D. Lončarević and J. Dostanić

*University of Belgrade, Institute of Chemistry, Technology and Metallurgy,
Njegoševa 12, 11000 Belgrade, Serbia. (hristina@ihm.bg.ac.rs)*

ABSTRACT

Conversion of sunlight energy via photocatalytic water splitting and photo-reforming of renewable biomass organic derivatives has been increasingly utilized for hydrogen production. Photocatalytic processes have been used due to their sustainability, environmental-safety, and effectiveness. Pt/N-doped titanate photocatalysts were synthesized via alkaline hydrothermal treatment, followed by $\text{Na}^+/\text{NH}_4^+$ ion exchange, impregnation and gaseous reduction. The activities of the photocatalysts were tested for hydrogen production via photocatalytic reforming of glycerol under simulated solar irradiation. The improved hydrogen production from photo-reforming of glycerol was attributed to the anatase active phase and surface area which enhanced the adsorption of glycerol onto the surface of catalysts; metallic Pt suppress the electron/hole recombination by trapping the photo-generated electrons; reduced band gap by incorporation of N into lattice of TiO_2 .

INTRODUCTION

Overcoming fossil fuel dependence in energy sector is great challenge in a last decade, regardless of increased use of alternative energy sources such as solar, wind, hydropower and geothermal energy. Hydrogen presented as efficient energy vector in utilization of sunlight, due to its high energy density and abundance from renewable sources. One of proposed strategies for efficient, environment friendly and reliable hydrogen production is photocatalytical water splitting. [1]

Among semiconductors fulfilling requirements for hydrogen production (valence band more positive than the $\text{O}_2/\text{H}_2\text{O}$ redox couple, conduction band more negative than $\text{H}_2\text{O}/\text{H}_2$ redox couple and resistance to photocorrosion) TiO_2 have been extensively studied in relation to H_2 production from water or biomass derivatives. [2] However, bare TiO_2 showed solar to hydrogen efficiencies under 5% which is limiting the industrial implementation of process. Different strategies are applied for improvement of efficiency for solar-light responsive photocatalysts.

Surface modification of TiO_2 with high work function metal cocatalyst (e.g., Pd, Au, Pt) suppress electron-hole pair recombination by forming Schottky junctions and accepting electrons from conduction band of TiO_2 to reduce hydrogen ions to molecular hydrogen. Doping of non-metals such as nitrogen extend absorption in visible light region of TiO_2 materials and allow improved separation of photo generated charge carriers. Sacrificial hole scavengers are commonly used for improvement of hydrogen production by directly reacting with positive holes, or intermediate $\cdot\text{OH}$ radicals, thus reducing recombination of hole-electron pairs, while scavengers undergo rapid and irreversible oxidation. Different factors influence hydrogen photocatalytic production from alcohols: a) titania phase composition and morphology, b) the choice of metal, c) alcohol oxidation potential, d) presence of hydrogen atoms in alpha positions with respect to hydroxyl group, e) byproducts generated in reaction. [3], [4]

The predominant byproduct of biodiesel production yields glycerol, which has led to waste disposal issues. Photo-reforming of glycerol in hydrogen production processes is one of proposed possibilities for developing sustainable and economically viable biodiesel production.

The aim of the study was to evaluate the efficiency of Pt/N-doped titanate photocatalysts for H_2 production from glycerol–water mixtures as well determining optimized concentration of glycerol at

ambient conditions which may provide an efficient and low-cost method for the production of renewable hydrogen.

METHODS

Titanate nanotubes were synthesized by a hydrothermal method, as previously reported by Kasuga et al. In this work, 4 g of the P25 TiO₂ were mixed with 250 mL of 10 M NaOH solution in a Teflon-lined autoclave at 150 °C for 24 h. Sodium titanate was vacuum filtered, and precipitate was redispersed 4 times in 2 M NH₄NO₃ solution for 24 h, to ensure complete ion-exchange reactions. Titanate photocatalyst loaded with Pt were synthesized by impregnation method using H₂PtCl₆ aqueous solution. Final catalysts were obtained by reduction in H₂ flow (8.5 mL/min) at 500 °C for 60 min (temperature rate 5°C/min). The photocatalytic activity of the prepared catalysts was tested towards the hydrogen production via photocatalytic water splitting/alcohol reforming process under simulated solar light. The photocatalytic tests were performed at 25 °C in a photocatalytic reactor equipped with standard reaction vessel, quartz immersion well and 100 W mercury-vapor lamp. Prior to each test reaction mixture consisting of 125 mg of photocatalyst, different concentration of aqueous glycerol solution was placed in a reaction vessel and purged for 45 min with Ar flow to remove oxygen from the suspension. The concentration of hydrogen in effluent gas was analyzed with a constant time interval sampling by gas chromatograph.

RESULTS AND DISCUSSION

The photocatalytic activity of synthesized photocatalysts were evaluated under simulated solar light in glycerol-water mixtures at ranging alcohol concentration from 0.2 mol/L to 1.6 mol/L. Glycerol, byproduct of trans-esterification of oils in biodiesel production, was selected as renewable sacrificial agent, due to removing rapidly and irreversibly photogenerated holes, or oxidants such as ·OH radicals.

Effect of glycerol concentration on hydrogen production activity over 0.5 wt% Pt/N-doped titanate catalysts is shown in Fig. 1. Addition of small amount of glycerol (0.2 mol/L) shows a very good improvement in hydrogen production activity. With increasing glycerol concentration up to 0.8 mol/L, an increase in the hydrogen production is observed with maximal rate of 15 mmol/gh. With further increase of glycerol concentration (1.6 mol/L), the hydrogen production activity is decreasing.

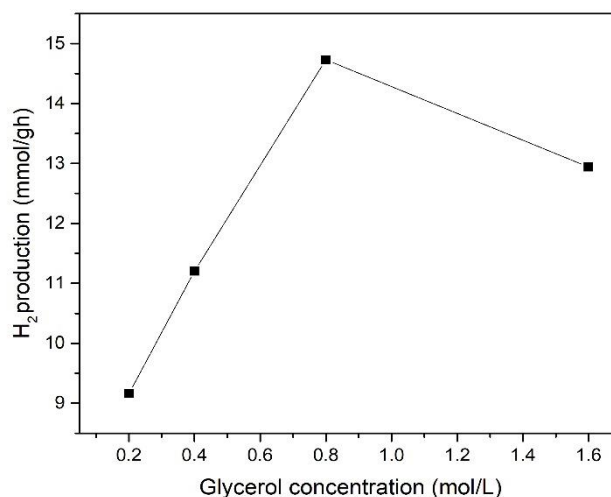


Figure 1. Effect of glycerol concentration on hydrogen production activity over 0.5 wt% Pt/N-doped titanate photocatalysts.

XRD pattern of N-doped titanate photocatalyst (presented in Fig. 2) showed anatase phase as main crystallite phase which attributed to improved photocatalytic activity.

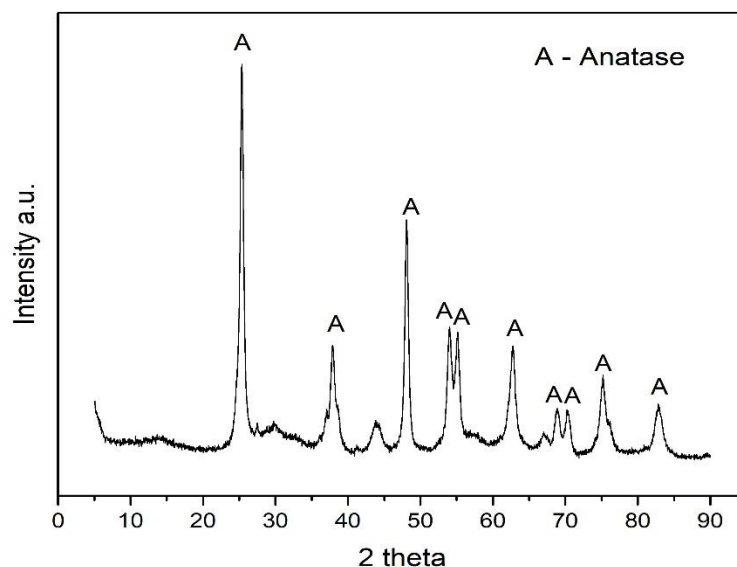


Figure 2. XRD pattern of N-doped titanate photocatalyst.

Parameters that could influence the optimum alcohol concentration for the glycerol-water mixture are viscosity and generated intermediates. At higher concentrations of glycerol solution become viscous which has effect on transport of reactants and products to and from the photocatalyst surface.

During glycerol photo-reforming a large number of intermediates can be formed such as acetic acid, acetaldehyde, glyceraldehyde, acetol, carbon dioxide, carbon monoxide, methanol, ethanol, glycolaldehyde, acetone and acrolein which already have been reported in the literature. Proposed mechanism involves the oxidation of glycerol to glycolaldehyde and formic acid and the secondary oxidation of glycolaldehyde to formic acid and formaldehyde followed by the simple photocatalytic oxidation of formic acid and formaldehyde to CO_2 . [5]

The photocatalyst surface is progressively covered by strongly adsorbed reaction intermediates and molecular fragments that restrict to some extent adsorption of compounds from the liquid phase, which could explain drop in hydrogen production rate.

Presence of metallic Pt is crucial in overcoming high H_2 overpotential, while N doping enabled improved sunlight harvesting, showed in DRS results where bandgap of N-doped titanate photocatalyst is red-shifted to 2.6 eV compared to TiO_2 .

CONCLUSION

In this work Pt/N-doped titanate photocatalysts were successfully synthesized and their photocatalytic activity was accessed towards hydrogen production under simulated solar light. The results showed that use of glycerol as biodiesel waste product enhanced photocatalytic activity compared to H_2 production from pure water. Parameters influencing the optimum alcohol concentration for the glycerol-water mixture were solution viscosity and great number of photogenerated intermediates that restrict to some extent adsorption on catalysts surface. Metallic Pt were crucial in suppressing electron/hole recombination.

Acknowledgement

This work was supported by the Ministry of Education, Science and Technological Development of the Republic of Serbia (Grants no. 451-03-9/2021-14/200026). Also, the article is based upon work from COST Action [Grant number: 18234], supported by COST (European Cooperation in Science and Technology) as well as work from Scientific bilateral cooperation between Republic of Serbia and Slovenia (Title of project: Adding value to biodiesel production – intensified conversion of glycerol to hydrogen and value-added bio-additives).

REFERENCES

- [1] I. Dincer, *Int. J. Hydrogen Energy*. 37 (2012) 1954–1971.
- [2] Z.H.N. Al-Azri, W.T. Chen, A. Chan, V. Jovic, T. Ina, H. Idriss, G.I.N. Waterhouse, *J. Catal.* 329 (2015) 355–367.
- [3] N. Denisov, J.E. Yoo, P. Schmuki, *Electrochim. Acta*. 319 (2019) 61–71.
- [4] F.J. López-Tenllado, J. Hidalgo-Carrillo, V. Montes-Jiménez, E. Sánchez-López, F.J. Urbano, A. Marinas, *Catal. Today*. 328 (2019) 2–7.
- [5] P. Panagiotopoulou, E.E. Karamerou, D.I. Kondarides, *Catal. Today*. 209 (2013) 91–98.

PHOTODEGRADATION OF DYES USING G-C₃N₄/TiO₂-BASED NANOCOMPOSITE

K. Milošević, D. Lončarević, J. Dostanić

*University of Belgrade, Institute of Chemistry, Technology and Metallurgy,
Department of Catalysis and Chemical Engineering
Njegoševa 12, 11000 Belgrade, Serbia. (ksenija.milosevic@ihtm.bg.ac.rs)*

ABSTRACT

Titanium dioxide is one of the most studied photocatalysts, using only the UV part of the light spectrum. There are various methods for improving the photocatalytic activity of TiO₂, such as activating TiO₂ in the visible part of the light spectrum. Titanium and carbon nitride-based hybrid photocatalyst was successfully synthesized by hydrothermal method followed by thermal treatment of a physical mixture of melamine and titania nanowires. The prepared nanocomposite was used to remove model pollutants - Methylene Blue (MB) and Acid Orange 10 (AO10) from its water solutions. Besides investigating the influences of cationic and anionic dyes on adsorption and photodegradation using solar light spectrum, varying the concentration of MB was examined under the visible light spectrum.

INTRODUCTION

In the present circumstances, various organic substances such as dyes, which are toxic, can be found in wastewater. Photocatalysts are very suitable for removing these pollutants and environmental protection because a naturally available energy source is sunlight. [1] When the photons start to act, the electrons from the photocatalyst's surface become excited in the valence band, so if the energy of the photon is higher than the bandgap, the electrons move into the conduction band, and a positive hole remains in the former electron's place. The excited electrons, reacting with oxygen, produce superoxide radicals or hydroperoxide radicals.[2] At the same time, oxidation of water using positive holes in the valence band occurs, which generates hydroxyl radicals and hydrogen ions. [3] These radicals interact with the pollutants in water.

Photocatalysts can also remove pollutants by the adsorption process. The removal of pollutants using sorption is a cheap, eco-friendly, and suitable method because of its simplicity and enablement to remove substances that can affect water ecosystems [4].

Titanates are considered promising photocatalysts; therefore, they have been highly researched. Titanium dioxide is safe, easy to prepare, cost-effective, non-toxic, and very stable metal oxide [4]. It is also one of the best photocatalysts because its redox potentials of conduction and valence band favor hydroxyl radical generation. TiO₂ is found to be a good material for immobilization and manipulation, which does not affect its photocatalytic properties [2,3,5,6].

The researchers focused on doping titanium dioxide with metal and non-metal components to reduce hole/electron recombination and extend the photoresponse of the catalyst to the visible light region. Hence, the influence of cocatalysts whose presence would increase the spectrum of activities, such as carbon nitride, is being investigated. [4,7,8]

Carbon nitride has a graphene-like polymer structure, does not contain metal, and is active as a catalyst in the visible part of the light spectrum. It is a thermally and chemically stable material, low-priced, and easy to synthesize. Researchers have developed g-C₃N₄-based photocatalysts for various uses, such as pollutant degradation. [6,8,9] Considering everything, producing a cocatalyst and nanocomposite made of g-C₃N₄ and TiO₂ would be an excellent opportunity to enhance the photocatalytic activity of both of these photocatalysts.

Herein, it is shown how the change of the concentration of model pollutants influences adsorption capacity and photodegradation rate and how anionic and cationic dye influence degradation.

MATERIALS AND METHODS

Materials

Commercial titanium dioxide (Aeroxide TiO₂ P25), consisting of 70 % anatase and 30 % rutile form, 52 m²/g surface area, 30 nm average particle diameter, was purchased from Evonik Degussa GmbH. Melamine (C₃H₆N₆) was obtained from Aldrich. Sodium hydroxide (NaOH) was purchased from Merck, Germany. Sodium nitrite (NaNO₂) was obtained from Alkaloid, Skopje. Hydrochloric acid (HCl), Acid Orange 10 (AO10), and Methylene Blue (MB) were also used in the experiment. All chemical reagents used in the synthesis of TiO₂ and g-C₃N₄/TiO₂ were of analytical grade without further purification.

Synthesis of TiO₂ nanowires

A commercial TiO₂ powder was used as a starting material. Titanium-dioxide nanowires were fabricated by hydrothermal synthesis [10]. A total of 3.33 g of TiO₂ powder and about 250 ml of 10 M NaOH were placed in the Teflon-lined stainless autoclave for the hydrothermal synthesis process. The autoclave was heated and stirred for 48 h at 165 °C. Upon completing the synthesis, the reaction mixture was left to cool down to room temperature, washed with 100 ml of 0.1 M HCl solution, and filtered in the vacuum. Then the precipitate was resuspended in 200 ml of 0.1 M HCl on a stirrer for a couple of hours, filtered, and washed with distilled water. The procedure was repeated once more to remove residual Na⁺ ions. After washing, the obtained precipitate was dried in the oven for 24 h at 110 °C. The as-synthesized titanate powder was composed of nanoribbons.

Synthesis of g-C₃N₄/TiO₂

For obtaining a hybrid catalyst, 0.5 g of nanoribbons fabricated by the method described above and 2.0 g of melamine were weighed. After making a physical mixture, the crucible was left in an annealing oven at 550 °C for two hours (step ramping rate of 3 °C/min). Subsequently, the hybrid photocatalyst was taken out from the oven and cooled down to room temperature.

Assessment of Photocatalytic Activities

The photocatalytic activity of the obtained catalysts was tested using model pollutants - MB and AO10 in an aqueous solution. The photocatalytic reactor consists of an open cylindrical thermostatic Pyrex cell, 250 mL volume, and a 300 W Osram Ultra Vitalux lamp, whose spectrum simulates sunlight. As a UV filter, 1 M HNO₂ solution was used. The dye concentration in the solution was monitored by UV/Vis spectrophotometer (Thermo Electron Nicolet Evolution 500) by recording the absorption spectrum of the dye solution. The measured mass (50mg) of the photocatalyst was poured into the reactor together with the dye solution, allowing it to stir in the dark until adsorption equilibrium was reached for two hours for MB and one hour for AO10. After the adsorption equilibrium was achieved, dye degradation was followed by taking the sample at a predetermined time, separating the dye solution and photocatalyst with a centrifuge, and measuring the absorbance of the dye solution (at a wavelength of 663 nm for MB and 475 nm for AO10).

RESULTS AND DISCUSSION

Samples TiO₂ and g-C₃N₄/TiO₂ were examined using scanning electron microscopy (SEM), shown in Figure 1. TiO₂ nanowires are numerous in quantity and clean, with no contamination attached to their surface. Their width is around 500 nm, and length 15 μm, The SEM examination of g-C₃N₄/TiO₂ showed different morphology, as some nanowires aggregate.

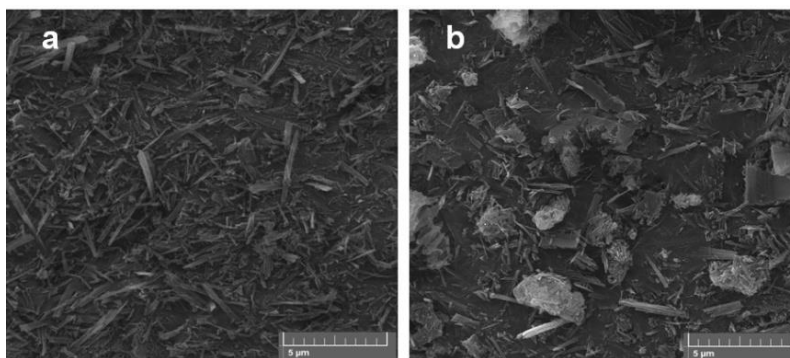


Figure 1 SEM images of a) TiO₂ nanowires, b) g-C₃N₄/TiO₂ hybrid photocatalyst.

The photocatalytic activity of g-C₃N₄/TiO₂ hybrid photocatalyst was evaluated using the MB and AO10 degradation as a representative system under light irradiation. The aqueous solution of MB and hybrid photocatalyst was stirred in the dark for 2 h to reach the adsorption equilibrium of photocatalyst and dye before it was exposed to visible light irradiation. It is observed from Fig. 2a that all samples exhibit a similar adsorption capacity for MB, approximately 1.1-2 ppm. When the concentration of MB is the lowest (2.5 ppm), the adsorption of MB is approximately 44 %, and when the concentration of MB is the highest (10 ppm), the adsorption of MB is around 19 %. Within 3 h, the percentage of degraded MB is approximately 70, 50, 40, and 30 % for solutions with 2.5, 5, 7.5, and 10 ppm of MB, respectively (Fig. 2b). In Figure 3, it is shown how the nature of anionic (AO10) and cationic (MB) dye affects the adsorption and degradation under solar light irradiation. The molar concentration of both dyes is the same. During 1 h, the aqueous solution of AO10 and photocatalyst was stirred in the dark to reach adsorption equilibrium, but the adsorption process did not occur. As is mentioned above, the adsorption of MB was approximately 30 %. This could be explained by negatively charged TiO₂ surface, which preferably adsorbs cationic dye. Using g-C₃N₄/TiO₂ photocatalyst after 4 hours, 69 % of MB from dye solution was degraded and 54 % of AO10, which concludes that degradation properties of cationic are better than for anionic dye.

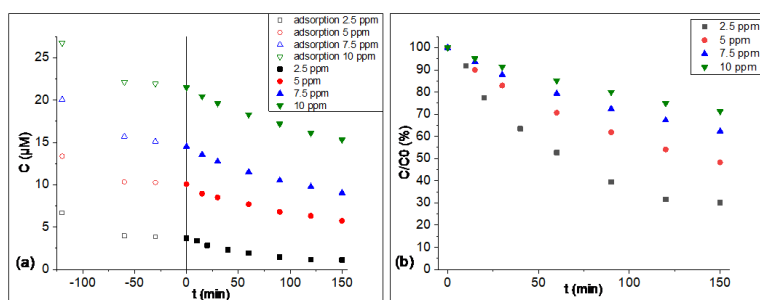


Figure 2. Adsorption and photocatalytic activity of the hybrid composite using visible light irradiation for MB removal from solutions with different dye concentrations expressed in a) μM, b) percentage of dye in solution.

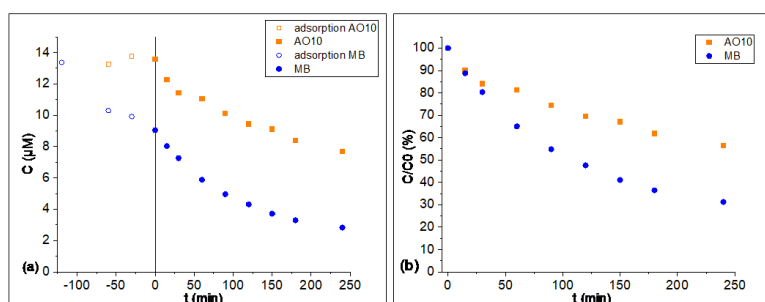


Figure 3. Adsorption and photocatalytic activity of the hybrid nanocomposite using solar light spectrum for MB and AO10 removal expressed in: a) μM, b) percentage of dye in solution

CONCLUSION

Hybrid photocatalyst, g-C₃N₄/TiO₂, has proven to be promising and cheap material for the degradation of different dyes. It is shown that it has the ability to degrade dyes using both visible and solar light spectrum. The adsorption of cationic dye was present, and adsorption of anionic dye did not occur due to the negatively charged surface of the photocatalyst. The degradation of both dyes was similar, and more than 50 % of both dyes were removed from the solutions for 4 hours using a solar light spectrum. However, better degradation was achieved with MB.

Acknowledgement

This work was financially supported by the Ministry of Education, Science and Technological Development of the Republic of Serbia (Grant No. 451-03-9/2021-14/200026). Also, the article is based upon work from COST Action [Grant number: 18234].

REFERENCES

- [1] L. Wang, C. Wang, X. Hu, H. Xue, H. Pang, Metal/Graphitic Carbon Nitride Composites: Synthesis, Structures, and Applications, *Chem. Asian J.* 11 (2016) 3305 – 3328.
- [2] U. G. Akpan, B. H.Hameed, Parameters affecting the photocatalytic degradation of dyes using TiO₂-based photocatalysts: A review, *Journal of Hazardous Materials* 170 (2009) 520-529.
- [3] C. Byrne, G. Subramanian, S. C. Pillai, Recent advances in photocatalysis for environmental applications, *Journal of Environmental Chemical Engineering* 6 (2018) 3531-3555.
- [4] S. De Gisi, G. Lofrano, M. Grassi, M. Notarnicola, Characteristics and adsorption capacities of low-cost sorbents for wastewater treatment: A review, *Sustainable Materials and Technologies*, 9 (2016) 10-40.
- [5] C. Xu, P.R. Ansuyadevi, C. Aymonier, R. Luque, S. Marre, Nanostructured materials for photocatalysis: a review, *ChemSoc Rev* 48 (2019) 3868.
- [6] P. A. K. Reddy, P. V. L. Reddy, E. Kwon, K. H. Kim, T. Akter, S. Kalagara, Recent advances in the photocatalytic treatment of pollutants in aqueous media, *Environment International* 91 (2016) 94–103.
- [7] A. Meng, L. Zhang, B. Cheng, J. Yu, Dual Cocatalysts in TiO₂ Photocatalysis, *Advanced Materials* 31 (2019) 1807660.
- [8] K.R. Reddy, CH.V. Reddy, M.N. Nadagounda, N.P. Shetti, S. Jaesool, T.M. Aminabhavi, Polymeric graphitic carbon nitride (g-C₃N₄)-based semiconducting nanostructured materials: Synthesis methods, properties, and photocatalytic applications: A review, *J of Environmental Management* 238 (2019) 25-40.
- [9] J. Wena, J. Xie, X. Chen, X. Li, A review on g-C₃N₄-based photocatalysts, *Applied Surface Science* 391 (2017) 72-123.
- [10] C. C. Tsai, H. Teng, Structural Features of Nanotubes Synthesized from NaOH Treatment on TiO₂ with Different Post-Treatments, *Chem. Mater.* 18 (2006) 367-373.

SURFACE ELECTRONIC STATE AT CeO₂-MODIFIED DIATOMITE AND SILICA GEL SUPPORTS

D. Nikolova¹, M. Gabrovska¹, J. Krstić², H. Kolev¹, Y. Karakirova¹, V. Radonjić², P. Tsvetkov³

¹*Institute of Catalysis, Bulgarian Academy of Sciences, 1113 Sofia, Bulgaria
(dimi@ic.bas.bg ; dimi_nik@abv.bg)*

²*University of Belgrade, ICTM-Department of Catalysis and Chemical Engineering,
11000 Belgrade, Serbia*

³*Institute of General and Inorganic Chemistry, Bulgarian Academy of Sciences,
1113 Sofia, Bulgaria*

ABSTRACT

The effect of cerium oxide modification of two different SiO₂ supports diatomite (macroporous natural origin material) and commercial silica gel (mesoporous industrial material) was examined. UV-vis diffuse reflectance and X-ray photoelectron spectroscopy measurements were used for estimation of the surface electronic state at both modified SiO₂ supports combine with data of X-ray diffraction, N₂ physisorption technique and electron paramagnetic resonance. Ce³⁺ ions were found in the supported CeO₂ structure over both SiO₂ supports after calcination at 400 °C. The CeO₂ modification reflects on the texture properties and surface electronic state by stronger Ce–O–Si bond in the case of modified CeO₂-silica gel support.

INTRODUCTION

CeO₂ is an interesting rare earth metal oxide used as constituent in multiple applications included catalysts, solid oxide fuel cells, solar cells, gas sensors, energy storage and etc.

The diatomite (D) as a natural SiO₂ source and its alternative silica gel (SIG) as a commercial SiO₂ product were a focus in our previous investigations as supports of nickel-based vegetable oil partial hydrogenation catalysts [1-4].

By the study of the model Ni/ceria systems [5], the uniform distribution of metallic Ni particles over reduced ceria surface was found. This has been explained as the result of surface defects (oxygen vacancies) acting as the nucleation sites for Ni particles with a smaller size and a higher particle density. It is shown by theoretical study with density functional (DFT) calculations that the nickel oxidation state is 2+ in CeO₂ and it remains metallic over reduced Ce₂O₃ [6, 7].

Inspired by these findings, we hypothesize a possible improvement in the catalytic performance of Ni-based catalysts in the reaction of partial hydrogenation of vegetable oils by increasing Ni⁰ dispersion and the availability of Ni atoms using CeO₂ modification of SiO₂ supports (diatomite or silica gel). In the present study, the surface electronic state of the modified SiO₂ supports is estimated by UV-vis diffuse reflectance (DRS) and X-ray photoelectron spectroscopy (XPS) measurements combine with data of X-ray diffraction (XRD), N₂ physisorption technique at -196 °C and electron paramagnetic resonance (EPR).

So far, no studies related to such CeO₂ modification of SiO₂ support in the catalysts for partial hydrogenation of vegetable oils have been reported in the literature.

EXPERIMENTAL

Diatomite (D) support was prepared from local crude diatomite (Prilep, Republic of North Macedonia) in our laboratories (ICTM-DCCE). The crude diatomite was mechanically, chemically and thermally treated to obtain the desired support characteristics (ω_{SiO₂}=97.8%). The commercial silica gel-C (SIG) with different textural characteristics to diatomite was used.

The deposition of 1 wt.% CeO₂ over both supports was done by a classical precipitation method using Ce(NO₃)₃·6H₂O and 0.9M Na₂CO₃ solutions at pH=10 and temperature of 60 °C, followed by calcination of the dried solid at 400 °C for 2 h. The concentration has been selected as appropriate to exclude possible re-oxidation of the future synthesized Ni-based catalyst during operation conditions due to the very well know property of CeO₂ as its high oxygen storage capacity. The CeO₂-modified diatomite and silica gel are denoted as CeO₂-D and CeO₂-SIG, respectively.

RESULTS AND DISCUSSION

In order to understand the contributions of the CeO₂ modifier, N₂ physisorption was done. The N₂ isotherm of diatomite with a barely noticeable hysteresis loop (Fig. 1) can be classified as type II, which is characteristic of macroporous materials, while the SIG isotherm with hysteresis loop H2 is type IV, typical of mesoporous materials.

Modification of silicate supports by CeO₂ causes a slight shift of the hysteresis loop position to a higher value of p/p₀ and a moderate decrease of the specific surface area. However, the types of corresponding isotherms remain unchanged.

The diffractograms of the modified supports (not shown) are very similar in the peak angle location and intensity. The absence of a separate ceria phase registration can be explained by the low CeO₂ content in the carriers.

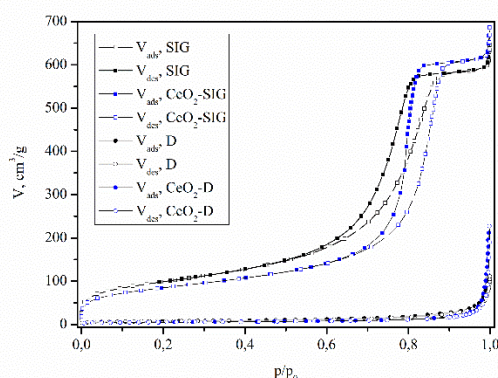


Figure 1. N₂ isotherms of the non-modified and CeO₂-modified diatomite and silica gel

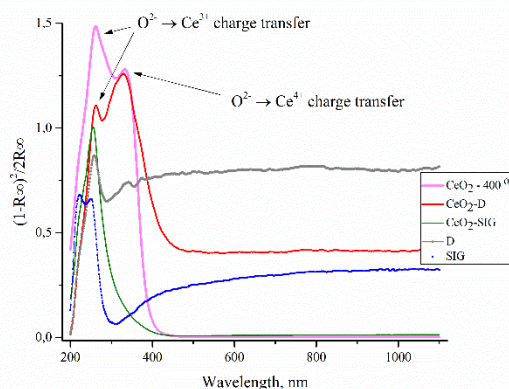


Figure 2. UV-Vis spectra of the non-modified and CeO₂-modified diatomite and silica gel

The characterization of the surface electronic state by DRS and Kubelka-Munk method shows that Ce ions deposition on both supports enhanced the absorption in the visible and especially ultraviolet region (Fig. 2). It must be noted that the presented adsorption values of CeO₂-SIG and CeO₂ samples are reduced 10 and 11 times, respectively, in order to facilitate comparison with the spectra of other samples. According to the literature, the registered bands at 253 nm for CeO₂-SIG and at 259 nm for CeO₂-D refer to the existence of O²⁻ → Ce³⁺ charge transfer. The bands at 327 nm in the spectrum of CeO₂-D and broad-band character toward 400 nm in the spectrum of CeO₂-SIG are due to the O²⁻ → Ce⁴⁺ charge transfer.

The registration of O²⁻ → Ce³⁺ charge transfer could be explained with the statement that supported ceria deviates slightly from stoichiometry and Ce³⁺ ions can be observed in the structure, without any reducing treatment [8]. The presence of such defects as in CeO₂ prepared by calcination of cerium hydroxide at 400 °C [9] has been established by EPR. In our case, the EPR signal was hard to identify at CeO₂-D and CeO₂-SIG due to the presence of stronger signals from such impurities as Fe³⁺ and Mn²⁺. However, a weak signal from Ce³⁺ sites with g=1.9464 is registered in the EPR spectrum of

bulk CeO₂ prepared as a reference by the same methodology as well as band of O²⁻ → Ce³⁺ charge transfer in the UV-vis spectrum.

Table 1. N₂ physisorption and XPS analyses data of the supports

Support	S _{BET} , m ² g ⁻¹	Micropore volume, cm ³ g ⁻¹	Mesopore volume, cm ³ g ⁻¹	Contribution (%)		Ce ⁴⁺ satellite position (eV)
				Ce ³⁺	Ce ⁴⁺	
D	25.8	0.010	0.061			
SIG	356	0.125	0.972			
CeO ₂ -D	18.3	0.007	0.046	53.55	46.45	916.9
CeO ₂ -SIG	306	0.111	1.000	50.66	49.34	917.7

Deconvoluted XPS spectra confirmed this Ce³⁺ phenomenon (Table 1). The contribution of Ce³⁺ state is the approximately the same at both CeO₂-D and CeO₂-SIG. The position of the Ce⁴⁺ satellite is registered at 916.9 and 917.7 eV for CeO₂-D and CeO₂-SIG, respectively (Table 1). The satellite position is higher by 0.8 eV in the CeO₂-SIG spectrum compared with that of CeO₂-D, indicating stronger Ce–O–Si bond during the partial dissolution of silica gel at pH=10. This stronger interaction between CeO₂ and SIG is visible also from modification of hysteresis loop in the N₂ isotherm of CeO₂-SIG, representing the formation of new mesopores (Table 1).

CONCLUSION

Two types of silica, naturally derived and artificial, were successfully modified with cerium oxide via the precipitation approach. Both Ce⁴⁺ the Ce³⁺ ions are observed in the structure of supported CeO₂ over diatomite and silica gel, which is an indication for stoichiometry deviation. The stronger Ce–O–Si bond in the case of modified CeO₂-SIG support reflects on the texture and surface electronic state.

Acknowledgement

The authors J.K and V.R. would like to thank the Ministry of Education, Science and Technological Development of Republic of Serbia (Grant No: 451-03-9/2021-14/200026) for financial support.

REFERENCES

- [1] M. Stanković, Ž. Čupić, M. Gabrovska, P. Banković, D. Nikolova, D. Jovanović, *React. Kinet. Mech. Catal.*, 2015, **115**(1), 105-127.
- [2] J. Krstić, M. Gabrovska, D. Lončarević, D. Nikolova, V. Radonjić, N. Vukelić, D.M. Jovanović, *Chem. Eng. Res. Des.*, 2015, **100**, 72-80.
- [3] M. Stanković, J. Krstić, M. Gabrovska, V. Radonjić, D. Nikolova, D. Lončarević, D. Jovanović, Chapter 8, In Book: *New Advances in Hydrogenation Processes – Fundamentals and Applications*. Edited by Maryam Takht Ravanchi.. InTech, 2017, **48**, 131-179.
- [4] M.V. Gabrovska, D.A. Nikolova, J.B. Krstić, D.R. Loncarević, P.T. Tzvetkov, M.G. Shopska, V.D. Radonjić, M.V. Stanković, D.M. Jovanović L.T. Spasov, D.B. Simeonov, *Bulg. Chem. Commun.*, 2018, **50**, 161-168.
- [5] Y. Zhou, J.M. Perket, A.B. Crooks, J. Zhou, *J. Phys. Chem. Lett.*, 2010, **1**, 1447-1453.
- [6] Z. Liu, D.C. Grinter, P.G. Lustemberg, T.-D. Nguyen-Phan, Y. Zhou, S. Luo, I. Waluyo, E.J. Crumlin, D.J. Stacchiola, J. Zhou, J. Carrasco, H. Fabio Busnengo, M.V. Ganduglia-Pirovano, S.D. Senanayake, J.A. Rodriguez, *Angew. Chem. Int. Ed.*, 2016, **55**, 7455-7459.
- [7] P.G. Lustemberg, P.J. Ramírez, Z. Liu, R.A. Gutiérrez, D.G. Grinter, J. Carrasco, S.D. Senanayake, J.A. Rodriguez, M.V. Ganduglia-Pirovano, *ACS Catal.*, 6(12) (2016) 8184-8191.

- [8] A. Bensalem, F. Bozon-Verduraz, M. Delamar, G. Bugli, *Appl.Cat. A: General*, 1995, **121**, 81-93.
- [9] E. Abi-Aad, A. Bennani, J.-P. Bonnelle, A. Aboukais, *J. Chem. Soc. Faraday Trans.*, 1995, **91**(1), 99-104.

INFLUENCE OF THE SURFACE SPECIES ON THE CATALYTIC PERFORMANCE OF Co-Pd CATALYSTS IN CO HYDROGENATION. PART 1. ROLE OF TITANIA SUPPORT

M. Shopska, I. Shtereva, K. Aleksieva, G. Kadinov

*Institute of Catalysis, Bulgarian Academy of Sciences,
Acad. G. Bonchev, St., Bldg. 11, Sofia 1113, Bulgaria, (shopska@ic.bas.bg)*

ABSTRACT

Activity and selectivity of (10%Co+0.5%Pd)/TiO₂ system in CO hydro-genation were studied in dependence of pretreatment mode, reduction and reaction temperature. It aimed to evaluate the information about influence of surface species and sites on catalytic performance. Samples were preliminary treated in oxidative, reductive, or inert gas flow and studied by chemisorption of H₂ and CO, TPR, XPS, EPR, *in situ* DRIFTS and catalytic measurements. Dependence on the mode of pretreatment and reduction temperature on the catalyst activity in CO conversion and selectivity to CH₄ were found. The reductive pretreatment resulted in an active sample characterized by bridged CO species on metal sites with weakened C-O bond that facilitated cleavage at lower temperatures and more bidentate carbonate species on average strength sites. The selective catalyst was prepared by pretreatment in air and revealed predomination of formate and monodentate carbonate species on strong adsorption sites of TiO₂.

INTRODUCTION

Main reactions in the process of CO hydrogenation are the synthesis of CH₄/hydrocarbons and water-gas shift reaction (WGSR). Methanation takes part on the metal particles composed of Co and Pd atoms [1–3]. WGSR occurs both on the reduced metal and on oxidized metal surface including metal ions in the support [4].

Present investigation shows results on activity and selectivity of (10%Co+0.5%Pd)/TiO₂ system in dependence of pretreatment mode, reduction and reaction temperature. It aimed to evaluate the information about influence of various surface species and sites on catalytic performance. Catalyst activity is not isolated property. It is accompanied by kind of selectivity in its work. It is necessary to vary the factors and adjust their effect in the catalyst creation so that the higher activity to be accompanied by improved selectivity.

METHODS

Samples were preliminary treated in air, H₂, or Ar and studied by chemisorption of H₂ and CO, temperature-programmed reduction (TPR), x-ray photoelectron spectroscopy (XPS), electron paramagnetic resonance (EPR), *in situ* DRIFTS in static and dynamic conditions of CO hydrogenation and catalyst activity measurements in flow reactor (CO:H₂ = 1:4, P = 1 atm, T_{reac} = 150–360 °C). Details were shown elsewhere [5, 6].

RESULTS AND DISCUSSION

Comparative analysis showed dependences on the pretreatment mode and reduction temperature on the catalyst activity in CO conversion and selectivity to CH₄. Data derived by different methods for the most active sample in CO conversion and that of high selectivity to CH₄ are shown in Table 1. The comparison was made taking 300 °C as reference reaction temperature.

Table 1. Data derived by TPR, XPS, chemisorption and catalytic measurements of catalyst (10%Co+0.5%Pd)/TiO₂.

Parameter		Active	Selective
Pretreatment		(red)	(ox)
T _{red} , (°C)		300	300
Co states (TPR)		Co ⁰ , Co ⁿ⁺	Co ⁰ , Co ⁿ⁺
R _{URM}		0.2	
Carbon (C1s)	Total, (at.%)	9.53	8.71
	CO ₃ , (%)	20	26
CH ₄ /CO ₂		3	65
D _{H100C} (T _{red}), (%)		3.6	3.7
H _{100C} /CO _s (T _{red})		2.9	2
CO _s /CO _w		0.8 (22/28)	1 (32.8/31.8)

Legend: R_{URM} – unreduced metal ratio (URM_{active}/URM_{selective}); CO₃ – surface carbon corresponding to carbonate(s); H_{100C} – H₂ adsorption measured at 100 °C after reduction at respective T_{red}; CO_w - weak (reversible) CO adsorption measured at room temperature after reduction at respective T_{red}; CO_s - strong (irreversible) CO adsorption; D_{H100C} - metal dispersion based on H_{100C} and determined after reduction at respective T_{red}.

XPS and EPR studies revealed Co²⁺, Co³⁺, Pd, Pd²⁺, Ti³⁺, and Ti⁴⁺ on the surface after the catalytic tests due to, in part, the ‘*ex-situ*’ measurements because the samples have already been reduced. XPS registered 8.71–10.06 at.% of carbon on the surface, certain part of which in a surrounding characteristic of carbonates.

The reductive pretreatment gave rise to an active sample with appearance of Ti³⁺ sites and O²⁻ vacancies [7, 8]. A lot of pure Co and Pd particles so as bimetallic ones were registered, Ti⁴⁺ and Co²⁺ ions, and lack or low level of metal-support interaction. The selective catalyst was prepared by pretreatment in air. TiO₂ was stabilized in relation to phase transformations with various sites for CO adsorption on the surface: Co and Pd particles, bimetallic particles with highly diluted Pd atoms on the surface, Ti³⁺, Ti⁴⁺, and Coⁿ⁺ ions, relatively low amount of O²⁻ vacancies, and metal particles with surface partially covered by reduced titania due to SMSI.

TPR study showed cobalt in metallic and ionic state in both samples independently on pretreatment and T_{red}. The amount of Coⁿ⁺ predominated in the selective sample.

CO and H₂ chemisorption indicated: (i) almost the same metal dispersion in both samples; (ii) higher H/CO_s ratio of 2.9 for the catalyst after reductive pretreatment; (iii) almost the same CO_s/CO_w ratio for both catalysts but CO adsorption was higher on the selective one. The results can be assigned to more CO adsorbed on metal ions in the active catalyst but existence of more CO in bridged form on separate Co and Pd particles in the selective catalyst.

The carbonate species formation on the samples/support proceeded by two distinct mechanisms: (i) through contact of CO with surface defects then with OH groups or (ii) directly *via* CO and surface OH group interaction [9]. The probability for their realization is different depending on the procedure of preliminary treatment of the catalyst. Both mechanisms could be equally operative in the case of an active sample, while in the case of selective catalyst the second mechanism is most probable.

The products ratio CH₄/CO₂ at the reaction temperature of 300 °C was 3 and 65 for the active and the selective catalyst. XPS study revealed higher carbon deposition on the surface of active sample but larger amount of carbonates on the surface of selective sample. The results could be explained with: (i) more sites for strong CO adsorption on the metal surface and for formate and monodentate carbonate species on the support in the selective catalyst that determine CO₂ formation to occur at higher temperatures during the catalytic process; (ii) more bidentate carbonate species on adsorption sites of average strength on the surface of the active catalyst; (iii) variation of the ratio linear/bridged

CO species on the surface of metal particles in the active catalysts, where the weakened C-O bond in bridged species facilitated cleavage at lower reaction temperatures. TiO₂ as reducible support, weak acid mainly with Lewis acid properties and Pd/TiO₂ are effective in WGS. This should be taken into account together with the other factors mentioned above attempting performance of an active catalyst with high selectivity.

CONCLUSION

Surface sites homogeneity (particles composition, energy of CO adsorption) depends on the pretreatment medium and reduction temperature and could promote higher selectivity to CH₄ during CO hydrogenation in bimetallic Co-Pd catalyst supported on titania.

Acknowledgement

This study was supported by BNSF (KP-06-H29-9/14.12.2018). The used equipment was part of INFRAMAT infrastructure (D01-155/28.08.2018).

REFERENCES

- [1] J.A. Rabo, A.P. Risch, M.L. Poutsma, Reactions of carbon monoxide and hydrogen on Co, Ni, Ru, and Pd metals, *J. Catal.*, 1978, **53**, 295.
- [2] P. Biloen, J.N. Helle, W.M.H. Sachtler, Incorporation of surface carbon into hydrocarbons during Fischer-Tropsch synthesis: Mechanistic implications, *J. Catal.*, 1979, **58**, 95.
- [3] L.E. Oi, M.-Y. Choo, H. V. Lee, H. C. Ong, S. B. A. Hamid, J. C. Juan, Recent advances of titanium dioxide (TiO₂) for green organic synthesis, *RSC Adv.*, 2016, **6**, 108741.
- [4] D.C. Grenoble, M.M. Estadt, D.F. Ollis, The chemistry and catalysis of the water gas shift reaction: 1. The kinetics over supported metal catalysts, *J. Catal.*, 1981, **67**, 90.
- [5] M. Shopska, G. Kadinov, I. Shtereva, Determination of metal dispersion in cobalt-palladium catalysts, *Rev. Roum. Chim.*, 2014, **59**, 219.
- [6] P. Stefanov, S. Todorova, A. Naydenov, B. Tzaneva, H. Kolev, G. Atanasova, D. Stoyanova, Y. Karakirova, K. Alexieva, On the development of active and stable Pd-Co/ γ -Al₂O₃ catalyst for complete oxidation of methane, *Chem. Eng. J.*, 2015, **266**, 329.
- [7] C.N. Satterfield, *Heterogeneous Catalysis in Industrial Practice*, McGraw-Hill. Inc., 1980.
- [8] A. Nobile, Jr., M. W. Davis, Jr., Importance of the anatase-rutile phase transition and titania grain enlargement in the strong metal-support interaction phenomenon in FeTiO₂ catalysts, *J. Catal.*, 1989, **116**, 383.
- [9] C. Weilach, C. Spiel, K. Föttinger, G. Rupprechter, Carbonate formation on Al₂O₃ thin film model catalyst supports, *Surf. Sci.*, 2011, **605**, 1503.

INFLUENCE OF RESIDENCE TIME ON THE DECOMPOSITION RATE OF OLEYLAMINE

S. Vidojkovic^{1,2}, R. Lindeboom¹, M. Mijajlovic³

¹*TU Delft, Faculty of Civil Engineering and Geosciences-Watermanagement Department, Stevinweg 1, 2628 CN, Delft, Netherlands*

²*University of Belgrade, Institute of Chemistry, Technology, and Metallurgy, Njegoseva 12, 11001 Belgrade, P.O.B. 473, Serbia (sonja66yu@yahoo.com)*

³*University of Nis, Faculty of Mechanical Engineering, Aleksandra Medvedeva 14, 18000 Nis, Serbia.*

ABSTRACT

Film forming amines (FFA) are organic feedwater additives used in the power industry for several decades. Even though, the utilization of FFA in power plants is highly dependent on their thermal stability in the high temperature water/steam environment, the scientific data are scarce. Oleylamine (OLA) is known to be a film forming amine commonly applied in power industry as a feedwater additive for the corrosion protection of the steam generators. The decomposition rate of OLA was studied at the temperatures up to 220 °C. For this purpose, the novel experimental high-temperature high-pressure stainless steel reactor was employed. The reactor was operational up to 300 °C/200 bar. For determination of the OLA concentration, the Bengal Rose method was used. In this paper, the effect of the residence time on the decomposition rate was presented. The obtained results demonstrated a high decomposition rate of OLA.

INTRODUCTION

Film forming amines are organic compounds added in the feedwater in power plants to prevent corrosion and deposition which are always associated with efficiency and reliability loss. FFA create a thin, impermeable film on the inner metal tube wall that constitutes a physical barrier between the metal wall and moisture containing corrosive impurities. Consequently, they reduce boiler tube failures, increase components life and decrease power generating cost. For several decades they are used worldwide in both nuclear and conventional plants for dosing in the feedwater during operation but also for lay-off period [1,2]. They were first used in SSSR since the beginning of the 1960s but over the last twenty years the application of FFA broadened, particularly in the western countries. It raised an increased interest of providing a scientific background on FFA behavior in water/steam cycle condition in order to facilitate their utilization and enable the highest benefit in power industry.

Film forming amines contain an aliphatic carbon chain with 10 to 22 saturated or unsaturated carbon atoms and one or several primary and/or secondary amine groups. General chemical formula for FFA is $R_1-[NH-R_2-]_n-NH_2$ where n is an integer between 0 and 7, R_1 is an unbranched aliphatic (such as alkyl or alkenyl) chain with 12 to 18 carbon atoms and R_2 is a short aliphatic chain (such as alkyl or alkenyl group) that usually contains 1 to 4 carbon atoms. A lone electron pair of the nitrogen atom in the functional amino group gives alkali properties to amines. The amine group of FFA represents a hydrophilic end of long hydrocarbon chain with a tendency to bind with the negatively charged metal (iron) surface. This connection leads to the formation of the monomolecular protective films on metal surfaces [3]. On the other side of the aliphatic carbon chain is a non-polar hydrophobic alkyl group giving non-wettable property to the film formed on the metal surface.

OLA, with the structural formula shown in Fig. 1 and molecular formula $C_{24}H_{53}N_3$, belongs to the amines with saturated carbon chain and has one primary and two secondary amino groups. The thermal stability of OLA directly influences its applicability in power plants and restricts its use. Consequently, the decomposition rate is the foremost factor that is needed to be explained in order to maintain safe, reliable and efficient plant operation. However, there is a lack of scientific data on thermolysis of ODA in various conditions of water/steam cycle of power plants, particularly fossil fuel power plants that normally work in wider temperature and pressure range (from 200 °C and 2.0 MPa to supercritical parameters) in comparison with nuclear plants. The objective of this work is to investigate the influence of the residence time on the decomposition rate of OLA in high temperature water.



Figure 1. Structural formula of OLA

METHODS

The novel high-temperature high-pressure stainless steel reactor (Fig.2) operational up to 300 °C/200bar was constructed for studying the thermal stability of OLA. The peculiarity of this stainless steel reactor is high versatility for performing different kind of high temperature experiments simulating various water processes that take place in the power plants. The reactor was equipped by sampling tube that serves to collect samples during the operation at different stages of the high-temperature experiments. Adsorption of OLA to the inner wall of the reactor vessel was precluded by a polytetrafluoroethylene (PTFE) liner. An experience of using liners as well as sampling bottles made of PTFE material to avoid adsorption of OLA was already proved in industry to be effective and recommended by manufacturers producing OLA for industrial facilities. Besides, in this experiment, additional precautionary measures were taken: 1) Before the experiment, the all equipment was saturated by washing with OLA emulsion. When the surfaces of the vessels are saturated with the OLA emulsion, the notable adsorption was not expected on the walls. 2) Additionally, the concentration of the OLA in the samples taken in the PTFE bottles was measured in certain time intervals and the change of the concentration was not observed. 3) The visual control of the PTFE liner was carried out and the OLA attached to the wall was not noticed. The reactor allows the permanent stirring.

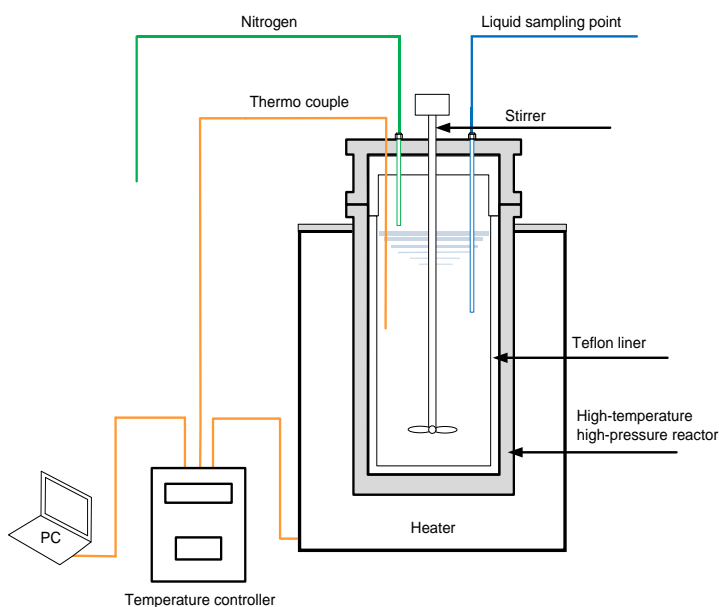


Figure 2. Scheme of the experimental high-temperature high-pressure reactor.

For this study, the 70 % OLA from Sigma Aldrich was used. The solutions were prepared using Mili-Q water. The concentration of the OLA emulsion used in the experiments was previously optimized and amounted to 5 ppm. OLA is low soluble in water because the long chain of amines interferes with hydrogen bonds between N atom of amine molecule and polar OH bonds in water. Therefore, to prepare a stable emulsion, OLA was carefully added to the warm Mili-Q water with permanent stirring. Having filled with the OLA emulsion, the reactor was sealed by a lid connected to the nitrogen gas tank that was used to remove air from the liquid. The experiments were conducted at the temperature of 220 °C and pressure of 20 bar. Bengal Rose analytical method [5, 6] was applied for determination of the OLA concentrations. Bengal Rose (4,5,6,7-Tetrachloro-2',4',5',7'-tetraiodofluorescein sodium salt) is Xanthene dye related to fluorescein. The sodium salt from Bengal Rose dye create with FFA a water-soluble colored complexes that are easy measured without any other further treatment. The detection limit of the method in the laboratory is 0.02 mg/l. The measurements were carried out by photometric technique using spectrophotometer Genesys 10S UV/VIS at the 560 nm that was recorded to be the wavelength with the maximum absorbance for OLA.

RESULTS AND DISCUSSION

A sharp drop of the OLA concentration with exposure time of 30 sec was observed, which indicates that OLA exhibits a very intensive decomposition during that time at the temperature of 220 °C. The obtained experimental results showed that the decomposed amount of OLA equaled 4.11% after the residence time of 5 s, but after 30 s it increased up to 24.66%. The decomposition reaction was confirmed to follow the first order kinetics as illustrated in Fig. 3. In the fossil fuel power plants, film forming amines are dosed into the condensate where the temperature of water is below 30 °C. With passage of the OLA through the plant the temperatures increase, and in front of the boiler the temperature reaches approximately 240 °C (in the subcritical power plants). This means that at the beginning of the feedwater system the decomposition of OLA is not anticipated and the OLA will form the protective film on the metal wall. In the close proximity to the boiler, the decomposition will occur but still the undecomposed OLA will have a protective effect on the tube wall. On the grounds that the residence time of OLA at a particular temperature point in the feedwater tube is of the order of a second, it is possible to assume that the decomposed amount of OLA will be much less than that observed for 30 s in this experiment. The temperature effect is not an issue in nuclear power plants due to the lower temperature ranges, during the power plant conservation (corrosion protection during shutdown), and in broad range of industrial plants operating at low temperatures.

The lack of published data on the thermolysis of OLA does not make possible the comparison of the results. In fact, the published results on the decomposition of pure FFA are rare and refer only to octadecylamine (ODA) which is the FFA with the longest history of utilization in energy sector and

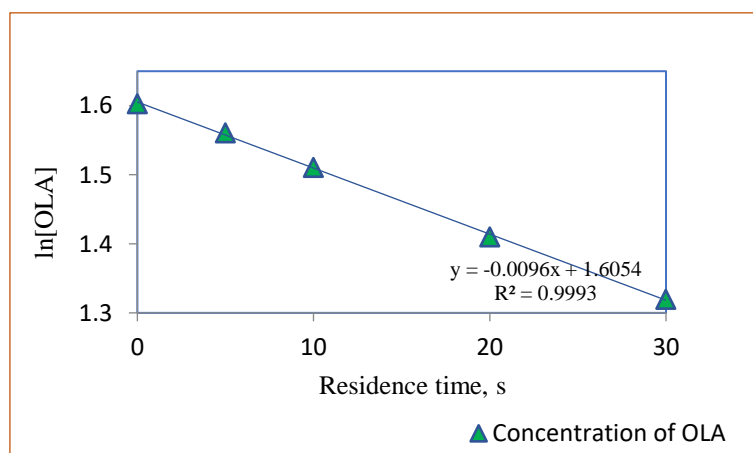


Figure 3. Relation between ln[OLA] and residence time

On the grounds that the residence time of OLA at a particular temperature point in the feedwater tube is of the order of a second, it is possible to assume that the decomposed amount of OLA will be much less than that observed for 30 s in this experiment. The temperature effect is not an issue in nuclear power plants due to the lower temperature ranges, during the power plant conservation (corrosion protection during shutdown), and in broad range of industrial plants operating at low temperatures.

proven records of effectiveness, while the data on other FFA are missing. The rapid decline of the OLA concentration immediately after its exposure to the high temperature of 220 °C acquired in this experimental study was found to be in agreement with the trend observed in ODA thermolysis study [3] performed at the temperatures of 233 °C and 343 °C.

The OLA concentrations used in this study corresponds to the realistic concentrations in power plants and the chosen temperature corresponds to the temperature in feedwater system. On the basis of the fact that using of FFA in industry is mostly based on the practical experience and suffer from significant deficiency of scientific information, this study provides significant scientific data on behavior of OLA in power plant water conditions which is of great importance for understanding the decomposition behavior of OLA, prediction its impact on steam generator operation and better selection of film forming amines.

CONCLUSION

This study led to a conclusion that the residence time is a substantial influencing factor in the process of thermal decomposition of OLA. The rate of thermal decomposition of OLA was confirmed to be high and after 30 s the amount of decomposed amine reached 24.66%. The constructed experimental reactor was proved to be reliable in simulation the power plant water/steam cycle conditions and thus capable of producing the experimental data for application in industry. In order to enable a complete prediction of the decomposition process of OLA, future research should provide more information on the effect of higher temperatures, additives and other amines on the OLA thermolysis.

Acknowledgement

This project has received funding from the European Union's Horizon 2020 research and innovation programme Marie Skłodowska-Curie Actions under grant agreement No 795275.

REFERENCES

- [1] B. Hoock, W. Hater, A. de Bache A., Thirteen years of experience with the treatment of the water-steam cycle of the MVV Enamic Power Plant with film-forming amines, *Power Plant Chemistry*, 2015, 17 (5), 283 – 293.
- [2] T. Petrova, Use of ODA at Russian Power Plants, *Power Plant Chemistry* 2017, 19 (2), 68-74.
- [3] I. Ya. Dubrovski, P. S. Ashev, L. N. Batalina, V. A. Loshkarev, On the ODA Behaviour in the Power Generation Cycle, *Trudy MEI*, 1980, 466, 26-31.
- [4] IAPWS TGD8-16, Technical Guidance Document: Application of Film Forming Amines in Fossil, Combined Cycle, and Biomass Power Plants, The International Association of the Properties of Water and Steam, Dresden, Germany, 2016.
- [5] A. Graf, Method for the Determination of Polyamines, European Patent Office, Munich, Germany, EP0562210 A1, 1993.
- [6] Katrin Stiller, Tobias Wittig, and Michael Urschey, The Analysis of Film-Forming Amines – Methods, Possibilities, Limits and Recommendations, *Power Plant Chemistry*, 2011, 13 (10), 602-611.

INFLUENCE OF THE SURFACE SPECIES ON THE CATALYTIC PERFORMANCE OF Co-Pd CATALYSTS IN CO HYDROGENATION. PART 2. ROLE OF ALUMINA AND SILICA SUPPORT

M. Shopska, I. Shtereva, H. Kolev, K. Aleksieva, S. Todorova, G. Kadinov

Institute of Catalysis, Bulgarian Academy of Sciences, Sofia 1113, Bulgaria. (shopska@ic.bas.bg)

ABSTRACT

Activity in CO conversion and selectivity to CH₄ of bimetallic catalysts Co-Pd/Al₂O₃ and Co-Pd/SiO₂ were studied in dependence of support, pretreatment mode, reduction and reaction temperature. Research was focused on the effect of surface sites and species on catalytic action. Samples were pretreated in air, H₂, or Ar and studied by H₂ and CO chemisorption, TPR, catalytic measurements, XPS, and EPR. The pretreatment in air resulted in formation of active samples with more pure Co and Pd particles and bridged CO species with weakened C-O bond that facilitated activation at lower temperatures. However, the high quota of unreduced metal and hydroxyl groups on the support with average strength sites for carbonate species adsorption facilitated WGSR. Selective catalysts were obtained by pretreatment in H₂ or Ar and were characterized by low level of unreduced metal, more bimetallic particles, more sites for strong adsorption of carbonate species on Al₂O₃.

INTRODUCTION

Main reactions in CO hydrogenation process on Co and Co-Pd supported catalysts are the synthesis of CH₄/hydrocarbons and water-gas shift reaction (WGSR). Methanation takes part on reduced Co and Pd. WGSR proceeds in presence of eight group elements independently on their state [1, 2]. Present paper shows results from studies of 10%Co+0.5%Pd catalysts related to activity and selectivity dependences on the type of support (Al₂O₃ or SiO₂), pretreatment, reduction and reaction temperature. The aim was to evaluate the factors determining the catalytic performance and how the activity could be optimized in relation to the selectivity.

METHODS

Precursors were pretreated in air, H₂ or Ar. Samples were studied by H₂ and CO chemisorption, temperature-programmed reduction (TPR), electron paramagnetic resonance (EPR), X-ray photoelectron spectroscopy (XPS). Catalytic activity measurements in CO hydrogenation were carried out at atmospheric pressure with reaction flow H₂:CO = 4, at T_{reac} ≤ 360 °C. Details can be found elsewhere [3, 4].

RESULTS AND DISCUSSION

CH₄/CO₂ products ratio decreased with the temperature increase for the samples pretreated in air. This effect was pronounced at reaction temperatures ≥300 °C. The reduction temperature change from 300 to 450 °C affected the samples' behaviour increasing in a similar way their conversion and selectivity. Comparative analysis showed that catalysts possessing high activity in CO conversion differ from those which were more selective to methane production (Table 1).

Table 1. Data derived by TPR, XPS, chemisorption and catalytic measurements (reaction temperature of 300 °C) with alumina- and silica-supported 10%Co+0.5%Pd catalysts.

Parameter	Support			
	SiO ₂		Al ₂ O ₃	
	Active	Selective	Active	Selective
Pretreatment	(ox)	(inert)	(ox)	(red)
T _{red} , (°C)	300	(300, 400) 450	300	(300) 400
Co states (TPR)	Co ⁰ , Co ⁿ⁺	Co ⁰	Co ⁰ , Co ⁿ⁺	Co ⁰ , Co ⁿ⁺
R _{URM}	14.1		3.3	
Carbon (C1s) Total, (at.%)	2.38	2.22	3.15	3.54
(XPS) CO ₃ , (%)	15	-	40	50
T _{reac} , (°C)	310*	300	300	300
CH ₄ /CO ₂	11.6*	No CO ₂	6.3	160
D _{H100C} , (%)	6	2.6	3.4	1
H _{100C} /CO _s	3.9	2.7	3.4	2.8
CO _s /CO _w	1.2	0.7	1.8	0.5
	(26.71/22.35)		(17.74/9.79) (6.03/13.07)	

Legend: R_{URM} – unreduced metal ratio (R_{URM} = URM_a/URM_s); CO₃ – surface carbon equivalent to carbonate(s); H_{100C} – H₂ adsorption measured at 100 °C after respective T_{red}; CO_w – weak CO adsorption at T_{room} after respective T_{red}; CO_s – strong CO adsorption at T_{room} after respective T_{red}; * – closest experimental data to T_{reac}; D_{H100C} – metal dispersion determined after reduction at respective T_{red}.

EPR spectra of all samples were registered after catalytic measurements at room temperature. The results showed a broad singlet line with g factor 2.2551±0.005, which is due to tetrahedral coordinated Co²⁺ ion. It is supposed that the line significantly broadens because of additional deformation of Co²⁺ tetrahedron (bimetallic systems), dipole-dipole inter-action between particles (10% Co), and bigger particles size. SiO₂ supported catalysts could be arranged concerning the amount Co²⁺ ions: (red) > (ox) > (inert). Probably, the samples pretreated in air and Ar have large amount of cobalt in other oxidation state (for example CoPd alloy particles, Co³⁺), which are diamagnetic. XPS registered Co²⁺, Co³⁺, Pd, and Pd²⁺ on the samples' surface, supporting EPR conclusions. The ions found in reduced materials were assigned to unreduced binary oxides phases and resulting from 'ex-situ' measurements. Carbon was registered on the samples and, partially, provided from carbonates. Carbonates were not observed on the SiO₂-supported sample pretreated in Ar. The amount of carbonates was larger on the Al₂O₃-supported samples indicating stronger adsorption sites [5]. The dependence on the pretreatment follows the same row (red) > (ox) > (inert).

The active catalysts were formed using pretreatment in air, where the presence of O₂ and H₂O is supposed. A higher metal dispersion was found after reduction. The catalysts demonstrated higher ratios of H_{100C}/CO_s and CO_s/CO_w, which was due to the adsorption on metal particles with a greater quota of bridged CO species. These species have weaker C-O bond allowing sample activation at lower reaction temperature. The abundance of irreversibly adsorbed CO on the active samples favours both main reactions. These samples have relatively more of pure Co and Pd particles that possess properties to activate WGS and should not be excluded as additional contributors to CO₂ production. A bigger quota of Coⁿ⁺ in the active catalysts (R_{URM}) allowed running of WGS in a higher extent leading to higher CO₂ content in the outlet gas flow. The dependence of catalyst activity in CO₂ formation on T_{reac} for the active Al₂O₃-supported sample supposed the existence of sites for carbonate(s) adsorption of, predominantly, middle strength [5] as supposed above according XPS data. The active samples have preserved in a higher extent the OH groups coverage after reduction compared to the selective ones thus favouring carbonate species formation upon CO adsorption. CO₂ production on the active catalysts was facilitated by three factors: abundance of CO_s species, a lot of Coⁿ⁺ ions, and high hydroxyl group coverage on the support giving ability to form carbonate species (in the case of Al₂O₃ support).

The catalysts of better selectivity to CH₄ formation were obtained by pretreatment in Ar or H₂ followed by reduction at high temperatures. This mode of pretreatment results in low level of unreduced metal, more bimetallic particles, lower amount of pure Pd particles, decreased metal dispersion and supposes removal of great amount of surface OH groups (especially in H₂ flow). Both the active and the selective samples worked in presence of reduced and ionic cobalt. However, the amount of the later was several times lower in the selective samples (in case of SiO₂ support almost all the cobalt was in metallic state). With Al₂O₃-supported selective sample the lower CO₂ production rate increasing reaction temperature and the higher level of carbonates on its surface, found by XPS study, are consistent with the existence of sites with stronger adsorption of carbonate-like species compared to the active catalyst [5]. Decreased rate of carbonate destruction with evolution of CO₂ diminished the rate of WGS and adsorbed CO on the selective catalysts was spent predominantly in CH₄ formation.

CONCLUSION

Supported on Al₂O₃ (SiO₂) Co-Pd catalysts active in CO conversion or selective to CH₄ showed similar characteristics. Active systems were prepared following pretreatment in air and they possessed larger amount of unreduced metal and bridged species of adsorbed CO, better preserved hydroxyl group coverage, and sites of middle strength for carbonates adsorption. Selective catalysts were prepared by pretreatment in H₂ or Ar flow and their performance was determined from a lower amount of CO_s, more reduced metal (even bimetallic particles formation) and strongly adsorbed carbonates species.

Acknowledgement

This research was supported by BNSF (KP-06-H29-9/14.12.2018). The used equipment is part of INFRAMAT infrastructure (D01-155/28.08.2018).

REFERENCES

- [1] J.A. Rabo, A.P. Risch, M.L. Poutsma, Reactions of carbon monoxide and hydrogen on Co, Ni, Ru, and Pd metals, *J. Catal.*, 1978, **53**, 295.
- [2] D.C. Grenoble, M.M. Estadt, D.F. Ollis, The chemistry and catalysis of the water gas shift reaction: 1. The kinetics over supported metal catalysts, *J. Catal.*, 1981, **67**, 90.
- [3] M. Shopka, G. Kadinov, I. Shtereva, Determination of metal dispersion in cobalt-palladium catalysts, *Rev. Roum. Chim.*, 2014, **59**, 219.
- [4] P. Stefanov, S. Todorova, A. Naydenov, B. Tzaneva, H. Kolev, G. Atanasova, D. Stoyanova, Y. Karakirova, K. Alexieva, On the development of active and stable Pd-Co/ γ -Al₂O₃ catalyst for complete oxidation of methane, *Chem. Eng. J.*, 2015, **266**, 329.
- [5] C. Weilach, C. Spiel, K. Föttinger, G. Rupprechter, Carbonate formation on Al₂O₃ thin film model catalyst supports, *Surf. Sci.*, 2011, **605**, 1503.

APPLICATION OF EPR SPECTROSCOPY FOR SILVER-BASED CATALYSTS CHARACTERIZATION

K. Aleksieva, Y. Karakirova, S. Todorova

*Institute of Catalysis, Bulgarian Academy of Sciences,
Acad. G. Bonchev, St., Bldg. 11, Sofia 1113, Bulgaria, (kati@ic.bas.bg)*

ABSTRACT

EPR spectra of oxidized 15Ag15CeO₂/SiO₂ registered in the temperature range 123–323 K show two overlapping signals – a broad line due to silver clusters and a narrow one due to the presence of Ag⁰ species. In view of the obtained EPR results it can suppose that Ag clusters in oxidized 15Ag15CeO₂/SiO₂ catalyst are destroyed and Ag⁺ and Ag⁰ are formed during catalytic reaction. EPR spectra of H₂-treated samples show that there is no EPR spectrum of silver clusters and only Ag⁰ were detected. After the catalytic reaction, the shape and parameters of EPR spectrum of reduced 15Ag15CeO₂/SiO₂ catalyst is not changed.

INTRODUCTION

The preferential CO oxidation in hydrogen rich gases (PROX) has been studied for application in polymer electrolyte membrane fuel cells (PEMFCs) to reduce CO in the fuel gases below 10 ppm. Catalysts, so far proposed for the PROX process, are based mainly on noble metals such as Pt, Rh, and Ru, deposited on different supports with or without promoters [1]. The working temperature of these catalysts is in the range 403–473 K [2]. It seems too high to match the subsequent reaction in PEMFC, which is usually carried out at 323–400 K [3]. The decrease in reaction temperature and the search for more economic catalysts for PROX are challenging objectives for the near future. Silver, another member of group IB, has been scarcely investigated as a PROX catalyst in spite of its high activity in low temperature CO oxidation in absence of hydrogen [4]. Reports concerning utilization of Ag as catalyst for selective CO oxidation are few and they examine only monometallic silver supported on SiO₂ or carbon and composites like Ag/Co and Ag/Mn oxides [5,6].

The main objective of our study to characterize Ag-based catalysts with the method of Electron Paramagnetic Resonance (EPR) spectroscopy.

SAMPLES AND METHODS

The Ag-Ce catalysts were obtained from a mixed aqueous solution of AgNO₃ and Ce(NO₃)₂·6H₂O. Bimetallic Ag-Ce were prepared. The silver and cerium contents in the bimetallic sample are 15 wt% Ag and 15 wt% Ce (sample denoted 15Ag15Ce). All samples were calcined and pretreated in pure O₂ 2h at 723 K before the catalytic test.

The EPR spectra were recorded at JEOL JES-FA 100 EPR spectrometer operating in X-band with standard TE₀₁₁ cylindrical resonator. The Varied Temperature Controller ES-DVT4 was used to permit detection of EPR spectra at temperatures from 123 to 323 K. Desired temperature can be easily obtained by sending liquid nitrogen at a temperature, which is controlled by the EPR spectrometer data system computer, to the sample area.

RESULTS AND DISCUSSION

EPR spectra of oxidized 15Ag15CeO₂/SiO₂ registered in the temperature range 123–323 K are shown in Figure 1. As can be seen this EPR spectrum consists of two overlapping EPR lines, indicated signal Si1 and signal Si2 in Figure 1. The signal Si1 is characterized with g factor 2.26. Based on the

previous EPR studies of supported Ag catalysts, [7] this signal can be assigned to Ag clusters with a general composition $\text{Ag}_n^{\delta+}$ where $(n - \delta^+)$ is an odd number and $n < 10$. The larger line width does not permit determining of the hyperfine structure, as a result of which the number of Ag species is not clear. This signal is expanded and shifted to lower field with reducing the recording temperature of the EPR spectra. The g value of signal Si2 is 2.0034 and most probably due to the Ag^0 . The g-factor of Ag^0 is reported to be isotropic and close to the free electron value 2.0023 [8]. This signal slightly broadening at temperature 173 K and at lower temperatures disappears.

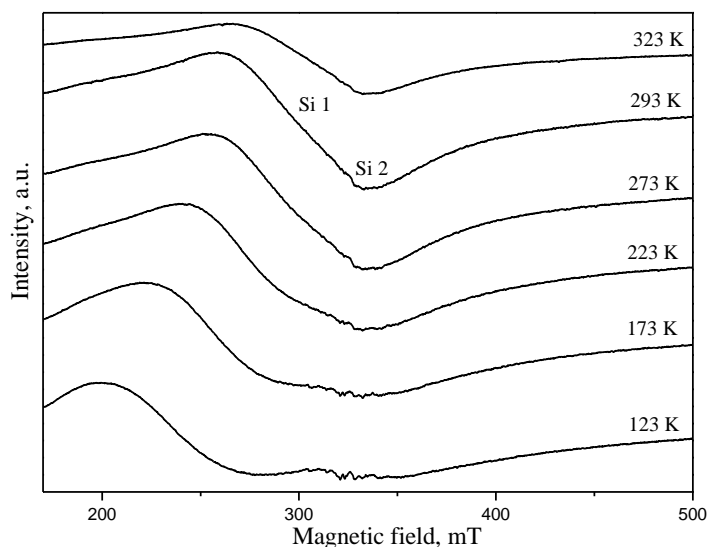


Figure 1. EPR spectra of oxidized 15Ag15CeO₂/SiO₂

After the catalytic reaction, the shape of EPR spectrum of 15Ag15CeO₂/SiO₂ catalyst is not changed, but the intensity and line width of the EPR signal is changed. During the reaction of CO oxidation in hydrogen-rich gases, the intensity of the EPR signal Si1 decreased and the intensity of Si2 slightly increased with the increasing of the reaction time. After 4 hours catalytic reaction, there is a narrowing of the EPR line Si1, which can be seen more clearly at a temperature above 273 K. The line width of signal Si2 after 4 hours catalytic test, strongly reduced at 173 K. The resonance field values of the EPR signals after catalytic test, remain constant.

In view of the obtained EPR results it can suppose that Ag clusters in oxidized 15Ag15CeO₂/SiO₂ catalyst are destroyed and Ag^+ and Ag^0 are formed during catalytic reaction. Ag^+ ion is diamagnetic with closed $4d^{10}$ electronic configuration and does not exhibit any ESR spectrum. As was mention before, Ag^0 is responsible for signal Si2 and its intensity slightly increased after catalytic test.

EPR spectra of H₂-treated samples show that there is no EPR spectrum of silver clusters and only Ag^0 were detected. After the catalytic reaction, the shape and parameters of EPR spectrum of reduced 15Ag15CeO₂/SiO₂ catalyst is not changed.

CONCLUSION

Based on the results given and discussed above it can be concluded that the introduction of ceria leads to the increase in the silver dispersion; the homogeneous distribution of Ag and ceria on the silica support; increases in bulk and subsurface oxygen. Supported silver catalysts are promising systems for selective oxidation of CO at low temperatures. The most suitable support among all studied is

SiO₂. Samples promoted with cerium oxide show better performance, most probably because more surface oxygen species are provided to the Ag.

Acknowledgement

This research was supported by BNSF (KP-06-H29-9/14.12.2018). This work was partially supported by the Bulgarian Ministry of Education and Science under the National Research Programme E+: Low Carbon Energy for the Transport and Households, grant agreement D01-214/2018. The used equipment is part of INFRAMAT infrastructure (D01155/28.08.2018).

REFERENCES

- [1] D. Teschner, A. Wootsch, O. Pozdnyakova-Tellinger, J. Kröhnert, E.M. Vass, M. Hävecker, S. Zafeiratos, P. Schnörch, P.C. Jentoft, A. Knop Gericke, R. Schlögl, Partial pressure dependent in situ spectroscopic study on the preferential CO oxidation in hydrogen (PROX) over Pt/ceria catalysts, *J. Catal.*, 2007, **249**, 318.
- [2] O. Korotkikh, R. Farrauto, Selective catalytic oxidation of CO in H₂: Fuel cell applications, *Catal. Today*, 2000, **62**, 249.
- [4] S. Imamura, H. Yamada, K. Utani, Combustion activity of Ag/CeO₂ composite catalyst, *Appl. Catal. A: General*, 2000, 192, 221
- [5] C. Güldür F. Balikçi, Selective carbon monoxide oxidation over Ag-based composite oxides, *Int. J. Hydrogen Energy*, 2002, **27**, 219
- [6] F.B. Derekaya and C. Güldür, Activity and selectivity of CO oxidation in H₂ rich stream over the Ag/Co/Ce mixed oxide catalysts, *Int. J. Hydrogen Energy*, 2010, **35**, 2247.
- [7] A. Abou-Kais, M. Jarjoui, J. C. Vedrine, P. C. Gravelle, Electron paramagnetic resonance (EPR) investigations on silica-supported silver catalysts and adsorbed oxygen species, *J. Catal.*, 1977, **47**, 399.
- [8] K. Chandrasekharan and V. S. Murty, Radiation-induced paramagnetic silver centers in LiNaSO₄, *Physica B: Physics of Condensed Matter*, 1995, **215**, 243

PHOTOCATALYTIC AND ELECTROCATALYTIC OXIDATION OF 2,4,6-TRICHLOROPHENOL ON IRON-DOPED NANOZIRCONIA CERAMIC

T. Savić¹, T. Novaković², N. Abazović¹, M. Čomor¹ and Z. Mojović¹

¹ Vinča Institute of Nuclear Sciences - National Institute of the Republic of Serbia, University of Belgrade, P.O. Box 522, 11000 Belgrade, Serbia.

² University of Belgrade, Institute of Chemistry, Technology and Metallurgy, Department for Catalysis and Chemical Engineering- National Institute of the Republic of Serbia, Njegoševa 12, 11000 Belgrade, Serbia.

ABSTRACT

Photocatalytic and electrocatalytic oxidation of 2,4,6-trichlorophenol (TCP) was investigated on pure and iron-doped zirconia matrix synthesized by solvothermal method from organometallic precursors. The doping of zirconia with Fe³⁺ ions had beneficial effect on its photocatalytic performance in degradation of TCP. Electrocatalytic investigation showed that TCP oxidation pathway depended on iron ions content in zirconia matrix.

INTRODUCTION

Chlorophenols are organic compounds widely used in various industries, resulting in the appearance of chlorophenols in different parts of environment. Chlorophenols are long-lasting, highly toxic pollutants of environment with extremely high toxicological impact on human organism causing damages and necrosis. [1]. In order to remove chlorophenols from water various photocatalysts and electrocatalysts have been investigated

Zirconia as eco-friendly ceramic material represents interesting choice for catalyst due to strong oxidizing and reducing ability [2]. It's application as photocatalyst is somewhat hindered due to wide band gap with absorption edge placed deep in UV region of solar spectrum. Doping of zirconia matrix with transition metal ions, such as iron [3], is usually performed in order to shift its spectral response towards visible part of the spectrum and enhance zirconia photocatalytic properties. The iron-doped zirconia also showed electrocatalytic activity [4] toward nitrite oxidation and reduction.

In this study, results of photo- and electro- catalytic activity of pure and iron-doped zirconia in reaction of oxidation of 2,4,6-trichlorophenol (TCP) are presented.

METHODS

Pure and iron doped zirconium oxide nanopowders were synthesized by solvothermal procedure [3]. Stoichiometric quantities of Fe ions of 0, 1, 5, 10 and 20 a. % were added to zirconium propoxide and obtained samples were denoted accordingly, as ZrO₂, 1-ZrO₂, 5-ZrO₂, 10-ZrO₂ and 20-ZrO₂. For photocatalytic experiments, 20 mg of catalyst was dispersed in 40 mL of TCP aqueous solution, (100 ppm). After equilibration in the dark for 1h, reaction dispersions were illuminated, and the aliquots were taken from the dispersions at regular time intervals. The electrochemical experiments were performed by Autolab PGSTAT302N with Ag/AgCl in 3 M KCl as a reference electrode and a platinum rod as a counter electrode. The working electrode was a glassy carbon electrode (GCE) (area = 0.0706 cm²) modified by investigated samples dispersed in 5 wt. % Nafion.

RESULTS AND DISCUSSION

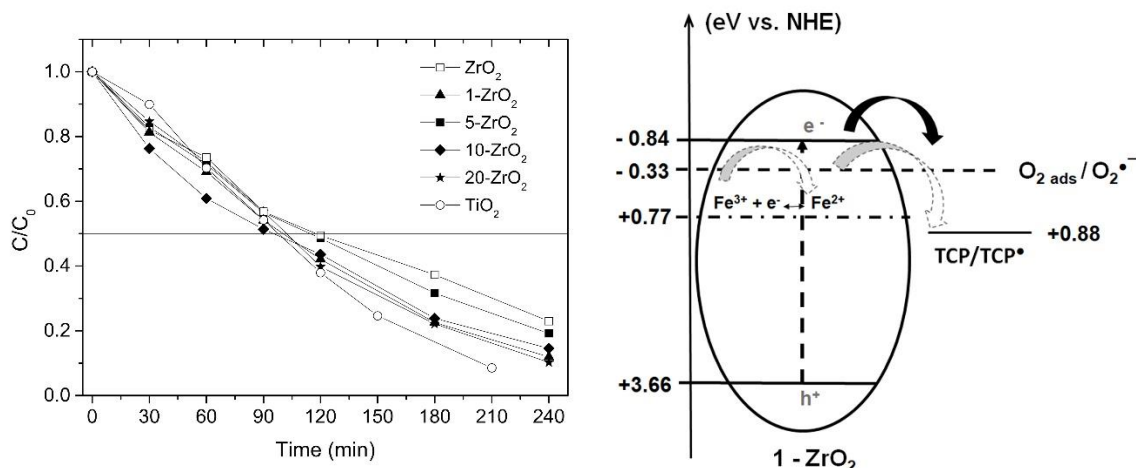


Figure 1. a) Kinetic curves of photocatalytic degradation of TCP on illuminated zirconia samples; b) Possible charge transfer processes in illuminated 1- ZrO_2 /TCP system.

Kinetic curves of photocatalytic degradation of TCP on illuminated zirconia samples are presented in Fig 1. Samples 1- ZrO_2 and 20- ZrO_2 were the most efficient photocatalysts. However, total organic carbon (TOC) measurements (not presented) have revealed that 1- ZrO_2 sample is the most efficient one; its efficiency is comparable with commercial Degussa P25 TiO_2 . Possible charge transfer processes are presented in Fig 2. Upon illumination, electron-hole pairs are formed in semiconductor. According to scheme, fate of photogenerated electrons from CB of semiconductor can be different: but according to potential positions, it is probably scavenged by surface oxygen forming superoxide radical anion, $O_2^{\bullet-}$. In mechanism proposed by Ji et al. [5] in reaction of superoxide radical anion with TCP, 2,6-dichlorohydroquinone and 2,6-dichloro-3-hydroxy-1,4-benzoquinone will be formed. Degradation of these compounds through aromatic ring cleavage will lead to formation of small molecular aliphatic carboxylic acids.

Cyclic voltammograms of GCE modified with investigated samples, recorded in 0.1 M H_2SO_4 showed a pair of redox peaks at the potential of 0.55 V vs. Ag/AgCl, that can be ascribed to the Fe^{2+}/Fe^{3+} oxidation/reduction process. The peak current was increased with the increase of quantity of iron ions in the zirconia matrices. Peak currents showed slight decrease with increase of cycling number that probably originated from releasing of iron species [4].

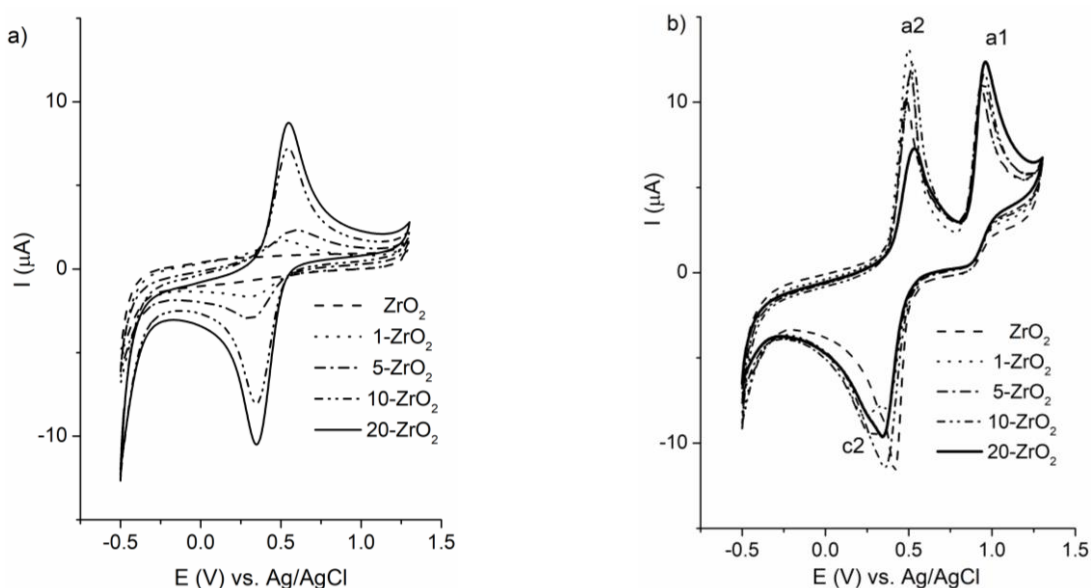


Figure 2. a) Cyclic voltammograms of ZrO_2 and iron-doped ZrO_2 in 0.1 M H_2SO_4 , scan rate 50 mVs^{-1} ; b) 5th cyclic voltammograms recorded on ZrO_2 and iron-doped ZrO_2 in 1 mM TCP + 0.1 M H_2SO_4 , scan rate 50 mVs^{-1} .

The electrooxidation of TCP was investigated using freshly prepared modified GCE. The irreversible anodic peak at 0.93 V designated as a1 corresponded to oxidation of hydroxyl group at TCP. The peak a1 charge increased with the increase of the iron ion content in the zirconia sample on the GCE, indicating that iron (iron oxide) doping increased electrocatalytic activity of ZnO_2 for oxidation of hydroxyl group of TCP. The peak current slightly decreased with cycling that is considered as electrode fouling due to formation of polyphenol film. The reversible pair of peaks (a2/c2) at lower potential was ascribed to the formation of quinones. The reversibility of the hydroquinone/quinone couple was close to unity for undoped and zirconia doped up to 5 % of Fe ions. The further increase of iron ions content led to decrease of the reversibility. The Q_{a2}/Q_{a1} ratio gives indication of fraction of TCP oxidized to quinone [6]. The highest value was obtained for 1- ZrO_2 and lowest for 20- ZrO_2 . This finding might indicate that electrooxidation of TCP on samples with high content of iron ions in zirconia matrix favors polyphenol film formation pathway.

CONCLUSION

Pure and Fe-doped zirconia nanopowders were solvothermally synthesized. The photocatalytic and electrocatalytic investigations of oxidation of 2,4,6-trichlorophenol (TCP) were performed. 1- ZrO_2 is the most efficient photocatalyst among synthesized samples in TCP photodegradation; superoxide radical anion is identified as the main radical species. Cyclic voltammograms of all investigated electrodes showed characteristic peak of oxidation of hydroxyl group at TCP and reversible pair of peaks ascribed to the formation of quinones. The amount of iron present in the sample influenced the pathway of TCP oxidation.

Acknowledgement

This work was supported by the Ministry for Education, Science and Technological Development of the Republic of Serbia (Grant No. 451-03-9/2021-14/200026 and 451-03-9/2021-14/200017).

REFERENCES

- [1] A. O. Adeola, *Medical & Analytical Chemistry International Journal*, 2018, 2(4), 000126.
- [2] K.C. Soni, S. C. Shekar, B. Singh, T. Gopi, *Journal of Colloid and Interface Science*, 2015, 446, 226–236.
- [3] M. V. Carević, T. D. Savić, N. D. Abazović, M. D. Mojović, T. B. Novaković, M. I. Čomor, *Ceramics International*, 2020, 46, 6820–6827
- [4] A. Doménech-Carbó, G. Herrera, N. Montoya, P. Pardo, J. Alarcón, M. T. Doménech-Carbó, M. Silva, *J. Electrochem. Soc.* 2014, 161, H539-H546
- [5] H. Ji, F. Cheng, X. Hu, W. Qin, J. Shen, *Chem. Eng. J* 2013, 2108, 183-190
- [6] F. Fernández, C. Berríos, E. Garrido-Ramírez, N. Escalona, C. Gutiérrez, M. S. Ureta-Zañartu, *J Appl Electrochem* 2014, 44, 1295–1306.

COBALT-DOPED ALUMINA CATALYSTS IN CATALYTIC OXIDATION OF TARTRAZINE INDUCED BY OXONE®

S. Marinović, T. Mudrinić, A. Ivanović-Šašić, B. Dojčinović, P. Banković, T. Novaković

*University of Belgrade, Institute of Chemistry, Technology and Metallurgy
Njegoševa 12, 11000 Belgrade, Serbia. (sanja@nanosys.ihtm.bg.ac.rs)*

ABSTRACT

In this work cobalt-doped alumina catalysts were synthesized using the sol-gel method. The calcination temperatures were 500 °C, 1000 °C and 1100 °C and the catalysts were denoted as CoA-500, CoA-1000 and CoA-110, respectively. The obtained catalysts were tested as Oxone® activators for the degradation of tartrazine azo-dye. The influence of the mass of catalyst and the reaction temperature was investigated. The catalyst mass and temperature increase were beneficial for the dye degradation rate. All three catalysts were found to be effective for tartrazine degradation in the presence of Oxone®.

INTRODUCTION

Cobalt-based catalysts are widely studied and applied in different processes. Cobalt nitrate and cobalt acetate are the most commonly used precursors in the preparation of the cobalt-based catalysts. These catalysts are usually prepared via impregnation on various oxide supports, such as Al₂O₃, SiO₂ or TiO₂ [1]. The cobalt-based catalysts have been largely used as oxidation catalysts in numerous environmental applications [2].

One of the applications of the cobalt-based catalysts is the activation of Oxone® (2KHSO₅×KHSO₄×K₂SO₄) in order to generate SO₄^{•-} radicals effective in the oxidative degradation of different organic pollutants in wastewaters [3]. Azo-dye tartrazine is mostly used in the food industry. The presence of tartrazine in wastewater may cause serious health problems. Therefore, the removal of tartrazine from industrial effluents can be regarded as a highly important goal [4].

In this work cobalt-doped alumina catalysts were used for the Oxone® “activation” in the catalytic oxidation of tartrazine dye as a water pollutant.

EXPERIMENTAL

The sol-gel method was used for the preparation of the Co(II)-doped alumina composites. Aluminum alkoxide was used as the precursor for boehmite sols. Aluminum isopropoxide was hydrolyzed at 80 °C in an excess amount of water. The hydrolysis was followed by a peptization with the appropriate amount of HNO₃ in order for a stable colloidal sol to be formed. The sol was kept at a constant temperature and under reflux conditions for a desired time, during which most of the alcohol evaporated [5]. In order for the Co/Al composite to be obtained, CoNO₃×6H₂O was added to a freshly prepared sol, in the amount that provides 40 mass% of Co with respect to Al. The doped boehmite sol was then gelled for 24 hours at 40 °C, and subsequently at 100 °C for another 24 hours. The gels were calcined at 500 °C, 1000 °C and 1100 °C for 5 h. These temperatures were selected in order for different structural phases of alumina (γ,δ-θ and α) to be obtained, with the goal of determining their catalytic diversity and selecting the most active phase. The obtained samples were denoted as CoA-500, CoA-1000 and CoA-1100, where Co stands for cobalt, the A stands for alumina and the number refers to the calcination temperature.

Catalytic tests were performed by stirring an aqueous tartrazine solution (C_{0,dye}=50 mg dm⁻³) in the presence of 0.130 mmol of Oxone®. The tests were conducted in a 500 cm³ Pyrex reactor thermostated using a Julabo MC 4 circular heater and equipped with a mechanical stirrer. The

following experimental parameters were investigated. The effect of the mass of the catalyst was investigated for CoA-500 catalyst in the range from 5 mg to 100 mg and at the reaction temperature of 30 °C. The effect of temperature was monitored for all three catalysts (CoA-500, CoA-1000 and CoA-1100) in the range from 30 °C to 60 °C. The moment of adding Oxone[®] to the reaction mixture was taken as the initial (0 min) moment of the reaction. With respect to this moment, aliquots were taken at the predetermined periods of time. Supernatant solutions were separated from the solid phase by centrifugation at 17000 rpm for 3 min and analyzed using the UV–Vis spectrophotometry (Thermo Scientific, Evolution 220 UV–Visible Spectrophotometer). The peak at 426 nm, indicating the decolorization of the solution, was monitored and analyzed.

RESULTS AND DISCUSSION

The sol-gel method was used for the synthesis of the Co/Al composites. The impregnation with cobalt, performed after the synthesis of alumina, could be an alternative synthesis method, which would provide catalysts with lower contents of Co. However, the impregnation was not chosen, mainly because a lower leaching of cobalt was intended to be achieved, and leaching usually occurs as a problem in this type of catalyst synthesis. ICP measurements showed that leaching was in the order of magnitude of ppb, which is acceptable. Another advantage of the applied synthesis method is that it results in a higher dispersity and more homogeneous distribution of cobalt comparing with those in impregnated samples. This leads to a better exposure of the catalytically active sites.

The influence of the mass of the catalyst was investigated for CoA-500 in the mass range from 5 mg to 200 mg (200 cm⁻³ of 50 mg dm⁻³ tartrazine solution; 40 mg of Oxone[®]; T=30 °C, reaction time of up to 240 min) (Fig.1). With the increase of the mass of the catalyst the degree of decolorization increased. For the mass of 100 mg a plateau, related to nearly 100% of decolorization, was reached after only 5 minutes. On the other hand, for the lowest mass, the total decolorization was not reached within the investigated time (240 minutes). For further investigations, a lower mass of catalyst was chosen for the monitoring of the occurrence and disappearance of other degradation products, detectable by UV–Vis spectra (Fig. 2).

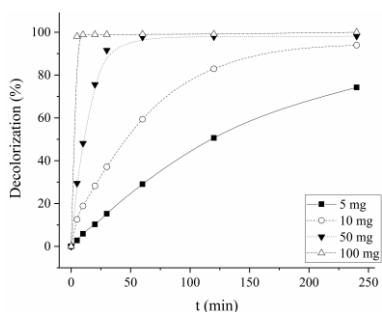


Figure 1. Influence of mass of catalyst CoA-500 on decolorization of tartrazine

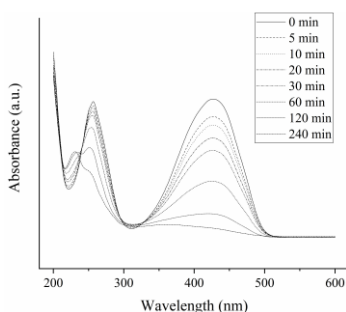


Figure 2. UV–Vis spectra for catalytic tests with 10 mg of the CoA-500 at 30 °C

The mass of the catalysts of 10 mg was chosen for the experiments conducted in order for the temperature influence on the efficiency of the catalysts to be investigated. Three catalysts: CoA-500, CoA-1000 and CoA-1100 were tested (Fig. 3). The rate of the decolorization of tartrazine under the investigated conditions was the highest for CoA-500 and the lowest for CoA-1100, for all investigated temperatures. Temperature increase

was beneficial for the dye decolorization rate. Under the investigated conditions, the total decolorization was achieved in the case of the reaction conducted at 60 °C for all three catalysts. In the case of CoA-500, almost complete decolorization was achieved after 240 min for all temperatures. On the other hand, for CoA-1100, the decolorization at 30 °C was much slower, and almost linear

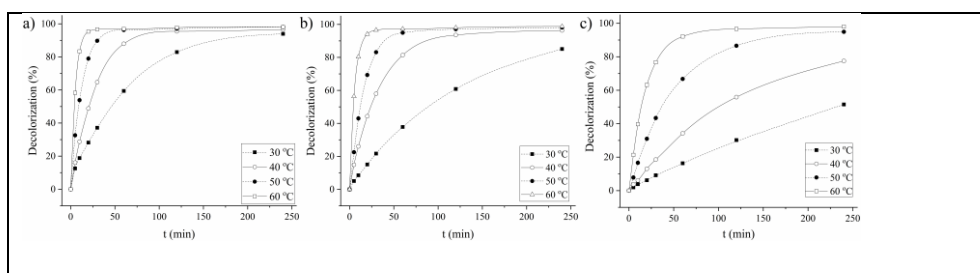


Figure 3. Decolorization of tartrazine solution at different temperatures using: a) CoA-500, b) CoA-1000 and c) CoA-1100

with time. Only 50% of the decolorization of the tartrazine was completed after 240 minutes. The results of the catalytic tests indicate that the gamma phase of the alumina was the most active in this reaction, under the selected test reaction conditions.

CONCLUSION

CoA-500, CoA-1000 and CoA-1100 were synthesized using the sol-gel method and tested as catalysts in a tartrazine solution decolorization. The role of the catalysts was to activate Oxone[®], thus yielding $\text{SO}_4^{\cdot-}$ radical that act as oxidizing species. The influence of the catalyst mass and temperature was investigated. The increase of temperature and the mass of the catalyst was beneficial for the reaction. Although CoA-500 catalyst was found to be the most active in the investigated reaction, all three catalysts were efficient. The cobalt-doped alumina materials were found to be promising catalysts in the Oxone[®] initiated tartrazine decolorization.

Acknowledgement

This work was financially supported by the Ministry of Education, Science and Technological Development of the Republic of Serbia (Grant No. 451-03-9/2021-14/200026).

REFERENCES

- [1] L. Fratolocchi, C. Giorgio Visconti, L. Lietti, *Applied Catalysis A: General*, 2020, 595, 117514.
- [2] A. Choya, B. de Rivas, J. R. González-Velasco, J. I. Gutiérrez-Ortiz, R. López-Fonseca, *Applied Catalysis A: General*, 2020, 591, 117381.
- [3] K.Y.A. Lin, J.T. Lin, X.Y. Lu, C. Hung, Y.F. Lin, *Journal of Colloid and Interface Science* 2017, 505, 728–735.
- [4] R. Jain, M. Bhargava, N. Sharma, *Industrial & Engineering Chemistry Research*, 2003, 42, 243–247.
- [5] Z. Mojović, T. Novaković, M. Mojović, T. Barudžija, M. Mitrić, *Science of Sintering*, 2019, 51, 339-351.

KINETIC AND THERMODYNAMIC STUDY OF THE OXIDATIVE CATALYTIC DEGRADATION OF ACID ORANGE 10 IN THE PRESENCE OF OXONE® AND COBALT BASED CATALYST

N. Jović-Jovičić, I. Ilić, A. Ivanović-Šašić, M. Ajduković, A. Milutinović-Nikolić

University of Belgrade – Institute of Chemistry, Technology and Metallurgy, National Institute, Department of Catalysis and Chemical Engineering, Njegoševa 12, 11000 Belgrade, Republic of Serbia (natasajovicjovicic.ihtm@gmail.com)

ABSTRACT

Catalytic degradation of Acid Orange 10 in the presence of Oxone® activated by Co-impregnated acid activated montmorillonite as catalyst was investigated. The catalytic experiments were performed at different temperatures in range from 303 to 333 K in order to determinate kinetics parameters. The kinetics data followed the first-order kinetics model. The activation energy of the investigated degradation process was calculated according to the Arrhenius equation.

INTRODUCTION

Degradation of pollutants present in effluents of textile industry received high attention since dyes and pigments from these effluents showed carcinogenic and mutagenic effects [1]. Most azo dyes have stable chemical structure, highly resistant to bio-treatment. Therefore, different physical-chemical methods such as adsorption or catalytic oxidative degradation have been employed in order to decrease concentration of pollutants in wastewaters of textile industry [1].

In this paper standard clay from Wyoming deposit with high content of montmorillonite was acid activated and then impregnated with cobalt, using incipient wetness impregnation method. The obtained catalyst was evaluated in oxidative degradation of Acid Orange 10 (AO10) with respect to degradation time and temperature. The kinetic and thermodynamic parameters were deduced from the catalytic tests. These data could be very useful in elucidating the nature of oxidative degradation process of investigated catalytic system.

EXPERIMENTAL

Materials

The sodium rich montmorillonite from Wyoming (MW) was supplied by The Clay Minerals Society repository (USA). MW was acid activated using HCl (35 wt. %, Lach-Ner). The $\text{Co}(\text{NO}_3)_2 \cdot 6\text{H}_2\text{O}$ (≥ 98 % purity), Oxone® ($2\text{KHSO}_5 \cdot \text{KHSO}_4 \cdot \text{K}_2\text{SO}_4$) and Acid Orange 10 (AO10, $\text{C}_{16}\text{H}_{10}\text{N}_2\text{Na}_2\text{O}_7\text{S}_2$) were purchased from Sigma Aldrich. The AO10 was tested as model pollutant.

Catalyst synthesis

The acid activation of MW was performed using previously described method with 4.5 M HCl [2] in order to improve textural properties of raw clay. The cation exchange capacity (CEC) after activation was determined by standard ammonium acetate method [3]. The cobalt was introduced in the amount equal to CEC value, following procedure of wetness impregnation method ($1.0\text{Co}/\text{MW}_A$) [4].

Catalytic test

The catalytic degradation was carried out in thermostated reactor at temperatures: 303, 313, 323 and 333 K. The catalytic test was performed using 10 mg of catalysts in 200 cm^3 dye solution ($C_{\text{dye}}=50\text{ mg dm}^{-3}$) in the presence of Oxone® (0.2 g dm^{-3}) with respect to predetermined time (10, 20, 30, 60, 120 and 240 min). Solid and liquid phase were separated by centrifugation at 17000 rpm for 3 min,

and analyzed using a Thermo Electron Nicolet Evolution 500 UV–VIS spectrophotometer. Characteristic AO10 UV absorption peak at 478 nm was used for degradation monitoring.

Applied kinetic and thermodynamic models

The obtained catalytic data for each investigated temperature were treated with different kinetic models [5]. The first-order kinetics model was found to be the most appropriate. In (Eq. 1) this model is given in exponential form:

$$Y_t = Xe^{-kt} + E \quad (\text{Eq. 1})$$

Where: X is the amplitude, k is the first-order rate constant, and E is the endpoint.

Arrhenius relationship was used to evaluate the activation energy of adsorption:

$$\ln k_1 = \ln A - \frac{E_a}{RT} \quad (\text{Eq. 2})$$

Where: k_1 is first-order kinetics rate constant, E_a is the Arrhenius activation energy (kJ/mol), A is the Arrhenius factor, R is the gas constant (8.314 J/mol K) and T is the temperature (K).

RESULTS AND DISCUSSION

The catalytic data together with the first-order kinetics models are given in Fig. 1a. The calculated kinetic parameters are presented in Table 1. The obtained k values are used to construct Arrhenius plot (Fig. 1b).

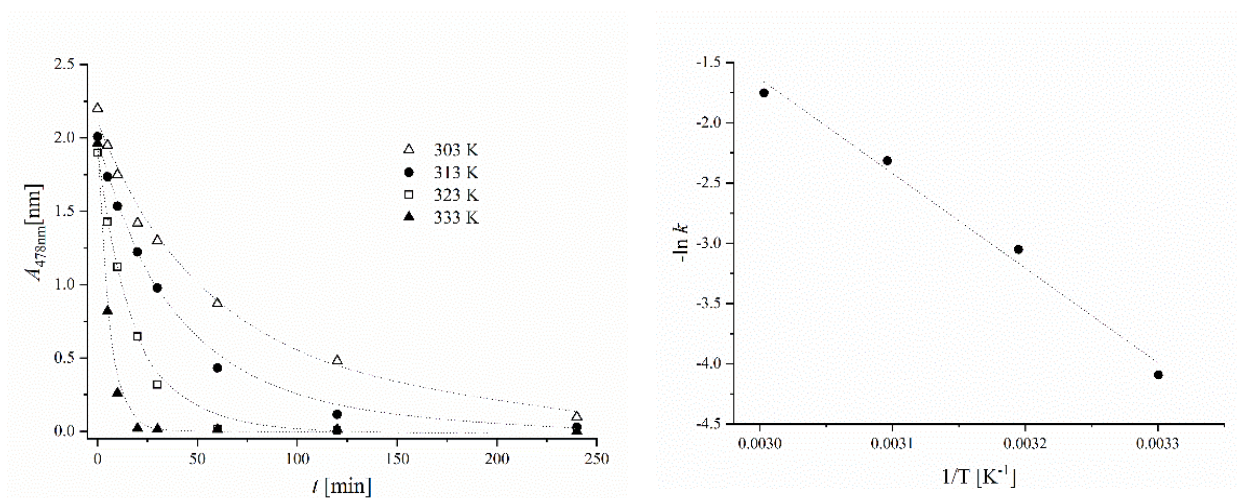


Figure 1. a) Experimental data and the first-order fitting curves for reaction of catalytic degradation of AO10 in the presence of 1.0Co/MW_A catalyst and Oxone® at different temperatures; b) Arrhenius plot of investigated process.

Table 1. Parameters calculated by fitting experimental data of catalytic degradation of AO10 with exponential fit (Eq. 1)

T [K]	k [min ⁻¹]	X [arb. unit]	E [arb. unit]	R^2	$\Sigma\sigma_i$
303	$1.67 \cdot 10^{-2} \pm$ $2.2 \cdot 10^{-3}$	$2.005 \pm$ 0.096	$0.099 \pm$ 0.022	0.989	$4.39 \cdot 10^{-2}$
313	$0.0251 \pm$ $7 \cdot 10^{-4}$	$1.972 \pm$ 0.022	$0.018 \pm$ 0.008	0.999	$2.72 \cdot 10^{-3}$
323	$0.0551 \pm$ $2.1 \cdot 10^{-3}$	$1.918 \pm$ 0.029	$0.0143 \pm$ 0.0083	0.998	$5.15 \cdot 10^{-3}$
333	$0.186 \pm$ $8 \cdot 10^{-3}$	$1.973 \pm$ 0.034	$0.001 \pm$ 0.0001	0.998	$4.87 \cdot 10^{-3}$

Where: X - amplitude of absorbance, E – endpoint of absorbance, k – first-order rate kinetics constant, R^2 – square of the coefficient of correlation, and $\Sigma\sigma_i$ – sum of squared deviations.

The process kinetics showed good agreement with the exponential fit with the squares of coefficients of correlation of ≥ 0.989 . Thus, the first-order kinetics for the investigated process was confirmed. Along with the increase of temperature of degradation process, the value of the first-order rate kinetics constant increased.

The activation energy E_a , obtained from slope of $\ln k_1$ plotted versus $1/T$ (Fig. 1b) has value of 1.16 kJ mol⁻¹. The obtained result was much lower than those previously reported in literature for similar processes of catalytic degradation of dyes [6].

CONCLUSION

The catalyst obtained by cobalt impregnation of acid activated montmorillonite was used for oxidative degradation of Acid Orange 10 dye in the presence of Oxone® at different temperature (303K - 333K). It was estimated that catalytic data obeyed first-order kinetics model, while calculated first-order rate constant (k_1) increased with temperature. The activation energy (E_a) for AO 10 degradation was evaluated using the k_1 values for investigated temperatures and Arrhenius equation. The obtained value for E_a of 1.16 kJ mol⁻¹ was much lower than those previously reported in literature for similar processes of catalytic degradation of dyes.

Acknowledgement

This work was financially supported by the Ministry of Education, Science and Technological Development of the Republic of Serbia (Grant No. 451-03-68/2020-14/200026).

REFERENCES

- [1] C. Fernández, M.S. Larrechi, M.P. Callao, Trends Anal. Chem., 2010, 29, 1202–1211.
- [2] Z. Vuković, A. Milutinović-Nikolić, J. Krstić, A. Abu-Rabi, T. Novaković, D. Jovanović, Mater. Sci. Forum, 2005, 494, 339-344.
- [3] Environmental Protection Agency, 1986. Method 9080 – Cation exchange capacity of soils (ammonium acetate). Available from <https://www.epa.gov/sites/production/files/2015-12/documents/9080.pdf> (verified May 2020).
- [4] F. Pinna, Catal. Today, 1998, 41, 129-137.
- [5] G. Lente, Deterministic kinetics in chemistry and systems biology. The dynamics of complex reaction networks, Springer. Briefs in Molecular Science, New York, 2015.
- [6] Z.C. Qin, Z.Z. Wang, Z.H. Feng, H. Z. Qi, Chinese Sci. Bull., 2011, 56, 3988-3992.

CORROSION PROTECTION OF STAINLESS STEEL BY ZrO₂ AND ZrO₂-TiO₂ SOL-GEL COATINGS

N. Radić¹, I. Stambolova², D. Stoyanova², N. Boshkov³ and N. Boshkova³

¹ *University of Belgrade, Institute of Chemistry, Technology and Metallurgy, Njegoševa 12, 11000 Belgrade, Serbia. (nradic@nanosys.ihm.bg.ac.rs)*

² *Institute of General and Inorganic Chemistry, Bulgarian Academy of Sciences, Acad. G. Bonchev Str, bl. 11, 1113 Sofia, Bulgaria*

³ *Institute of Physical Chemistry Acad. "R. Kaishev", Bulgarian Academy of Sciences, Acad. G. Bonchev Str, bl. 11, 1113 Sofia, Bulgaria*

ABSTRACT

Sol gel ZrO₂ and ZrO₂-TiO₂ composite coatings were deposited on stainless steel substrates and treated at 300 and 500°C, respectively. X-ray diffraction analyses (XRD) have proved the cubic ZrO₂ phase in zirconia coatings, while the composites coatings possess amorphous structure. The AFM analyses revealed typical island structure. It was registered that Zr-Ti composites are amorphous after treatment even at 500°C. The corrosion and electrochemical behavior of the samples was evaluated by potentiodynamic polarisation (PDP) under DC conditions. The coatings treated at 500°C exhibit higher corrosion resistance than the other sample types. This could be explained by the amorphous structure of the composites, which slows down the ionic and electron conductivity and the stabilizing role of ZrO₂ on the mechanical properties of titania.

INTRODUCTION

Nowadays, stainless steel is one of the most widely used structural material due to its good corrosion and heat resistance as well as mechanical properties. In chloride containing environments (salt, sea water, and soil) several phenomena such as stress induced corrosion, pitting corrosion, and intergranular corrosion often occurs. In order to solve this problem the researchers have applied surface modifications using various types of ceramic oxide coatings [1]. The nanosized TiO₂ has been used in different areas: solar energy conversion, fuel cells, paints and photocatalysts, due to its high chemical stability, availability and low cost [2]. Recently, titania films have been applied for protection of stainless steel [3]. Since TiO₂ has a low mechanical stability it is usually mixed with other oxides, especially ZrO₂. The preparation of corrosion resistant coatings by means of sol-gel method has several advantages such as higher degree of chemical purity and easier control of stoichiometry as well as the possibility to apply the layers onto large-sized substrates [4]. In the present work, the coatings based on ZrO₂ and ZrO₂-TiO₂ were deposited on stainless steel substrates from corresponding alkoxides as precursors using dip-coating technique and corrosion tests were performed.

METHODS

Zirconium precursor solution Z was prepared from ethanol solution of ZrOCl₂·8H₂O (p. a.) with small quantity of acetylacetone (AcAc). Another solution T was prepared using (Ti(OBu)₄) and AcAc dissolved in 2-propanol. For the preparation of zirconia-titania coatings both solutions were mixed in molar ratio Z:T = 50: 50. In both solutions polyethylene glycol (PEG) Mw=400 was added as structure directing agent. After ultrasonic cleaning of the substrates in ethanol for 10 min, they were immersed in each of the respective precursor solutions and withdrawn at a rate of 30 mm/min. After each application, the samples were air-dried, after which the temperature was raised up to 300 ° C for 1 h. The procedure was repeated 5 times, after which the samples were divided into 2 batches - treated at

300°C and 500°C, respectively. The ZrO₂ samples were designated as Z3 and Z5, while the composites ZrO₂-TiO₂ were marked as T3 and T5, respectively.

The phase compositions of the samples were studied by X-ray diffraction (XRD) with CuK α -radiation (Philips PW 1050 apparatus). The surface topography was investigated by means of Atomic Force microscope (AFM) (NanoScopeV system, Bruker Inc.) operating in tapping mode in air. The corrosion behavior and protective ability of the samples were studied and evaluated by application of potentiodynamic polarisation (PDP) curves at DC conditions. Potentiodynamic curves were performed for characterization of the anodic behavior and evaluation of the corrosion properties of the coatings at conditions of external polarization in the model test medium of 3,5% NaCl using a VersaStat 4 (PAR) unit. These tests were carried out at room temperature in a three-electrode electrochemical cell with a volume of 250 mL and at a scan rate of 1 mV/s.

RESULTS AND DISCUSSION

The XRD analyses of zirconia samples confirm the presence of low crystallized monoclinic ZrO₂ phase (JCPDS card 02-0464) with polycrystalline nature, while the composite coatings possess amorphous structure. The roughness of ZrO₂ coating (Z5) is 39 nm. After corrosion attack it retains almost the same value – about 45 nm. Coatings T3 and T5 have a significantly lower roughness compared to ZrO₂ ones: R_q is 4.9 nm and 15 nm, respectively (Figure 1).

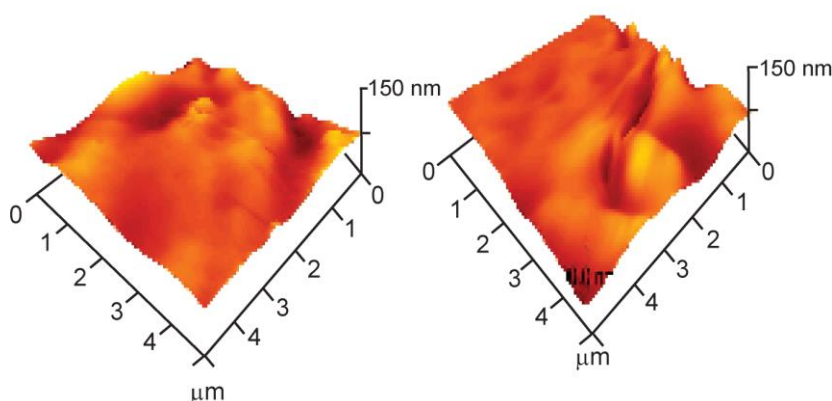


Figure 1. 3D topography of T5 coatings before(a) and after corrosive test(b)

After immersion in a corrosive medium, the roughness increases slightly. It is well visible that the corrosion potential of T5 (-660 mV) is more positive compared to T3 (-720 mV). (Figure 2). The corrosion current density value of T3 is $1,3 \cdot 10^{-5}$ A.cm⁻² and that of T5 – $1,4 \cdot 10^{-5}$ A.cm⁻², i.e. their corrosion current density values are very close in that case. Generally, it can be also observed that in the anodic area the course of the curves looks very close. Additionally, a "plateau" of the anodic current densities (width of ~ 500 mV) exists which means that in this potential area the dissolution process practically does not depend on the changes (shifts) of the potential.

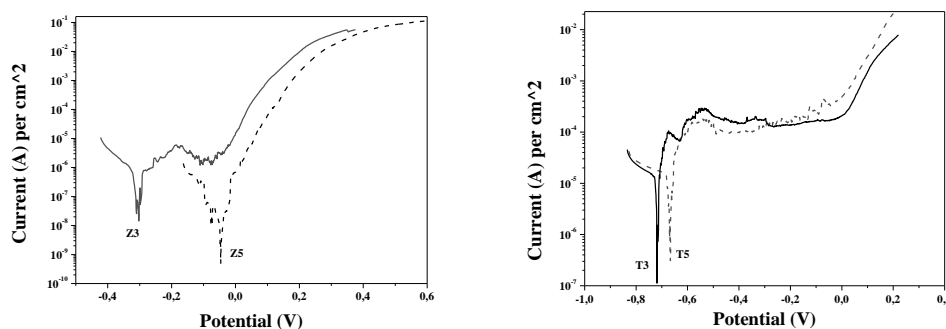


Figure 2.
Potentiodynamic
polarization curves
in 3.5% NaCl
solution of ZrO₂
(left) and ZrO₂-
TiO₂ coatings
(right)

Concerning the ZrO₂ coatings (Fig. 2, left) it can be registered that the corrosion potential of Z5 (-50 mV) is more positive compared to Z3 (-300 mV) which difference is greater compared to the other composite coatings. The corrosion current density value of Z3 is $7,4 \cdot 10^{-7}$ A.cm⁻² and that of Z5 is $1,9 \cdot 10^{-7}$ A.cm⁻². Contrary to the previous case, their anodic branches distinguish with steeper slopes (higher current densities) which means that the dissolution process will occur with increased mass damages under external anodic polarization. The lower corrosion protection properties of the ZrO₂ probably is due to the crystalline nature of the samples, which leads to deeper and more pronounced boundaries between individual grains, which accelerate the inter crystalline corrosion processes between the grains. On the contrary, the amorphous structure of the zirconia-titania composite films slows down the ionic and electron conductivity thus enhances their protection ability.

CONCLUSION

Corrosion resistant zirconia and zirconia-titania coatings were obtained by sol-gel method using inorganic zirconium precursors, containing polyethylene glycol. The XRD analyses revealed crystallized monoclinic ZrO₂ phase, while the composite coatings possess amorphous structure. The AFM analyses revealed typical island structure. After the corrosion tests significant signs of corrosion as cracks, craters etc. are not observable. The potentiodynamic measurements of ZrO₂ coatings have proved that the dissolution process will occur with increased mass damages under external anodic polarization. The higher corrosion stability of composite samples is probably due to amorphous structure and stabilizing effect of ZrO₂ on the mechanical properties of titania coatings.

Acknowledgement

The authors are grateful to the financial support of Bulgarian National Science Fund at the Ministry of Education and Science, Project No KP-06-H37/16 “New environmentally friendly one- and multi-layer coatings for corrosion protection of structural materials with wide application” and “Mono- and poly-component catalytic systems for waste water and polluted air purification from model contaminants”- Cooperation of the Bulgarian Academy of Sciences and the Serbian Academy of Sciences and Arts.

REFERENCES

- [1] D. Wang, G. Bierwagen, Sol gel coatings on metals for corrosion protection, *Progr. Org. Coat.* 2009, 64, 327-338
- [2] I. Stambolova, M. Shipochka, V. Blaskov, A. Loukanov, S. Vassilev, *J. Photochem. Photobiol. B*: 2012, 117, 19-26
- [3] A. Ghasemi, T. Shahrabi, A. Oskuie, H. Hasannejad, S. Sanjabei, *J. Alloys Comp.* 2010, 504, 237-242
- [4] A. Durán, Y. Castro, M. Aparicio, A. Conde & J. J. de Damborene, *Intern. Mater. Rev.* 2016, 175-192.

PREFERENTIAL CO OXIDATION IN HYDROGEN-RICH GASES OVER Ag CATALYSTS SUPPORTED ON DIFFERENT SUPPORTS

S. Todorova¹, H. Kolev¹, J-P. Holgado², A. Caballero²

¹Institute of Catalysis, Bulgarian Academy of Sciences, Acad. G. Bonchev St., Block 11, 1113 Sofia, Bulgaria

²Instituto de Ciencia de Materiales and Dpto. Química Inorgánica, CSIC-University of Sevilla, Sevilla, Spain

ABSTRACT

Silver samples were prepared by impregnation of different supports (SiO₂, Al₂O₃, ZSM-5 (Si:Al=100)) with aqueous solution of AgNO₃. The catalysts were characterized by X-ray diffraction, X-ray photoelectron spectroscopy, temperature-programmed reduction and high-resolution SEM. It is established that the support has an important effect on the Ag phase composition, oxidation state, particle size distribution, and interaction between silver and the support. Samples supported on SiO₂ show better performance in the preferential CO oxidation in hydrogen rich gases.

INTRODUCTION

The preferential CO oxidation in hydrogen rich gases (PROX) is a simple, efficient, and economic method for CO removal from hydrogen rich streams in comparison with other methods as membrane separation or pressure swing methods. The catalysts employed previously for CO removal are based mainly on noble metal such as Au, Pd, Ru and Rh and metal oxide catalysts, such as CuO–CeO₂ [1-3]. The decrease in reaction temperature and the search for more economic catalysts for PROX are challenging objectives for the near future. Among the members of IB group (Cu, Ag, Au) the silver has been scarcely investigated as a PROX catalyst in spite of its high activity in low temperature CO oxidation in absence of hydrogen [4-7]. Qu et al [8-10], showed that supported Ag is a promising catalyst for this reaction at low temperature. The catalyst showed their maximum CO conversion in the range 30 °C–50 °C. Also, they demonstrated that the particle size and the presence of sub-surface oxygen species are determinant for achieving high selectivity in the PROX reaction. In previous studies aimed at the investigation of carriers such as MnO₂, CeO₂ and SiO₂ and Ag loading [10], we found that the most active catalyst is 15Ag/SiO₂.

This paper is a part of our research targeting into the influence of the support on the properties of the silver catalysts in the PROX reaction.

SAMPLES AND METHODS

The 15 wt% silver was loaded on SiO₂, Al₂O₃, ZSM-5 (Si:Al=100) supports by impregnation with aqueous solution of AgNO₃. All samples were calcined and pretreated in pure O₂ 2h at 450°C before the catalytic test. The prepared catalysts were characterized by XRD, TPR, XPS, high resolution SEM, O₂-TPD and tested in PROX reaction (1% CO, 1% O₂, 45 % H₂ and N₂).

RESULTS AND DISCUSSION

According to the XRD data (Fig.1), silver is in a form of Ag⁰ (01-087-0719) in Ag/SiO₂ sample while X-ray patterns of Ag/ZSM-5 and Ag/Al₂O₃ contain line of Ag₂O, indicating the presence of small quantity of silver oxide. The particles size calculated using Sherrer equation are 47 nm for Ag/SiO₂, 27,5 nm for Ag/Al₂O₃ and 30 nm for Ag/ZSM-5.

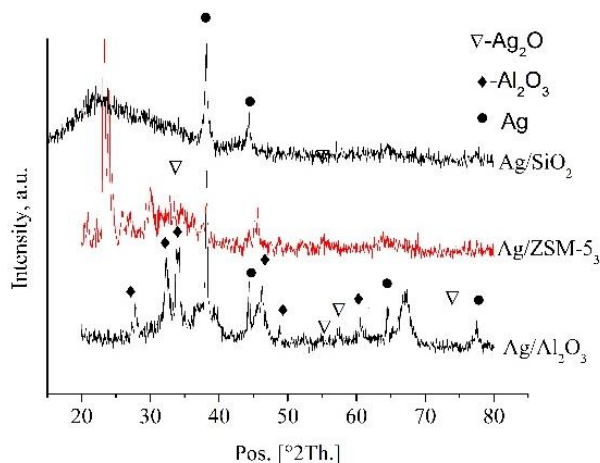


Figure 1. XRD data of all studied samples after treatment 2 h at 450 C in oxygen.

All these XRD data are with good coincidence with data from SEM. A bimodal distribution of sizes is found for Ag/Al₂O₃: the big particles (>50 nm) and particles with sizes in the range 10-20 nm are observed. In all the cases, particles are pseudospherical. The same is situation for Ag/ZSM-5: big particles above 30 nm and particles with sizes below 10 nm. For Ag/ZSM-5, not all the particles are pseudospherical, but some of them appear elongated.

Two reduction peaks are observed in the TPR profile of the samples supported on Al₂O₃ and SiO₂. Only one peak is observed for Ag-ZSM-5. According to the literature data the hydrogen consumption below 100°C is associated with the reduction of silver from the oxide-like species known in the literature as the form of adsorbed oxygen [12].

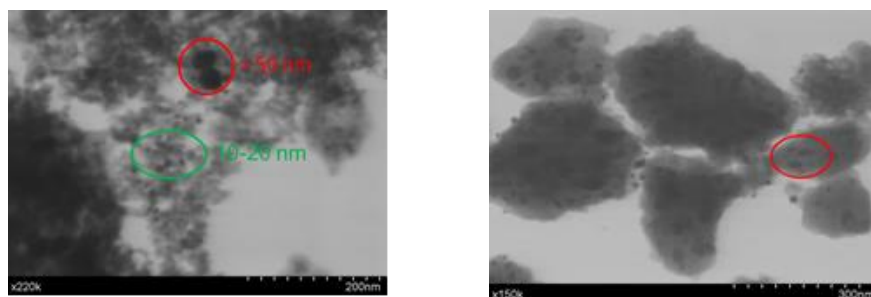


Figure 2. STEM image of Ag/Al₂O₃ (A) and Ag/ZSM-5 (B) after calcination

The reduction peak at 120 °C in the TPR spectra of Ag-ZSM-5 could be ascribed to the reduction of Ag₂O [12, 13]. XRD data pointed the presence of silver oxide in samples supported on Al₂O₃ and ZSM-5.

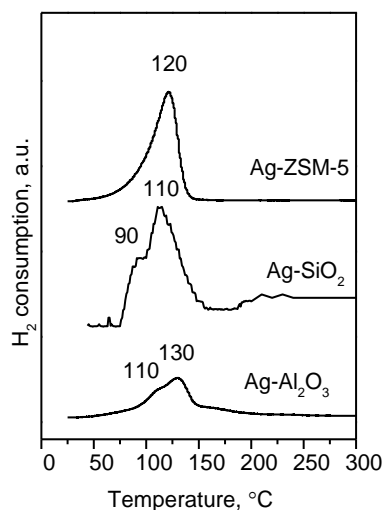


Figure 3. TPR spectra of spectra of all catalysts pretreated with O₂ at 450 °C

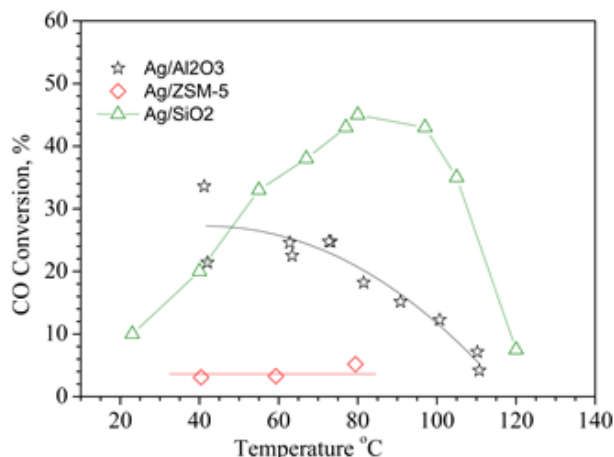


Figure 4. CO conversion degree with catalyst bed temperature on Ag supported on different supports

The preliminary catalytic tests using different supports showed that the catalyst with better performance is Ag/SiO₂. For all samples selectivity to CO₂ decreases with temperature increases, which is in coincidence with literature data and it is attributed to the fact that activation energy of H₂ oxidation was found to be considerably higher than that of CO oxidation. XPS experiments carried out on Ag/SiO₂ after pretreatment in oxygen show that both Ag⁺ and Ag⁰ are present on the surface [11].

CONCLUSION

It is established that the support has an important effect on the Ag phase composition, oxidation state, particle size distribution, and interaction between silver and the support. Samples supported on SiO₂ show better performance in the PROX.

Acknowledgement

This work was supported by the Bulgarian Ministry of Education and Science under the National Research Program E+: Low Carbon Energy for the Transport and Households, grant agreement D01-214/2018. The experiments were performed with equipment included in the National Infrastructure INFRAMAT D01-155/28.08. 2018.

REFERENCES

- [1] R.H. Liu, N.S. Gao, F. Zhen, Y.Y. Zhang, L. Mei, X.W. Zeng, *Chem. Eng. J.*, 225 (2013), 245–253;
- [2] F.G. Wang, K.F. Zhao, H.J. Zhang, Y.M. Dong, T. Wang, D.N. He *Chem. Eng. J.*, 242 (2014), 10–18;
- [3] L. Wang, J. Chen, A. Patel, V. Rudolph, Z. Zhu, *Appl. Catal. A: Gen.*, 447–448 (2012), 200–209;
- [4] S. Imamura, H. Yamada, K. Utani, *Appl. Catal. A: General*, 192 (2000) 221–226;
- [5] K. Song, S. Kang, S.D. Kim, *Catal. Lett.*, 49 (1997) 65–68;
- [6] Zhenping Qu, Shutian Zhou, Weicheng Wu, Can Li, Xinhe Bao, *Catal. Lett.*, 101 (2005) 21–26;
- [7] D.S. Afanasev, O.A. Yakovina, N.I. Kuznetsova, A.S. Lisitsyn, *Catal. Commun.* 22(2012) 43–47.
- [8] X Zhang, Z Qu, F Yu and Y Wang *Chin. J. Catal.* 34 (2013) 1277–90.

- [9] Z Qu, M Cheng and C Shi *J. Nat. Gas. Chem.* 14 (2005) 4–12.
- [10] Z Qu, M Cheng, C Shi and X Bao *Chin. J. Catal.* 23 (2002) 460.
- [11] S. Todorova, H.G Kolev, M.G. Shopska, G.B Kadinov, J.P. Holgado, A Caballero *Bulg. Chem. Comm.* (2018) 50 17-23.
- [12] G. V. Mamontov, T. I. Izaak, O. V. Magaev, A. S. Knyazev, and O. V. Vodyankina *Russ. J. Phys. Chem. A.* 85 (9) (2011) 1540–1545;
- [13] T. Furusawa, K. Seshan, J. Lercher, L. Lefferts, K. Aika, *Appl. Catal. B: Environmental*, **37** (2002) 205–216;

*D - Nonlinear Dynamics,
Oscillatory Reactions,
Chaos*

VARIOUS DYNAMICAL STATES IN THE BRAY- LIEBHAFSKY OSCILLATORY REACTION- FROM PERIODICITY TO INTERMITTENT CHAOS

A. Ivanović-Šašić¹, S. Maćešić², Ž. Čupić¹ and Lj. Kolar-Anić^{1,2}

¹*University of Belgrade, Institute of Chemistry, Technology and Metallurgy, National Institute of Republic of Serbia, Belgrade, 11000 Serbia (ana.ivanovic@nanosys.ihtm.bg.ac.rs)*

²*University of Belgrade, Faculty of Physical Chemistry, Belgrade, 11000 Serbia*

ABSTRACT

The Bray-Liebhafsky (BL) is one of the most analyzed oscillatory reaction both experimentally and numerically. Most of the experimentally obtained dynamical states of this reaction realized in a continuously fed well stirred tank reactor (CSTR) are successfully simulated. Beside others, numerous structured chaotic dynamical states were obtained between each two periodic states in the period doubling rout to chaos with respect to specific flow rate as the control parameter. It was an universal scenario throughout the whole mixed-mode region, as well as throughout other mixed-mode regions obtained under different initial conditions. However, the intermittent oscillations consistent of chaotic mixture of large-amplitude relaxation oscillations, grouped in bursts and small-amplitude sinusoidal ones or even quiescent parts between them known as gaps were also generated experimentally in the Bray–Liebhafsky reaction by varying different parameters such as temperature, flow rate or reactant concentrations under CSTR conditions. Nevertheless, it will be shown here that intermittent oscillations can be simulated by already published model of the BL reaction network.

Acknowledgement

Support from the Ministry of Education, Science and Technological Development of the Republic of Serbia (Grant Numbers 172015 and 45001, and Contract numbers 451-03-9/2021-14/200026 and 451-03-9/2021-14/200146), is gratefully acknowledged by AIŠ, SM, ŽČ and LjKA.

REFERENCES

- [1] W. C. Bray, *J. Am. Chem. Soc.*, **43** (1921), 1362.
- [2] W. C. Bray and H. A. Liebhafsky, *J. Am. Chem. Soc.*, **53** (1938), 38.
- [3] A. Z. Ivanović, Ž. D. Čupić, M. M. Janković, Lj. Z. Kolar-Anić, S. R. Anić, *Phys. Chem. Chem. Phys.*, **10** (2008), 5848.
- [4] Bubanja, I. N., Ivanovic-Šašić, A., Čupić, Ž., Anić, S., and Kolar-Anić, Lj. *Russ. J. Phys. Chem. A* **91** (2017), 2525.
- [5] Bubanja, I. N., Maćešić, S., Ivanović-Šašić, A., Čupić, Ž., Anić, S., and Kolar-Anić, Lj., *Phys. Chem. Chem. Phys.*, **18** (2016), 9770
- [6] Itana Nuša Bubanja, Ana Ivanovic-Šašić, Željko Čupić, Slobodan Anić and Ljiljana Kolar-Anić, *Frontiers in Chemistry*, **8** (2020), 560274

DYNAMICS OF HYDROXIDE-ION-DRIVEN AUTOCATALYTIC REACTION NETWORKS

Á. Tóth

University of Szeged, Department of Physical Chemistry and Materials Science, Szeged, Hungary

ABSTRACT

In biochemistry, hydrogen bonding is an essential structure forming factor, therefore function and activity of enzymes strongly depend on the pH of the medium. Acid-base equilibria are needed to maintain physiological pH to attenuate fluctuations in hydrogen ion concentration. Redox reactions generally change the pH and because their rate depends on it, they often autocatalytic with respect to hydrogen ion. The positive feedback can provide the fundamental nonlinearity necessary in controlling far-from-equilibrium systems. However, an autocatalytic reaction under the mild conditions of organic molecules must interact with the acid-base equilibria present. Imines, for example, hydrolyze with their rate depending on the pH of the solution. For those, where hydrolysis rate is negligible in acidic medium, we show that their clock reaction, both substrate-depleting and autocatalysis driven, is a result of the delicate interplay between the autocatalytic hydroxide ion production and the acid-base equilibria of the components. With the addition of a reaction removing hydroxide ion we can, in principle, obtain oscillatory dynamics in an open system.

A BZ ASSEMBLAGE WORKING FOR A DAY

F. Muzika, J. Górecki

*Institute of Physical Chemistry Polish Academy of Sciences,
Kasprzaka 44/52, 01-224 Warsaw, Poland. (fmuzika@ichf.edu.pl).*

ABSTRACT

Our work is focused on the experimental observation of Belousov-Zhabotinsky reaction oscillations in ferriin loaded Dowex 50w beads in a batch reactor open to the atmosphere. We investigated the conditions for the maximum oscillation lifetime and the change of wave regimes as the answer to the applied potential. The catalyst-free solution in the batch reactor is a mixture of concentrated sulphuric acid, NaBrO₃, and different ratios of malonic acid and 1,4 cyclohexanedione. We are using three types of cation Dowex 50w beads, namely type x2, x8, which differ by their level of crosslinking and cation exchange capacity. Their mesh size is 16-50 and 50-100. We investigate the influence of such parameters as the distance between a bead and the electrode and the value of electrode potential on the oscillations. Moreover, we study the character of oscillations in the function of the number of adjacent beads and the layout of the beads. The reduction of formation of CO₂ bubbles has been achieved by choice of Dowex beads type, solution composition, and usage of acetone. We report oscillations with stable amplitude and varying period and lifetime over 19 hours and oscillations with decreasing amplitude with a lifetime of 10 hours. The investigated media and beads type seem to be promising candidates for experimental realization of chemical computers based on interacting oscillators.

INTRODUCTION

Ever since we record ideas, we can find stories about the creation of something artificial, which can perform tasks like humans. One example is a clay creature build to fulfil given duties described in an old Egyptian story [1], a being made of soil though not liquid or purely organic in its nature. The need for thinking, automatic machines able to perform repetitive tasks on assembly lines, and control such processes appeared at the end of the 19th century. One of the first “liquid computers” was the hydraulic algebraic machine, followed by hydraulic integrators, mappers, and up to fluid logic in 1960, later followed by Belousov-Zhabotinsky computers (1985), other types of reaction-diffusion computers. These developed through liquid brain robots and maze solvers into current techniques of liquid marbles, vesicles, and droplet logic systems [2]. There was a parallel development of non-liquid computers, which eventually proven themselves in WWII due to Alan Turing’s computer breaking Enigma code [3]. Our current focus is to deepen techniques proposed by Kuze et al. [4] using electric potential and incorporating groups of connected beads to assess their dynamic behavior in reaction to electric potential as a first step towards creating marble logic assemblages [5] with an electric interface.

EXPERIMENTAL

Used chemicals: Deionized water. Sulphuric acid 95% from Chempur Poland, malonic acid 99% from Sigma-Aldrich (Japan), 1,4 cyclohexanedione 98% from Sigma-Aldrich (Germany), NaBrO₃ 99% from Fluka (Netherlands). Ferriin solution 0.025M from Sigma-Aldrich (Switzerland). Acetone 99.5% from Avantor Performance Materials Poland S.A. Dowex 50w-x2/x8 hydrogen form (50-100) mesh/(16-50) mesh from Sigma-Aldrich (USA).

Beads are loaded prior to the experiment, 50w-x2 are loaded with $4.66 \cdot 10^{-9}$ mol/bead in average, 50w-x8 are loaded with $1.89 \cdot 10^{-7}$ mol/bead in average. Ambient temperature is maintained at 23°C. The experimental setup is shown in Fig. 1. The glass reactor, which is, prior to its usage thoroughly washed with acetone to remove/inhibit remaining Br ions [5], is filled with catalyst free reaction solution of volume 5ml. Ferroin loaded beads are placed inside reactor with BZ solution near the electrode, using different spatial arrangements. Colour change of beads due to BZ reaction occurrence is recorded on CCD camera using lenses with 110x magnification. Resulting videos are cut and decomposed into frames by Ffmpeg program. Frames are put into stack using ImageJ program, resliced and put into montages of reslices. Each montage is divided into three colour channels, red, green, blue, where green channel is equivalent to brightness channel with values of brightness 0-255. The brightness channel of each montages is analyzed for oscillation periods per each bead.

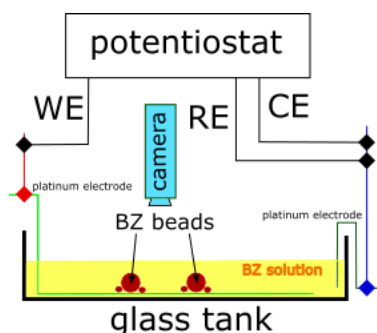


Figure 1. Schematic diagram of experimental setup. WE – working electrode, RE- reference electrode, CE – counter electrode.

RESULTS AND DISCUSSION

Electric potential creates activator species for BZ reaction, HBrO_2 , according to reaction: $\text{BrO}_3^- + 2e^- + 3\text{H}^+ \rightarrow \text{HBrO}_2 + \text{H}_2\text{O}$. The negative potential on working electrode attracts activator molecules, while positive potential is attracting Br^- [4]. According to our observations, after application of positive potential, bubbles occur near electrode and on beads much more frequently. Using different than glass reactor lead into change of colour and structural integrity of whole reactor body, due to sorption of bromide ions. These inhibitor ions were later diffusing into new solutions inhibiting the BZ reaction completely. This effect could be avoided by washing the reactor with acetone for period of 7+ days before the reactor body became unusable, and on some occasions, damaged by mere CO_2 bubbles. Each experiment consists of several electric potential changes, while keeping the original batch solution. Therefore, each presented part of experiment shows initial concentration of species in negative time values in subscript. The first experiment shows 2nd change of potential in the row (potential change from 0V to -1.5V) with two beads not touching the electrode and a ring of seven coupled beads touching the working electrode by bead number 3, see Fig. 2A).

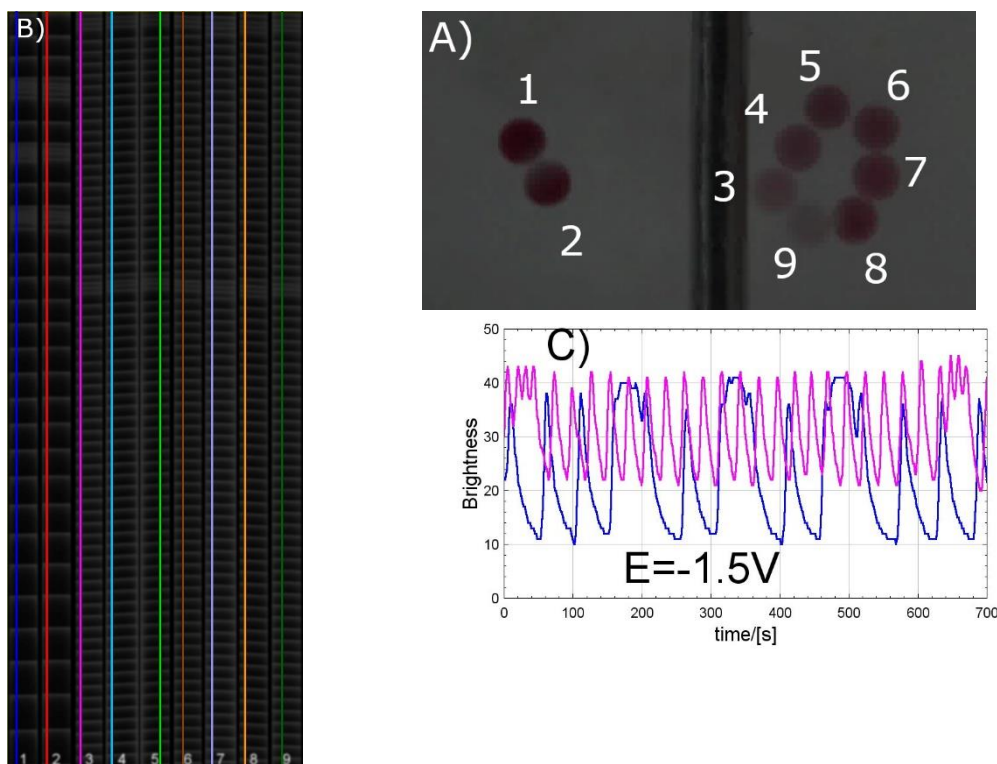


Figure 2. The first experiment showing 2nd change of potential, from 0V to -1.5V, time length 1799 seconds, A) layout of beads Dowex 50w- x2 (50-100) mesh and beads numbering, B) space-time plot of brightness intensity in each bead, C) oscillation in beads number 1(blue) and 3(magenta), colour respective to B), zoomed time. $[\text{NaBrO}_3]_{(-1800\text{s})}=0.45\text{M}$, $[\text{malonic acid}]_{(-1800\text{s})}=0.4\text{M}$, $[\text{H}_2\text{SO}_4]_{(-1800\text{s})}=0.9\text{M}$. Diameter of the electrode is 0.43mm.

Interesting part of this particular experimental set is observation of bursts in both groups of beads, see Fig 2B). Beads number 1 and 2 oscillate with much slower pace, 60 seconds at the beginning and slowing down to 80 seconds in the end of this experiment, bursts occur as 6, 5 and 6 peaks with 150 second period between beginning of each burst. For seven coupled beads, general oscillation period is holding at 28 ± 2 seconds whole experimental set, which burst go with period 600 seconds and three peaks, see Fig. 2C).

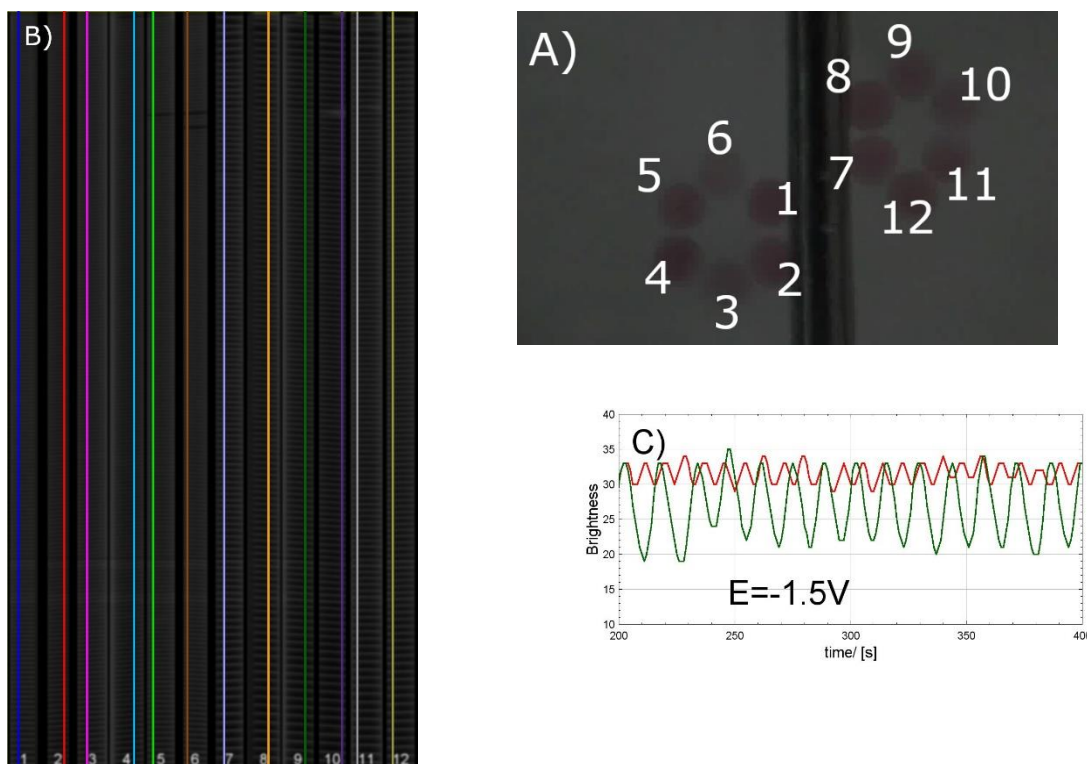


Figure 3. The second experiment showing 2nd change of potential, from 0V to -1.5V, time length 1794 seconds. A) layout of beads Dowex 50w-x2 (50-100) mesh and beads numbering B) space-time plot of brightness intensity in each bead, C) oscillation in beads number 2(red) and 9(green), colour respective to B), zoomed time. $[\text{NaBrO}_3]_{(-1900\text{s})}=0.45\text{M}$, $[\text{malonic acid}]_{(-1900\text{s})}=0.4\text{M}$, $[\text{H}_2\text{SO}_4]_{(-1900\text{s})}=0.9\text{M}$. Diameter of the electrode is 0.43mm

The second experiment shows two equivalent group of 6 beads, see Fig. 3B). While the left group starts the experimental cascade without applied potential with period 30 seconds and slowing down to 50 seconds, right group goes into spiral waves oscillating with period 19 ± 2 seconds. After negative potential is applied, left group goes into superspiral waves with period 8 ± 2 slowing down eventually to 13 ± 2 seconds, right group is uninfluenced in its period and spiral wave behaviour, see Fig. 3B). With shorter period, amplitude of oscillations is smaller, see Fig. 3C).

The third experiment shows combination of two Dowex types, type x2 (16-50)mesh and type x8 (50-100) mesh, while it is also possible to see diminishing amplitude of brightness by naked eye, see Fig. 4A). While both groups operate with same period 17 ± 2 seconds, see Fig. 4B), C), both their current group behaviour and their evolution behaviour differs. The left group operates as quadruple spiral wave with center in bead 1, while it started as a wave coming from bead number 5, went through changing of origin of the wave and into a triple spiral wave with center in bead 1. Positive electric potential had no effect on this group. The right group has origin of waves simultaneously in bead 6 and 10, while it changes to bead 6 and 11 after application of positive potential. The central beads operate over 19 hours, while the small bead up 10 hours, while their brightness amplitude is continuously decreasing.

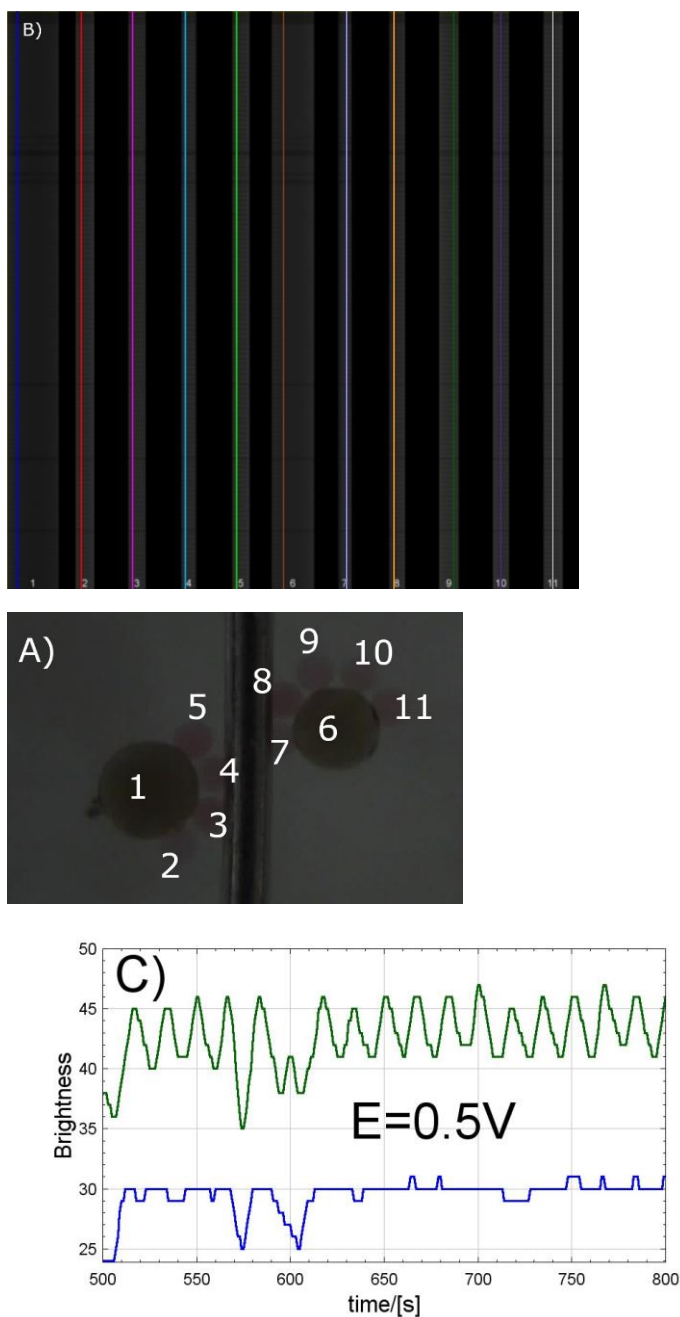


Figure 4. The third experiment showing 8th change of potential, from 0V to 0.5V, time length 2035 seconds. A) layout of beads Dowex 50w -x8 (12-50)mesh(bigger ones)/ -x2 (50-100)mesh and beads numbering, B) montage of eighth set in the row with applied potential 0.5V, B) space-time plot of brightness intensity in each bead, C) oscillation in bead numbers 1(blue) and 9 (dark green), colour respective to B). [NaBrO₃]_(-13000s)=0.45M, [malonic acid]_(-13000s)=0.4M, [H₂SO₄]_(-13000s)=0.9M. Diameter of the electrode is 0.43mm.

The fourth experiment deals again with combination of different type of beads, but also uses equimolar solution of malonic acid and 1,4 cyclohexanedione, see Fig. 5A). The small beads oscillate with period 10 ± 1 seconds while the big beads start around 200 second period and shorten the period to 20 ± 2 seconds by the end of the experimental set, see Fig. 5B), C). The long period appears as blinking eye and ends up as wave patterns looking like a blossomed rose. The wave in left group of beads starts with separate oscillations of beads 3 and 4 and changes into a travelling wave from bead 5 without applied potential, after application of negative potential, the origin of waves go to beads 3,4 touching the electrode. The right group is more dynamic, starting separate oscillations of beads 8 and 9 while forming the origin of travelling waves in beads 7 and 11 without applied potential. After the application of negative potential, the travelling wave originates from beads 7 and 10, then transforms into spiral wave with center in bead 6, and then traveling waves occur and originate from bead 8 and 9 touching the electrode.

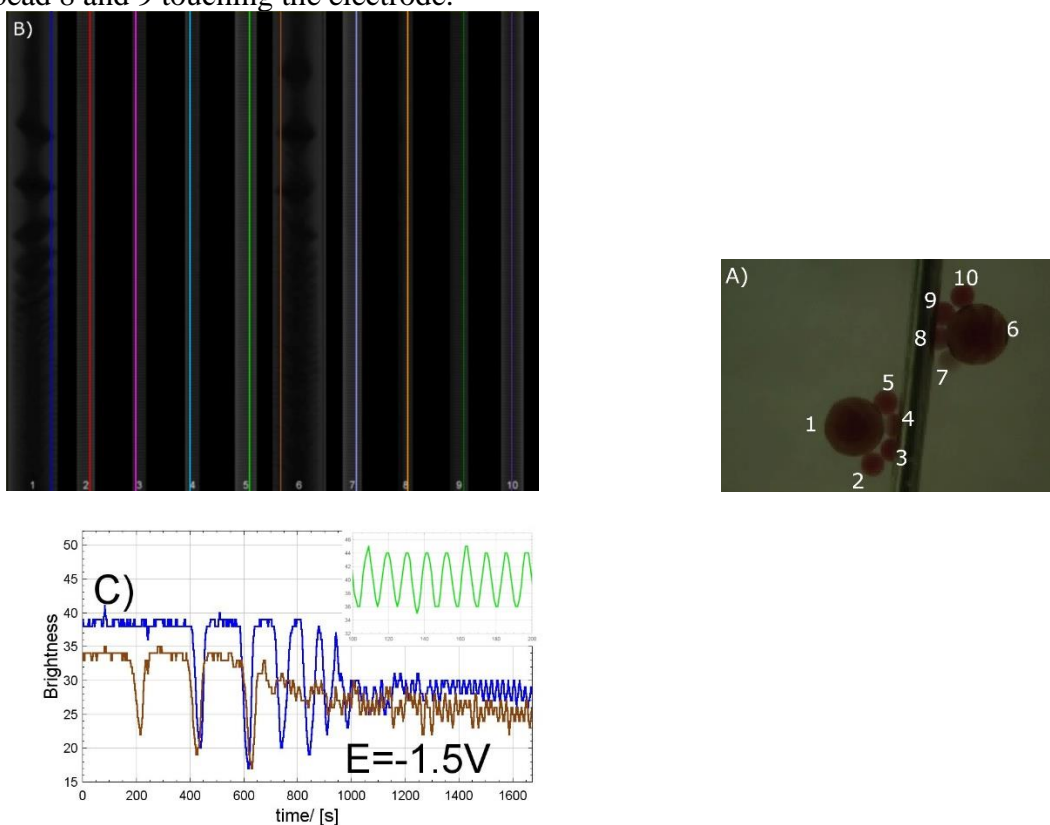


Figure 5. The fourth experiment showing 2nd change of potential, from 0V to -1.5V, time length 1674 seconds. A) layout of beads Dowex 50w -x8 (12-50)mesh (bigger ones)/ -x2 (50-100)mesh and beads numbering, B) space-time plot of brightness intensity in each bead, C) oscillation in bead numbers 1 (blue), 6(brown) and 5(green-zoomed), colour respective to B). $[\text{NaBrO}_3]_{(-1900\text{s})} = 0.45\text{M}$, $[\text{malonic acid}]_{(-1900\text{s})} = 0.2\text{M}$, $[\text{1,4-cyclohexanedione}]_{(-1900\text{s})} = 0.2\text{M}$, $[\text{H}_2\text{SO}_4]_{(-1900\text{s})} = 0.9\text{M}$. Diameter of the electrode is 0.43mm.

CONCLUSION

Experimental sets with various layouts have been performed while electric potential has been applied. We have observed bursts, travelling waves, and group behaviour like spiral waves inside BZ bead assemblage. Most importantly, the electrode can be the origin of wave signal, as shown in the work by Kuze et al. [4]. The repeatability of such process seems to be currently limited, influenced by layout of BZ assemblage and type of BZ solution. Ion exchange resins with smaller mesh value,

having more ferroin loaded, seem to be able to operate more than 19 hours without creation of CO₂ bubbles compared to resins with high mesh value and less ferroin loaded, which can oscillate up to 10 hours.

We will focus further into new layouts and higher concentration of ferroin loaded into beads to increase its oscillation/operation lifetime to get closer to liquid marble logic technique [5] operating more than a day.

Acknowledgement

This publication is part of a project that has received funding from the European Union's Horizon 2020 research and innovation programme under the Marie Skłodowska-Curie grant agreement No. 847413

Scientific work published as part of an international co-financed project founded from the programme of the Minister of Science and Higher Education entitled "PMW" in the years 2020 - 2024; agreement no. 5005/H2020-MSCA-COFUND/2019/2

REFERENCES

- [1] Vachala, Břetislav. Člověk ze země. Golem ve staroegyptské povídce. Vachala, Břetislav. Dějiny a současnost. Kulturně historická revue. 31, č. 3, (2009,) s. 25-27
- [2] Adamatzky A. Phil. Trans. R. Soc. B **374**: 20180372 (2019). DOI: 10.1098/rstb.2018.0372
- [3] Copeland, B.J. "Ultra". Encyclopedia Britannica, 4 Apr. 2019, <https://www.britannica.com/topic/Ultra-Allied-intelligence-project>. Accessed 31 May 2021.
- [4] Kuze M., Horisaka M., Suematsu N. J., Amemiya T., Steinbock O. and Nakata S., J. Phys. Chem. A **123**, 4853–4857 (2019).
- [5] Gorecki J., Bose A., Frontiers in Chemistry **8**, 2020, 580703; DOI=10.3389/fchem.2020.580703
- [6] Somboon T., Wilairat P., Müller S.C. and Kheowan On-U., Phys. Chem. Chem. Phys. **17**, 2015, 7114-7121

IMPACT OF D₂O ON SPONTANEOUS OSCILLATORY PEPTIDIZATION OF SELECTED α -AMINO ACIDS

A. Fulczyk¹, E. Łata¹, E. Talik², T. Kowalska¹ and M. Sajewicz¹

¹*Institute of Chemistry, University of Silesia, 9 Szkolna Street, 40-006 Katowice, Poland
(teresa.kowalska@us.edu.pl)*

²*Department of Physics of Crystals, University of Silesia, 75 Pułku Piechoty 1, 41-500 Chorzów, Poland*

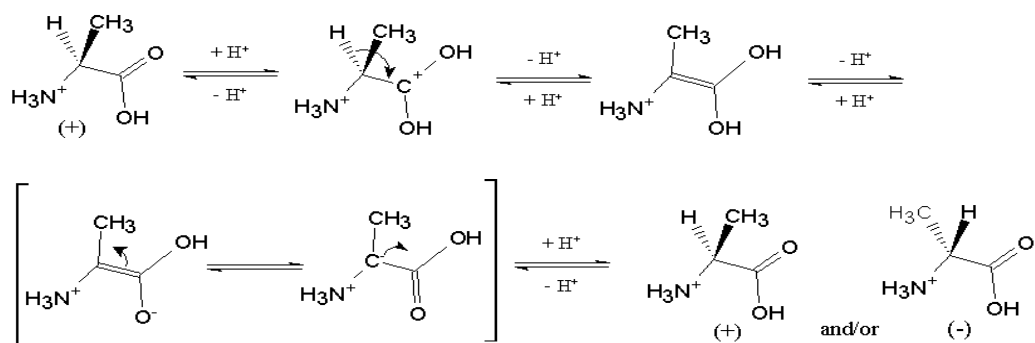
ABSTRACT

Earlier, we have demonstrated spontaneous oscillatory chiral inversion and spontaneous oscillatory peptidization running with proteinogenic α -amino acids in the parallel. These processes might have been of certain importance in the prebiotic history of Earth, i.e., in the period of chemical evolution. In fact, spontaneous oscillatory peptidization can be regarded as a sequence of elementary steps which in certain sense simulate Life. On the other hand, it is a well recognized fact that heavy water (D₂O) considerably slows down life processes of all organisms and when dispensed in considerable amounts to organisms on a higher level of cellular organization (e.g., to mammals), it can exert even a lethal effect. As proteinogenic α -amino acids can be regarded as the smallest building blocks of all living matter, now we are interested to find out, if D₂O can hamper spontaneous oscillatory peptidization of proteinogenic α -amino acids. In our study, we focused on three endogenous (L-Cys, L-Pro, L-Ala) and two exogenous (L-Met, L-Hyp) α -amino acids and we managed to demonstrate that D₂O strongly inhibits spontaneous oscillatory peptidization of all these compounds. It is noteworthy to add that out of five α -amino acids investigated so far, which can be divided into two groups of endogenous and exogenous species, two endogenous species (L-Cys and L-Pro) undergo spontaneous oscillatory peptidization following the circadian rhythm, whereas two exogenous ones (i.e., L-Met and L-Hyp) do not. The third endogenous species (L-Ala) first undergoes two initial oscillations which are damped (not periodic) and the oscillatory changes are on a scale of about 10 hours (as estimated with use of the Fourier Transform approach) and after that, the system reaches a steady state.

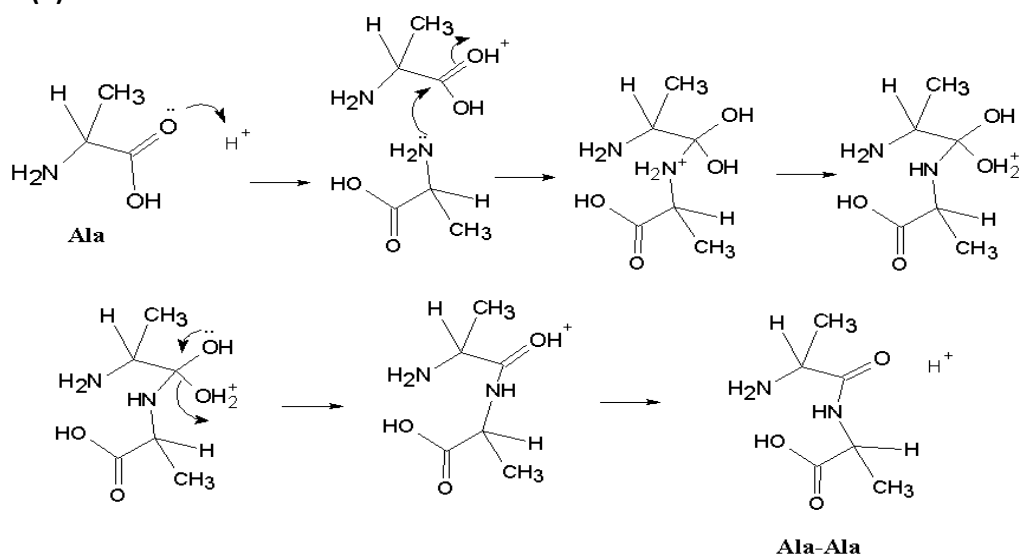
INTRODUCTION

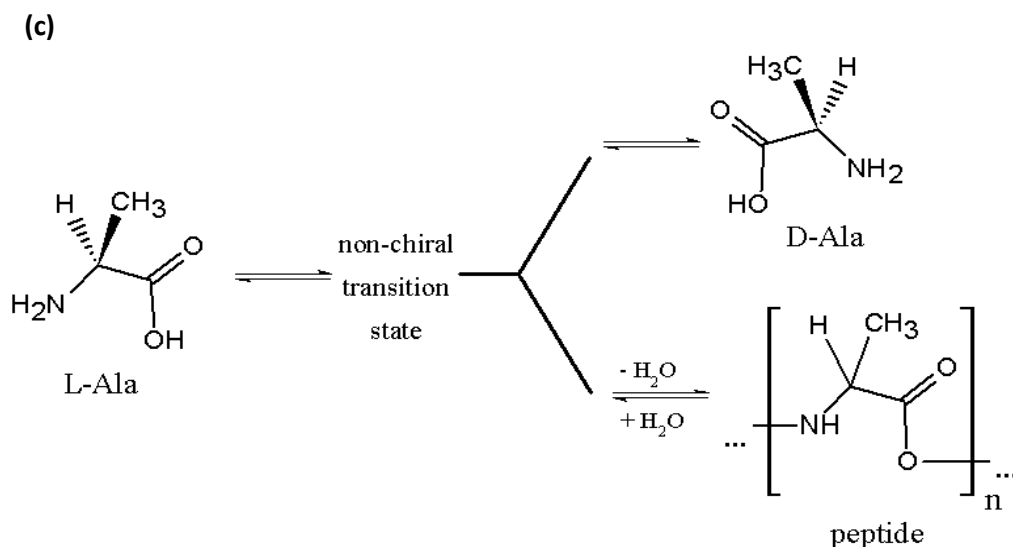
Our studies (e.g., [1-5]) were the first ones to demonstrate spontaneous oscillatory chiral inversion and spontaneous oscillatory peptidization of α -amino acids running in the parallel in the aqueous-organic solutions. These two processes can be schematically presented upon an example of L-Ala (Scheme 1).

(a)



(b)





Scheme 1. (a) Molecular mechanism of chiral inversion for L-Ala. (b) Molecular mechanism of peptidization for L-Ala. (c) General scheme of the mechanisms of chiral inversion and peptidization of L-Ala running in the parallel (adapted from [15]).

It seems quite probable that these two processes might have been running in the parallel in the so-called “Primordial Broth” also, i.e., in the period of chemical evolution preceding on Earth biological evolution and independently postulated in the 1920s by A. Oparin and J.B.S. Haldane in their theories on the origin of Life. As proteinogenic α -amino acids can be regarded as the smallest building blocks of all living matter, it seemed interesting to find out, if D₂O can hamper spontaneous oscillatory peptidization of proteinogenic α -amino acids in the way roughly resembling obstruction (or even termination) of life of most organisms, and particularly of those with a higher level of cellular organization [6-10].

In order to verify our assumption as to the hampering effect of D₂O on spontaneous oscillatory peptidization of proteinogenic α -amino acids, we selected three exogenous (L-Cys, L-Pro, L-Ala) and two endogenous (L-Met, L-Hyp) species and dissolved them in a liquid mixture of organic solvent + X, 70:30 (v/v), where organic solvent: acetonitrile or methanol, and X: H₂O + D₂O, with the percent contribution of D₂O equal to 0, 5, 10, 20, and 30%. The α -amino acid solutions in pure D₂O were also considered. Then these solutions were stored for certain periods of time in the darkness at 21±0.5 °C and the experiments to check an impact of D₂O were carried out with use of the high-performance liquid chromatography (HPLC), mass spectrometry (MS) and scanning electron microscopy (SEM).

METHODS

In our experiments, the non-chiral high-performance liquid chromatographic (HPLC) system was used to demonstrate spontaneous oscillatory peptidization of L-Cys, L-Met, L-Pro, L-Hyp, and L-Ala in an absence of heavy water. To this effect, the oscillatory concentration changes of the monomer of a given species were recorded, which occurred due to the oscillatory peptidization–depeptidization process. In order to investigate an impact of D₂O on peptidization, mass spectrometry (MS) and scanning electron microscopy (SEM) were employed. MS was used to assess the dynamics and formation yields of the lower soluble peptides depending on proportions of D₂O in a given solution

and the spectra were recorded after 7 days sample storage period in the darkness at 21 ± 0.5 °C. The obtained mass spectra were in the first instance regarded as fingerprints which allowed instantaneous visual comparison of the number and intensity of signals. SEM was used to assess the dynamics and formation yields of the higher insoluble peptides and micrographs were recorded for the same samples after one months sample storage period in the darkness at 21 ± 0.5 °C. The obtained micrographs were also regarded as fingerprints which allowed visual comparison of the sizes and yields of insoluble peptides, also depending on proportions of D_2O in a given solution.

RESULTS AND DISCUSSION

The results of our investigations are summarized in a series of five papers, each focusing on a single α -amino acid (L-Cys, [11]; L-Met, [12]; L-Pro, [13]; L-Hyp, [14]; and L-Ala, [15]).

The HPLC registration of spontaneous oscillatory concentration changes of each α -amino acid monomer was carried out in relatively short time intervals of ca. 15 min, providing quasi-kinetic results in form of the time series reflecting dynamics of the peptidization–depeptidization process spontaneously running in a given solution. In that case, either MeOH + H₂O, or ACN + H₂O, 70:30 (v/v) was used as a solvent. Further, the time series valid for each individual α -amino acid was Fourier-transformed in order to detect periodicity of the observed oscillations (or otherwise). For the sake of example, in Fig. 1 we present the time series and the Fourier transform curve valid for L-Pro.

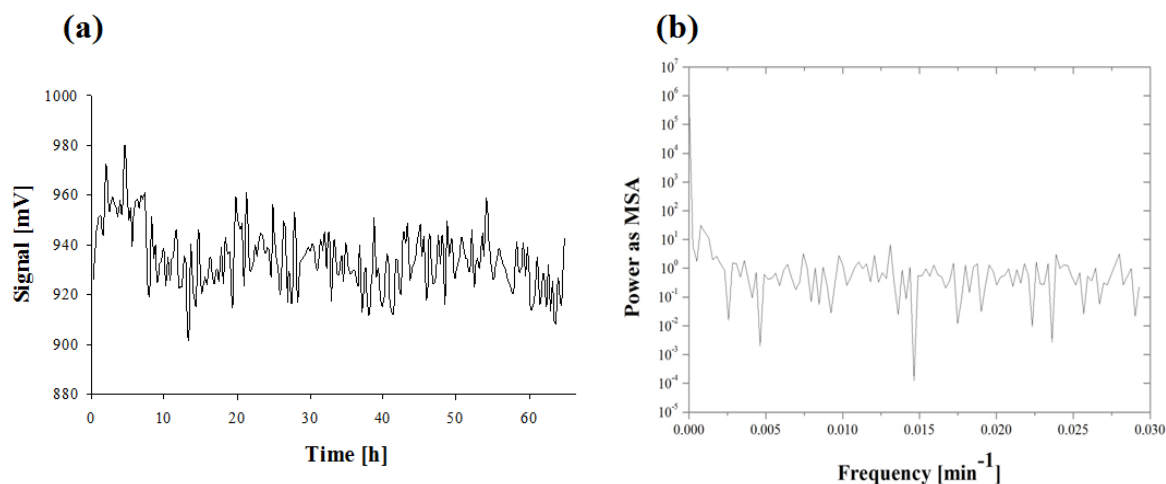


Figure 1. (a) Time series of chromatographic peak heights at $t_R \approx 5.46$ min for the monomeric L-Pro in MeOH + H₂O, 70:30 (v/v) recorded by means of HPLC with the ELSD detector in the time range from 0 h to 65 h sample storage time. (b) Power spectrum calculated from the time series of the chromatographic peak heights shown in Fig. 1(a) (adapted from [13]).

From the Fourier transformation of the time series valid for the investigated α -amino acids it came out that with two endogenous species (L-Cys and L-Pro) the circadian rhythm of the oscillatory concentration changes was observed as equal to ca. 24 h and ca. 20.8 h, respectively, and with two exogenous species (L-Met and L-Hyp) no periodicity was observed. With the third endogenous species (L-Ala), the oscillatory pattern was still different. After two initial and damped (not periodic) oscillations which lasted for about 10 hours, the investigated system reached a steady state.

Dissolution of each investigated α -amino acid in pure heavy water resulted in an almost complete extinction of the oscillations, as confirmed by means of HPLC. In the search for a better nuanced insight in susceptibility of each individual α -amino acid to the $H^+ \leftrightarrow D^+$ ion exchange in the environment of heavy water, with each compound we prepared a series of solutions in a liquid mixture

of organic solvent + X, 70:30 (v/v), where organic solvent: acetonitrile or methanol, and X: H₂O + D₂O with the percent contributions of D₂O equal to 0, 5, 10, 20, and 30%. For the sake of comparison, the α -amino acid solutions in pure D₂O were also checked. An impact of different proportions of D₂O on the dynamics and yields of the soluble lower peptides was assessed with use of MS, and the analogous impact of different proportions of D₂O on the dynamics and yields of the insoluble higher peptides was assessed with use of SEM. Irrespective of the measuring technique employed, in both cases the obtained instrumental results (either mass spectra, or micrographs) were in the first instance considered as fingerprints which allowed rapid visual inspection and comparison of the effects exerted by D₂O. Selected results are presented in Figs 2 and 3.

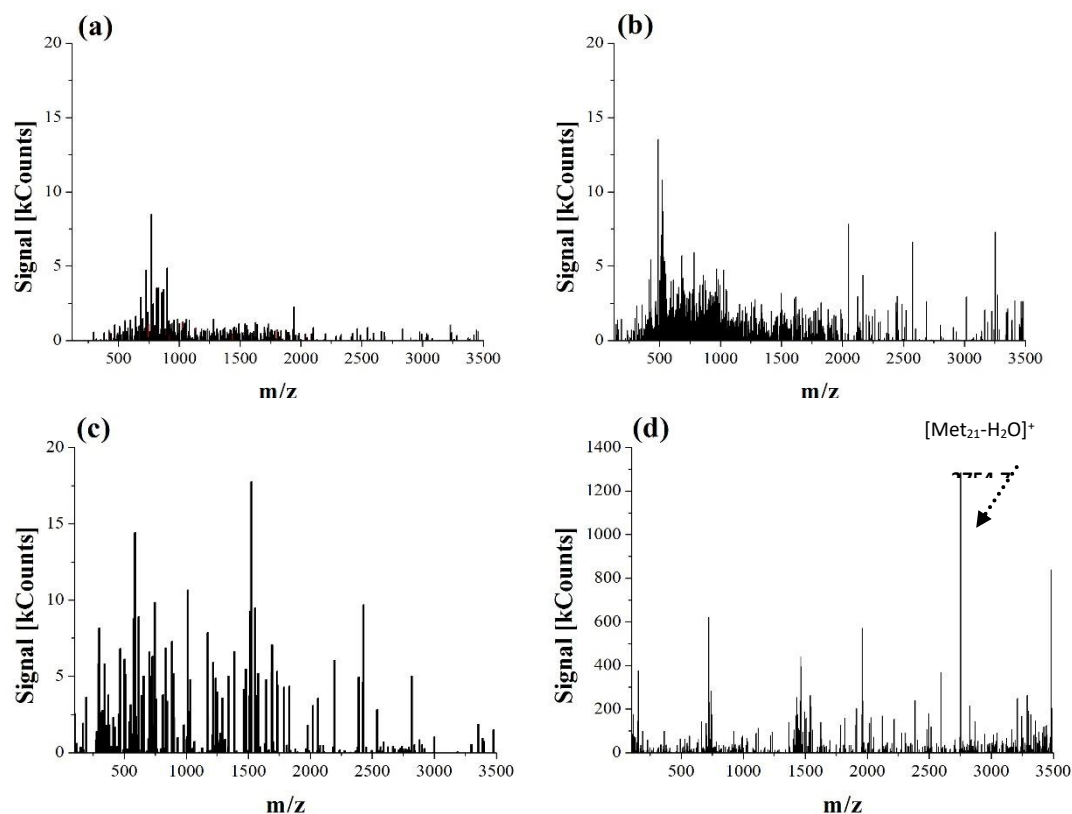


Figure 2. Mass spectra recorded for L-Met dissolved in ACN + X, 70:30 (v/v), where X: the binary mixture of H₂O + D₂O in the changing volume proportions; (a) 5% D₂O; (b) 20% D₂O; (c) 30% D₂O and (d) L-Met dissolved in pure D₂O (adapted from [12]).

From the results obtained with use of MS, the following conclusions were drawn: For the two sulfur-containing α -amino acids (L-Cys and L-Met), the higher were the proportions of D₂O in solution, the higher were the yields of soluble lower peptides [11, 12]. For L-Hyp and L-Ala, the higher were the proportions of D₂O in solution, the lower were the yields of soluble lower peptides [14, 15]. For L-Pro, initially the yields of soluble lower peptides were declining and at the 10% D₂O level, practically full extinction of soluble lower L-Pro-derived peptides was observed, but from the 20% D₂O level on, these yields rather unexpectedly started growing [13]. From the results obtained with use of SEM, the following observation was made: D₂O inhibits formation of insoluble higher peptides with each investigated compound and this effect is at least semi-quantitatively dependent on the contents of D₂O in solution.

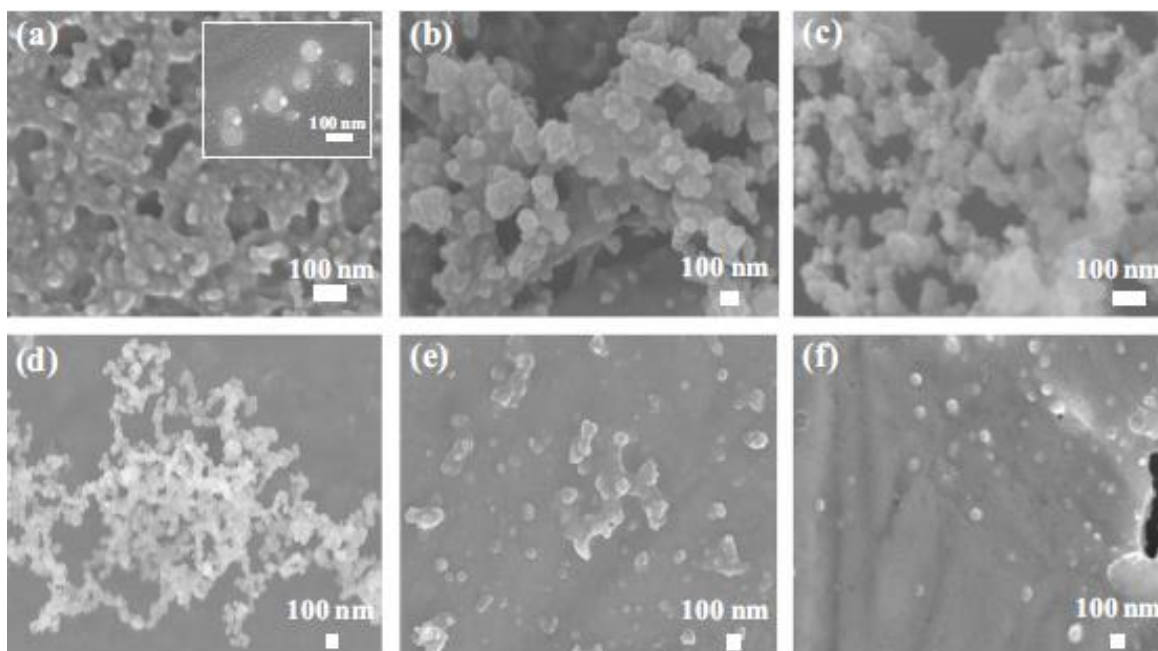


Figure 3. Scanning electron micrographs recorded for the L-Cys-derived peptides retrieved from the samples dissolved in ACN + X, 70:30 (v/v), where X: the binary mixture of H₂O + D₂O in the changing volume proportions; (a) 0% D₂O, $\times 100,000$; (b) 3% D₂O, $\times 50,000$; (c) 10% D₂O, $\times 100,000$; (d) 20% D₂O, $\times 30,000$; (e) 30% D₂O, $\times 35,000$; (f) 100% D₂O, $\times 37,000$ (adapted from [11]).

CONCLUSIONS

Main conclusion derived from the results presented in a series of papers ([11-15]) is that heavy water inhibits spontaneous oscillatory peptidization of all five proteinogenic α -amino acids and strongly affects peptide yields. An extent of this inhibition remains in relation to chemical structure of the test compounds and to the percentage contribution of D₂O. With all α -amino acids considered, the amount of 30% D₂O in solution is enough to practically extinguish all spontaneous peptidization. This proportion (30% D₂O) remains in agreement with the findings of some research groups claiming that replacement of H₂O in a mammalian organism with 30% D₂O can exert lethal effect. It was also established that inhibition of peptidization is stronger with these amino acids which in their structure incorporate the pyrrolidine ring and the secondary $>$ NH amino group (L-Pro and L-Hyp) than with those with the primary amino group, $-NH_2$ (L-Cys, L-Met).

Further it was established that two endogenous species (L-Cys and L-Pro) follow the circadian rhythm of the oscillatory concentration changes (equal to ca. 24 h and ca. 20.8 h, respectively), and two exogenous species (L-Met and L-Hyp) show no periodicity of its oscillations. With the third endogenous species (L-Ala), the oscillatory pattern is still different. After two initial and damped (not periodic) oscillations which last for about 10 hours, the investigated system reaches a steady state.

REFERENCES

- [1] M. Sajewicz, R. Piętka, A. Pieniak, T. Kowalska, *Acta Chromatogr.*, 2005, **15**, 131-149
- [2] M. Sajewicz, M. Matlengiewicz, M. Leda, M. Gontarska, D. Kronenbach, T. Kowalska, I.R. Epstein, *J. Phys. Org. Chem.*, 2010, **23**, 1066-1073
- [3] M. Sajewicz, M. Gontarska, D. Kronenbach, M. Leda, T. Kowalska, I.R. Epstein, *J. Syst. Chem.*, **1**:7 (2010); DOI:10.1186/1759-2208-1-7
- [4] M. Sajewicz, M. Dolnik, T. Kowalska, I.R. Epstein, *RSC Adv.*, 2014, **4**, 7330-7339
- [5] A. Maciejowska, A. Godziek, E. Talik, M. Sajewicz, T. Kowalska, I.R. Epstein, *J. Chromatogr. Sci.*, 2016, **54**, 1301-1309
- [6] J.J. Katz, H.L. Crespi, D.M. Czajka, A.J. Finkel, *Am. J. Physiol.*, 1962 **203**, 907-913
- [7] P. Bachner, D.G. McKay, D. Rittenberg, *Proc. Natl. Acad. Sci. USA*, 1964, **51**, 464-471
- [8] C.P. Richter, *Proc. Soc. Exp. Biol. Med.*, 1976, **152**, 677-684
- [9] C.P. Richter, *Proc. Natl. Acad. Sci. USA*, 1977, **74**, 1295-1299
- [10] U. Kanto, A.J. Clawson, *J. Nutrit.*, 1980, **110**, 1840-1848
- [11] A. Fulczyk, E. Łata, M. Dolnik, E. Talik, T. Kowalska, M. Sajewicz, *Reac. Kinet. Mech. Cat.*, 2018, **125**, 555-565
- [12] A. Fulczyk, E. Łata, E. Talik, T. Kowalska, M. Sajewicz, *Reac. Kinet. Mech. Cat.*, 2019, **126**, 939-949
- [13] A. Fulczyk, E. Łata, E. Talik, T. Kowalska, M. Sajewicz, *Reac. Kinet. Mech. Cat.*, 2019, **128**, 599-610
- [14] A. Fulczyk, E. Łata, E. Talik, T. Kowalska, M. Sajewicz, *Reac. Kinet. Mech. Cat.*, 2020, **128**, 17-28
- [15] A. Fulczyk, E. Łata, E. Talik, T. Kowalska, M. Sajewicz, *Reac. Kinet. Mech. Cat.*, submitted

A METHODOLOGY FOR VERTICAL TRANSLATION BETWEEN MOLECULAR AND ORGANISMAL LEVEL IN BIOLOGICAL FEEDBACK LOOPS

J. W. Dietrich^{1, 2}

¹Lab XU44, Endocrinology Department, Medical Hospital I, Bergmannsheil University Hospitals, Ruhr University of Bochum, Bochum, NRW, Germany (johannes.dietrich@ruhr-uni-bochum.de)

²Ruhr Center for Rare Diseases (CeSER), Bochum, NRW, Germany.

ABSTRACT

Feedback loops are among the primary network motifs in living organisms, ensuring survival via homeostatic control of key metabolites and physical properties. However, from a scientific perspective, their characterization is unsatisfactory since the usual modelling methodology is incompatible with the physiological and biochemical basis of metabolic networks. Therefore, any “vertical translation”, i.e. the study of the correspondence between molecular and organismal levels of causality, is difficult and in most cases impossible.

As a viable solution, we demonstrate an alternative modelling platform for biological feedback loops that is based on key biochemical principles, including mass action law, enzyme kinetics, binding of mediators to transporters and receptors, and basic pharmacological properties. Subsequently, we show how this framework can be used for translating from molecular to systems-level behaviour.

Basic elements of the proposed modelling platform include Michaelis-Menten kinetics defining nonlinear dependence of the output $y(t)$ on an input signal $x(t)$ with the Hill-Langmuir equation $y(t) = G * x(t)^n / (D + x(t)^n)$, non-competitive inhibition for linking stimulatory and inhibitory inputs with $y(t) = G + x_1(t) / ((D + x_1(t)) * (1 + x_2(t) / K_I))$ and processing structures for distribution and elimination.

Depending on the structure of the feedback loop, its equifinal (steady-state) behaviour can be solved in form of polynomials, with a quadratic equation for the simplest case with one feedback loop and a Hill exponent of 1, and higher-grade polynomials for additional feedback loops and/or integer Hill exponents > 1 . As a companion to the analytical solution, a flexible class library (CyberUnits) facilitates computer simulations for studying the transitional behaviour of the feedback loop.

Unlike other modelling strategies in biocybernetics and systems biology, this platform allows for straightforward translation from the statistical properties of single molecules on a “microscopic” level to the behaviour of the whole feedback loop on an organismal “macroscopic” level. An example is the Michaelis constant D , which is equivalent to $(k_{-1} + k_2) / k_1$, where k_1 , k_{-1} and k_2 denote the rate constants for the association and dissociation of the enzyme-substrate or receptor-hormone complex, respectively. From the perspective of a single molecule the rate constants represent the probability (per unit time) that the corresponding reaction will happen in the subsequent time interval. Therefore $1/k$ represents the mean lifetime of the complex. Very similar considerations apply to the other described constants of the feedback loop.

In summary, this modelling technique renders the translation from a molecular level to a systems perspective possible. In addition to providing new insights into the physiology of biological feedback loops, it may be a valuable tool for multiple disciplines of biomedical research, including drug design, molecular genetics and investigations on the effects of endocrine disruptors.

INTRODUCTION

In life sciences, the function of organisms uses to be described on several and distinct levels of causality, ranging from the behaviour of single elementary particles to the performance of whole living creatures and even social interactions. While approaches remaining on one level only are able to successfully provide physiological insights and while they are usable for practical purposes, including clinical reasoning and epidemiological decision making, the translation between the levels of causality is difficult and, in most cases, virtually impossible [1]. A methodology bridging this gap is highly needed, but previous approaches were unsatisfactory [2].

An example of this dilemma that is both typical and significant is feedback control systems. Feedback loops are fundamental network motifs and information processing structures in living organisms, providing means for homeostatic control of vital parameters including the concentration of key metabolites and important physical properties. Unfortunately, the usual methodology for the mathematical description of feedback loops as linear time-invariant (LTI) systems is not readily compatible with biochemical insights and theories [2]. It is, therefore, impossible to draw conclusions from physicochemical processes to the corresponding response of the organism and vice versa.

Here, we suggest an alternative modelling platform for systems biology that is able to establish compatibility between the distinct levels of causal description, thereby providing a framework for vertical translation between molecular and organismal levels of interaction. Additionally, we demonstrate how this framework can be exploited to translate between different levels of causality.

METHODS

Based on (but not restricted to) requirements of endocrinology and metabolism we developed a metamodel, containing elements that can be mapped to empirically testable biochemical and physiological data [3, 4]. This modelling platform has been successfully applied to different hormonal feedback loops, including thyroid homeostasis, the hypothalamus-pituitary-adrenal axis and insulin-glucose homeostasis [3, 5, 6]. Its main elements include (1) coupling the concentration of a substance (e.g. a hormone or metabolite) to its elimination and distribution and modelling this process as analog signal memory with intrinsic adjustment (ASIA element) [7], (2) saturation kinetics based on the Michaelis-Menten-Hill formalism representing enzymatic processes, receptor kinetics and other forms of signal transduction mechanisms [8, 9] and (3) non-competitive inhibition for the description of negative feedback [8, 9].

ASIA elements describe the steady-state concentration of a substance with

$$y_{\infty} = \frac{\alpha x_{\infty}}{\beta}$$

as a function of an input signal x_{∞} , the inverse of the volume of distribution (α) and a clearance exponent (rate constant) β that depends with

$$\beta = \frac{\ln(2)}{t_{1/2}}$$

on the half-life of the respective substance [7]. The transitional behaviour is described with

$$y(t) = \frac{\alpha x(t)}{\beta} + K e^{-\beta t}.$$

Michaelis-Menten (MiMe) kinetics describe the nonlinear dependence of an output signal $y(t)$ on an input signal $x(t)$ with

$$y(t) = \frac{Gx(t)}{D + x(t)}$$

They are a well-characterised universal formalism for modelling enzymatic processes and receptor-mediated signal-transduction mechanisms.

The combined effect of stimulating (x_1) and inhibiting (x_2) input signals can be modelled as non-competitive divisive inhibition (NoCoDI) process with

$$y(t) = \frac{Gx_1(t)}{[D + x_1(t)] \left[1 + \frac{x_2(t)}{K_I} \right]}$$

with K_I being the dissociation constant of x_2 [3, 4].

Putting these elements together delivers a closed formalism (MiMe-NoCoDI loop) describing a nonlinear feedback control system based solely on elements that are mappable to basic biochemical or pharmacological properties (Fig. 1). The constant parameters of the feedback loop belong to different classes of physical properties: G_1 , G_2 and G_3 are extensive properties, i.e. they depend on the size of the organism, whereas D_2 is an intensive property, independent of the body mass or size.

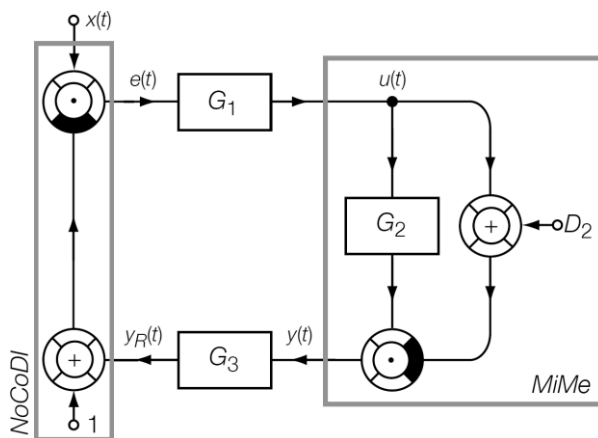


Figure 1. The smallest and simplest implementation of a MiMe-NoCoDI loop. G_3 corresponds to $1/K_I$ in the equation describing non-competitive inhibition. x : setpoint; e : control error; u : manipulated variable; y : controlled variable; y_R instantaneous value.

Combining the equations for the single blocks and solving for a selected signal delivers e.g. for the controlled variable $y(t)$

$$y(t) = \frac{G_1 G_2 x(t)}{D_2 + D_2 G_3 y(t) + G_1 x(t)}$$

and for the manipulated variable $u(t)$

$$u(t) = \frac{G_1 x(t)}{1 + \frac{G_3 G_2 u(t)}{D_2 + u(t)}}$$

as recursive solutions for the temporal development of the system [3].

In order to arrive at an equifinal solution describing the steady-state behaviour of the systems (in terms of input and constant parameters only), we define

$$a = D_2 G_3,$$

$$b = D_2 + G_1 x(t)$$

and

$$c = -G_1 G_2 x(t),$$

so that the equation for y may be expressed as

$$ay(\infty)^2 + by(\infty) + c = 0$$

with the two solutions

$$y(\infty)_{1,2} = \frac{-b \pm \sqrt{b^2 - 4ac}}{2a}.$$

The positive solution represents the fixpoint (set point) of the feedback control system [3]. For k parallel feedback loops we obtain the recursive universal equation

$$u(t) = \frac{G_1 x(t)}{\prod_{k=1}^n \frac{G_{2k+1} G_{2k} u(t)}{D_{2k} + u(t)}}$$

with the equifinal solution

$$a_m u^m(\infty) + a_{m-1} u^{m-1}(\infty) + \dots + a_1 u(\infty) + a_0 = 0,$$

where $m = k + 1$ [3].

As an extension of this mathematical formulation, a class library was developed for the programming languages Object Pascal and S that facilitates the development of simulation programs for this kind of information processing structure. It has been made available as an open-source project (CyberUnits Bricks) [10]. The class hierarchy is shown in Fig. 2. Non-visual classes support numeric simulation, visual classes the generation of block diagrams.

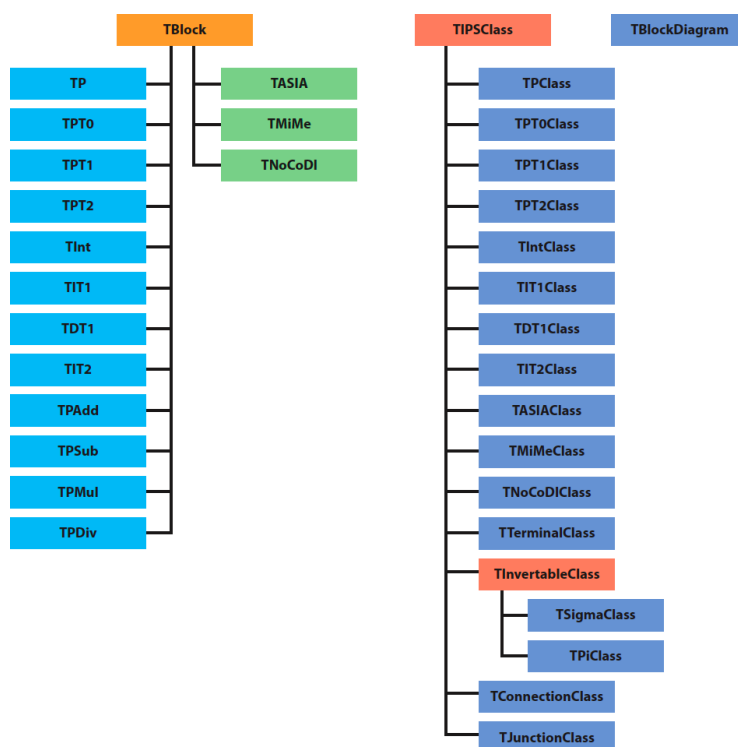
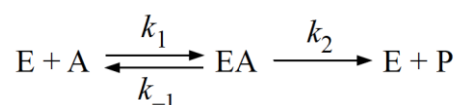


Figure 2. Class hierarchy of the CyberUnits Bricks library. Non-visual classes are shown on the left (descendants of *TBlock*), visual classes on the right (descendants of *TIPSClass*).

RESULTS AND DISCUSSION

Parameters representing extensive properties can be derived from body size. If determined with biochemical research they can be translated to whole-body values with appropriate scaling factors, representing e.g. the mass or volume of organs or compartments. Examples include the gain factors (G) of the presented equations and the α parameters of ASIA elements.

The process of vertical translation is more complex for intensive properties, e.g. dissociation constants (D and K_I coefficients of the specified equations). It is important to note that D is a lumped parameter that incorporates the rate constants for the reactions involved in enzyme kinetics:



with

$$D = \frac{k_{-1} + k_2}{k_1}$$

This can be used for translating from molecular properties to the whole-body behaviour of a feedback loop. In the example of the simple MiMe-NoCoDI loop shown in Fig. 1, this can be achieved by redefining a and b as

$$a = \frac{k_{-1} + k_2}{k_1} G_3$$

and

$$b = \frac{k_{-1} + k_2}{k_1} + G_1 x(t)$$

and using these parameters for the above-mentioned quadratic equation. Fig. 3 shows how the controlled variable depends on selected rate constants.

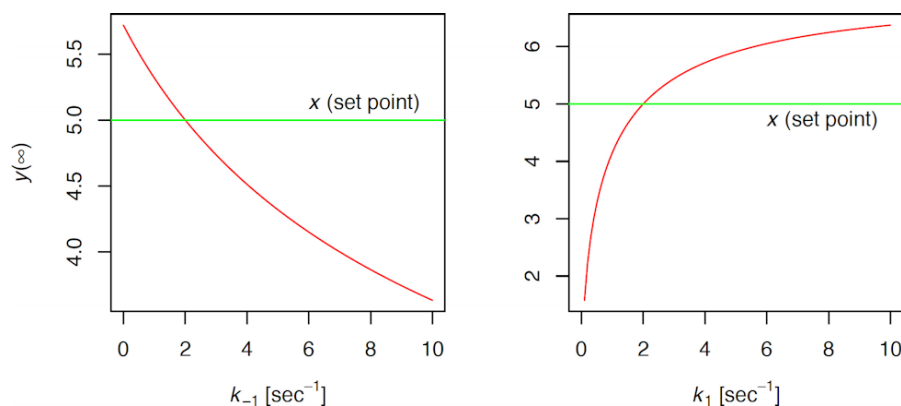


Figure 3. Controlled variable y in relation to the rate constants for the dissociation of the enzyme-substrate complex.

After appropriate rescaling, the same relationships also apply to statistical properties on the level of single molecules, since the rate constants can be expressed as the probability of the corresponding equation occurring in the subsequent time interval or as the inverse mean lifetime of the complex. By translating properties of a feedback loop to rate coefficients it is possible to verify the conclusions with computer simulations of molecular reactions, e.g. based on the Gillespie algorithm [11, 12], and to integrate this theory with the methodology of stoichiometric network analysis [13].

Some of the results shown here are still partly preliminary and require future research for a more systematic investigation and validation of the vertical relationships between causal levels.

If this method can be successfully implemented it might be a valuable tool, e.g. for the research on endocrine disruptors and genetic syndromes and for the early phases of drug design, which is more and more supported by computational methods.

CONCLUSION

The method presented here allows for translating between molecular processes and the behaviour of embedding feedback loops on the level of the whole organism, a previously unsolved challenge. This is accomplished by “high-fidelity” modelling of feedback control systems based on a parametrically isomorphic approach and by applying the insights to the statistical properties of chemical reactions. The new methodology may be a useful tool for multiple fields of biomedical research.

Acknowledgement

JWD is co-owner of the intellectual property rights for the patent “System and Method for Deriving Parameters for Homeostatic Feedback Control of an Individual” (Singapore Institute for Clinical Sciences, Biomedical Sciences Institutes, Application Number 201208940-5, WIPO number

WO/2014/088516). The author wants to express his gratitude to Ljiljana Kolar-Anić (Faculty of Physical Chemistry, University of Belgrade) and Željko D Čupić (Department of Catalysis and Chemical Engineering, University of Belgrade) for valuable discussions and suggestions.

REFERENCES

- [1] Noble R, Tasaki K, Noble PJ, Noble D: Biological Relativity Requires Circular Causality but Not Symmetry of Causation: So, Where, What and When Are the Boundaries? *Front Physiol* 2019, 10:827.
- [2] Tretter F, Wolkenhauer O, Meyer-Hermann M, Dietrich JW, Green S, Marcum J, Weckwerth W: The Quest for System-Theoretical Medicine in the COVID-19 Era. *Front Med (Lausanne)* 2021, 8:640974.
- [3] Dietrich JW, Boehm BO: Equilibrium behaviour of feedback-coupled physiological saturation kinetics. In: *Cybernetics and Systems 2006. Volume 1*, edn. Edited by Trappl R. Vienna: Austrian Society for Cybernetic Studies; 2006: 269-274.
- [4] Dietrich JW, Boehm BO: Die MiMe-NoCoDI-Plattform: Ein Ansatz für die Modellierung biologischer Regelkreise. *GMS - German Medical Science* 2015(60. Jahrestagung der GMDS e.V.):DocAbstr. 284.
- [5] Berberich J, Dietrich JW, Hoermann R, Muller MA: Mathematical Modeling of the Pituitary-Thyroid Feedback Loop: Role of a TSH-T3-Shunt and Sensitivity Analysis. *Front Endocrinol (Lausanne)* 2018, 9:91.
- [6] Dietrich JW, Tesche A, Pickardt CR, Mitzdorf U: Thyrotropic Feedback Control: Evidence for an Additional Ultrashort Feedback Loop from Fractal Analysis. *Cybernetics and Systems* 2004, 35(4):315-331.
- [7] Dietrich JW: Signal Storage in Metabolic Pathways: The ASIA Element. *kybernetiknet* 2000, 1 (3, 2000):1-9.
- [8] Cornish-Bowden A: *Fundamentals of Enzyme Kinetics*. Weinheim: Wiley-Blackwell; 2012.
- [9] Gutfreund H: *Kinetics for the Life Sciences*. Cambridge: Cambridge University Press; 1995.
- [10] Dietrich JW: CyberUnits Bricks. In., 1.1.1 edn; 2015-2021.
- [11] Cao Y, Samuels DC: Chapter 5 Discrete Stochastic Simulation Methods for Chemically Reacting Systems. In: *Computer Methods, Part A*. edn.; 2009: 115-140.
- [12] Gillespie DT: A General Method for Numerically Simulating the Stochastic Time Evolution of Coupled Chemical Reactions. *Journal of Computational Physics* 1976, 22:403-434.
- [13] Cupic Z, Macesic S, Novakovic K, Anic S, Kolar-Anic L: Stoichiometric network analysis of a reaction system with conservation constraints. *Chaos* 2018, 28(8):083114.

NULLCLINES. A SIMPLE EXPLANATION OF COMPLICATED PHENOMENA

G. E. Schmitz

Université Libre de Bruxelles, Ecole Polytechnique, CP165/63, Av. F. Roosevelt 50, 1050 Brussels, Belgium

ABSTRACT

To simply explain the sometimes-surprising results obtained with acidic solutions of hydrogen peroxide, iodate and iodine, we study the properties of the concentration space. The shape of the trajectories is determined by the slow manifold which can be reduced to a one-dimensional curve, the nullcline. In iodate-rich systems, it has the classic S-shape which explains the Bray-Liebhafsky oscillations, their domain of existence and the effect of additions of different reagents. In low iodate systems, it can be more complicated and explains the unusual behavior of the iodine oxidation by hydrogen peroxide. The observed effects of oxygen are qualitatively explained by its effect on the nullcline.

KEYWORDS

Slow manifold, nullcline, hydrogen peroxide, iodate, iodine.

MOTION IN THE CONCENTRATIONS SPACE

Figure 1 shows an example of the evolution of iodine and iodide concentrations during Bray-Liebhafsky (BL) oscillations. Instead of representing changes over time, it is also possible to represent the concentration of iodide as a function of that of iodine as in Fig. 1d. This article will show the interest of such a representation. The composition of the system is represented by a point in the space of concentrations. Its evolution is represented by a curve, the trajectory. It is impossible to visualize it because it has as many dimensions as the number of chemical compounds, but we can represent its projection on a plane. Figure 1d is the projection of the trajectory of the BL system on the iodide-iodine plane. Its shape suggests that it is attracted by a limit cycle but with a decreasing size because the H_2O_2 concentration decreases over time (Fig.1c).

To study the properties of the concentration space, we use the concepts of the SNA (Stoichiometric Network Analysis) [1, 2]. There are two types of compounds, those which appear in a stoichiometric equation, the external compounds, and those which do not appear, the internal compounds. During the BL reaction, there are alternately periods where iodate is reduced to iodine according to reaction R and periods where iodine is oxidized to iodate according to reaction O. Iodate, iodine and hydrogen peroxide are external compounds.

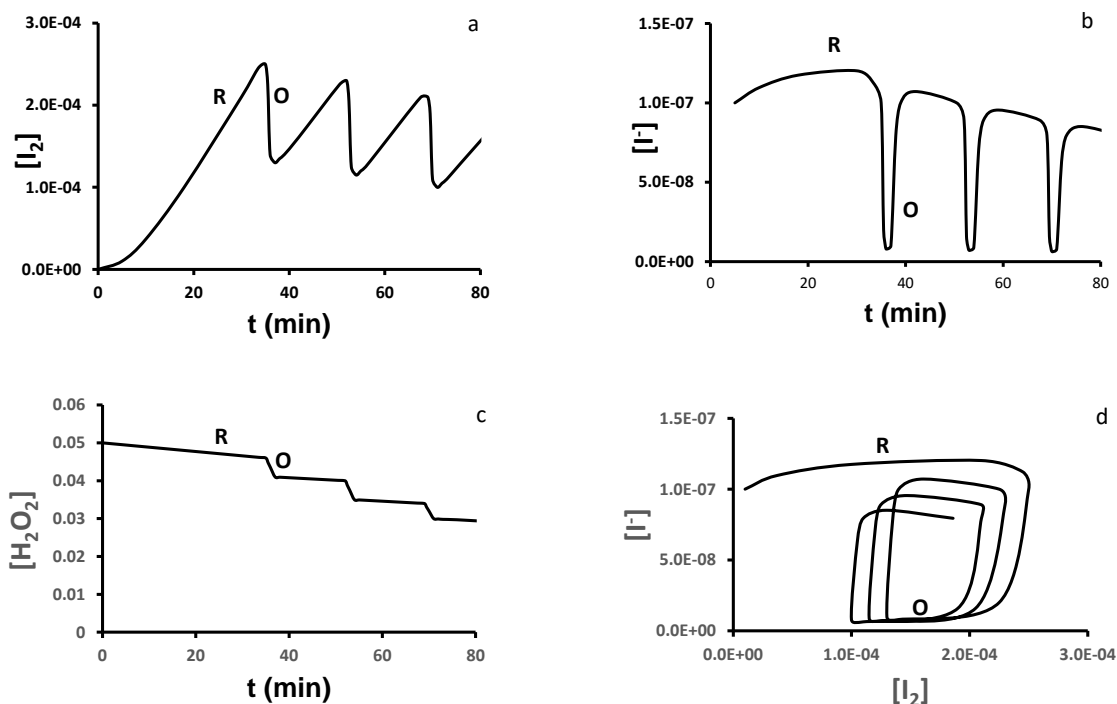
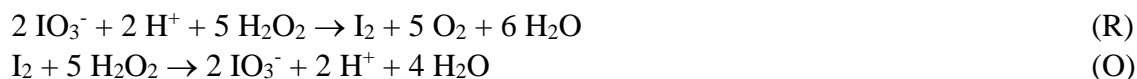


Figure 1. BL oscillations at 60°C, $[\text{HClO}_4]_0 = 0.0625 \text{ M}$, $[\text{NaIO}_3]_0 = 0.10 \text{ M}$, $[\text{H}_2\text{O}_2]_0 = 0.05 \text{ M}$.



These reactions have a complicated mechanism involving several intermediates, the internal compounds in much lower concentrations than those appearing in the R and O reactions. This difference in concentrations scales results in differences in time scales. If we start from any point in the concentration space, the system rapidly evolves towards a hypersurface where we obtain one of the R or O reactions. This is the slow manifold. The different time scales correspond to a fast evolution towards the slow manifold followed by a much slower evolution on it. This slow evolution is usually that which one observes experimentally. We do not distinguish between "critical manifold" and "slow manifold" [3, 4] but note that the trajectory, even strongly attracted by the slow manifold, does not follow it exactly.

The concentration $[\text{H}^+]$ changes little during the BL reaction and it can be assumed that it is constant. The concentration $[\text{H}_2\text{O}_2]$ decreases slowly but, if one considers only the duration of one oscillation, one can neglect its variation. This leaves two external compounds, iodine and iodate. Their concentrations are not independent, they are linked by the balance of iodine atoms.

$$[\text{Total I}] = [\text{IO}_3^-] + 2 [\text{I}_2] + \text{small terms from the internal compounds} \quad (1)$$

There is therefore only one independent variable left and the slow manifold has only one dimension. The trajectory follows a more or less complicated line in the space of concentrations called nullcline. It suffices to study the properties of the nullcline, or of its projection on a plane, to describe the observed phenomena.

PROPERTIES OF THE NULLCLINE

Figure 2 shows the nullcline calculated with the model we have proposed [5, 6] and its recent variant [7]. Nullclines are calculated by solving the system of analytical equations $dC_i/dt = 0$ where C_i represents the concentrations of the internal compounds. The trajectories are calculated by integrating the system of differential equations for all the compounds with the function ode15s of Matlab. Under the conditions of Fig.1, the upper and lower branches of the nullcline in Fig.2 are stable. The middle branch is unstable. When the system is on the upper branch, $[I_2]$ increases and we get the reaction R. When the system reaches the value $[I_2]_{\max}$, $[I_2]$ still increases and the system must quit the nullcline. It rapidly evolves towards the lower branch where $[I_2]$ decreases and reaction O is obtained. When the system reaches the value $[I_2]_{\min}$, $[I_2]$ still decreases and the system rapidly evolves towards the upper branch. This gives a limit cycle. Its size decreases when $[H_2O_2]$ decreases, which explains the experimental curve in Fig.1d.

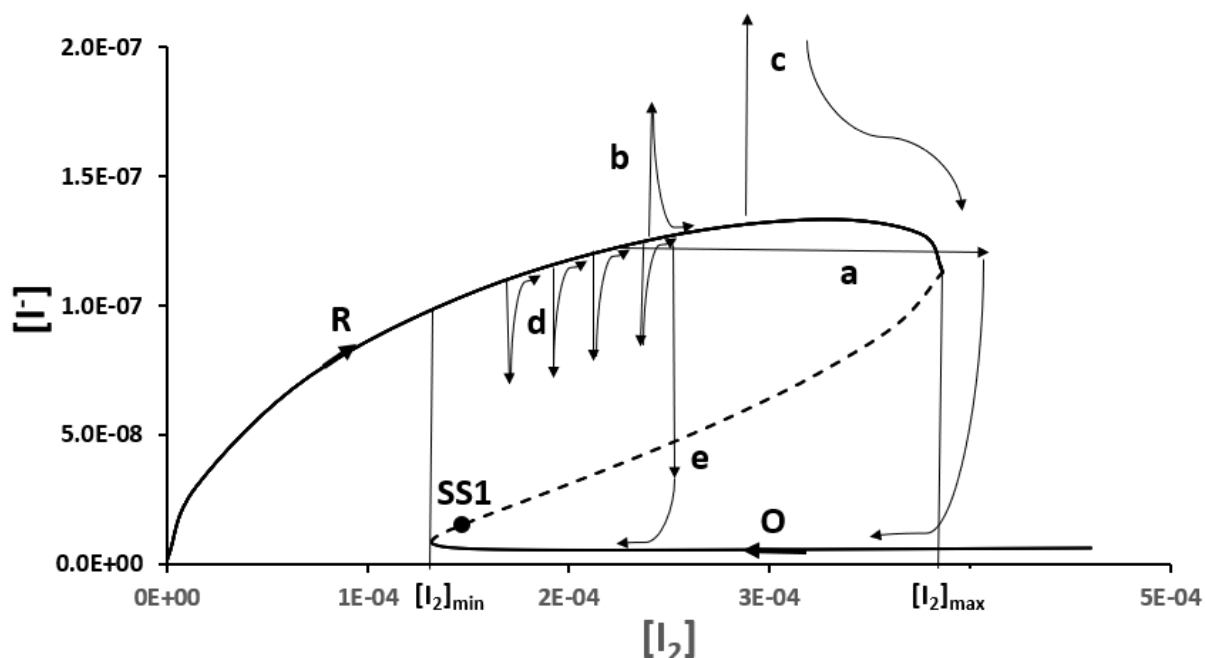


Figure 2. Example of nullcline and effects of additions during the period R (see text).

There is a point in the concentrations space where the rates of the reactions R and O are equal and where the only global reaction is the decomposition $2 H_2O_2 \rightarrow 2 H_2O + O_2$. It is the catalytic steady state (SS1). Oscillations are obtained when it is unstable. If the concentration is $[H^+]$ increased, the amplitude of the oscillations decreases, the shape of the nullcline changes, and the catalytic steady state becomes stable. If the concentration $[H^+]$ is decreased the value of $[I_2]_{\max}$ increases and can become greater than the solubility of iodine. The catalytic steady state is still unstable but one can no longer observe oscillations because the iodine produced by the reaction R precipitates or passes into the gas phase. The effects of $[H_2O_2]$ and $[H^+]$ on the nullcline explains why oscillations can only be observed in a limited range of concentrations. The shape of the nullcline also explains some surprising observed effects of additions during the reaction R.

- The addition of iodine can cause the iodine to disappear. This addition can move the system to the right of point $[I_2]_{\max}$ and cause a transition to the reaction O (arrow a in figure 2).

- The addition of a small amount of I^- has little effect (arrow **b**) but the addition of a larger amount of I^- can cause a fast decrease in the concentration of I^- . Arrow **c** in figure 2 shows that a sufficient amount of I^- causes a transition to the reaction O with a very small concentration of I^- .

- Additions of several small amounts of Ag^+ have little effect but a single addition of a larger amount causes an almost instantaneous transition to the reaction O. AgI precipitation brings the system below the R branch of the nullcline. If it remains in the basin of attraction of this branch, it quickly returns after each small addition (arrows **d**). If it arrives below the unstable branch of the nullcline (arrow **e**), it is attracted by the O branch. This is a case of overdose.

IODINE OXYDATION BY H_2O_2

We have studied the kinetics of the iodine oxidation by H_2O_2 in solutions containing iodate concentrations of the order of 0.01 mol/l and an iodine concentration greater than $[I_2]_{max}$ [5, 6]. Under these conditions, reaction O usually begins as soon as the reactants are mixed and the concentration of iodate has no effect on the kinetics. On the other hand, if there is no or very little iodate initially, reaction O only appears after a long period, sometimes hours or even days. Furrow [8] had measured the absorbances at 460 and 354 nm over time, which makes it possible to calculate the concentrations of I_2 and I_3^- . We thank him very much for having sent us the details of his experiments, of which Fig. 3 gives an example. We have used our model to calculate the trajectories under these conditions and obtained curves similar to the experimental curves. We have then calculated the nullcline and got a surprising result.

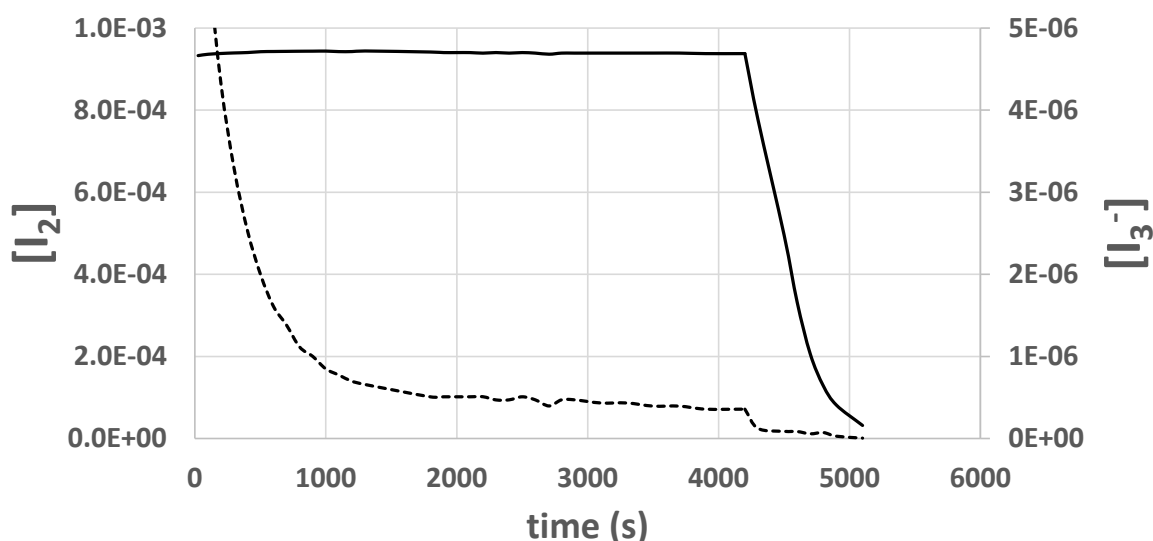


Figure 3. Evolution of $[I_2]$ (line, left scale) and $[I_3^-]$ (dashes, right scale) during an experiment in Table IV of ref. 8. $[HClO_4]_0 = 0.10$ M, $[H_2O_2]_0 = 0.088$ M, $[I_2]_0 = 9.3 \times 10^{-4}$ M, $[I^-]_0 = 1.1 \times 10^{-5}$ M, no iodate initially.

Figure 4 shows that a new branch of the nullcline appears when the concentration $[Total\ I]$ is small. The left branch is the one studied above with the steady state SS1. On the new branch on the right, there are two steady states, one stable (SS2), the other unstable (SS3). These two steady states are very close to the maximum value of $[I_2]$ given by the mass balance (1), that is $[Total\ I]/2$.

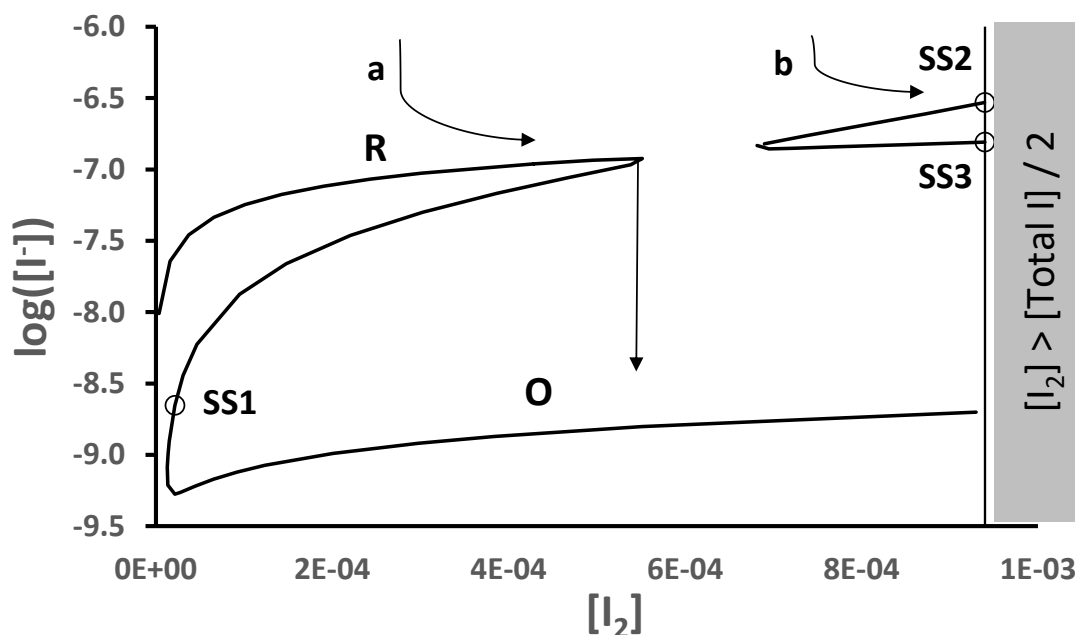


Figure 4. Calculated nullcline under the conditions of Fig.3.

The arrows indicate the direction of the trajectories. For a given value of [Total I], oscillations are obtained if the initial solution contains enough iodate (arrow **a**). If it does not contain, or very little, iodate as in the experiment of Fig. 3, the system goes to state SS2 (arrow **b**). The system remains in the state SS2 during the horizontal part of the experimental curve in Fig 3.

It remains to explain the sudden appearance of reaction O. If the behavior of the system changes, a constraint must have changed, and it can only be the concentration of an external compound because the concentrations of the internal compounds are determined by the nullcline. In the SS2 state, $[H^+]$ and $[I_2]$ are constant and therefore also $[IO_3^-]$. There seems to be only one external compound left, H_2O_2 , the concentration of which slowly decreases. This could be an explanation when the initial H_2O_2 concentration is small but in the case of Fig. 3 its variation is much too small. To explain the transition, we must take into account another external compound, oxygen.

EFFECTS OF OXYGEN ON THE BL REACTION

R. M. Noyes [10] had studied these effects and had even proposed that they could explain the oscillations. This explanation has been discarded but it is well established that oxygen can have important effects on the BL reaction [11-14]. Oxygen can oxidize iodide in acidic solution. The non-radical pathway of the reaction $I^- + H^+ + \frac{1}{2} O_2 \rightarrow HOI$ is very slow but a radical pathway can be fast. This reaction was added to our model as a global reaction with an unknown light-catalyzed radical mechanism that deserves further experimental study. It allows qualitative explanation of the observed effects of oxygen on the oscillations [5, 6]. We now show that it explains also the transition in Fig. 3.

Comparison of Fig.4 and Fig.5a shows that the right branch of the nullcline shifts to the right when the oxygen concentration increases. Oxygen is produced while the system is in the state SS2 and the SS2 and SS3 states approach. When oxygen reaches a critical concentration, they meet and disappear. We have a saddle-node bifurcation. The system which was in the stable SS2 state is now attracted by the lower branch of the nullcline and the reaction O starts. This bifurcation explains why the rate of disappearance of iodine in Fig. 3 is maximum just after the transition. It also explains why the moment of appearance of the transition is not reproducible. The concentration of oxygen in the solution

depends on the rate of its transfer to the gas phase and therefore on many factors such as the stirring rate [9] and the interphase area [13]. It is difficult to control nucleation and bubble growth and the supersaturation of the solution in oxygen can become very large. Moreover, since radical reactions can be initiated by light [15], the critical oxygen concentration depends on it. The effects of oxygen explain why Stanisavljev [9] observed that the period preceding the reaction O has a stochastic character. A phenomenon seems stochastic when it depends on a parameter that we ignore or do not control.

The effect of $[I_2]$ on the concentrations of internal compounds shown by the nullcline depends on $[H^+]$, $[H_2O_2]$, $[O_2]$ and on $[Total\ I]$ but not on $[IO_3^-]$ given by the balance (1). However, the trajectories depend on it. Fig. 4 shows that the trajectory goes to the SS2 state if the total iodine is added mainly in the form of I_2 , as in the experiments of Furrow [8] and Stanisavljev [9] and goes to the left branch of the nullcline giving oscillations for the same value of $[Total\ I]$ if the total iodine is added mainly as iodate. Changing the values of $[H^+]$, $[H_2O_2]$, $[O_2]$ and $[Total\ I]$ gives several different shapes of the nullcline with several kinds of bifurcations between them. An example is given by Fig. 5b calculated with a low value of $[O_2]$. If $[O_2]$ increases, we obtain Fig. 4 after a global bifurcation giving the appearance of a limit cycle without modification of the steady states.

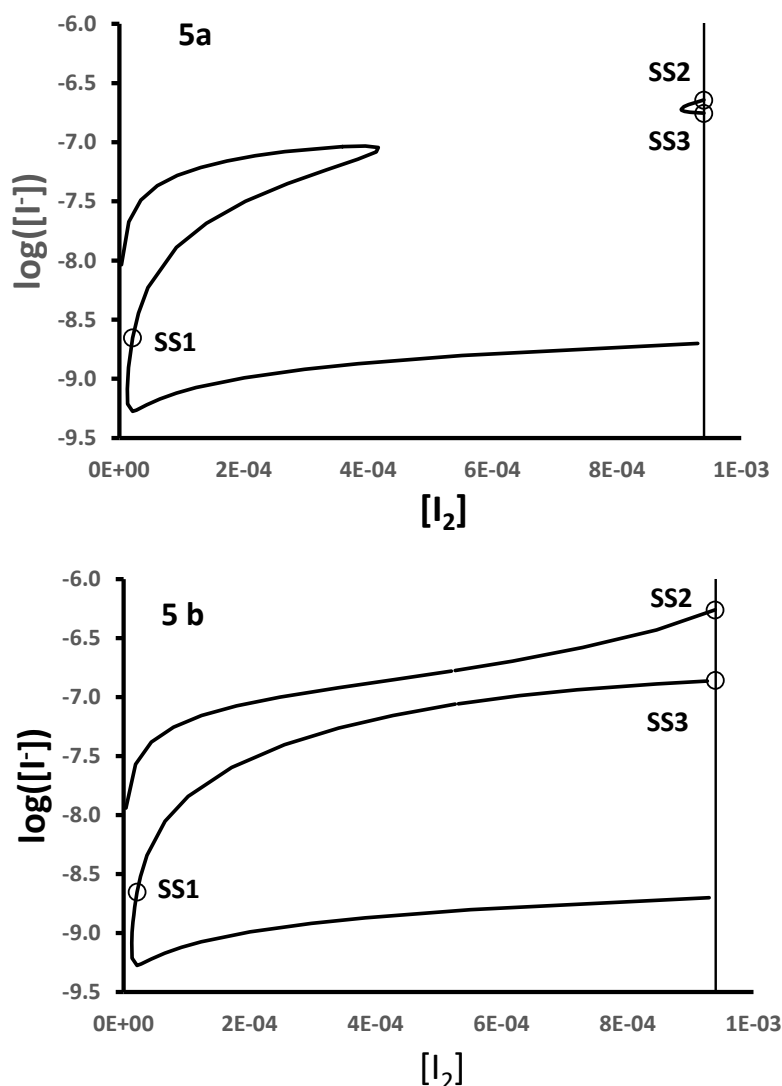


Figure 5. Shapes of the nullcline under the conditions of Fig.3 calculated with the proposed model [7] and different concentrations of oxygen: 1.05×10^{-3} M (Fig.5a), 8.0×10^{-4} M (Fig.4), 2.6×10^{-4} M (Fig.5b)

CONCLUSIONS

The study of nullclines makes it possible to simply explain various experimental observations relating to the reaction of BL, effects of concentrations on oscillations and effects of additions of compounds during this reaction. It also explains what seems to be a period of induction before the reaction O if there is no iodate initially. It is actually not an induction period. It is a quasi-steady state different from the catalytic steady state usually studied. The appearance of the O reaction is due to a saddle-node bifurcation occurring when $[O_2]$ increases. The nullcline can have different shapes and several kinds of bifurcations can be observed.

Acknowledgement

We thank Prof. Stanley Furrow for his experimental results and his very valuable comments.

REFERENCES

- [1] G. Schmitz, Lj. Kolar-Anić, S. Anić, and Ž. Čupić, Stoichiometric Network Analysis and Associated Dimensionless Kinetic Equations. Application to a Model of the Bray-Liebhafsky Reaction, *J. Phys. Chem. A*, 2008, 112 (51), 13452-13457.
- [2] Lj. Kolar-Anić, Ž. Čupić, G. Schmitz and S. Anić, Improvement of the stoichiometric network analysis for determination of instability conditions of complex nonlinear reaction systems, *Chem. Engineering Sci.* 2010, 65, 3718–3728.
- [3] Ž. Čupić, A. Ivanović-Šašić, St. Blagojević, Sl. Blagojević, Lj. Kolar-Anić and S. Anić, Return map analysis of the highly nonlinear Bray-Liebhafsky reaction model, *Reac. Kinet. Mech. Cat.* 2016, 118, 27-38.
- [4] A. Ivanović, Ž. Čupić, S. Marinović, G. Schmitz and Lj. Kolar-Anić, Critical manifold of the model for Bray-Liebhafsky oscillatory reaction, *Proceedings of Physical Chemistry 2010*, Belgrade, 21-24 September 2010, 236-238.
- [5] G. Schmitz, Iodine oxidation by hydrogen peroxide in acidic solutions, Bray-Liebhafsky reaction and other related reactions, *Phys. Chem. Chem. Phys.* 2010, 12, 6605-6615.
- [6] G. Schmitz, Iodine oxidation by hydrogen peroxide and Bray-Liebhafsky oscillating reaction: effect of the temperature, *Phys. Chem. Chem. Phys.* 2011, 13, 7102-7111.
- [7] G. Schmitz and S. Furrow, Kinetics of I(+3) reactions and consequences for other iodine reactions, *Reac. Kinet. Mech. Cat.* 2022, submitted
- [8] S. Furrow, Reactions of Iodine Intermediates in Iodate-Hydrogen Peroxide Oscillators, *J. Phys. Chem.* 1987, 91, 2129-2135.
- [9] D. R. Stanisavljev, K. Z. Stevanović and I. M. Bujanja, Outsized stochasticity of iodine oxidation with hydrogen peroxide and its implications on the reaction mechanism, *Chem. Phys. Letters* 2018, 706, 120-126.
- [10] K. R. Sharma and R. M. Noyes, Oscillations in chemical systems. 13. A detailed molecular mechanism for the Bray-Liebhafsky reaction of iodate and hydrogen peroxide, *J. Am. Chem. Soc.* 1976, 98 (15), 4345-4361.
- [11] G. Schmitz, Effects of oxygen on the Bray-Liebhafsky reaction, *Phys. Chem. Chem. Phys.* 1999, 1, 4605.
- [12] K. Kissimonová, I. Valent, L. Adamčíková and P. Ševčík, Numerical simulations of the oxygen production in the oscillating Bray-Liebhafsky reaction, *Chem. Phys. Letters* 2001, 341, 345-350.
- [13] A. Olexová, M. Mrákavová, M. Melicherčík and L. Treindl, The autocatalytic oxidation of iodine with hydrogen peroxide in relation to the Bray-Liebhafsky oscillatory reaction, *Collect. Czechoslov. Chem. Commun.* 2006, 71, 91–106.

- [14]M. Radenković, S. Anić, Lj.Kolar-Anić, The oxygen evolution in the Bray-Liebhafsky reaction, in Book of papers of XII Yugoslav Symposium on Electrochemistry, Society of Chemists and Technologists in Bosnia and Herzegovina, 1991, pp.207-208.
- [15]S. Kéki, G. Székely and M. T. Beck, The Effect of Light on the Bray-Liebhafsky Reaction, J. Phys. Chem. A 2003, 107, 73-75.

THREE DECADES OF OSCILLATORY CARBOXYLATION REACTIONS OF ALKYNES: PAST, PRESENT AND FUTURE

K. Novakovic

School of Engineering, Newcastle University, Newcastle upon Tyne, NE1 7RU, UK

ABSTRACT

First reported in 1997, oscillatory carbonylation reactions of alkynes are still attracting our attention. Here, we summarize work thus far and share a vision of where these mesmerizing chemical oscillators may take us. We showcase a range of substrates, catalysts and solvents that successfully yield oscillations in redox potential, pH, turbidity and release reaction heat in a pulsatile manner. Moving towards prospective applications we look into transitioning this oscillatory carbonylation reaction from small molecule substrates and catalysts to oscillatory reactions using polymeric substrates and catalysts, which are seen as the way forward in the formulation of oscillatory (pulsatile) materials.

Starting from oxidative carbonylation of alkynes such as $\text{PhC}\equiv\text{CH}$ and $\text{MeC}\equiv\text{CH}$ in the acid-free PdI_2 – KI – MeOH system for the synthesis of Z- and E-diesters of α,β -unsaturated acids at mild temperatures (e.g. 20 °C) and elevated pressures (e.g. 20 bar) [1], Temkin et al. found that, at certain concentrations of $\text{PhC}\equiv\text{CH}$, PdI_2 , KI and NaOAc , exposed to atmospheric pressure of CO/O_2 mixture, this reaction system can exhibit self-oscillations in Pt electrode potential and pH, while consuming CO/O_2 gasses in a step-like manner (Figure 1a) [2].

The reaction was conducted in a well-stirred and closed batch reactor at 40 °C and atmospheric pressure of CO/O_2 mixture.[2] Oscillations proceeded for 3.5 h, until 95% of phenylacetylene was converted to phenyl maleate (I), phenyl fumarate (II), and dimethoxylactone (III) (Figure 1a); making this reaction the first oscillatory reaction showcasing the formation of more complex molecules from a simple one in a solution of a metal complex. Similarly, prolonged oscillations were achieved when PdI_2 was replaced with $\text{K}_2\text{Pd}_2\text{I}_4$, suggesting that the process of initial dissolution of PdI_2 (by reaction with KI) is not crucial for the occurrence of oscillation.[6] Gorodskii et al. continued to study oxidative carbonylation of alkynes, seeking to understand elements of the reaction mechanism responsible for its self-oscillatory mode. In addition to phenylacetylene they confirmed three more alkynes as viable substrates yielding self-oscillatory mode of the reaction: methylacetylene, propargyl alcohol and 1,1-dimethylprop-2-ynol (Figure 1b).[3] They showed that the change in agitation speed (from 250-900 rpm) did not have an effect on observed oscillations, their amplitude and period, suggesting that gas diffusion through the l-g interface is not driving the occurrence of oscillations, i.e. oscillations are chemically driven, rather than diffusion driven.

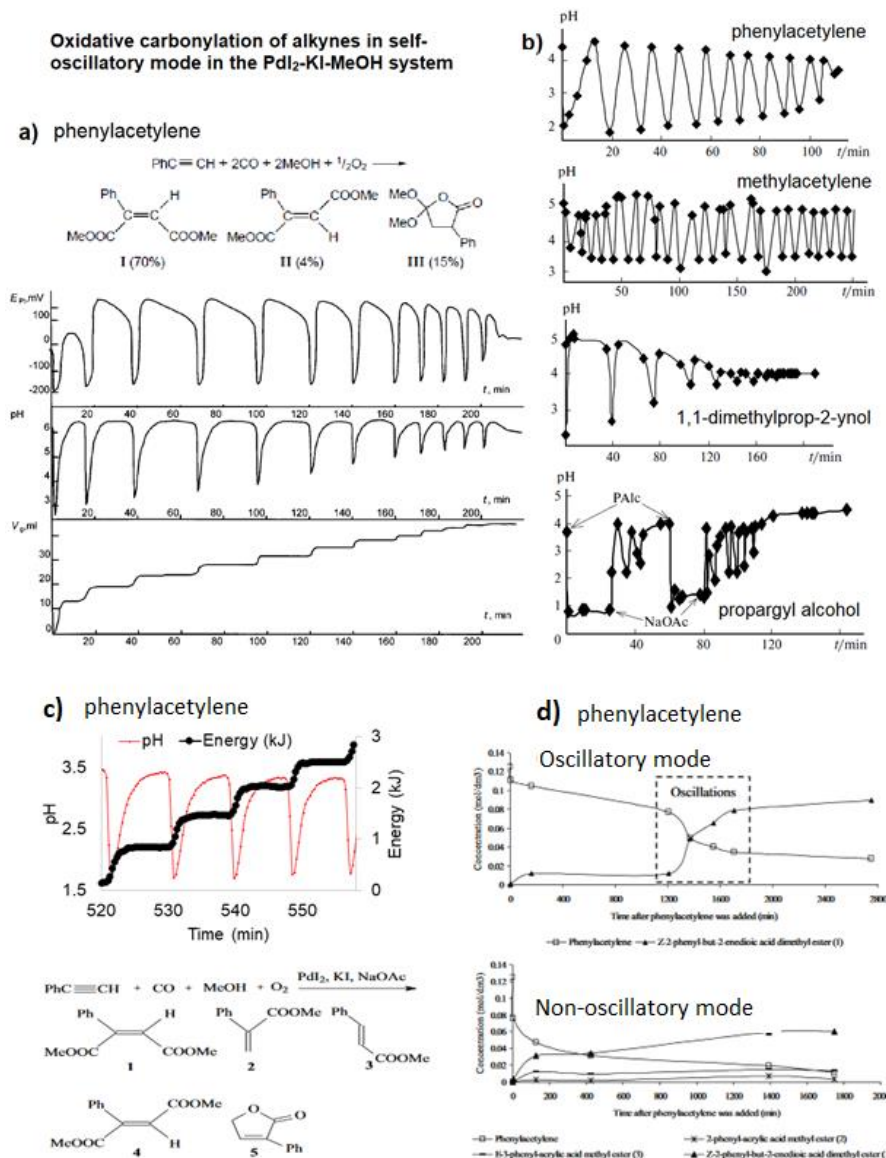


Figure 1. a) Oscillations of the platinum electrode potential (E_{Pt}), pH, and volume of the gas mixture CO-O₂ (V_g , ml) consumed in the course of reaction at 40 °C. Initial concentrations: [PdI₂]=0.01 mol/L, [KI]= 0.4 mol/L, [PhC≡CH]= 0.1 mol/L, [NaOAc] = 0.0024 mol/L; solvent used was methanol and total volume of the solution was 10 ml. Water (2 mmol) was added together with methanol to maintain the constant concentration of water at the initial level (approx. 0.2 mol/L). Adopted from [2]; b) Oscillations in the pH using same concentrations of substrate, PdI₂ and KI as in (a) but with a broader range of substrates; Agitation speed = 700 rpm and [CO]:[O₂]=3:2; Adopted from [3] c) Synchronize oscillations in pH and heat release; First methanol (400ml) and PdI₂ (2.03 g, 5.60 mmol) were stirred at 550 rpm and the temperature was set at 40°C. Following KI (37.39 g, 225 mmol) and NaOAc (114 mg, 1.40 mmol) in 50 ml of methanol were added, and after a further 20 min, simultaneous purging of the system with CO and Air (50 ml/min each) commenced. Thirty minutes after purging started, phenylacetylene (6.2 ml, 56.5 mmol) was added. Adopted from [4]; d) The product formation in oscillatory and non-oscillatory mode (related to PdI₂ granularity). Adopted from [5].

Furthermore, while all four substrates produce oscillations in electrode potential and pH under the same initial conditions (Figure 1b), they showed different induction times, periods and amplitudes of oscillations; suggesting core similarity in the reaction mechanism with subtle differences caused by a difference in a substrate. They also observed that once damped upon alkyne consumption, oscillations can be restarted by the addition of fresh amounts of substrate and reported that in the case of phenylacetylene and methylacetylene, methanol (used both as solvent and reactant), can be replaced with n-butanol and self-oscillatory mode still occurs. They also noted that NaOAc can be used to alter the pH of the solution and speed-up onset of the oscillations (demonstrated with propargyl alcohol as substrate, Figure 1b). Furthermore, experimental study revealed that in general, oscillation period increases with the increase in initial concentration of KI, a decrease in the initial concentration of PdI₂, and an increase in the fraction of O₂ (in CO-O₂ mixture). In the search for the mechanism behind the observed oscillations, role of oxidants, I₂ and H₂O₂, was experimentally studied and showcased as relevant to pH values recorded, as well as the induction period and onset of oscillations. Various mechanisms were postulated and a range of Pd species were considered as having a role in the mechanism (HPdI, PdI₂I₂, IPdOOH, Pd⁰). [6] It was proposed that the transitions between oxidation states of palladium occur by non-linear and self-catalyzed steps with significantly different rate constants; leading to fast re-distribution of palladium species between different oxidation states and linking formation and consumption of these species to the appearance of oscillations.

Interest in the oscillatory nature of the oxidative carbonylation of alkynes was taken by Novakovic et al. who in addition to experimentally confirming pH oscillations in a palladium-catalyzed phenylacetylene oxidative carbonylation reaction, also recorded synchronized oscillations in the reaction heat output which were exothermic with no corresponding endotherm and in phase with a pH fall (Figure 1c). [4] By performing experiments in a reaction calorimeter energy release during oscillations was recorded and it was shown that it follows a staircase function, indicating a stepwise product formation. Further studies of the product formation in the oscillatory carbonylation reaction of phenylacetylene, revealed that occurrence of pH oscillations influences product selectivity. [5,7] As shown in Figure 1d, when operating in oscillatory mode at 40°C a high selectivity towards the formation of Z-2-phenyl-but-2-enedioic acid dimethylester (denoted as Product 1 in Figure 1c, reaction scheme) was recorded. Furthermore, product formation was suppressed until oscillations occurred when a steep increase in reaction rate was observed. [5] Broadening studies of oscillatory carbonylation of phenylacetylene to a wider temperature range (0-40°C) showed that reaction temperature affects product selectivity. [8] Study noted that the conversion of phenylacetylene to products recorded at 0–20 °C follows kinetic laws (conversions increase as the temperature increases) which becomes less apparent at 30 °C and is not followed at 40 °C, suggesting thermodynamic reaction control. Experiments showcased the ability of oscillatory carbonylation reactions to proceed in self-oscillatory mode for days and weeks with no further addition of either a substrate or catalyst. Experimentally Parker and Novakovic [9] showed that synchronous with pH oscillations, oscillations in turbidity take place, indicating oscillatory cycling between soluble and insoluble catalytic species (postulated to be Pd⁺² and Pd⁰ respectively) in autocatalytic mode. Further experimental studies of phenylacetylene carbonylation demonstrated the existence of self-oscillatory mode when the water concentration in the system is increased (0–30 vol%, mixed with methanol). [10] Addition of water transformed oscillations in pH from regular oscillations to stepwise behavior. These findings show dilution with water as a significant mean in tailoring amplitude, period and duration of oscillations, but also as a way to reduce overall toxicity.

Versatility of substrates, catalysts and solvents which can lead to self-oscillatory mode of these carbonylation reactions [2-10] was expanded further with the polymeric substrates (pegylated mono and dialkyne [11-13]) and polymeric catalysts (Pd-polyacrylate, proline-functionalised chitosan-Pd, chitosan-palladium catalysts [12, 13]), and less toxic ethanol, Figure 2a,b. Transitioning oscillatory

carbonylation reactions from solution chemistry to polymer science opened new opportunities and led to recent reports of pulsatile hydrogels capable of drug release in a stepwise manner (Figure 2c, d) [14]. Isakova and Novakovic demonstrated a proof-of-concept self-oscillatory chitosan macrogel, employing the palladium-catalysed oxidative carbonylation reaction as the driving force of its oscillations. The reported hydrogel was composed of highly biocompatible components and a novel imine-functionalised chitosan-palladium catalyst with zero leaching rates (Figure 2c). During the synthesis macrogels were loaded with FDA-approved model drug fluorescein and following when used in place of catalyst in oxidative carbonylation reaction, shown to rhythmically release the model drug. The step-wise release pattern corresponded to the step-wise dynamics of pH decrease in methanol water, while in pure methanol, the changes in pH had an oscillatory mode, accompanied by mirrored oscillations in fluorescein concentration. (Figure 2d).

Combining oscillatory chemical reactions and smart hydrogels has been previously reported by Yoshida et al. [15] who synthesized and studied BZ-gels as a way forward in producing novel functional oscillatory materials. What oscillatory carbonylation reactions have showed so far indicates that these systems have a better potential to achieve meaningful applications due to reaction being long lived, and both substrate and catalyst being a polymer and therefore possible to contain within the hydrogel as interpenetrating polymer network or via grafting process. PEGylated alkyne substrates as well as Pd-chitosan as a catalyst enable reduced toxicity, relevant for medical applications. Also using ethanol in place of methanol brings toxicity of the system down, with further use of water in place of a portion of solvent being beneficial. As this is carbonylation reaction, CO is required in low concentrations (mM). Although we can focus on replacing CO with less toxic counterparts, we need to note endogenous production (12 ml/day) and physiological functions of CO [16], blood CO levels and body CO stores [17] that may serve as a trigger of oscillations in pulsatile hydrogels in vivo.

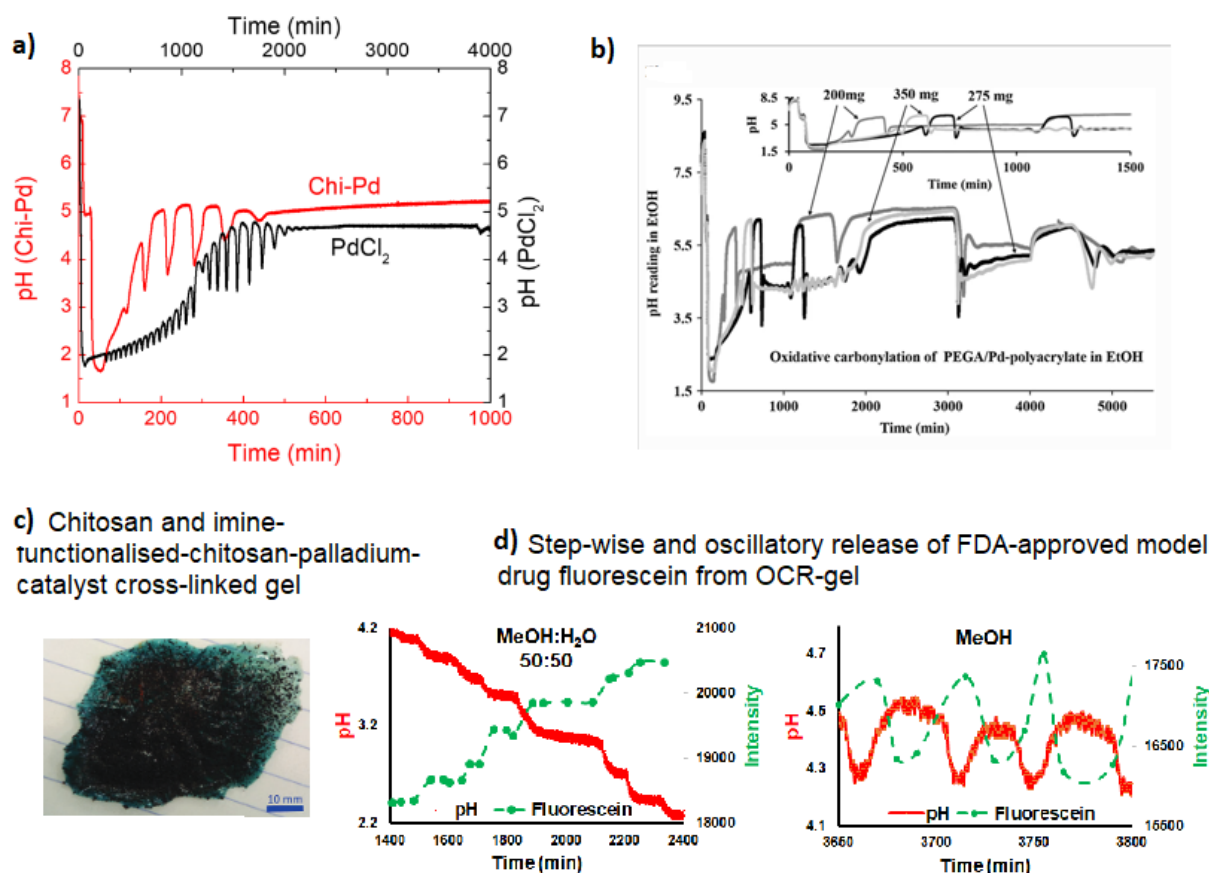


Figure 2. a) pH oscillations in dialkyne-functionalised poly(ethylene glycol) (PEGDAC) carbonylation system using PdCl₂ and non-functionalised chitosan-palladium catalysts (Chi-Pd). Adopted from [13] b) pH recorded in the oxidative carbonylation reaction using monoalkyne functionalized polyethylene glycol PEGA/Pd-polyacrylate in EtOH. PEGA=200 mg, 275 mg and 350 mg; [KI]=250 mmol; Pd-polyacrylate=200 mg; EtOH=100 mL; CO=15 mL/min and air=15 mL/min. Adopted from [12]; c) chitosan and imine-functionalised palladium-bearing chitosan polymer (Chi-IM-PdCl₂ macrogel) top view. Adopted from [14]; d) pH-controlled release of model drug fluorescein as a function of time in methanol:water and methanol systems. Adopted from [14].

To advance these reaction systems further, modelling studies are needed. Recently Kolar-Anic group used Stoichiometric Network Analysis to examine instabilities in oscillatory carbonylation of poly(ethylene glycol)methylether acetylene [18] and also expand on the previously proposed reaction network in order to obtain a more realistic reaction model [19]. In the new model, direct autocatalytic steps were replaced with autocatalytic loops and expressions for reaction rates correspond to their stoichiometry in accordance to mass action kinetics. Joining experimental and modelling efforts aims to accelerate the development of oscillatory materials and achieve their application in mechanoresponsive tissue engineering, chronopharmacotherapy, soft robotics and beyond.

REFERENCES

- [1] B. Gabriele, M. Costa, G. Salern and G. P. Chiusoli, *J. Chem. Soc., Perkin Trans.*, No. 1, 83 (1994)
- [2] A. V. Malashkevich, L. G. Bruk and O. N. Temkin, *J. Phys. Chem. A.*, 101, 9825 (1997)
- [3] S. N. Gorodskii, E. S. Kalenova, L. G. Bruk and O. N. Temkin, *Izv. Akad. Nauk, Ser. Khim.*, No. 7, 1452 (2003)

- [4] K. Novakovic, C. Grosjean, SK Scott, A Whiting , MJ Willis, AR Wright, Chem. Phys. Lett, 435(1-3), 142-147 (2007)
- [5] K. Novakovic, C. Grosjean, S.K. Scott, A. Whiting, M.J. Willis, A.R. Wright, PCCP 2008, 10(5), 749-753 (2008)
- [6] N. Gorodskii, A. N. Zakharov, A. V. Kulik, L. G. Bruk and O. N. Temkin, Kinet. Katal., 42 (2), 280 (2001)
- [7] C. Grosjean, K. Novakovic, S.K. Scott, A. Whiting, M.J. Willis, A.R. Wright, J Mol Cat A: Chemical, 284(1-2), 33-39, (2008)
- [8] J. Parker, K. Novakovic, ChemPhysChem, 18(15), 1981-1986 (2017)
- [9] J. Parker, K. Novakovic, React. Kinet. Mech. Catal. , 1-13 (2016)
- [10] J. Parker, K. Novakovic, React. Kinet. Mech. Catal. , 123(1), 113–124 (2018)
- [11] L. Donlon, K. Novakovic, Chem. Commun., 50(98), 15506-15508 (2014)
- [12] A. Isakova, J. Parker, C.J. Nwosu, J.R. Howse, K. Novakovic, React. Kinet. Mech. Catal., 127(1), 161-174 (2019)
- [13] A. Isakova, G.E. Parkes, B.J. Murdoch, P.D. Topham, K. Novakovic, Eur. Polym. J, 109, 537-543 (2018)
- [14] A. Isakova, K. Novakovic, J. Mat. Chem.y B, (30), 5003-5010 (2018)
- [15] R. Yoshida, Adv Mater (2010)
- [16] L. Wu and R. Wang, Pharmacol Rev (2005)
- [17] J Coburn, J Intern Med (2009)
- [18] Z. Cupic, S. Macesic, K. Novakovic, S. Anic, Lj. Kolar-Anic, Chaos 28, 083114 (2018)
- [19] S. Macesic, Z. Cupic, K. Novakovic, J. Parker, S. Anic, Lj. Kolar-Anic, MATCH Communications in Mathematical and in Computer Chemistry 81(1), 5-34 (2019)

REACTION NETWORK ANALYSIS OF CIRCADIAN AND ULTRADIAN RHYTHMS OF CYANOBACTERIA IN A PHOTOBIOREACTOR

I. Schreiber*[†], F. Muzika* and J. Červený[†]

**Department of Chemical Engineering, University of Chemistry and Technology, Prague, Czech Republic*

†Department of Adaptive Biotechnologies, Global Change Research Institute, Academy of Science of the Czech Republic, Brno, Czech Republic

ABSTRACT

Reaction network analysis assumes that stoichiometric equations are given for each reaction step together with power law rate expressions. On output, elementary subnetworks (known also as elementary modes or extreme currents) are identified and their capacity for displaying dynamical instabilities, such as bistability and oscillations, is evaluated by examining the associated Jacobian matrix. This analysis is qualitative and does not assume the rate values of coefficients and concentrations of chemical components. In the next step, the subnetworks are combined to form the entire network and its stability is deduced from the stability of the constituting subnetworks. In the final step, this combination principle is used in a quantitative manner for kinetic parameter estimation of the unknown/unspecified rate coefficients by applying linear optimization to a set of constraint equations balancing linearly combined subnetworks with the corresponding rate expressions. From mathematical point of view, this is a special case of convex optimization.

From the application point of view, the outlined theory is applied to experimentally measured activity of photosynthesizing diazotrophic cyanobacteria in a photobioreactor. In particular, we focus on biochemical processes giving rise to experimentally observed change from a steady state to oscillatory dynamics. The oscillations in cyanobacteria come from either a circadian clock synchronized with external light/dark cycle or from an internal ultradian cycle, which is active even in the absence of external environmental cues. For the former, we examine models of circadian clock associated with a network involving the KaiABC proteins and their regeneration via a transcriptional network, for the latter, a compartmental model of carbon-nitrogen metabolism is analyzed.

For the metabolic model the set of unknown kinetic parameters is estimated via linear optimization so that the dynamics displayed by the model coincides with the experimentally observed emergence of oscillations.

ON THE INTERACTION OF EDTA WITH THE H₂O₂-NASCN-NAOH-CUSO₄ OSCILLATOR - FROM TRIVIAL ASSUMPTION TO A NEW KINETIC MECHANISM

P. Oliwa, M. Orlik

Faculty of Chemistry, University of Warsaw, ul. Pasteura 1, 02-093 Warsaw, Poland

Email: morlik@chem.uw.edu.pl

ABSTRACT

Oscillatory chemical reactions have been successfully studied for several decades. Recently, interest has been growing in coupled oscillators or single systems chemically perturbed by adding a substance that interacts with key intermediates of oscillatory systems. One of the most interesting systems of this type is the H₂O₂ - SCN⁻ - OH⁻ - Cu²⁺ oscillator discovered by Orbán [1] (which is often referred to as the Orbán-Epstein oscillator), and later studied in various research groups (cf. e.g. [2, 3, 4]), including our group (cf. e.g. [5, 6]).

In our recent extensive potentiometric and spectrophotometric studies of the effect of Cu²⁺ concentration on the dynamics of the Orbán-Epstein oscillator, modified by addition of EDTA, for a certain concentration range of [EDTA] < [CuSO₄], only transient damping of the oscillation amplitude was observed. Discovered in this way, non-trivial chemical interaction of EDTA with the oscillatory system made it possible to propose a new kinetic reaction mechanism of these phenomena, based on the perturbation of the oscillator feedback loops. The proposed chemical reaction scheme [7] has been illustrated by its numerical modeling, allowing for the estimation of the rate constants of individual reaction steps. Furthermore, the previously proposed [5] mechanism of differences in potentiometric responses of various inert electrodes was confirmed. In conclusion, the oscillatory H₂O₂ - SCN⁻ - OH⁻ - Cu²⁺ reaction has become a dynamic sensor of EDTA interactions with the components of the feedback loops.

REFERENCES

- [1] M. Orbán: Oscillations and Bistability in the Cu(II)-Catalyzed Reaction between H₂O₂ and KSCN. *J. Am. Chem. Soc.* **1986**, *108*, 6893-6898.
- [2] Y. Luo, M. Orbán, K. Kustin, I.R. Epstein: Mechanistic Study of Oscillations and Bistability in the Cu(II)-catalyzed Reaction Between H₂O₂ and KSCN, *J. Am. Chem. Soc.*, **1989**, *111*, 4541-4548.
- [3] Ž. D. Čupić, E. Greco, R. Cervellati: New Experimental and Mechanistic Investigation on the KSCN-H₂O₂-NaOH-Cu(II)-catalyzed Oscillating Orbán–Epstein Reaction: Inhibitory Effects by Diphenols, *Int. J. Chem. Kinet.*, **2015**, *47*, 82-92.
- [4] R. Cervellati, E. Greco, S. N. Blagojević, S. Anić, Ž. D. Čupić: Experimental and Mechanistic Study of the Inhibitory Effects by Phenolics on the Oscillations of the Orbán-Epstein Reaction. *React. Kinet. Mech. Cat.* **2018**, *123*, 125–139.
- [5] A. Wiśniewski, K. Pekala, M. Orlik: Kinetic model of the H₂O₂ – SCN⁻ - OH⁻ - Cu²⁺ Oscillator and its Application to the Interpretation of the Potentiometric Responses of Various Inert Electrodes Monitoring the Reaction Course”, *J. Phys. Chem. A*, **2010**, *114*, 183-190.
- [6] M. Jędrusiak, A. Wiśniewski, M. Orlik, „The Model of „Minimal Oscillator” Derived from the Kinetic Mechanism of the H₂O₂-NaSCN-NaOH-CuSO₄ Dynamical System”, *Int. J. Chem. Kin.*, **2015**, *7*, 791-802
- [7] P. Oliwa, M. Orlik, submitted for publication, **2021**

EXPERIMENTAL SETUP FOR CONTINUOUS MEASUREMENTS OF GASEOUS OXYGEN PRODUCTION IN BRAY-LIEBHAFSKY OSCILLATOR

I. N. Bubanja and D. Stanisavljev

*Faculty of Physical Chemistry, University of Belgrade, Studentski trg 12-16, Belgrade, Serbia
(itana.bubanja@ffh.bg.ac.rs)*

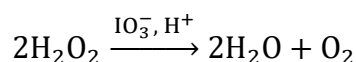
ABSTRACT

Experimental setup for tracing gas evolution in Bray-Liebhafsky (BL) oscillatory reaction was designed. It enables simultaneous and continuous recording of potential changes as well as relative gaseous pressure above BL reaction mixture. Since one serious problem in establishing reaction mechanism is limited number of techniques for monitoring reaction components, development of the cheap method for measuring evolved oxygen may be valuable.

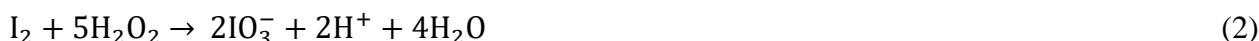
INTRODUCTION

Even though, chemical oscillators are known and studied for almost hundred years, there are still doubts about their full mechanism and dynamics. This could be due to the lack of sensitive and selective methods, by which reactive and unstable reaction components can be followed. Moreover, stable components may be difficult to determine experimentally due to the interfering reactions of the matrix components.[1]

One of the simplest chemical oscillators is the Bray–Liebhafsky (BL) reaction. It represents catalytic decomposition of hydrogen peroxide into water and oxygen, in the presence of hydrogen and iodate ions [2,3]:



This hydrogen peroxide decomposition is the result of two complex pathways:



Their mechanisms involve several intermediate species, such as I_2 , I , HIO and HIO_2 [4,5], as well as free radicals [6]. The question that is still open is how slow iodine oxidation (2) to I(+5) component, can periodically dominate process since oxidation of I(+1) intermediates is related to a high energetic barrier.[7] Olexová and coworkers studied this BL subsystem without any additional substances, and from their experiments, the importance of gaseous oxygen becomes evident as the reaction induction period was considerably diminished in the absence of mixing or in other words controlling oxygen escape from the reaction mixture.[8] Our recently published papers [9,10] also indicate the importance of gaseous phase in this subsystem of BL reaction, so the purpose of this work was to investigate the possibility of monitoring gas pressure above BL reaction mixture. Dissolved oxygen during BL reaction was commonly monitored using Clark electrode[11]. To the best of our knowledge, evolution of gaseous oxygen in BL reaction was studied by Ševčík and coworkers [12]. They measured evolved oxygen by the means of displaced volume of water by oxygen from collecting

reservoir.[12] Although we believe that Ševčík et al. introduced useful measurement technique for evolved gas, we hope that our procedure is more practical for continuous monitoring.

METHODS

All experiments were performed in a batch reactor, protected from light. Temperature was kept constant by a PolyScience thermostat (accuracy ± 0.1 °C) connected to a reaction vessel. BL reaction dynamics was followed simultaneously by the potentiometric method and by measurements of the gas pressure above reaction mixture.

For potentiometric measurements platinum electrode, as a working electrode, and mercury sulfate as a reference electrode, were used. A data acquisition voltmeter (PC-MultiLab EH4 16-bit ADC), coupled with a personal computer, was used for electrode potential recording in time. For homogenization of the reaction mixture a magnetic stirrer was used (stirring rate was 1200 rpm). Initial concentrations of the reactants were $[\text{KIO}_3]_0 = 7,23 \times 10^{-2}$ M, $[\text{H}_2\text{SO}_4]_0 = 4,92 \times 10^{-2}$ M, $[\text{H}_2\text{O}_2]_0 = 8,28 \times 10^{-3}$ M (corresponds to $6,21 \times 10^{-4}$ mol in 75 mL of reaction mixture), and the order by which the aqueous reactant solutions were added was: potassium iodate, sulfuric acid, and hydrogen peroxide solution when system stabilized at constant temperature ($T = (62,0 \pm 0,2)$ °C). All stock solutions were prepared with deionized water (18 M Ω cm) and all chemicals were p.a. grade. Moreover, two thermometers were used to control the temperature of the reaction mixture and the gaseous phase above it.

For pressure measurements a relative pressure sensor giving output signal of 1 V at 100 mBar was used. Accompanying sensor electronics were provided by "Measuring instruments Miljković Budimir et al". Before experiments took place pressure sensor was calibrated with standard U manometer tube. Since the temperature of the gaseous phase was known ($T = (57,0 \pm 0,2)$ °C) as well as gaseous volume above reaction mixture, with ideal gas approximation, the moles of produced oxygen were calculated. Overall schematic view of experimental setup is given at Figure 1.

RESULTS AND DISCUSSION

At Figure 2, besides typical BL oscillogram (potential versus time diagram) produced oxygen moles over time during BL reaction are given as well. It should be said that besides oxygen, water and iodine vapor may contribute to overall pressure. Pressure over the mixture is measured relatively to atmospheric pressure and only after desired temperature of the reaction mixture was established all valves were closed and pressure reading was taken as zero. In this way water vapor pressure was excluded from reading. Moreover, due to very low value of Henry's constant (about 3×10^{-5} mol/(dm³ Pa)) and since iodine concentration in solution was far below solubility limit, its contribution to overall pressure was negligible. As a result pressure step-like jumps during chemical oscillations, may be satisfactorily related to evolved oxygen.

As it can be seen from Figure 2, slightly before oscillation took place a step-like jump occurred for produced oxygen. Moreover, this step-like jump is the highest for the first oscillation and it gradually decreases for second and third oscillation. From Figure 2. can be estimated that during first oscillation number of produced oxygen moles is 45 μmol while during second and third oscillation is 27 μmol and 16 μmol respectively. Due to the small decomposed peroxide after third oscillation, for two final oscillations pressure changes are of the order of experimental noise. Therefore, suggested method for estimation of evolved oxygen may be used before the approach of the final monotonous dynamic reaction state.

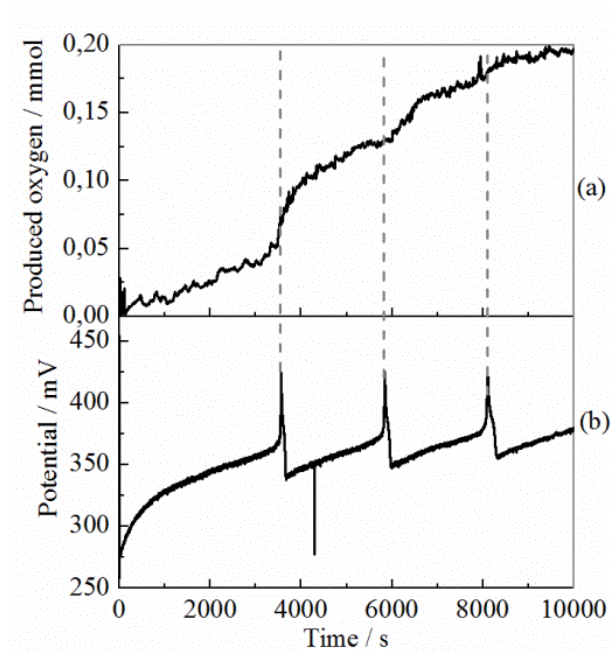


Figure 1. Schematic view of the experimental setup

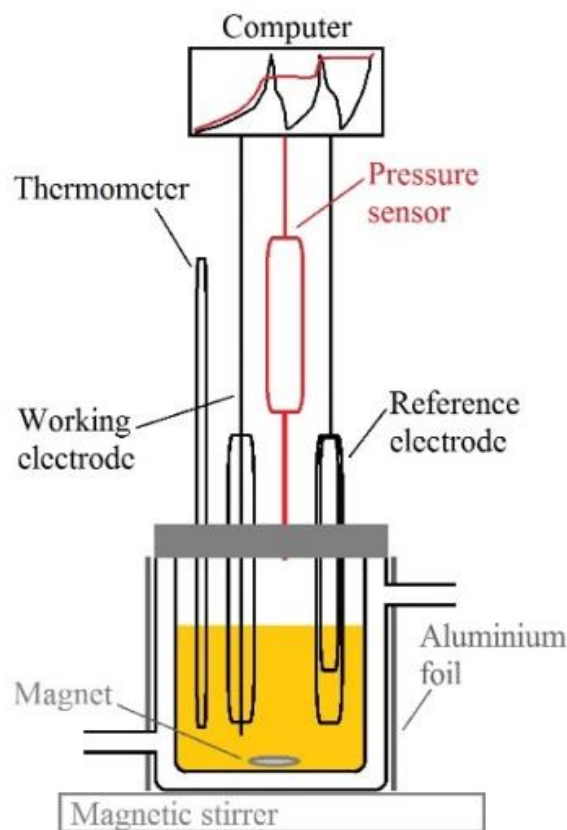


Figure 2. Simultaneous monitoring of BL reaction dynamics (a) Number of produced oxygen moles during BL reaction and (b) potential versus time oscillatory evolution.

CONCLUSION

Improved design of the experimental setup for monitoring BL oscillatory reaction dynamics enabled simultaneous recording of potential and gaseous pressure changes over time. From pressure measurements with approximation of ideal gas the number of produced oxygen moles in gaseous phase above reaction mixture was calculated and estimated per oscillation. Given experiments offer possibility for development of the convenient procedure for continuous monitoring of the hydrogen-peroxide degradation during the reaction. They can contribute to better experimental characterization of this complicate process and further investigation of its mechanism.

Acknowledgement

This work was partially supported by Ministry of Education, Science and Technological Development of Republic of Serbia (Grant No: 451-03-9/2021-14/200146)

REFERENCES

- [1] D. Stanisavljev, I. N. Bubanja and K. Stevanović, *Reac. Kinet. Mech. Cat.*, 2016, **118**, 143–151.
- [2] W. C. Bray, *J. Am. Chem. Soc.* 1921, **43**, 1262–1267.
- [3] W. C. Bray and H. A. Liebhafsky, *J. Am. Chem. Soc.* 1931, **53**, 38–44.
- [4] S. Furrow, *J. Phys. Chem.* 1987, **91**, 2129–2135.
- [5] G. Holló, K. Kály-Kullai, T.B. Lawson, Z. Noszticzius, M. Wittmann, N. Muntean, S.D. Furrow, G. Schmitz, *J. Phys. Chem. A* 2014, **118**, 4670–4679.

- [6] D. R. Stanisavljev, M. C. Milenković, A. D. Popović-Bijelić, M. D. Mojović, *J. Phys. Chem. A* 2013, **117**, 3292–3295.
- [7] K. Z. Stevanović, I. N. M. Bujanja, D. R. Stanisavljev, *Chem. Phys. Lett.* 2017, **684**, 257–261.
- [8] A. Olexová, M. Mrákavová, M. Melicherčík, L. Treindl, *Collect. Czech. Chem. Commun.* 2006, **71**, 91–106.
- [9] K. Z. Stevanović, I. N. M. Bujanja, and D. R. Stanisavljev, *J. Phys. Chem. C* 2019, **123**, 16671–16680.
- [10] D. R. Stanisavljev, K. Z. Stevanović, I. N. M. Bujanja, *Chem. Phys. Lett.* 2018, **706**, 120–126.
- [11] L. C. Clark Jr, R. Wolf, D. Granger and Z. Taylor, *J. Appl. Physiol.* 1953, **6**(3), 189–193.
- [12] P. Ševčík, K. Kissimonová, L. Adamčíková, *L. J. Phys. Chem. A* 2000, **104**, 3958–3963.

DEVELOPMENT OF A SMART HYDROGEL OSCILLATOR

J. Leach and K. Novakovic

*Newcastle University, School of Engineering, Newcastle upon Tyne NE1 7RU, United Kingdom.
(J.C.Leach2@newcastle.ac.uk)*

ABSTRACT

The overall aim of this work is the synthesis and characterisation of hydrogels that have the ability to oscillate in volume to ultimately achieve an autonomous pulsed release system for drugs. To create a material capable of achieving this feat the incorporation of components that can produce oscillations in pH are required. Thorough testing of these components is required to ensure fulfilment of this role. The main components of this hydrogel include a polymeric catalyst and substrate that can work in tandem to produce a conformational response of a hydrogel system at specific intervals. Prior to assembling the hydrogels, the functionality of the catalyst and substrate require confirmation for yielding pH oscillations over longer periods of time (e.g. days).

INTRODUCTION

The palladium-catalysed oxidative carbonylation reaction, named *BT-GN reaction* after the core contributors **Br**uk, **Te**mk**i**n, **Go**rodsky and **No**vakovic, has garnered an attention due to its ability to oscillate in pH, redox potential, turbidity and heat of a reaction. [1-3] It is a unique example of organic oscillatory chemical reactions taking place under lab conditions where more complex products are formed from simple starting materials. Currently these reaction systems have attracted interest for use as a driving force for smart materials and in particular pH responsive hydrogels. [4] This is due to the hydrogels' ability to react to environmental changes in pH generated by these oscillatory processes. The system that uses phenylacetylene (PhAc) as a substrate is the most studied due to the ability to easily analyse the products. [5] Typically, this system employs PdI₂ as a catalyst, and oscillations can last for days in a batch reactor. It is possible to vary the period and amplitude of the oscillations by adjusting the concentration of catalyst, substrate, water content and temperature of reaction. [6-8] There is also evidence to show that temperature has an effect on product selectivity in the oscillatory mode. [9]

More recently oscillations in pH were reported for a *BT-GN reaction* with a alkyne-functionalised polymeric substrate (poly(ethylene glycol) methyl ether acetylene, abbreviated to PEGA) in the place of PhAc. This created more opportunity for the application of *BT-GN reaction* in smart materials. [10] Following this, Isakova *et al.* showed that oscillations with the *BT-GN reaction* can be achieved with more than just the PdI₂ as a catalyst. Showing oscillations with the catalysts PdCl₂, Pd(OAc)₂, L-Cat and P-Cat. [11] Isakova then showed incorporation of PdCl₂ bound to chitosan fabricated into a macrogel producing oscillations in pH with PhAc. The result of this leads us to research on display here as we attempt to combine a palladium bound catalyst with the polymeric substrate (PEGA) to create a self-oscillating autonomous system.

METHODOLOGY

Chemicals

Palladium (II) chloride ($\geq 99.9\%$, PdCl₂), chitosan medium molecular weight (190-310 kDa, deacetylation degree of 75-85% and a viscosity of 200-800cPs), 2 pyridinecarboxaldehyde (99%), sodium chloride (ACS reagent, $\geq 99.0\%$), methanol (HPLC Plus, $\geq 99.9\%$), ethanol (absolute, for HPLC 99.8%), phenylacetylene (98%, PhAc), N-(3-dimethylaminopropyl)-N'-ethylcarbodiimide hydrochloride (EDCI), 4 pentynoic acid (95%), 4-(dimethylamino)pyridine (ReagentPlus®, $\geq 99\%$,

DMAP), poly(ethylene glycol) methyl ether (average Mn ~2,000, flakes), Dichloromethane (suitable for HPLC, ≥99.8%, contains amylene as stabilizer) all provided by Sigma Aldrich; naphthalene (extra pure), potassium iodide (≥99% GPR RECTAPUR®, KI) all provided by VWR Chemicals; buffer solutions: pH 2.00 (glycine), pH 7 (phosphate) and pH 10 (borate) (all NIST Standard, ready to use for pH measurement) all provided by Fisher Chemical; pure air, carbon monoxide (CO), argon and nitrogen (N₂) were all supplied by BOC.

Synthesis of chitosan-2-pyridylimine

Chitosan (500 mg), 2-pyridine carboxaldehyde (300 mg), ethanol (50 mL) and a stir bar are added to a round bottom flask with a quick fit condenser attached and placed into an oil bath set to 85°C and left for 12 hours. The resulting mixture is then vacuum filtered using a Buchner funnel and washed three times with ethanol (50 mL) to produce light brown flakes. The flakes are then analysed by IR to confirm imine functionalisation.

Synthesis of sodium tetrachloropalladate (II) solution

Palladium (II) chloride (100 mg), sodium chloride (200 mg) and a stir bar are added to methanol (50 mL) in a 100 ml conical flask and stirred until dissolution occurs.



Synthesis of Chi-IM-PdCl₂

Chitosan-2-pyridylimine (500 mg) is added to sodium tetrachloropalladate (II) solution (50 mL) and stirred overnight to produce an orange precipitate, a mixture of Chi-IM-PdCl₂. The orange precipitate is washed with potassium iodide (KI) dissolved into methanol.

Synthesis of poly(ethylene glycol) methyl ether acetylene

Using a glovebox with an inert nitrogen atmosphere, poly(ethylene glycol) methyl ether (mPEG) (5 g), DMAP (40 mg) and 4-pentynoic acid (295 mg) were placed into a 100 mL Schlenk flask. In a separate 100 mL Schlenk flask EDCI (575 mg) is added. Both Schlenk flasks had a stir bar added and are then sealed with an injectable septum while in an inert atmosphere. The Schlenk flasks are then transferred to a Schlenk line. On the Schlenk line, the flasks and a bottle of dichloromethane (DCM) with a septum are vacuumed and filled with an inert argon atmosphere. Using a glass leur lock syringe purged with argon DCM (15 mL) was added to the flask containing mPEG. Using the same syringe DCM (10 mL) was added to the flask containing EDCI. Both flasks were continually stirred. Once the contents of both flasks dissolve the flask containing mPEG-DCM is transferred to an ice-methanol water bath. The EDCI-DCM is added dropwise to the mPEG-DCM flask using a clean glass leur lock syringe purged with argon. After 30 minutes the ice-methanol bath and Schlenk line are removed, the solution is further stirred at room temperature for 48 hours. After 48 hours the PEGA solution is added to a separating funnel with cold 1M NaOH (3°C, 100 mL) and shaken vigorously before separating the organic and aqueous layer into two separate flasks. This is performed in triplicate on the organic phase. After completing this set of washes the organic phase is washed in triplicate with deionised water. The resulting organic phase is then dried using anhydrous magnesium sulphate before being filtered into a 100 mL rotary evaporation flask and a rotary evaporator is used to remove any excess DCM. The remaining solution is added dropwise to cold diethyl ether (3°C, 100 mL) with constant stirring. The resulting precipitate, a white powder that is PEGA, is then vacuum filtered and dried. This white powder is then taken for NMR to confirm the presence of the alkyne functionalisation.

Palladium catalysed oxidative carbonylation (BT-GN) reactions

All experiments were performed using a LabVIEW setup, with pH probes and temperature probes all calibrated using NIST standard buffers. The temperature for all these experiments was maintained with a water bath at 20°C.

Chi-IM-PdCl₂ with PEGA in Ethanol

In the conical flask, Chi-IM-PdCl₂ (200 mg), PEGA (200 mg) and KI (4.15 g) was added to ethanol (100 mL). The flask was then placed into the reaction setup and logging of the pH and temperature was started in conjunction with the purging of CO and air at 15 ml/min.

Reused Chi-IM-PdCl₂ with PEGA in Ethanol

In the conical flask, used Chi-IM-PdCl₂ (200 mg), PEGA (200 mg) and KI (4.15 g) was added to ethanol (100 mL). The flask was then placed into the reaction setup and logging of the pH and temperature was started in conjunction with the purging of CO and air at 15 ml/min.

Recovery of Chi-IM-PdCl₂ for BT-GN reaction

The conical flasks containing Chi-IM-PdCl₂ used in the *BT-GN reaction* is filtered using a Buchner filtration setup. It is then washed with methanol (100 mL) three times before being left to dry under vacuum for 3 hours.

RESULTS AND DISCUSSION

Chi-IM-PdCl₂ with PEGA in Ethanol

Initial runs using fresh Chi-IM-PdCl₂ and PEGA last for approximately 1000 minutes. The pH drops to 5 before raising to 6.6 and maintain a pH between these two values. The period of the oscillations starts at around 300 minutes before dropping to smaller intervals as the oscillations comes to a stop. While the oscillations are short when compared to previous oscillatory reactions for PdI₂/PEGA and PdI₂/PhAc systems the presences of oscillations are a net positive towards the goal of producing smart materials with the *BT-GN reaction* as a driving force.

Used Chi-IM-PdCl₂ with PEGA in Ethanol

Upon using recovered catalyst from the previous reaction, the oscillations last for just under 6000 minutes. The pH drops to 3.5 before rising to a high of 6.5 and fluctuates within that range. The period of the oscillations starts from a high of 600 minutes at the start and drops as every time the pH drops until the oscillations stop at around 6000 minutes.

These results indicate that catalyst type strongly determine characteristics of the oscillatory behaviour. This behaviour has been shown to be replicable in our studies. Understanding the cause behind the increase in longevity in oscillations could be the key behind using Chi-IM-PdCl₂ and PEGA as a driving force to produce an autonomous mechanical oscillatory system that can last for several days.

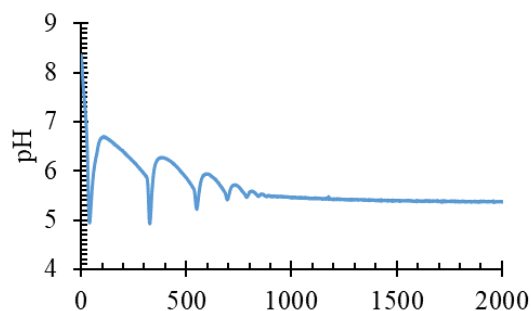


Figure 1. A graph showing oscillations in pH with Chi-IM-PdCl₂ and PEGA in ethanol over 2000 minutes.

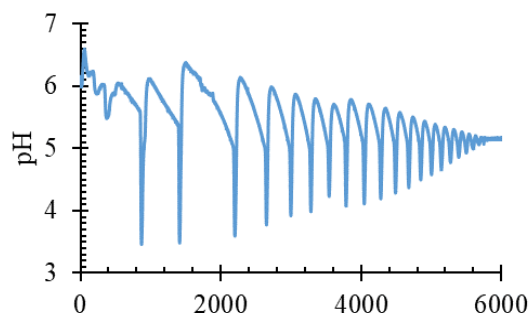


Figure 2. A graph showing oscillations in pH with used Chi-IM-PdCl₂ and PEGA in ethanol over 6000 minutes.

REFERENCES

- [1] A.V. Malashkevich , A. Lev , G. Bruk and O. N. Temkin , *J. Phys. Chem. A*, 1997, **101**, 9824—9827
- [2] V. R. Khabibulin , A. V. Kulik , I. V. Oshanina , L. G. Bruk , O. N. Temkin , V. M. Nosova , Y. A. Ustynyuk , V. K. Bel'skii , A. I. Stash , K. A. Lysenko and M. Y. Antipin , *Kinet. Catal.*, 2007, **48**, 228—244
- [3] K. Novakovic, C. Grosjean, S. K. Scott, A. Whiting, M. J. Willis and A. R. Wright, *Chem. Phys. Lett.*, 2007, **435**, 142—147
- [4] A. Isakova and K. Novakovic, *Eur. Polym. J.*, 2017, **95**, 430 —439
- [5] C. Grosjean, K. Novakovic, S. K. Scott, A. Whiting, M. J. Willis and A. R. Wright, *J. Mol. Catal. A: Chem.*, 2008, **284**, 33 —39
- [6] K. Novakovic, A. Mukherjee, M. Willis, A. Wright, S. Scott and A. R. Wright, *Phys. Chem. Chem. Phys.*, 2009, **11**, 9044
- [7] J. Parker and K. Novakovic, *React. Kinet., Mech. Catal.*, 2016, **118**, 73 —85
- [8] J. Parker and K. Novakovic, *React. Kinet., Mech. Catal.*, 2018, **123**, 113 —124
- [9] J. Parker and K. Novakovic, *ChemPhysChem*, 2017, **18**, 1981 —1986
- [10] L. Donlon and K. Novakovic, *Chem. Commun.*, 2014, **50**, 15506 —15508
- [11] A. Isakova and K. Novakovic, *J. Mater. Chem. B*, 2018, **6**, 5003—5010

CIRCADIAN RHYTHM FUNCTION COUPLING TO THE UPGRADED HYPOTHALAMIC-PITUITARY-ADRENAL (HPA) AXIS WITH INCORPORATED ARGININE VASOPRESSIN

A. S. Stojiljković¹, A. Stanojević², A. Ivanović-Šašić³, Ž. Čupić³ and Lj. Kolar-Anić^{2,3}

¹ *Institute of General and Physical Chemistry, University of Belgrade, Studentski trg 12/V, P.O. Box 45, Belgrade, Serbia (alek.stoj@gmail.com)*

² *Faculty of Physical Chemistry, University of Belgrade, Studentski trg 12-16, 11000 Belgrade, Serbia*

³ *Institute of Chemistry, Technology and Metallurgy, University of Belgrade, Njegoševa 12, 11000 Belgrade, Serbia.*

ABSTRACT

An upgraded model of the Hypothalamic-Pituitary-Adrenal (HPA) axis has been developed that advances our previously proposed low-dimensional HPA model by including the effects of arginine vasopressin (AVP) that is a key modulator of HPA axis function. The upgraded model allows us to emulate AVP effects on HPA axis dynamics individually and in synergy with the corticotropin-releasing hormone (CRH). In this work, we examine how coupling of the circadian function through summarised reaction steps describing CRH and AVP biosynthesis in the same neuronal cell group of the hypothalamic paraventricular nucleus (PVN) affects HPA axis dynamics. Results of numerical simulations show that coupling of the circadian function through both, CRH and AVP summarised biosynthesis reaction steps simultaneously, emulates best the HPA axis dynamics, in line with literature findings.

INTRODUCTION

The hypothalamic-pituitary-adrenal (HPA) axis represents a complex neuroendocrine system that couples the functions of hypothalamus, pituitary and adrenal glands to preserve the organism's homeostasis under physiologically normal and various stressful conditions. For that purpose, a proper oscillatory dynamics of HPA axis comprising hormones, with ultradian oscillations (period of 20 minutes to 2 hours) superimposed on circadian oscillations (period of about 24 hours), is an essential precondition [1].

The aim of this study is to examine the coupling conditions between ultradian and circadian rhythms of the hormones of the upgraded HPA axis model with incorporated arginine vasopressin (AVP), using modelling of reaction mechanism and numerical simulations. For that purpose, a low-dimensional model with five dynamic variables is employed as the initial model [2]. The upgraded low-dimensional model is now consisted of six dynamic variables: the corticotropin-releasing hormone (CRH), arginine vasopressin (AVP), adrenocorticotrophic hormone (ACTH), cortisol (CORT), aldosterone (ALDO) and cholesterol (CHOL), as the only precursor of all steroid hormones.

MODEL AND METHODS

The pre-existing low-dimensional HPA model [2] has been extended to describe arginine vasopressin (AVP) effects on adrenocorticotrophic hormone (ACTH) release (Table 1).

Table 1. Summarised reaction steps associated with arginine vasopressin (AVP) that are incorporated in the upgraded low-dimensional model of the HPA axis

$\xrightarrow{k_1} \text{AVP}$	(R1)
$\xrightarrow{k_2} \text{AVP}$	(R2)
$\text{AVP} \xrightarrow{k_3} \text{ACTH}$	(R3)
$\text{CRH} + \text{AVP} \xrightarrow{k_4} \text{ACTH}$	(R4)
$\text{AVP} \xrightarrow{k_5} \text{P}_3$	(R5)

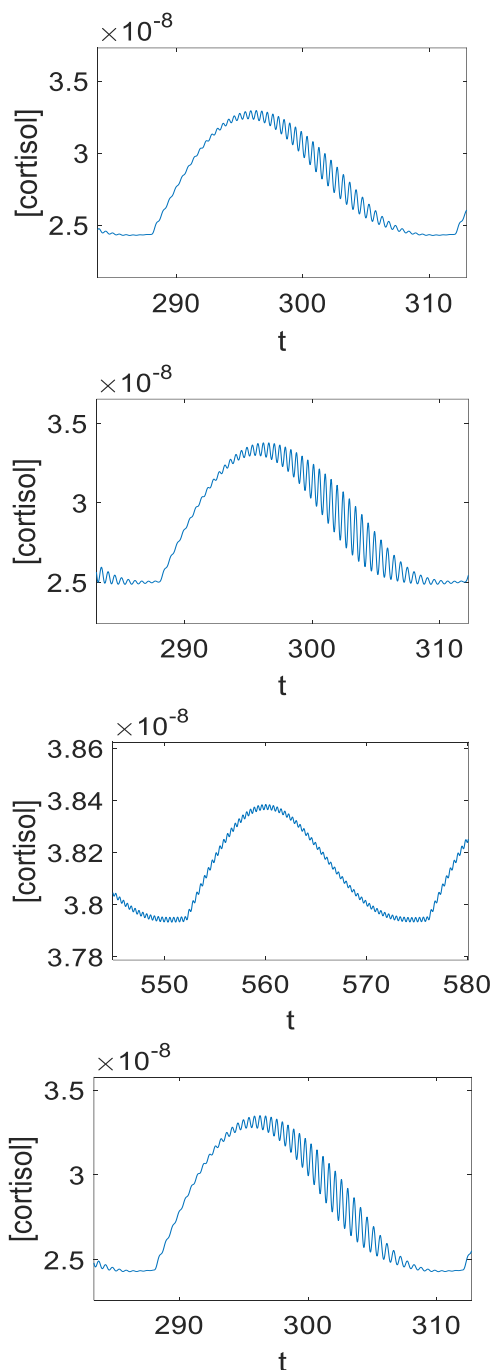
All reaction steps presented in Table 1 describe end-results of a series of complex biochemical processes. In more detail, series of processes of the biosynthesis of AVP in the parvicellular part of the hypothalamic paraventricular nucleus (PVN), and in the magnocellular neurosecretory system of the hypothalamus, resulting in corresponding inflows of AVP into the pituitary portal system are described by reaction steps (R1) and (R2), respectively. Reaction step (R3) describes summarised series of complex biochemical processes resulting in ACTH secretion stimulated by AVP originating from both of these neuronal populations. Series of complex biochemical reactions leading to ACTH production and release due to a strong synergistic effect of CRH and AVP on ACTH secretion by the pituitary gland, are summarised by reaction step (R4) [3]. Reaction step (R5) describes summarised series of complex biochemical processes leading to the elimination of AVP.

Numerical simulations were conducted using the Matlab software package and the ode15s solver routine based on the Gear algorithm for integration of stiff differential equations. In all simulations, the absolute and relative tolerance errors were $3 \cdot 10^{-20}$ and $1 \cdot 10^{-14}$, respectively. The initial concentrations, expressed in mol dm^{-3} and designated as M, were: $[\text{CHOL}]_0 = 3,4 \cdot 10^{-4}$ M, $[\text{CRH}]_0 = 1 \cdot 10^{-12}$ M, $[\text{AVP}]_0 = 1 \cdot 10^{-12}$ M, $[\text{ACTH}]_0 = 8 \cdot 10^{-8}$ M, $[\text{CORT}]_0 = 4 \cdot 10^{-8}$ M and $[\text{ALDO}]_0 = 1,5 \cdot 10^{-9}$ M. If not otherwise stated, the rate constants were: $k_1 = 1,83 \cdot 10^{-8} \text{ mol dm}^{-3} \text{ min}^{-1}$, $k_2 = 1,537 \cdot 10^{-9} \text{ mol dm}^{-3} \text{ min}^{-1}$, $k_3 = 7,79 \cdot 10^{-3} \text{ min}^{-1}$, $k_4 = 1,098 \cdot 10^9 \text{ mol}^{-1} \text{ dm}^3 \text{ min}^{-1}$ and $k_5 = 1,386 \cdot 10^{-1} \text{ min}^{-1}$. The circadian rhythm function $D = d_1 - 0,079145093 \cdot d_2 + \{0,064 \cdot \sin(2\pi t/1440) + 0,12 \cdot \text{abs}[\sin(\pi t/1440)]\} \cdot d_2$ is used to couple to the upgraded model through the reaction steps describing biosynthesis of CRH and AVP in the same neuron cell groups of the hypothalamic PVN.

RESULTS

Couplings of the circadian function D to the upgraded HPA model through reaction steps related to the inflows of CRH and AVP into the system from the same neuron cell group and sharing the same rate constant $= 1,830 \cdot 10^{-8} \text{ mol dm}^{-3} \text{ min}^{-1}$, have been examined *in silico* for inflow reaction steps both individually and simultaneously (Figure 1.). These results were further compared with those obtained from the initial HPA model, where CRH is the only species that influence ACTH secretion. The same value for rate constant is used. Namely, when function D is coupled to the upgraded model through CRH and AVP inflow reaction steps simultaneously (Figure 1, case (3)), results show decrease of the amplitude of [CORT] ultradian oscillations compared to those obtained by the coupling of function D through CRH inflow reaction step solely (Figure 1, case (1)). On the other hand, function D coupling through solely AVP inflow reaction step (R1), produces very low amplitude of ultradian oscillations (A_{UD}), that are uniformly superimposed on circadian [CORT] oscillations of also low circadian amplitudes (A_{CD}) (Figure 1, case (2)). By comparing the results obtained by coupling the function D through CRH inflow to the initial minimal HPA model that does not include AVP (Fig. 1, (0)) and the upgraded model with AVP using the same rate constant value for CRH inflow (Fig. 1, (1)), it can be noticed that cortisol A_{UD} is higher in the upgraded HPA model,

which is in better agreement with experimentally measured values reported in the literature. Taken together, A_{UD} increases between the examined cases in the following manner: $A^{(2)}_{UD} < A^{(0)}_{UD} < A^{(3)}_{UD} < A^{(1)}_{UD}$. There are numerous studies on humans indicating several-fold increased [CORT] due to CRH and AVP acting synergistically on corticotrope cells that could fall into the domain of A_{UD} [4-6].



- (0)** **Figure 1.** Temporal evolution of cortisol concentration ([CORT]) emulated using the minimal or the upgraded model of HPA axis dynamics with the circadian function being coupled through CRH and/or AVP inflow. Daily changes in blood cortisol concentration emulated using: **(0)** the minimal HPA axis model without AVP, when the rate constant of CRH inflow is $1,830 \cdot 10^{-8} \text{ M}$; **(1)** the upgraded HPA axis model with AVP, when the rate constant of CRH inflow is $1,830 \cdot 10^{-8} \text{ M}$ and AVP inflow is disregarded; **(2)** the upgraded HPA axis model with AVP, when the rate constant of AVP inflow is $1,830 \cdot 10^{-8} \text{ M}$ and CRH inflow is disregarded; **(3)** the upgraded HPA axis model with AVP, when the rate constant of CRH and AVP inflow are both $1,830 \cdot 10^{-8} \text{ M}$.
- (2)** Of note, when function D is coupled to the model simultaneously through these inflow reaction steps (3) or only through CRH inflow reaction step, (1) parameters of the circadian function D were: $d_1 = 0,840978$ and $d_2 = 0,957$. On the other hand, when function D is coupled through AVP inflow reaction step (R1) solely (2), corresponding parameters were: $d_1 = 1,1331072$ and $d_2 = 0,957$. In the initial HPA model, (0) with CRH as the only species that influence ACTH secretion, $d_1 = 0,88524$ and $d_2 = 0,957$ were parameters of function D coupling only through CRH inflow reaction step. Time is given in hours (h) and cortisol concentration in mol dm^{-3} .
- (3)**

Circadian function D coupling through the CRH inflow reaction step only will result in [AVP] minimum appearing around 8 o'clock in the morning (8 h) and [AVP] maximum around midnight (24 h). This is in contrast with [AVP] extreme values appearance when the function D is coupled through CRH and AVP inflow reaction steps simultaneously (data not shown). Since [AVP] reaches

its minimum in the early evening, around 18-20 o'clock, and a maximum around 2-6 o'clock in the morning [7], the best agreement with experimental results could be achieved when the daily function D is coupled to the model through both, CRH and AVP inflows simultaneously. Additionally, it has been pinpointed in the literature that both parvocellular CRH and AVP participate in the generation of a circadian ACTH and CORT rhythm [8]. In line with these experimental findings, results obtained using the upgraded model favour coupling of the circadian function through CRH and AVP inflow reaction steps simultaneously.

CONCLUSION

The pre-existing low-dimensional mathematical model of HPA axis dynamics is extended to include AVP. This enhances the comprehensiveness and physiological plausibility of the model, while preserving its tractability to mathematical analysis and simulation. A step forward is made by finding the appropriate conditions for coupling between ultradian and circadian rhythms of the HPA axis hormones. However, the proposed model still needs further improvements and refinements for examination of AVP and CRH effects and synergistic influence on the HPA axis dynamics.

Acknowledgement

This study was supported by Ministry of Education, Science and Technological Development of the Republic of Serbia (Contracts no. 451-03-9/2021-14/200146, 451-03-9/2021-14/200026 and 451-03-9/2021-14/200051).

REFERENCES

- [1] C. Tsigos and G. P. Chrousos, *Journal of Psychosomatic Research* (2002) **53**, 865-871.
- [2] V. M. Marković, Ž. Čupić, S. Maćešić, A. Stanojević, V. Vukojević and Lj. Kolar-Anić, *Mathematical Medicine and Biology* (2016) **33** (1), 1–28.
- [3] F. A. Antoni, *Frontiers in Neuroendocrinology* (1993) **14** (2), 76-122.
- [4] R. A. Salata, D. B. Jarrett, J. G. Verbalis, A. G. Robinson, *The Journal of Clinical Investigation* (1988) **81**(3), 766-774.
- [5] C. R. DeBold, W. R. Sheldon, G. S. DeCherney, R. V. Jackson, A. N. Alexander, W. Vale, J. Rivier, and D. N. Orth, *The Journal of Clinical Investigation* (1984) **73**(2), 533-538.
- [6] J.H. Liu, K. Muse, P. Contreras, D. Gibbs, W. Vale, J. Rivier, S. S. C. Yen, *The Journal of Clinical Endocrinology & Metabolism* (1983) **57** (5), 1087-1089.
- [7] ML Forsling, H Montgomery, D Halpin, RJ Windle, DF Treacher, *Experimental Physiology* (1998) **83** (3), 409-418.
- [8] George P. Chrousos, *Endocrinology* (1998) **139** (2), 437–40.

STOICHIOMETRIC NETWORK ANALYSIS OF THE MODEL OF OSCILLATORY CARBONYLATION OF PEGA IN OPEN REACTOR

S. Maćešić¹ K. Novaković², Lj. Kolar-Anić¹

¹ University of Belgrade, Faculty of Physical Chemistry, Studentski trg 12-16, 11000 Belgrade, Serbia, e-mail: stevan.macesic@ffh.bg.ac.rs

² Newcastle University, School of Engineering, Merz Court, Newcastle upon Tyne, NE1 7RU, United Kingdom

ABSTRACT

Subset of reactions of the model of palladium-catalysed oscillatory carbonylation of PEGA was analyzed. Stability analysis was then performed using stoichiometric network analysis (SNA). It was found that considered sub-model can simulate Andronov-Hopf and saddle-node bifurcations.

INTRODUCTION

Extensive studies of oscillatory carbonylation reactions in the presence of the polymeric substrate and polymeric catalysts[1, 2] raised necessity to have realistic mechanism which can accurately predict system behavior. With aim to achieve this goal a realistic model capable to reproduce oscillatory behavior of considered system was derived.[3] In this paper the minimal set of model's reactions which can result in oscillatory dynamics is analyzed.

MODEL

Considered subset of reactions is presented in the Table 1. This sub-model consists of 9 reactions of the original model. Concentrations of CH₃OH, O₂ and CO and PEGA are in excess, therefore assumed as constant and included in the corresponding rate constants k_i . The species H₂O and PEGP are the products of reactions and consequently they do not appear in the reaction rates. Concentrations c_1 - c_{11} in Table 1 correspond to PdI₄²⁻, Int₁, HI, Int₂, Int₃, Pd, I⁻, Pd₂I₄²⁻, I₂, Pd₂I₆²⁻, H⁺ respectively while k_1 - k_{10} and k_{-12} are related rate constants.

Table 1. Submodel of the mechanism of oscillatory carbonylation of PEGA proposed by Maćešić et al[3]

$\text{PdI}_4^{2-} + \{\text{CH}_3\text{OH} + \text{CO}\} \rightarrow \text{Int}_1 + \text{HI}$	$r_1 = k_1 c_1$	(R ₁)
$\text{Int}_1 + \text{PEGA} \rightarrow \text{Int}_2$	$r_2 = k_2 c_2$	(R ₂)
$\text{Int}_2 + \{\text{CH}_3\text{OH} + \text{CO}\} \rightarrow \text{Int}_3 + \text{HI}$	$r_3 = k_3 c_4$	(R ₃)
$\text{Int}_3 \rightarrow \text{PEGP} + \text{Pd} + 2\text{I}^-$	$r_4 = k_4 c_5$	(R ₄)
$\text{PdI}_4^{2-} + \text{Pd} \rightarrow \text{Pd}_2\text{I}_4^{2-}$	$r_7 = k_7 c_1 c_6$	(R ₇)
$\text{Pd}_2\text{I}_4^{2-} + \text{I}_2 \rightarrow \text{Pd}_2\text{I}_6^{2-}$	$r_8 = k_8 c_8 c_9$	(R ₈)
$\text{Pd}_2\text{I}_6^{2-} + 2\text{HI} \rightarrow 2\text{PdI}_4^{2-} + 2\text{H}^+$	$r_9 = k_9 c_{10} c_3^2$	(R ₉)
$2\text{HI} + \{0.5\text{O}_2\} \rightarrow \text{I}_2 + \text{H}_2\text{O}$	$r_{10} = k_{10} c_3^2$	(R ₁₀)
$\text{H}^+ + \text{I}^- \rightarrow \text{HI}$	$r_{-12} = k_{-12} c_{11} c_7$	(R ₋₁₂)

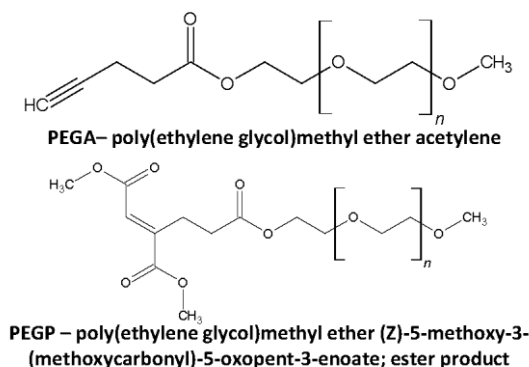


Figure 1. Structural formulas of PEGA and PEGP

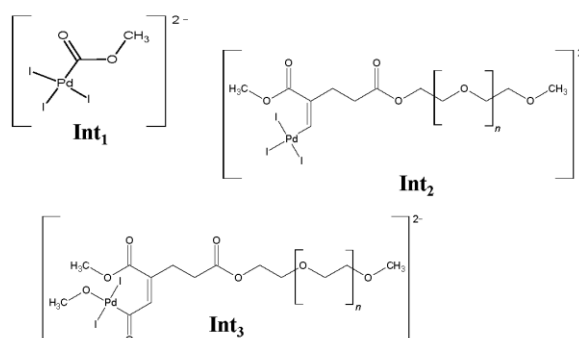


Figure 2. Structural formulas of Int₁, Int₂ and Int₃

STOICHIOMETRIC NETWORK ANALYSIS

Stoichiometric network analysis (SNA)[4] is very powerful method for stability analysis of complex reaction network which allows steady-state stability evaluation solely based on reaction network structure. Foundation of this method is decomposition of the reaction network into set of steady-state sub-networks and expressing reaction rates $r_{ss,i}$ at the steady state as linear combination of new parameters, current rates j_i , using relation $\mathbf{r}_{ss} = \mathbf{E}\mathbf{j}$ where \mathbf{E} is the matrix of extreme currents and \mathbf{j} is the vector of current rates. Matrix \mathbf{E} consists of nonnegative elements while each column represents one possible reaction pathway in the steady-state. Using new parameters kinetic equations can be written as $\mathbf{dx}/dt = \text{diag}(\mathbf{h})\mathbf{S}\text{diag}(\mathbf{E}\mathbf{j})\mathbf{x}^{\mathbf{K}}$, where $x_i = c_i/c_{i,ss}$ ($c_{i,ss}$ is steady-state concentration of intermediate species i , $i=1,2,\dots,11$), $h_i = 1/c_{i,ss}$ represents reciprocal steady-state concentration of species i , \mathbf{S} is stoichiometric matrix while \mathbf{K} is a matrix of the order of reactions. Stability of the steady state requires calculation of the eigenvalues λ_i of Jacobian matrix which in SNA notation has following form $\mathbf{M} = \mathbf{S}\text{diag}(\mathbf{E}\mathbf{j})\mathbf{K}^T\text{diag}(\mathbf{h})$. Eigenvalues are root of characteristic polynomial which in this case has form

$$|\lambda\mathbf{I} - \mathbf{M}| = \sum_{i=0}^n \alpha_i \lambda^{n-i} = \lambda^8 + \alpha_1 \lambda^7 + \alpha_2 \lambda^6 + \alpha_3 \lambda^5 + \alpha_4 \lambda^4 + \alpha_5 \lambda^3 + \alpha_6 \lambda^2 + \alpha_7 \lambda + \alpha_8 \quad (1)$$

= 0

where α_i represents coefficients of characteristic polynomial. Coefficients α_9 - α_{11} are equal to 0 as a consequence of conservation constraints. Eigenvalues can be evaluated using Hurwitz determinants but in this particular case α -approximation was most convenient. According to α -approximation steady state is unstable if there is at least one negative coefficient α_i of characteristic polynomial given in equation (1).

RESULTS AND DISCUSSION

Matrices **S**, **K** and **E** for the model presented in Table 1 are presented in equation 2-4:

$$\mathbf{S} = \begin{bmatrix} -1 & 0 & 0 & 0 & -1 & 0 & 2 & 0 & 0 \\ 1 & -1 & 0 & 0 & 0 & 0 & 0 & 0 & 0 \\ 1 & 0 & 1 & 0 & 0 & 0 & -2 & -2 & 1 \\ 0 & 1 & -1 & 0 & 0 & 0 & 0 & 0 & 0 \\ 0 & 0 & 1 & -1 & 0 & 0 & 0 & 0 & 0 \\ 0 & 0 & 0 & 1 & -1 & 0 & 0 & 0 & 0 \\ 0 & 0 & 0 & 2 & 0 & 0 & 0 & 0 & -1 \\ 0 & 0 & 0 & 0 & 1 & -1 & 0 & 0 & 0 \\ 0 & 0 & 0 & 0 & 0 & -1 & 0 & 1 & 0 \\ 0 & 0 & 0 & 0 & 0 & 1 & -1 & 0 & 0 \\ 0 & 0 & 0 & 0 & 0 & 0 & 2 & 0 & -1 \end{bmatrix} \begin{matrix} \text{PdI}_4^{2-} \\ \text{Int}_1 \\ \text{HI} \\ \text{Int}_2 \\ \text{Int}_3 \\ \text{Pd} \\ \text{I}^- \\ \text{Pd}_2\text{I}_4^{2-} \\ \text{I}_2 \\ \text{Pd}_2\text{I}_6^{2-} \\ \text{H}^+ \end{matrix} \quad (2)$$

$$\mathbf{K} = \begin{bmatrix} 1 & 0 & 0 & 0 & 0 & 0 & 0 & 0 & 0 \\ 0 & 1 & 0 & 0 & 0 & 0 & 0 & 0 & 0 \\ 0 & 0 & 0 & 0 & 0 & 0 & 2 & 2 & 0 \\ 0 & 0 & 1 & 0 & 0 & 0 & 0 & 0 & 0 \\ 0 & 0 & 0 & 1 & 0 & 0 & 0 & 0 & 0 \\ 0 & 0 & 0 & 0 & 1 & 0 & 0 & 0 & 0 \\ 0 & 0 & 0 & 0 & 0 & 0 & 0 & 0 & 1 \\ 0 & 0 & 0 & 0 & 0 & 1 & 0 & 0 & 0 \\ 0 & 0 & 0 & 0 & 0 & 1 & 0 & 0 & 0 \\ 0 & 0 & 0 & 0 & 0 & 0 & 1 & 0 & 0 \\ 0 & 0 & 0 & 0 & 0 & 0 & 0 & 0 & 1 \end{bmatrix} \begin{matrix} \text{PdI}_4^{2-} \\ \text{Int}_1 \\ \text{HI} \\ \text{Int}_2 \\ \text{Int}_3 \\ \text{Pd} \\ \text{I}^- \\ \text{Pd}_2\text{I}_4^{2-} \\ \text{I}_2 \\ \text{Pd}_2\text{I}_6^{2-} \\ \text{H}^+ \end{matrix} \quad (3)$$

$$\mathbf{E}^T = [1 \quad 1 \quad 2] \mathbf{E}_1 \quad (4)$$

where rows of matrices **S** and **K** correspond to the following intermediate species: PdI_4^{2-} , Int_1 , HI , Int_2 , Int_3 , Pd , I^- , $\text{Pd}_2\text{I}_4^{2-}$, I_2 , $\text{Pd}_2\text{I}_6^{2-}$, H^+ respectively.

Analysis of the coefficients of characteristic polynomials α_i has shown that this sub-model can simulate both Andronov-Hopf (AH) and saddle-node (SN) bifurcations. Numerical analysis allowed us to determine conditions under which AH and SN bifurcations emerge. It was found that steady-states with lower steady-state concentrations of PdI_4^{2-} and H^+ compared to the steady-state concentrations of remaining species play important role in the emergence of instabilities but it has to be accompanied by additional species in order to produce AH or SN bifurcation. In case of SN bifurcation it is required that lower steady-state concentrations of PdI_4^{2-} and H^+ is accompanied by low steady-state concentrations of I_2 . On the other hand, for the emergence of AH bifurcation to occur low steady-state concentration of PdI_4^{2-} and H^+ need to be accompanied by low steady-state concentration of $\text{Pd}_2\text{I}_4^{2-}$.

CONCLUSION

Essential subset of reactions of the model of palladium-catalysed oscillatory carbonylation of PEGA was analyzed using SNA. It was found that model can exhibit Andronov-Hopf and saddle-node bifurcations. Emergence of the saddle-node bifurcation is conditioned by low steady-state concentration of PdI_4^{2-} and H^+ accompanied by low concentration of I_2 while low steady-state

concentration of PdI_4^{2-} and H^+ accompanied by low steady-state concentration of $\text{Pd}_2\text{I}_4^{2-}$ is essential for the emergence of Andronov-Hopf bifurcation.

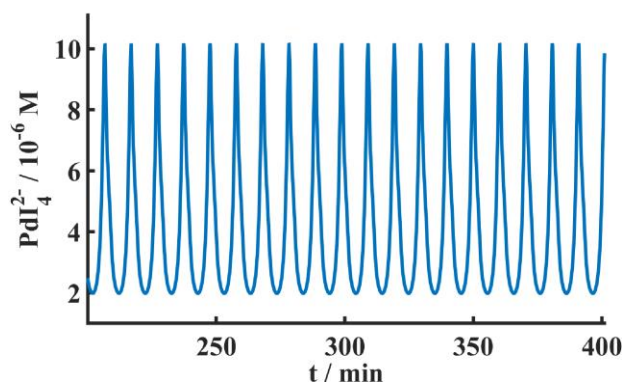


Figure 1. Oscillatory dynamics of the model presented in Table 1 obtained in numerical simulation for: $h_1 = 2 \times 10^5 \text{ M}^{-1}$, $h_2 = 1 \times 10^4 \text{ M}^{-1}$, $h_3 = 1 \times 10^4 \text{ M}^{-1}$, $h_4 = 1 \times 10^4 \text{ M}^{-1}$, $h_5 = 1 \times 10^4 \text{ M}^{-1}$, $h_6 = 1 \times 10^4 \text{ M}^{-1}$, $h_7 = 1 \times 10^4 \text{ M}^{-1}$, $h_8 = 2.5 \times 10^5 \text{ M}^{-1}$, $h_9 = 1 \times 10^4 \text{ M}^{-1}$, $h_{10} = 1 \times 10^4 \text{ M}^{-1}$, $h_{11} = 2.3 \times 10^5 \text{ M}^{-1}$, $j_1 = 1 \times 10^{-4} \text{ M min}^{-1}$. Initial dimensionless concentrations x_1 - x_{11} were all equal to 0.99

Acknowledgement

KN would like to acknowledge UK Engineering and Physical Sciences Research Council (EPSRC) grant number EP/N033655/1 for financial support. Support from the Ministry of Education, Science and Technological Development of the Republic of Serbia (Grant Numbers 172015 and 45001, and Contract numbers 451-03-9/2021-14/200026 and 451-03-9/2021-14/200146), is gratefully acknowledged by SM, ŽČ and LjKA.

REFERENCES

- [1] A. Isakova, B. J. Murdoch, K. Novakovic, *Phys. Chem. Chem. Phys.* 2018, 20, 9281–9288.
- [2] A. Isakova, K. Novakovic, *J. Mater. Chem. B.* 2018, 30, 5003-5010.
- [3] S. Macesic, Z. Cupic, K. Novakovic, J. Parker, S. Anic, Lj. Kolar-Anic, *MATCH-COMMUN MATH CO.* 2019, 81, 5–34.
- [4] B. L. Clarke, *Cell Biochem. Biophys.* 1988, 12 (1), 237–253.

AUTOCATALYSIS OF HIO AND ASSOCIATED REACTION-DIFFUSION FRONTS IN THE MODEL OF BRAY-LIEBHAFSKY REACTION

S. Maćešić¹ and Ž. Čupić²

¹ *University of Belgrade, Faculty of Physical Chemistry, Studentski trg 12-16, 11000 Belgrade, Serbia, e-mail: stevan.macesic@ffh.bg.ac.rs*

² *University of Belgrade, Institute of Chemistry, Technology and Metallurgy, Njegoševa 12, 11000 Belgrade, Serbia*

ABSTRACT

Analysis of the HIO autocatalytic production in the model of Bray-Liebhafsky reaction was carried out. 1D reaction-diffusion simulations were performed on the two subsets of reactions of the BL model responsible for functioning of the cycle where autocatalytic production of HIO occurs. Characteristics of these two reaction subsets and reaction-diffusion fronts emerging from them were analysed.

INTRODUCTION

The Bray-Liebhafsky (BL)[1,2] reaction is the decomposition of hydrogen-peroxide in the presence of iodate and hydrogen ions into water and oxygen. The process of BL reaction can be represented with following net reaction



Decomposition of H_2O_2 is a complex process known for wide range of dynamical states such as simple oscillation, mixed-mode oscillations and chaos which are the result of present autocatalytic cycles. Combined presence of the autocatalysis and diffusion results in the emergence of reaction-diffusion fronts which propagate with constant velocity and constant shape. Therefore, in this paper we focus on the investigation of reaction-diffusion fronts which are the consequence of two pathways where autocatalytic production of HIO occurs.

MODEL

The model of the BL oscillatory reaction, M(1-6, 8)[3, 4] is given in Table 1. This model consists of seven reactions, among which three are reversible. There are five intermediates species I^- , HIO, HIO_2 , I_2 , I_2O (whose concentrations are denoted by c_2 - c_6 respectively in expressions for reaction rates in Table 1) essential for the dynamics, and reactant H_2O_2 (concentration denoted by c_1) required for the initiation of the reaction. Concentrations of O_2 , H_2O , H^+ , and IO_3^- can be considered constant due to much slower temporal evolution and therefore are incorporated in the values of the rate constants.

Table 1. Model of Bray-Liebhafsky reaction M (1-6, 8)[3, 4]

$\text{IO}_3^- + \text{I}^- + 2\text{H}^+ \xrightleftharpoons[k_{-1}]{k_1} \text{HIO} + \text{HIO}_2$	$r_1 = k_1 c_2, r_{-1} = k_{-1} c_3 c_4$	(R1)
$\text{HIO}_2 + \text{I}^- + \text{H}^+ \xrightarrow{k_2} \text{I}_2\text{O} + \text{H}_2\text{O}$	$r_2 = k_2 c_2 c_4$	(R2)
$\text{I}_2\text{O} + \text{H}_2\text{O} \xrightleftharpoons[k_{-3}]{k_3} 2\text{HIO}$	$r_3 = k_3 c_6, r_{-3} = k_{-3} c_3^2$	(R3)
$\text{HIO} + \text{I}^- + \text{H}^+ \xrightleftharpoons[k_{-4}]{k_4} \text{I}_2 + \text{H}_2\text{O}$	$r_4 = k_4 c_2 c_3, r_{-4} = k_{-4} c_5$	(R4)
$\text{HIO} + \text{H}_2\text{O}_2 \xrightarrow{k_5} \text{I}^- + \text{H}^+ + \text{O}_2 + \text{H}_2\text{O}$	$r_5 = k_5 c_1 c_3$	(R5)
$\text{I}_2\text{O} + \text{H}_2\text{O}_2 \xrightarrow{k_6} \text{HIO} + \text{HIO}_2$	$r_6 = k_6 c_1 c_6$	(R6)
$\text{IO}_3^- + \text{H}^+ + \text{H}_2\text{O}_2 \xrightarrow{k_8} \text{HIO}_2 + \text{O}_2 + \text{H}_2\text{O}$	$r_8 = k_8 c_1$	(R8)

Numerical simulations were carried out by solving the following set of reaction-diffusion equations:

$$\begin{aligned}
 \frac{dc_1}{dt} &= D \frac{d^2 c_1}{dx^2} - r_5 - r_6 - r_8 \\
 \frac{dc_2}{dt} &= D \frac{d^2 c_2}{dx^2} - r_1 + r_{-1} - r_2 - r_4 + r_{-4} + r_5 \\
 \frac{dc_3}{dt} &= D \frac{d^2 c_3}{dx^2} + r_1 - r_{-1} + 2r_3 - 2r_{-3} - r_4 + r_{-4} - r_5 + r_6 \\
 \frac{dc_4}{dt} &= D \frac{d^2 c_4}{dx^2} + r_1 - r_{-1} - r_2 + r_6 + r_8 \\
 \frac{dc_5}{dt} &= D \frac{d^2 c_5}{dx^2} - r_4 - r_{-4} \\
 \frac{dc_6}{dt} &= D \frac{d^2 c_6}{dx^2} + r_2 - r_3 + r_{-3} - r_6
 \end{aligned} \tag{2}$$

where expressions for r_i are defined in Table 1 while $D = 10^{-5} \text{ cm}^2 \text{ s}^{-1}$ represents the diffusion coefficient which was considered to be the same for all species.

NUMERICAL SIMULATIONS

Numerical simulations were carried out in a thin layer of solution where 1D diffusion is present. For 1D reaction-diffusion simulations Python *odeint* function from *scipy* module was used. In simulations no flux boundary condition was used.

RESULTS AND DISCUSSION

Previous analysis[5] of the model M(1-6, 8) found that interaction between HIO, HIO₂ and I₂O forms destabilizing feedback cycle which can lead to the emergence of oscillatory dynamics. Since autocatalysis is responsible for the formation of destabilizing feedback cycle, the understanding the mechanism of autocatalysis is of great importance. By analysing reaction pathways it was found that

there are two pathways which can lead to autocatalytic production of HIO. First pathway is made from reactions R_1 , R_2 , R_3 , and R_5 and results in cubic autocatalysis of HIO with net reaction



while the second is comprised from reactions R_{-1} , R_2 , R_3 , and R_8 with net reaction



To compare the validity, the characteristics and the efficiency of the found autocatalytic cycles 1D reaction-diffusion simulations of pathways I (R_1 , R_2 , R_3 , and R_5) and II (R_{-1} , R_2 , R_3 , and R_8) were carried out. In reaction-diffusion simulations, conditions which correspond to the thin layer of solution, where 1D diffusion is present were emulated. In performed simulations, initial solution for both pathways contained H_2O_2 in the abundance while small amount of HIO was added into a narrow region of solution with width=0.15 cm. In both cases distance was set to be 1.5 cm. Addition of small amount of HIO in both cases resulted in the emergence of reaction-diffusion fronts which confirmed that both pathways are autocatalytic. Results of numerical simulations can be seen in Figure 1.



Figure 1. Results of numerical 1D reaction-diffusion simulations of: a) pathway I (R_1 , R_2 , R_3 and R_5) b) pathway II (R_{-1} , R_2 , R_3 and R_8). In both cases, initial conditions were: $[\text{H}_2\text{O}_2]_0 = 1 \times 10^{-2} \text{ M}$ with $[\text{HIO}]_0 = 1 \times 10^{-6}$ added into narrow region of solution (region width 0.15 cm). Initial concentrations of remaining species were set to 0.

Furthermore, it was found that in pathway I it took around 500 min for reaction-diffusion fronts to obtain constant shape while in case of pathway II they were formed almost instantaneously. To understand the strength of these autocatalytic pathways, velocity of the reaction-diffusion fronts was determined. Velocities were calculated by analysing the position of inflection point x_{inf} (where second derivative of concentration over distance equals to zero, $\partial^2 c_3 / \partial x^2 = 0$) as a function of time (see Figure 2) and linear dependence was found in both cases. It was found that reaction-diffusion fronts in pathway I propagate considerably slower compared to those found in pathway II. Velocities of pathway I and II are $v_{\text{I}} = 5.88 \times 10^{-4} \text{ cm s}^{-1}$ and $v_{\text{II}} = 1.31 \times 10^{-2} \text{ cm s}^{-1}$, respectively. Obtained results strongly suggest that pathway II is considerably more efficient in autocatalytic production of HIO. This can be explained by the fact that in pathway II the autocatalytic production of HIO occurs through reactions R_{-1} , R_2 , and R_3 while reaction R_8 allows continuous supply of HIO_2 which grants uninterrupted functioning of autocatalytic cycle. On the other, hand, in pathway I all reactions are incorporated in the autocatalytic production of HIO, which makes it much less efficient.

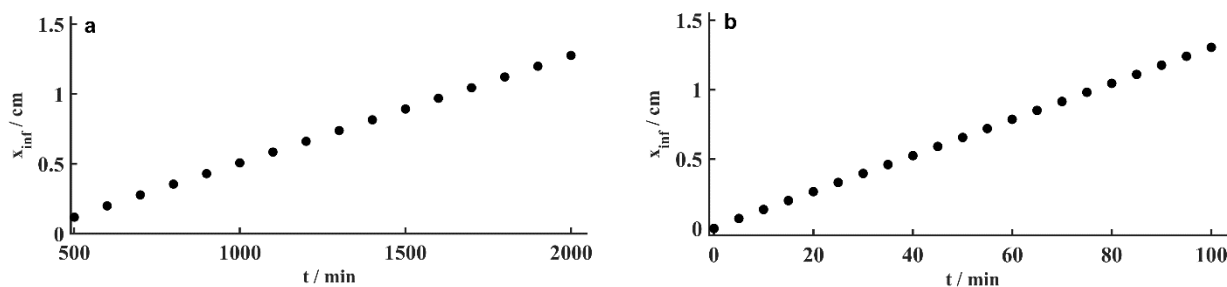


Figure 2. Dependence of the inflection point x_{inf} over time for: a) pathway I b) pathway II

CONCLUSION

The autocatalysis of HIO in the model M(1-6, 8) of BL reactions was analysed. Reaction pathway analysis has shown that two pathways can lead to the autocatalytic production of HIO in the considered model. The first pathway consists of reactions R_1 , R_2 , R_3 , and R_5 , while second is formed from R_{-1} , R_2 , R_3 , and R_8 . 1D reaction-diffusion simulations of both pathways confirmed the presence of the autocatalysis of HIO through the emergence of reaction-diffusion fronts. It was found that reaction-diffusion fronts obtained in pathway I propagates considerably slower than those found in pathway II. This suggests much greater efficiency of the autocatalytic production of HIO in pathway II.

Acknowledgement

Support from the Ministry of Education, Science and Technological Development of the Republic of Serbia (Grant Numbers 172015 and 45001, and Contract numbers 451-03-9/2021-14/200026 and 451-03-9/2021-14/200146), is gratefully acknowledged by SM and ŽČ.

REFERENCES

- [1] W. C. Bray, *J. Am. Chem. Soc.*, 1921, 43, 1262.
- [2] W. C. Bray and H. A. Liebafsky, *J. Am. Chem. Soc.*, 1931, 53, 38; 896; 2074.
- [3] Lj. Kolar-Anić, Đ. Mišljenović, S. Anić, G. Nicolis, *React. Kinet. Catal. Lett.* **1995**, 54, 35–41.
- [4] Lj. Kolar-Anić, Ž. Čupić, G. Schmitz, S. Anić, *Chem. Eng. Sci.* **2010**, 65, 3718–3728.
- [5] G. Schmitz, Lj. Kolar-Anić, S. R. Anić, Ž. Čupić, *J. Phys. Chem. A*, **2008** 112(51), 13452-13457.

QUANTUM ASPECTS AND IMPLICATIONS OF ELECTROCOALESCENCE PROCESS

A.M. Spasic¹, V. Manojlovic², M. Jovanovic²

¹*Institute for Technology of Nuclear and Other Mineral Raw Materials, Dept. of Chem.Engng., 86 F. d'Esperey St., 11000 Belgrade, Serbia. (a.spasic@itnms.ac.rs)*

²*Dept. of Tech. & Met., University of Belgrade, 4 Karnegijeva St., 11000 Belgrade, Serbia*

ABSTRACT

This is a brief presentation of multi-decennial work, at first as applied research and development (R&D), and later on as a fundamental research. In the pilot plant for uranium extraction from wet phosphoric acid the solution of entrainment problem was realized, that is breaking of double emulsions was explained, in some extent. Possible quantum aspects and implications, based on electrohydrodynamics principles and a theory or program of decoherence are discussed.

INTRODUCTION

Rheology or nano-rheology of emulsions and double emulsions play an important role in some physical, chemical, and biochemical processes, for example, the coalescence or electrocoalescence (EC), the life of biological cells, the polymer conformations and stability, DNA and other macromolecular structures. Some phenomena and events in these processes, for example, coalescence, and/or more precisely EC, are not deep enough presented or understood in a scientific literature. Therefore, one of the main objectives was a try to elucidate, in some extent, these phenomena and events [1-7]. The selected, representative, process is a sequence of coalescence or EC during the breaking of double emulsion on an inclined plate in the lamellar coalescer; this system, double emulsion can be presented as a “sandwich“: droplet H_3PO_4 -film [synergistic mixture 0.5 M D2EHPA-0.125 M TOPO in dearomatized kerosene (DTK)] structure submerged into-the droplet homo-phase continuum H_3PO_4 , see Fig. 1. Here, the possible idea related to this system, in a quantum mechanical framework, may be applied; than the complex composite system is the droplet-film (object S) + the droplet homophase continuum (environment E), that is (S+E).

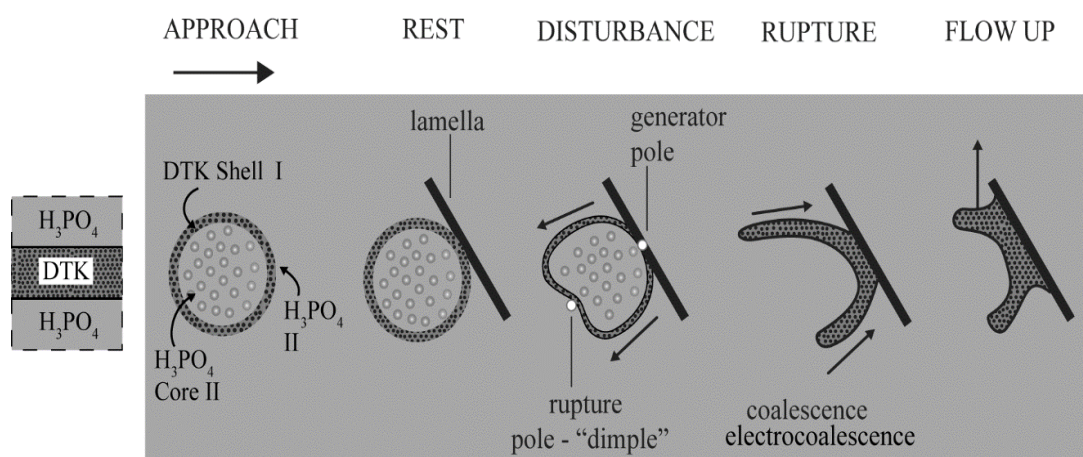


Figure 1. Breaking of the selected double emulsion at an inclined plate, a schematic presentation of all process sequences that occur in the lamellar coalescer.

EC PROCES IN A FRAME OF DECOHERENCE THEORY

A frame of decoherence, in a wider sense, consider possible effects of environmental influence on the open macroscopic quantum systems (OMQS). The dynamics of isolated quantum systems are reversible and governed by Schrodinger's equation, while these for OMQS are irreversible, where the environment E act on the composite system S changing its state [1, 7]. Here the interaction Hamiltonian $H_{S+E} \equiv H_{\text{int}}$ present a two-body observable, coupling that of the system S and environment E; hence, the composite system's Hamiltonian is expressed as

$$H = H_S \otimes \hat{I}_E + \hat{I}_S \otimes H_E + H_{\text{int}} \quad (1)$$

the cycles of formation, duration and destruction of double emulsion may be considered to be open macroscopic quantum system (OMQS) under specified conditions. Also, the process of coalescence or EC, as presented here, can be regarded as electro-mechanical oscillators (EMO) or clusters conformational limit. When the conformations are attributed to the finite number of coupled EMO with strong interactions between them, S, immersed in an environment of an almost infinite number of EMO with weak interactions among them, E, then the complex composite system is S + E. These interactions will produce some effect on the complex composite system, in particular on the N-particle or N-EMO entanglement.

Possible biological systems in a frame of decoherence theory

A number of different sources of decoherence can be found in some biological systems, which may be warm, wet, and noisy, interacting with environment, thus permitting to be considered as OMQS. Here a brief discussion of several possible ideas, will be presented; DNA molecule modeled as a sequence of quantum entangled EMO, and the brain modeled as a quantum entangled "core shell" structure [1]. At first, it is possible to present the system's environment as a kind of quantum bath, and to study the resultant interactions between the system S and the bath E. Hence, for example, the spin-boson Hamiltonian, presented by Leggett et al., defined as

$$H = -\frac{1}{2}\Delta\sigma_x + \frac{1}{2}\varepsilon\sigma_z + \sum_{\alpha} \left(\frac{p_{\alpha}^2}{2m_{\alpha}} + \frac{1}{2}m_{\alpha}\omega_{\alpha}^2x_{\alpha}^2 \right) + \frac{1}{2}\sum_{\alpha} C_{\alpha}x_{\alpha} \quad (2)$$

this Hamiltonian describes a two-level system (TLS) interacting with an infinite bath of harmonic oscillators. Here, σ_z is a Pauli sigma matrix which describes the state of a TLS with energy gap ε , Δ represent the low tunneling energy between the two levels (Leggett used a tunneling frequency instead of energy, and $\hbar\Delta$ appears in Eq. (2) instead). Further on, the TLS is coupled to the bath of harmonic oscillators identified by subscript α , described by frequency, mass, position and momentum $\omega_{\alpha}, m_{\alpha}, x_{\alpha}$ and p_{α} , respectively. The third term presents the standard energy of a simple harmonic oscillator, and the final term describes the coupling to the position of the α th oscillator [1, 8].

(1) Genetics - DNA as a sequence of quantum entangled EMO; - all nitrogen basis in DNA, T-A linked by two weak hydrogen bonds and C-G linked by three weak hydrogen bonds, regardless to the minor difference in their molar masses, are represented by finite number of coupled EMO constituting the system S; - the EMO are coupled along the strands, with some weak interactions, and between the strands, with weak interactions, constituting the double DNA helix E; - the double DNA helix E is submerged in the bath-environment E'; - the bath consists of a very big, almost infinite, number of the harmonic EMO with ultra-weak interactions among them; - the system S and the double DNA

helix E are immersed in the bath-environment E', thus constituting the complex composite system S+E+E'.

(2) Electroneurophysiology - the brain as a quantum entangled multiple „core-shell“ structure; - taking into account the “sandwich” system which present the double emulsion as a “core-shell” structure, see figure 1, it is possible to consider the four brain parts - frontal, temporal, parietal, and occipital, as one, close to the elliptical, “core-shell” - chain system; - all brain parts consist of coupled EMO; - inside each particular brain part, the EMO are coupled among them with a strong interactions; - between the brain parts the EMO are coupled with some weak interactions; - such “core-shell”-chain system may be considered as the OMQS S; - the brain, as an OMQS of the second kind, enabling decoherence, is immersed in the environment E; - here, the term environment means the air surrounding the human beings on the earth; - this air, environment, is full of electromagnetic waves, each having the one particular frequency among almost infinite possible number; - weak and ultra-weak interactions occur between the brain S and environment E; - the overall quantum entangled complex composite system is “core-shell”-chain-environment system S+E. Note: the terms “strong”, “weak”, “some weak”, and “ultra-weak” interactions are of a hierarchical qualitative nature.

PHYSICAL AND PHILOSOPHICAL CONTENTS

The selected double emulsion, or droplet-film structure immersed in the droplet homo-phase “continuum”, including its cycles of the formation, duration, and destruction, presented in this work, was considered as a close to the OMQS, under specified conditions. The EC process is explained as a kind of EMO conformational limit. Beside the solution of particular entrainment problem in chemical engineering, or in *extended chemical engineering* (heat, mass, momentum, and electron transfer phenomena), developed results and ideas are intended to be a perspective basis for modeling quantum decoherence in some biological systems.

Acknowledgement

Min. of Sci., Republic of Serbia, Grants: 101822, 142034, 34009, 46010.

REFERENCES

- [1] A.M. Spasic, *Rheology of Emulsions*, Academic Press, Elsevier, 2018. [2] A.M. Spasic, J.M. Jovanovic, V. Manojlovic, M. Jovanovic, *J. Colloid Interface Sci.* 2016; 479 165-172.
- [3] A.M. Spasic et al. CHISA 1987-2020 All Congresses, Prague, CZ.
- [4] A.M. Spasic, J.M. Jovanovic, M. Jovanovic, *Adv. Colloid Interface Sci.* 2012; 174 31-49.
- [5] J-P. Hsu, A.M. Spasic, *Interfacial Electroviscoelasticity and Electrophoresis*, CRC Press-Taylor & Francis, Boca Raton London New York, 2010.
- [6] A.M. Spasic In: A.V. Delgado (Ed.) *Interfacial Electrokinetics and Electrophoresis*, Marcel Dekker Inc.: New York, 2002.
- [7] A.M. Spasic et al, PHYSICAL CHEMISTRY 1992-2018 All Conferences. Belgrade, Serbia.
- [8] D. Abbott, P.C.W. Davis, A.K. Pati (Eds.) *Quantum aspects of life*, Imperial College Press: London, 2008 [Foreword by Sir Roger Penrous].

IMPACT OF D₂O ON PEPTIDIZATION OF L-ALANINE

A. Fulczyk¹, E. Łata¹, E. Talik², T. Kowalska¹ and M. Sajewicz¹

¹*Institute of Chemistry, University of Silesia, 9 Szkolna Street, 40-006 Katowice, Poland
(teresa.kowalska@us.edu.pl)*

²*Department of Physics of Crystals, University of Silesia, 75 Pułku Piechoty 1, 41-500 Chorzów,
Poland*

ABSTRACT

The investigation was carried out to collect experimental evidence on the effect of heavy water (D₂O) on spontaneous peptidization of proteinogenic α -amino acids upon an example of L-alanine (L-Ala). As analytical techniques, we used high-performance liquid chromatography with the diode array detection (HPLC-DAD), mass spectrometry (MS), and scanning electron microscopy (SEM). Growing proportions of D₂O in the reaction mixture result in decreasing yields of both, the soluble lower molecular weight peptides and the insoluble higher molecular weight peptides.

INTRODUCTION

The object of our interest was L-Ala, which is the simplest chiral (endogenous and proteinogenic) α -amino acid with as low molar weight, as 89.09 g mol⁻¹ only. It plays many vital roles in human organism, involved in the glucose-alanine cycle [1]. It is puzzling to what extent the process of spontaneous oscillatory peptidization of proteinogenic α -amino acids may be sensitive to heavy water (D₂O) known for its lethal effect on higher organisms. With some mammals, this effect was established at 30% D₂O of the organism's body weight [2]. On the other hand, the simplest organisms (e.g., bacteria, protozoa and algae) have proved to be largely resistant to the toxic effects of D₂O at the expense of slowing down their life processes [3].

METHODS

In our experiment, high-performance liquid chromatography with diode array detection (HPLC-DAD) was used to demonstrate spontaneous oscillatory peptidization of L-Ala in an absence of D₂O and no oscillatory peptidization in its presence. A freshly prepared L-Ala sample stored for 142 h in MeOH + H₂O (70:30, v/v), was traced with aid of the achiral HPLC-DAD system. The goal was to separate the monomeric L-Ala from the spontaneously formed peptides and to trace its varying amounts, as represented by the changing peak heights of the L-Ala monomer (with the changes resulting from alternate processes of spontaneous peptidization and hydrolytic degradation of peptides). For the sake of comparison, the behaviour of the freshly prepared L-Ala solution in D₂O was also recorded by means of the HPLC-DAD system. In the next step, mass spectrometry (MS) and scanning electron microscopy (SEM) were used to study an impact of D₂O on peptidization of L-Ala. All L-Ala solutions used for the MS and SEM tests were prepared at a concentration of 1 mg mL⁻¹ either in pure D₂O, or in the binary liquid mixtures MeOH + X, 70:30 (v/v), where X: the binary mixture of H₂O + D₂O in the changing volume proportions of 30:0, 25:5, 20:10, 10:20 and 0:30. Mass spectrometry allows recording mass spectra for the monomeric L-Ala and the lower soluble peptides formed during the 7-days storage period in the darkness at 21±0.5 °C. The insoluble higher peptides which self-separate from the solution by sedimentation were recorded for the same samples using the scanning electron microscopy after one month of sample storage period under the unchanged conditions.

RESULTS AND DISCUSSION

Data obtained from HPLC-DAD dissolved in the aqueous-organic solvent presented the changing L-Ala peak heights, when plotted against sample storage time ($t_R \approx 4.43$ min). The non-linear signal intensity changes in the function of time were observed, equivalent to the respective concentration changes. To assess whether the HPLC-DAD signal recorded for the monomeric L-Ala contains a significant periodic component, a Fourier transform was performed on the data and the power spectrum calculated for the peak of L-Ala was plotted. L-Ala first undergoes two initial oscillations which are damped (not periodic) and the oscillatory changes are on a scale of ca. 10 hours. After that time, the system reaches a steady state [4]. For L-Ala dissolved in pure D_2O , no significant changes of signal intensity (perceptibly higher than instrumental noise) were observed, witnessing to practically full inhibition of the oscillatory peptidization (Fig. 1).

The obtained mass spectra (Fig. 2) were regarded as fingerprints which allowed visual comparison of the number and intensity of signals. With the L-Ala sample stored in an absence of heavy water (D_2O), the mass spectrum shows significant amounts of high intensity signals, predominantly in the range of the m/z values below 2000. An increasing content of D_2O up to 30% causes a slow and gentle blanking of the mass spectrometric signals, whereas the 100% D_2O content does not result in any further significant change of the MS pattern. Signal at m/z 689 marked on the plots most probably originates from the cation built of the nanomeric peptide and the methanol and water adducts, $[Ala + CH_3OH + H_2O]^+$.

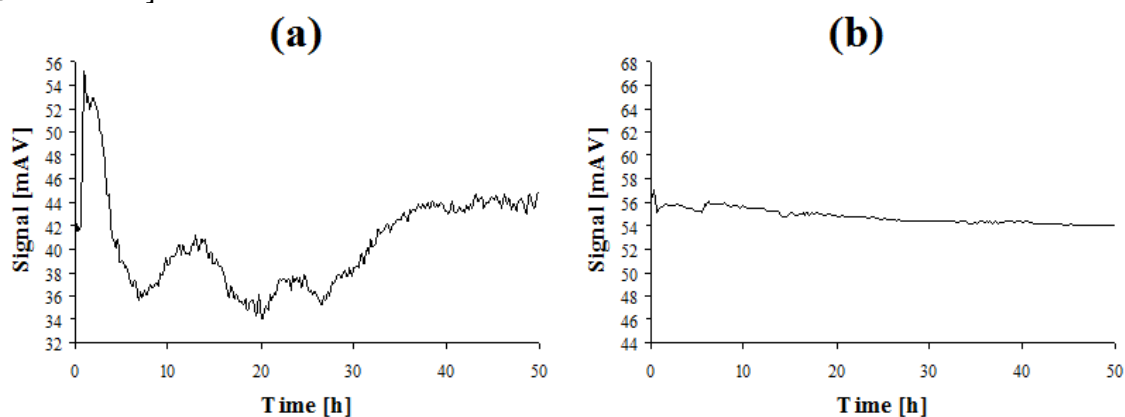


Figure 1. Time series of the chromatographic peak heights at $t_R \approx 4.43$ min for the monomeric L-Ala in: (a) MeOH + H_2O , 70:30 (v/v) and (b) pure D_2O , recorded with the DAD detector in the time range from 0 h to 50 h sample storage time.

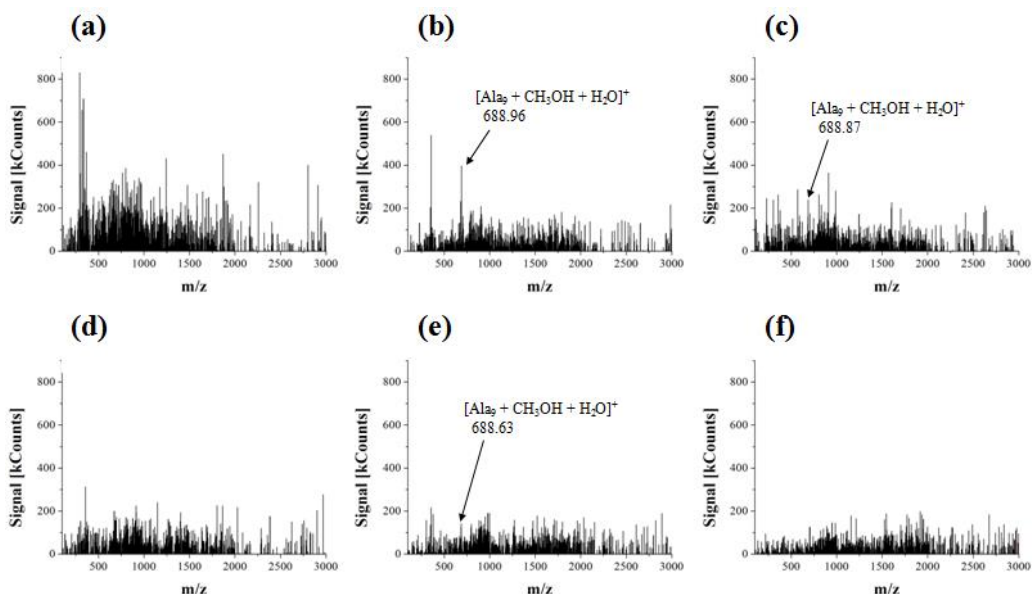


Figure 2. Mass spectra recorded for L-Ala dissolved in MeOH + X, 70:30 (v/v), where X: the binary mixture of H₂O + D₂O in the changing volume proportions; (a) 0% D₂O; (b) 5% D₂O; (c) 10% D₂O; (d) 20% D₂O; (e) 30% D₂O and (f) L-Ala dissolved in pure D₂O (adapted from [4]).

Selected micrographs which illustrate the observed regularities are given in Fig. 3. The micrographs of the higher and mostly insoluble peptides derived from L-Ala show a decrease in peptide yields with the increasing amounts of D₂O in solution. For the L-Ala sample which underwent peptidization in an absence of D₂O the resulting peptide structures resemble elongated and outstretched filaments. On the micrographs obtained for 30% D₂O, rare clusters of the fine-grained peptidization products can be seen.

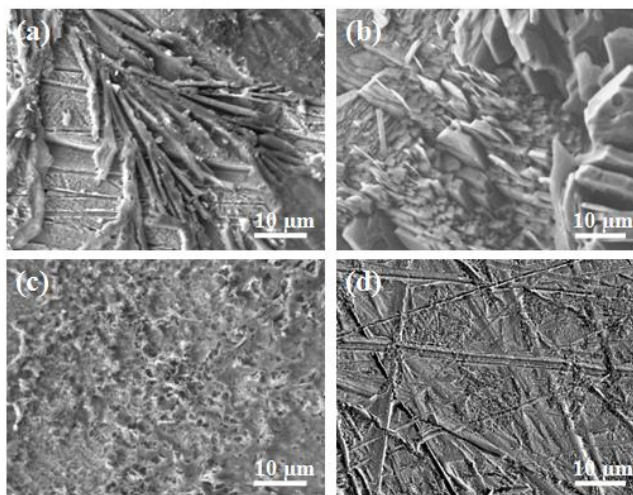


Figure 3. Scanning electron micrographs recorded for the L-Ala-derived peptides retrieved from the samples dissolved in MeOH + X, 70:30 (v/v), where X: the binary mixture of H₂O + D₂O in the changing volume proportions; (a) 0% D₂O, × 2,000; (b) 5% D₂O, × 2,000; (c) 10% D₂O, × 2,000; (d) 30% D₂O, × 2,000 (adapted from [4]).

CONCLUSIONS

In this study, we examined an influence of heavy water (D_2O) on spontaneous oscillatory peptidization of L-Ala. With use of HPLC-DAD, we demonstrated the nature of this process in an absence of D_2O . The L-Ala solution first undergoes two initial oscillations which are damped and the oscillatory changes are on a scale of ca. 10 hours. After that time, the system reaches a steady state. With the mass spectra recorded for the samples with the increasing proportions of D_2O in solution, a general trend is observed of the lowering yields of the soluble L-Ala-derived peptides. With use of SEM, gradual shift of peptidization equilibria is observed toward the lower peptides with the increasing proportions of D_2O in solution.

REFERENCES

- [1] P. Felig, *Metabolism*, 1973, 22, 179-207
- [2] C.P. Richter, *Proc. Natl. Acad. Sci. USA*, 1977, 74, 1295-1299
- [3] L.A. Litvinenko, L.A. Kravchuk, S.B. Petrikevich, V.G. Sakharovskii, J.G. Ivanitskaia, D.E. Guliamova, *Mikrobiologiya*, 1992, 61, 1030-1037
- [4] A. Fulczyk, E. Łata, E. Talik, M. Dolnik, T. Kowalska, M. Sajewicz, *Reac. Kinet. Mech. Cat.*, <https://doi.org/10.1007/s11144-020-01783-y>

TANGENTIAL MODEL OF MICROTUBULES

S. Zdravković and S. Zeković

*Univerzitet u Beogradu, Institut za nuklearne nauke Vinča, 11001 Beograd, Serbia.
(szdjidji@vin.bg.ac.rs)*

ABSTRACT

Microtubules (MTs) represent basic components of a cytoskeleton. The present work studies nonlinear dynamics of MTs assuming tangential oscillations of the dimers. We introduce a two component model and show that the dynamics of MTs can be explained in terms of breather solitary waves.

INTRODUCTION

MTs are the basic components of the cytoskeleton, existing in eukaryotes [1]. They are long structures that spread between a nucleus and cell membrane, playing essential role in the shaping and maintenance of cells and in cell division. Also, they represent a network for motor proteins. More information about MT structure and function can be found in a review [2].

MT is a hollow cylindrical polymer. Its surface is formed usually of 13 long structures called protofilaments (PFs), representing a series of electric dipoles called dimers. For most of the models the dimer's internal structure is not taken into consideration.

There are a few models describing the nonlinear dynamics of MTs, based on the crucial fact that MTs are ferroelectrics as the dimers are electric dipoles [3]. Each model can be seen as either longitudinal or angular. The first nonlinear model was longitudinal one, introduced almost 30 years ago [3]. Its improved and more general version is the so-called u -model [2,4]. Two commonly used mathematical procedures were explained within the u -model in Ref. [5].

TANGENTIAL MODEL OF MICROTUBULES

An overview of a couple of models, both longitudinal and angular, can be found in the review [5]. All of them are one component models. The purpose of this paper is to introduce a two component angular one. It was pointed out that the MT represents a ferroelectric system. Interaction of a single dimer with surrounding ones, that do not belong to the same PF, can be modelled by W-potential energy, or potential for short [3]. This is a function $f_w = -ax^2 + bx^4 - cx$, having two minima. We assume that all parameters are positive. It is crucial to understand the meaning of these minima. The existence of the two minima means that there are two possible positions for the dimer. To be more precise, there are two directions of electric fields, \vec{E}_1 and \vec{E}_2 , around which the dimer can oscillate. One of them is shown in Fig. 1. A resultant internal electric field $\vec{E} = \vec{E}_1 + \vec{E}_2$ is in the direction of PF. We may expect that the dimer oscillates around \vec{E} , but any displacement would move it towards the directions of either \vec{E}_1 or \vec{E}_2 . This means that the dimer's position in the direction of \vec{E} is not stable and corresponds to the maximum of the function f_w .

The values of the longitudinal \vec{p}_z , radial \vec{p}_r , and tangential \vec{p}_θ components of electric dipole moment are known [6]. The component p_z is in the direction of MT. The oscillation of the dimer is

in the tangential plane, which means that $\vec{p}_r \cdot \vec{E}_1 = 0$ and the relevant moment here is

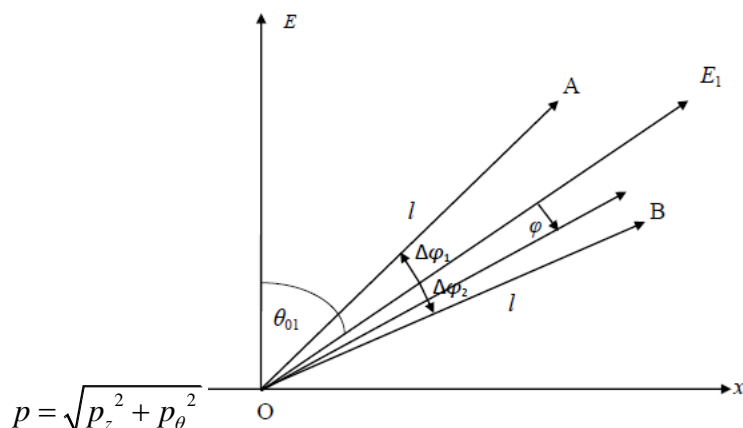


Figure 1. A schematic representation of the dimer's oscillations.

In Fig. 1, the dimer oscillates around the direction of \vec{E}_1 . The angle between PF and \vec{E}_1 is $\theta_{01} \equiv \theta_0$. A coordinate determining the displacement from the direction of \vec{E}_1 is φ . Its position with respect to the direction of PF is θ . The amplitude positions of the dimer are OA and OB. Hence, $\Delta\varphi_1 \leq \varphi \leq \Delta\varphi_2$, $\Delta\varphi_1 < 0$ and $\Delta\varphi_2 > 0$. The value θ_0 corresponds to the minimum of the W-potential [7].

The Hamiltonian for MT can be written as [7]

$$H = \sum_n \left[\frac{I}{2} \dot{\varphi}_n^2 + \frac{k}{2} (\varphi_{n+1} - \varphi_n)^2 - \frac{A}{2} \theta_n^2 + \frac{B}{4} \theta_n^4 - C \theta_n - p E_1 \cos \varphi_n \right]. \quad (1)$$

We recognize the kinetic energy, potential energy of the interaction between neighbouring dimers belonging to the same PF in the nearest neighbour approximation, and W-potential. The potential energy which would explain the interaction between neighbouring dimers belonging to different PFs is neglected [8]. The very last term comes from the fact that the dimer is the electric dipole existing in the field of all other dimers, where $p > 0$ is an electric dipole moment. It is assumed that $E_1 > 0$ [7].

From $\theta = \theta_0 + \varphi$ and Eq. (1) we obtain the dynamical equation of motion $I\ddot{\varphi}_n = k(\varphi_{n+1} + \varphi_{n-1} - 2\varphi_n) - A_0\varphi_n - C_0\varphi_n^2 - B_0\varphi_n^3$, where $B_0 = B - pE_1/6$, $A_0 = -A + 3B\theta_0^2 + pE_1$, $C_0 = 3B\theta_0$ [7]. To solve it, we use a semi-discrete approximation [9]. This means that we assume small oscillations, i. e. $\varphi_n = \varepsilon \Phi_n$, $\varepsilon \ll 1$, and look for wave solutions in the form

$$\Phi_n(t) = F_1(\xi)e^{i\theta_n} + \varepsilon \left[F_0(\xi) + F_2(\xi)e^{i2\theta_n} \right] + \text{cc} + O(\varepsilon^2), \quad (2)$$

where $\xi = (\varepsilon nl, \varepsilon t)$, $\theta_n = nql - \omega t$, ω is the optical frequency of the linear approximation, $q = 2\pi/\lambda$ is a wave number, cc represents complex conjugate terms and F_0 is real. A crucial point is that the function F_1 represents an envelope, which is treated in a continuum limit, while $e^{i\theta_n}$, including discreteness, is a carrier component of the wave. After rather tedious mathematics, including a continuum limit $nl \rightarrow z$, we come up with a conclusion that the functions $F_0(\xi)$ and $F_2(\xi)$ can be expressed through $F_1(\xi)$, while $F_1(\xi)$ is a solution of the solvable nonlinear Schrödinger equation (NLSE) [9]. The final result, that is the solution of the equation of motion, is (work in progress):

$$\varphi_n(t) = 2A' \operatorname{sech}(\Phi_1) \left\{ \cos(\Phi_2) + A' \operatorname{sech}(\Phi_1) \left[\mu/2 + \delta \cos(2\Phi_2) \right] \right\}, \quad (3)$$

where $\Phi_1 = (nl - V_e t)/L$ and $\Phi_2 = \Theta nl - \Omega t$. A very tedious parameter selection can be found in Ref. [7]. It suffices now to mention that the wave velocity V_e can be obtained using the idea of a coherent mode (CM), assuming that the envelope and carrier wave velocities are equal, i. e. $V_e = \Omega/\Theta$. This means that the function $\varphi_n(t)$, shown in Fig. 2 for CM and a certain set of the parameters [7], is the same at any position n . This is a modulated solitary wave called a breather.

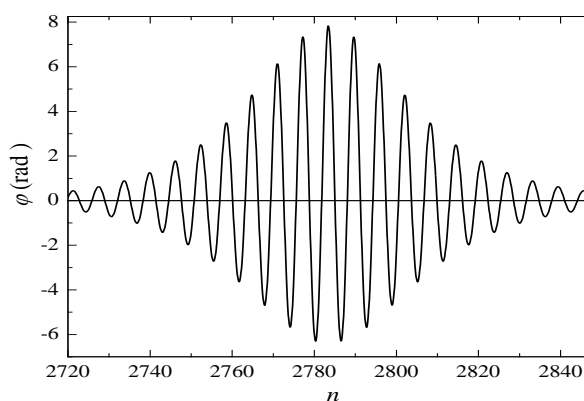


Figure 2. The function $\varphi_n(t)$ as a function of n for $t = 50\text{ns}$. The CM is assumed.

CONCLUSION AND FUTURE RESEARCH

The model explained here is a mechanical one. An example that shows the relevance of the mechanical models is kinocilium, a component of vestibular hair cells of the inner ear [10]. Also, MTs are believed to be a source of electrodynamics activity of cells and have been modelled as nonlinear RLC transmission lines, which is very important for fighting some diseases [11]. Therefore, MTs are both mechanical and electrical systems. Regarding their modelling, the best that should be done is to work towards more component models that would take both characteristics into consideration [12]. Our approach here is a classical one and NLSE should not be confused with the quantum SE.

Acknowledgement

We thank our colleague Alexandr N. Bugay for his collaboration with us.

REFERENCES

- [1] P. Dustin, *Microtubules*, Springer, Berlin, 1984.
- [2] S. Zdravković, *J. Serb. Chem. Soc.* **82** (2017) 469.
- [3] M.V. Satorić, J.A. Tuszyński, R.B. Žakula, *Phys. Rev. E* **48** (1993) 589.
- [4] S. Zdravković *et al.*, *Chaos Solitons Fract.* **45** (2012) 1378.
- [5] S. Zdravković, *Mechanical Models of Microtubules*. In *Complexity in Biological and Physical Systems*, Ed. by R. Lopez-Ruiz, IntechOpen, 2018, Chapter 1.

-
- [6] J.E. Schoutens, J. Biol. Phys. **31** (2005) 35.
- [7] S. Zdravković *et al*, Two component model of microtubules and continuum approximation. Submitted to Chaos Soliton Fract.
- [8] P. Drabik, S. Gusarov, A. Kovalenko, Biophys. J. **92** (2007) 394.
- [9] S. Zdravković, J. Nonlin Math. Phys. **18**, Suppl. 2 (2011) 463.
- [10] M.V. Sataric, D.L. Sekulic, B.M. Sataric, S. Zdravkovic, Progress Biophys. Molec. Biology **119** (2015) 162.
- [11] F.T. Ndjomatchoua *et al*, Chaos **26** (2016) 053111.
- [12] A.N. Bugay, Nonlin. Phenomena Complex Sys. **18** (2015) 236.

MICRO-QUANTITATIVE ANALYSIS OF TYROSINE

L. Negrojević, A. Lončar and J. P. Maksimović

*University of Belgrade, Faculty of Physical Chemistry, Studentski trg 12-16, 11000 Belgrade,
Republic of Serbia*

ABSTRACT

The biological importance of tyrosine interactions with iodine led us to investigate the possibilities of quantitative determination of tyrosine in the Bray-Liebhafsky reaction using the pulse perturbation technique. For this purpose, a bifurcation diagram with respect to temperature was obtained, and the response of the Bray-Liebhafsky system to tyrosine perturbations was examined. Tyrosine affects the temporal evolution of the system quantitatively in the micromolar range of concentrations. This finding suggests the possibility of using a Bray-Liebhafsky matrix to quantify tyrosine.

INTRODUCTION

Tyrosine (Tyr) is an amino acid [1]. Together with iodine, it is the main ingredient of thyroid hormones [2]. Therefore, it was natural to investigate if it reacts with the iodine species in the Bray-Liebhafsky (BL) reaction. Moreover, having significant experience with the BL reaction as a matrix for micro-quantitative determination of analyte concentrations [3,4], we decided to determine which concentrations of tyrosine could be examined in the same system.

METHODS

The experiments were performed in a continuous stirred-tank reactor (CSTR) at a stirring speed of 900 rpm and a specific flow rate of $9.72 \times 10^{-3} \text{ min}^{-1}$. The temporal evolution of the system was monitored using a Pt electrode and an Ag/AgCl reference electrode. The bifurcation diagram with respect to temperature was determined in the temperature range of 49.7 - 44.9 °C.

All reactants used are p.a. degree of purity. The concentration of reaction species in the BL system was: $[\text{H}_2\text{O}_2] = 0.2006 \text{ M}$, $[\text{H}_2\text{SO}_4] = 0.0550 \text{ M}$ and $[\text{KIO}_3] = 0.0590 \text{ M}$. Tyrosine perturbations were performed at a temperature of 46.0 °C in a concentration range of 1.1558 to 13.8702 μM .

RESULTS AND DISCUSSION

The sensitivity of the pulse perturbation analysis technique is heavily dependent on the distance of the system from the bifurcation point [5]. Thusly, potentiometric traces of different dynamic states were recorded (Figure 1) and the bifurcation diagram was obtained (Figure 2). Since the bifurcation point was present around 46.5 °C, the Bray-Liebhafsky matrix was perturbed with tyrosine below this temperature, namely at 46.0 °C, to ensure that the system was sensitive enough towards the perturbations.

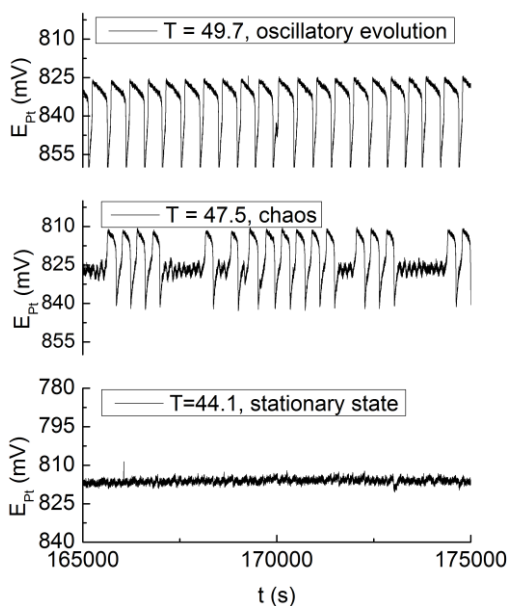


Figure 1. The potentiometric traces of three different dynamic states of the BL reaction obtained using a Pt electrode, in order of decreasing temperature.

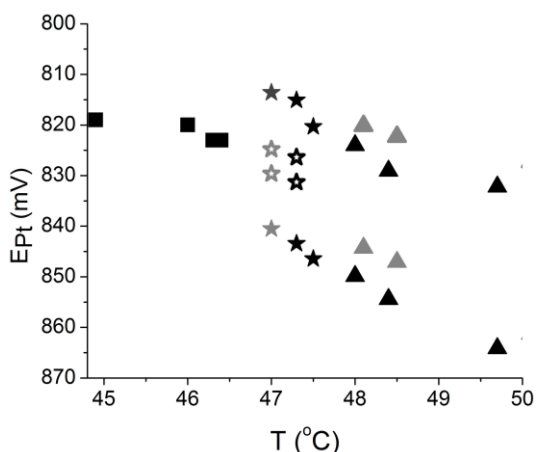


Figure 2. Bifurcation diagram for the BL system.

Squares represent stationary states; full stars represent amplitude values of more intense oscillations while hollow stars represent amplitudes values of less intense oscillations in chaos; triangles represent amplitudes of oscillations in oscillatory period; black are the values obtained by decreasing temperature and gray are the values obtained by raising the values of temperature.

The addition of tyrosine affected the temporal evolution of the Bray-Liebafsky matrix (Figure 3). Typical system response to tyrosine perturbation is the appearance of two oscillations (Figure 4). To determine if there were correlations between the concentration and the first preoscillatory period (t_1), the period between two oscillations (Δt_2), the time elapsed between the start and the termination of the oscillatory phase (t_{end}), three different calibration diagrams were obtained. All of the diagrams were formed by plotting the respective time against the concentration of tyrosine used to perturb the system. Adjusted R-Square coefficients in the investigated range of Tyr concentrations for t_1 , Δt_2 , and t_{end} were 0.9291, 0.9751, and 0.9236, respectively.

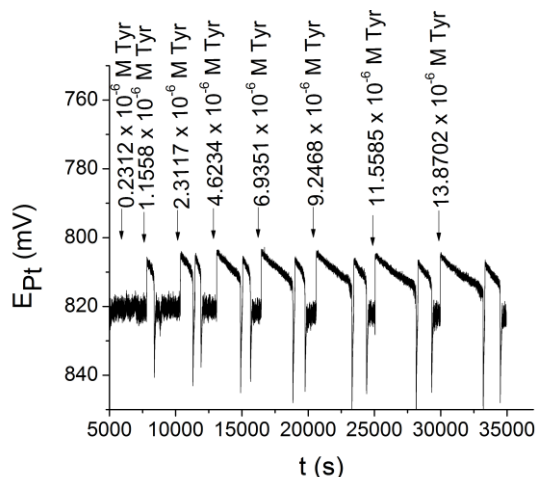


Figure 3. The potentiometric trace of the perturbation of the BL matrix with increasing concentrations of tyrosine at 46 °C.

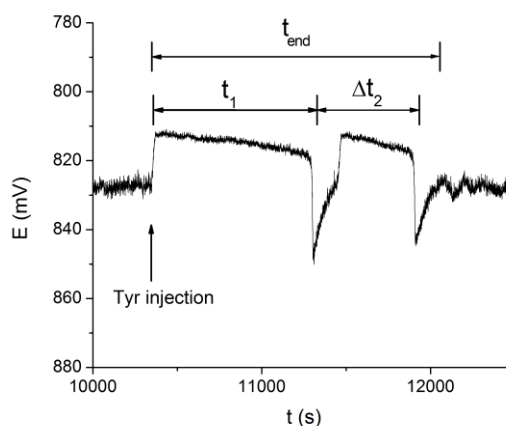


Figure 4. Typical BL system response after tyrosine perturbation.

As Δt_2 proved to be the superior predictor of concentration in the range of concentrations of 2.3117 μM to 13.8702 μM , compared to t_1 and t_{end} , its respective calibration diagram is shown in Figure 5. Parameters obtained from a linear fit of the Δt_2 diagram are shown in Table 1, as are the adjusted R-Square coefficients for the calibration diagrams of their respective time periods.

Table 1. Linear fit parameters of the calibration diagram shown in Figure 5.

Parameter	Slope (M s^{-1})	Intercept (s)	Adj. R-Square
Δt_2	6.0×10^7	482	0.9751

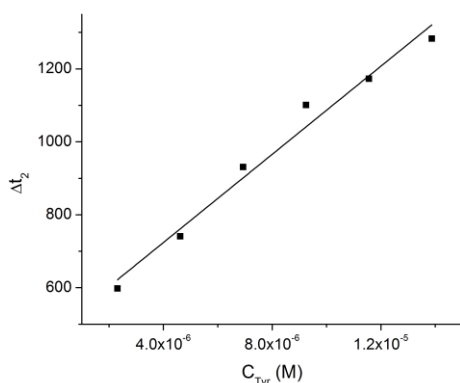


Figure 5. The calibration diagram obtained by plotting Δt_2 against added concentrations of tyrosine into the BL matrix at 46.0 °C.

CONCLUSION

In this paper, the effect of tyrosine on the Bray-Liebhafsky reaction was investigated. The addition of tyrosine to the BL matrix quantitatively affects the temporal evolution of the system. The high adjusted R-square value between the period between the two oscillations (Δt_2) and the tyrosine concentration indicates the possibility of using the parameter Δt_2 for the micro-quantitative determination of tyrosine in the range from 2.3117 μM to at least 13.8702 μM . Further research may be directed towards optimizing the conditions in the reactor for greater precision in determining this analyte.

Acknowledgement

This work was supported by the Ministry of Education, Science and Technological Development of the Republic of Serbia, contract number: 451-03-9/2021-14/200146. The authors are thankful to Professor Emeritus Ljiljana Kolar-Anić for useful suggestions and proof help of this article.

REFERENCES

- [1] J. P. Greenstein and M. Winitz, Chemistry of the amino acids. John Wiley, New York, 1961.
- [2] G. K. Pal, Textbook of Medical Physiology. India: Ahuja Publishing House, Endocrine Physiology, 2007.
- [3] J. P. Maksimović, Lj. Z. Kolar-Anić, S. R. Anić, D. D. Ribič, N. D. Pejić, J. Braz. Chem. Soc., 2011, **22(1)**, 38-48.
- [4] N. D. Pejić, J. P. Maksimović, S. M. Blagojević, S. R. Anić, Ž. D. Čupić, Lj. Z. Kolar-Anić, J. Braz. Chem. Soc., 2012, **23(8)**, 1450-1459.
- [5] N. Pejić, S. Blagojević, S. Anić, Lj. Kolar-Anić, Anal. Bioanal. Chem., 2007, **389**, 2009-2017.

E - Electrochemistry

ELECTROCHEMICAL DEPOSITION OF NEODYMIUM AND PRASEODYMIUM ON MOLYBDENUM FROM MOLTEN FLUORIDE

D. Feldhaus¹, V.S. Cvetković², N.M. Vukićević², T.S. Barudžija³, B. Friedrich¹ and J.N. Jovićević²

¹*RWTH Aachen University, IME Process Metallurgy and Metal Recycling, Intzestrassse 3, 52056 Aachen, Germany. (DFeldhaus@ime-aachen.de).*

²*University of Belgrade, Institute of Chemistry, Technology and Metallurgy, Njegoševa 12, 11000 Belgrade, Republic of Serbia.*

³*University of Belgrade, Institute for Nuclear Sciences Vinča, P.O.Box 522, 11001 Belgrade, Republic of Serbia.*

ABSTRACT

Neodymium and praseodymium were electrochemically co-deposited onto Mo cathode applying constant potential, from fluoride-based molten salts containing the corresponding rare earth oxides. According to the recorded voltammograms, it appears that in the investigated system, the electrodeposition of neodymium proceeds as a two-step reduction process: Nd(III)→Nd(II) and Nd(II)→Nd(0), whilst the praseodymium deposition proceeds as an one-step reduction process: Pr(III)→Pr(0). However, it was also recognized that at the same time a substantial amount of NdF₂ was formed as a result of the disproportionation reaction between the electrodeposited Nd metal and Nd(III) present in the electrolyte.

The deposit on the working electrode surface was recorded by optical microscopy and analyzed by X-ray diffraction (XRD). The analysis made upon the applying the potentiostatic deposition regime has shown Nd/Pr metals present on the molybdenum cathode.

INTRODUCTION

Recycling in the context of the circular economy is becoming increasingly important, including the field of neodymium iron boron magnets, which are used in applications such as computer hard drives, hybrid and electric vehicles (HEVs/EVs) and wind turbines [1]. Neodymium and praseodymium rare earth elements are components of NdFeB magnets. There are various approaches to the recovery of rare earth elements (REEs) from the end-of-life magnets, such as hydrometallurgical and pyrometallurgical processes, liquid metal extraction, molten salt electrolysis [2]. An effective recycling process of these magnets could make rare earth mining and subsequent process steps up to the metal partially obsolete [3]. One recycling route for magnets is, firstly, to oxidise magnet powder. The next step is to melt these oxides which separates the ingredients into an iron rich metal phase and a REE rich slag. In the last step of this route, the rare earth elements, namely neodymium, praseodymium and dysprosium, can be won in the molten salt electrolysis.

Therefore, in this work, the deposition behaviour of neodymium and praseodymium from the fluoride molten salts system was investigated. More specifically, the reaction mechanism of neodymium and praseodymium deposition was studied in the fluoride based molten salts containing the rare earth oxides, in order to provide the appropriate potential for increase of Nd and Pr metal deposited on the cathode surface. Using a molten fluoride salts electrolyte instead of chloride ones is expected to provide advantages like higher current efficiencies, lower hygroscopicity and higher conductivity. However, there is a number of challenges remaining connected to the composition of the electrolyte based on neodymium, praseodymium, lithium fluoride and neodymium and praseodymium oxides and their influence on all aspects of desired effective metals deposition.

EXPERIMENTAL

The electrochemical experiments were conducted in a steel cell described elsewhere [4,5], with a three-electrode system: a working electrode (WE) molybdenum (Mo, 2 mm diameter, EWG 99.95%), a counter electrode (CE) high purity glassy carbon (GC, 4 mm diameter, >99.99% HTW SIGRADUR® G) and a reference electrode (RE) tungsten (W, 1 mm diameter, EWG 99.95%). The chemicals used for the experiments and the composition of the electrolyte used are shown in Table 1.

Table 1. Composition of the electrolyte

Component	Supplier	Purity	Weight percentage [wt.-%]	Molar ratio [mol.-%]
NdF ₃	Treibacher, Althofen, Austria	≥99.9%	63.17	35.26
PrF ₃		≥99.9%	20.96	11.90
LiF		≥99.5%	12.02	51.99
Nd ₂ O ₃		≥99.9%	1.92	0.64
Pr ₆ O ₁₁		≥99.9%	1.92	0.21

To prepare the electrolyte, the fluorides have been dried in a furnace for 24 h at 523 K. They were then manually mixed and molten in a high purity graphite crucible to homogenise the melt. This process is conducted in a vacuum induction furnace at up to 1373 K which is able to operate at overpressure to counteract the high vapour pressure of the fluorides, under 1800 mbar of argon. The oxides were also dried in a furnace for 24 h at about 393 K before they have been added to the electrolyte.

The electrochemical measurements have been conducted at a process temperature of 1323 K, controlled by a thermocouple type B, and under a continuous flow of argon to prevent oxidation. An IviumStat potentiostat (5 A/10 V; Ivium Technologies) was used for electrochemical measurement: cyclic voltammetry (CV using various scan rates in 50–300 mV/s range) and chronopotentiometry (deposition experiments were carried out for up to 240 min at different constant overpotentials).

The surface of the working electrode obtained after deposition was examined by an optical microscope (Keyence; model VH-Z100R, Japan). The deposits and the remaining electrolyte on the electrode were analysed by X-ray diffraction (XRD) with Philips PW 1050 powder diffractometer at room temperature with Ni filtered CuK α radiation ($\lambda = 1.54178 \text{ \AA}$), scintillation detector within 20–85° 2 θ range in steps of 0.05 and scanning time of 5 s per step.

RESULTS AND DISCUSSION

An example of the cyclic voltammograms recorded on the Mo working electrode in the fluoride-based molten salts containing rare earth oxide Nd₂O₃ and Pr₆O₁₁ are shown in Figure 1.

In the electrolyte with Nd₂O₃ and Pr₆O₁₁, the anodic and cathodic current peaks are not very clearly defined. In the presence of Nd₂O₃ and Pr₆O₁₁, there are three cathodic (C₁, C₂, C₃) and three anodic (A₁, A₂, A₃) current waves to be recognized. The peak C₁ at $\approx -400 \text{ mV vs. W}$ should reflect the reduction of Nd(III) to Nd(II), the cathodic peak C₂ at $\approx -550 \text{ mV vs. W}$ should record the further reduction of Nd ions to the metal, namely Nd(II) to Nd(0). At further negative applied potential around -800 mV vs. W , the third cathodic peak C₃ is most probably a reflection of the reduction of Pr(III) to Pr(0) metal. The anodic current waves (A₃ at $\approx -600 \text{ mV vs. W}$, A₂ $\approx -350 \text{ mV vs. W}$ and A₁ $\approx -200 \text{ mV vs. W}$) should reflect the reverse processes to those presented by C₁, C₂ and C₃, in other words, dissolution of the deposited praseodymium to Pr(III) (A₃ peak) and neodymium to Nd(III), (A₂ and A₁ peaks). In addition, only when the slow scan rates were used (20 and 50 mVs⁻¹), the anodic current wave A₁, which corresponds to oxidation of Nd(II) \rightarrow Nd(0), could be detected.

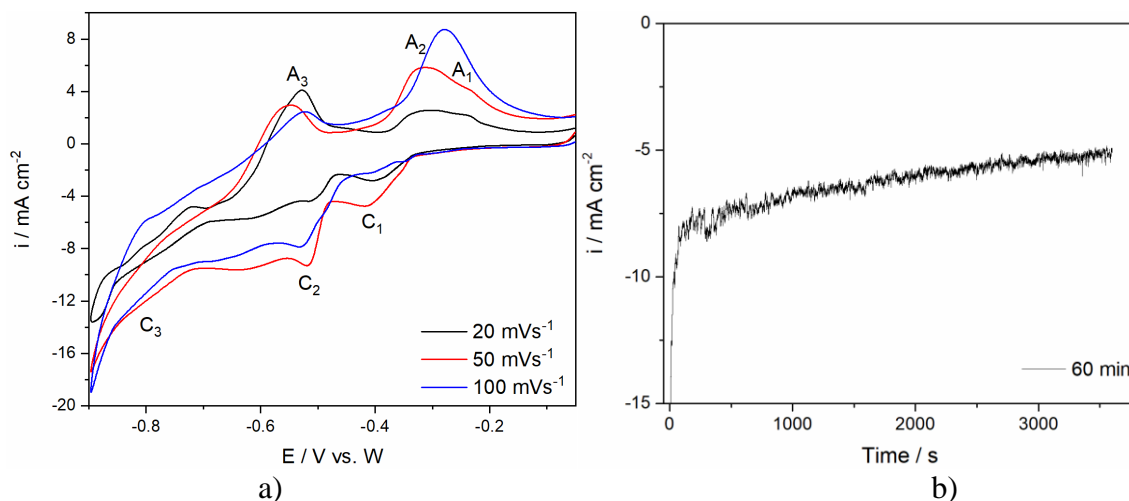


Figure 1. a) CV recorded on Mo working electrode in molten $\text{NdF}_3+\text{PrF}_3+\text{LiF}+\text{Nd}_2\text{O}_3+\text{Pr}_6\text{O}_{11}$ electrolyte, with different scan rates; b) potentiostatic deposition on Mo from the same electrolyte for 60 min at constant potential of - 900 mV vs. W; $T=1323$ K.

The appearance of the Mo cathode surface under an optical microscope after constant potential deposition at - 900 mV vs. W for 1 h from the used electrolyte is presented in Figure 2.a).

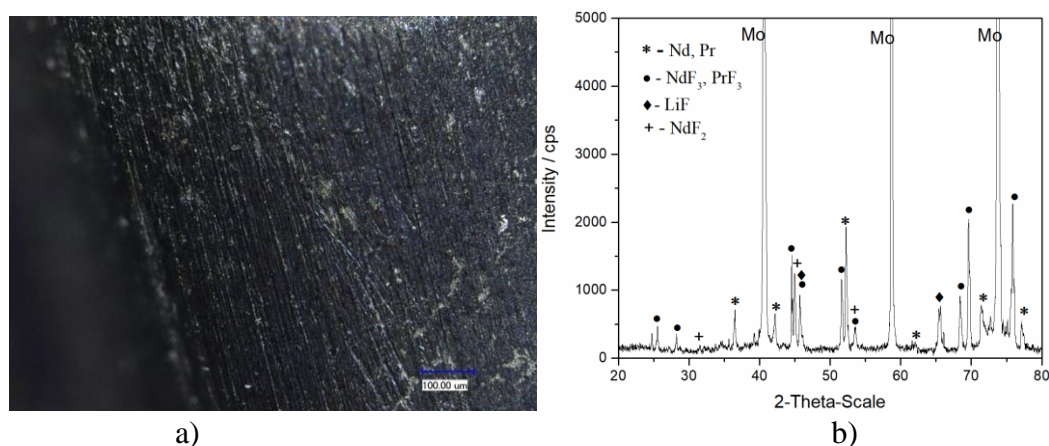


Figure 2. a) Optical image of the surface of the Mo cathode after deposition from molten $\text{NdF}_3+\text{PrF}_3+\text{LiF}+\text{Nd}_2\text{O}_3+\text{Pr}_6\text{O}_{11}$ electrolyte, at - 900 mV vs. W for 3600 s, at 1323 K (the solidified electrolyte was removed from the electrode); b) XRD pattern of the Mo working electrode from Figure 1.a).

To ensure that Li will not be present in the deposit, the deposition was performed at - 900 mV vs. W, which was a potential only ≈ 100 mV more negative than the peak potential value of the cathodic peak C_3 . The chosen potential was cathodic enough to sustain Nd and Pr metal deposition, with a deposition current density of ≈ -6 mAcm^{-2} , Figure 1.b). There is obvious evidence of the deposit other than the solidified electrolyte which has been removed before the photo was taken. The XRD pattern of the same working electrode and the deposit thereon is given in Figure 2.b). The diffractogram revealed the presence of Nd and Pr metal in substantial quantity and verified that the proper potential was applied for deposition. Unfortunately, in the diffractograms recorded, it is difficult to distinguish between the possible peaks belonging only to Nd and only to Pr, because of the high similarity of their crystal lattices. Nd and Pr metal both have hexagonal crystal lattice and very similar lattice parameters. Therefore, although the peaks are characteristic of either of the two

metals, we had to attribute to both of them, Nd and Pr [JCPDS No. 03-065-3424 for Nd, and JCPDS No. 01-089-2921 for Pr]. Well defined peaks reflecting the presence of Nd/Pr metal on the working electrode surface could be recognized by the following 2θ values: $36.40^\circ/36.27^\circ$; $41.83^\circ/41.89^\circ$; $52.3^\circ/52.14^\circ$; $62.05^\circ/62.16^\circ$, $71.75^\circ/71.45^\circ$, $77.33^\circ/77.01^\circ$. However, the presence of the melt residue (NdF_2 , NdF_3 , PrF_3 , LiF) could not be avoided. Evidence of NdF_2 , which was formed during the potentiostatic deposition process due to the disproportionation reactions between Nd metal deposited and Nd(III) ions present in the electrolyte, was rather well pronounced [4,5].

CONCLUSION

Neodymium and praseodymium were successfully electrodeposited on Mo cathode by applying constant potential from fluoride-based Nd, Pr and Li molten salts containing rare earth oxides (Nd_2O_3 and Pr_6O_{11}). It seems that in the investigated systems, the reduction of Nd(III) ions to the metal proceeds as a two-step reduction process: $\text{Nd(III)} \rightarrow \text{Nd(II)}$ and $\text{Nd(II)} \rightarrow \text{Nd(0)}$, whilst the reduction of Pr(III) ions to the metal is a one-step reduction process: $\text{Pr(III)} \rightarrow \text{Pr(0)}$. It appears, also, that these reactions under the applied conditions are reversible and transport- controlled because the electrolyte was not stirred. The results recorded by the electrochemical techniques applied on the system used suggested that Nd and Pr metal can be electrochemically deposited on Mo electrode, and the XRD analysis confirmed the assumption.

Acknowledgement

V.S.C. and N.M.V. acknowledge the financial support for the investigation received from the Ministry of Education, Science and Technological Development of the Republic of Serbia (Grant No.451-03-9/2021-14/200026). Part of the research was supported by the funds of the bilateral research project (ID: 451-03-01344/2020-09/8) supported by the Ministry of Education, Science and Technological Development of the Republic of Serbia and German Academic Exchange Service (DAAD).

REFERENCES

- [1] O. Diehl, M. Schönfeldt, E. Brouwer, A. Dirks, K. Rachut, J. Gassmann, K. Güth, A. Buckow, R. Gauß, R. Stauber, O. Gutfleisch, *J. Sustain. Metall.*, 2018, **4**, 163–175.
- [2] Y. Yang, C. Lan, L. Guo, Z. An, Z. Zhao, B. Li, *Sep. Purif. Technol.*, 2020, **233**, 116030.
- [3] M.C. Bonfante, J.P. Raspini, I.B. Fernandes, S. Fernandes, L. M.S. Campos, O. E. Alarcon, *Renew. Sustain. Energy Rev.*, 2021, **137**, 110616.
- [4] V.S. Cvetković, D. Feldhaus, N.M. Vukićević, T.S. Barudžija, B. Friedrich, J.N. Jovićević, *Metals*, 2020, **10**, 576.
- [5] V.S. Cvetković, N.M. Vukićević, D. Feldhaus, T.S. Barudžija, J.S. Stevanović, B. Friedrich, J. N. Jovićević, *Int. J. Electrochem. Sci.*, 2020, **15**, 7039-7052.

MORPHOLOGY OF ALUMINIUM ELECTRODEPOSITED ON ALUMINIUM FROM AlCl_3 +UREA SOLVATE IONIC LIQUID

V.S. Cvetković, N.M. Vukićević and J.N. Jovićević

University of Belgrade, Institute of Chemistry, Technology and Metallurgy, Department of Electrochemistry, Njegoševa 12, 11000 Belgrade, Republic of Serbia. (v.cvetkovic@ihtm.bg.ac.rs)

ABSTRACT

The ionic liquid, made of urea and AlCl_3 , known as deep eutectic solvent (DESs) has already shown to be low-cost electrolyte suitable for aluminum electrodeposition. By applying appropriate potentiostatic or galvanostatic electrolysis regime, aluminium is successfully electrodeposited from the deep eutectic solvent onto aluminium substrate at nearly room temperatures. Morphologies of the produced deposits were characterized by scanning electron microscopy (SEM) and chemical composition by energy-dispersive X-ray (EDX) analysis. The electrodeposited aluminium displayed different morphology depending on the deposition conditions applied.

INTRODUCTION

Because of outstanding thermal properties, electric conductivity, light weight, and good corrosion resistance aluminium and its alloys are very significant [1,2,3]. It is now common knowledge that aluminium cannot be electrodeposited from aqueous electrolyte because its standard potential is much more negative than standard potential of hydrogen evolution (-1.662 V vs NHE). Therefore, the majority of the electrolytes investigated for possible Al electrodeposition are inorganic molten salts at elevated temperatures, mostly composed from AlCl_3 and NaCl, KCl and LiCl [4,5]. Research efforts have also been directed towards finding even more suitable non aqueous electrolytes applicable for Al deposition close to room temperatures. It was found that novel electrolytes, called ionic liquids (ILs), might be suitable for the electrodeposition of reactive metals including Al and Al alloys [2,6]. One of those appeared to be the mixture of aluminium chloride and 1-ethyl-3-methylimidazolium chloride ([EMIm]Cl) [2]. Although able to operate at near room temperatures the ionic liquids are expensive and very hygroscopic, and thus unsuitable for industrial electrolysis.

A new class of low cost ionic liquids with increased stability in air called deep eutectic solvents (DESs) was reported not long ago [7]. DESs are systems produced from an eutectic mixture of Lewis or Brønsted acids and bases, consisting of a different anionic and/or cationic species [7]. DESs have proven to possess several advantages over traditional ILs such as low vapor pressure, high solubility for metal salts, easy preparation. Research done so far showed that DES is very promising electrolyte for electrodeposition and dissolution of a number of metals and alloys including aluminium [7].

Our previous study has shown that aluminium can be successfully electrodeposited from deep eutectic system, based on AlCl_3 +urea, onto glassy carbon and aluminium at near room temperatures [8]. This paper focuses on the conditions leading to different aluminium morphology electrodeposited onto aluminium substrate. This is very important having in mind possibility that this system is considered suitable for electrochemical renewable energy source [9].

EXPERIMENTALS

Electrochemical measurements and electrodeposition processes were conducted in three-electrode electrochemical cell made of Pyrex glass, under dry argon atmosphere. High purity aluminium (Al, 99.999%, Alfa Products, Thiokol/Ventron division, USA) was used as electrodes material. Aluminium wire 3 mm in diameter served as the reference electrode, a rectangular shovel of aluminium was used as the counter electrode and 0.5 cm^2 plate of aluminium was employed as the

working electrode. Previous to each experiment aluminium electrodes were mechanically polished with sand paper and etched as reported earlier [8].

Deep eutectic solvent (DES) used as the electrolyte was made from anhydrous aluminium chloride (used as received, >99%, Aldrich Chemical Company, Inc.) and urea (used as received, p.a. Carlo Erba, France) with molar ratio of 1.6:1. The process of the electrolyte preparation was specified in our previous work [8].

Electrochemical techniques used for examination of aluminium deposition/dissolution processes were cycling voltammetry (CV), potentiodynamic polarization curves, chronoamperometry and chronopotentiometry with an electrochemical workstation (EG&G model PAR 273A) regulated by Power Suite software (Princeton Applied Research, USA). Electrochemical study was carried out at three different temperatures: 25 °C, 35 °C and 50 °C. The galvanostatic and potentiostatic electrodepositions were done at 35 °C. The electrolyte was not stirred. After deposition working electrode was washed with absolute ethanol (C₂H₅OH, Zorka-Pharma, Šabac, Serbia) to remove any electrolyte residue and then dried before further deposit analysis. The morphological forms and chemical composition of the deposits obtained were determined by scanning electron microscopy assembled with energy dispersive X-ray spectroscopy (SEM, TESCAN Digital Microscope; model VEGA3, Brno, Czech Republic and EDX-Oxford INCA 3.2, UK).

RESULTS AND DISCUSSION

Examples of cyclic voltammograms recorded on the Al cathode within the same potential range at three different temperatures are presented in Figure 1. It appeared that working temperature significantly influences aluminium electrodeposition process in the electrolyte used (made of 1.6:1 molar ratio AlCl₃:urea). The maximum peak current densities of both cathodic and anodic peaks recorded increased several times when working temperature was enlarged by ten degrees Celsius. The charge encompassed by the recorded cathodic and anodic currents was also increased considerably as the result of said temperature change. The cathodic charge (reflecting aluminium deposition) was more or less equal to anodic charge (reflecting dissolution of the deposited aluminium) showing reasonable reversibility of the two opposite processes (Al(III) ↔ Al) under applied conditions and the DES chosen. The voltammograms suggest aluminium deposition potential close to – 50 mV vs. Al irrespective of working temperature. From the point of possible use of the system in batteries this can be considered as positive. However, the deposition and dissolution current densities recorded by voltammograms were rather low, less than 100 μA cm⁻². This should not be surprising, because low conductivity of the electrolyte used at applied temperatures is known.

Scanning electron micrographs and chemical composition of the aluminium electrodeposited onto aluminium by applying constant deposition potential of – 250 mV vs. Al at 35 °C are presented in Figure 2. The deposits of very high specific surface area were obtained showing pure aluminium with complex three-dimensional morphology. It was the deposit made of the flake-like dendrites randomly oriented predominantly formed as the upper layer, and positioned over lower layer of densely grown much smaller needle-like crystallites. This implies that, immediately after nucleation, the deposit proceeds to grow under 3D diffusion control. These crystallites could be a problem for some future renewable power source.

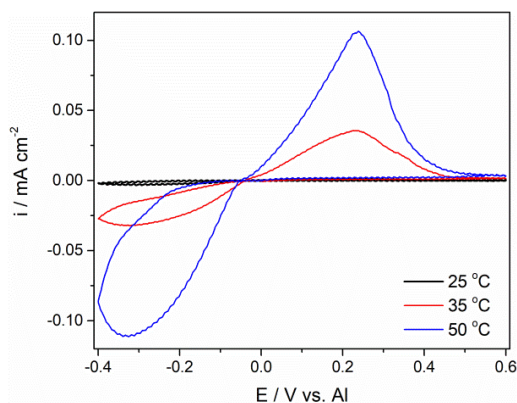


Figure 1. CV recorded on Al working electrode at different temperatures; potential range: $E_{\text{INITIAL}} = 000 \text{ mV} \rightarrow E_{\text{CATHODIC}} = -400 \text{ mV} \rightarrow E_{\text{ANODIC}} = 600 \text{ mV} \rightarrow E_{\text{FINAL}} = 000 \text{ mV}$ vs. Al; sweep rate = 10 mVs^{-1} .

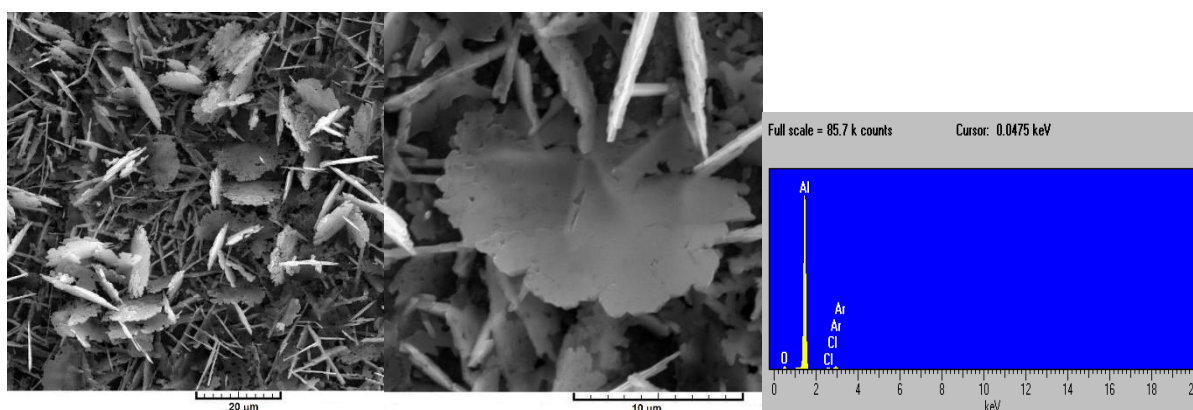


Figure 2. a) and b) SEM images (magnification: 1500x and 6000x) and c) EDX analysis of aluminium deposits obtained at $35 \text{ }^\circ\text{C}$ on Al after potentiostatic regime at -250 mV vs. Al, during 30 min.

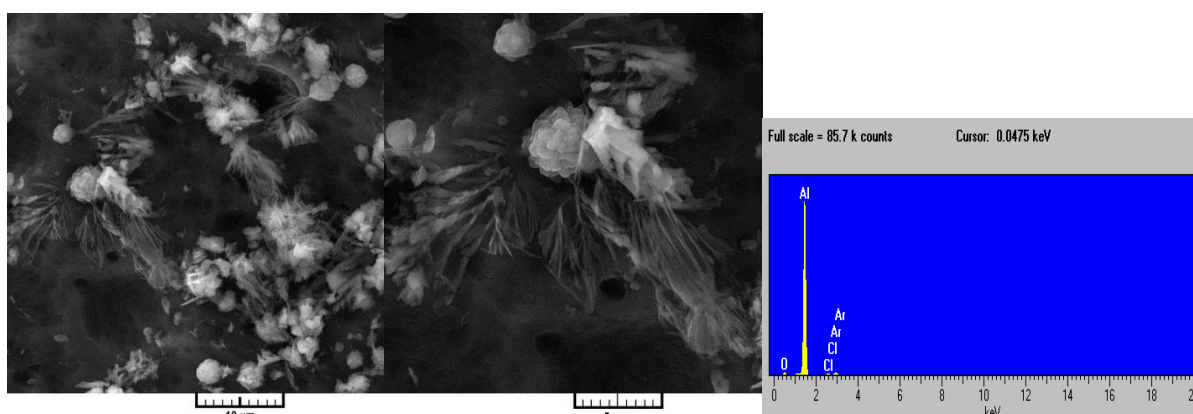


Figure 3. a) and b) SEM images (magnification: 5000x and 10000x) and c) EDX analysis of the aluminium deposits onto Al substrate obtained at a current density of -2 mA cm^{-2} for 30 min at $T = 35 \text{ }^\circ\text{C}$.

SEM micrographs and chemical compositions of the aluminium electrodeposited onto aluminium substrate from the chosen electrolyte at $35 \text{ }^\circ\text{C}$ under constant current density of -2 mA cm^{-2} are presented in Figure 3. The obtained aluminium deposit was tree-dimensional consisting of grains in

different sizes and crystal shapes. Apparently, crystal grains as the most dominant form were grouped randomly into more or less separate agglomerates. The shape of the grains seems to be changing from the form of crystalline boulders and nodular grains to a very complex and irregular morphology almost from the beginning of the deposition. The dendrites were formed on the boulders and grains as highly branched crystallites of various shapes that grew oriented towards the bulk of the electrolyte. These highly developed 3D crystallite forms are expected result of the diffusion controlled deposition of the aluminium under applied condition. Applied deposition current density of -2 mA cm^{-2} provoked cathodic overpotential in the range of -1000 mV vs. Al at $35 \text{ }^\circ\text{C}$. It was again apparent that a uniform Al deposit layer could not be put down onto the Al substrate under the experimental conditions described.

CONCLUSION

Aluminum was successfully electrodeposited on Al by applying constant potential or constant current density, from deep eutectic solvent (AlCl_3 :urea = 1.6:1).

Although successfully electrodeposited onto aluminium at a temperature ranging from $25 \text{ }^\circ\text{C}$ to $50 \text{ }^\circ\text{C}$ it was apparent that a uniform Al deposit layer could not be put down onto the aluminium substrate under the experimental conditions described. Instead, aluminium deposits consisting of great number of crystallites of various shapes were obtained. These findings should arise caution in the circles considering the used system as promising for rechargeable batteries.

The deposit obtained by applying constant deposition potential makes denser surface population than the deposit made by applying constant deposition current density which consists of randomly distributed groups of individual grains. However, in both cases no compact deposit covering whole substrate is possible but individual flake-like, dendrites of different shapes, needles, boulders and crystalline grains.

Acknowledgement

V.S.C. and N.M.V. acknowledge the financial support for the investigation received from the Ministry of Education, Science and Technological Development of the Republic of Serbia (Grant No. 451-03-9/2021-14/200026).

REFERENCES

- [1] M. Paunovic, M. Schlesinger, *Fundamentals of Electrochemical Deposition*, 2nd ed., John Wiley & Sons, Inc., Hoboken, USA, 2006.
- [2] K.K. Maniam, S. Paul, *Coatings*, 2021, **11**, 80.
- [3] H.M.A. Abood, N.L. Dawood, *Int. J. Sci. Res.*, 2015, **4**, 753–760.
- [4] G.R. Stafford, C.L. Hussey, R.C. Alkire, D.M. Kolb (Eds.), *Adv. Electrochem. Sci. Eng.*, Wiley-VCH Verlag GmbH, New York, Weinheim, pp. 275–348, 2001.
- [5] M. Ueda, *J. Solid State Electrochem.*, 2017, **21**, 641–647.
- [6] T. Tsuda, G.R. Stafford, C.L. Hussey, *J. Electrochem. Soc.*, 2017, **164**, H5007–H5017.
- [7] E.L. Smith, A.P. Abbott, K.S. Ryder, *Chem. Rev.*, 2014, **114**, 11060–11082.
- [8] V.S. Cvetković, N.M. Vukićević, N. Jovićević, J.S. Stevanović, J.N. Jovićević, *Trans. Nonferrous Met. Soc. China*, 2020, **30**, 823–834.
- [9] M. Angell, C-J. Pan, Y. Rong, C. Yuan, M-C. Lin, B-J. Hwang, H. Dai, *PNAS*, 2017, **114**, 834–839.

IMPACT OF CURRENT DENSITY ON THE ELECTROCHEMICAL DEGRADATION OF PHENOL AT PbO₂-GNR ANODE

T. Brdarić, B. Savić, D. Aćimović, D. Vasić Anićijević, M. Ječmenica Dučić, I. Perović and M. Momčilović

University of Belgrade, VINČA Institute of Nuclear Sciences - National Institute of the Republic of Serbia, Mike Petrović Alasa 12-14, 11001 Belgrade, Serbia. (tanja.brdaric@vin.bg.ac.rs).

ABSTRACT

This paper presents the impact of current density on the degradation efficiency of phenol by electrochemical oxidation in the base media on a new hydrothermally synthesized PbO₂-GNR (lead dioxide – graphene nanoribbon) anode. The morphological characteristics of materials was obtained using field emission scanning electron microscopy (FESEM). The electrochemical oxidation were performed in galvanostatic mode applying current densities of 50 and 100 mA cm⁻² in 0.1 M Na₂SO₄. Experimental results have shown that the degradation efficiency increased with increasing applied current density and electrolysis time. After 60 minutes of the electrolysis the degradation efficiency of the phenol was 98.6 % and 49.4 % on current densities 100 and 50 mA cm⁻², respectively. The newly synthesized anode material PbO₂-GNR can be successfully used in the treatment of phenol-contaminated wastewater.

INTRODUCTION

A serious problem of the global ecosystem and human health is the pollution of water sources and surface waters caused by industrial wastewater, inadequate waste disposal, and unsettled flow of sanitary wastewater.

In recent decades, great efforts have been made to improve water treatment technologies and establish legislation, especially in the field of an economy that exploits the largest amounts of solid and liquid waste and wastewater. One of the most common organic pollutants in industrial and municipal wastewater, which belong to the highly toxic, are phenols and their derivatives, chlorinated, nitrated, and methylated phenols. The simplest representative of phenolic compounds is phenol. Phenol is an aromatic, organic compound with molecular formula - C₆H₅OH [1]. Electrochemical oxidation has been investigated as a potential application for the decontamination of wastewater containing organic pollutants. The anode material has a significant influence on the application of electrochemical oxidation. Thus, the development of new anode materials with improved electrooxidation performance, electrochemically more stable and cheaper compared to standard anodes, is among key strategies in the future research in the field of electrochemical depollution. With the development of nanomaterials of metal nanoparticles and metal oxides, carbon nanomaterials and composites, better efficiency of electrochemical decomposition is achieved. In our previous paper [2] a nanocomposite PbO₂-GNR material was synthesized and applied for the first time as anode for the degradation of a mixture of phenols. However, despite the considerable efficiency of the degradation of phenol mixture, the fundamental principles beyond the degradation process are rather complex and require further investigation to be fully understood.

In this contribution, the nanocomposite material based on PbO₂-GNR nanocomposite synthesized in [2] is additionally morphologically characterized, and applied as the anode for degradation of pure phenol in aqueous solution. Within the experiments, the research is focused on the examination of electrochemical oxidation of phenol on the synthesized PbO₂-GNR anode (lead dioxide-graphene nanoribbon), on current density of 50 and 100 mA cm⁻².

METHODS

PbO was synthesized using the procedure proposed by Alagar et al. [3] with a small modification. This modification is explained in detail in the paper Savic et al. [2]. The nanosized PbO₂ was prepared by the hydrothermal method using synthesized PbO. The PbO₂-GNR nanocomposite was obtained by mixing the synthesized PbO₂ nanoparticles with commercial GNR in deionized water, a ratio of 3:1 (v/v %) on a magnetic stirrer for 3 hours, ie until a homogeneous suspension was achieved. The sample was dried at 70 °C. After that, obtained PbO₂-GNR nanopowder was dispersed in dimethylformamide (DMF) by sonication for 2 h (5 mg mL⁻¹) and 500µL suspension were applied dropwise to the SS electrodes.

FESEM was applied for testing morphological characteristics. Electrochemical oxidation was performed in a closed, undivided, thermostated two-electrode cell. A stainless steel electrode was used as a counter electrode. The modified steel electrode with PbO₂-GNR was a working electrode. Electrochemical oxidation of phenol was performed in the galvanostatic regime on current densities of 50 and 100 mA cm⁻². Concentration of phenol was 25 mg L⁻¹ in Na₂SO₄ (0.1M) solution as electrolyte. The experiments were carried out at room temperature, 25 ± 1 °C.

Phenol extraction and determination was performed by the standard method EN 12673: 1998 [4]. Qualitative and quantitative analysis of phenol was performed by gas chromatography with mass detector on the device 7890B GC System, 5977MSD manufactured by Agilent Technologies, USA. It is very important to determine the degradation efficiency of a given process and it is determined by following expression:

$$\varepsilon = \frac{(c_0 - c)}{c_0} 100$$

where are:

ε - degradation efficiency in %,

c_0 - concentration of phenol at the beginning of the process in (mg L⁻¹),

c - concentration of phenol after application of the process in (mg L⁻¹).

RESULTS AND DISCUSSION

The micrographs presented in Figures 1. shows the synthesized PbO₂ powder, at different magnifications.

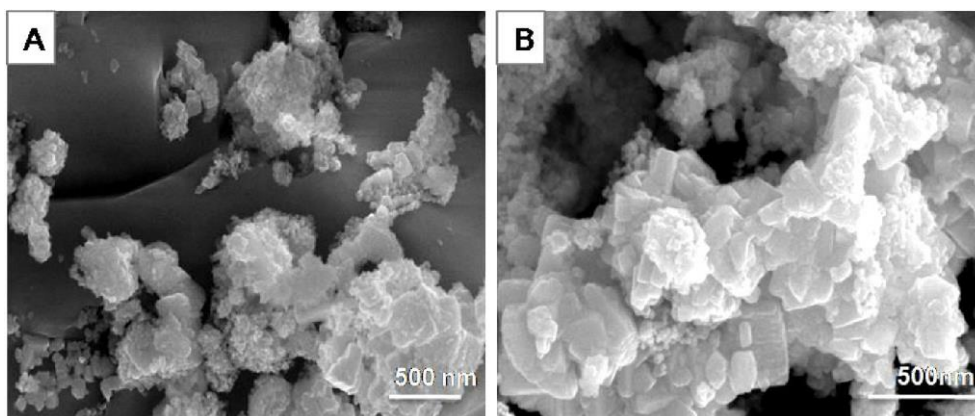


Figure 1. FESEM micrographs of PbO₂: A) magnification 50,000 × and B) magnification 80,000 ×

The powder sample consists of agglomerates of irregular shapes and different sizes. At higher magnification (Figure 1B), it is noticed that the agglomerate is composed of interconnected grains of predominantly plate shape.

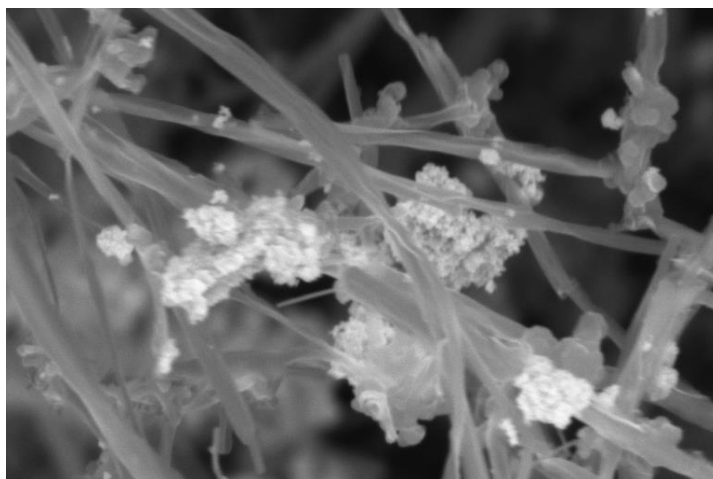


Figure 2. FESEM micrographs of PbO₂ magnification 50,000 ×

FESEM image (Figure 2) confirmed the presence of PbO₂ nanoparticles on the nanoribbon GNR.

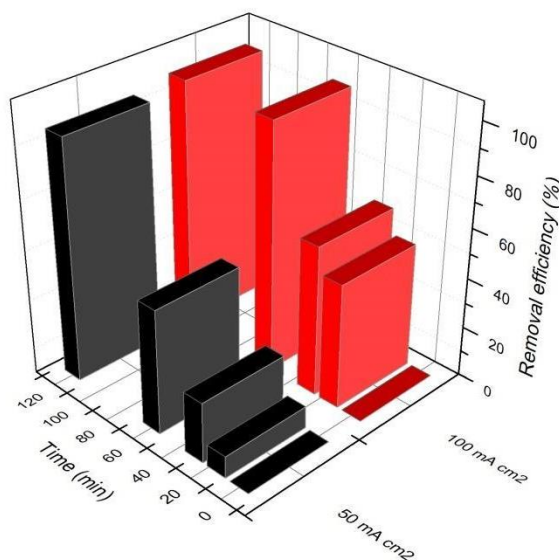


Figure 3. The degradation efficiency of phenol

Figure 3 shows degradation efficiency of phenol on PbO₂-GNR electrode at applied current densities of 50 and 100 mA cm⁻². As expected, with increasing of applied current density, the degradation efficiency increased and a time required to complete the degradation process decreased. After 60 minutes the degradation efficiency of the phenol was 98.6 % and 49.4 % on current densities 100 and 50 mA cm⁻², respectively. These results are ascribed to an increase in the concentration of reactive •OH radicals at higher current densities. It is well known that phenols is oxidized indirectly via adsorbed hydroxyl radicals on non-active electrode like PbO₂ and PbO₂-GNR. Thus, higher concentration of •OH radicals at higher current densities at the same electrolysis time contributes to higher percentage of degradation efficiency. The obtained results follow the same trend as the previously reported results of the other authors with small distinctions [5, 6].

CONCLUSION

A previously synthesized nanocomposite PbO₂-GNR anode with considerable efficiency for the electrooxidation of phenol mixture was additionally morphologically characterized and successfully applied as anode for electrooxidative degradation of pure phenol aqueous solution. Particularly, the results indicated that the current density is an important factor and significantly affect the efficiency of electrochemical oxidation of phenols. The presented research results show the possibilities of PbO₂-GNR electrode application, in real systems, especially for decontamination of phenol-containing sulphate wastewater from the textile industry. It was shown that electrode modification with nanocomposite PbO₂-GNR enlarges the size of the active surface and the diffusion layer of the electrode. All the results indicated that the current density is an important factor and significantly affects the efficiency of electrochemical oxidation of phenols.

The presented research results show the possibilities of PbO₂-GNR electrode application, in real systems, especially for sulphate wastewater from the textile industry.

In addition, it provides a starting point for the extensive further investigations in the field of nanocomposite-based anodes for the electrooxidative removal of various organic pollutants. Moreover, investigation of the fundamental principles beyond the observed electrode performance of the prepared nanocomposite will also be the subject of future research.

Acknowledgement

The authors would like to thank the Ministry of Education, Science and Technological Development of the Republic of Serbia for the financial support to the research through institutional funding (Contract number 451-03-9/2021-14/200017).

REFERENCES

- [1] M. Soto-Hernández, M. P. Tenango, R. Garcia-Mateos, Phenolic Compounds: Natural Sources, Importance and Applications. IntechOpen, 2017.
- [2] B. Savić, D. Stanković, S. Živković, M. Ognjanović, G. Tasić, I. Mihajlović, T. Brdarić, Applied Surface Science, 2020, 529, 147120.
- [3] M. Alagar, T. Theivasanthi, A. K. Raja, Journal of Applied Sciences, 2012, 12, 398–401.
- [4] EN 12673:1998 Water quality – Gas chromatographic determination of some selected chlorophenols in water, European Committee for Standardization, 1998.
- [5] X. Duan, F. Ma, Z. Yuan, X. Jin, L. Chang, Journal of the Taiwan Institute of Chemical Engineers, 2013, 44, 95–102.
- [6] X. Duan, C. Zhao, W. Liu, X. Zhao, L. Chang, Electrochimica Acta, 2017, 240, 424–436.

DEGRADATION OF RHODAMINE B DYE ON GRAPHITE ANODE: KINETIC AND ELECTROCHEMICAL BEHAVIOR

T. Brdarić, D. Aćimović, B. Savić, D. Vasić Anićijević, M. Ječmenica Dučić, I. Perović and D. Maksin

University of Belgrade, VINČA Institute of Nuclear Sciences - National Institute of the Republic of Serbia, Mike Petrović Alasa 12-14, 11001 Belgrade, Serbia. (tanja.brdaric@vin.bg.ac.rs).

ABSTRACT

The aim of this study was to investigate the removal efficiency of Rhodamine B dye from NaCl aqueous solution by electrochemical oxidation on the graphite anode with a specific focus on the kinetics of the process. After 60 minutes of galvanostatic electrolysis on the applied current density of 25 mA cm⁻² removal efficiency of about 97.6% was obtained. The degradation of Rhodamine B fitted well with the first-order kinetics.

INTRODUCTION

Rhodamine B, [9-(o-Carboxyphenyl)-6-(diethylamino)-3H-xanthen-3-ylidene] diethylammonium chloride, is a synthetic dye used as colorant in food, textile, leather, paper, etc [1]. According to the literature data, rhodamine B exhibits some carcinogenic and toxic effects on humans and animals. Due to health and environmental risk, great efforts had been made to develop the methods for Rhodamine B detection and degradation [2].

Advanced oxidation processes have shown up as a good alternative technique for decontamination of synthetic dyes, when conventional technologies are ineffective. Some of them, like photocatalysis, electrocoagulation, Fenton oxidation, sonochemical degradation and electrochemical techniques have been widely studied in literature as a treatment for many synthetic dyes [3, 4].

Electrochemical oxidation has stood out as a degradation method due to its simplicity, economy and environmental compatibility, because it does not require the addition of toxic chemical reagents [5]. Due to its intensive absorption in the visible region, spectrophotometry is an excellent method for the detection of Rhodamine B [6].

Current anode materials that are used for electrooxidation of Rhodamine B mainly involve noble and transition metals/metal oxides (IrO₂, RuO₂, PbO₂, TiO₂, SnO₂) [7, 8]. Also, research interests to use carbonaceous materials as anodes are increasing in recent years, since the development of advanced, high-surface carbonaceous materials opens novel possibilities [9]. Graphite represents a common, cheap and stable anode material with satisfactory mechanical properties, prone to oxidation and dissolution, thus being a satisfactory model anode and excellent support for innovative carbon materials [10]. Due to these properties, it represents a good base for further modification and improvement of efficiency of electrooxidation of dyes and organic pollutants from aqueous solutions.

In this study, the electrochemical behavior of Rhodamine B in NaCl-aqueous solution on graphite anode was investigated. Particular attention was paid to the investigation of oxidation kinetics, using UV-Vis spectrometry for determination of Rhodamine B concentration. The presented results establish the basic model system for future investigations of electrooxidative removal of various organic pollutants, using carbon-based anode materials.

METHODS

For the experiments 1x10⁻⁴ M solution of Rhodamine B in 0.05 M NaCl was used. Electrochemical measurements and oxidation were carried out on the Gamry Instrument - Interface 1000 Potentiostat/Galvanostat/ZRA06230 (Gamry Instruments, USA).

For cyclic voltammetry a three-electrode glass cell was utilized. Graphite, platinum and Ag/AgCl electrodes were used as working, counter and reference electrodes, respectively. Cyclic voltammetry was carried out at -1 to 2.5 voltage range and scanning rate of 100 mV s^{-1} . There were 10 cycles recorded, and since no change among them was observed, only the last cycle is shown.

In order to study the effect of electrolysis time on Rhodamine B degradation rate, experiments were performed in two-electrode electrolytic cell (working electrode was graphite, counter electrode was platinum) at constant current density of 25 mA cm^{-2} at room temperature.

During the electrolysis, the electrolyte aliquots were taken in different time intervals and absorbance at maximum absorbance peak (at 554.5 nm) were recorded on UV/Vis spectrophotometer Lambda 35 (Perkin Elmer, SAD).

Determination of Rhodamine B concentration in electrolyte was based on calibration curve. Removal efficiency was calculated according to following equation:

$$\text{Removal efficiency}(\%) = \frac{c_0 - c}{c_0} 100$$

where c_0 is initial concentration, c is concentration in taken aliquot in time, t of electrolysis.

RESULTS AND DISCUSSION

The cyclic voltammetry experiments were performed in order to confirm the Rhodamine B oxidation and examine the electrochemical behavior of the Rhodamine B on graphite electrode. The cyclic voltamograms in the absence and the presence of Rhodamine B are presented in Figure 1a. The rise of oxidation current at 1.14 V compared to blank electrolyte, indicates an oxidation process of Rhodamine B at the electrode surface. The cyclic voltamogram curve of Rhodamine B shows one anodic peak at $+1.14 \text{ V}$ ($I_{pa} = 0.0012 \text{ mA}$) in the forward scan and one cathode peak at 0.58 V ($I_{pc} = 0.0018 \text{ mA}$) in the reverse scan, suggesting that electrochemical oxidation is a quasi-reversible process ($I_{pc}/I_{pa} = 1.5$) (Figure 1a).

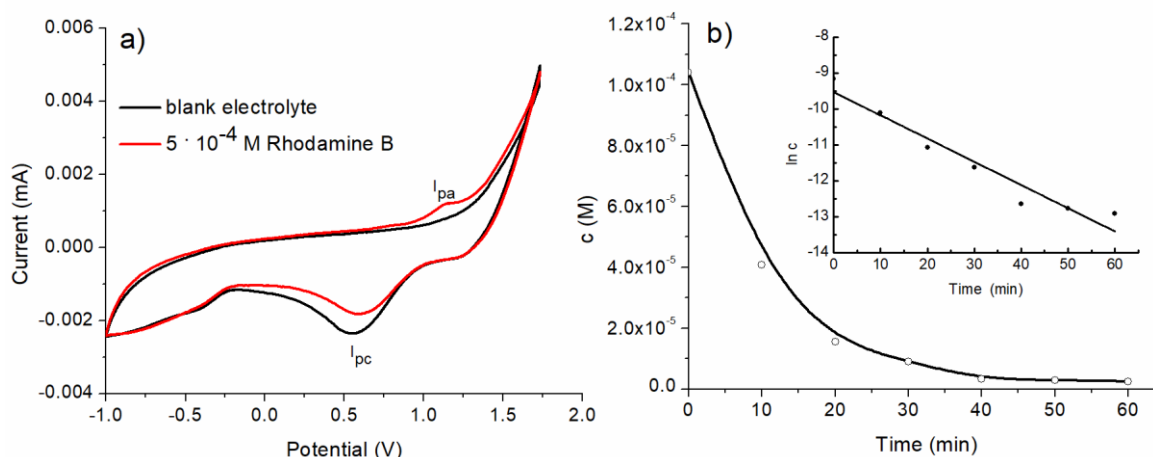


Figure 1. a) Cyclic voltamograms of Rhodamine B dye ($1 \times 10^{-4} \text{ M}$) and blank electrolyte at graphite working electrode, scan rates 100 mV s^{-1} ; b) Concentration profiles of Rhodamine B dye ($1 \times 10^{-4} \text{ M}$) at current density 25 mA cm^{-2} ; insert: relationship of the $\ln c$ versus time (relation of $\ln C$ and time).

It can be seen from the concentration profile presented in Figure 1b, that the electrochemical degradation of Rhodamine B was very fast within the initial 10 minutes. Determined removal

efficiency is about 61%. After 40 minutes removal efficiency is 96.91% and degradation rate slowly declining up to 60 min. 60 minutes after electrolysis treatment, the removal efficiency was 97.6 %.

In order to simulate the experimentally obtained degradation profile of Rhodamine B first-order kinetic reaction equation was used:

$$\ln C = \ln C_0 - kt$$

where k is the first-order reaction rate constant (min^{-1}) and C is concentration of Rhodamine B at time t . The linear relationship of $\ln C$ versus to time (insert Figure 1b) confirms that the degradation of Rhodamine B by electrolysis follows first-order kinetics. The determined rate constant is 0.0646 min^{-1} and the regression coefficient, R_2 is bigger than 0.94.

Observed first (or pseudo-first) order kinetics is in a good agreement with previous research data of Rhodamine B degradation in similar electrochemical conditions [9, 11]. In combination with the obtained remarkable efficiency of the dye removal, it points to the large amount of available chlorine and OH radicals at achieved potentials, so that the indirect oxidation of Rhodamine B is independent on their concentration, and/or to the direct oxidation of dye on the anode [12].

CONCLUSION

Oxidation of Rhodamine B was confirmed on the graphite anode, at the potential 1.14 V vs. Ag/AgCl reference electrode. A cathode peak at 0.58 V in the reverse direction indicates a quasi-reversible process.

Based on the results of electrooxidative degradation experiment, Rhodamine B has been effectively removed by graphite–Pt electrochemical system by applying current density of 25 mA cm^{-2} . At initial concentration $1 \times 10^{-4} \text{ M}$, 97.6% of Rhodamine B has been removed within 60 minutes of electrooxidation. The degradation process can be described by first-order kinetics.

High efficiency of the investigated electrooxidation process confirms the general potential of use of carbon-based anodes in the removal of organic pollutants from aqueous solutions, and paves a way for the extensive future research including various pollutants and anode materials.

Acknowledgement

The authors would like to thank the Ministry of Education, Science and Technological Development of the Republic of Serbia for the financial support to the research through institutional funding (contact number 451-03-9/2021-14/200017)

REFERENCES

- [1] L. Feng, X. yan Li, L. hong Gan, and J. Xu, *Electrochim. Acta*, 2018, 290, 165–175.
- [2] D. Sun, X. Yang, *Food Anal. Methods*, 2017, 10, 2046–2052.
- [3] P. V Nidheesh, R. Gandhimathi, *Desalin. Water Treat.*, 2014, 52, 37–41.
- [4] E-S. El-Ashtouky, N. Amin, *J. Hazard. Mater.*, 2010, 179, 113–119.
- [5] D. Medeiros, D. Araújo, C. Sáez, C. A. Martínez-huitle, M. A. Rodrigo, *Appl. Catal. B Environ.*, 2015, 167, 454–459.
- [6] H. Ngo, V. Nguyen, T. Manh, T. Toan, N. Triet, N. Binh, N. Hoan, T. Thien, D. Khieu, *J. Nanomater.*, 2020, 1-14.
- [7] M. Kothari, K. Shah, *Water Sci. Technol.*, 2020, 81, 720–731.
- [8] A. Ahmad, M. Priyadarshini, S. Das, M. Ghangrekar, 2021, *J. Hazardous, Toxic, Radioact. Waste*, 25, 4021012.
- [9] R. Rathinam, M. Govindaraj, K. Vijayakumar, S. Pattabhi, *Desalin. Water Treat.*, 2016, 57, 16995–17001.

- [10] R. Kakhki, *Russ. J. Appl. Chem.*, 2016, 89, 480–488.
- [11] A. Kaur, R. Kaur, H. Kaur, *Moroccan J. Chem.*, 2016, 4, 1–4.
- [12] D. Maharana, J. Niu, D. Gao, Z. Xu, J. Shi, *Water Environ. Res.*, 2015, 87, 304–311.

COMPOSITE of AgX ZEOLITE WITH CARBONIZED POLYANILINE FOR ELECTROANALYTICAL SENSING OF PHENOL COMPOUNDS

I. Stojković Simatović¹, M. Petković¹, R. Hercigonja¹, N. Cvjetičanin¹, A. Jović¹, D.M.F. Santos² and B. Šljukić^{1,2*}

¹University of Belgrade – Faculty of Physical Chemistry, Studentski trg 12–16, 11158 Belgrade, Serbia. (biljka@ffh.bg.ac.rs)

²CeFEMA, Instituto Superior Técnico, University of Lisbon, Avenida Rovisco Pais, 1049–001 Lisbon, Portugal.

ABSTRACT

Ag⁺ cation-exchanged X zeolite was prepared by ion-exchange procedure and characterized by chemical analysis and scanning electron microscopy. The zeolite was subsequently used for the preparation of a composite with carbonized polyaniline. The electroanalytical response of the composite in the presence of phenol compounds (phenol, p-nitrophenol, and p-aminophenol) in acidic media was studied by voltammetric techniques. The results indicate that the composite electrode is suitable for phenol and p-nitrophenol sensing in aqueous media, while no response was obtained in p-aminophenol presence.

INTRODUCTION

Among different organic water pollutants, phenol and its derivatives are extremely toxic to humans, causing irritation of skin, eyes, and mucous membranes after acute (short-term) inhalation or dermal exposures [1,2]. In the present work, the potential application of composite electrodes based on zeolites and carbonized polyaniline for monitoring phenol compounds in acidic aqueous media is addressed. The main issue related to the electrochemical sensing of phenol compounds is electrodes fouling with time. Thus, phenols oxidation at different electrodes (metal, metal oxides, and carbon) was explored in different electrolytes (H₂SO₄, Na₂SO₄, and NaCl) to assess the mechanism and nature of electrode deactivation phenomena [3]. Adsorption of intermediates generated during oxidation was found to lead to early deactivation of the electrode, while the formation of polymeric films is promoted with time. Furthermore, it was shown that, depending on the electrode material, electrode regeneration can be achieved by anodic polarization. Zeolite-based electrodes can be exploited to improve the electrocatalytic responses with reduced overpotentials and increased voltammetric/ampereometric signals allowing low detection limits and high sensitivities. Similarly, new nitrogen-containing carbon nanomaterials synthesized by carbonization of nanostructured conducting polymer polyaniline (PANI) were also shown to be electrocatalytic active for the oxidation of different metals and ions.

EXPERIMENTAL

The Ag⁺ cation-exchanged zeolite was prepared from synthetic 13X (Union Carbide) zeolite by standard ion-exchange procedure [4]. The morphology of the zeolite was examined using a JEOL JSM-6610LV scanning electron microscope.

Carbonized polyaniline (c-PANI-SSA) was prepared by the gram-scale template-free oxidative polymerization of aniline with ammonium peroxydisulfate as an oxidant in 5-sulfosalicylic acid aqueous solution, followed by carbonization of produced PANI [5,6].

Electrochemical studies were carried out using Gamry PCI4/750 potentiostat in 0.1 M H₂SO₄ as supporting electrolyte, and with platinum as counter electrode and saturated calomel electrode (SCE) as a reference electrode. Working electrodes were prepared by mixing AgX with c-PANI-SSA in

25:75 wt.% ratio and then ultrasonically dispersing in 2% polyvinylidene difluoride solution in N-methylpyrrolidone. The prepared suspension was dropped onto glassy carbon support and dried at 100°C.

RESULTS AND DISCUSSION

The composition of the prepared AgX zeolite was determined by chemical analysis and found to correspond to $\text{Ag}_{80}\text{Na}_7(\text{AlO}_2)_{87}(\text{SiO}_2)_{105}$ with Si/Al ratio of 1.2 and Ag/Al ratio of 0.92.

Morphology of the studied zeolite was observed by SEM revealing partially agglomerated particles of typical polyhedral shape, **Figure 1**. The particles were observed to be of ca. 0.5 - 1.0 μm in size.

CV of AgX/c-PANI-SSA composite electrode in 1 mM phenol solution in 0.1 M H_2SO_4 revealed an anodic peak at ca. 0.65 V vs. SCE corresponding to phenol oxidation, **Figure 1B** [1]. The phenol electrooxidation is rather complex and, generally, benzoquinone and hydroquinone are the main oxidation products (in the absence of chlorides) along with traces of catechol and carboxylic acids. Namely, direct electrooxidation of phenol proceeds through several steps starting with the phenol molecules adsorption on the electrode surface, followed by their oxidation to form radicals and subsequent oxidation of formed radicals to hydroquinone and then to benzoquinone. Though these radicals might be involved in polymerization reaction in acidic media with formation of the mentioned passivating film, the response of AgX/c-PANI-SSA was found to be stable.

It should be mentioned that phenol oxidation on the individual components of the composite, i.e., pure AgX and c-PANI-SSA, as well as on the glassy carbon support, was also explored. Significantly lower peak currents were recorded in these cases.

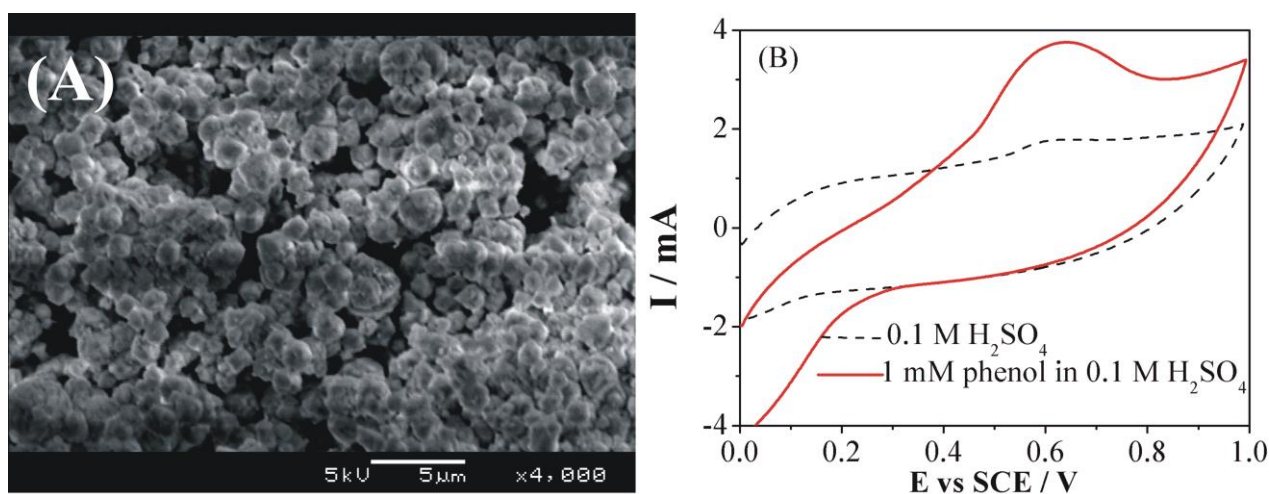


Figure 1. SEM images of AgX zeolite (A) and CV of AgY/c-PANI-SSA composite electrode in 0.1 M H_2SO_4 in the absence and in the presence of 1 mM phenol (B) at polarisation rate of 0.01 V s^{-1} .

The favorable electrochemical sensing performance was attributed to the synergistic effect of zeolite and carbonized polyaniline components. The 3D porous network zeolite structure offers a large active interface for electrooxidation of phenol. The approach of guest molecules and their interaction with zeolites is determined by the number and location of the exchanged cations, with cations occupying mainly three types of sites in FAU framework. Carbonized polyaniline provides high electronic conductivity, thus facilitating charge transport.

CV of AgX/c-PANI-SSA composite electrode in 1 mM p-nitrophenol solution in 0.1 M H_2SO_4 revealed an anodic peak at ca. 1.3 V vs. SCE corresponding to p-nitrophenol oxidation in addition to

the peaks in the 0.4 - 0.6 V vs. SCE region. No peak could be observed at the CV of AgX/c-PANI-SSA electrode in 1 mM p-aminophenol solution in 0.1 M H₂SO₄, thus excluding this composite electrode for potential application for aminophenol sensing in acidic media.

In order to explain the absence of anodic peaks in the CV obtained in p-aminophenol solution, the energies of the highest occupied molecular orbitals (HOMO) at B3LYP/6-311G(d,p) level were estimated to be -5.21 eV, -6.22 eV, and -7.14 eV for p-aminophenol, phenol, and p-nitrophenol, respectively. Lower/higher values for p-aminophenol/p-nitrophenol compared to phenol are due to the electron donating/withdrawing nature of the substituent, which is reflected in the lower/higher oxidation potential compared to the reference compound. As the measured oxidation potential of phenol is lower than the one for p-nitrophenol by ca. 0.65 V, energies of the HOMO orbitals imply that the oxidation potential of p-aminophenol lies beyond the potential range in which the CV measurements were performed.

CONCLUSIONS

AgX zeolite was prepared by exchanging Ag⁺ ion with Na⁺ ion in the 13X parent zeolite. SEM analysis showed that polyhedral-like morphology of NaX precursor was preserved. AgX zeolite was used for building a composite with carbonized polyaniline and tested for electroanalytical sensing of phenol compounds in acidic media. Thus, phenol and p-nitrophenol oxidation was detected in a rapid, low-cost, and reliable way. Conversely, aminophenol oxidation could not be detected.

Acknowledgement

The authors would like to thank professor Gordana Ćirić-Marjanović and associate professor Aleksandra Janošević Ležaić for the synthesis of carbonized polyaniline used in this work. This work was partially supported by the Ministry of Education, Science and Technological Development of the Republic of Serbia (Contract no. 451-03-9/2021-14/200146), as well as by the Fundação para a Ciência e a Tecnologia, Portugal (research contract in the scope of programmatic funding UIDP/04540/2020 (D.M.F. Santos) and contract no. IST-ID/156-2018 (B. Šljukić)).

REFERENCES

- [1] A. Jović, A. Đorđević, M. Čebela, I. Stojković Simatović, R. Hercigonja, B. Šljukić, *Journal of Electroanalytical Chemistry*, 2016, 778, 137–147.
- [2] B. Šljukić, C. E. Banks, A. Crossley, R. G. Compton, *Analytica Chimica Acta*, 2007, 587(2), 240-246.
- [3] D. Funo, C. Carlesi Jara, G. Saracco, V. Specchia, P. Spinelli, *Journal of Applied Electrochemistry*, 2005, 35, 405–411.
- [4] R. Hercigonja, V. M. Radak, *Colloids and Surfaces*, 1992, 64, 191-195.
- [5] N. Gavrilov, I. A. Pašti, M. Vujković, J. Travas-Sejdic, G. Ćirić-Marjanović, S.V. Mentus, *Carbon*, 2012, 50, 3915–3927.
- [6] A. Janošević, I. Pašti, N. Gavrilov, S. Mentus, G. Ćirić-Marjanović, J. Krstić, J. Stejskal, *Synthetic Metals*, 2011, 161, 2179–2184.
- [7] M. J. Frisch, *Gaussian 09 Revision D.01*, Gaussian Inc, Wallingford CT, 2009.

ELECTROCHEMICAL OXIDATION AND INTERACTION OF NEWLY SYNTHESIZED ACRIDINE DERIVATIVES WITH DNA

J. Rupar¹, M. Aleksić¹, V. Dobričić², O. Čudina², J. Brborić² and N. Gavrilov³

University of Belgrade, Faculty of Pharmacy, ¹Department of Physical Chemistry and Instrumental Methods (jelena.rupar@pharmacy.bg.ac.rs)

²Department of Pharmaceutical Chemistry, Vojvode Stepe 450, 11000 Belgrade, Serbia

³University of Belgrade, Faculty of Physical Chemistry, Studentski Trg 12-15, 11000 Belgrade, Serbia (gavrilov@ffh.bg.ac.rs).

ABSTRACT

Oxidation of newly synthesized acridine derivatives was studied using cyclic voltammetry at glassy carbon electrode. Oxidation occurs as irreversible, diffusion-controlled process at pH 4.6 for compounds 1-3 and as adsorption controlled process for compound 4. The interaction between newly synthesized acridine compounds (compounds 1-4) and dsDNA was studied using a multilayer dsDNA biosensor applying square wave voltammetry. Peak current corresponding to deoxyadenosine decreased after 30 minutes of interaction suggesting interaction with dsDNA.

INTRODUCTION

It has been proven that acridine derivatives may be used as anti-inflammatory, anticancer and antimicrobial agents [1]. Activity of acridine derivatives can be attributed to their semiplanar structure and to their redox properties as they can intercalate between double stranded DNA (dsDNA) base pairs [2]. Synthesis and activity testing for acridine derivatives has been the subject of many research papers [3] as well as investigation of their redox activity [4]. DNA-drug interaction can be investigated using DNA biosensor where the adsorbed DNA at glassy carbon electrode (GCE) surface undergoes charge-transfer reactions, producing signals which correspond to deoxyguanosine (dG) and deoxyadenosine (dA) oxidation.

The aim of this work was to investigate the oxidation of some newly synthesized acridine derivatives [3] and their interaction with dsDNA.

METHODS

Voltammetric measurements were performed using a μ Autolab analyzer (EcoChemie, Utrecht, The Netherlands) controlled by the GPES 4.9 software. A conventional three-electrode system was used with Ag/AgCl as a reference (3.00 M KCl) and Pt as an auxiliary electrode. A GCE (d = 3 mm, CH Instruments, Inc., Austin, TX, USA) was used as the working electrode. Before the measurements, the GCE was polished on a smooth polishing pad with an aqueous slurry of Al₂O₃ powder (particle size 0.05 μ m). After polishing, the GCE was sonicated in bidistilled water for 2 minutes and then in absolute ethanol for 2 minutes. Calf thymus DNA (dsDNA, $MW_r = 10 - 15 \times 10^6$) was obtained from Sigma-Aldrich, and acridine derivatives: (S)-methyl 2-(acridin-9-ylamino)-3-phenylpropanoate (compound 1), (S)-methyl 2-(acridin-9-ylamino)-3-(1H-imidazol-4-yl)propanoate (compound 2), (S)-methyl 2-(acridin-9-ylamino)-3-(1-methyl-1H-indol-3-yl)propanoate (compound 3) and (S)-2-(acridin-9-ylamino)-3-(1-methyl-1H-indol-3-yl)propanoic acid (compound 4) were synthesized in our laboratory [3]. Final concentrations of the compounds 1-4 (2.4×10^{-4} M for cyclic voltammetry (CV) and 1×10^{-4} M for square wave voltammetry (SWV)) were obtained by diluting the stock solution with appropriate volume of supporting electrolyte (acetate buffer, pH 4.6). Solutions were

de-aerated for 10 minutes with high purity nitrogen. The experiments were performed at room temperature (25 °C).

The multilayer DNA biosensor was prepared by covering the surface of glassy carbon electrode successively with three drops of DNA (5 μL , 73.95 $\mu\text{g mL}^{-1}$) [4]. After placing each drop on the top of the electrode surface, the electrode was dried under nitrogen atmosphere, and rinsed with water to remove the unabsorbed DNA. The DNA biosensor was immersed in acridine derivative solutions and allowed to incubate for 30 minutes. After the incubation time, the biosensor was removed from the solution, washed with bidistilled water in order to remove the unbounded molecules and placed in the electrochemical cell containing only the supporting electrolyte.

The transduction for biosensor was performed using SW voltammetry. The experimental parameters for SWV were: frequency 25 Hz, potential increment 0.001 V, effective scan rate of 0.0025 V/s and pulse amplitude of 0.005 V. Oxidation of acridine derivatives was examined using CV. CV was performed between 0 V and +1.6 V. Scan rate was ranging from 10 mV/s up to 100 mV/s with step potential of 0.005 V.

RESULTS AND DISCUSSION

The oxidation of synthesized acridine derivatives (compounds 1-4) of 2.4×10^{-4} M was studied by CV at pH 4.6. The cyclic voltammograms were recorded in three successive scans at a scan rate 10 – 100 mV/s (Fig. 1). Anodic peak which appeared at $E_p \sim 0.9 - 1.0$ V was of interest for our research since the oxidation of the synthesized compounds was monitored during the DNA interaction study. The corresponding cathodic peak was absent, meaning that the oxidation process of compounds was irreversible. The scan rate effect on the compounds oxidation peak was monitored. The peak current increased linearly with the square root of v for compounds 1-3 indicating that the oxidation process was diffusion controlled [5]. The corresponding slopes of $\log I_p$ vs. $\log v$ dependences, which were close to theoretical value of 0.5 for diffusion controlled process, proved the diffusion nature of the oxidation of the compounds 1-3.

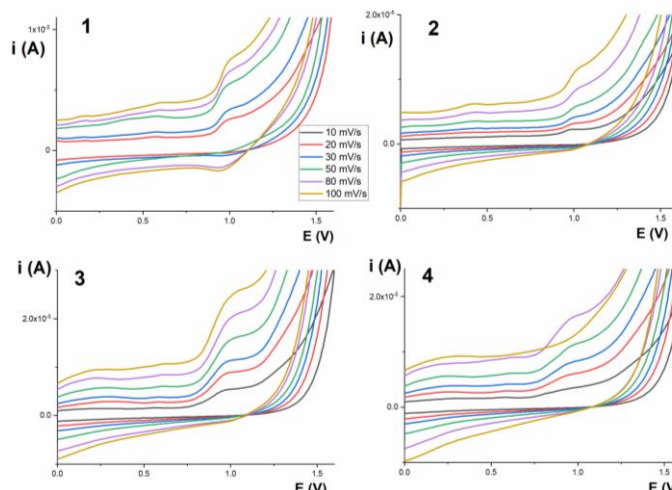
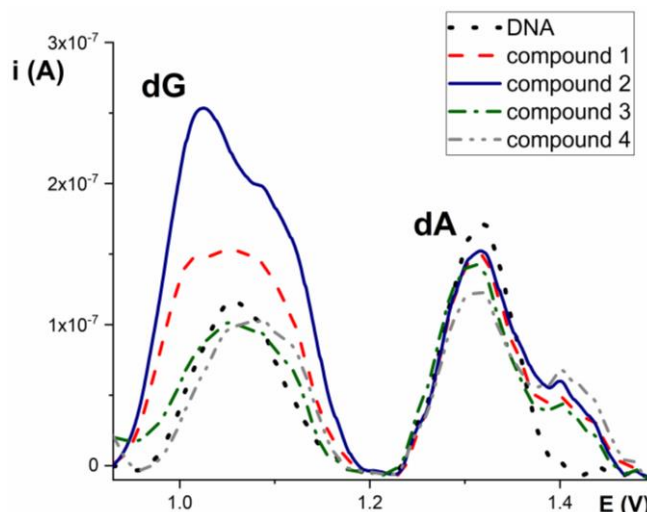


Figure 1. Cyclic voltammograms of compounds 1-4 at different scan rates

Table 2. Equations I_p vs. $v^{1/2}$ or I_p vs. v and $\log I_p$ vs. $\log v$ for compounds 1- 4

Co mp	I_p vs. $v^{1/2}$ or I_p vs. v	$\log I_p$ vs. $\log v$
1	I_p (A) = $3.34 \times 10^{-6} v^{1/2}$ (V/s) $^{1/2}$ - 7.11 $\times 10^{-8}$, $R^2 = 0.9904$	$\log I_p$ (A) = $0.55 \log v$ (V/s) - 5.44
2	I_p (A) = $1.84 \times 10^{-6} v^{1/2}$ (V/s) $^{1/2}$ + 1.91×10^{-9} , $R^2 = 0.8960$	$\log I_p$ (A) = $0.45 \log v$ (V/s) - 5.80
3	I_p (A) = $1.34 \times 10^{-5} v^{1/2}$ (V/s) $^{1/2}$ - 1.18 $\times 10^{-7}$, $R^2 = 0.9788$	$\log I_p$ (A) = $0.47 \log v$ (V/s) - 4.03
4	I_p (A) = $2.72 \times 10^{-5} v$ (V/s) - 6.13 $\times 10^{-8}$, $R^2 = 0.9989$	$\log I_p$ (A) = $0.93 \log v$ (V/s) - 4.71

On the other hand, compound 4 showed linear dependence of I_p vs. v , and the $\log I_p$ vs. $\log v$ curve slope close to the unity value, indicating its adsorption nature. (Table 1).

**Figure 2.** SW voltammograms of acridine derivatives interaction with DNA

The interaction of compounds with dsDNA was examined using SWV at pH 4.6. The changes in the purine base (deoxyguanosine, dG and deoxyadenosine, dA) oxidation peak currents were monitored after the incubation of DNA biosensor with 1×10^{-4} M solutions of synthesized compounds during 30 minutes [6].

As the oxidation peak of compounds and dG of DNA overlapped, only the change in dA peak was informative.

After the interaction, the height of the dA peak decreased (comparing to control dsDNA biosensor) indicating an interaction. According to the results presented in Figure 2, compound 4 indicated most intensive interaction with DNA, probably as a consequence of its adsorption at GCE.

CONCLUSION

The oxidation of compounds was examined applying cyclic voltammetry using a glassy carbon electrode and it occurred as irreversible, diffusion controlled process for compounds 1-3 and adsorption controlled process for compound 4. The glassy carbon electrode covered with three drops of dsDNA solution was used as electrochemical biosensor with aim to examine the possible

interaction of compounds with DNA. The results of our study indicate potential chemotherapeutical role for used compounds, where compound 4 has the most intensive interaction considering the dA peak current decrease.

Acknowledgement

Research was funded by the Ministry of Education, Science and Technological Development, Republic of Serbia through Grant Agreement with University of Belgrade-Faculty of Pharmacy No: 451-03-9/2021-14/200161 and University of Belgrade-Faculty of Physical Chemistry No: 451-03-68/2020-14/200146 and the Science Fund of the Republic of Serbia (PROMIS program, RatioCAT, no. 606224).

REFERENCES

- [1] J. S. Rugar, V. D. Dobričić, M. M. Aleksić, J. S. Brborić, O. A. Čudina, *Kragujevac J. Sci.* 2018, 40, 83-101.
- [2] R. A. Hutchins, J. M. Crenshan, D. E. Graves, W. A. Denny, *Biochemistry*, 2003, 42, 13754-13761.
- [3] J. Rugar, V. Dobričić, J. Grahovac, S. Radulović, Ž. Skok, J. Ilaš, M. Aleksić, J. Brborić, O. Čudina, *RSC Med. Chem.*, 2020, 11, 378-386.
- [4] J. Rugar, M. M. Aleksić, V. Dobričić, J. Brborić, O. Čudina, *Bioelectrochemistry*, 2020, 135, 107579.
- [5] A. Shah, A. M. Khan, R. Qureshi, F. L. Ansari, M. F. Nazar and S. S. Shah, *Int. J. Mol. Sci.* 2008, 9, 1424-1434.
- [6] J. Rugar, M. Aleksić, V. Dobričić, O. Čudina, J. Brborić, S. Vladimirov, 14th International Conference on Fundamental and Applied Aspects of Physical Chemistry 2018, Belgrade, Serbia, 379-382.

THE SYNTHESIS AND CHARACTERIZATION OF ZnMn_2O_4 IN AN AQUEOUS SOLUTION OF ZnCl_2

J. Senćanski¹, N. Nikolić², S. Blagojević¹ and I. Stojković Simatović³

¹University of Belgrade, Institute of General and Physical Chemistry, Studentski trg 12-15, 11000 Belgrade, Republic of Serbia (sencanskijelena@yahoo.com)

²University of Belgrade, Institute for Multidisciplinary Research, Kneza Višeslava 1, 11030 Belgrade, Republic of Serbia

³University of Belgrade, Faculty of Physical Chemistry, Studentski trg 12-15, 11000 Belgrade, Republic of Serbia

ABSTRACT

This work provides the synthesis and characterization of ZnMn_2O_4 that may be a potential replacement for the hazardous cathode materials used in commercial Li-ion batteries, as well as the examination of its electrochemical properties in an aqueous solution of ZnCl_2 . Due to the fact that commercial Li-ion batteries contain toxic and flammable electrolyte, there is a need for their replacement with less harmful substance.

INTRODUCTION

This work aims to design an ecological Zn-ion battery using the glycine nitrate procedure by which sub-micron sized particles are obtained. ZnMn_2O_4 , according to the data reported, has a stable capacity in both aqueous and organic electrolytes. Zhang *et al.* examined ZnMn_2O_4 as the cathode material in 3M aqueous solution of $\text{Zn}(\text{CF}_3\text{SO}_3)_2$. The measurement by galvanostatic charge and discharge gave a capacity of 150 mAh g^{-1} with a capacity retention of 94% after 500 cycles at rate of 500 mA g^{-1} . Sheklar *et al.* examined the electrochemical properties of ZnMn_2O_4 as an anode in 1M NaClO_4 dissolved in 1:1 (v/v) mixture of ethylene carbonate with diethyl carbonate. The measurement was performed by galvanostatic charge and discharged obtaining the capacity of 170 mAh g^{-1} with the retention of 1000 cycles at rate of 100 mA g^{-1} . This work provides the synthesis, crystallographic and morphological analysis as well as the electrochemical properties of the material in the aqueous solution of zinc salt.

METHODS

The glycine nitrate combustion method was applied to synthesize ZnMn_2O_4 . The solutions of 1M $\text{Mn}(\text{NO}_3)_2 \cdot 6\text{H}_2\text{O}$ and $\text{Zn}(\text{NO}_3)_2 \cdot 6\text{H}_2\text{O}$ in stoichiometric ratio were mixed and glycine was added (glycine/ $\text{NO}_3=1.2$). The solution was combusted at 200°C until complete combustion, and thereafter annealed for four hours at 800°C in air.

XRPD data are collected using the Rigaku Ultima IV powder diffractometer with Ni-filtered $\text{Cu K}\alpha$ radiation in the interval of 4 to $90^\circ 2\theta$ with the step of 0.02° (scanning speed 2° min^{-1}). The unit cell refinement was performed using the Le Bail full pattern profile fitting method [3] implemented in FullProf software [4].

The sample morphology was analyzed using the scanning electron microscope (Tescan VEGA TS 5130MM) operating at 20 kV accelerating voltage.

Cyclic voltammetry was performed using the Gamry PCI4/300 Potentiostat/Galvanostat at the polarization rate 10 and 50 mV s^{-1} . The three electrode system was used (a counter electrode was platinum, reference SCE, and working electrode was glossy carbon electrode on which was pasted

cathode material, carbon black as well as polyvinylidene difluoride in ratio 85:10:5). The paste was obtained according to reference [5]. The measurement was performed at 25 °C.

RESULTS AND DISCUSSION

The diffractogram calculated shows a good agreement with the data reported in the literature [6] and shown in **Fig. 1**; the pattern is refined to the $I4_1/amd$ space group with lattice parameters: $a= b= 5.7185(8) \text{ \AA}$, $c= 9.268(2) \text{ \AA}$.

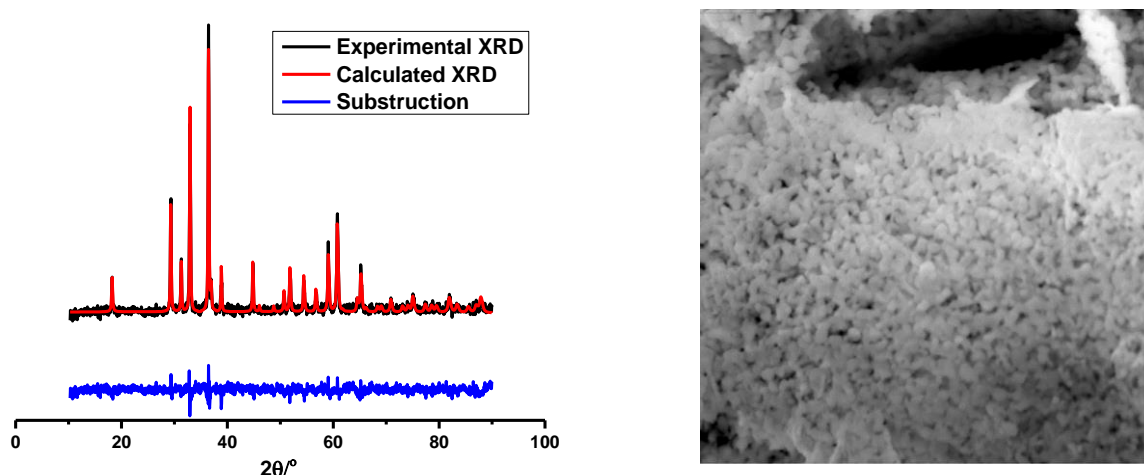


Figure 1. a) refined XRD pattern of the material synthesized, b) SEM micrographs at magnification of 10 000x

SEM imaging revealed the irregular to prismatic shaped bridged particles composing the partly porous microstructure **Fig. 1.b**. Taking into account submicroscopic dimensions of particles and their coalescence a high specific surface may be predicted to zinc ions absorption, but their coalescence will affect to zinc ion insertion, and, consequently, to a capacity amount. The material's electrochemical properties are tested by cyclic voltammetry.

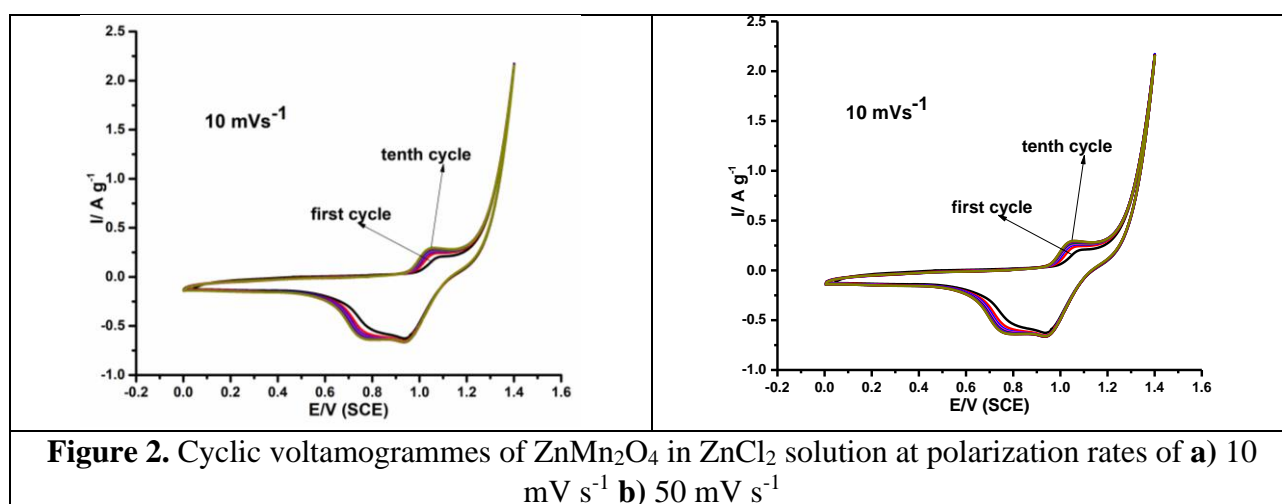


Figure 2. Cyclic voltammogrammes of $ZnMn_2O_4$ in $ZnCl_2$ solution at polarization rates of a) 10 mV s^{-1} b) 50 mV s^{-1}

Low, however, a stable capacity may be observed from **Fig. 2 a) and b)**. The average discharge capacity for 10 mV s^{-1} amounting to 10.33 mAh g^{-1} , as well as 4.1 mAh g^{-1} for 50 mV s^{-1} are low

compared to the theoretical capacity of the material, 224 mAh g⁻¹. Lower distance of the peaks for a lower rate means that the process of insertion and de-insertion of zinc ions is more reversible compared to a higher rate. The consequence is that distinction of anode and cathode peaks is higher for the higher rate (0.26V) compared to the lower rate (0.11V), as may be observed from **Fig 2**. In practice, these results show that the material may be used for low rates as well as for high rates. The reason for low capacity lies in the fact that the coalescence of the sub-micron particles gave rise in the total particle specific surface area reduction, thus amount of the inserted Zn ions is reduced. Zinc ions may be inserted and de-inserted only through the opened surface part of the particles. Since the low capacity values, the research needs to be directed to improve this disadvantage by doping the material with different metal, or using different salt aqueous solution.

CONCLUSION

This work presents the results of characterization of ZnMn₂O₄ cathode material synthesized using the glycine nitrate procedure. This material was characterized by XRPD showing the lattice parameters obtained were in a good agreement with the data reported in literature. The morphological characterization predicted a low capacity, due to the presence of sub-micron particles and their coalescence, that was proven by cyclic voltammetry, in the aqueous solution of ZnCl₂. Owing to the results obtained, the material might be used for both low and high rates. Research should be continued in order to improve the capacity by doping the material with some other ion, or using an aqueous solution of some other salt.

Acknowledgement

This work was supported by the Ministry of Education, Science and Technological Development of the Republic of Serbia, contract numbers: 451-03-9/2021-14/ 200051, 451-03-9/2021-14/200053, 451-03-9/2021-14/200146.

REFERENCES

- [1] N. Zhang, F. Cheng, Y. Liu, Q. Zhao, K. Lei, C. Chen, J. Chen, *Journal of the American Chemical Society*, 2016, 138, 12894-12901.
- [2] B. C. Sekhar, P. Packiyalakshmi, N. Kalaiselvi, *Royal Society of Chemistry Advances*, 2017, 7, 20057-20061.
- [3] A. Le Bail, H. Duroy, J. L. Fourquet, *Materials Research Bulletin* 1988, 23, 447-452.
- [4] J. Rodriguez-Carvajal, *Physica B* 1993, 192, 55-69.
- [5] J. Senćanski, D. Bajuk-Bogdanović, D. Majstorović, E. Tchernychova, J. Papan, M. Vujković, *Journal of Power Sources*, 2017, 342, 690-703.
- [6] Y. Yanyan, Y. Zhao, L. Xiao, and L. Zhang, *Electrochemistry communications*, 2008, 10, 1117-1120.

HYDROGEN EVOLUTION AT NICKEL/NICKEL OXIDE/CARBON COMPOSITES ELECTROCHEMICALLY PREPARED IN ALGINATE SOLUTION

J. Rupar¹, A. Janošević Ležaić¹ and N.Gavrilov²

¹*University of Belgrade, Faculty of Pharmacy, Department of Physical Chemistry and Instrumental Methods (jelena.rupar@pharmacy.bg.ac.rs)*

²*University of Belgrade, Faculty of Physical Chemistry, Studentski Trg 12-15, 11000 Belgrade, Serbia (gavrilov@ffh.bg.ac.rs).*

ABSTRACT

In this work, carbon materials enriched in nickel (Ni) and nitrogen (N), obtained by carbonization of electrochemically synthesized alginate-based gels, were analyzed in 1 M potassium hydroxide (KOH) to assess their catalytic activity towards hydrogen evolution reaction (HER). SEM and elemental analysis confirmed the presence of Ni in all samples. Electrochemically active surface area (ECSA) was obtained from measured cyclic voltammograms (CVs), namely characteristic Ni²⁺/Ni³⁺ oxidation/reduction transition in synthesized composite materials. Sample Ni5AlgRiv, which in addition to Ni, contains a small percentage of N, dominantly formed by β-Ni(OH)₂, showed highest electro-catalytic activity for HER, with currents reaching few mA/cm².

INTRODUCTION

Development of cheap, stable and highly active catalyst for hydrogen evolution reaction (HER) is one of the prerequisites for future hydrogen based economy [1]. Pure nickel and its oxides/hydroxides have been shown to possess some of these qualities [2]. New venue of research now combine these properties with those of carbon based materials, mainly graphene oxide (GO) and reduced graphene oxide (rGO), to obtain highly conductive and stable composites [3].

This work investigates the possibility of electrochemical preparation of nickel/ nickel oxide/carbon composites based on sodium alginate and its use in HER. Ni/NiO nanoparticles are embedded in carbon support after drying and carbonization procedure.

METHODS

Ivium V01107 Potentiostat/Galvanostat (Ivium Technologies B.V., The Netherlands) was used for electrochemical measurements in a standard three-electrode cell. Surface morphology and composition was probed using PhenomTM ProX Desktop SEM (ThermoFisher ScientificTM, USA) with integrated EDS detector.

Synthesis of samples. Four samples synthesized within this work were obtained by oxidation of the nickel electrode where locally formed Ni²⁺ ions crosslink alginate chains. Prior to synthesis Ni electrode is mechanically cleaned to remove possible impurities. Metal contaminants were further removed by 0.1 M HCl treatment, while the organic impurities were removed with acetone. Electrode cleaning procedure was repeated before each synthesis. Samples Ni2Alg2.5V and Ni2Alg2.5V were obtained from 2% solution alginate at a voltage of 2.5 V and 2.0 V, respectively, relative to graphite electrode, for 30 minutes. Sample Ni5Alg2V was synthesized from a 5% solution of alginate, while, samples Ni5AlgRiv2V was synthesized from a 5% solution of alginate in 0.1% ethacridine lactate, at 2.0 V, for 30 min. After removal of the formed gel from the electrode, the samples were dried for 24 hours, at room temperature in air.

Carbonization of the sample. Drying was followed by carbonized in inert atmosphere (Ar) at a temperature of 800°C for 2h. The obtained samples are marked by addition of the prefix C to the name of the sample.

RESULTS AND DISCUSSION

SEM photographs, of all samples show bright spots that represent conducting nickel species evenly distributed on the carbon support. Elementary analysis of sample surfaces revealed that Ni is present in all samples. The highest atomic content of Ni (Table 1) was obtained for CNi5Alg2V, synthesized from a 5% solution of alginate. In the sample CNi5AlgRiv2V, in addition to C, O, Ni and Na, a small amount of N was observed, due to the presence of ethacridine lactate in the forming solution.

Table 1. EDS results for atomic and weight content and electrochemically active surface area (ECSA) for obtained carbonized samples

	CNi2Alg2.5V		CNi2Alg2V		CNi5Alg2V		CNi5AlgRiv2V	
	At. %	Weight %	At. %	Weight %	At. %	Weight %	At. %	Weight %
C	81.72	63.83	83.61	66.61	80.75	60.02	77.7	58.38
O	10.67	11.1	9.41	9.98	10.12	10.02	9.94	9.95
Ni	5.7	21.75	5.26	20.47	7.52	27.31	6.68	24.53
Na	1.34	2	1.34	2.04	1.14	1.62	1.18	1.7
N	/	/	/	/	/	/	3.44	3.01
ECSA / cm ²	4.7381		5.3809		2.5476		1.5476	

To assess the electrochemically active surface area (ECSA) prepared electrodes are cycled between 0 and 0.5 V to obtain characteristic Ni²⁺/Ni³⁺ transition (Fig 2, left). Oxidation/reduction peaks are shifted for different samples which depends on the type of oxide/hydroxide formed (α and/or β), thickness/size of formed particles, and local interaction with supporting carbon [4]. Based on peak positions, surface of CNi2Alg2.5V is almost exclusively formed by α -Ni(OH)₂ [4]. CNi2Alg2V and CNi5Alg2V are covered by a mix of α and β hydroxides while CNi5AlgRiv2V is predominantly β -Ni(OH)₂. Surface areas are determined by integration of respective oxidation/reduction peaks and normalization with the specific charge density of this process, which is 420 $\mu\text{C cm}^{-2}$. Obtained ECSA values are given in Table 1 and are used in current density calculations.

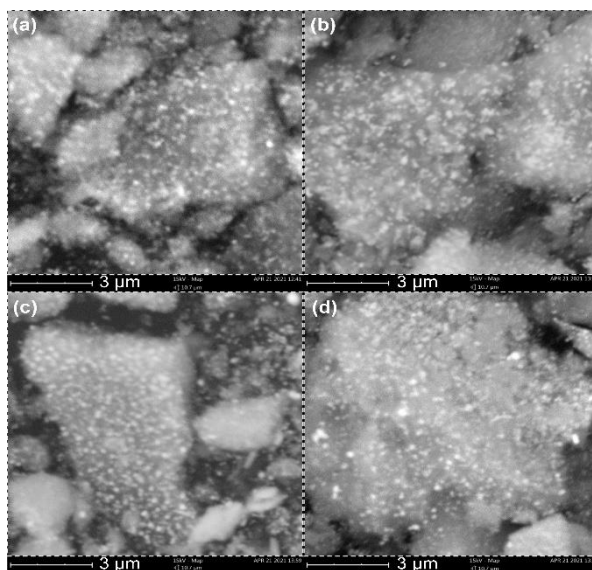


Figure 1. SEM micrographs of: CNi2Alg2.5V (a), CNi2Alg2V (b), CNi5Alg2V (c) and CNi5AlgRiv2V (d)

Hydrogen evolution was examined in 1M KOH deaerated solution with the cyclic voltammograms given in Fig 2, right. Materials can be compared based on onset potential i.e potential at which some arbitrary current value is attained or, as done here, by comparing current densities at a fixed potential value (measured currents are normalized to ECSA). Samples Ni2Alg2 and Ni2Alg2.5 show rather low activity toward HER which might be attributed to the materials being mainly in the form of α -Ni(OH)₂ and slightly lower surface nickel content. Conversely, Ni5AlgRiv shows good electrocatalytic activity which is on par with some Ni/rGO composites [1] with currents reaching few mA/cm². In spite having comparable Ni at. % Ni5AlgRiv2V has lowest ECSA leading to the conclusion that the β -Ni(OH)₂ should be much more active towards HER than α -Ni(OH)₂ in line with [5].

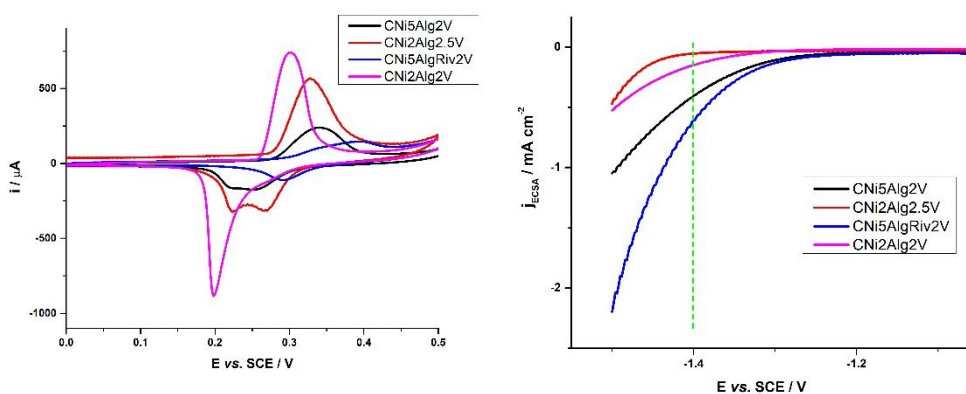


Figure 2. Oxidation/reduction CVs of composites for ECSA calculation, 1M KOH (left), 20 mV s⁻¹. (b) HER in 1M KOH, 20 mV s⁻¹(right)

CONCLUSION

Herein we report a simple method to manufacture carbon composite materials enriched in Ni and N, as potential catalysts for HER. Our results demonstrate that synthesized composite have varied activity toward HER depending on the type of nickel species present. Composite with predominantly β -Ni(OH)₂ shows good electro-catalytic activity, which might be connected with incorporated nitrogen in the carbon structure of this composites.

Acknowledgement

Research was funded by the Ministry of Education, Science and Technological Development, Republic of Serbia through Grant Agreement No: 451-03-68/2020-14/200146 and No: 451-03-9/2021-14/200161 and the Science Fund of the Republic of Serbia (PROMIS program, RatioCAT, no. 606224).

REFERENCES

- [1] M. J. Gomez, A. Loiacono, L. A. Perez, E. A. Franceschini, G. I. Lacconi, ACS Omega, 2019, 4, 1, 2206–2216.
- [2] M. Wang, Z. Wang, X. Gong, Z. Guo, Renewable Sustainable Energy Rev., 2014, 29, 573–588.
- [3] H. Ahmad, M. Fan, D. Hui, Composites Part B: Engineering, 2018, 145, 270–280.
- [4] I. G. Casella, M. R. Guascito, M. G. Sannazzaro, Journal of Electroanalytical Chemistry, 1999, 462, 2, 202–210.
- [5] A. Y. Faid, A. O. Barnett, F. Seland, S. Sunde, Electrochimica Acta, 2020, 361, 137040.

*F - Biophysical Chemistry,
EPR Investigations of Bio-systems*

ROLE OF PRO-INFLAMMATORY S100 PROTEINS IN AMYLOID-NEUROINFLAMMATORY CASCADE IN NEURODEGENERATIVE DISEASES.

L. A. Morozova-Roche

Department of Medical Biochemistry and Biophysics, Umeå University, Umeå, SE 90781, Sweden.

ABSTRACT

The amyloid cascade is central for the neurodegeneration disease pathology, including Alzheimer's and Parkinson's diseases, and remains the focus of much current research. Increasing evidence has accumulated demonstrating critical role of pro-inflammatory S100A9 in the amyloid-neuroinflammatory cascade in these diseases. We have demonstrated that S100A9 protein is intrinsically amyloidogenic and able to form amyloids both *in vitro* and *in vivo* in cell models and in neurodegenerative diseases. In Alzheimer's disease, deciphering the interaction between proinflammatory S100A9 protein and A β peptide and their co-aggregation mechanisms are particularly important since these lead to amyloid plaques formation and neural cytotoxicity. By using the combination of mass and charge distributions of amyloids together with reconstruction of the differences between them and detailed microscopy reveals that co-aggregation involves templating of S100A9 fibrils on the surface of Abeta42 amyloids. Kinetic analysis further corroborates that the surfaces available for the Abeta42 secondary nucleation are diminished due to the coating by S100A9 amyloids, while the binding of S100A9 to Abeta42 fibrils is validated by a microfluidic assay. We demonstrate that synergy between charge detection mass spectroscopy, microscopy, kinetic and microfluidic analyses opens new directions in interdisciplinary research.

Interactions of S100A9 with small molecules as potential regulators of its amyloid aggregation and functions, including interactions with NCAM1 peptide constructs, oleuropein aglycone, polyoxometalates and DOPA-derivatives, are discussed in the light of their potential therapeutic applications.

ANTIOXIDANT ENZYMES IN BLOOD OF WOMEN WITH UTERINE HYPERPLASIA

A. Todorović, D. Drakulić, L. Gavrilović, V. Stojiljković, N. Popović, N. Đorđević,
N. Todorović Vukotić, J. Miletić, S. Pejić, S. B. Pajović

University of Belgrade, VINČA Institute of Nuclear Sciences – National institute of the Republic of Serbia, P.O.Box 522, 11001 Belgrade, Republic of Serbia. (anato@vin.bg.ac.rs)

ABSTRACT

The literature emphasizes the involvement of oxidative stress in the etiopathogenesis of many uterine diseases. Antioxidant system (AOS) represents the protective mechanism used by cells to neutralize overproduced reactive oxygen species (ROS) and prevent oxidative stress. We have previously shown that in gynecological patients with various diagnoses, the reproductive and other factors may be associated with antioxidant capacity and the ability to defend against oxidative damage. In this study, we examined the changes in expression of antioxidant enzymes (AOE): superoxide dismutases (SOD), catalase (CAT), glutathione peroxidase (GPx), and glutathione reductase (GR) in the blood of women with endometrial hyperplasia. Our results indicate that hyperplasia induces perturbation in oxidative balance, particularly in glutathione redox cycle enzymes.

INTRODUCTION

According to the World Health Organization (WHO) classification system, simple endometrial hyperplasia (SH) refers to diffuse and variably sized glands with a normal ratio of glands to stroma. This type of hyperplasia is characterized by a spectrum of changes in the endometrium ranging from slight alterations seen in the late proliferative phase of the menstrual cycle to irregular, hyperchromatic lesions that are similar to endometrial adenocarcinoma [1].

There is growing literature evidence on the involvement of oxidative stress in the etiopathogenesis of various uterine diseases including endometriosis, pre-eclampsia and unexplained infertility. Antioxidant system (AOS) represents the protective mechanisms used by cells to neutralize reactive oxygen species (ROS) and prevent oxidative stress. The most important enzyme components in antioxidant system are superoxide dismutase (SOD), catalase (CAT), glutathione peroxidase (GPx) and glutathione reductase (GR). Various studies demonstrated that compared to control, patients with benign and malignant changes in the genital tract have increased level of lipid peroxidation and altered antioxidant enzyme (AOE) activities in both peripheral blood and tissue [2].

We have previously shown that in gynecological patients with various diagnoses, the reproductive and other factors may be associated with antioxidant capacity and the ability to defend against oxidative damage [3]. In this study, we wanted to further examine the changes of antioxidant enzymes (SOD, CAT, GPx, and GR) expression, to better understand the changes in AOE activities found in patients with SH.

METHODS

This study utilized blood samples obtained from 30 subjects admitted to the Department of Gynecology and Obstetrics for gynecological evaluation within routine checkups or for abnormal uterine bleeding. The samples were taken after obtaining the informed consent. The study was conducted prospectively and it was approved by the Human Studies Ethics Committee of the Clinical Centre (No. 27/06-2006). The protocol was consistent with the World Medical Association Declaration of Helsinki (Ethical Principles for Medical Research Involving Human Subjects). Based on diagnosis and histological examination, subjects were divided into the following groups: healthy

control patients (C, $n = 15$, 49 ± 3 yr) and patients with hyperplasia simplex endometrii (SH, $n = 15$, 48 ± 1 yr). None of the subjects had undergone hormone therapy or any other medical treatment 6 months before sampling.

Venous blood samples were collected into heparinized tubes on the same day as endometrial biopsy. The protein levels of SOD, CAT, GPx, and GR were assayed by Western blot analysis as described previously [4].

Due to a non-Gaussian distribution of values, nonparametric Mann-Whitney U test was used to compare enzyme levels between SH patients and control subjects. A 2-tailed $p < 0.05$ was considered statistically significant. All data were analyzed using IBM SPSS Statistics version 23 and GraphPad Prism 4 software.

RESULTS AND DISCUSSION

Despite the incidence, treatment protocols for SH have not been standardized. The choice depends on lesion severity, patient age and medical history, but further progression of clinical diagnostic and treatment requires a better understanding of the molecular mechanisms that influence the disease. Oxidative stress seems to be important for disease development since it starts in the early stages of gynaecological pathologies [5].

Our study confirmed the existence of oxidative imbalance in women with SH. Results showed that among examined protein levels in the blood of SH patients, the GPx level was significantly increased (133.2%, $p < 0.05$), and the GR level was decreased (80.6%, $p < 0.01$), compared to healthy controls. The protein levels of CuZnSOD and CAT in SH patients were comparable between groups (**Figure 1**).

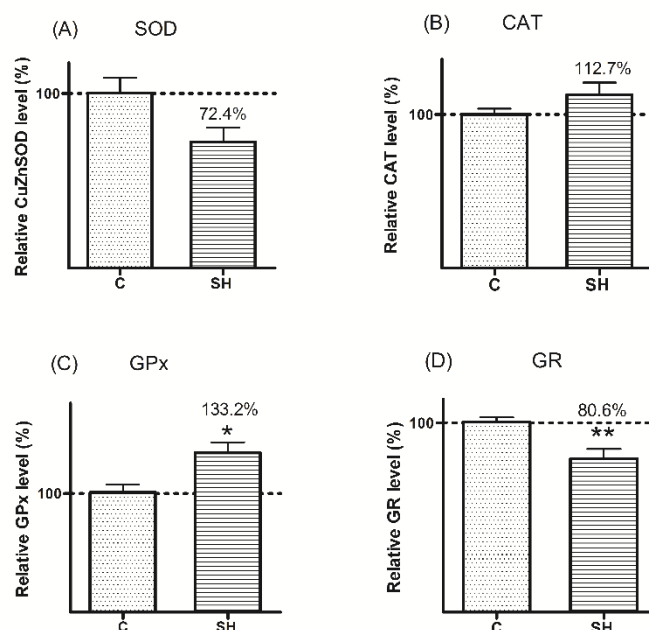


Figure 1. Relative protein levels of (A) CuZnSOD, (B) CAT, (C) GPx, and (D) GR in blood of healthy subjects (controls, C) and patients diagnosed with hyperplasia simplex (SH). Data are presented as the mean \pm SEM, whereas the values of controls are set as 100%. * $p < 0.05$, ** $p < 0.01$ vs. controls.

In our previous work, we reported significantly decreased activity of SOD in the blood of patients with SH [3]. Based on the unchanged SOD level detected in the current study, the results can be explained by inhibition of the enzyme activity that was not caused by the changes in its expression. Phosphorylation of proteins, for example, is one of the typical post-expressional mechanisms for the regulation of SOD activity. Transient phosphorylation of cytoplasmic SOD was firstly reported by Csar et al. [6] and it could explain the reduction of SOD activity in the blood of SH patients. Enzymatic activity of SOD could also be reduced by the peroxynitrite and myeloperoxidase system modification [7, 8], as well as by nitration, phosphorylation, glutathionylation, glycation, etc. The consequences of these modifications include altered structure and function of the protein, modulation of the catalytic activity, susceptibility to proteolysis, and disturbed signal transduction [9].

Similar to SOD, the CAT level in patients with SH was also unchanged. It seems that CAT functioning was unaffected by the existence of SH, although its adequate activity might be important for the disposal of free radicals and maintenance of the redox status of the cells. Unchanged expression and activity of CAT in SH patients could be elucidated by a decreased H_2O_2 production due to reduced SOD activity, but also by the role of CAT in the H_2O_2 removal. In the presence of high H_2O_2 concentration, CAT is the most effective for its metabolizing, but the glutathione system plays a critical role in the presence of low concentrations of H_2O_2 and other peroxides [10]. Ota et al. observed that CAT level was higher in patients with endometriosis than in controls. They hypothesized that GPx was not sufficient to dispose excessive free radicals in endometrium, so CAT was mobilized to support the neutralization [11].

GPx and GR are complementary pair of enzymes and important components of the glutathione redox system. GPx reduces toxic hydroperoxides, formed as a result of oxidative stress, while GR converts oxidized glutathione to the reduced form which GPx uses as an obligate co-substrate for normal enzyme activity. The significance of all components of the glutathione redox cycle is based on the great importance of glutathione molecules (GSH). They participate directly in free radicals neutralization and maintain vitamins C and E in their active forms. They are also involved in the regulation of the cell cycle, cell death, and many other important physiological processes [12]. Since GR is involved in sustaining the intracellular reducing environment by maintaining a high ratio of reduced to oxidized forms of GSH (GSH/GSSG), the inhibition of GR leads to the accumulation of GSSG, resulting in oxidative stress [13]. In our study, increased GPx and reduced GR levels observed in SH patients, might induce a reduction in GSH level, increasing the sensitivity to oxidative stress. This is particularly important for SH patients that are already in a state of oxidative stress since GSH deficiency enhances the cell's vulnerability to oxidative stress and the possibility of hyperplasia progression to adenocarcinoma [14].

CONCLUSION

Presented results provide evidence about AO disturbance in the blood of SH patients, with particular regard to glutathione redox cycle enzymes GPx and GR. Findings indicate the complex mechanisms that link the AO system with this endometrial disease and point to the need for further research to elucidate the mechanisms of observed AO shift.

Acknowledgement

This work is supported by the Ministry of Education, Science and Technological Development, Republic of Serbia (grant no. 451-03-9/2021-14/20017-0902107).

REFERENCES

- [1] V. Chandra, J.J. Kim, D.M. Benbrook, A. Dwivedi, R. Rai, *J Gynecol Oncol.*, 2016, **27**, e8.
- [2] J. Lu, Z. Wang, J. Cao, C. Yaoxing, D. Yulan, *Reprod Biol Endocrinol.*, 2018, **16**, 80.
- [3] S. Pejic, J. Kasapovic, A. Todorovic, V. Stojiljkovic, S.B. Pajovic, *Biol Res.*, 2006, **39**, 619-629.
- [4] N. Popović, S. Pajović, V. Stojiljković, S. Pejić, A. Todorović, I. Pavlović, L. Gavrilović, *Folia Biol.*, 2017, **65**, 43–54.
- [5] G.J. Burton, E. Jauniaux, *Best Pract Res Clin Obstet Gynaecol.*, 2011, **25**, 287-299.
- [6] X.F. Csar, N.J. Wilson, P. Strike, L. Sparrow, K.A. McMahon, A.C. Ward, J.A. Hamilton, *Proteomics*, 2001, **1**, 435-443.
- [7] F. Yamakura, T. Matsumoto, T. Fujimura, H. Taka, K. Murayama, T. Imai, K. Uchida, *Biochim Biophys Acta.*, 2001, **1548**, 38-46.
- [8] F. Yamakura, T. Matsumoto, K. Ikeda, H. Taka, T. Fujimura, K. Murayama, E. Watanabe, M. Tamaki, T. Imai, K. Takamori, *J Biochem.*, 2005, **138**, 57-69.
- [9] F. Yamakura, H. Kawasaki, *Biochim Biophys Acta.*, 2010, **1804**, 318-325.
- [10] S.A. Comhair, S.C. Erzurum, *Am J Physiol Lung Cell Mol Physiol.*, 2002, **283**, L246-255.
- [11] H. Ota, S. Igarashi, N. Sato, H. Tanaka, T. Tanaka, *Fertil Steril.*, 2002, **78**, 804-809.
- [12] N. Ballatori, S.M. Krance, S. Notenboom, S. Shi, K. Tieu, C.L. Hammond, *Biol Chem.*, 2009, **390**, 191-214.
- [13] C. Cereser, S. Boget, P. Parvaz, *A Revol Toxicology*, 2001, **163**, 153-162.
- [14] N. Traverso, R. Ricciarelli, M. Nitti, B. Marengo, A.L. Furfaro, M.A. Pronzato, U.M. Marinari, C. Domenicotti, *Oxid Med Cell Longev.*, 2013, **2013**, 972913.

FTIR ANALYSIS OF XYLEM VESSEL CELL WALLS IN TWINING STEM OF *Dioscorea balcanica*

J. Simonović Radosavljević¹, K. Radotić¹, D. Janošević², G. Mouille³, and A. Lj. Mitrović¹

¹ Institute for Multidisciplinary Research, University of Belgrade, Kneza Višeslava 1, 11000 Belgrade, Republic of Serbia (jasna@imsi.rs)

² University of Belgrade, Faculty of Biology, Studentski trg 16, Belgrade, Republic of Serbia

³ INRA, Institut Jean-Pierre Bourgin, UMR1318 INRAAgroParisTech, ERL3559 CNRS, Saclay Plant Sciences, 78026 Versailles, French Republic

ABSTRACT

Using stem cross sections of *Dioscorea balcanica*, as a model, we detected changes in anatomy and structural organization of xylem vessel cell walls (CWs) linked to stem twining in liana plants. UV microscopy, scanning electron microscopy and Fourier transform infrared (FTIR) microspectrometry were used. Different microfibrils orientation in vessel CWs of twisted compared to straight internodes, revealed by histological examination, coincide with the lower lignin content, the lower amount of xylan and cellulose, and the higher amount of xyloglucan, showed by FTIR. Xylem vessels resist high mechanical strain developed in twisted internodes by decreased CW rigidity (lower lignin content) and extensibility (higher xyloglucan content), and increased elasticity (lower xylan content).

INTRODUCTION

In liana plants anatomical and morphological adaptations to mechanical strain involve high flexibility of the stem tissue structures, achieved by structural changes in the cell walls (CWs) of different tissues: fibers, xylem (vessels and tracheids) and parenchyma [1].

Xylem vessels are elongated hollow cells subjected to high pressure of surrounding tissues resisted by their highly lignified walls to prevent cell collapse. This could be particularly relevant for herbaceous perennial lianas [2], such as *D. balcanica*.

We used UV microscopy, scanning electron microscopy (SEM) and Fourier transform infrared (FTIR) microspectrometry to analyze structural changes in vessel CWs of liana plant *D. balcanica* related to stem twining.

METHODS

Plant material: *Dioscorea balcanica* Košanin, family Dioscoreaceae, is an herbaceous monocotyledonous dioecious tuberous perennial liana, an endemic, endangered species and a Tertiary relict of Balkan Peninsula [3]. Stem cross sections (free-hand sectioning with a razor blade) of straight and twisted internodes (**Figure 1A**) were used.

Microscopy analysis: For SEM: dried free-hand stem sections were coated with gold, analyzed, and photographed with a TESCAN VEGA 3 SB at 20 kV (TESCAN, Brno, Czech Republic). For fluorescence microscopy (UV 358 nm - excited autofluorescence): unstained stem sections were mounted in glycerol, observed, and photographed by light-fluorescence Zeiss Axiovert microscope (Carl Zeiss GmbH, Gottingen, Germany).

Fourier transform infrared (FTIR) microspectrometry: An area of 50 μm x 50 μm in the vessel CWs was selected. Spectra were collected using a ThermoNicolet Nexus spectrometer (Madison, WI) with a Continuum microscope accessory; 20 spectra for each internode in transmission mode with 4 cm^{-1} resolution. Spectra were baselined and normalized [4]. The spectra of corresponding internodes from 2 plants were similar, so here we present the spectra of selected internodes.

Statistical analysis: Student's t-test for independent samples was used to determine the significance of the difference (at level 0.05) between average values for every individual wavenumber of the FTIR spectra, as described previously [5]. The obtained t-values (Y-axis) were plotted against the wavenumbers of the spectrum (X-axis).

RESULTS AND DISCUSSION

Using stem cross sections of *Dioscorea balcanica*, as a model, we detected changes in anatomy and structural organization in xylem vessel CWs linked to stem twining in liana plants. Our previous results obtained by light microscopy revealed no differences either in the structure or in lignification of, both, sclerenchyma or parenchyma cells between straight and twisted internodes. The difference was visible only by SEM, and FTIR microspectrometry [6]. Changes in parenchyma CW structure related to stem twining include: lower amount of xyloglucan and cellulose, and higher amount of xylan and lignin (with modified organization) [6].

In the present study, UV microscopy showed no difference in lignification of vessel CWs between straight and twisted internodes (**Figure 1C**, and **Figure 1E**), but SEM images indicate the difference in microfibrils orientation – vessel CWs in twisted internodes (tension side) showed cellulose microfibrils oriented almost parallel to the stem axis (**Figure 1B**), while in **Figure 1D**, in straight internodes cellulose microfibrils are oriented at very high microfibril angle to the stem axis.

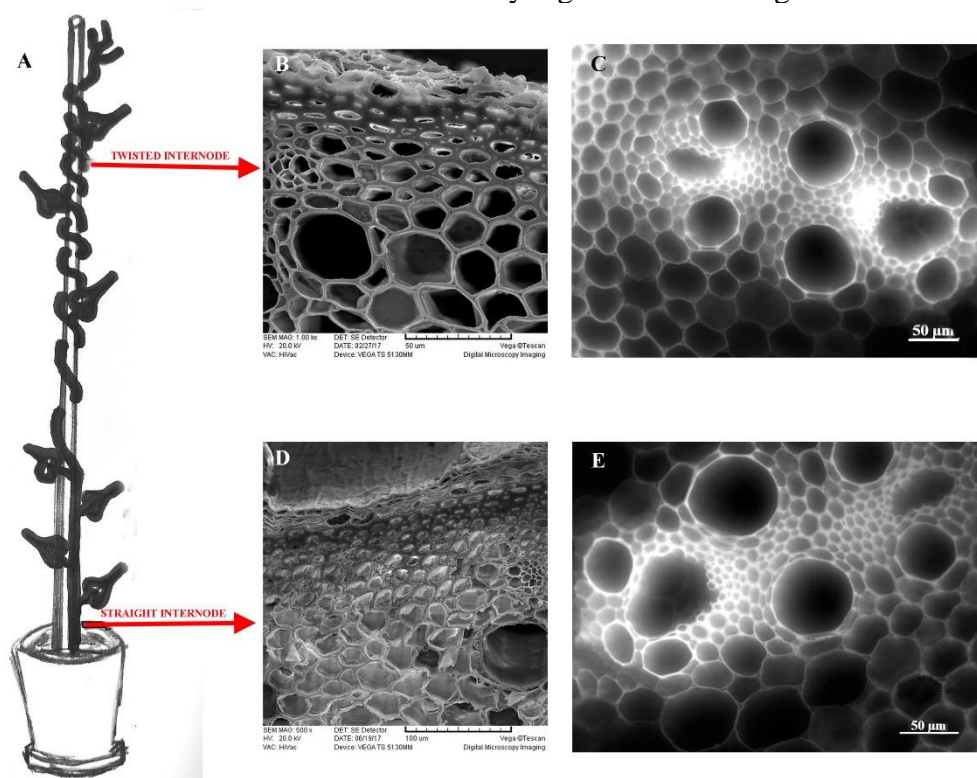


Figure 1. Scheme of experimental plant (A); SEM micrographs of twisted (B) and straight (D) internode; UV – excited autofluorescence of twisted (C) and straight (E) internode, n=8.

Figure 2 shows overlaid FTIR spectra of CWs of vessels of the straight and twisted internodes in the region 800–1800 cm^{-1} . The band at 896 cm^{-1} is characteristic for anomeric b-linkage of glucose in xyloglucan [7]. The region from 900 - 1100 cm^{-1} is specific for polysaccharides (xyloglucan). The interaction of cellulose fibrils and a matrix are mediated by changes in the amount of non-cellulosic polysaccharides and lignin [8]. Hemicelluloses interact with cellulose providing CW structural strength: xyloglucan binds to the surface of cellulose tethering cellulose microfibrils together [9]

controlling cell wall extensibility [10], while xylan and cellulose fibrils bonding affects CW elasticity [11].

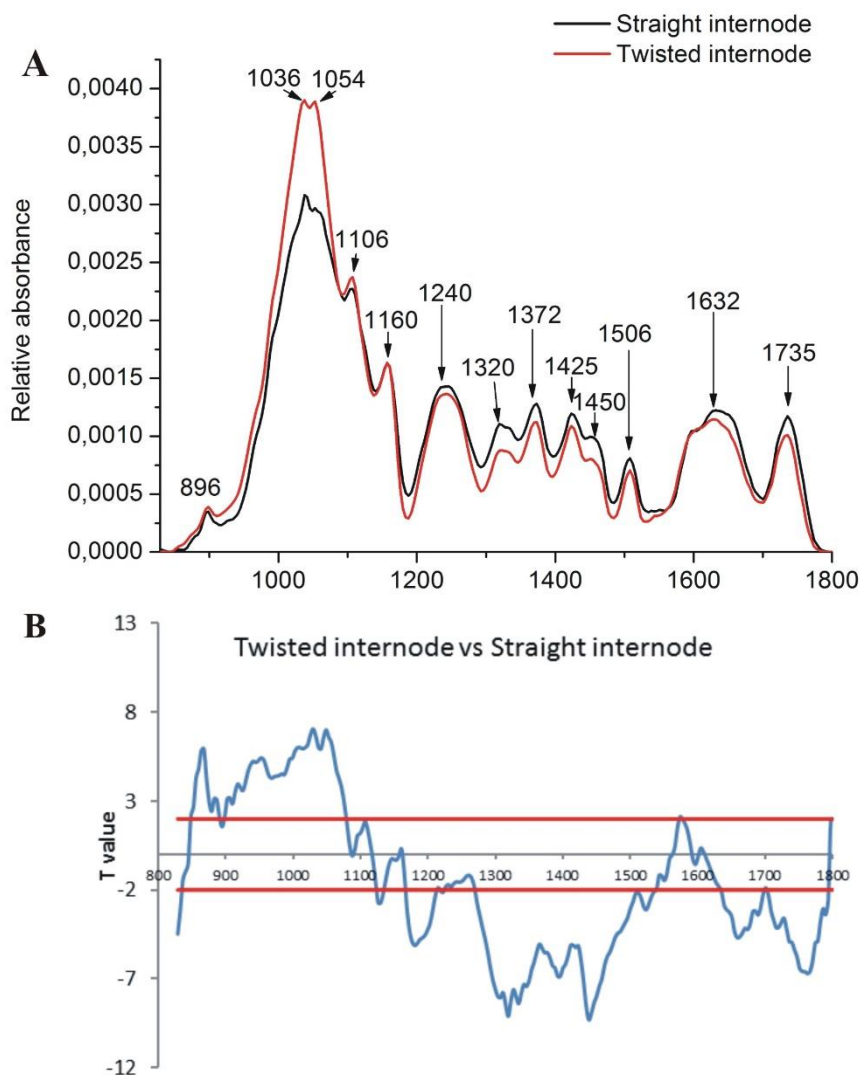


Figure 2. A) overlaid FTIR spectra of vessel CWs of straight and twisted internodes in the region 800–1800 cm^{-1} ; B) t test for twisted versus straight internodes (horizontal red lines— 5% significance threshold)

Four distinct vibration bands that were related to cellulose, viz. the antisymmetric C–O–C bridge stretching vibration at 1160 cm^{-1} , CH_2 wagging vibration at 1320 cm^{-1} , the C–H bending vibration at 1372 cm^{-1} and the C–OH bending vibration of the CH_2 –OH group at 1425 cm^{-1} were found [11–13]. The bands at 1240 cm^{-1} (the C–O stretching in the O=C–O group), 1451 cm^{-1} (CH_2 symmetric bending on the xylose ring) and 1735 cm^{-1} (carbonyl group vibration, the C=O stretching vibrations in the O=C–OH group of the glucuronic acid units) are characteristic for xylan [12–14]. The bands at 1506 cm^{-1} (aromatic skeletal vibrations) and 1596 cm^{-1} (C=C aromatic ring vibrations plus C=O stretch) are characteristic for guaiacyl and syringyl lignin [15, 16]. The 1632 cm^{-1} band is characteristic of C=bond in the lignin monomer side chain [17, 18].

T test (**Figure 2B**, right y-axis, black line) was used for the evaluation of differences in the mean of absorbances at specific wavelengths between vessels of twisted versus straight internode. The amount of xylan (absorbances at 1735, 1451, 1240 cm^{-1}) and cellulose are higher in vessels CWs of

straight internodes (**Figure 2B**). Contrary, the amount of xyloglucan (from 900 to 1100 cm^{-1}) is higher in vessels CWs of twisted internodes (**Figure 2B**). Lignin content is lower (wavenumber at 1506 cm^{-1}) in vessel CWs of twisted internodes.

CONCLUSION

According to the results obtained by UV microscopy and SEM, as well as FTIR microspectroscopy, different cell types (xylem vessels, and parenchyma, as cells with different shape/structure/function ratio) developed different CW structural changes to support a twisting force and resist mechanical strain established in twisted internodes. Opposite to parenchyma cells, xylem vessels showed lower lignin, xylan and cellulose content, but higher xyloglucan content, resulting in decreased CW rigidity and extensibility but increased elasticity.

Acknowledgement

This work was supported by the Ministry for Science of the Republic of Serbia (Grants no. 451-03-9/2021-14/200053 and 451-03-9/2021-14/ 200178).

REFERENCES

- [1] S. Isnard, W. K. Silk, *American Journal of Botany*, 2009, **96**, 1205–1221.
- [2] S. Carlquist, *Aliso*, 1985, **11**, 139–157.
- [3] V. Pulević, *Glasnik Republičkog zavoda za Zaštitu Prirode. Prirodnjački Muzej u Titogradu*, 1973, **16**, 33–34 (in Serbian).
- [4] S. Robin, M. Lecomte, H. Höfte, G. Mouille, *J. Appl. Stat.*, 2003, **30**, 669–681.
- [5] G. Mouille, S. Robin, M. Lecomte, S. Pagant, H. Höfte, *Plant Journal*, 2003, **35**, 393–404.
- [6] J. Simonović Radosavljević, J. Bogdanović Pristov, A. Lj. Mitrović, G. Steinbach, G. Mouille, S. Tufegdžić, V. Maksimović, D. Mutavdžić, D. Janošević, M. Vuković, G. Garab, K. Radotić, *Cellulose*, 2017, **24**, 4653–4669.
- [7] M. Kačurakova, A. C. Smith, M. J. Gidley, R. H. Wilson, *Carbohydr. Res.*, 2002, **337**, 1145–1153.
- [8] L. A. Donaldson, J. P. Knox, 2012, *Plant Physiol.*, **158**, 642–653.
- [9] C. Somerville, S. Bauer, G. Brininstool, M. Facette, T. Hamann, J. Milne, E. Osborne, A. Paredez, S. Persson, T. Raab, 2004, *Science*, **306**, 2206–2211.
- [10] J. S. Kim, G. Daniel, 2012, *Planta*, **236**, 35–50.
- [11] D. J. Cosgrove, M. C. Jarvis, 2012, *Front. Plant. Sci.*, **3**, 204.
- [12] C. Y. Liang, K. H. Basset, E. A. McGinnes, R. H. Marchessault, *Tappi*, 1960, **43**, 232–235.
- [13] R. H. Marchessault, *Pure Appl. Chem.*, 1962, **5**, 107–129.
- [14] M. Akerholm, L. Salmen, *Polymer*, 2001, **42**, 963–969.
- [15] R. H. Atalla, U. P. Agarwal, *Science*, 1985, **227**, 636–638.
- [16] O. Faix, *Holzforschung*, 1991, **45**, 21–27.
- [17] E. Pretsch, J. Seibl, W. Simon, *Tabellen zur strukturaufklärung organischer verbindungen mit spektroskopischen methoden*. Springer Verlag, Berlin Heidelberg, 1982.
- [18] K. Radotić, S. Todorović, J. Zakrzewska, M. Jeremić, *Photochem. Photobiol.*, 1998, **68**, 703–709.

INVESTIGATION OF THE SCAVENGING POTENCY OF SELECTED NEUROTRANSMITTERS AND THEIR METABOLITES TOWARDS IMIDAZOLYL RADICALS

A. Lončar, L. Negrojević, D. Dimić and J. Dimitrić Marković

Faculty of Physical Chemistry, University of Belgrade, Studentski trg 12-16, 11000 Belgrade, Serbia. (ddimic@ffh.bg.ac.rs)

ABSTRACT

The antiradical potency of several neurotransmitters and their metabolites – dopamine, 3,4-dihydroxyphenylacetic acid (DOPAC), catechol, 3-metoxytyramine (3-MT), and homovanillic acid (HVA), with water as a solvent, towards substituted imidazole radicals, was investigated according to three most common mechanisms. By calculating the enthalpy of reaction for each suggested mechanism, using thermodynamic parameters obtained through DFT simulations, the preferred reaction mechanism was determined for each molecule.

INTRODUCTION

The modern lifestyle exposes us to pollutants and radiation more than ever. These factors contribute to the overproduction of extremely reactive radicals in our bodies. The harmful effect of radicals on biological systems is considered to be one of the main causes of aging. The development of various neurodegenerative disorders may also be caused by radicals. While this may sound grim, the detrimental effects of radical species can be relieved to some degree, with the help of antioxidants [1].

Besides regulating neurological processes within the nervous system, neurotransmitters contribute to its antioxidant protection. This fact makes research into the mechanisms of their antioxidant activity appealing. The structures of the chosen neurotransmitters are shown in Figure 1.

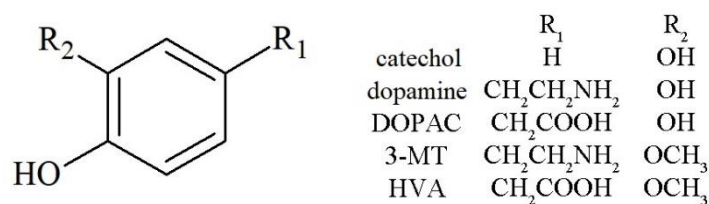


Figure 1 - Structures of the investigated antioxidants.

The imidazole moiety is an important part of numerous compounds that play a vital role in biological systems. It makes up molecules that play a significant role in the allergic response. Also, it is an essential part of nucleic acids, as it is the key part of purine nitrogen bases. The structures of the imidazole-based radicals that were examined are shown in Figure 2.

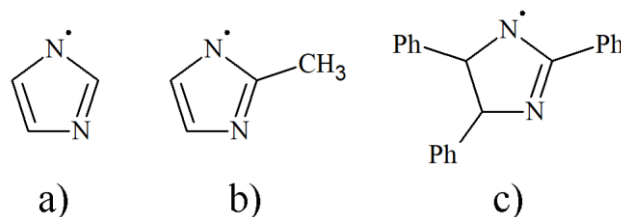


Figure 2 – Structures of a) 1-imidazolyl, b) methyl-1-imidazolyl, c) 2,4,5-triphenyl-1-imidazolyl radicals

METHODS

All of the starting molecules (ArOH, RNH), radicals (ArO·, RN·), cation radicals (ArOH⁺·), and anions (R⁻, ArO⁻) were optimized using Gaussian09 Program Package [2]. The selected method was DFT, with the M06-2X [3] functional and 6-311G++(d,p) basis set. Solvation was also taken into account, using the CPCM solvation model for water.

There are several mechanisms by which antioxidant reactions most commonly occur [1], one of which is based on the Hydrogen Atom Transfer (HAT) to the radical, thus stabilizing it. The second mechanism is the Single Electron Transfer followed by Proton Transfer (SET-PT), where the antioxidant transfers the electron to the radical in the first step, after which the proton is transferred from the cation-radical form of the antioxidant to the anion of the radical in the second. The last mechanism considered in this contribution is the Sequential Proton Loss Electron Transfer (SPLET), where the antioxidant releases a proton in the first reaction and then reacts with the radical, creating a stable anion of the radical in the second.

The enthalpies associated with the respective reaction steps (ΔH_{BDE} , ΔH_{IP} , ΔH_{PDE} , ΔH_{PA} , ΔH_{EDE}) were calculated by subtracting the standard enthalpies of the compounds participating in the reactions [1].

RESULTS AND DISCUSSION

Enthalpies obtained from Gaussian optimization are shown in Table 1.

Thermodynamic calculations showed that the most probable mechanism for R2 and R3 was HAT, while the most probable mechanism for R1 was SPLET. The values for ΔH_{IP} were higher than the respective values for ΔH_{BDE} and ΔH_{PA} , therefore this is not a plausible mechanism in water.

R1 was the most reactive radical ($\Delta H_{PA} = -207 \text{ kJ mol}^{-1}$ for R1 reaction with DOPAC), and it had no additional bonded groups. The exchange of proton in the first step is expected because of the electronegative nitrogen atom. On the other hand, R2 and R3 were stabilized thanks to the positive inductive effect present in the molecules (owing to the fact that additional groups were bonded onto the primary imidazole ring), delocalizing the electrons in the structure, thus making it less reactive ($\Delta H_{BDE} = -65 \text{ kJ mol}^{-1}$ for R2 and $\Delta H_{BDE} = -24 \text{ kJ mol}^{-1}$ for R3 for reaction with DOPAC). The hydrogen atom transfer can be explained by the spin delocalization throughout radicals.

Table 1. Thermodynamic parameters of the reaction between investigated molecules and radical species (in kJ mol⁻¹)

Neurotransmitter	Radical	HAT		SET-PT		SPLET	
		ΔH_{BDE}	ΔH_{IP}	ΔH_{PDE}	ΔH_{PA}	ΔH_{ETE}	
Catechol	R1	-15	349	-364	-205	190	
	R2	-62	131	-193	-34	-28	
	R3	-21	138	-160	-1	-21	
Dopamine	R1	-22	336	-358	-202	181	
	R2	-69	118	-187	-31	-37	
	R3	-28	126	-154	2	-30	
DOPAC	R1	-18	345	-363	-207	189	
	R2	-65	127	-192	-36	-29	
	R3	-24	135	-159	-2	-21	
HVA	R1	-2	338	-339	-177	176	
	R2	-48	120	-168	-6	-42	
	R3	-7	127	-135	27	-35	
3-MT	R1	-6	328	-334	-173	167	
	R2	-53	110	-163	-2	-51	
	R3	-12	118	-130	32	-44	

When considering the structures of the examined antioxidants, dopamine, DOPAC and catechol produced the most stable anions and radicals after the reaction with imidazolyl radicals, with $\Delta H_{PA,R1}$ being around -200 kJ/mol⁻¹, for example. These molecules are characterized by the strong hydrogen bond between protonated and deprotonated aromatic OH groups in formed radicals/anions. When the reaction enthalpies for these three molecules are compared it is clear that the aliphatic chain groups do not influence the calculated values significantly. These groups would have important effect in case of various protonation/deprotonation equilibria, as they are the source of hydrogen atoms that could be exchanged [1]. Once the OH group was changed by OCH₃ group, the enthalpies of reactions were lowered. In reaction with R1 the enthalpies of reaction for 3-MT and HVA were -334 kJ and -339 kJ mol⁻¹, respectively. The reaction enthalpies for these two metabolites according to the HAT mechanism for reactions with R2 and R3 were reduced for 10 kJ mol⁻¹ when compared with three others molecules with catechol moiety. This is a consequence of a weak hydrogen bond formed between oxygen atom and OCH₃ group. The same trend in values for parameters was observed for dopamine/3-MT and DOPAC/HVA pairs.

CONCLUSION

The antioxidative activity of several neurotransmitters and their metabolites (dopamine, catechol, DOPAC, HVA, and 3-MT) towards N-centered imidazole radicals was investigated. Most of the examined reactions were exothermic and spontaneous, thus proving possible antiradical activity, which is very dependent on the structure of the interacting radical. Knowing that the mechanism with the lowest enthalpy is the most likely one, the most probable mechanisms were deduced for radicals: 1-imidazolyl – SPLET, 2-methyl-1-imidazolyl and 2,4,5-triphenyl-1-imidazolyl (R3) – HAT. The least reactive radical was R3, having the least negative enthalpy, while the most reactive one was R1. The importance of intramolecular hydrogen bond is also proven for the reactivity of investigated species.

Acknowledgment

The authors acknowledge the Ministry of Education, Science and Technological Development of the Republic of Serbia for the financial support (Agreement No. 451-03-9/2021-14/200146 and 451-03-9/2021-14/200378)

REFERENCES

- [1] D. Dimić, D. Milenković, J. Dimitrić Marković and Z. Marković, *Physical Chemistry Chemical Physics* 19, 2017, 12970–12980.
- [2] Y. Zhao, D.G. Truhlar, *Theoretical Chemistry Accounts* 120, 2008, 215–241.
- [3] M.J. Frisch et al., *Gaussian 09, Revision C.01* (Gaussian, Inc., Wallingford, CT, 2009).

FLAXSEED OIL PREVENTS TRIMETHYLTIN-INDUCED UP-REGULATION OF ECTONUCLEOTIDASES ACTIVITIES IN THE RAT HIPPOCAMPUS

N. Mitrović¹, M. Dragić², M. Zarić¹, J. Martinović¹ and I. Grković¹

¹ *Department of Molecular Biology and Endocrinology, VINČA Institute of Nuclear Sciences-National Institute of the Republic of Serbia, University of Belgrade, Belgrade, Serbia*

² *Department for General Physiology and Biophysics, Faculty of Biology, University of Belgrade, Belgrade, Serbia*

ABSTRACT

This study aimed to investigate the effects of trimethyltin (TMT)-induced hippocampal neurodegeneration and the beneficial effects of flaxseed oil (FSO) consumption on ectonucleotidase activities in the hippocampus of female rats. Animals were pretreated with FSO (1 ml/kg, orally) for two weeks then received a single dose of TMT (8 mg/kg, i.p.), and application of FSO continued for twenty-one days. Data have shown that FSO prevented TMT-induced up-regulation of ATP/ADP hydrolysis rates, while AMP hydrolysis remained unchanged in all examined groups. These findings support beneficial neuroprotective properties of FSO against TMT-induced neurotoxicity and hint at a promising preventive use of FSO in hippocampal degeneration and dysfunction.

INTRODUCTION

Trimethyltin (TMT) is an organotin neurotoxicant that selectively targets the limbic region, particularly the hippocampus, and induces selective and progressive hippocampal neurodegeneration and gliosis, representing a useful tool to recapitulate critical features of most common neurodegenerative disorders such as Alzheimer disease (AD) or temporal lobe epilepsy [3].

In response to central nervous system (CNS) injury, injured cells massively release adenosine-5'-triphosphate (ATP) into the extracellular space, where it acts as a "danger signal" and activates specific ligand-gated P2X channels and G-protein coupled P2Y receptors, promoting microglial chemotaxis and phagocytosis as well as release of pro-inflammatory cytokines [1]. The levels of ATP in the extracellular space are tightly controlled by ecto-nucleoside triphosphate diphosphohydrolases (NTPDases)/ecto-5'-nucleotidase (eN) enzyme chain [2]. Three distinct membrane-bound NTPDases (NTPDase1-3) are expressed in CNS and hydrolyze ATP/ADP to AMP. AMP is a substrate for extracellular ATP degradation's final and rate-limiting step, catalyzed by eN, thus producing extracellular adenosine [2]. NTPDase/eN enzymes act together as an immune checkpoint since they degrade pro-inflammatory ATP and generate anti-inflammatory adenosine, thus determining the inflammatory state of the tissue [1]. Accordingly, NTPDase/eN enzyme chain might be a promising target for controlling the progression of neurodegenerative diseases.

Since their broad spectrum of pharmacological and biological activities, natural products such as flaxseed oil (FSO) may be promising alternatives for the prevention/amelioration of neurodegenerative diseases [5]. Thus, the present study aimed to evaluate the potential changes in ectonucleotidase activities after TMT intoxication. Also, we evaluated whether pretreatment with flaxseed oil (FSO) as an anti-inflammatory compound might prevent these potential changes.

METHODS

Animals. All experiments were conducted on 10-week-old female intact female Wistar rats (200–220 g) following the European Community Council Directive of 86/609/EEC and 010/63/EU for

animal experiment. The authorized Ethical Committee approved research procedures. Animals were housed (3–4/cage) under standard conditions.

Experimental groups and treatments. A total of 20 female rats were randomly divided into the following groups (5 rats per group): **INT**- without any treatment; **FSO**- received FSO (Granum®, 1 ml/kg, orally) for 5 weeks; **TMT**- received a single dose of TMT (8 mg/kg, i.p.) and **FSO+TMT**- pretreated with FSO for two weeks and then received a single dose of TMT and application of FSO continued for twenty one more days. All animals were decapitated by a small animal guillotine (Harvard apparatus) 24 h after the last injection, and brains were isolated.

Preparation of crude membrane fraction. Individual hippocampi were dissected for immediate preparation of crude membrane fraction as previously described [4]. The protein content was determined using bovine serum albumin (BSA) as a standard.

Functional ectonucleotidase assays. The NTPDase and eN activities were evaluated by measuring the formation of inorganic phosphate upon addition of ATP, ADP, or AMP to hippocampal crude membrane preparations. Briefly, an aliquot containing 10 µg of total proteins was resuspended in assay buffer; preincubated for 10 min at 37 °C; and incubated with the 1 mM ATP, 1 mM ADP for 10 min, or 1 mM AMP for 30 min, at 37 °C. The level of inorganic phosphates liberated by enzyme actions was determined by the Malachite green method [4]. All samples were run in triplicate, and each sample was expressed as mean ± SEM (in nmol Pi/mg protein/min).

Data analysis. Data were analyzed with a two-way ANOVA followed by Tukey's multiple-comparison post hoc test using Origin 8.0 software package. The values of $p < 0.05$ or less were considered statistically significant.

RESULTS AND DISCUSSION

For ATP/ADP hydrolysis significant effects of TMT, FSO treatment and the interaction were obtained: ATP- the effect of TMT ($F_{1,16} = 57.88$; $P < 0.0001$), FSO treatment ($F_{1,16} = 22.08$; $P = 0.0002$) and the interaction ($F_{1,16} = 14.05$; $P = 0.0018$); ADP- the effect of TMT ($F_{1,16} = 19.91$; $P = 0.0004$), FSO treatment ($F_{1,16} = 9.768$; $P = 0.0065$) and the interaction ($F_{1,16} = 16.35$; $P = 0.0009$). FSO alone did not produced any significant effect on ATP/ADP/AMP hydrolysis rates, thus the effect of TMT was compared to INT group. Post hoc analyses showed that TMT induced significant up-regulation of ATP (249.58 ± 7.68 nmol Pi/mg/min) and ADP hydrolysis levels (128.45 ± 9.88) ($p < 0.001$) compared to controls (135.08 ± 10.11 nmol Pi/mg/min for ATP and 46.74 ± 3.32 nmol Pi/mg/min for ADP). Treatment of TMT animals with FSO significantly decreased relative ATP/ADP hydrolysis levels (176.27 ± 7.44 nmol Pi/mg/min for ATP and 59.50 ± 4.92 nmol Pi/mg/min for ADP) ($p < 0.001$) compared to TMT. Examined treatments did not alter AMP hydrolysis rates (Specific eN activities for experimental groups are as follow: INT- 55.88 ± 3.39 nmol Pi/mg/min; FSO- 56.22 ± 3.35 nmol Pi/mg/min; TMT- 56.50 ± 2.60 nmol Pi/mg/min; FSO+TMT- 59.97 ± 4.41 nmol Pi/mg/min).

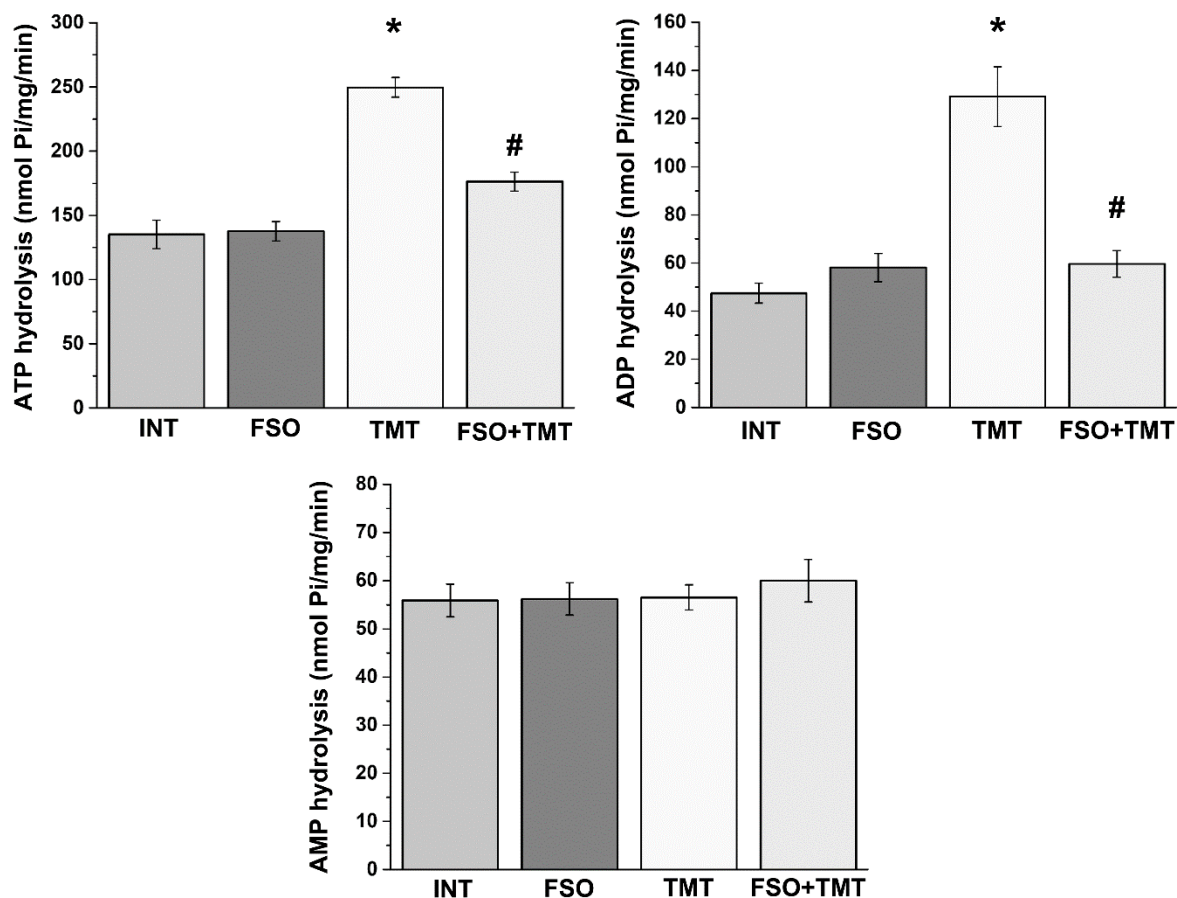


Figure 1. Specific ectonucleotidase activity in the presence of ATP, ADP, and AMP. Significance level: * $p < 0.001$ in respect to INT; # $p < 0.001$ in respect to TMT.

In response to various neurodegenerative disorders, a large amount of extracellular ATP, released from injured neurons and activated glial cells, acts as a “danger signal” and activates specific P2 receptors, promoting microglial chemotaxis [1]. Enhanced activity of NTPDases may represent a defense mechanism against excess levels of extracellular ATP, thereby preventing P2 receptor desensitization and hyperactivation of microglia from overstimulation by ATP [1]. Pretreatment with FSO prevented TMT-induced increase in ATP/ADP hydrolysis rates probably by preventing neuronal injury [5] and consequent massive release of ATP.

CONCLUSION

The current findings indicate that administration of FSO may have anti-inflammatory potential by preventing cell death and thus alterations of ectonucleotidases activities and consequent development of neurodegenerative disorders.

Acknowledgment

This work was supported by the Ministry of Education, Science and Technological Development, Republic of Serbia, Contract No. 451-03-1/2021-16/14 – 0902102.

REFERENCES

- [1] S.C. Robson, J. Sévigny, H. Zimmermann, *Purinergic Signal.*, 2006, 2, 409–430.
- [2] H. Zimmermann, M. Zebisch, N. Sträter, *Purinergic Signal.*, 2012, 8, 437–502.

-
- [3] E. Pompili, C. Fabrizi, L. Fumagalli, F. Fornai, *J. Neural Transm.*, 2020, 127, 987–998.
- [4] N. Mitrović, I. Guševac, D. Drakulić, M. Stanojlović, J. Zatković, J. Sevigny, A. Horvat, N. Nedeljković, I. Grković, *Gen. Comp. Endocrinol.* 2016, 1, 100–107.
- [5] N. Mitrović, M. Dragić, M. Zarić, N. Nedeljković, I. Grković, No Title, *Metab. Brain Dis.* (2021). doi:10.21203/rs.3.rs-277617/v1.

ORAL D-GALACTOSE INTAKE PROVOKES REGION-SPECIFIC CHANGES OF GLUTAMATERGIC SIGNALING COMPONENTS IN THE BRAIN OF ADULT MALE WISTAR RAT

J. Martinović, M. Zarić, I. Gusevac Stojanović, N. Mitrović, I. Grković, and D. Drakulić

*University of Belgrade, Vinča Institute of Nuclear Science -National Institute of the Republic of Serbia, Mike Petrovića Alasa 12-14, 11000 Belgrade, Republic of Serbia.
(jelenazlatkovic@vin.bg.ac.rs)*

ABSTRACT

Extended lifespan highlights brain aging as an emerging worldwide problem. D-galactose (d-gal) is broadly used in animal aging studies as its chronic administration mimics aging-associated alterations, such as cognitive impairment in humans. This age-related cognitive impairment may be associated with alteration in synaptic structure and function, including changes in the glutamatergic system. Hence, we examined the effects of 6-weeks oral d-gal intake (200 mg/kg and 500 mg/kg) on protein expression of components involved in glutamatergic signaling in the prefrontal cortex (PFC) and hippocampus (HIP) of adult male Wistar rats. Decreased levels of vesicular glutamate transporter 1 (vGlut1) and NMDAR 2B subunit (NR2B) and a downward trend of postsynaptic density protein 95 (PSD-95) were observed solely in the PFC. Investigated components in the HIP were only slightly modified. These findings suggest the need for further research regarding region-specific glutamate involvement in age-related changes.

INTRODUCTION

Age-related cognitive impairments might be associated with alterations in synaptic structure and function, including changes in the glutamatergic system. Proteins involved in glutamate exocytosis, such as vesicular glutamate transporter 1 (vGlut1), refills synaptic vesicles with glutamate for a new round of exocytosis a critical role as they determine levels of this neurotransmitter in the synaptic cleft. Precisely, reduced vGlut1 has been highly correlated with the degree of cognitive impairment in humans [1]. The postsynaptic membrane receives glutamate signals and transfers them into the postsynaptic cell. Comprised of a high concentration of receptors and joint cytoskeletal and signaling proteins, the postsynaptic specialization is visible as a thickening of the postsynaptic membrane known as the postsynaptic density (PSD). N-methyl-D-aspartate subtype of glutamate receptor (NMDAR) is an abundant constituent of the PSD. NMDARs are anchored in the PSD by protein-protein interactions between the cytoplasmic C-terminal tails of their NR2 subunits and the PDZ domains of PSD-95. This abundant PSD protein forms a two-dimensional lattice immediately under the postsynaptic membrane. Hence, PSD-95 plays a role in the precise assembly and spatial organization of NMDAR and coupling these receptors to downstream signaling events [2].

NMDAR, a glutamate receptor essential for maintaining numerous neurological functions in both physiological and pathophysiological conditions, is in native conformation tetramer made of NR1 subunits with at least one type of NR2 subunit. Aging seems to affect everything from the number and functionality of NMDAR to the expression of its subunits and their composition within various brain regions. NR2B subunit is mainly affected by the aging process, showing greater mRNA and protein expression declines than NR1 or NR2A subunits across cortical and hippocampal regions [3].

D-galactose (d-gal) is widely exploited in animal aging studies since its chronic administration mimics age-related learning and memory impairments in humans [4]. To our knowledge, no research was focused on the NMDA receptor system in the synaptic compartment following chronic oral d-

gal treatment. Hence, we aimed to determine the effects of 6 weeks oral d-gal intake on protein expression of components included in glutamatergic signaling in a crude synaptosomal fraction (P2) of the PFC and HIP of adult males Wistar rats.

METHODS

All experimental procedures complied with the Ethical Committee for the Use of Laboratory Animals of Vinča Institute of Nuclear Science - National Institute of the Republic of Serbia, University of Belgrade (protocol number 02/11) and European Communities Council Directive (2010/63/EU) guidelines. For the 6 weeks-lasting experiments, rats were randomly assigned to three groups: control animals (Con) and rats receiving either 200 mg/kg (200 mg/kg) or 500 mg/kg d-gal (500 mg/kg). D-gal was dissolved in tap water, and target concentration was adjusted according to rats' d-gal dose and body weight. Control animals drank pure tap water. After decapitation with a guillotine (Harvard Apparatus, Holliston, MA, USA), brains were removed, and PFC and HIP were dissected for preparation of P2 fraction using the previously described method [5]. After determining protein concentration using the modified method of Lowry [6], Western blot analysis was performed. Samples were loaded onto 10 % SDS polyacrylamide gel, and electrophoresis was carried out using a mini protein system (Bio-Rad Laboratories, Inc., USA). The proteins were electrophoretically transferred onto PVDF membranes (Imobilon-P membrane, Millipore, USA), blocked for 1h with 5 % BSA in TBST (50 mM Tris-HCl, pH 7.4, 150 mM NaCl, 0.1 % Tween 20), and incubated with primary and secondary antibodies (**Table 1**).

Table 1. List of primary and secondary antibodies used for Western blot analysis

Antigen	Manufacturer and Catalog No	Species
PSD 95	MAB1598, Merck Millipore Corporation, USA	mouse monoclonal
NR2B	ab93610, Abcam, UK	mouse monoclonal
vGlut1	ab134283, Abcam, UK	mouse monoclonal
β -actin	sc-1615, Santa Cruz Biotechnology Inc., USA	goat polyclonal
mouse IgG	sc-2318, Santa Cruz Biotechnology Inc., USA	donkey
goat IgG	sc-2033, Santa Cruz Biotechnology Inc., USA	donkey

Following incubation with antibodies, an enhanced chemiluminescence (ECL) system (Immobilon Western Chemiluminescent HRP Substrate, Millipore, USA) was poured on the membranes. Immunoreactive bands were detected on X-ray films in the dark chamber. β -actin as quantified and used as a loading control. The signal intensity was evaluated using the Image J software package, and results were expressed relative to the control value (set as 100%).

All data were expressed as means \pm S.E.M. Results were analyzed using One-way ANOVA followed by a posthoc Tukey's test. $p < 0.05$ was defined as statistically significant.

RESULTS AND DISCUSSION

In the HIP, a significant effect of d-gal treatment was detected only on vGlut1 protein level ($F = 3.835$, $p < 0.05$), and *post-hoc* analysis revealed a significantly lower vGlut1 level in 500 mg/kg compared to the 200 mg/kg ($p < 0.05$). In the PFC, One-way ANOVA revealed a significant effect of d-gal treatment on vGlut1 ($F = 5.823$, $p < 0.01$) and NR2B protein level ($F = 18.29$, $p < 0.001$), while *post-hoc* test showed a statistically significant decrease of vGlut1 ($p < 0.05$) and NR2B ($p < 0.01$, $p < 0.001$, respectively) in both treated groups compared to Con. D-gal treatment did not affect the PSD-95 protein level in the PFC and HIP (**Figure 1**).

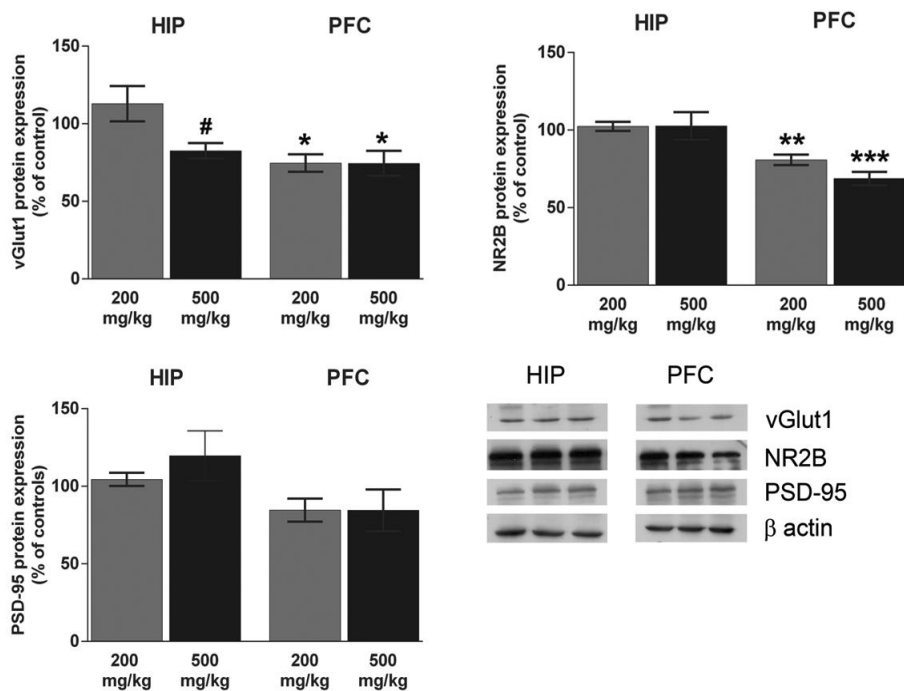


Figure 1. Effect of D-galactose treatment applied in two doses (200 mg/kg and 500 mg/kg) on components of glutamatergic signaling in the hippocampus (HIP) and prefrontal cortex (PFC). Data are presented as the mean \pm SEM, and the values of the control group were set as 100 %. * symbols indicate significant difference control vs. d-gal groups (* $p < 0.05$, ** $p < 0.01$, *** $p < 0.001$) while # represents the difference between two d-gal groups (# $p < 0.05$).

Detected region-specific changes of vGlut1 and NR2B proteins suggest compromised glutamatergic synapses homeostasis in the PFC but not in the HIP. Herein reported a decreased level of vGlut1 in the PFC indicates jeopardized glutamate import into synaptic vesicles, resulting in diminished glutamate content in the synaptic cleft. Our findings are similar to those published by Dawson and co-workers who reported a functionally intact glutamate pool in the frontal cortex but age-dependent changes in presynaptic modulation of glutamate release [1]. Furthermore, the literature emphasizes that the most consistent age-related change in the glutamatergic system is the loss of glutamate receptors [7]. The observed decrease of NR2B subunit in the PFC indicate region-specific NMDAR modulation. Indeed, studies suggest that the NMDA receptors in the cerebral cortex are more vulnerable to aging changes than those in the hippocampus [3].

Interestingly, the protein level of PSD-95 stayed unaltered regardless of group and brain region. Considering that PSD-95 may be crucial for the synapse interaction with downstream signaling, its preserved level may prevent further propagation of the potential detrimental signal. Still, the exact effect will be determined in future research.

CONCLUSION

To our knowledge, we are the first to report changes in the expression of synapse-located proteins in rats following chronic oral d-gal treatment. Our results represent valuable data guiding us into further research on region-specific modulation of NMDA receptors in the aging brain.

Acknowledgment

This work was supported by the Ministry of Education, Science and Technological Development of the Republic of Serbia (grant no 451-03-9/2021-14/200017-0902102).

REFERENCES

- [1] R. Dawson Jr., D.R. Wallace, M.J. Meldrum, *Neurobiol. Aging.*, 1989, **10**(6), 665-668.
- [2] M.V. Doucet, A. Harkin, K.K. Dev, *Pharmacol Ther.*, 2012, **133**(2):218-229.
- [3] K.R. Magnusson, B.L. Brim, S.R. Das, *Front. Aging Neurosci.*, 2010, **2**, 11.
- [4] S. Sadigh-Eteghad, A. Majdi, S. K. McCann, J. Mahmoudi, M.S. Vafaei, M.R. Macleod, *PLoS One*, 2017, **12**, e0184122.
- [5] M. Stanojlovic, A. Horvat, I. Gusevac, I. Grkovic, N. Mitrovic, I. Buzadzic, D. Drakulic, *Folia Biol. (Praha)*, 2014, **60**, 123-132.
- [6] M.A. Markwell, S.M. Haas, L.L. Bieber, N.E. Tolbert, *Anal. Biochem.*, 1978, **87**, 206-210.
- [7] T.P. Wong, *MJM*, 2002, **6**, 104-114.

INVESTIGATION OF STRUCTURAL AND CONFORMATIONAL CHANGES IN Na/K-ATPase INDUCED BY DECAVANADATE

B. P. Bondžić¹, Z. Džambaski¹, T. Parac Vogt², A. M. Bondžić³

¹ *Institute of Chemistry, Technology and Metallurgy, University of Belgrade, Njegoševa 12, 11000 Belgrade, Serbia*

² *Department of Chemistry, KU Leuven, Celestijnenlaan 200F, Leuven, Belgium*

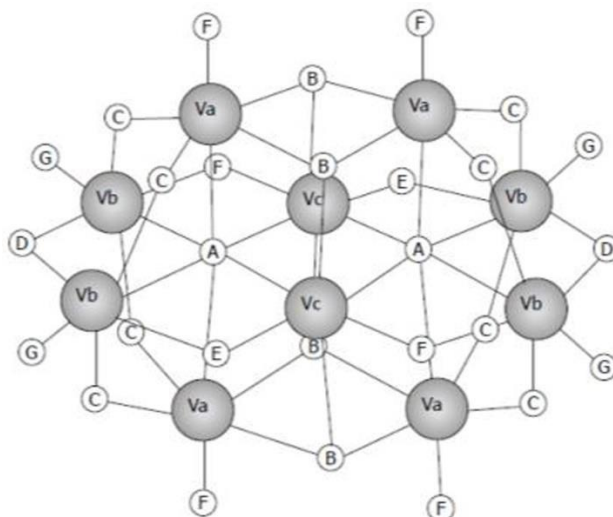
³ *Vinča Institute of Nuclear Sciences, National Institute of the Republic of Serbia, University of Belgrade, P.O. Box 522, 11000 Belgrade, Serbia (aleksandrab@vin.bg.ac.rs)*

ABSTRACT

The decavanadate compounds (V10) have strong anticancer activity that is not yet fully understood. However, the cell proliferation seems to impact P-type ATPases. In this paper insights into structural and conformational changes of Na/K-ATPase induced by decavanadate were obtained using CD and 51V NMR spectroscopy. The CD measurements indicated the changes in α helix content and increase in disordered after addition of increasing concentration of decavanadate. 51V NMR spectra indicated the interaction of the enzyme with a specific vanadate species. The changes of the correspondent vanadate NMR signals were reflected in the broadening of the observed V10 NMR signals and changing of ratio of characteristic peaks. New peak was observed in 51V NMR spectra and was ascribed as vanadate–sucrose complex.

INTRODUCTION

Polyoxometalates (POMs) are attracting considerable attention due to their unique structural characteristics and chemical properties. The research on anticancer properties of POMs is an active area of study, due to the number of papers that reported promising anti-tumor activities of POMs. Vanadium is a trace element widely distributed in plants and animals although its essential role for humans is yet to be clarified. After discovery that the "muscle inhibitor factor" isolated from horse muscle containing ATP and responsible for Na/K-ATPase inhibition was, in fact, vanadate, vanadium's impact in biology, pharmacology and medicine was rapidly increased [1]. Na/K-ATPase is a transmembrane protein which regulates many cellular functions, including those associated with tumor cell growth. The alterations in overall Na/K-ATPase activity and relative subunit abundance were observed in carcinoma cell lines obtained from a variety of tissues. Recent studies demonstrated the modulation of Na/K-ATPase activity induced by some POM compounds, suggesting their potential anticancer activity [2]. However, mechanism of the POMs action and the induced structural and conformational changes of the enzymes have not been yet elucidated. The aim of this study was to obtain molecular insight into structural and conformational changes of Na/K-ATPase induced by decameric vanadate species $(\text{NH}_4)_6\text{V}_{10}\text{O}_{28}\times 5\text{H}_2\text{O}$ (Scheme 1). The influence on the secondary and tertiary structure of Na/K-ATPase was investigated by Circular Dichroism (CD) and 51V Nuclear Magnetic Resonance (NMR).



Scheme 1. The structure of V_{10} ($V_{10}O_{28}^{6-}$). V_a , V_b and V_c represent the three different types of vanadium atoms described in the text.

EXPERIMENTAL

Chemicals. Na/K-ATPase from the porcine brain cortex, NaCl, KCl, $MgCl_2$, HCl, and Tris-HCl were purchased from Sigma-Aldrich (Germany). The stock solutions of decavanadate were prepared in accordance with previously published procedure [2].

Apparatus. CD spectra were recorded with a Jasco 1500 spectrophotopolarimeter equipped with a Peltier thermostatic system under constant nitrogen flux at 37 °C and with a 0.1cm quartz cuvette. 51V NMR measurements were performed on Bruker Avance II+ at 600 MHz.

RESULTS AND DISCUSSION

The circular dichroism spectra of Na/K-ATPase in the presence of increasing concentration of sodium decavanadate show a negative maximum at 225nm and positive maxima in region below 200nm. Additionally, the one isosbestic point at 204nm was observed (Figure 1). Hence, from circular dichroism spectra we can conclude that adding V10 induce significant changes in secondary and tertiary structure of enzyme. With increasing concentration of V10, CD signals at 225nm and below 200nm are decreasing. These changes are primarily indicative of changes in α helix whereas changes in peak below 200 nm reflect both, decrease in α helix content and increase in disordered or "other" structure. The presence of only one isosbestic point is indicative of existence of a two transition states i.e. folded and unfolded state, without accumulation of significant stable intermediate form.

Decavanadate, with a formula of $V_{10}O_{28}^{6-}$, has a unique structure (Scheme 1). Using 51V NMR spectroscopy three different types of vanadium atoms could be distinguished, marked as V10a, V10b and V10c with ratio of 2 : 2 : 1 [3]. In addition, 51V NMR spectrum of decavanadate solution can contain several metavanadate species (VO_3^-), such as monomeric vanadate (V1, orthovanadate species (VO_4^{3-})), dimeric vanadate (V2), tetrameric vanadate (V4) and pentameric vanadate (V5) (Figure 2).

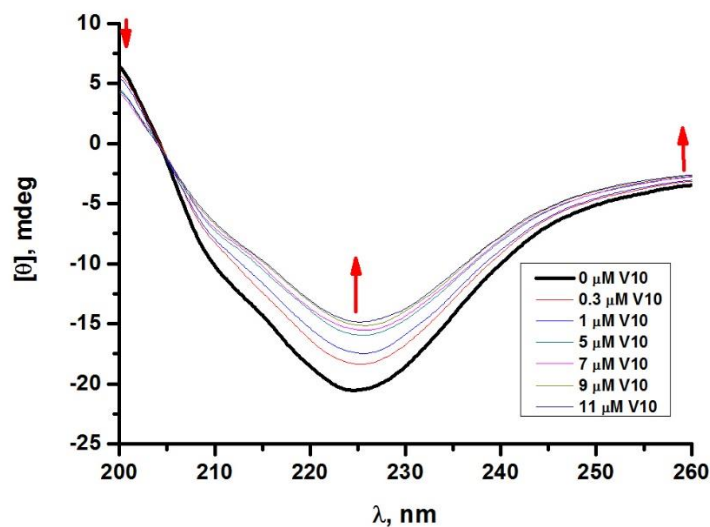


Figure 1. CD spectra of Na/K-ATPase in presence of increasing concentration of V10

In general, it was found that the interaction of the protein with a specific vanadate (V) species induced changes in the intensity and shape of the correspondent vanadate NMR signals. In the present study, broadening of the observed V10 NMR signals and changing of ratio of characteristic peaks showed that V10 interacts with the Na/K pump. In our NMR spectrum we can observe new peak marked as C as well. This NMR signals were ascribed to vanadate–sucrose complexes. Sucrose is the constituent of commercially available Na/K ATPase [4].

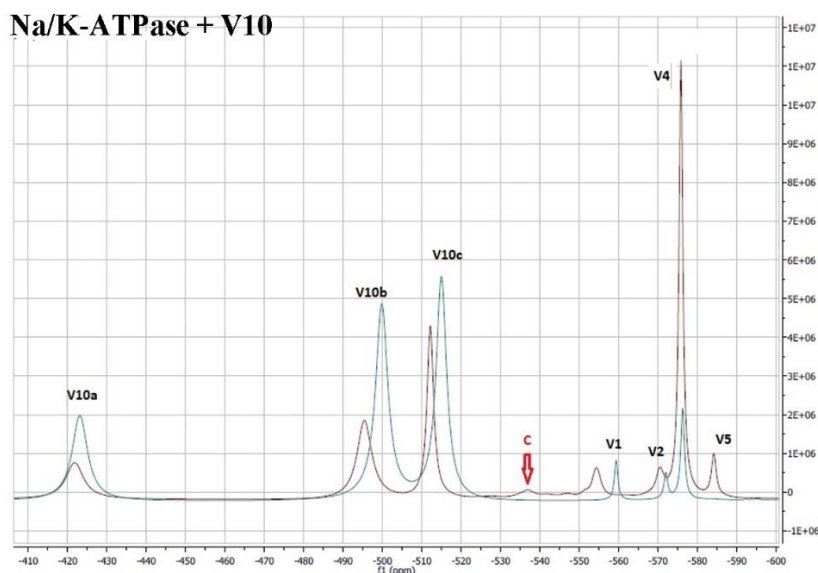


Figure 2. ^{51}V NMR spectra of V10 without (green line) and with Na/K-ATPase (red line).

CONCLUSION

In this work we investigated interaction of decavanadate and Na/K-ATPase interaction using Circular Dichroism and 51V NMR. The obtained results indicated that decavanadate induces significant changes in secondary and tertiary structure of enzyme. Additionally, 51V NMR confirm interaction with enzyme that is reflected in appears of broadening of V10 NMR signals and changing of ratio of characteristic peaks. The detailed knowledge of the molecular basis of decavanadate-proteins will allow better understand the processes associated with the anticancer applications of decavanadate.

Acknowledgement

This work was supported by the Ministry for Science of the Republic of Serbia (Grants no. 172023) and COST action CM 1203.

REFERENCES

- [1] L. C. Cantley, L. Josephson, R. Warner, M. Yanagisawa, Lechene, et al., Vanadate is a potent (Na,K)-ATPase inhibitor found in ATP derived from muscle, *Journal of Biological Chemistry*, 1977, 252, 7421-7423.
- [2] D. Krstić, M. Čolović, N. Bošnjaković-Pavlović, A. Spasojević-de Bire, V. Vasić, Influence of decavanadate on rat synaptic plasma membrane ATPases activity, *General Physiology and Biophysics*, 2009, 28, 302-308.
- [3] S. Ramos, J. J. G. Moura, M. A. Aureliano, Comparison between Vanadyl, Vanadate, and Decavanadate Effects in Actin Structure and Function: Combination of Several Spectroscopic Studies, *Spectroscopy: An International Journal*, 2012, 27, 5, 355-359.
- [4] M. Aureliano, V.M.C. Madeira, Interactions of vanadate oligomers with sarcoplasmic reticulum Ca^{2+} -ATPase, *Biochimica et Biophysica Acta (BBA)-Molecular Cell Research*, 1994, 1221, 259–271.

KINETICS OF ADSORPTION OF THE BOVINE SERUM ALBUMIN ON THE SILVER NANOPARTICLES

A. M. Bondžić¹, D. Jovanović², A. R. Leskovac¹, Z. Džambaski³, B. P. Bondžić³

¹ *Vinča Institute of Nuclear Sciences, National Institute of the Republic of Serbia, University of Belgrade, P.O. Box 522, 11000 Belgrade, Serbia*

² *Faculty of Physical Chemistry, University of Belgrade, Studentski trg 12–16, 11000 Belgrade, Serbia*

³ *Institute of Chemistry, Technology and Metallurgy, National Institute of the Republic of Serbia, University of Belgrade, Njegoševa 12, 11000 Belgrade, Serbia
(aleksandrab@vin.bg.ac.rs)*

ABSTRACT

In this study, the kinetics of bovine serum albumin (BSA) adsorption from aqueous solutions on the methionine stabilized silver nanoparticles (AgNPs) was investigated. The influence of the parameters such as contact time and BSA initial concentration on the adsorption capacity of AgNPs were tested. By increasing the contact time up to 30 min, the percentage of adsorbed BSA was increased. After this time, no changes were observed, indicating that the equilibrium state was reached. Investigation of the initial concentration-effect showed that the percentage of BSA adsorption increased with increasing BSA concentration until the available binding sites were saturated. After that, more BSA molecules were left unadsorbed. To elucidate the adsorption kinetic, pseudo-first-order, pseudo-second-order, and intraparticle diffusion kinetic models were applied. The pseudo-second-order well described the adsorption process and intraparticle diffusion model rate laws, and the intraparticle diffusion is the sole rate-controlling step.

INTRODUCTION

Adsorption of proteins on surfaces constitutes an important and very active research field due to its impact on different areas [1]. For example, when a biological system contacts artificial material, its biocompatibility is closely related to the cellular response. Additionally, the amount, orientation and the conformational state of the protein are important factors in the cell-protein-mediated response. Also, from a more fundamental research perspective, the protein adsorption process is of interest due to the complex nature of the biological systems. Ideally, one would like to understand how the protein concentration, buffer, pH, ionic strength etc., can influence protein adsorption. This work clarified the influence of the contact time and BSA initial concentration on the adsorption mechanism. Besides, kinetic parameters and the reaction order were determined. Based on these results, we gained better insight into the interaction, and conjugate formation between BSA and methionine stabilized silver nanoparticles.

EXPERIMENTAL

Chemicals. Bovine serum albumin (BSA), AgNO₃, L-methionine, KOH were purchased from Sigma-Aldrich (Germany). The stock solution of BSA was prepared in a 10mM phosphate buffer, pH 7.4.

Synthesis of AgNPs. Silver nanoparticles with L-methionine as a reducing and capping agent were synthesized as previously reported [2].

Apparatus. UV/Vis spectra were recorded on Lambda 35 UV/Vis spectrometer, Perkin Elmer, with a thermostatted 1.00 cm quartz cell at 25 °C. All spectra were background-subtracted against deionized water.

Batch mode adsorption studies. The effect of contact times on the adsorption amount of various concentrations of BSA was studied in a batch mode of operation for the specific contact times (0–72 h). The other experimental parameters were kept constant during the experiments.

RESULTS AND DISCUSSION

The effect of contact time on the adsorption of BSA on the surface of AgNPs was investigated for different concentrations of BSA. The amount of adsorbed BSA on AgNPs as adsorbent surfaces was presented as a function of contact time (Figure 1). Figure 1 showed that when increasing the contact time, the percentage of adsorbed BSA increased. The amount of adsorbed BSA was the highest after 30 min. After this time, changes in the adsorbed amount of BSA were not observed, indicating that after 30 min the equilibrium state was reached. The effect of the initial BSA concentration on the concentration retained in the adsorbent phase was studied at equilibrium time. Different concentrations of BSA (5 μM ; 10 μM ; 20 μM ; 40 μM and 50 μM) were chosen. The dependence of q_t in the function of BSA equilibrium concentration was presented in Figure 2. q_t was calculated according to equation (1):

$$q_e = \frac{([BSA]_0 - [BSA]_{eq})V}{W} \dots \quad (1)$$

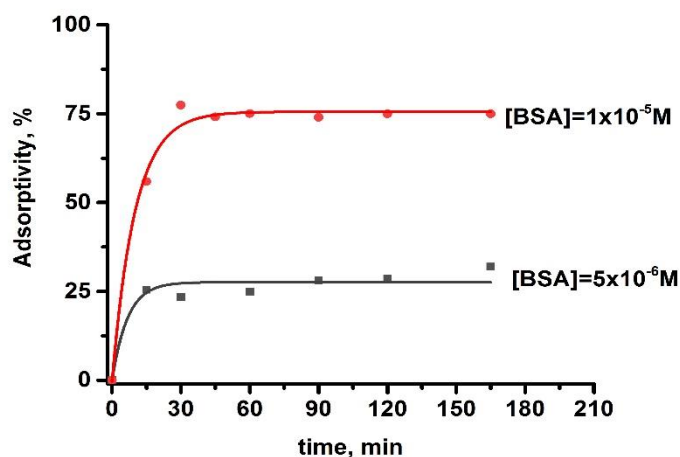


Figure 1. The effect of contact time and initial concentration on BSA adsorption on the AgNPs surfaces at 37°C.

where q_e is the concentration retained in the adsorbent phase (q_e , mg/g), $[BSA]_0$ and $[BSA]_{eq}$ are the initial and equilibrium BSA concentration at any time (mol/dm^3), respectively. V is the volume of solution (dm^3), and W is the mass of the adsorbents (g).

Figure 2 showed that the percentage of BSA adsorption increased with increasing BSA concentration. Besides, the available binding sites were saturated, and more BSA molecules were left unadsorbed. These results indicated that energetically favorable sites became involved with the increase of BSA concentration in the aqueous solution [6].

To elucidate the kinetics of the BSA adsorption process on L-Met stabilized AgNPs, the pseudo-first-order, the pseudo-second-order and the intraparticle diffusion kinetic models were applied. The results are summarized in Table 1. Compared with the pseudo-first-order kinetic model, the pseudo-

second-order kinetic model fits the experimental data better with correlation coefficients (R^2) higher than 0.99. These results suggest that BSA adsorption on AgNPs follows the pseudo-second-order model, which was applied based on the assumption that the limiting step may be a chemisorptions process involving valency forces *via* sharing (or exchange) of electrons between adsorbate and adsorbent [3]. To further understand the adsorption kinetics, the intraparticle diffusion kinetics model was tested to elucidate the diffusion mechanism and obtain the intraparticle diffusion parameter k_I . This kinetic model indicated that intraparticle diffusion is the sole rate-controlling step.

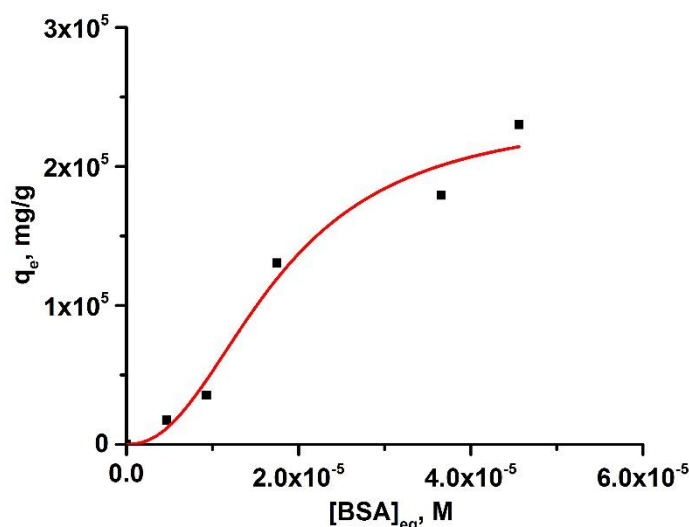


Figure 2. The dependence of the concentration of BSA retained in the adsorbent phase, q_e , in the function of BSA equilibrium concentration. The incubation time was 30 min at 37 °C.

Table 1. Kinetic parameters of pseudo first-order, pseudo second-order models and the Weber-Morris intraparticle diffusion model for BSA on methionine stabilized AgNPs. ($[BSA]_0 = 1 \times 10^{-5}$ M, $[AgNPs] = 0.00127$ g L⁻¹, T = 37 °C, pH 7.4).

Pseudo-first-order model	k_1 , min ⁻¹	0.03666±0.03094
	q_e , mgg ⁻¹	247±12
	R^2	0.25983
Pseudo-second-order model	k_2 , min ⁻¹	$(1.97±0.01) \times 10^{-5}$
	q_e , mgg ⁻¹	38172 ± 340
	R^2	0.99952
Intraparticle-diffusion model	k_I , min ⁻¹	0.00186 ± 0.00061
	I, mgg ⁻¹	37805 ± 1908
	R^2	0.94969

CONCLUSION

In this study, AgNPs are identified to be an effective adsorbent for the adsorption of BSA molecules from the aqueous medium. The adsorption is highly dependent on contact time and initial BSA concentration. It has been observed that the adsorption percentage increased with an increase in the contact time and becomes gradual after 30 min. Additionally, the adsorption percentage increased

with the increasing initial concentration of BSA. Adsorption kinetics follows pseudo-second-order kinetics, and intraparticle diffusion is the rate-controlling step.

Acknowledgement

Science and Technological Development of the Republic of Serbia, grant numbers: 451-03-9/2021-14/200017 and 451-03-68/2021-14/200026. The authors would like to thank dr Bojana Laban for sending aliquots of silver nanoparticles.

REFERENCES

- [1] S. H. Brewer, W.R. Glomm, M. C. Johnson, M. K. Knag, S. Franzen, Probing BSA binding to citrate-coated gold nanoparticles and surfaces. *Langmuir*, 2005, 21, 9303–9307.
- [2] B. Laban, U. Ralević, S. Petrović, A. Leskovic, D. Vasić-Anićijević, M. Marković, V. Vasić, Green synthesis and characterization of nontoxic L-methionine capped silver and gold nanoparticles, *Journal of Inorganic Biochemistry*, 2020, 204, 110958.
- [3] Y. S. Ho, G. McKay, Pseudo-second order model for sorption processes. *Process Biochemistry*, 1999, 34, 451–465.

INFLUENCE OF ULTRAVIOLET B (UV-B) IRRADIATION ON ANTIOXIDANT CAPACITY AND FLUORESCENCE CHARACTERISTICS OF SOYBEAN (*GLYCINE MAX L.*) SEEDS

D. Bartolić, M. Stanković, M. Prokopijević and K. Radotić

University of Belgrade, Institute for Multidisciplinary research (IMSI), Kneza Višeslava 1, 11030 Belgrade, Republic of Serbia. (dragana.bartolic@imsi.rs)

ABSTRACT

UV-B light, plays a crucial role as a signal for inducing plant response and development of specific photomorphogenic responses. The UV radiation may have a damaging effect on cellular components and macromolecules in seeds, which may influence seed quality. We compared *Glycine max L.* seeds exposed to UV-B radiation for 1 h with non-irradiated seeds (control). The antioxidant activity was estimated using a DPPH assay. The seeds' fluorescence characteristics were studied by fluorescence excitation-emission matrices. According to the obtained results the UV-B irradiated seeds possess a significantly higher free radical scavenging activity compared to the control. The fluorescence analysis showed differences in the spectral emission profiles of irradiated seeds compared to the control seeds. The results imply that 1h seed exposure to UV-B increases free radical content which may alter the structures of cellular macromolecules resulting in degradation of some of the fluorophores.

INTRODUCTION

Plants are constantly exposed to ultraviolet radiation from the sunlight, UV-A (320–390 nm) and UV-B (280–320 nm) [1]. The damaging effect of ultraviolet radiation is visible in cellular components and macromolecules due to the production of reactive oxygen species (ROS) and their free radical reactions [2, 3]. Increasing interest in the effects of UV-B radiation on plants as well as important mechanisms of defense to stress and damage caused by the radiation is a topic of numerous research studies.

Soybean (*Glycine max L.*) is a widespread annual legume and one of the most important plant protein sources from its edible seeds. Soybean varieties have expressed differences in their antioxidant activities [4]. Total phenolic composition, anthocyanin and flavonoid content influence the antioxidative properties of soybean seeds. It was demonstrated that antioxidants from some varieties of soybean seeds provide some health benefits, particularly in their seed hulls [4].

In the present work, the antioxidant activity and fluorescence of soybean seeds were investigated before (control) and after 1h of UV-B radiation treatment.

METHODS

Soybean (*Glycine max L.*) seeds were purchased from the local market in Belgrade, Republic of Serbia. We compared soybean (*Glycine max L.*) seeds exposed to UV-B radiation for 1 h with non-irradiated seeds (control). The seeds were irradiated by a UV-B lamp (312 nm, 15 W Hg, Sankyo Denki, Japan) for 1h. UV light was positioned at 50 cm distance from the seeds.

After grinding in a mill, soybean seeds were further homogenized with liquid nitrogen to obtain a fine powder. Antioxidant activity (AA %) was measured using a 2,2-Diphenyl-1-picrylhydrazyl (DPPH, Sigma-Aldrich, USA) assay. The sample was added in the reaction mixture containing 0.1 mM DPPH in 70 % ethanol and shaken in the dark. The aliquots were taken after 30 min and placed in microplate wells where absorbance was measured at 517 nm in UV-VIS microplate reader (Tecan Infinite M Nano+, Switzerland). Pure deionized water was used as blank while 0.1 mM DPPH was

considered as a control. Antioxidant activity was calculated as a percentage of depleted DPPH-reagent.

The fluorescence steady-state measurements were recorded using an F13-221 P spectrofluorimeter (JobinYvob, Horiba, French Republic). The ranges of the excitation spectra were 260 nm to 380 nm, while the range for the recorded fluorescence emission spectra was 270 nm to 515 nm. The spectral bandwidth of 2 nm was applied for both the excitation and emission slits.

RESULTS AND DISCUSSION

The antioxidant capacity of soybean seeds non-irradiated (control) and UV-B irradiated are presented in **Figure 1**. Our results showed that treating the soybean (*Glycine max* L.) seeds with UV-B light for 1h significantly increased the DPPH[•] scavenging activity. Several studies revealed that the UV-B irradiation caused changes in the production of some compounds (flavonoids and phenolic) in several plant species. It has been reported that the UV-B irradiation induced changes in the plants' response regarding the increased content of radical-scavenging compounds, such as antioxidant enzymes and non-enzyme antioxidant compounds [5, 6].

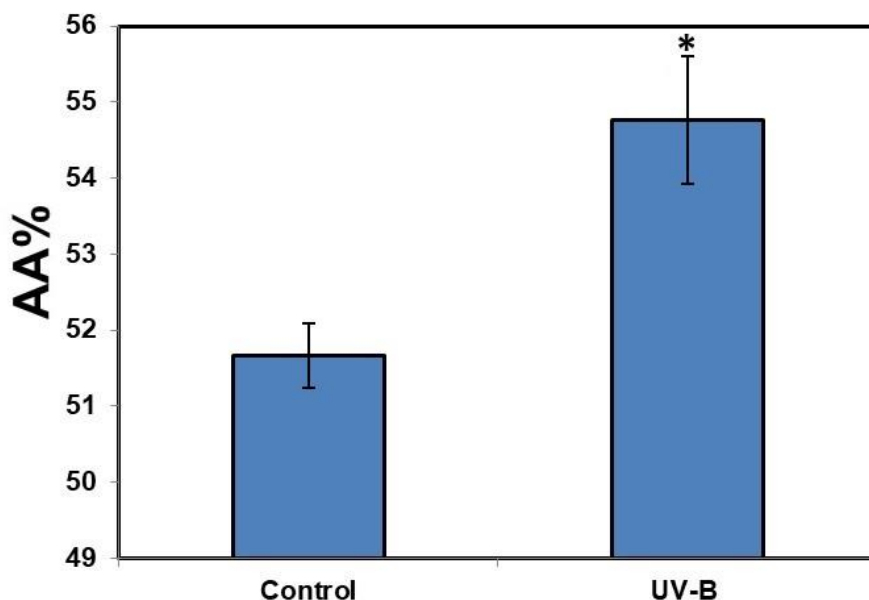


Figure 1. Effects of 1 h- UV-B irradiation on antioxidant capacity in soybean seeds. Each value is expressed as the means \pm SD (n = 3). Asterisk (*) indicates a significant difference at $p < 0.05$.

Representative excitation-emission matrices (EEMs) of the non-irradiated and the UV-B irradiated soybean seeds are shown in **Figure 2**. The comparison of the EEMs reveals the characteristic high fluorescence regions with excitation-emission wavelength peaks at 280/355 nm, 290/400 nm, and 370/465 nm. This could arise from different types of fluorophores, such as proteins and phenolics. The averaged emission spectra of the analyzed seeds are shown in **Figure 3**. Differences were observed concerning the spectral shape, emission peak positions, as well as intensity. Our results showed that the peak intensity at 290/400 nm was higher in the control samples and decreased after being exposed to UV-B light for 1h. This could be explained by the degradation of some of the seeds' fluorophores under UV-B stress conditions.

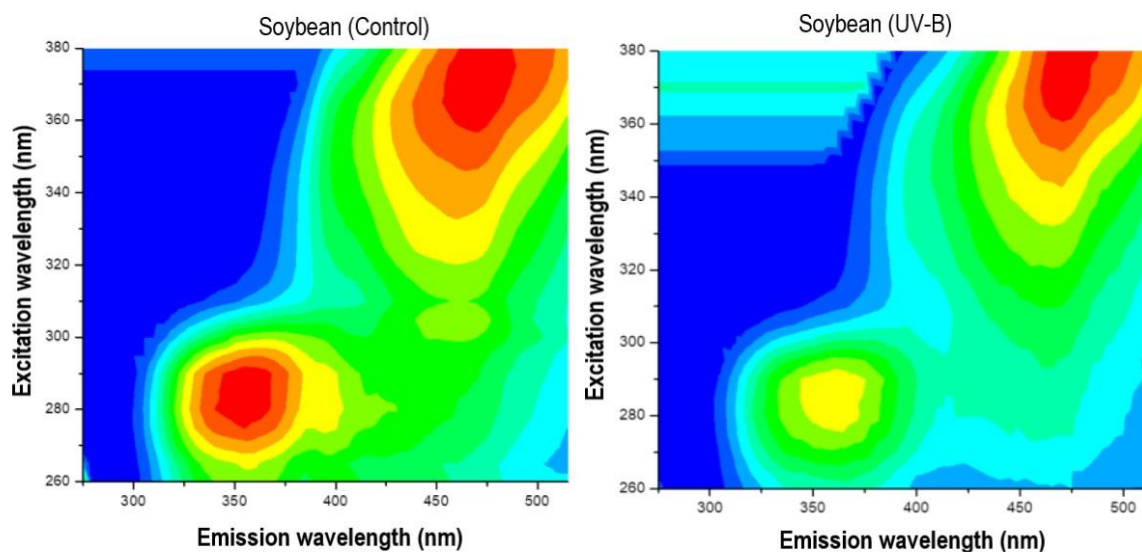


Figure 2. EEMs of the control and UV-B irradiated soybean seeds.

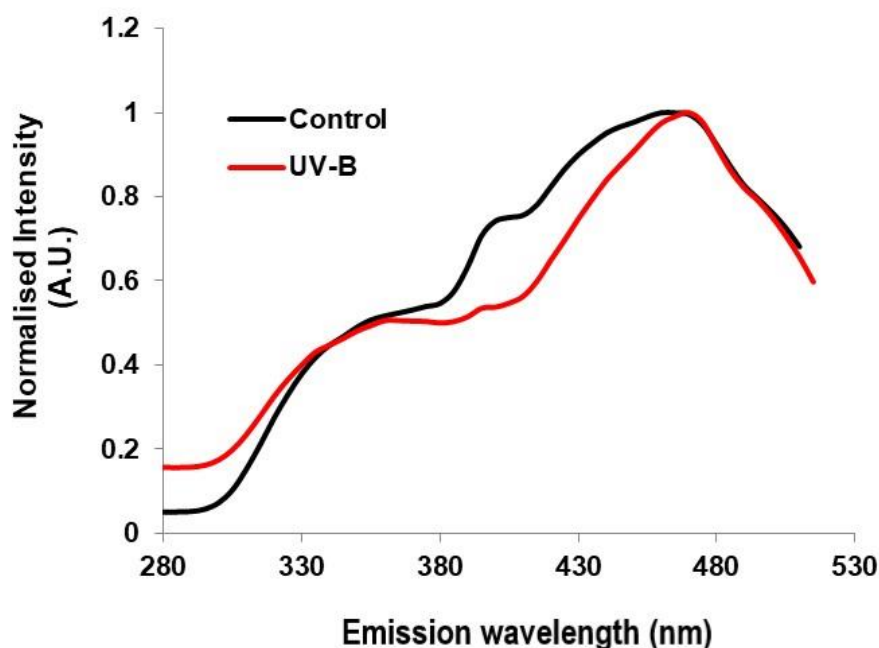


Figure 3. Overlay of the normalized emission spectra for control (dark line) and UV-B irradiated (red line) soybean seeds. The spectrum of each sample is an average of the 25 spectra recorded for various excitation wavelengths.

CONCLUSION

Our results show that 1h- UV-B irradiation induces the increase of antioxidant capacity in soybean seeds. The effect of UV-B irradiation is visible in the decreased fluorescence peak intensities of the treated seeds compared to the control. The production of ROS and free radical reactions after exposure to UV light may alter the structures of cellular macromolecules resulting in degradation of some of the fluorophores. It may be useful for the improved soybean seeds quality. The results of this study

indicate that EEM fluorescence analysis could contribute to a better understanding of fluorescence species in UV-B-irradiated seeds.

Acknowledgement

This work was supported by the Ministry for Science of the Republic of Serbia (Grant no. 451-03-9/2021-14/200053).

REFERENCES

- [1] R. F. Pournavab, E. B. Mejía, A. B. Mendoza, L. R. S. Cruz, M. N. Heya, *Agronomy*, 2019, 9, 269.
- [2] C. A. Mazza, P. I. Giménez, A. G. Kantolic, C. L. Ballaré, *Physiologia Plantarum*, 2012, 147, 3, 307-315.
- [3] A. Ali, M. A. Rashid, Q. Y. Huang, C.-L. Lei, *Environmental Science and Pollution Research*, 2017, 24, 8392–8398.
- [4] P. G. Peiretti, M. Karamać, M. Janiak, E. Longato, G. Meineri, R. Amarowicz, F. Gai, *Agronomy*, 2019, 9, 153.
- [5] H. Köhler, R. A. Contreras, M. Pizarro, R. Cortés-Antíquera, G. E. Zúñiga, *Frontiers in Plant Science*, 2017, 8, 921.
- [6] C. Xu, S. Natarajan, J. H. Sullivan, *Environmental and Experimental Botany*, 2008, 63, 39-48.

CHEMICAL MODIFICATION OF HEMICELLULOSE ISOLATED FROM CORNCOBS TO OBTAIN HYDROGEL FOR ENZYME IMMOBILIZATION

D. Spasojević,¹ M. Prokopijević¹, O. Prodanović¹, N. Pantić¹, K. Radotić¹ and R. Prodanović²

¹ University of Belgrade, Institute for Multidisciplinary Research, Kneza Višeslava 1, 11000 Belgrade, Serbia. (dragica@imsi.rs)

² University of Belgrade, Faculty of Chemistry, Studentski trg 12-16, 11000 Belgrade, Serbia.

ABSTRACT

Hemicellulose rich in xylan was isolated from corncobs. Functional groups were introduced first by carboxymethylation and then by coupling with tyramine via carbodiimide-mediated reaction. Obtained hydrogel was tested for horseradish peroxidase (HRP) immobilization within microbeads, formed in an emulsion based enzymatic polymerization reaction. This model system showed that modified hemicellulose isolated from corncob is a suitable candidate for enzyme or small molecule immobilization for different purposes.

INTRODUCTION

Hemicelluloses are large group of polysaccharides and represent about 20-40% of the plant biomass [1]. Corncobs are especially rich in xylan-type hemicelluloses, with its content of 25-35% (w/w) [2]. Enzyme-mediated crosslinking provides non-invasive and non-toxic method for *in situ* forming of hydrogels. Hydrogels are polymer network structures filled with water [3]. Horseradish peroxidase (HRP) is one of the most studied peroxidases from plants and one of the most commonly used enzymes for cross-linking of polymers into a hydrogel. Chemical modification of polymers introduces new functional groups that promote enzyme immobilization and adsorption to the gel [4].

The aim of this work was to modify isolated hemicellulose in a way that it can easily form hydrogels by enzymatic cross-linking and to test it as a carrier for enzyme or small molecules.

METHODS

Isolation and chemical modification of hemicellulose

Xylan-rich hemicellulose was isolated from ground corncobs by alkaline extraction method and then carboxymethylated two times using chloroacetic acid [5]. 0.25 g of the obtained carboxymethyl hemicellulose was dissolved in 25 mL 0.1 M HEPES (4-(2-hydroxyethyl)-1-piperazineethanesulfonic acid) buffer solution pH 6.5. 0.18 g tyramine hydrochloride was added into solution and at the same time 0.1 g EDC (1-ethyl-3-(3-dimethylaminopropyl)carbodiimide hydrochloride) and 0.012 g NHS (N-hydroxysuccinimide), with constant stirring. The reaction was left overnight at room temperature and afterwards the reaction mixture was dialyzed against water. After dialysis, the solution was frozen and lyophilized to obtain dry powder.

Preparation of hydrogel and enzyme immobilization

Dry powder of hemicellulose coupled with tyramine was dissolved in 0.05 M Tris buffer pH 7 (such that its final concentration in the 0.3 mL mixture would be 3%), and 0.5 U of HRP and 3 U of glucose oxidase (with glucose it will act as a source of hydrogen peroxide for HRP) were added. After adding glucose in final concentration of 0.133 M, the mixture was rapidly poured into 0.6 mL of solution of 3% Span 80 in Light Mineral Oil, and stirred for 15 min on magnetic stirrer. The reaction was stopped by adding 1 mL of 0.5% Triton X-100 solution in water with 0.5 mM H₂O₂, and the stirring was continued for 5 more minutes. After that, the solution was centrifuged and obtained hydrogel microbeads washed 4-5 times. Supernatants from washing were collected and combined to measure

the unbound activity, and microbeads were resuspended in Tris buffer with 5mM CaCl₂ and left at the 4 °C till use.

HRP activity assay

Obtained microbeads were tested for HRP immobilization. Enzyme activity was measured in the initial supernatant and hydrogel microbeads using pyrogallol and H₂O₂ as substrates. For unbound activity 0.1 mL of supernatant was added into 1 mL of 13 mM solution of pyrogallol and 9.7 mM H₂O₂ in 0.1 M Tris buffer pH 7.0. Absorbance at 420 nm was followed for the first 3 min, and the enzyme activity was calculated by using extinction coefficient of purpurogallin (12 mg⁻¹ cm²). For immobilized enzyme, 100 µL of sample (concentration of microbeads in suspension approximately 20%) was resuspended in 3 mL of 13 mM solution of pyrogallol in 0.1 M Tris buffer. Reaction was started by adding 30 µL of 0.97 M H₂O₂ and performed under constant stirring. Every minute aliquot was taken, filtrated and absorbance at 420 nm was measured. One HRP unit was defined as the amount of enzyme that produces 1 mg of purpurogallin in 20 s at 20 °C. Specific activity of immobilized enzyme was calculated per volume of hydrogel. Enzyme “leakage” from microbeads was measured after 24 h in the buffer solution they were stored.

RESULTS AND DISCUSSION

During chemical modifications of xylan-type hemicellulose isolated from corncobs, carboxymethyl groups were introduced first within polysaccharide chains. Tyramine-hemicellulose was synthesized utilizing EDC-NHS coupling chemistry to couple amine in tyramine to the carboxylic acid group of the polymer. Glucose oxidation by glucose oxidase enabled slow release of hydrogen peroxide that could prevent HRP substrate inactivation. Modified polymer showed the hydrogel formation ability induced by peroxidase and hydrogen peroxide. As a proof of concept, tyramine-hemicellulose was tested for HRP encapsulation within hydrogel microbeads made in a peroxidase induced emulsion polymerization reaction.

The results of HRP immobilisation are shown in Table 1, where Sp is the specific activity of the immobilized enzyme in units/mL of microbeads suspension (the activity of free HRP - lyophilized powder is 150–250 units/mg of enzyme).

Table 1. Microbeads specific activity, unbound activity and enzyme leakage.

modified hemicellulose hydrogel	
Sp (U/mL)	0.138
Unbound act. (U)	0.108
Leakage (U)	0.008

CONCLUSION

Hemicellulose isolated from corncobs was modified, introducing carboxymethyl and tyramine groups. Modified biopolymer was capable to form hydrogel in the reaction with hydrogen peroxide and peroxidase. HRP was successfully immobilized within microbeads.

The results obtained in the present work showed that hemicellulose modified by carboxymethylation with chloroacetic acid, followed by carbodiimide coupling reaction for

introducing tyramine moiety, has a good potential for enzyme immobilisation. Further studies are planned for optimisation and testing immobilization method.

Acknowledgement

This work was supported by the Ministry of Education, Science and Technological Development of the Republic of Serbia Grant No. 451-03-68/2020-14/200053 (University of Belgrade-Institute for Multidisciplinary Research).

REFERENCES

- [1] X. Peng, J. Ren, R. Sun, *Biomacromolecules* 2010, 11, 3519–3524.
- [2] E. G. Cuneyt, H. Unlu, and O. Atıcı, *Carbohydrate Polymers*, 2009, 76, 585-592.
- [3] W. Song, J. Ko, Y. H. Choi, N. S. Hwang, *APL Bioengineering*, 2021, 5, 021502.
- [4] D. Spasojevic, O. Prodanovic, M.G. Pirtea, K. Radotic, R. Prodanovic, *Hemijaska Industrija*, 2014, 68, 117–122.
- [5] D. Spasojević, M. Prokopijević, O. Prodanović, N. Zelenović, N. Polović, K. Radotić, R. Prodanović, *Macromolecular Research*, 2019, 27, 764–771.

CIP - Каталогизација у публикацији
Народна библиотека Србије, Београд

544(082)
621.35(082)
577.3(082)
543.42(082)

**INTERNATIONAL Conference on Fundamental and Applied Aspects of Physical Chemistry
(15; 2021; Beograd)**

Physical Chemistry 2021: proceedings: the Conference is dedicated to the 30th Anniversary of the founding of the Society of Physical Chemists of Serbia and 100th Anniversary of Bray-Liebhaafsky reaction. Vol. 1 / 15th International Conference on Fundamental and Applied Aspects of Physical Chemistry, September 20-24, 2021, Belgrade, Serbia; [organized by The Society of Physical Chemists of Serbia in cooperation with Institute of Catalysis Bulgarian Academy of Sciences ... [et al.]]; [editors Željko Čupić and Slobodan Anić]. - Belgrade: Society of Physical Chemists of Serbia, 2021 (Belgrade: Jovan). - VI, 344 str.: ilustr.; 30 cm

Tiraž 200. - Bibliografija uz svaki rad.

ISBN 978-86-82475-38-5
ISBN 978-86-82475-40-8 (niz)

а) Физичка хемија -- Зборници б) Електрохемијско инжењерство -- Зборници в) Биофизичка хемија -- Зборници г) Спектроскопија -- Зборници

COBISS.SR-ID 53316617

